Physics of Atomic Nuclei, Vol. 65, No. 5, 2002, pp. 753–762. Translated from Yadernaya Fizika, Vol. 65, No. 5, 2002, pp. 787–796.

NUCLEI
Experiment

Moments of the Response Function for the ^{2}H Nucleus at $q = 1.05$ fm^{-1}

A. Yu. Buki, N. G. Shevchenko, I. A. Nenko, V. N. Polishchuk, A. A. Khomich, and S. V. Dmytriyeva[1)]

Kharkov Institute for Physics and Technology, ul. Akademicheskaya 1, 61108 Kharkov, Ukraine

Received September 4, 2000; in final form, February 26, 2001

Abstract—In an ee' experiment, the transverse and the longitudinal response function are measured for the ^{2}H nucleus at $q = 1.05$ fm^{-1}, and their moments of orders -1, 0, 1, and 2 are obtained.

1. INTRODUCTION

Present-day experiments studying electron scattering on nuclei make it possible to determine transverse and longitudinal response functions. Measurements performed for nuclei of extremely light elements revealed that, at 3-momentum transfers in the region $q > 1.5$–2.0 fm^{-1}, the relevant response functions are determined primarily by quasielastic electron–nucleon scattering treated within relatively simple models of the nucleus [1]. As soon as the momentum transfer falls below 1.5 fm^{-1}, electron–nucleus interaction becomes more complicated, while the response functions appear to be more sensitive, in some aspects, to the structure of nuclei and to the properties of the nucleon–nucleon interaction that determine this structure. In this connection, we note that, although the deuteron, which is the simplest few-nucleon system, is one of the most promising subjects for studying the intranuclear interaction of nucleons, its response functions have been measured only at high momentum transfers ($q = 1.5$, 2.0, 2.5 fm^{-1} [2]). The present study is aimed at extending experimental explorations of response functions for the ^{2}H nucleus to the model-dependent region of low momentum transfers.

2. PROCEDURES FOR DETERMINING RESPONSE FUNCTIONS

2.1. Measurements in ee' experiments yield the spectra of scattered electrons with respect to their final energies E'. Each such spectrum is usually measured at a single value of the initial electron energy E_0 and a single value of the scattering angle θ. Upon the relevant normalization, the readings of the measuring equipment used are transformed into the double-differential cross section $d^2\sigma(\theta, E_0, E')$ for electron scattering. This cross section can be expressed in terms of some function $R_\theta(q, \omega)$ that will be referred to as the angular response function and which is defined as

$$R_\theta(q,\omega) = d^2\sigma(\theta, E_0, E')[\sigma_M(\theta, E_0)G^2(Q^2)]^{-1}, \quad (1)$$

where $\sigma_M(\theta, E_0) = \{\alpha\cos(\theta/2)/[4\pi E_0 \sin^2(\theta/2)]\}^2$ is the Mott cross section, $G(Q^2) = (1 + Q^2/18.24)^{-2}$ is proton electric form factor, α is the fine-structure constant, $\omega = E_0 - E'$ is the energy transfer to the nucleus involved, and $Q = (q^2 - \omega^2)^{1/2}$ is the 4-momentum transfer in fm^{-1} units. In the case of electron scattering on nuclei, the 3-momentum transfer has the form

$$q = \sqrt{4(E_0 + E_e)[(E_0 + E_e) - \omega]\sin^2(\theta/2) + \omega^2}, \quad (2)$$

where

$$E_e = 4Z\alpha/(3R) \quad (3)$$

is a correction that takes into account the distortion of the incident electron wave by the Coulomb field of the nucleus characterized by the charge number Z and the radius R of the equivalent uniform distribution.

According to [3], the angular response function is related to the transverse (T) and the longitudinal (L) response function $[R_{T/L}(q, \omega)]$ by the equation

$$R_\theta(q,\omega) = \lambda^2 R_L(q,\omega) + (\lambda/2 + \tan^2(\theta/2))R_T(q,\omega), \quad (4)$$

where $\lambda = Q^2/q^2$. From this equation, it can be seen that, knowing two values of $R_\theta(q, \omega)$ that correspond to different values of θ, but identical values of q and ω,

[1)]Kharkov State University, pl. Svobody 4, 61077 Kharkov, Ukraine.

1063-7788/02/6505-0753$22.00

one can easily determine $R_T(q,\omega)$ and $R_L(q,\omega)$. As follows, however, from expression (2), two functions $R_\theta(q,\omega)$ measured at different angles but each with its own initial electron energy that is constant for it can have not more than one common point in the $q\omega$ plane of arguments. In order to obtain, from a limited number of experimental angular functions, a set of values of R_T and R_L, it is necessary to integrate and partly to extrapolate the functions R_θ referring to the same θ, whereupon it is possible to find, from two functions $R_{\theta 1}$ and $R_{\theta 2}$ ($\theta_1 \neq \theta_2$), which are continuous in the variables q and ω, the values of R_T and R_L over the entire region of the arguments that is common to these functions.

2.2. A feature common to all experiments aimed at determining response functions is that such experiments require much expensive time of accelerator operation. In this connection, the problem of optimizing such measurements is of great practical importance, and experience that we gained in exploring this problem revealed that some of its solutions can significantly reduce the costs of such investigations and enhance their efficiency. Below, we consider two aspects of this problem.

2.2.1. As was indicated above, the quantities R_L and R_T are determined from the interpolation of the experimental functions R_θ. The higher the accuracy of the interpolation of data, the closer the behavior of the functions R_θ along the line of interpolation to a linear dependence. On this basis, it was shown (see, for example, [4]) that, in the $q\omega$ plane of arguments, the family of lines

$$\omega_j = a + b_j q^2, \tag{5}$$

where a is a constant that is approximately equal to the mean nucleon binding energy in the nucleus being considered and b_j is a variable that specifies the jth line, determines the most convenient directions for the interpolation—that is, the directions along which the derivative of the function R_θ undergoes the smallest changes.

For the purpose of interpolation, the data were approximated by various functions. If the results obtained from fits to the data in terms of a few functions are such that the corresponding values of χ^2 are close, the accuracy of the interpolation is characterized by the amplitude of the scatter of these functions. If the statistical uncertainties are preset, the scatter of the approximating functions is not reduced considerably upon increasing, above some value, the number of points in the region where the fitting is performed. It follows that, in the $q\omega$ region being considered, a reduction of the step between the points below some value, which depends on the errors in $R_\theta(q,\omega)$, does not improve the accuracy of the interpolation.

By using some models for the functions R_θ, we sampled versions of measurements with various steps in the momentum transfer. As a result, we found that, in the region around $q \approx 1$ fm^{-1}, it is meaningless to reduce the momentum-transfer step below some 0.1 fm^{-1} for the functions R_θ measured at a single value of the angle θ with the errors of $\geq 5\%$, since, in this case, the approximating functions become indistinguishable in terms of the χ^2 criterion.

2.2.2. The errors in the functions $R_{T/L}$ are determined by the errors in measuring the functions R_θ; if the latter are assumed to be statistical, it follows from Eq. (4) that

$$\Delta_S R_T = \frac{1}{v_2 - v_1}\sqrt{(\Delta R_{\theta,1})^2 + (\Delta R_{\theta,2})^2}, \tag{6a}$$

$$\Delta_S R_L = \frac{1}{\lambda^2}\frac{1}{1 - v_1/v_2} \times \sqrt{(\Delta R_{\theta,1})^2 + (v_1/v_2)^2(\Delta R_{\theta,2})^2}. \tag{6b}$$

Here and below, the subscript 1 (2) labels quantities measured at the smaller (larger) of the two scattering angles; the subscript S indicates a statistical character of the error; and $v_i = \lambda/2 + \tan^2(\theta_i/2)$, $i = 1, 2$. Expressions (6a) and (6b) demonstrate that, at given values of $\Delta_S R_{\theta,i}$, the closer the angle θ_1 to 0° and the angle θ_2 to 180°, the smaller the errors in the response functions. Under actual experimental conditions, the minimum and the maximum value of θ for a given value of q is determined by the accelerator energy range and by the design of the experimental facility used.

The statistical error in a measurement depends on the number N of counts in the measuring equipment over the exposure time. The quantity N is related to the function R_θ by the equation

$$R_\theta(q,\omega) = cN[\sigma_{\mathrm{M}}(\theta, E_0)G^2(Q^2)xt]^{-1}. \tag{7}$$

Here, c is a constant that characterizes the experimental facility used; t is the exposure time; and x is the product of quantities measured within a single run,

$$x = \tau E' I, \tag{7a}$$

where τ is the target thickness in the direction of the electron flux I traversing it. According to the Poisson distribution, we have $\Delta N = \sqrt{N}$. Taking this into account and using expressions (4), (6a), (6b), and (7), we obtain the relative errors $\delta_S R_{T/L} = \Delta_S R_{T/L}/R_{T/L}$ in the form

$$\delta_S R_T = \frac{1}{\gamma}\frac{1}{v_2 - v_1}\sqrt{\frac{A_1}{t'_1} + \frac{x_1}{x_2}\frac{\sigma_{\mathrm{M},1}}{\sigma_{\mathrm{M},2}}\frac{A_2}{1 - t'_1}} \tag{8a}$$

$$\times\sqrt{\frac{c}{R_L\sigma_{\mathrm{M},1}G^2(Q^2)x_1T}},$$

$$\delta_S R_L = \frac{1}{\lambda^2}\frac{1}{1-v_1/v_2} \tag{8b}$$

$$\times\sqrt{\frac{A_1}{t_1'}+\left(\frac{v_1}{v_2}\right)^2\frac{x_1}{x_2}\frac{\sigma_{\mathrm{M},1}}{\sigma_{\mathrm{M},2}}\frac{A_2}{1-t_1'}}$$

$$\times\sqrt{\frac{c}{R_L\sigma_{\mathrm{M},1}G^2(Q^2)x_1T}},$$

where $\gamma = R_T/R_L$; $A_i = \lambda^2 + v_i\gamma$; $T = t_1 + t_2$; $t_1' = t_1/T$; and the factor

$$\sqrt{\frac{c}{R_L\sigma_{\mathrm{M},1}G^2(Q^2)x_1T}}, \tag{9}$$

which appears in both expressions, can be considered as a unit of measurement for $\delta_S R_{T/L}$. The values of $E_{0,i}$ that correspond to given θ_i, ω, and q are determined by Eq. (2). In order that expressions (8a) and (8b) could be used in planning an experiment, it is necessary to make a preliminary assumption concerning the value of γ. In the case of quasielastic electron scattering on the nucleons of the ^{2}H nucleus, the approximation of scattering on free nucleons yields a good approximation to γ; that is,

$$\gamma = \frac{q^2}{2M^2}\left(\mu_p^2+\mu_n^2\right), \tag{10}$$

where M is the nucleon mass and μ_p and μ_n are, respectively, the proton and the neutron magnetic moment.

Since expressions (8a) and (8b) depend differently on t_1', different values of t_1' correspond to minimal values of $\delta_S R_T$ and $\delta_S R_L$. From this, it follows that the choice of t_1' is also dependent on which response function is of prime interest in the experiment being planned.

We will now show how one can use the above expressions in choosing conditions in experiments of the type being discussed.

In our experiment, the measurement at the small angle of $\theta_1 = 55^\circ$ was ensured by the use of the new gas target GM-2. For the measurements at a large scattering, use could be made of GM-2 as well or of the earlier gas-target version GM-1. Since the features of these targets were different, we had to assess two versions of the measurements:

(i) $\theta_1 = 55^\circ$ (GM-2), $\quad \theta_2 = 130^\circ$ (GM-2);

(ii) $\theta_1 = 55^\circ$ (GM-2), $\quad \theta_2 = 160^\circ$ (GM-1).

One gas target GM-2 is arranged and tuned in order to perform an experiment according to version 1. In the measurements, the advantage of GM-2 over GM-1 consists in that the former is much less sensitive to the background.

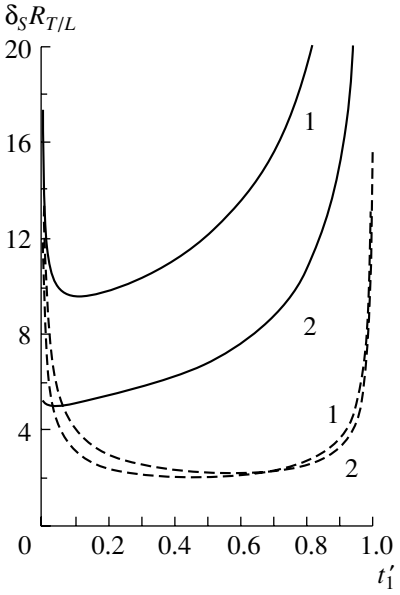

Fig. 1. Errors in the response functions versus the exposure time t_1' at a small angle: (solid curves) $\delta_S R_T(q,\omega)$ and (dashed curves) $\delta_S R_L(q,\omega)$. The figures 1 and 2 on the curves indicate the version of measurement (see main body of the text).

In version 2, a greater value of the angle θ_2 is achieved, while the effective target thickness τ of GM-1 is approximately twice as large as that of GM-2. At the same time, an experiment in that case is complicated by the needed replacement of the targets in going over from the measurements at one angle to the measurements at the other angle and by additional tunings that are associated with this replacement and which are more involved for GM-2, requiring additional time of accelerator operation.

The result of the calculation by formulas (8a) and (8b) for measurements in the region of the maximum of the quasielastic-scattering peak ($\omega = q^2/2M$) at $q = 1$ fm^{-1} and $I_1 = I_2$ is displayed in Fig. 1 for the remaining conditions specified as above. It can be seen that, at the minimum of the functions $\delta_S R_T(t_1')$, version 2 yields a value that is one-half as large as that in the case of version 1. This distinction means that, in order to achieve identical statistical accuracies in measuring the functions R_T, the required time of accelerator operation is four times smaller in the case of version 2. This was a crucial argument in choosing the latter.

The calculation of version 2 shows that the functions $\delta_S R_T(t_1')$ and $\delta_S R_L(t_1')$ attain minima at $t_1' = 0.03$ and $t_1' = 0.55$, respectively. But in the case of

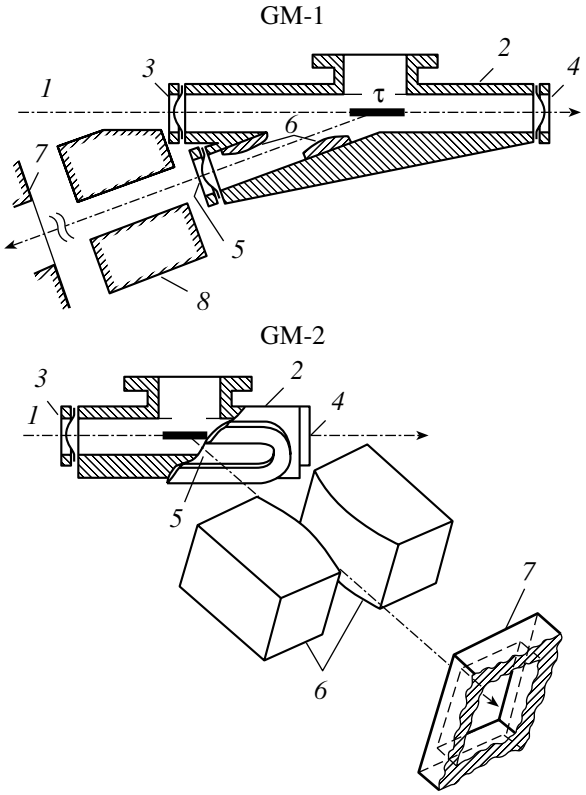

Fig. 2. Layout of the gas targets GM-1 and GM-2.

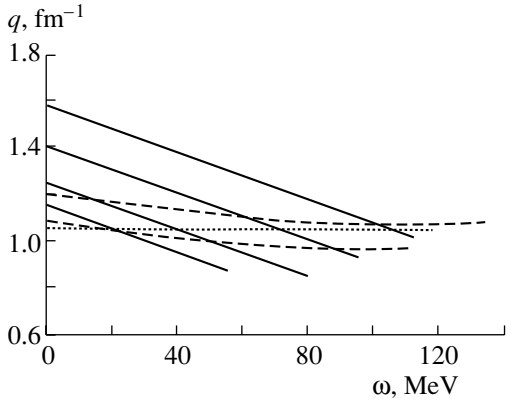

Fig. 3. Coordinates of the experimental spectra in the $q\omega$ plane for the measurements at the scattering angles of (solid lines) $\theta = 160°$ and (dashed line) $\theta = 55°$. The dotted line represents the coordinates of the sought functions $R_{T/L}(q, \omega)$.

$t'_1 = 0.3$, each of the quantities $\delta_S R_T$ and $\delta_S R_L$ exceeds its minimum only by 15%. Since we are equally interested both in the transverse and in the longitudinal response function, this relationship between the durations of the exposures was used in the measurements.

3. DESCRIPTION OF THE EXPERIMENT AND DATA PROCESSING

Measurements were performed in an electron beam from the LUE-300 linear electron accelerator installed at the Kharkov Institute for Physics and Technology. With the exception of what is concerned with the gas targets, the experimental facility and the procedure of measurements were described in detail elsewhere [4]. In the present article, we will therefore only briefly touch upon the basic points of this part of the investigation, but we will dwell at some length on the design of the gas targets.

3.1. High-energy electrons were scattered on ^{2}H nuclei within gas targets and found their way to a double-focusing magnetic spectrometer [5]; on traversing it, they were recorded by an eight-channel scintillation Cherenkov telescope [6].

The experiment employed two gas targets GM-1 and GM-2. Either target was rated to the pressure of 100 atm at normal temperature for the gas under study. The GM-1 target was intended for measurements only at the scattering angle of $\theta = 160°$. The operating range of GM-2 was 50°–130°. The layout of the targets is displayed in Fig. 2.

The electron beam along the line *1* passes through a high-pressure vessel (*2*), traversing the foils of the inlet (*3*) and the outlet (*4*) window. Electrons that were scattered by the gas over the segment τ (effective target thickness) arrived, through the foil of the window (*5*) and a slit collimator (*6*), at the collimator of a spectrometer (*7*). Electrons that were scattered by the gas beyond the segment τ and by the foils of the windows *3* and *4* are screened from the spectrometer by a lead shield (*8*) in the case of GM-1 or by the collimator *6* in the case of GM-2.

The basic design distinction between the targets consists in the arrangement of their collimators: in GM-1, the collimator is within the high-pressure vessel and is tightly fixed in it, while the collimator of GM-2 is arranged directly in the scattering chamber and its position is fixed with respect to the spectrometer. In the last case, the spectrometer is rotated together with the target collimator; this makes it possible to perform measurements within the width of the window *5*.

The conditions under which the electrons traverse the target are determined by the diameter of the primary electron beam; by the dimensions of the windows *3*, *4*, and *5*; by the radiation thickness of the foils; and by the shapes and the material of the working surfaces of the collimators *6*.

In the experiment being described, the diameter of the electron beam was 2–4 mm. The oval window *5* of the GM-2 target had dimensions of 115×16 mm. All the remaining windows of both

targets were round and had a diameter of 20 mm. The thicknesses of the titanium foils of the windows were 0.15 and 0.3 mm. For electrons that entered the spectrometer, the thickness of the target filled with deuterium was 1.2×10^{-2} to 1.8×10^{-2} radiation-length units. The radius of curvature of the working surfaces of the lead collimators was 500 mm in GM-1 and 1000 mm in GM-2. In order to reduce boundary effects, the convex surfaces of the collimators were covered with a tungsten layer of thickness 0.3 mm. Estimates show that, in structures like those that are discussed here, the background from boundary effects does not exceed 10^{-5} of the measured cross section.

3.2. In order to obtain each spectrum of the electrons scattered on ^{2}H nuclei, we performed three measurements under identical conditions:

(a) measurements of the background from an empty gas target;

(b) measurements of elastic scattering on ^{4}He nuclei;

(c) measurements of scattering on ^{2}H nuclei.

At all stages of the measurements, we determined the number of counts corresponding to random coincidences in the detecting equipment. Their contribution did not exceed 1% of the size of the sought effect.

The scattering of the electrons from the halo of the primary beam on the collar of the target inlet window was the main source of the background from the empty target. This background depended on the quality of guiding the electron beam to the target and on the efficiency of shielding from the scattered halo electrons (the corresponding design elements in Fig. 2 are the following: *8* for GM-1 and *6* for GM-2). The ratio of the number of counts in the equipment for the case of an empty target (background) to the number of counts at the maximum of the quasielastic peak was 0.1–2% at $\theta = 55^\circ$ and 1–7% at $\theta = 160^\circ$. The distinction between the background conditions of the measurements is explained by the fact that the thickness of the collimator screening the spectrometer of the GM-2 target was three times larger than that of the shield of the GM-1 target.

3.3. Upon correcting the results of the measurements for random coincidences, the background from the empty target was subtracted, channel-by-channel, from the spectra of ^{2}H and ^{4}He. The resulting spectra were corrected for radiative effects according to the calculations presented in [7].

We measured elastic scattering on ^{4}He nuclei in order to obtain the absolute values of the cross sections for the spectra of ^{2}H. For a reference, we employed the form factor for the ground state of the ^{4}He nucleus, representing it as

$$F^2(q) = (1 - (a^2q^2)^6)^2 e^{-2b^2q^2}, \qquad (11)$$

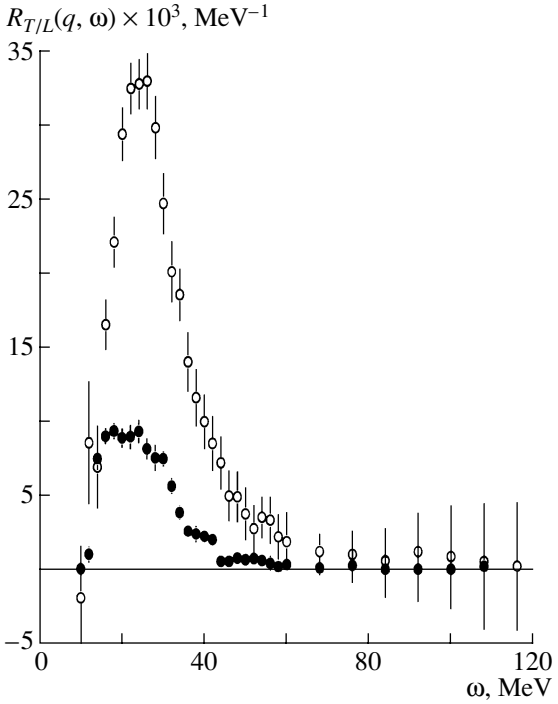

Fig. 4. Experimental values of the response functions for the ^{2}H nucleus at $q = 1.05$ fm^{-1}: (closed circles) $R_T(q, \omega)$ and (open circles) $R_L(q, \omega)$.

where the parameter values of $a = 0.315$ fm and $b = 0.675$ fm were borrowed from [8].

Thus, six functions R_θ were obtained as the result of measurements at the scattering angle of $\theta = 160^\circ$ for the initial electron energies of $E_0 = 114, 126, 141,$ and 158 MeV and at the scattering angle of $\theta = 55^\circ$ for the initial electron energies of $E_0 = 230$ and 260 MeV. From Fig. 3, it can be seen that, best of all, the results of the measurements correspond to determining the function $R_{T/L}$ for $q = 1.05$ fm^{-1}.

The response functions $R_T(q, \omega) \pm \Delta_S R_T(q, \omega)$ and $R_L(q, \omega) \pm \Delta_S R_L(q, \omega)$ found for this momentum-transfer value are displayed in Fig. 4. The quantities $\Delta_S R_{T/L}$ reflect the statistical errors in the original spectra upon introducing radiative corrections. The total error $\Delta R_{T/L}$ includes, in addition to $\Delta_S R_{T/L}$, the uncertainty that stems from going over to the absolute values of the experimental cross sections. The latter consists of the error $\Delta_{\text{el}} R_{T/L}$, which is associated with statistics of a series of measurements of the cross sections for elastic scattering on ^{4}He nuclei, and the error $\Delta_F R_{T/L}$, which reflects the uncertainty in the reference form-factor function (11). Upon taking into account the different origins of

the errors being considered, we obtain

$$\Delta R_{T/L} = \sqrt{(\Delta_s R_{T/L})^2 + (\Delta_{\rm el} R_{T/L})^2} + \Delta_F R_{T/L}. \quad (12)$$

The relative values of the errors $\Delta_{\rm el}R$ and $\Delta_F R$ are the following:

$$\delta_{\rm el} R_T = 0.05 \quad \text{and} \quad \delta_F R_T = 0.02,$$

$$\delta_{\rm el} R_L = 0.02 \quad \text{and} \quad \delta_F R_L = 0.02.$$

4. MOMENTS OF RESPONSE FUNCTIONS

4.1. Sum rules form a basis of one of the less model-dependent computational approaches. As the result of calculations based on sum rules, one obtains moments of the response functions in the form

$$S^{(k)}_{T/L}(q,\omega_f) = \int\limits_{\omega^+}^{\omega_f} R_{T/L}(q,\omega)\omega^k d\omega, \quad (13)$$

where the symbol ω^+ means that the lower limit of the integral in Eq. (13) is equal to the energy transfer corresponding to the peak of quasielastic electron scattering on a nucleus; however, the integral receives no contribution from the process itself. In the calculation of the moments, the upper limit of the integral takes the value of $\omega_f = q$ (photon point) or $\omega_f = \infty$. In the last case, the moments are denoted by $S^{(k)}(q)$.

The data in Fig. 4 cover the main part of the area of the quasielastic-scattering peak. However, the upper limit of the integral on the right-hand side of Eq. (13) lies beyond the range of actual measurements. For this reason, the procedure for evaluating the moments involves representing the response functions, up to some value ω_x of the energy transfer, by a set of experimental values $R^{\rm expt}(q,\omega_i)$ and extrapolating them for $\omega > \omega_x$ in terms of an analytic function $R^{\rm theor}(q,\omega)$ whose explicit form follows from theoretical ideas of the nucleus. Within this approach, expression (13) takes the form

$$S^{(k)}_{T/L}(q,\omega_f) = S^{{\rm expt},(k)}_{T/L}(q,\omega_x) + S^{{\rm theor},({\rm k})}_{T/L}(q,\omega_x,\omega_f), \quad (14)$$

where

$$S^{{\rm expt},(k)}_{T/L}(q,\omega_x) = \int\limits_{\omega^+_{\rm el}}^{\omega_x} R^{\rm expt}_{T/L}(q,\omega)\omega^k d\omega, \quad (14a)$$

$$S^{{\rm theor},(k)}_{T/L}(q,\omega_x,\omega_f) = \int\limits_{\omega_x}^{\omega_f} R^{\rm theor}_{T/L}(q,\omega)\omega^k d\omega. \quad (14b)$$

4.2. An investigation of the asymptotic behavior of the response functions in ω is a problem in itself, which will be considered in a separate publication. In order to evaluate their moments, we employ here the expression that was proposed in [1, 9, 10] and which, in the case of $q = {\rm const}$, can be represented in the form

$$R^{\rm theor}_q(\omega) = C_q \omega^{-\alpha}, \quad (15)$$

where the parameter values found in the present study are the following:

$$C_{q,L} = 123 \pm 7\ {\rm MeV}^{\alpha_L - 1} \quad \text{and} \quad \alpha_L = 2.82 \pm 0.07$$

for the function R_L;

$$C_{q,T} = 35.4 \pm 2.0\ {\rm MeV}^{\alpha_T - 1} \text{ and } \alpha_T = 2.93 \pm 0.15$$

for the function R_T.

4.3. Substituting expression (15) into the integral in Eq. (14b), we obtain

$$S^{{\rm theor},(k)}(q,\omega_x,\omega_f) = \frac{C_q}{\alpha - k - 1}\left(\omega_x^{-\alpha+k+1} - \omega_f^{-\alpha+k+1}\right). \quad (16)$$

According to (14), the statistical error for the moments has the form

$$\Delta_S S^{(k)}(q,\omega_f) = \sqrt{\left[\Delta_S S^{{\rm expt},(k)}(q,\omega_x)\right]^2 + \left[\Delta_S S^{{\rm theor},(k)}(q,\omega_x,\omega_f)\right]^2}. \quad (17)$$

The values found for the functions $S^{(k)}_L(q)$ and $\Delta_S S^{(k)}_L(q)$ with the aid of expressions (14), (16), and (17) are displayed in Fig. 5 versus ω_x. It can be seen that, within the errors, the moments are independent of ω_x, but the errors in these momenta are minimal at some values of this quantity. For the eventual values of $S^{(k)}(q)$, we took those of them that correspond to the smallest errors.

The results that we obtained here for the moments of the response functions are quoted in Tables 1 and 2—specifically, the results in Table 1 correspond to the nuclear reference frame comoving with the center of mass of the nucleus and its fragments upon the interaction (c.m.), while the results in Table 2 correspond to the laboratory frame (lab). Here and below, the moments in the c.m. and in the laboratory frame are labeled with the symbols "^" and "~", respectively.

The data are given here in terms of the above two reference frames because the results of relevant calculations are quoted in the different reference frames and because the relations between these different presentations of the moments are simple only for $k = 0$, 1 (in the case of $k = 0$, these quantities merely take identical values in the two reference frames, and this

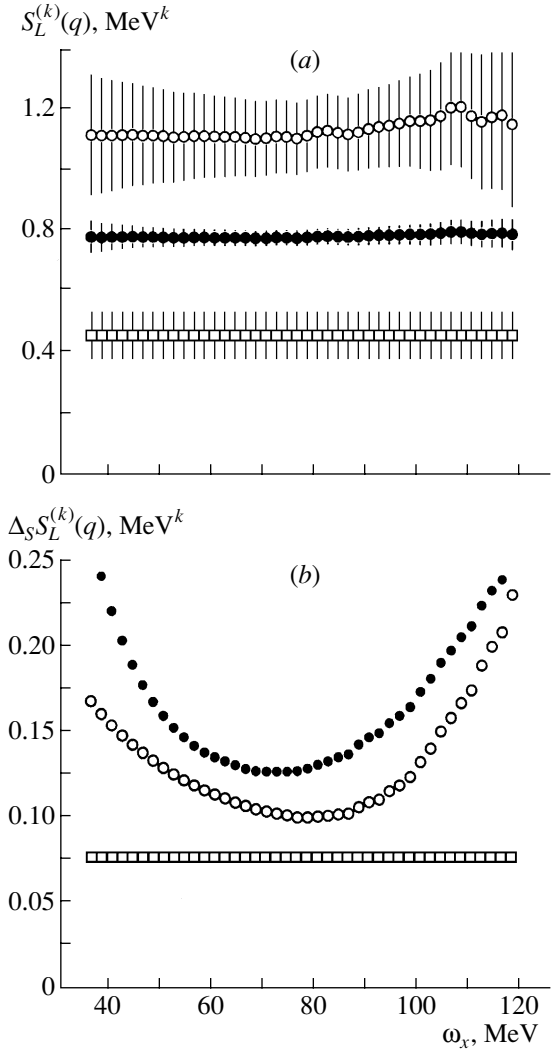

Fig. 5. Values of (a) moments of the longitudinal response function and (b) their errors versus the point ω_x at which the experimental data were matched with the extrapolating function: (open boxes) $S_L^{(-1)}(q) \times 5$ and $\Delta_S S_L^{(-1)}(q) \times 5$, (closed circles) $S_L^{(0)}(q)$ and $\Delta_S S_L^{(0)}(q) \times 5$, and (open circles) $S_L^{(1)}(q) \times 0.06$ and $\Delta_S S_L^{(1)}(q) \times 0.05$.

is the reason why they are not given in Table 2), the relationships between the errors in the different reference frames being rather complicated for all values of $k \neq 0$.

The integral S^{theor} appearing in the definition (14) of the moments is not, strictly speaking, an experimental value because the integrand in (14b), albeit containing parameters determined by experimental data, is not known for $\omega \to \infty$—its behavior there is hypothetical and by no means can be verified. In order to display the contribution of the quantity S^{theor} to the moments found here, the ratios $D^{(k)} = S^{\text{theor},(k)}/S^{(k)}$

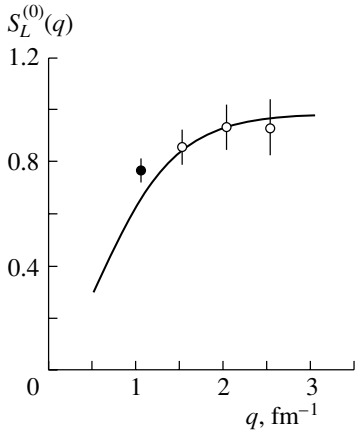

Fig. 6. Zeroth moment of the longitudinal response function: (open circles) data from [2], (closed circle) value obtained in the present study, and (curve) results of the calculations from [13].

and the ratios $\Delta_S D^{(k)} = \Delta_S S^{\text{theor},(k)}/S^{(k)}$, which are related to the statistical errors in measuring the parameters of expression (15), are quoted in the tables.

5. DISCUSSION OF THE RESULTS AND CONCLUSIONS

5.1. The calculations of the $k = -1$ response-function moment that are known to the present authors were performed within the Fermi gas model [11] and within the hydrodynamic model [12]. Neither of these is adequate to few-nucleon systems, but, for want of other calculations, we used them for the theoretical estimate of $S_L^{(-1)}(q)$ for the ^{2}H nucleus. As a result, it was found for the moment in question that, at $q = 1.05$ fm^{-1}, $\hat{S}_L^{(-1)}(q) = 0.045$ MeV^{-1} in [11] and $\hat{S}_L^{(-1)}(q) \approx 0.09$ MeV^{-1} in [12]—that is, these estimates agree (with allowance for their scatter) with the experimental values.

5.2. Some results of the calculations for the $k = 0$, 1 moments are quoted in Table 3, along with their ratios to the experimental values. Here, the theoretical values were obtained by interpolating the numerical results from other studies. Since those studies present the calculations for $q = 1$ fm^{-1} or $q = 200$ MeV/c, the error of the interpolation to $q = 1.05$ fm^{-1} is insignificant (about a few tenths of a percent of the eventual values obtained).

5.2.1. Figure 6 displays the experimental results for $S_L^{(0)}(q)$ and the result of the calculation from [13]. It can be seen that the value found for the zeroth moment supplements data from [2] in the sense that it lies beyond the region $q > 1.5$ fm^{-1}, where the cross section for electron scattering on a light nucleus is

Table 1. Moments of the response functions $S^{(k)}_{T/L}(q,\omega_f)$ for the ^{2}H nucleus at $q = 1.05\,\mathrm{fm}^{-1}$ in the c.m. frame [the values of the moments are supplemented with the total experimental error (first line) and its statistical component (second line)]

k	ω_f	$\hat{S}^{(k)}_L(q,\omega_f)$, MeV^k	ω_x, MeV	$D \pm \Delta_S D$, %	$\hat{S}^{(k)}_T(q,\omega_f)$, MeV^k	ω_x, MeV	$D \pm \Delta_S D$, %
-1	∞	0.090 ± 0.017 ± 0.015	69	0.6 ± 0.2	0.027 ± 0.003 ± 0.002	69	0.3 ± 0.2
0	∞	0.771 ± 0.045 ± 0.025	71	5.3 ± 1.7	0.217 ± 0.018 ± 0.007	71	3.2 ± 2.2
1	∞	18.5 ± 2.4 ± 2.0	79	26 ± 10	3.99 ± 0.78 ± 0.67	73	21 ± 16
	q	16.4 ± 1.6 ± 1.2	77	18 ± 6	3.70 ± 0.54 ± 0.42	71	15 ± 11
2	q	676 ± 130 ± 116	77	48 ± 16	128 ± 45 ± 42	73	45 ± 31

Table 2. Moments of the response functions $S^{(k)}_{T/L}(q,\omega_f)$ for the ^{2}H nucleus at $q = 1.05$ fm^{-1} in the laboratory frame [the values of the moments are supplemented with the total experimental error (first line) and its statistical component (second line)]

k	ω_f	$\tilde{S}^{(k)}_L(q,\omega_f)$, MeV^k	ω_x, MeV	$D \pm \Delta_S D$, %	$\tilde{S}^{(k)}_T(q,\omega_f)$, MeV^k	ω_x, MeV	$D \pm \Delta_S D$, %
-1	∞	0.029 ± 0.002 ± 0.001	69	1.4 ± 0.3	0.0091 ± 0.0007 ± 0.0002	69	0.8 ± 0.6
1	∞	27.4 ± 2.8 ± 2.2	79	19 ± 7	6.46 ± 0.93 ± 0.74	71	14 ± 11
	q	25.3 ± 2.1 ± 1.5	77	14 ± 4	6.20 ± 0.71 ± 0.50	71	11 ± 7
2	q	1172 ± 177 ± 151	77	36 ± 12	244 ± 61 ± 54	71	31 ± 22

Table 3. Calculated values of the moments S^{theor} for $k = 0, 1$ and their ratios $S^{\mathrm{theor}}/S^{\mathrm{expt}}$ to the experimental values

	$S^{(0)}_L(q)$	$S^{(0)}_T(q)$	$\tilde{S}^{(1)}_L(q)$, MeV			$\hat{S}^{(1)}_L(q)$, MeV	$\tilde{S}^{(1)}_T(q)$, MeV
S^{theor}	0.658 [13]	0.259 [14]	28.1 [15]	26.8 [14]	23.7 [13]	18.6 [10]	9.48 [14]
$S^{\mathrm{theor}}/S^{\mathrm{expt}}$	0.85 ± 0.05	1.20 ± 0.10	1.03 ± 0.11	0.98 ± 0.10	0.87 ± 0.09	1.01 ± 0.11	1.47 ± 0.21

close to the sum of the cross sections for scattering on its constituent nucleons:

$$S^{(0)}_L(q)/Z \simeq 1. \qquad (18)$$

Violation of the equality in (18) is a manifestation of the nuclear structure; therefore, the value of the moment $S^{(0)}_L(q = 1.05\ \mathrm{fm}^{-1})$ is sensitive to distinctions in its calculations. From Table 3, it can be seen that the experimental values of $S^{(0)}(q)$ are poorly reproduced by the quoted theoretical values. In this connection, it is interesting to note that the ratio $\gamma^{(0)} = S^{(0)}_T(q)/S^{(0)}_L(q)$ for the calculated values from [13, 14] is 0.395, the experimental value being 0.281 ± 0.016; at the same time, a simple calculation for electron scattering on a free proton and a free neutron [see Eq. (10)] yields 0.265. The agreement between the last two values within the experimental error suggests that, in the region $q < 1.5$ fm^{-1}, the ratio $\gamma^{(0)}$ is less dependent on the nuclear structure than the quantities $S^{(0)}_T(q)$ and $S^{(0)}_L(q)$ taken separately. If this is indeed so, expression (10) can be used as a test of theoretical calculations of $S^{(0)}_T(q)$ and $S^{(0)}_L(q)$ for momentum-transfer values in the range $q \approx 1$–1.5 fm^{-1}.

5.2.2. Let us now compare our result for the moment $S^{(1)}_L(q)$ with data of other measurements and with the results of theoretical calculations.

Figure 7 displays the result of our study for $\hat{S}^{(1)}_L(q)$ and the estimates of this moment from [16, 17], which were obtained from measurements only at small angles rather than within the usual procedure of separating the functions R_T and R_L. In view of this, the results presented in [16, 17] call for an additional discussion. By way of example, we indicate that all of the measurements reported in [16] were performed at the

same scattering-angle value of $\theta = 14°$. Under these conditions, the contribution of the transverse component to the angular response function is assumed to be relatively modest, its major part being due to scattering on the magnetic moments of the nucleons. In order to eliminate the contribution from the proton magnetic moment, the longitudinal response function was determined in [16] as

$$R_L(q,\omega) = R_\theta(q,\omega)/u_p(\theta,q), \qquad (19)$$

where the correction

$$u_p(\theta,q) = 1 + \left(\frac{1}{2} + \tan^2\frac{\theta}{2}\right)\mu_p^2\frac{q^2}{2M^2} \qquad (20a)$$

was calculated in the approximation of electron scattering on a free proton. In order to eliminate the contribution from scattering on a neutron as well, the data presented in [16] were rescaled in our study by taking into account the correction

$$u_{p+n}(\theta,q) = 1 + \left(\frac{1}{2} + \tan^2\frac{\theta}{2}\right)(\mu_p^2 + \mu_n^2)\,\frac{q^2}{2M^2}. \qquad (20b)$$

The function u_{p+n} changes from 1.14 at $q = 1.02$ fm^{-1} to 1.38 at $q = 1.71$ fm^{-1}. The data being considered do not involve the extrapolation of the response function; therefore, they represent, as was indicated in [16], a lower bound on the first moment. According to the present-day ideas of the behavior of the function $R_L(q,\omega\to\infty)$, the inclusion of the extrapolation increases them by 15 to 20%. The experimental values of $\hat{S}_L^{(1)}(q)$ from [16] [that is, those that include the correction in (20a)] are represented by boxes in Fig. 7; the values shown in this figure by open circles were obtained by taking into account the correction in (20b) and by multiplying the result by a factor of 1.15.

As to the value of $\hat{S}_L^{(1)}(q = 1.5\ \text{fm}^{-1})$ from [17], we note that it was obtained from an interpolation of measurements at two scattering-angle values of $\theta = 77.5°$ and 84°. This interpolation is not correct since the angular factor in expression (4) is not fixed in this case, so that the resulting function is not characterized by a specific value of the scattering angle—that is, it is not a function R_θ. The uncertainty in the angle leads to an error in the moment value. In the case being considered, this error can be estimated at 6%. The extrapolation of the function R_L was taken into account in [17] by calculating it on the basis of the Durand model [18], but the correction for the contribution of the function R_T was not included there (see the footnote on page 912 in [14]). The diamond in Fig. 7 represents the value of $\hat{S}_L^{(1)}(q = 1.5\ \text{fm}^{-1})$ as given in [17], while the triangle stands for this result

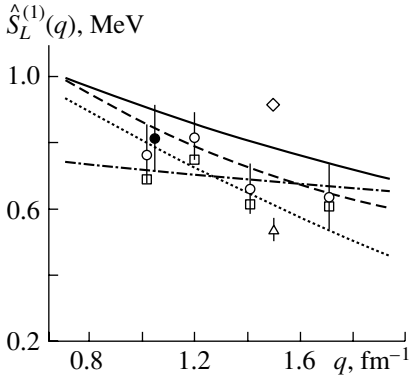

Fig. 7. Ratio of the first moment of the longitudinal response function to $q^2/(2M)$ (data and results of the calculations are presented in the c.m. frame). The points represent (open boxes) data from [16], (open diamond) result from [17], (open circles and open triangle) same data upon the introduction of corrections, and (closed circle) value obtained in the present study. The solid, the dashed, the dash-dotted, and the dotted curve depict the results of the calculations performed in [15], [14], [13], and [10], respectively.

corrected with allowance for (20b), the corresponding correction being equal to 1.7 in this case. The relative values of the experimental errors in the corrected data are identical to those in [16, 17].

With allowance for the corrections introduced above, Fig. 7 indicates that all experimental data considered in this study are consistent and that the general character of their dependence on the momentum transfer is similar to that which is predicted by theoretical calculations.[2)] It can be seen that, according to these data, the results of the calculations performed in [13, 14], as well as those from [10], stand out as those that are the closest to the experimental data. In what is concerned with the last study, it should be noted that, despite the good agreement between the results of this study and experimental data, its calculations at $q = 2$ and $\sqrt{10}$ fm^{-1} yield $\hat{S}_L^{(1)}(q)[q^2/(2ZM)]^{-1} = 0.43$ and 0.15, respectively, whereas the asymptotic behavior of this function must lead to 0.5.

5.3. Let us summarize the basic results of this study.

[2)]The calculations of $S_L^{(1)}(q)$ that are presented in [13–15] were performed in the laboratory frame; in order to display their results in Fig. 7, they were rescaled to the c.m. frame with the aid of the expression $\tilde{S}^{(1)}(q) = \hat{S}^{(1)}(q) + q^2/(2AM)S^{(0)}(q)$. Since the values of A required for this were borrowed from [13], the corresponding lines in the region $q < 1.5$ fm^{-1}, where the zeroth moment is sensitive to the choice of model, can deviate by a few percent from the results quoted by the authors of [14, 15].

(i) We have considered the problem of optimally choosing conditions for measuring nuclear response functions.

(ii) The gas target GM-2 has been created for the measurements reported in this article.

(iii) The transverse and the longitudinal response function for the ^{2}H nucleus have been measured at $q = 1.05$ fm^{-1} up to $\omega = 118$ MeV.

(iv) The experimental values of the moments $S_L^{(k)}(q)$ and $S_T^{(k)}(q)$ have been determined for $k = -1$, 0, and 1. The values of $S_L^{(2)}(q, \omega_f = q)$ and $S_T^{(2)}(q, \omega_f = q)$ have also been found.

The results of our measurements have revealed the following:

(a) The experimental values of $S^{(0)}(q)$ differ from the results of the calculations reported in [13, 14] by 2 to 3 values of $\Delta S^{(0)}(q)$, but the experimental result for the ratio $S_T^{(0)}(q)/S_L^{(0)}(q)$ is close to the result of the calculation for electron scattering on the system formed by a free proton and free neutron.

(b) The value obtained for $S_L^{(1)}(q)$ complies with data presented in [16, 17]; the entire body of experimental values of $S_L^{(1)}(q)$ is compatible with the results of the calculations from [13, 14].

ACKNOWLEDGMENTS

We are grateful to A.E. Zatserklyanyi and L.G. Levchuk for stimulating discussions.

REFERENCES

1. G. Orlandini and M. Traini, Rep. Prog. Phys. **54**, 257 (1991).
2. S. Dytman *et al.*, Phys. Rev. C **38**, 800 (1988).
3. T. de Forest, Jr., and J. D. Walecka, Adv. Phys. **15**, 1 (1966).
4. A. Yu. Buki *et al.*, Yad. Fiz. **58**, 1353 (1995) [Phys. At. Nucl. **58**, 1271 (1995)].
5. N. G. Afanas'ev *et al.*, Yad. Fiz. **5**, 318 (1966) [Sov. J. Nucl. Phys. **5**, 223 (1966)].
6. V. N. Polishchuk *et al.*, Preprint No. 72-40, KhFTI (Institute for Physics and Technology, Kharkov, 1972).
7. L. W. Mo and Y. S. Tsai, Rev. Mod. Phys. **41**, 205 (1969); D. B. Isabelle and G. R. Bishop, Nucl. Phys. **45**, 209 (1963).
8. J. S. McCarthy *et al.*, Phys. Rev. C **15**, 1396 (1977).
9. V. Tornow *et al.*, Nucl. Phys. A **348**, 157 (1980).
10. W. Leidemann and H. Arenhövel, Nucl. Phys. A **381**, 365 (1982).
11. A. L. Fetter and J. D. Walecka, *Quantum Theory of Many-Particle System* (McGraw-Hill, New York, 1971).
12. C. Garcia-Recio *et al.*, Nucl. Phys. A **507**, 385 (1990).
13. R. Schiavilla *et al.*, Phys. Rev. C **40**, 1484 (1989).
14. V. D. Éfros, Ukr. Fiz. Zh. **25**, 907 (1980).
15. E. V. Inopin and S. N. Roshchupkin, Yad. Fiz. **17**, 1008 (1973) [Sov. J. Nucl. Phys. **17**, 526 (1973)].
16. A. Yu. Buki *et al.*, in *Program and Abstracts of Papers of the 25th Conference on Nuclear Spectroscopy and Structure of Atomic Nucleus, Leningrad, 1975,* p. 321; A. Yu. Buki *et al.*, Yad. Fiz. **24**, 457 (1976) [Sov. J. Nucl. Phys. **24**, 237 (1976)].
17. É. L. Kuplennikov *et al.*, Yad. Fiz. **24**, 22 (1976) [Sov. J. Nucl. Phys. **24**, 11 (1976)].
18. L. Durand, Phys. Rev. **123**, 1392 (1961).

Translated by A. Isaakyan

Physics of Atomic Nuclei, Vol. 65, No. 5, 2002, pp. 763–775. From Yadernaya Fizika, Vol. 65, No. 5, 2002, pp. 797–809.

NUCLEI
Experiment

Investigation of the Formation of Residual Nuclei from Radioactive ^{237}Np and ^{241}Am Targets in Reactions with 660-MeV Protons*

J. Adam[1], A. R. Balabekyan[2], R. Brandt[3], V. P. Dzhelepov†, S. A. Gustov, V. G. Kalinnikov, M. I. Krivopustov, I. V. Mirokhin, J. Mrazek[4], R. Odoj[5], V. S. Pronskikh, O. V. Savchenko, A. N. Sosnin, A. A. Solnyshkin, V. I. Stegailov, and V. M. Tsoupko-Sitnikov

Joint Institute for Nuclear Research, Dubna, Moscow oblast, 141980 Russia

Received November 22, 2000; in final form, August 21, 2001

Abstract—The burning of radioactive waste is investigated. Targets from ^{241}Am and ^{237}Np were irradiated with 0.66-GeV proton beams. The cross sections for the formation of 60 and 80 residual nuclei from ^{237}Np and ^{241}Am are determined. The experimental results are compared with the theoretical cross sections calculated by the cascade–evaporation model. © *2002 MAIK "Nauka/Interperiodica".*

The present study was initiated by the prominent scientist and outstanding personality V.P. Dzhelepov. The preliminary results were reported by him at the JINR Scientific Council. This investigation is one of the last initiated by V.P. Dzhelepov with great enthusiasm, but his untimely death prevented him from seeing the final results. The death of V.P. Dzhelepov is an irreparable loss for Russian science and for all those who knew him and worked with him.

1. INTRODUCTION

The transmutation of fission products and actinoids produced at atomic power stations has aroused great interest in the last decade. Estimations made by various groups [1, 2] indicate that, in the case of transmutation of all transuranium elements (TUE), radiation risk due to their leakage from deep-underground storage systems must be compared with the natural radioactivity of the uranium ore after 10^3 yr and not after 5×10^6 yr (as in the case of untreated wastes). But in this case, treatment of TUE at all stages of the fuel cycle becomes a more difficult problem.

Estimations of radiation risk of spent nuclear fuel show that, after the extraction of the uranium–plutonium actinoid group and such fission products as ^{90}Sr and ^{137}Cs, the main risk for the population can be associated with ^{241}Am and ^{237}Np [3]. Among actinoids, ^{241}Am makes the greatest contribution. The particularly hazardous effect of ^{237}Np is due to its mass predominance and a high migration ability, which increases the probability of its penetration into the human body through food chains [4].

Investigation of ^{237}Np and ^{241}Am transmutation dynamics in the flow of thermal neutrons of various densities shows that the higher the density of neutrons, the smaller the number of various actinoids noticeably contributing to the radioactivity of wastes [4]. For solving the problem of transmutation, high-current proton accelerators must be used to produce neutron fluxes of 10^{17} cm^{-2} s^{-1} for transmutation purposes. In some recent publications, both transmutation of actinoids under the effect of neutron irradiation and their spallation and fission under the effect of proton and ion beams are investigated [5].

The parameters of the hadron–nucleon cascade form a basis for calculating electronuclear setups, their targets, and the blanket effect. These parameters are calculated with a number of codes using models of different accuracies for the cascade approximation. As is shown in [6], the best test for various codes is a comparison of the calculated and experimental yields of residual nuclei. From the experimental point of view, a determination of the independent cross sections for the yields of short-lived nuclear products from a monoisotope target is the most important

*This article was submitted by the authors in English.

†Deceased.

[1]On leave from Nuclear Physics Institute, Řež, CZ-25068 Czech Republic.

[2]Yerevan State University, ul. A. Manukiana 1, Yerevan, 375049 Armenia.

[3]Institut für Physikalische, Kern- und Makromolekular Chemie, Philipps-Universität, Marburg, Germany.

[4]Nuclear Physics Institute, Řež, CZ-25068 Czech Republic.

[5]Forschungszentrum, Julich, Germany.

1063-7788/02/6505-0763$22.00

Table 1. Characteristics of $^{237}_{93}$Np and $^{241}_{95}$Am targets

Target	Half-life, yr	Total mass-attenuation coefficient for γ rays of energy 300 keV, cm^2/g	Density of oxide, g/cm^3	Weight, g	Thickness, mm	Activity, mCi	Beam intensity, 10^{14} p/min	Irradiation time, min
$^{237}_{93}$Np	$2.144(7) \times 10^6$	0.498	11.1	0.742	0.193	0.523	2.64	5
				0.742	0.193	0.523	2.66	30
$^{241}_{95}$Am	432.2(7)	0.508	11.7	0.177	0.043	601	2.72	5
				0.183	0.044	621	2.58	30

for comparison [7]. The experimental cross sections for residual nuclei in radioactive ^{241}Am and ^{237}Np targets are undoubtedly important for the projects of transuranium-waste transmutation in a direct proton beam [8]. The present article deals with an investigation of the cross sections for the formation of residual nuclei in ^{241}Am and ^{237}Np targets.

2. EXPERIMENTAL METHOD

The experiment was performed in an external beam of the phasotron installed at the Laboratory of Nuclear Problems at the Joint Institute for Nuclear Research (JINR, Dubna). The beam current was 1.2 μA. Targets from NpO_2(Np) and AmO_2(Am) were exposed to a 660-MeV proton beam. The target and beam characteristics are presented in Table 1. The irradiated target samples were hermetically packed in aluminum capsules with a weight of 78.8 g and the dimensions shown in Fig. 1.

A specific feature of such experiments is that the high self-radiation of the targets used often produces a background that makes it difficult to measure the yield of product nuclei. For example, the activity of the ^{241}Am target is about 600 mCi, while the intensity of the γ radiation (I_γ) is distributed over energy (E_γ) in such a way that $\sum I_\gamma(E_\gamma < 103$ keV$) : \sum I_\gamma(103 < E_\gamma < 400$ keV$) : \sum I_\gamma(E_\gamma > 400$ keV) is $0.392 : 0.831 \times 10^{-4} : 0.912 \times 10^{-5}$. The intensities I_γ are given for the decay probability, and the remaining 60% occur through the electron-conversion channel. During the measurement, such a γ-radiation-intensity distribution allowed the background from the radioactive targets to be reduced with filters. We used a 10-mm Pb + 2-mm Cd + 1-mm Cu filter to increase the solid angle for ^{241}Am by a factor of about 700. For ^{237}Np, the energy (E_γ) distribution of the γ radiation (I_γ) differs from that for ^{241}Am: $\sum I_\gamma(E_\gamma < 100$ keV$) : \sum I_\gamma(100 < E_\gamma < 400$ keV$) : \sum I_\gamma(E_\gamma > 400$ keV) is $0.167 : 0.548 : 0.0168$. But we used the same filter for the ^{237}Np target to optimize the detector loading and the measurement geometry. Figure 2 shows the efficiency curves for our HPGe detector that were obtained with and without the filter.

The self-absorption correction for the γ radiation in the target (C_A) was calculated with the density and dimensions of the targets by the formula [9]

$$C_A = (\mu D/(1 - e^{-\mu D}))^{-1}, \qquad (1)$$

where μ is the total attenuation coefficient for a given γ ray in the source material and D is the target thickness. This correction for γ rays of energy higher than 300 keV proved to be less than 1.5% in the ^{241}Am target and less than 5% in the ^{237}Np target and may be neglected. The profile and the position of the beam during the irradiation of the targets were controlled by a two-coordinate proportional chamber. To monitor the beam, the reaction ^{27}Al$(p, 3pn)^{24}$Na was used. In [10], the cross section for this reaction at a proton energy of 660 MeV was found to be 10.8 ± 0.7 mb. A further investigation of this reaction [11] yielded new values of the reaction cross section at an energy higher than 800 MeV, but, in our energy range, its value did not change [12]. In our calculation, we used the cross section for the reaction ^{27}Al$(p, 3pn)^{24}$Na (see above). Aluminum foils of the same dimensions as the targets were used for monitoring. The weight of each aluminum foil was 99 mg. The targets were irradiated in two steps: 5-min exposure for the measurement of short-lived residual nuclides and 30-min exposure for long-lived ones.

The induced activity of the targets was measured by two detectors, an HPGe detector with an efficiency of 20% and an energy resolution of 1.8 keV (1332-keV ^{60}Co) for the ^{241}Am target and a Ge(Li) detector with an efficiency of 4.8% and a resolution of 2.6 keV (1332-keV ^{60}Co) for the ^{237}Np target. The γ spectrum was recorded with the aid of a high-rate multichannel buffer MASTER 921 (^{241}Am) and a four-input multichannel buffer MASTER 919

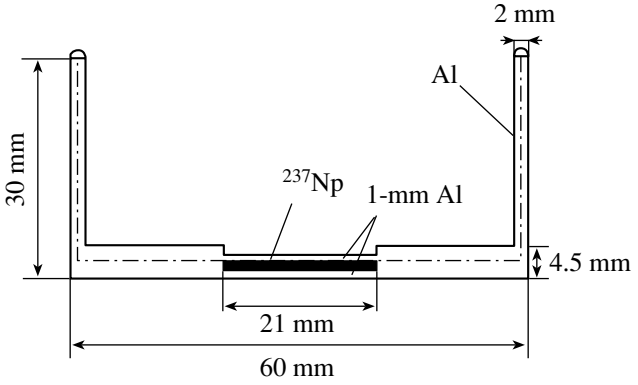

Fig. 1. Targets from $^{237}_{93}$Np and $^{241}_{95}$Am in an aluminum capsule.

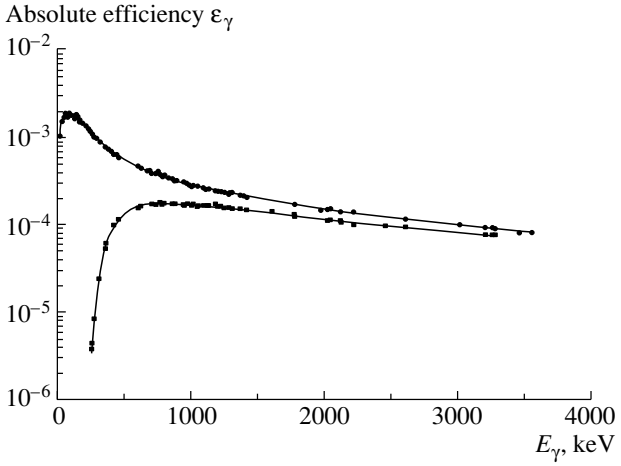

Fig. 2. Detector-efficiency curves for the source-to-detector distance of 25 cm: (●) without a filter and (■) with a 1-mm Cd + 1-mm Cu + 10-mm Pb filter.

(^{237}Np), which automatically determined the dead time.

The measurement of the first targets (short exposures) started 10 min after the end of irradiation. These targets were measured 17 times for 17 h. The measurement time varied from 5 min to 3 h, the distances between the target and the detector being 150 cm for ^{241}Am and 100 cm for ^{237}Np. The second targets (30-min exposures) were measured 11 times for 30 d with exposures from 5 to 50 h and respective distances of 100 and 60 cm. The code DEIMOS [13] was used in the interactive mode for spectrum handling. This code determines the area S_γ and the position K_γ of the peak and the upper limit on the peak area $S_\gamma(\mathrm{lim})$, which cannot be found at the given background level. At the same time, the exact energy E_γ and intensity I_γ of the peaks can be obtained. When the spectrum handling had been finished, the data were "cleaned" from background lines and single and double escape peaks. The peak intensities were corrected by subtraction of the single and double escape peaks. The corrected line intensities were used to determine the half-life of each line, including the complex (doublet) lines. The identification of residual nuclei was based on their γ-transition energies, intensities, and half-lives compared with the data from [14]. A more detailed analysis and checking of the data after identification of the residual nuclei for the ^{241}Am target were performed with a special code. This analysis was based on a comparison of the ratios of our experimental $I_\gamma(\mathrm{lim})$ ($< -S_\gamma(\mathrm{lim})$) and published $I_\gamma(\mathrm{lit})$ intensities of the transitions (including unobserved ones) for each decaying identified nucleus. Knowing the half-lives of the multiplet components, we also analyzed such complex lines. We found 1025 γ lines in 28 spectra measured for ^{241}Am targets; 166 of them had different energies E_γ. Determining the half-lives of those 166 lines, we found that 34 of them are doublets and 5 are triplets. A special system of codes was created for a complex analysis of the experimental data. This system is described in detail in [15].

The cross sections for the formation of residual nuclei a, $\sigma_a(E_\gamma(j))$, were determined for each line in all of the measured spectra $i = 1, 2, \ldots, n$ with a correction for the dead time [Eq. (2), Table 2],

$$\sigma_a(E_\gamma(j), i) = S_i(E_\gamma(j)) \tag{2}$$
$$\times \lambda_a(t_3(\mathrm{real}, i)/t_3(\mathrm{live}, i))/[N_p N_{\mathrm{targ}} \varepsilon_\gamma(E_\gamma(j))$$
$$\times I_j(E_\gamma(j))(1 - e^{-\lambda_a t_1})e^{-\lambda_a t_2(i)}(1 - e^{-\lambda_a t_3(\mathrm{real},i)})],$$

where $S_i(E_\gamma(j))$ is the number of recorded photons of energy $E_\gamma(j)$ in the ith spectrum; λ_a [s^{-1}] is the decay constant for nucleus a; N_p is the flux of particles [s^{-1}] on the target; N_{targ} is the number of nuclei on 1 cm^2 of the target surface; $\varepsilon_\gamma(E_\gamma(j))$ is the absolute recording efficiency for photons with the energy $E_\gamma(j)$; $I_\gamma(E_\gamma(j))$ is the intensity per decay of γ rays of energy $E_\gamma(j)$; and t_1, $t_2(i)$, $t_3(\mathrm{real}, i)$, and $t_3(\mathrm{live}, i)$ are the exposure time, waiting time, real, and live time of measurement, respectively.

The components of the doublet lines are genetically related (Gen = 1, decay of the parent nucleus a and of the daughter nucleus b) or independent (Gen = 0, nuclei a', b'). The number of γ rays from the decay of nucleus b recorded in the ith measurement is

$$S_i(E_{\gamma(b)}) = \left\{ Ae^{-\lambda_a t_2(i)} \left(1 - e^{-\lambda_a t_3(\mathrm{real},i)}\right) \right. \tag{3}$$
$$\left. + Be^{-\lambda_b t_2(i)} \left(1 - e^{-\lambda_a t_3(\mathrm{real},i)}\right) \right\} \frac{t_3(\mathrm{live}, i)}{t_3(\mathrm{real}, i)}.$$

Substituting the known λ_a and λ_b and the measured values $S_i(E_\gamma(b))$, $t_2(i)$, $t_3(\mathrm{real}, i)$, and $t_3(\mathrm{live}, i)$, we

Table 2. Residual nuclei from the reactions $^{241}\mathrm{Am}(p, xpyn)X$

Residual nuclei	$T_{1/2}$	E_γ, keV	I_γ	Cross section, mb	Number of measurements
^{48}Sc	1.820(4) d	c983.500(1)	1.0	1.35 ± 0.19	7
		c1312.100(30)	0.975	1.04 ± 0.10	7
^{48}V	15.970(10) d	c983.50(3)	0.999	3.52 ± 0.17	7
		c1312.00(3)	0.9739(20)	3.37 ± 0.14	7
^{52}V	3.750(10) min	1434.100(10)	1.000(10)	2.3 ± 0.6	1
^{52}Mn	5.590(10) d	c744.233(13)	0.906(4)	1.81 ± 0.20	1
		c935.544(12)	0.949(3)	1.9 ± 3.4	4
		1434.090(17)	1.000(3)	1.71 ± 0.12	1
^{54}Mn	312.5(5) d	c834.830(21)	0.9998(2)	10.1 ± 0.4	9
^{56}Mn	2.580(1) h	846.750(20)	0.9887(30)	6.7 ± 1.6	7
^{72}Ga	14.100(11) h	c834.030(30)	0.9563	1.5 ± 0.7	9
^{72}As	1.080(5) d	c833.990(30)	0.795	4.2 ± 0.5	8
^{76}As	1.1000(30) d	c559.10(5)	0.447(8)	4.5 ± 1.6	5
^{76}Br	16.19(22) h	c559.09(5)	0.740	0.6 ± 1.9	5
^{82}Br	1.470(20) d	c554.320(20)	0.706(4)	7.55 ± 0.30	5
		c619.070(20)	0.431(5)	10.5 ± 0.9	10
		c698.330(20)	0.279(4)	8.5 ± 0.9	2
		c776.490(30)	0.834	8.68 ± 0.30	7
		c827.810(30)	0.2419(25)	7.3 ± 0.6	5
		c1043.970(30)	0.2736(33)	6.5 ± 0.6	5
		c1317.47(5)	0.2694(33)	8.0 ± 0.4	5
		1474.82(8)	0.1660(17)	8.6 ± 0.7	2
^{84}Br	6.470(6) h	c554.35(10)	0.624(8)	12 ± 5	5
		c619.11(10)	0.380	6 ± 7	10
		c698.37(10)	0.263(7)	2.5 ± 0.8 (fix.)	2
		c776.52(10)	0.844	1.4 ± 1.7	7
		c827.83(10)	0.210(6)	7 ± 11	5
		c1044.08(10)	0.321	2.5 ± 0.4 (fix.)	5
		c1317.43(10)	0.237(6)	10 ± 12	5
^{84}Rb	32.77(14) d	c881.610(3)	0.690(20)	6.9 ± 0.4	5
^{86}Rb	18.82(2) d	1076.6(1)	0.0878	2.02 ± 0.30	1
^{89}Rb	15.15(14) min	c657.77(6)	0.0998(52)	4 ± 8	4
		c947.73(7)	0.0922(46)	23 ± 6	1
		1031.92(6)	0.58(3)	10.6 ± 0.8	4
		1248.14(6)	0.423(23)	10.7 ± 1.4	3
		2195.92(11)	0.1334(87)	23 ± 5	1
^{91}Sr	9.52(6) h	c555.60(10)	0.617(6)	0.9 ± 7.0	17
		c1024.30(10)	0.334	15.0 ± 1.8	10
^{92}Sr	2.710(10) h	1383.90(6)	0.9(1)	11.8 ± 0.5	12
^{93}Sr	7.32(10) min	590.28(5)	0.665(18)	13.4 ± 2.7	3
		875.73(6)	0.239(13)	7.1 ± 2.8	1
^{84m}Y	40(1) min	793.0(3)	0.986	3.1 ± 0.9	1
^{87}Y	3.350(10) d	484.90(5)	0.922(10)	4.40 ± 0.29	6
^{88}Y	106.6(4) d	898.021(19)	0.940(4)	6.6 ± 0.6	3
		1836.01(4)	0.9936(2)	6.1 ± 0.5	3
^{91m}Y	49.71(4) min	555.57(10)	0.949(6)	14 ± 4	17
^{95}Y	10.30(10) min	954.20(20)	0.19	18 ± 4	1
^{89}Zr	3.270(10) d	909.20(10)	0.9987	3.79 ± 0.29	1
^{95}Zr	63.98(6) d	c724.23(4)	0.4444(60)	36.0 ± 2.0	4
		756.74(4)	0.5486	38 ± 4	5
^{97}Zr	16.90(5) h	cd657.92(10)	0.9135(11)	20.7 ± 0.4	8
		cd743.36(10)	0.9093(6)	19.5 ± 0.8	3
^{92m}Nb	10.15(2) d	c935.44(10)	0.99	0.6 ± 0.4	4

Table 2. (Contd.)

Residual nuclei	$T_{1/2}$	E_γ, keV	I_γ	Cross section, mb	Number of measurements
^{95}Nb	33.15(5) d	c765.83(4)	1.0	16.8 ± 2.1	8
^{96}Nb	23.35(5) h	460.03(6)	0.276(11)	15 ± 2.0	3
		568.86(6)	0.546(22)	12.5 ± 0.6	8
		c719.56(15)	0.0713(4)	35 ± 18	4
		c778.22(10)	0.950	13 ± 2	10
		810.25(7)	0.0969(61)	15 ± 4	8
		c849.90(10)	0.203(10)	13.2 ± 1.7	10
		1091.31(6)	0.484(22)	13.8 ± 0.4	7
		1200.19(6)	0.197(10)	14.7 ± 0.9	4
^{97}Nb	1.200(12) h	c657.92(10)	0.9834(11)	13.3 ± 0.8	17
^{98m}Nb	51.30(40) min	c722.50(10)	0.707(65)	12.2 ± 0.7	17
		787.20(10)	0.93(8)	15 ± 0.7	9
^{99}Mo	2.750(8) d	c739.500(15)	0.1219	44.1 ± 1.3	10
^{96}Tc	4.30(10) d	c778.22(4)	0.9976	2.71 ± 0.29	10
		812.54(4)	0.820(35)	2.65 ± 0.14	6
		c849.86(4)	0.976(38)	2.78 ± 0.19	10
^{104}Tc	18.4(10) min	358.00(10)	0.89	28 ± 8	1
		c884.40(10)	0.110(12)	14 ± 8	1
^{103}Ru	39.35(5) d	497.080(13)	0.889(28)	63 ± 4	8
^{105}Ru	40440(22) h	676.36(8)	0.157(5)	40 ± 4	6
		c724.30(3)	0.473	33.0 ± 1.3	15
^{105}Rh	1.470(1) d	318.90(10)	0.192	77 ± 13	2
^{106m}Rh	2.170(34) h	717.20(10)	0.294(34)	13.8 ± 2.5	2
		748.50(10)	0.197(23)	21 ± 5	1
		1529.40(10)	0.178(24)	17 ± 4	1
^{108}Rh	5.90(20) min	581.10(20)	0.586	9.5 ± 1.9	1
		c947.10(20)	0.4974	13.9 ± 1.9	1
^{112}Pd	21.05(5) h	cd617.40(20)	0.43(60)	18 ± 3	9
		cd694.80(20)	0.0345(8)	$41 \pm 9 + e$	8
^{106m}Ag	8.46(10) d	c1045.83(8)	0.2955(96)	2.4 ± 0.4	5
		1527.65(19)	0.163(13)	2.6 ± 0.5	1
^{110m}Ag	252.2(3) d	c657.70(10)	0.947	21 ± 11	8
		884.70(10)	0.729	11.2 ± 2.6	3
^{112}Ag	3.140(20) h	617.40(20)	0.43(6)	20.4 ± 1.7	13
^{115}cd	2.230(4) d	492.350(4)	0.0803(33)	18 ± 4	1
		527.900(7)	0.274(11)	19.3 ± 0.9	7
^{117m}cd	3.36(5) h	c552.900(20)	0.997(10)	6.9 ± 0.7	15
^{116m}In	54.15(16) min	1097.30(20)	0.557(15)	13.5 ± 0.9	7
		1293.54(15)	0.850(20)	17.3 ± 0.5	10
^{117m}In	1.940(12) h	cd552.90(20)	0.469(50)	21.4 ± 1.0	15
^{118m}In	4.45(5) min	1050.8(5)	0.820(82)	6.8 ± 1.3	1
		c1229.5(5)	0.96(10)	6.2 ± 1.3	2
^{116m}Sb	5.000(11) h	1050.8(5)	0.82(8)	7.0 ± 1.5	7
		c1229.5(5)	0.96(10)	7.7 ± 0.6	8
^{120}Sb	5.760(21) d	c1023.3(4)	0.994(3)	10.8 ± 0.3	10
		1171.7(3)	1.0	10.4 ± 2.0	10
^{122}Sb	2.700(10) d	564.24(4)	0.7	14.0 ± 0.5	10
^{124}Sb	60.200(30) d	c602.72(4)	0.9792	10.1 ± 0.6	10
		c1691.00(4)	0.4876(49)	10.2 ± 0.6	6
^{126}Sb	12.40(10) d	414.80(20)	0.98	7.5 ± 0.9	2
		c695.00(20)	0.997	6.84 ± 0.29	8
		c697.00(20)	0.289(70)	12.1 ± 2.2	6
		c720.50(20)	0.538(24)	10.9 ± 0.9	4

Table 2. (Contd.)

Residual nuclei	$T_{1/2}$	E_γ, keV	I_γ	Cross section, mb	Number of measurements
		856.70(20)	0.176(9)	6.5 ± 2.3	3
^{127}Sb	3.85(50) d	473.0(4)	0.247(9)	7.4 ± 1.2	2
		685.7(5)	0.353	7.2 ± 0.5	5
		783.7(5)	0.145(5)	7.4 ± 0.9	2
^{128}Sb	9.010(30) h	c743.30(10)	1.00(5)	10.6 ± 1.1	9
		754.00(10)	1.00(5)	1.8 ± 0.5	2
		c813.60(20)	0.130(20)	11 ± 7	6
^{119m}Te	4.69(5) d	1136.75(7)	0.0772(7)	4.7 ± 1.5	1
		1212.73(7)	0.667	3.72 ± 0.15	6
^{121}Te	16.78(35) d	573.139(11)	0.803(17)	5.3 ± 0.5	5
^{131m}Te	1.25(80) d	782.49(4)	0.0778(12)	18 ± 4	3
		822.78(4)	0.0612(8)	5.4 ± 1.2	1
^{132}Te	3.260(34) d	cd630.22(9)	0.137(6)	11.2 ± 0.9	3
		cd667.69(8)	0.987(2)	7.1 ± 1.2	12
		*d*772.60(8)	0.762(19)	6.2 ± 0.3	7
^{124}I	4.180(21) d	c602.72(4)	0.605	10.3 ± 0.3	10
		c1691.02(4)	0.1041(12)	12.8 ± 0.8	6
^{126}I	13.02(7) d	388.630(11)	0.340(7)	31 ± 10	4
		c666.330(12)	0.330(7)	6.0 ± 1.9	6
^{130}I	12.36(1) h	536.090(20)	0.99(2)	8.1 ± 0.6	14
		c668.540(10)	0.961(25)	11.8 ± 0.6	4
		c739.480(20)	0.823(23)	10.7 ± 3.0	17
^{131}I	8.04(1) d	364.480(11)	0.812(16)	14.2 ± 0.9	6
		636.793(20)	0.812(16)	13.5 ± 2.7	1
^{132}I	2.2846(4) h	667.70(10)	0.99	8.3 ± 1.2	6
^{133}I	20.80(10) h	529.872(11)	0.863(17)	9.3 ± 0.5	9
^{134}I	52.6(4) min	c847.025(25)	0.954(19)	2.7 ± 1.2	5
		c884.090(25)	0.649(9)	5.2 ± 0.9	7
^{132}Cs	6.48(2) d	c667.5(1)	0.974	6.2 ± 1.8	7
^{136}Cs	13.16(3) d	818.514(12)	0.997	6.01 ± 0.18	6
		1048.070(20)	0.798(30)	7.16 ± 0.24	6
		1235.360(23)	0.200(7)	9.2 ± 0.6	2
^{140}Ba	12.74(5) d	537.274(20)	0.2439(21)	$11.1 \pm 2.5 +$ f	1
		cd487.029(19)	0.459(4)	4.1 ± 0.5	6
		cd815.780(30)	0.2364(17)	3.9 ± 0.6	4
		cd1596.17(6)	0.9540(8)	3.4 ± 0.3	11
^{140}La d	1.680(18)	c487.029(19)	0.459(4)	9.3 ± 0.5	6
		c815.780(30)	0.2364(17)	6.3 ± 0.6	4
		c1596.17(6)	0.9540(8)	7.09 ± 0.27	11
^{135}Ce	17.69(19) h	606.760(20)	0.1881(54)	17.0 ± 2.6	4
^{145}Eu	5.93(5) d	893.738(24)	0.684	1.65 ± 0.20	4
^{146}Eu	4.59(3) d	747.20(12)	0.98	1.16 ± 0.18	3
^{154}Tb	21.4(5) h	c536.25(10)	0.013	60 ± 40	14
		c722.10(20)	0.058	13 ± 6	17
^{156}Tb	5.35(10) d	534.29(6)	0.67(7)	1.8 ± 0.5	1
^{198}Au	2.700(2) d	411.790(10)	0.955	1.33 ± 0.21	1
^{206}Bi	6.240(3) d	c537.50(5)	0.304	$3.2 \pm 0.7 +$ g	1
		803.10(5)	0.989	1.33 ± 0.21	1
		c881.01(5)	0.662(7)	0.5 ± 0.5	5
^{240}Am	2.120(13) d	880.80(5)	0.251(4)	46.5 ± 1.1	10
		987.76(6)	0.731(10)	44.7 ± 0.7	11

Note: The following notation is used here: (c) complex peak, (d) peak corresponding to the decay of daughter nuclei, (e) together with ^{112}Ag, (f) admixture of ^{206}Bi, and (g) admixture of ^{140}Ba.

Table 3. Formation of nuclei in the reactions ^{241}Am$(p, xpyn)X$ (complex peaks)

No.	Gen	E_γ, keV	$T_{1/2}$	Residual nuclei	Cross section, mb	Type of cross section	χ^2
1	1	487.029(19)	12.74 d	^{140}Ba	4.1 ± 0.5	C	0.3
	1	487.029(19)	1.68 d	^{140}La	9.3 ± 0.5	I	
2	0	536.090(20)	12.36 h	^{130}I	8.1 ± 0.6	C	0.3
	0	536.25(10)	21.40 h	^{154}Tb	60 ± 40	C	
3	1	552.900(20)	3.36 h	^{117m}Cd	6.9 ± 0.7	C	1.0
	0	552.900(20)	1.94 h	^{117m}In	21.4 ± 1.0	C	
4	0	554.320(20)	1.47 d	^{82}Br	7.55 ± 0.30	I	0.3
	0	554.35(10)	6.47 h	^{82m}Rb	12 ± 5	C	
5	1	555.60(10)	9.52 h	^{91}Sr	0.9 ± 7.0	C	2.4
	1	555.57(10)	49.71 min	^{91m}Y	14 ± 4	I	
6	0	559.10(5)	1.10 d	^{76}As	4.5 ± 1.6	C	0.9
	0	559.09(5)	16.19 h	^{76}Br	0.6 ± 1.9	C	
7	0	602.72(4)	60.20 d	^{124}Sb	10.1 ± 0.6	I	0.9
	0	602.72(4)	4.18 d	^{124}I	10.3 ± 0.3	I	
8	1	617.40(20)	21.05 h	^{112}Pb	18 ± 0.3	C	1.3
	1	67.40(20)	3.14 h	^{112}Ag	20.4 ± 1.7	I	
9	0	919.070(20)	1.47 d	^{82}Br	10.5 ± 0.9	I	2.9
	0	619.11(10)	6.47 h	^{82m}Rb	6 ± 7	C	
10	1	630.22(9)	3.26 d	^{132}Te	11.2 ± 0.9	C	0.6
	1	630.19(2)	2.30 h	^{132}I	–	I	
11	1	657.92(10)	16.90 h	^{97}Zr	20.7 ± 0.4	C	2.2
	1	657.92(10)	1.20 h	^{97}Nb	13.3 ± 0.8	I	
	0	657.77(6)	15.15 min	^{89}Rb	4 ± 8	C	
12	0	666.3(2)	12.40 d	^{126}Sb	–	I	0.8
	0	666.330(12)	13.02 d	^{126}I	6.0 ± 1.9	I	
13	1	667.69	3.26 d	^{132}Te	7.1 ± 1.2	C	2.4
	1	667.70(10)	2.28 h	^{132}I	8.3 ± 1.2	I	
	0	667.5(1)	6.48 d	^{132}Cs	6.2 ± 1.8	I	
14	1s	694.80(20)	21.05 h	^{112}Pd	$41 \pm 9 + e$	C	0.8
	0	695.00(20)	12.40 d	^{126}Sb	6.84 ± 0.29	I	
15	0	698.330(20)	1.47 d	^{82}Br	8.5 ± 0.9	I	1.2
	0	698.37(10)	6.47 h	^{82m}Rb	2.5 ± 0.8(fix.)	C	
	0	697.00(20)	12.40 d	^{126}Sb	12.1 ± 2.2	I	
16	0	719.56(15)	23.35 h	^{96}Nb	35 ± 18	I	1.0
	0	720.50(20)	12.40 d	^{126}Sb	10.9 ± 0.9	I	
17	0	722.50(10)	51.30 min	^{98m}Nb	12.2 ± 0.7	I	1.7
	0	722.10(20)	21.40 h	^{154}Tb	13 ± 6	C	
18	0	724.23(4)	63.98 d	^{95}Zr	36.0 ± 2.0	C	0.9
	0	724.30(30)	4.44 h	^{105}Ru	33.0 ± 1.3	C	
19	0	739.500(15)	2.75 d	^{99}Mo	44.1 ± 1.3	C	1.3
	0	739.480(20)	12.36 h	^{130}I	10.7 ± 3.0	C	

Table 3. (Contd.)

No.	Gen	E_γ, keV	$T_{1/2}$	Residual nuclei	Cross section, mb	Type of cross section	χ^2
20	0	744.233(13)	5.59 d	^{52}Mn	1.81 ± 0.20	C	1.2
	0	743.36(10)	16.90 h	^{97}Zr	19.5 ± 0.8	C	
	0	743.30(10)	9.01 h	^{128}Sb	10.6 ± 1.1	C	
21	0	776.490(30)	1.47 d	^{82}Br	8.68 ± 0.30	I	1.5
	0	776.52(10)	6.47 h	^{82m}Rb	1.4 ± 1.7	C	
22	0	778.22(10)	23.35 h	^{96}Nb	13 ± 2	I	2.3
	0	778.22(4)	4.30 d	^{96}Tc	2.71 ± 0.29	I	
23	0	812.54(4)	4.30 d	^{96}Tc	2.65 ± 0.14	I	
	0	813.60(20)	9.01 h	^{128}Sb	11 ± 7	C	
24	1	815.780(30)	12.74 d	^{140}Ba	3.9 ± 0.6	C	1.8
	1	815.780(30)	1.68 d	^{140}La	6.3 ± 0.6	I	
25	0	827.810(30)	1.47 d	^{82}Br	7.3 ± 0.6	I	0.8
	0	827.83(10)	6.47 h	^{82m}Rb	7 ± 11	C	
26	0	834.830(21)	312.5 d	^{54}Mn	10.1 ± 0.4	I	0.6
	0	834.030(30)	14.10 h	^{72}Ga	1.5 ± 0.7	C	
	0	833.990(30)	1.08 d	^{72}As	4.2 ± 0.5	C	
27	0	846.750(20)	2.58 h	^{56}Mn	6.7 ± 1.6	C	2.0
	0	847.025(25)	52.6 min	^{134}I	2.7 ± 1.2	C	
28	0	849.90(10)	23.35 h	^{96}Nb	13.2 ± 1.7	I	1.9
	0	849.86(4)	4.30 d	^{96}Tc	2.78 ± 0.19	I	
29	0	881.610(30)	32.77 d	^{84}Rb	6.9 ± 0.4	C	2.6
	0	881.01(5)	6.24 d	^{206}Bi	0.5 ± 0.5	C	
30	0	884.40(10)	18.4 min	^{104}Tc	14 ± 8	C	1.9
	0	884.090(25)	52.6 min	^{134}I	5.2 ± 0.9	C	
31	0	935.544(12)	5.59 d	^{52}Mn	1.9 ± 0.3	C	3.2
	0	934.44(10)	10.15 d	^{92m}Nd	0.6 ± 0.4	I	
32	0	983.500(10)	1.82 d	^{48}Sc	1.35 ± 0.19	I	0.2
	0	983.50(3)	15.97 d	^{48}V	3.52 ± 0.17	C	
33	0	1024.30(10)	9.52 h	^{91}Sr	15.0 ± 1.8	C	1.7
	0	1023.3(4)	5.76 d	^{120}Sb	10.8 ± 0.3	I	
34	0	1043.970(30)	1.47 d	^{82}Br	6.5 ± 0.6	I	2.8
	0	1044.08(10)	6.47 h	^{82m}Rb	2.5 ± 0.4fix	C	
35	0	1229.5(5)	4.45 min	^{118m}In	6.2 ± 1.3	C	
	0	1229.5(5)	5.00 h	^{118m}Sb	7.7 ± 0.6	I	
36	0	1312.100(30)	1.82 d	^{48}Sc	1.04 ± 0.10	I	0.2
	0	1312.00(3)	15.97 d	^{48}V	3.37 ± 0.14	C	
37	0	1317.47(5)	1.47 d	^{82}Br	8.0 ± 0.4	I	1.5
	0	1317.43(10)	6.47 h	^{82m}Rb	10 ± 12	C	
38	1	1596.17(6)	12.74 d	^{140}Ba	3.4 ± 0.3	C	5.2
	1	1596.17(6)	1.68 d	^{140}La	7.09 ± 0.27	I	
39	0	1691.00(4)	60.20 d	^{124}Sb	10.2 ± 0.6	I	1.1
	0	1691.02(4)	4.18 d	^{124}I	12.8 ± 0.8	I	

Note: C is cumulative cross section, while I is independent cross section.

Table 4. Cross sections for the formation of residual nuclei from a ^{237}Np target

Residual nuclei	Type of decay and cross section	Experimental cross section, mb	Theoretical cross section, mb	Residual nuclei	Type of decay and cross section	Experimental cross section, mb	Theoretical cross section, mb
^{48}Sc	I(β^-)	5.2 ± 1.5	–	^{122}Sb	C(β^-, ε)	18.4 ± 1.7	13.75 ± 0.22
^{48}V	C(β^+)	0.89 ± 0.2	–	^{124}Sb	C(β^-)	16.68 ± 2.0	13.08 ± 0.22
^{56}Mn	C(β^-)	25.35 ± 4.5	0.006 ± 0.006	^{126}Sb	C(β^-)	13.91 ± 2.0	17.74 ± 0.22
^{74}As	I($\beta^\pm$)	3.58 ± 0.5	1.16 ± 0.09	^{127}Sb	C(β^-)	14.74 ± 2.0	22.25 ± 0.22
^{83}Rb	C(ε)	6.13 ± 0.2	14.23 ± 0.1	^{128}Sb	C(β^-)	90.2 ± 1.3	19.66 ± 0.52
^{84}Rb	C($\beta^\pm$)	13.33 ± 0.3	20.25 ± 0.69	^{132}Te	C(β^-)	12.83 ± 3.0	3.2 ± 0.17
^{86}Rb	C(β^-, ε)	17.72 ± 2.0	31.19 ± 0.56	^{133m}Te	C(β^-)	18.44 ± 1.8	0.42 ± 0.006
^{85}Sr	C(ε)	9.6 ± 2.0	14.28 ± 0.18	^{124}I	I(β^+, ε)	17.29 ± 2.0	19.65 ± 0.31
^{91}Sr	C(β^-)	29.11 ± 3.0	25.02 ± 0.4	^{131}I	C(β^-)	20.36 ± 1.9	30.55 ± 0.49
^{87}Y	C(β^+, ε)	6.65 ± 0.1	7.04 ± 0.28	^{134}I	C(β^-)	12.86 ± 1.5	2.04 ± 0.14
^{88}Y	C(β^+, ε)	10.44 ± 0.9	17.7 ± 0.15	^{136}Cs	I(β^-)	9.14 ± 0.4	3.57 ± 0.15
^{89}Zr	C(β^+, ε)	4.62 ± 0.5	6.83 ± 0.19	^{138}Cs	C(β^-)	14.93 ± 1.4	0.49 ± 0.03
^{95}Zr	C(β^-)	59.24 ± 6.0	40.27 ± 0.07	^{131}Ba	C(β^+, ε)	71.09 ± 13	16.82 ± 0.22
^{95}Nb	C(β^-)	22.31 ± 2.0	49.25 ± 13	^{140}Ba	C(β^-)	22.92 ± 2.0	0.28 ± 0.03
^{99}Mo	C(β^-)	73.13 ± 6.0	36.33 ± 0.2	^{145}Eu	C(β^+, ε)	0.83 ± 0.01	0.025 ± 0.01
^{95m}Tc	C(β^+, ε)	2.32 ± 0.15	0.63 ± 0.03	^{146}Eu	I(β^+, ε)	4.2 ± 0.2	0.006 ± 0.006
^{96}Tc	C(β^+, ε)	5.65 ± 0.9	1.73 ± 0.13	^{147}Eu	C(β^+, ε)	1.93 ± 0.3	0.006 ± 0.006
^{103}Ru	C(β^-)	62.91 ± 1.0	22.39 ± 0.16	^{146}Gd	C(β^+, ε)	1.39 ± 0.02	-
^{105}Ru	C(β^-)	19.63 ± 2.0	12.32 ± 0.01	^{152}Tb	C(β^+, ε)	26.77 ± 3.0	-
^{106m}Rh	I(β^-)	55.32 ± 3.0	2.09 ± 0.05	^{171}Lu	C(β^+)	2.41	-
^{106m}Ag	Iβ^+)	6.18 ± 0.8	0.82 ± 0.036	^{185}Os	C(ε)	2.76 ± 0.1	-
^{110m}Ag	I(β^-, ε)	17.97 ± 2.0	2.05 ± 0.1	^{188}Pt	C(ε)	0.46 ± 0.08	-
^{115g}Cd	C(β^-)	64.61 ± 6.0	3.14 ± 0.16	^{206}Po	C(ε)	3.78 ± 0.7	2.65 ± 0.1
^{117m}Cd	C(β^-)	17.44 ± 4.0	1.27 ± 0.11	^{230}Pa	I(ε)	1.6 ± 0.15	23.54 ± 0.19
^{125}Sn	C(β^-)	6.59 ± 0.4	7.47 ± 0.22	^{234}Np	C(β^+, ε)	2.21 ± 0.4	75.0 ± 1.16
^{118m}Sb	I(β^+, ε)	10.36 ± 1.3	9.04 ± 0.14	^{238}Np	C(β^-)	15.77 ± 1.4	-
^{120}Sb	I(β^+, ε)	14.71 ± 1.6	13.68 ± 0.04				

calculate the coefficients A and B by the least squares method from several measurements $i = 1, 2, \ldots$ and determine the cross sections for genetically related residual nuclei as

$$\sigma_a = A\frac{\lambda_a(\lambda_b - \lambda_a)}{K_b(1 - \exp(-\lambda_a t_1))}, \quad (4)$$

$$\sigma_b = B\frac{\lambda_b}{K_b(1 - \exp(-\lambda_b t_1))} + A\frac{\lambda_a^2}{K_b\lambda_b(1 - \exp(-\lambda_a t_1))}, \quad (5)$$

where

$$K_b = N_p N_{\text{targ}}\varepsilon(E_\gamma)I_\gamma(E_\gamma, b). \quad (6)$$

If we replace the coefficient A by A' and the coefficient B by B', Eq. (2) will be valid for the independent decay of nuclei a' and b'. Then, the cross sections for the formation of residual nuclei can be found from the

Table 5. Cross sections for the formation of residual nuclei from a ^{241}Am target

Residual nuclei	Type of decay and cross section	Experimental cross section, mb	Theoretical cross section, mb	Residual nuclei	Type of decay and cross section	Experimental cross section, mb	Theoretical cross section, mb
^{48}Sc	I(β^-)	1.11 ± 0.09	–	^{108}Ph	I(β^-)	11.6 ± 1.5	6.0 ± 0.18
^{18}V	C(β^+)	3.44 ± 0.11	–	^{112}Pd	C(β^-)	21 ± 0.7	4.76 ± 0.20
^{52}V	C(β^-)	2.3 ± 0.6	–	^{106m}Ag	I(β^+, β^-)	2.5 ± 0.3	1.57 ± 0.05
^{52}Mn	C(β^+, ε)	1.74 ± 0.11	–	^{110m}Ag	I(β^-, ε)	11.6 ± 2.4	3.86 ± 0.12
^{54}Mn	I(ε)	10.1 ± 0.4	–	^{112}Ag	I(β^-)	20.4 ± 1.6	3.40 ± 0.26
^{56}Mn	C(β^-)	6.7 ± 1.6	–	^{115}Cd	C(β^-)	19.2 ± 0.9	6.70 ± 0.30
^{72}Ga	C(β^-)	1.5 ± 0.7	0.38 ± 0.09	^{117m}Cd	C(β^-)	6.9 ± 0.7	2.66 ± 0.05
^{72}As	C(β^+, ε)	4.2 ± 0.5	0.022	^{116m}In	I(β^-)	16.4 ± 0.8	5.44 ± 0.13
^{76}As	I(β^-)	4.5 ± 1.6	1.45 ± 0.06	^{117m}In	C(β^-)	21.4 ± 1.0	9.87 ± 0.35
^{76}Br	C(β^+)	0.6 ± 1.8	0.02 ± 0.01	^{118m}In	I(β^-)	6.5 ± 0.9	4.71 ± 0.21
^{82}Br	I(β^-)	8.0 ± 0.3	4.79 ± 0.13	^{118m}Sb	I(β^+, ε)	7.6 ± 0.6	8.72 ± 0.09
^{84}Br	C(β^-)	9.2 ± 1.4	1.16 ± 0.07	^{120}Sb	I(β^+, ε)	10.8 ± 0.3	12.9 ± 0.6
^{84m}Br	I(β^-)	2.7 ± 0.6	–	^{122}Sb	C(β^-, ε)	14.0 ± 0.5	13.2 ± 0.1
^{82m}Rb	C(β^+, ε)	2.1 ± 1.0	1.84 ± 0.08	^{124}Sb	C(β^-)	10.2 ± 0.4	13.4 ± 0.2
^{84}Rb	C(β^+, β^-)	6.9 ± 0.4	13.1 ± 0.2	^{126}Sb	C(β^-)	7.3 ± 0.7	9.56 ± 0.23
^{86}Rb	C(β^-)	2.02 ± 0.29	13.6 ± 0.1	^{127}Sb	C(β^-)	7.3 ± 0.5	9.07 ± 0.19
^{89}Rb	C(β^-)	11.1 ± 1.5	1.98 ± 0.13	^{128}Sb	C(β^-)	3.3 ± 1.0	3.51 ± 0.08
^{91}Sr	C(β^-)	15.0 ± 1.7	5.61 ± 0.20	^{119m}Te	I(β^+, ε)	3.73 ± 0.15	11.2 ± 0.30
^{92}Sr	C(β^-)	11.8 ± 0.5	3.03 ± 0.07	^{121}Te	C(β^+, ε)	5.3 ± 0.5	29.3 ± 0.4
^{93}Sr	C(β^-)	10.4 ± 2.2	1.09 ± 0.10	^{131m}Te	I(β^-)	6.5 ± 1.1	3.18 ± 0.13
^{84m}Y	I(β^+, ε)	3.1 ± 0.9	–	^{132}Te	C(β^-)	6.7 ± 0.5	1.30 ± 0.08
^{87}Y	C(β^+, ε)	4.40 ± 0.27	9.22 ± 0.22	^{124}I	I(β^+, ε)	10.6 ± 0.8	17.6 ± 0.2
^{88}Y	C(β^+, ε)	6.2 ± 0.4	20.5 ± 2.4	^{126}I	I(β^+, β^-)	6.8 ± 1.8	20.6 ± 0.5
^{91m}Y	C(β^-)	14 ± 4	28.9 ± 5.0	^{130}I	I(β^-)	10.0 ± 0.9	16.5 ± 0.5
^{95}Y	C(β^-)	17.4 ± 3.6	3.69 ± 0.22	^{131}I	C(β^-)	14.1 ± 0.9	20.2 ± 0.5
^{89}Zr	C(β^+, ε)	3.79 ± 0.27	11.0 ± 0.4	^{132}I	I(β^-)	8.3 ± 1.2	9.03 ± 0.14
^{95}Zr	C(β^-)	36.3 ± 1.7	18.3 ± 0.4	^{133}I	C(β^-)	9.3 ± 0.5	6.18 ± 0.14
^{97}Zr	C(β^-)	20.4 ± 0.4	7.22 ± 0.32	^{134}I	C(β^-)	4.3 ± 0.7	0.980 ± 0.07
^{92m}Nb	I(β^+, ε)	0.6 ± 0.4	9.42 ± 0.37	^{132}Cs	I(β^+, β^-)	6.2 ± 1.7	12.2 ± 0.4
^{95}Nb	C(β^-)	16.8 ± 2.0	41.8 ± 0.5	^{136}Cs	C(β^-)	6.6 ± 0.5	2.05 ± 0.04
^{96}Nb	I(β^-)	13.6 ± 0.3	18.8 ± 0.4	^{140}Ba	C(β^-)	3.64 ± 0.24	0.045 ± 0.03
^{97}Nb	C(β^-)	13.3 ± 0.8	24.4 ± 0.5	^{140}La	I(β^-)	7.4 ± 0.5	0.113 ± 0.03
^{98m}Nb	I(β^-)	13.9 ± 0.5	21.8 ± 0.4	^{135}Ce	C(β^+, ε)	17.0 ± 2.5	3.75 ± 0.05
^{99}Mo	C(β^-)	44.1 ± 1.3	42.2 ± 0.5	^{145}Eu	C(β^+, ε)	1.65 ± 0.19	0.045 ± 0.02
^{96}Tc	C(β^+, ε)	2.71 ± 0.28	3.40 ± 0.10	^{146}Eu	C(β^+, ε)	1.16 ± 0.17	0.022 ± 0.01
^{104}Tc	C(β^-)	22 ± 6	23.9 ± 0.3	^{154}Tb	C(β^+, ε)	13 ± 6	–
^{103}Ru	C(β^-)	62.9 ± 3.4	43.7 ± 0.5	^{156}Tb	C(ε)	1.7 ± 0.5	–
^{105}Ru	C(β^-)	33.8 ± 1.2	29.0 ± 0.7	^{198}Au	C(β^-)	1.33 ± 0.20	–
^{105}Rh	C(β^-)	77 ± 13	36.8 ± 0.7	^{206}Bi	C(ε)	1.21 ± 0.25	1.19 ± 0.20
^{106m}Rh	I(β^-)	15.0 ± 2.3	27.9 ± 0.3	^{240}Am	I(ε)	45.3 ± 0.8	–

relations

$$\sigma_a = A' \frac{\lambda_a}{K_b(1-\exp(-\lambda_a t_1))}, \quad (7)$$

$$\sigma_b = B' \frac{\lambda_b}{K_b(1-\exp(-\lambda_b t_1))}. \quad (8)$$

We also obtained a similar equation for triplet lines. The results of the analysis of the multiplet peaks are presented in Table 3. In some cases, we performed the fixed-value fitting of one of these cross sections (σ_a, σ_b, or σ_c). Small values of χ^2 prove correctness of the analysis of complex lines for residual nuclei.

About 60 residual nuclei from the ^{237}Np target and 80 residual nuclei from the ^{241}Am target were found. The results are demonstrated in Tables 4 and 5. The errors in the tables are the largest deviation of the given cross section from the average-weighted cross section for several measurements.

3. EXPERIMENTAL RESULTS AND DISCUSSION

The cross sections for the formation of nuclei from the ^{231}Np and ^{241}Am targets are shown in Tables 4 and 5. The final results for the ^{241}Am target are presented in Table 5. For 44 nuclei, the cross sections were determined from several γ transitions: the average-weighted value was found from two γ transitions in 33 cases, from three in seven cases, from four in one case, and from six in three cases (Table 2). Gamma transitions assigned to the decay of the residual nuclei ^{7}Be, ^{22}Na, ^{24}Na, ^{27}Mg, and ^{28}Al were detected. The first three nuclei could be formed in the $p + {}^{241}$Am and $p + {}^{27}$Al reactions (targets packed in the aluminum capsule). If we assume that they appear in the Al capsule, we obtain the following cross sections for their formation: $\sigma(^{7}\mathrm{Be}) = (5.5 \pm 0.5)$ mb, $\sigma(^{22}\mathrm{Na}) = (16.4 \pm 1.4)$ mb, and $\sigma(^{24}\mathrm{Na}) = (12.3 \pm 1.1)$ mb. These values agree within the errors with the known values of the cross sections for the formation of ^{7}Be, ^{22}Na, and ^{24}Na nuclei on an Al target exposed to 660-MeV protons [16]: $\sigma(^{7}\mathrm{Be}) = 5.0$ mb, $\sigma(^{22}\mathrm{Na}) = 15.0$ mb, and $\sigma(^{24}\mathrm{Na}) = 10.8$ mb. The residual nuclei ^{27}Mg and ^{28}Al could be produced in the (n,p) and (n,γ) reactions on an ^{27}Al target. Using the values presented in the literature for these reactions, $\sigma(\mathrm{Al}(n,p)^{27}\mathrm{Mg}) = 52.5$ mb [17] and $\sigma(\mathrm{al}(n,\gamma)^{28}\mathrm{Al}) = (230 \pm 5)$ mb [18], we can estimate the flux of the secondary and background neutrons in which the aluminum capsule finds itself (Fig. 1). It is 4×10^{12} n/min ($E_n > 4.5$ MeV) from the first reaction and 2×10^{11} n/min from the second one.

The tables show not only the type of the cross sections for the formation of the given residual nucleus (I is an independent cross section, while C is a cumulative cross section), but also the decay mode of this nucleus (β^- or β^+ decay or electron capture). For the sake of comparison, the theoretical cross sections calculated on the basis of the cascade–evaporation model are also presented [19].

The theoretical calculations were based on a simulation of 10^6 events. Since the calculation yields only independent cross sections for the residual nuclei, a correction was introduced for the experimental cumulative cross sections to make the comparison valid. The isobar chain ($A = \mathrm{const}$) of β-decaying n and m residual nuclei, together with their isomers (one nucleus is able to form more than one isomer), can be represented as follows:

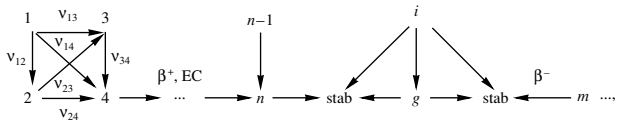

where odd numbers denote the formation of isomeric states of the residual nuclei whose ground states are denoted by even numbers; $\nu_{k,k+1}$, $\nu_{k,k+2}$, and $\nu_{k,k+3}$ are the branching ratios for the decay of the isomeric state (k is odd); and $\nu_{l,l+1}$ and $\nu_{l,l+2}$ (l is even) are the branching ratios for the decay of the ground states. The cumulative yield of the nth residual nucleus is calculated by the generalized formula that follows from the physical interpretation of the independent and cumulative yields:

$$\sigma_n^{\mathrm{cum}} = \sigma_n^{\mathrm{ind}} + \sum_{m=1}^{n-1} B_{mn}\sigma_m^{\mathrm{ind}}, \quad (9)$$

$$B_{mn} = \nu_{mn} + \sum_{l_1>m}^{n-1} \nu_{ml_1}\nu_{l_1 n} + \sum_{l_2>l_1}^{n-1}\sum_{l_1>m}^{n-2} \nu_{ml_1}\nu_{l_1 l_2}\nu_{l_2 n} + \ldots.$$

Here, $\nu_{mn} \equiv 0$ for odd m if $n - m > 3$ or for even m if $n - m > 2$. For even isobars, there exists a nucleus g (and its isomer i) near the stability line that disintegrates through β^- decay, β^+ decay, and electron capture. The formation of such nuclei is characterized by independent cross sections. Tables 4 and 5 demonstrate the theoretical cross sections for the ground states of the residual nuclei. The calculation accuracy parameter (deviation factor) could be the mean ratio

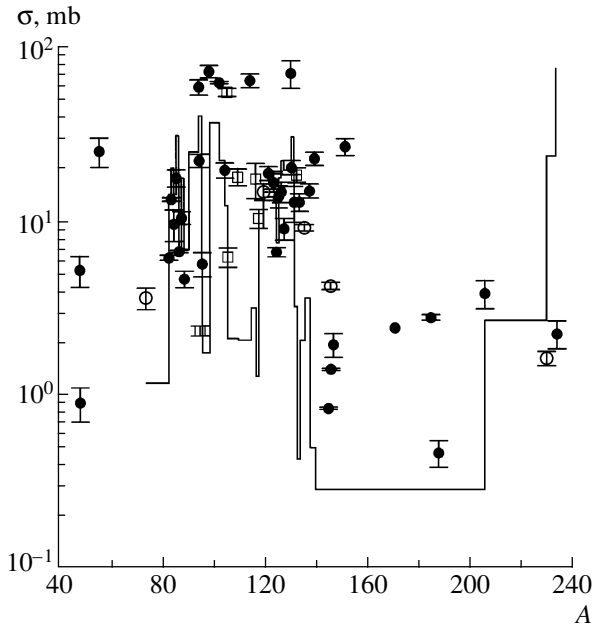

Fig. 3. Dependence of the cross sections for the formation of residual nuclei on the mass number of these nuclei for the ^{237}Np target. Points represent experimental data: (●) cumulative cross section, (○) independent cross section, and (□) isomeric cross section. The histogram corresponds to the calculations based on the cascade–evaporation model.

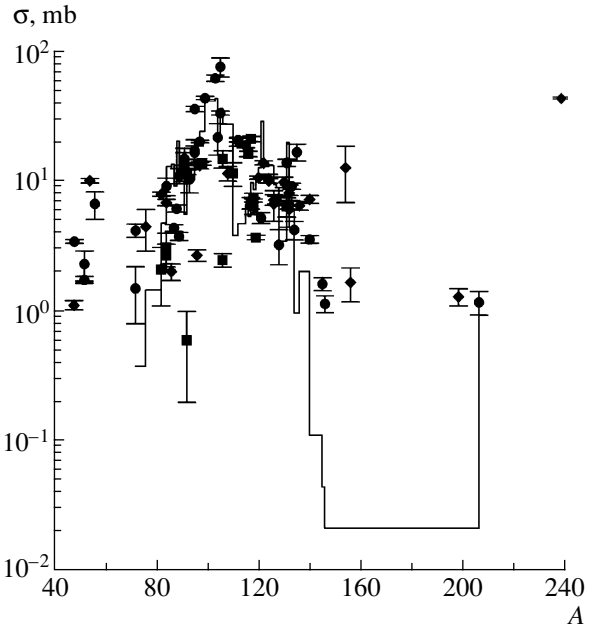

Fig. 4. Dependence of the cross sections for the formation of residual nuclei on their mass number for an ^{241}Am target. Points represent experimental data: (⧫) independent cross section, (■) isomeric cross section, and (●) cumulative cross section. The histogram corresponds to the calculations based on the cascade–evaporation model.

of the calculated cross section $\sigma_{\mathrm{calc}}(i)$ to the experimental cross section $\sigma_{\mathrm{expt}}(i)$; that is,

$$\langle H\rangle = 10^{\sqrt{\langle(\log[\sigma_{\mathrm{calc}}(i)/\sigma_{\mathrm{expt}}(i)])^2\rangle}}, \qquad (10)$$

with the standard deviation being $S(\langle H\rangle) = 10^{\sqrt{a}}$, where

$$a = \left\langle \left[\left| \log\left(\frac{\sigma_{\mathrm{calc}}(i)}{\sigma_{\mathrm{expt}}(i)}\right)\right| - \log(\langle H\rangle)\right]^2 \right\rangle. \qquad (11)$$

On the basis of the data in Tables 4 and 5, we obtain

^{237}Np $\quad \langle H\rangle = 12.1, \quad S(\langle H\rangle) = 7.6;$

^{241}Am $\quad \langle H\rangle = 4.9, \quad S(\langle H\rangle) = 3.3.$

Such a comparison with theoretical calculations agrees with a similar one in [6]. We hope that our experimental results will help to improve theoretical models for such reactions.

Figures 3 and 4 show the cross sections for the formation of residual nuclei versus their mass number. The residual nuclei are seen to be fission products [20]. However, the nuclei with $A > 160$, i.e., with mass numbers close to the target mass number, were formed only by spallation. As is seen from Tables 4 and 5 and from the figures, residual nuclei with a half-life from a few minutes to a few months dominate. They decay to stable isotopes. The cross sections for some residual nuclei—^{95m}Tc, ^{106m}Ag, ^{110m}Ag, and ^{118m}Sb—are small; that is why they became an exception to the basic dependence. This is due to the fact that only isomer states of these residual nuclei were recorded. In [21], it was shown that, for proton–nucleus reactions in a target from tin isotopes, the isomeric ratio of the cross section for high-spin-state formation to that for the formation of a low-spin state depends on the number of emitted neutrons and can be as large as 6 to 7. For example, it is $\sigma(^{95g}\mathrm{Tc}(9/2^+))/\sigma(^{95m}\mathrm{Tc}(1/2^-)) \sim 7$ for the ^{95}Tc nucleus. Therefore, we can conclude that the cross sections for the isomeric nuclei dropping out of the basic dependence (Figs. 3, 4) can be increased by the cross section for the ground state; then, these points could fall on the curve too. Analyzing the types of formation of residual nuclei, we can see that the experimental numbers of neutron-rich and neutron-deficient nuclei are equal. Our results were compared with the results of [5]. The comparison shows that, because of the great intensity of our beam [three orders of magnitude higher ($1.3 \times 10^{16} p$/h)], the number of residual nuclei is larger than in [5].

ACKNOWLEDGMENTS

We are grateful to the personnel of the phasotron for providing good parameters of the beams. We also

thank the Directorate of the Laboratory of High Energies of JINR for providing us with radioactive targets.

REFERENCES

1. P. Kusters, Atomwirtschaft **35**, 287 (1990).
2. W. Gudowski, Nucl. Phys. A **654**, 436 (1999).
3. Yu. P. Sivintchev, Atomic Technique out of Boundary **2**, 1 (1992); **11**, 11 (1992).
4. A. S. Nikiforov, At. Energ. **70**, 188 (1991).
5. M. I. Krivopustov *et al.*, Preprint No. E1-97-59, OIYaI (Joint Inst. for Nuclear Research, Dubna, 1997); J. Radioanal. Nucl. Chem. **222**, 267 (1997); M. Ochs *et al.*, Preprint No. E1-99-1, OIYaI (Joint Inst. for Nuclear Research, Dubna, 1999).
6. V. F. Batiaev, Candidate's Dissertation (Joint Inst. for Nuclear Research, Dubna, 1999).
7. Yu. E. Titarenko *et al.*, Nucl. Instrum. Methods Phys. Res. A **414**, 73 (1998).
8. T. Nishida and Y. Nakahara, Kerntechnik **50**, 3 (1987).
9. L. Moens *et al.*, Nucl. Instrum. Methods **187**, 451 (1981).
10. J. B. Cumming, Annu. Rev. Nucl. Sci. **13**, 261 (1963).
11. R. Michel *et al.*, Nucl. Instrum. Methods Phys. Res. B **103**, 185 (1995).
12. Yu. V. Aleksandrov *et al.*, in *Abstracts of the XLVI Meeting on Nuclear Spectroscopy and Nuclear Structure, Moscow, 1996,* p. 221.
13. J. Frana, Acta Polytech. — Nukleonika **38**, 127 (1998).
14. N. Reus and W. Westmeier, At. Data Nucl. Data Tables **29**, 1 (1983).
15. J. Adam *et al.*, Preprint No. P10-2000-28, OIYaI (Joint Inst. for Nuclear Research, Dubna, 2000).
16. K. Michel and P. Nagel, NEA/OECD, NSC/DOC(97)-1 (Paris, 1997).
17. H. R. Heydegger, A. L. Turkevich, A. van Ginneken, and P. N. Walpole, Phys. Rev. C **14**, 1506 (1976).
18. S. S. Lomakin, V. N. Petrov, and P. S. Samoilov, *Radiometry of Neutrons by the Activation Method* (Moscow, 1983).
19. A. Polanski, A. N. Sosnin, and V. D. Toneev, Preprint No. E2-91-562, OIYaI (Joint Inst. for Nuclear Research, Dubna, 1991); F. G. Zheregy and J. J. Musulmanbekov, Preprint No. B3-10-84-873, OIYaI (Joint Inst. for Nuclear Research, Dubna, 1984).
20. V. S. Barashenkov and V. D. Toneev, *Interactions of High-Energy Particles and Nuclei with Nuclei* (Atomizdat, Moscow, 1972), p. 568.
21. V. E. Alexandryan *et al.*, Yad. Fiz. **59**, 592 (1996) [Phys. At. Nucl. **59**, 560 (1996)].

Physics of Atomic Nuclei, Vol. 65, No. 5, 2002, pp. 776–784. Translated from Yadernaya Fizika, Vol. 65, No. 5, 2002, pp. 810–818.

NUCLEI
Experiment

Isomeric Ratios of the Cross Sections for Sn(p, $xpyn$)X Reactions

V. É. Aleksandryan, J. Adam[1),2)], A. R. Balabekyan[1)], A. S. Danagulyan, V. G. Kalinnikov[1)], M. I. Krivopustov[1)], and G. Musulmanbekov[1)]

Yerevan State University, ul. A. Manukiana 1, Yerevan, 375049 Armenia

Received September 25, 2000; in final form, August 3, 2001

Abstract—In proton–nucleus reactions, the ratios of the cross sections for 18 isomeric pairs were measured by the induced-activity method as functions of the initial-proton energy and of the number of emitted nucleons. The isotopic effect and the cross sections for charge-exchange reactions are discussed. The experimental values of the cross sections for disintegration reactions like $(p, xpyn)$ are compared with the theoretical values calculated on the basis of the cascade–evaporation model. © *2002 MAIK "Nauka/Interperiodica".*

1. INTRODUCTION

The present article reports on part of a series of studies that we performed using 0.66-, 1-, and 8.1-GeV proton beams in irradiating targets from enriched tin isotopes [1, 2]. The use of a high-energy proton beam ($E_p = 8.1$ GeV) enabled us to obtain new data on the mechanism of formation of light ($A < 40$) and medium-mass ($60 < A < 80$) nuclei. The formation of these nuclei is described by the intranuclear-cascade model combined with the statistical multifragmentation model (SSM) [1, 2]. Our experimental data are compared with the results obtained on the basis of the cascade–evaporation model [3] and on the basis of the SSM, where a liquid–gas phase transition is taken into account for a hot excited nucleus formed after the completion of the cascade [4].

In addition to the formation of light and medium-mass nuclei, these investigations recorded a large number of nuclei featuring isomeric states. Such isomeric pairs obtained at high energies of incident particles were studied in [5–8]. In this article, we discuss the energy dependence of the isomeric ratios of the cross sections and their dependence on the number of emitted nucleons.

2. EXPERIMENTAL PROCEDURE

Targets from the enriched tin isotopes ^{112}Sn (92.6%), ^{118}Sn (98.7%), ^{120}Sn (99.6%), and ^{124}Sn (95.9%) were irradiated by proton beams accelerated to energies of 1 or 8.1 GeV at the synchrophasotron of the Laboratory of High Energies at the Joint Institute for Nuclear Research (JINR, Dubna). The beam intensities amounted to 4.97×10^{12} or 2.27×10^{13} proton/h, respectively. The reaction $^{27}\mathrm{Al}(p, 3pn)^{24}\mathrm{Na}$, whose cross sections at the above energy values are known to be 10.8 ± 0.8 mb [9] and 8.65 ± 0.05 mb [10], is used to monitor the beams. After the lapse of some time from irradiation, the γ activity induced in the targets was measured by γ spectrometers equipped with HpGe detectors, the source–detector distances being 8, 15, and 26 cm in these measurements. The regular measurements of the γ spectra of the irradiated targets were performed for one year in order to single out long-lived residual nuclei. The residual nuclei were identified according to characteristic γ lines and known half-lives [11]. The γ spectra were processed by means of the DEIMOS code [12].

We obtained the production cross sections for 18 residual nuclei in the ground and in an isomeric state. The results are quoted in the tables.

3. EXPERIMENTAL RESULTS AND DISCUSSION

For all four target species, Table 1 displays the experimental values of the cross sections for residual nuclei from ^{123}Sn to ^{84}Rb and the cross sections for light isotopes ^{44}Sc and ^{52}Mn. For almost all residual nuclei, we obtained the cross-section values at $E_p =$ 1 and 8.1 GeV. Nuclei of the ^{44}Sc and ^{52}Mn isotopes were formed only at $E_p = 8.1$ GeV, while the isomeric state ^{52m}Mn ($T_{1/2} = 21.1$ min) was detected only with the ^{118}Sn target. The table gives types of cross sections, the independent (I) and the cumulative (C) one, along with the decay types (β^-, β^+) and spin–parities (I^P). For the errors in the cross-section values, we took the largest deviation of the cross sections

[1)]Joint Institute for Nuclear Research, Dubna, Moscow oblast, 141980 Russia

[2)]Nuclear Physics Institute, CZ-25068 Řež, Czech Republic

Table 1. Cross sections for the formation of residual nuclei, σ (in mb), for ^{112,118,120,124}Sn targets at $E_p = 1$ and 8.1 GeV

Residual nucleus	Cross-section type	I^P	^{112}Sn		^{118}Sn			^{120}Sn			^{124}Sn		
			8.1 GeV		1 GeV	8.1 GeV		1 GeV	8.1 GeV		1 GeV	8.1 GeV	
			Expt.	Calc.	Expt.	Expt.	Calc.	Expt.	Expt.	Calc.	Expt.	Expt.	Calc.
^{123m}Sn	I$^-$	$3/2^+$									35 ± 1	52.7 ± 1.5	
^{123g}Sn	I$^-$	$11/2^-$											
^{124}Sb	I$^-$	3^-									1.2 ± 0.1	2.4 ± 0.3	
^{122}Sb	I$^-$	2^-									2.7 ± 0.3	4.4 ± 0.5	
^{120}Sb	I$^+$	8^-						0.43 ± 0.40	1.10 ± 0.12		1.37 ± 0.20	1.9 ± 0.3	
^{118}Sb	I$^+$	8^-			0.46 ± 0.03	1.4 ± 0.3		1.16 ± 0.10	1.9 ± 0.2		1.06 ± 0.15	1.2 ± 0.1	
^{117}Sb	I$^+$	$5/2^+$			2.7 ± 0.4	7.5 ± 1.5	22.6	2.2 ± 0.2	3.2 ± 0.3				
^{116m}Sb	I$^+$	8^-			1.00 ± 0.15	2.4 ± 0.2	7.447	1.15 ± 0.02	1.07 ± 0.10		0.84 ± 0.14	0.44 ± 0.05	
^{116g}Sb	I$^+$	3^+			1.8 ± 0.2	4.6 ± 0.6		1.00 ± 0.15	1.00 ± 0.15				
^{115}Sb	I$^+$	$5/2^+$			2.2 ± 0.4	4.05 ± 0.25	8.766	2.0 ± 0.2	1.60 ± 0.15		0.78 ± 0.08	0.62 ± 0.05	
^{117m}Sn	I	$11/2^-$			16.3 ± 1.5	41.8 ± 2.5	0.847	11.5 ± 3.0	17.3 ± 2.0	26.875	11 ± 1	12.6 ± 1.2	9.73
^{113g}Sn	C$^+$	$1/2^-$			9.2 ± 1.0	19 ± 2	2.275	10 ± 1	6.5 ± 1.0	9.625	5.5 ± 1.0	3.6 ± 0.5	4.54
^{110}Sn	C$^+$	0^+	32.2 ± 2.0	43.47	2.7 ± 0.2	2.9 ± 0.3	4.4	1.7 ± 0.1	1.0 ± 0.1	2.375	0.75 ± 0.06	0.40 ± 0.04	1.135
^{117g}In	I$^-$	$9/2^+$			8.3 ± 0.6	14.3 ± 1.0	5.398	5.5 ± 0.5	14.3 ± 0.5	27	3.85 ± 0.40	10.4 ± 1.4	14.15
^{117m}In	I$^-$	$1/2^-$			3.6 ± 0.2	6.0 ± 0.6		2.1 ± 0.3	2.36 ± 0.16		0.95 ± 0.20	1.20 ± 0.25	
^{116m}In	I$^-$	5^+			7.25 ± 0.70	13 ± 1	30.7	10 ± 1	11.4 ± 1.0	17.68	9.24 ± 0.70	10.1 ± 0.3	11.15
^{114m}In	I$^-$	5^+			15.1 ± 1.5	31.2 ± 2.8	18.62	17.8 ± 0.4	16 ± 2	16.63	16.3 ± 1.5	15.3 ± 0.5	10.54
^{113g}In	I	$1/2^-$			1.8 ± 0.1	20.5 ± 0.15	18.55	1.2 ± 0.2	1.7 ± 0.2	16.75	0.74 ± 0.06	0.75 ± 0.03	9.61
^{111}In	C$^+$	$9/2^+$	103.6 ± 10.0	63.38	18.6 ± 1.0	26.8 ± 2.0	14	16.1 ± 0.9	12.8 ± 2.0	13.38	10.1 ± 1.0	6.5 ± 0.4	6.975
^{110g}In	I$^+$	7^+	11.1 ± 1.0	34.23	7.2 ± 0.2	8.7 ± 0.5	10.53	6.5 ± 0.5	5.4 ± 0.2	6.75	3.85 ± 0.30	2.6 ± 0.2	3.447
^{110m}In	I$^+$	2^+	13.8 ± 1.0		1.8 ± 0.2	3.85 ± 0.30		2.1 ± 0.3	2.25 ± 0.20		0.95 ± 0.20	1.10 ± 0.78	
^{109}In	C$^+$	$9/2^+$	45.7 ± 2.0	32.95	10.2 ± 0.2	11.1 ± 0.9	7.175	7.3 ± 0.4	6.40 ± 0.65	7.25	3.6 ± 0.2	2.60 ± 0.25	2.595
^{108m}In	I$^+$	6^+	2.8 ± 1.0	10.85	3.6 ± 0.3	3.2 ± 0.4	1.9	3.03 ± 0.15	1.9 ± 0.2	1.375	1.45 ± 0.20	0.72 ± 0.20	0.487
^{108g}In	C$^+$	1^-	12.9 ± 1.3		1.5 ± 0.2	1.02 ± 0.17		0.82 ± 0.08	0.58 ± 0.15		0.40 ± 0.08	0.28 ± 0.13	
^{107}In	C$^+$	$9/2^+$	17.5 ± 1.0	11.25	2.6 ± 0.2	2.3 ± 0.2	1.675	2.0 ± 0.1	1.20 ± 0.04	1		0.35 ± 0.10	0.487
^{117m}Cd	C$^-$	$11/2^-$						1.9 ± 0.2	1.42 ± 0.26	9.375	3.4 ± 0.3	4.1 ± 0.5	8.8
^{117g}Cd	C$^-$	$1/2^+$						0.93 ± 0.03	0.98 ± 0.22		1.13 ± 0.15	1.30 ± 0.15	

Table 1. (Contd.)

Residual nucleus	Cross-section type	I^P	^{112}Sn		^{118}Sn			^{120}Sn			^{124}Sn		
			8.1 GeV		1 GeV	8.1 GeV		1 GeV	8.1 GeV		1 GeV	8.1 GeV	
			Expt.	Calc.	Expt.	Expt.	Calc.	Expt.	Expt.	Calc.	Expt.	Expt.	Calc.
^{115g}Cd	C^-	$1/2^+$			0.91 ± 0.90	1.26 ± 0.10	7.65	1.9 ± 0.1	2.8 ± 0.3	10.38	4.1 ± 0.4	4.5 ± 0.6	9.8
^{111m}Cd	I	$11/2^-$			4.8 ± 0.3	7.5 ± 0.5	12.5	5.9 ± 0.4	7.1 ± 0.7	16.5	7.0 ± 0.7	5.5 ± 0.2	13.18
^{104}Cd	C^+	0^+	10.5 ± 1.1	14.57	1.8 ± 0.2	1.71 ± 0.20	2.35	1.5 ± 0.3	0.94 ± 0.08	2.5	0.7 ± 0.2	0.48 ± 0.17	0.73
^{1113}Ag	C^-	$1/2^-$			(1.06 ± 0.13)[a)]				2.1 ± 0.2	4.25	4.7 ± 0.5	5.7 ± 1.0	5.8
^{112}Ag	I^-	2^-			0.82 ± 0.08	0.5 ± 0.1	2.425	2.4 ± 0.6	2.6 ± 0.2	4.375	5.6 ± 0.8	(6.3 ± 0.7)[a)]	5.31
^{111}Ag	I^-	$1/2^-$				4.7 ± 0.2	3.85	3.9 ± 0.4	4.8 ± 0.2	6.125	7.6 ± 0.8	9.1 ± 1.1	5.92
^{110m}Ag	I^-	6^-			1.6 ± 0.2	2.75 ± 0.30	3.975	3.7 ± 0.4	3.8 ± 0.5	5.625	5.7 ± 0.7	5.1 ± 0.5	5.89
^{106m}Ag	I^{+-}	6^-	3.75 ± 0.30	4.85	7.5 ± 0.7	8.4 ± 1.0	8.85	6.9 ± 1.0	6.5 ± 0.7	9.125	7.0 ± 0.5	4.9 ± 0.5	7.42
^{105g}Ag	C^+	$1/2^-$	31.7 ± 0.3	10.55	21 ± 2	22.8 ± 1.0	9.65	18.6 ± 0.8	12.4 ± 1.5	9.375	11.5 ± 1.0	7.8 ± 1.2	4.825
^{104g}Ag	I^+	5^+	15.8 ± 1.0	8.875	9.0 ± 0.9	7.1 ± 0.3	5.4	7.9 ± 0.5	5.3 ± 0.4	5.875	4.8 ± 0.2	2.8 ± 0.1	2.433
^{104m}Ag	I^+	2^+	12.5 ± 1.2		2.75 ± 0.45	3.0 ± 0.3		3.2 ± 0.3	1.93 ± 0.10		1.3 ± 0.3	1.0 ± 0.1	
^{103}Ag	C^+	$7/2^+$	17.8 ± 2.0	13.2	7.0 ± 0.4	5.6 ± 1.0	4.725	5.5 ± 0.6	3.5 ± 0.2	3.975	2.0 ± 0.25	1.68 ± 0.16	1.094
^{112}Pd	C^-	0^+			0.27 ± 0.03	0.72 ± 0.10	0.4		1.94 ± 0.19	1.125	0.8 ± 0.1	1.7 ± 0.2	2.392
^{101}Pd	C^+	$5/2^+$	12.0 ± 1.2	22.4	9.45 ± 0.80	10.0 ± 1.5	11.62	7.7 ± 1.0	4.9 ± 0.5	6.5	5.1 ± 0.8	3.8 ± 0.7	4.177
^{100}Pd	C^+	0^+	12.1 ± 1.3	18.2	7.7 ± 0.8	6.4 ± 0.8	6.92	5.9 ± 0.3	3.9 ± 0.1	5.5	3.0 ± 0.3	1.48 ± 0.06	1.95
^{99}Pd	C^+	$5/2^+$			1.2 ± 0.1	0.77 ± 0.08	2.17	1.18 ± 0.20	0.46 ± 0.05	1.625	0.70 ± 0.08	0.23 ± 0.02	0.32
^{102g}Rh	I^{+-}	6^+	(2.61 ± 0.39)[a)]	1.525	4.2 ± 1.2	5.8 ± 1.0	5.275		4.7 ± 0.4	6.625	6.7 ± 0.7	3.4 ± 0.6	5.8
^{102m}Rh	I^{+-}	2^-	(1.0 ± 0.1)[a)]		1.4 ± 0.3	2.5 ± 0.7			1.9 ± 0.2			1.25 ± 0.20	
^{101m}Rh	I^+	$9/2^+$	(13.4 ± 1.0)[a)]	5.275	6 ± 1	6.4 ± 0.7	8.325	9.2 ± 0.9	8 ± 1	8.35	6.3 ± 0.8	3.8 ± 0.5	6.2
^{101g}Rh	I^+	$1/2^-$	(4.5 ± 0.5)[a)]		5.1 ± 0.6	5.26 ± 0.60		5.1 ± 0.6	4.1 ± 0.4		4.6 ± 0.5	2.75 ± 0.30	
^{100}Rh	I^+	1^-	(19.2 ± 2.0)[a)]	7.55	8.6 ± 1.4	8.7 ± 0.9	7.825	10.3 ± 1.3	6.26 ± 0.70	7	7.2 ± 0.8	5.0 ± 0.5	4.42
^{99m}Rh	I^+	$9/2^+$	$(14.9 \pm 1.5)^*$	10.8	9.1 ± 1.0	8.4 ± 1.2	6.575	7.2 ± 0.4	5.5 ± 0.5	7.125	4.94 ± 0.35	3.0 ± 0.2	2.76
^{99g}Rh	I^+	$1/2^-$	3.0 ± 0.4		1.48 ± 0.20	1.75 ± 0.30		2.0 ± 0.2	1.30 ± 0.13		0.9 ± 0.2	0.45 ± 0.04	
^{103}Ru	C^-	$3/2^+$	0.34 ± 0.02	0.075	0.50 ± 0.05	0.86 ± 0.07	1.325	1.5 ± 0.1	1.5 ± 0.2	2.75	3.3 ± 0.4	4.1 ± 0.4	3.57
^{97}Ru	I^+	$5/2^+$	18.0 ± 1.5	23.2	15.7 ± 2.0	10.0 ± 0.9	14.22	11.5 ± 2.1	9.9 ± 1.0	13.125	8.8 ± 0.9	5.7 ± 0.4	7.02
^{95}Ru	C^+	$5/2^+$	5.14 ± 0.20	11.25	4.5 ± 0.3	1.66 ± 0.15	3.83	3.1 ± 0.4	1.44 ± 0.20	2	1.34 ± 0.39	0.57 ± 0.20	1.1354
^{94}Ru	C^+	0^+	3.6 ± 0.4	4.175	1.5 ± 0.3	1.2 ± 0.2	0.825	0.98 ± 0.03	0.71 ± 0.07		0.78 ± 0.22	0.65 ± 0.13	0.122

Table 1. (Contd.)

Residual nucleus	Cross-section type	I^P	^{112}Sn		^{118}Sn			^{120}Sn			^{124}Sn		
			8.1 GeV		1 GeV	8.1 GeV		1 GeV	8.1 GeV		1 GeV	8.1 GeV	
			Expt.	Calc.	Expt.	Expt.	Calc.	Expt.	Expt.	Calc.	Expt.	Expt.	Calc.
^{96}Tc	I^+	7^+	3.86 ± 0.41	5.45	7.2 ± 0.8	8.4 ± 1.6	7.275	6.4 ± 0.8	5.6 ± 0.8	9.375	6.5 ± 0.6	4.4 ± 0.5	5.6
^{95g}Tc	I^+	$9/2^+$	10.6 ± 1.3	11.45	8.3 ± 0.6	10.6 ± 1.0	8.6	8.4 ± 0.6	7.5 ± 1.0	8.75	5.35 ± 0.30	5.88 ± 0.60	5.39
^{95m}Tc	I^+	$1/2^-$	1.27 ± 0.17		1.05 ± 0.06	1.25 ± 0.04		0.98 ± 0.07	0.67 ± 0.07		0.47 ± 0.05	0.47 ± 0.05	
^{94m}Tc	I^+	7^+	8.7 ± 0.9	11.325	7.14 ± 0.40	7.2 ± 0.7	5.9	6.4 ± 0.3	5.4 ± 0.5	5.5	3.6 ± 0.4	3.2 ± 0.3	2.47
^{94g}Tc	I^+	2^+	1.86 ± 0.22		1.4 ± 0.3	1.1 ± 0.1		0.76 ± 0.15	0.72 ± 0.10		0.30 ± 0.05	0.28 ± 0.03	
^{93g}Tc	I^+	$9/2^+$	7.96 ± 0.60	7.25	5.14 ± 0.50	4.3 ± 1.0	2.625	4.6 ± 0.5	3.50 ± 0.35	1.625	2.40 ± 0.35	1.6 ± 0.4	0.69
^{93m}Tc	C^+	$1/2^-$			2.1^*	1.00 ± 0.25		0.6 ± 0.1					
^{96}Nb	I^-	7^+	0.41 ± 0.03	0.025	0.39	0.5 ± 0.07	0.35	0.46 ± 0.04	0.72 ± 0.14	0.75	0.97 ± 0.10	1.0 ± 0.12	0.65
^{95g}Nb	C^-	$9/2^+$	$(0.13 \pm 0.03)^{a)}$	0.1	0.72 ± 0.11	1.0 ± 0.1	0.825	0.84 ± 0.04	1.35 ± 0.43	0.625	1.2 ± 0.2	1.6 ± 0.2	1.298
^{95m}Nb	I^-	$1/2^-$	$(0.20 \pm 0.02)^{a)}$		0.88 ± 0.15	0.80 ± 0.08							
^{90}Nb	I^+	8^+	13 ± 1	6.225	9.5 ± 1.0	10.1 ± 1.1	2.95	9.1 ± 0.9	8.4 ± 0.8	2.625	5.15 ± 0.35	6.6 ± 0.6	1.176
^{93m}Mo	I^+	$21/2^+$	2.2 ± 0.1	15.05	3.8 ± 0.4	3.96 ± 0.20	13.425	3.56 ± 0.30	3.66 ± 0.20	12.65	3.4 ± 0.3	2.93 ± 0.15	7.99
^{90}Mo	C^+	0^+	4.9 ± 0.5	1.321	2.1 ± 0.1	2.2 ± 0.2	0.275	1.54 ± 0.20	1.58 ± 0.10	0.125	0.85 ± 0.15	0.85 ± 0.03	0.041
^{87}Zr	C^+	$9/2^+$	$(3.8 \pm 0.5)^{a)}$	4.05		9.3 ± 1.1	1.6	5.2 ± 0.5	6.7 ± 0.6	0.875		4.52 ± 0.50	0.81
^{86}Zr	C^+	0^+	6.57 ± 0.60	1.725	2.7 ± 0.3	4.0 ± 0.2	0.525	2.0 ± 0.2	2.9 ± 0.2	0.625	1.12 ± 0.20	1.7 ± 0.1	0.081
^{87m}Y	I^+	$9/2^+$	$(14.3 \pm 1.5)^{a)*}$	14.375	$(9.9 \pm 1.0)^*$	5.8 ± 0.8	10.6	4.1	6.4 ± 0.6	9.125		5.17 ± 0.60	5.64
^{87g}Y	I^+	$1/2^-$			5.55 ± 0.60	3.4 ± 0.6		1.2 ± 0.3	1.8 ± 0.2			1.8 ± 0.2	
^{86m}Y	I	8^+	5.65 ± 0.20	6.5	4.1 ± 0.4	5.8 ± 0.2	2.925	3.45 ± 0.20	5.17 ± 0.25	2.36	2.0 ± 0.2	4.1 ± 0.2	1.014
^{86g}Y	I^+	4^+	1.85 ± 0.25		1.2 ± 0.1	2.80 ± 0.38		1.17 ± 0.20	2.0 ± 0.2		0.74 ± 0.22	1.47 ± 0.12	
^{84m}Rb	I	6^-		2.725		1.45 ± 0.44	3.575		1.57 ± 0.15	4.5		2.23 ± 0.15	3.6
^{84g}Rb	I^{+-}	2^-	$(1.4 \pm 0.1)^*$			1.75 ± 0.53			1.57 ± 0.15			1.74 ± 0.20	
^{52g}Mn	I^+	6^+	1.95 ± 0.15			1.74 ± 0.20			1.33 ± 0.33			1.04 ± 0.10	
^{52m}Mn	I^+	2^+				0.41 ± 0.05							
^{44m}Sc	I^+	6^+	2.3 ± 0.2			1.95 ± 0.20			2.1 ± 0.3			1.46 ± 0.20	
^{44g}Sc	I^+	2^+	1.3 ± 0.3			0.93 ± 0.20			1.0 ± 0.1			0.69 ± 0.20	

[a)] $E_p = 0.66$ GeV.

* Cumulative.

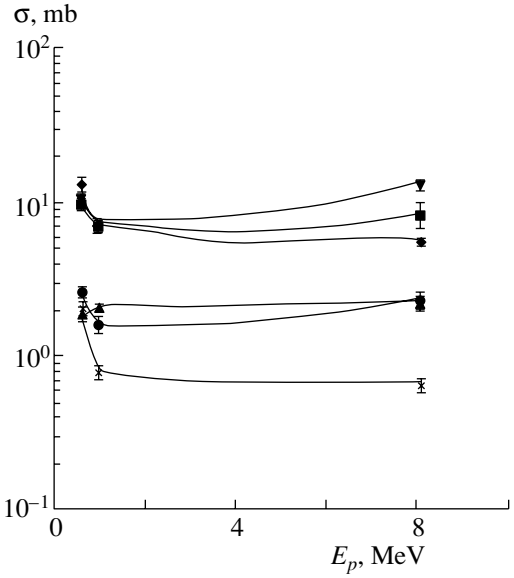

Fig. 1. Cross sections for certain reactions versus the proton energy: (●) ^{120m}Sb, (♦) ^{106m}Ag, (▲) ^{90}Mo, (▼) ^{116m}In, (■) ^{96}Tc, and (×) ^{115}Sb.

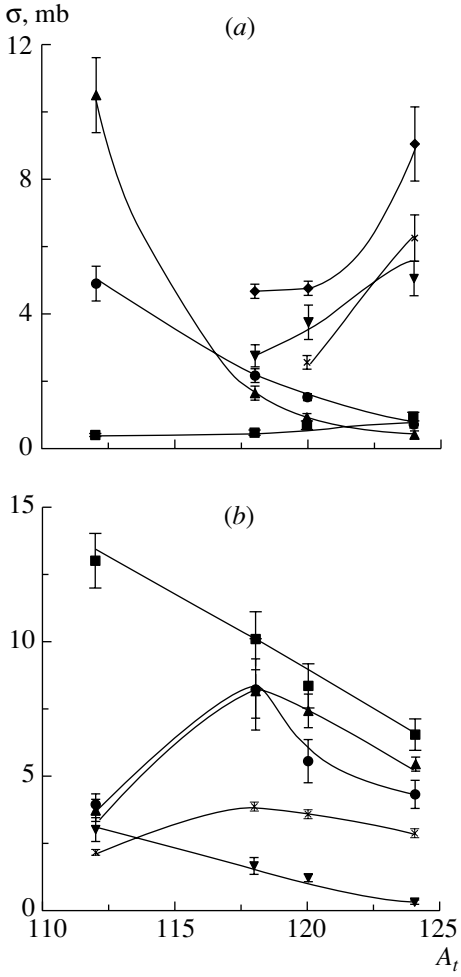

Fig. 2. Cross sections for the formation of residual nuclei versus the target mass number A_t ($E_p = 8.1$ GeV): (*a*) nuclei undergoing β^+ and β^- decays [(●) ^{90}Mo, (▲) ^{104}Cd,(■) ^{96}Nb, (×) ^{112}Ag, (♦) ^{111}Ag, and (▼) ^{110m}Ag] and (*b*) high- and low-spin nuclei [(●) ^{96}Tc, (▲) ^{106m}Ag, (×) ^{93m}Mo, (■)^{90}Nb, and (▼) ^{99g}Rh].

in various measurements of the γ spectra from the mean cross section; these include statistical errors in determining the efficiencies of the detectors, the number of particles in the beam, and the number of nuclei in the target.

We considered charge-exchange reactions of the (p, xn) type that lead to the formation of Sb isotopes, simple $(p, 2N)$ (N stands for nucleons) reactions, and $(p, xpyn)$ disintegration reactions. Our main objective was to obtain and to discuss the cross sections for the formation of high-spin isomeric states and to investigate the dependences of isomeric ratios on the number of emitted nucleons. In order to determine the independent values of the cross sections, we also calculated the cross sections for the formation of parent isotopes (the results are presented in Table 1). In addition, we calculated the cross sections for the formation of neutron-deficient and neutron-rich nuclei (Table 1) in order to investigate the isotopic effect.

Charge-exchange reactions proceeding at the proton energy of $E_p = 0.66$ GeV in targets from separated tin isotopes were discussed in detail elsewhere [13]. By comparing the cross sections for the above reactions at the three values of the proton energy, we find that their energy dependence is weak. For some reactions, the cross sections increase by a factor of about 2 upon going over from $E_p = 0.66$ to 8.1 GeV, while, for others, the cross sections decrease or remain constant within the experimental errors (see Table 1 and Fig. 1). In [13], the cross sections were calculated on the basis of the model of quark–gluon strings [14], which describes the fast stage of pSn interaction. Since a weak energy dependence was observed, we can draw a conclusion about the character of emitted neutrons—namely, the formation of $(x-1)$ neutrons in (p, xn) reactions is caused by the evaporation mechanism [13].

As can be seen from Table 1, the cross sections for the formation of product nuclei in disintegration reactions are weakly dependent on energy. Using the data from [8] at $E_p = 0.66$ GeV, we can compare the cross sections at three values of the proton energy. In some cases, the cross sections first decrease in going over from $E_p = 0.66$ to 1 GeV and then slowly increase upon going over to $E_p = 8.1$ GeV (Fig. 1). The total cross sections for reactions induced by protons in Cd isotopes exhibit such an energy dependence [15] (mass region of tin nuclei). In many cases, the cross sections first decrease and then remain constant.

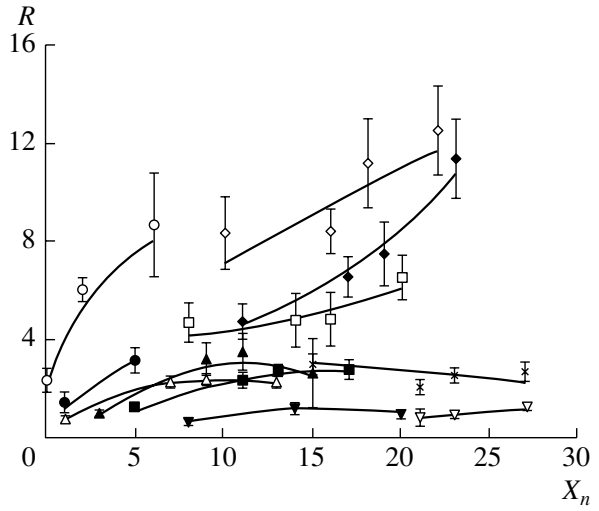

Fig. 3. Isomeric ratios R of the cross sections versus the number X_n of emitted neutrons ($E_p = 8.1$ GeV): (•) ^{117}Cd, (○) ^{117}In, (△) ^{110}In, (▲) ^{108}In, (◇) ^{95}Tc, (□) ^{99}Rh, (♦) ^{94}Tc, (■) ^{86}Y, (▼) ^{95}Nb, (▽) ^{84}Rb, and (×) ^{104}Ag.

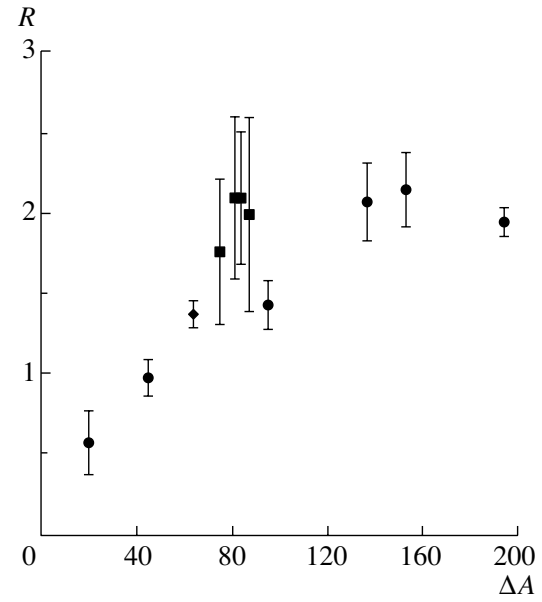

Fig. 4. Isomeric ratios R [for ^{44}Sc$(6^+, 2^+)$] versus the number ΔA of emitted nucleons according to data from (•) [5], (♦) [6], and (■) this study.

Now, we discuss the isotopic effect {the dependence of the cross sections for the formation of residual nuclei on the third projection of the target isospin $[T_3 = (N_t - Z_t)/2]$ and on the third projection of the residual-nucleus isospin $[t_3 = (N - Z)/2]$}. Table 1 presents the values of the cross sections for 20 residual nuclei undergoing β^- decay. As can be seen from Fig. 2*a* and from Table 1, the cross sections for the formation of these nuclei increase with increasing number of neutrons in the target nucleus. On the contrary, the cross sections decrease for all β^+-active nuclei. This means that the reaction cross sections depend on the nucleonic content of the target nucleus and residual nuclei. Figure 2*b* shows the cross sections for the formation of high-spin states of residual nuclei versus the target mass number (that is, versus the number of emitted neutrons). As can be seen from this figure, the cross sections in question first increase, attain a maximum, and then decrease; at the same time, the cross sections for the formation of low-spin nuclei decrease steadily with increasing number of emitted neutrons (^{99g}Rh, $I = 1/2^-$). The initial increase in the cross sections for high-spin states with increasing target mass number A_t can be explained by an increase in the number of cascade particles, so that the nucleus acquires a high angular momentum upon their emission. As the number of emitted neutrons increases, the fraction of evaporated particles also grows. Together with photons emitted in the deexcitation process, these particles lead to a decrease in the probability of the formation of high-spin states—that is, to the broadening of the aftercascade spin distribution and, consequently, to the smoothing of the spin dependence of the reaction cross section. Furthermore, it is known that the reaction cross sections decrease with increasing number of emitted particles. From Fig. 2*b*, it can also be seen that the cross sections for the formation of the 8^+ state of a residual β^+-active nucleus ^{90}Nb slowly decrease with increasing A_t (by a factor of 2 in response to a change in A_t from 112 to 124), whereas $\sigma(^{99g}\mathrm{Rh}(1/2^-), \beta^+)$ decreases by a factor of about 7 upon going over from the target nucleus of ^{112}Sn to that of ^{124}Sn. In the case of ^{90}Nb, the isotopic effect is operative, and the character of the variation in the cross section differs from that for other high-spin nuclei.

In Table 2, the so-called isomeric ratios $R = \sigma(I_\mathrm{h})/\sigma(I_\mathrm{l})$ of the cross sections for the formation of high-spin and low-spin states are given for 18 isometric pairs. It can be noted that, for the majority of nuclei of the Tc isotopes, the ratios R are great and exhibit a strong dependence on the number of emitted nucleons. This ratio increases by a factor greater than 2 upon going over the ^{112}Sn to the ^{124}Sn target (see Table 2 and Fig. 3). For the neighboring ^{95}Nb nucleus, the isomeric ratio R is predominantly below unity and is nearly invariable within the experimental errors in passing from one target to another. The same is true for ^{84}Rb as well.

Table 2. Isomeric ratios of the cross sections, $R = \sigma(I_h)/\sigma(I_l)$, for residual nuclei in reactions on ^{112,118,120,124}Sn target nuclei at $E_p = 1$ and 8.1 GeV

residual nucleus	^{112}Sn	^{118}Sn		^{120}Sn		^{124}Sn	
	8.1 GeV	1 GeV	8.1 GeV	1 GeV	8.1 GeV	1 GeV	8.1 GeV
^{117}Cd$(11/2^-, 1/2^+)$				2.04 ± 0.20	1.46 ± 0.41	3.00 ± 0.45	3.15 ± 0.50
^{117}In$(9/2^+, 1/2^-)$		2.3 ± 0.3	2.34 ± 0.50	2.60 ± 0.47	6.00 ± 0.46	4.05 ± 0.990	8.67 ± 2.10
^{116}Sb$(8^-, 3^+)$		0.56 ± 0.10	0.52 ± 0.08	1.15 ± 0.21	1.07 ± 0.19		2.17
^{110}In$(7^+, 2^+)$	0.8 ± 0.1	3.9 ± 0.4	2.30 ± 0.22	3.1 ± 0.5	2.40 ± 0.23	4.05 ± 0.91	2.36 ± 0.25
^{108}In$(6^+, 1^-)$	0.22 ± 0.13	2.40 ± 0.35	3.10 ± 0.64	3.7 ± 0.4	3.30 ± 0.93	3.65 ± 0.91	2.60 ± 1.39
^{104}Ag$(5^+, 2^+)$	1.26 ± 0.15	3.27 ± 0.62	2.37 ± 0.35	2.45 ± 0.32	2.75 ± 0.25	3.65 ± 0.88	2.80 ± 0.39
^{102}Rh$(6^+, 2^-)$	2.61 ± 0.39	3.00 ± 1.06	2.30 ± 0.75		2.47 ± 0.33	3.69 ± 0.86	2.72 ± 0.60
^{101}Rh$(9/2^+, 1/2^-)$	(2.94 ± 0.44)[a)]	1.20 ± 0.23	1.22 ± 0.24	1.8 ± 0.3	1.93 ± 0.29		1.38 ± 0.23
^{99}Rh$(9/2^+, 1/2^-)$	(4.97 ± 0.80)*	6.15 ± 1.10	4.8 ± 1.1	3.6 ± 0.5	4.26 ± 0.64	1.38 ± 0.25	6.6 ± 0.9
^{95}Tc$(9/2^+, 1/2^-)$	8.34 ± 1.49	7.90 ± 0.63	8.40 ± 0.96	8.6 ± 0.9	11.2 ± 1.2	5.44 ± 1.25	12.5 ± 1.87
^{95}Nb$(9/2^+, 1/2^-)$	0.65 ± 0.12	0.82 ± 0.16	1.20 ± 0.25			11.37 ± 1.30	
^{94}Tc$(7^+, 2^+)$	4.70 ± 0.73	5.1 ± 1.1	6.55 ± 0.80	8.4 ± 1.8	7.5 ± 1.3	(0.96 ± 0.17)[a)]	11.4 ± 1.6
^{93}Tc$(9/2^+, 1/2^-)$			4.30 ± 1.46	7.67 ± 1.53		12.0 ± 3.4	
^{87}Y$(9/2^+, 1/2^-)$		1.80 ± 0.27	1.8 ± 0.3	3.40 ± 0.76	3.55 ± 0.53		2.87 ± 0.52
^{86}Y$(8^+, 4^-)$	3.00 ± 0.43	3.42 ± 0.50	2.1 ± 0.3	2.95 ± 0.40	2.59 ± 0.30		2.7 ± 0.4
^{84}Rb$(6^-, 2^-)$			0.83 ± 0.35		0.96 ± 0.14	2.7 ± 0.82	1.28 ± 0.13
^{52}Mn$(6^+, 2^+)$			4.24 ± 0.71				
^{44}Sc$(6^+, 2^+)$	1.77 ± 0.45		2.1 ± 0.5		2.1 ± 0.5		2.0 ± 0.6

[a)] $E_p = 0.66$ GeV.
* Cumulative.

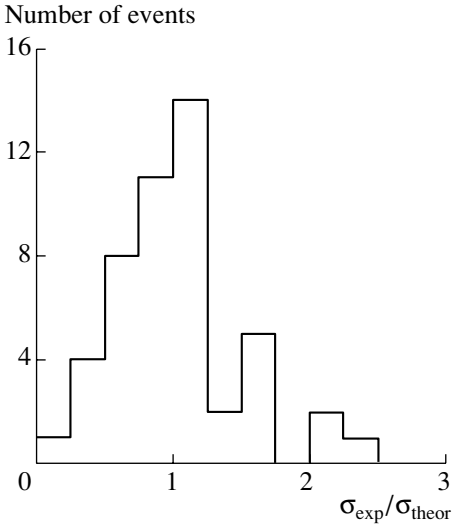

Fig. 5. Results obtained by comparing the experimental values of the cross section for the ^{124}Sn target with the results of the calculations based on the cascade–evaporation model.

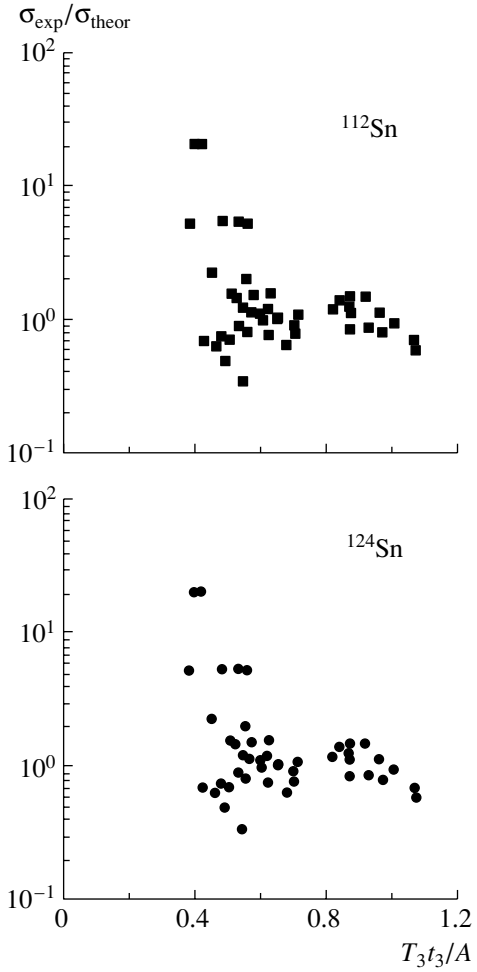

Fig. 6. Ratios of the experimental values of the cross sections for the ^{112}Sn and ^{124}Sn targets at $E_p = 8.1$ GeV to the results of the calculations based on the cascade–evaporation model versus the product T_3t_3/A of the third projections of the nuclear isospins.

For the simple reactions $^{118}\mathrm{Sn} + p \to {}^{116m}\mathrm{Sb} + 3n$, $^{112}\mathrm{Sn} + p \to {}^{110}\mathrm{In} + 2p + n$, and $^{112}\mathrm{Sn} + p \to {}^{108}\mathrm{In} + 2p + 3n$, the ratio R is less than unity. It grows as the number of emitted neutrons increases and then remains constant. This can be explained by the fact that the emission of three neutrons or of two protons and one neutron does not generate a high angular momentum of the residual nucleus; as a result, a high-spin state is formed with a lower probability after deexcitation than a low-spin state. As the number of cascade nucleons increases, a higher angular momentum is transferred to the residual nucleus, with the result that the probability of the formation of a high-spin state increases. The same is true for the residual nucleus ^{117}In as well. Although $R > 1$ for the simple reaction $^{118}\mathrm{Sn}(p, 2p)^{117}\mathrm{In}$, this ratio increases by a factor greater than 3 at $E_p = 8.1$ GeV (see Table 2 and Fig. 3) for the reactions where a larger number of neutrons is emitted from ^{124}Sn. Figure 3 displays R as a function of the number X_n of emitted neutrons. It can be noted that, for $X_n \geq 9$, the isomeric ratio remains constant for many isomeric pairs [with the exception of $^{95}\mathrm{Tc}(9/2^+, 1/2^-)$ and $^{94}\mathrm{Tc}(7^+, 2^+)$]. From the data presented in Table 2, it follows that, within the experimental errors, R is independent of energy. This is not so for the ^{117}In nucleus, in which case the ratio R increases for the ^{120}Sn and ^{124}Sn targets upon going over from $E_p = 0.66$ GeV [8] to $E_p = 1$ and 8.1 GeV (Table 2).

Relying on the experimental isomeric ratios of the cross sections at the proton energy $E_p = 0.66$ GeV from [8] and on the yields of photonuclear reactions at $E_{\gamma\,\mathrm{max}} = 4.5$ GeV [15] for the same enriched tin isotopes, we can draw the following conclusions: (i) In many cases, the isomeric ratios are almost equal for proton–nucleus and photonuclear reactions; that is, these ratios are independent of the projectile type, but they depend on the individual properties of the residual nucleus. (ii) The isomeric ratios of the cross sections and of the yields remain constant with increasing number of emitted neutrons (for $X_n > 9$). This is true for almost all isomeric pairs, including $^{44}\mathrm{Sc}(6^+, 2^+)$ (except for the case where the residual nuclei are those of Tc). For ^{44}Sc nuclei formed in proton–nucleus reactions at high proton energies, the isomeric ratio R of the cross sections versus the number of emitted nucleons is shown in Fig. 4 for a wide region of target masses. It can be seen that R first grows and then remains constant.

Thus, we have corroborated here the conclusions

drawn in [8, 15], where the character of variations of the isomeric ratios of the cross sections and yields was discussed qualitatively. In other words, we can state that the character of their variations is associated with the presence of a neutron halo in heavy tin isotopes (evaporation of neutrons from the nuclear surface) and with the occurrence of the absorption of negative secondary pions by the surface quasideuterons ($\pi^- + d \to n + n$), along with the cascade–evaporation process.

For the above disintegration reactions at $E_p = 8.1$ GeV, we have calculated the cross sections on the basis of the cascade–evaporation model [16]. For the ground nuclear states, the results of the calculations are in satisfactory agreement with the experimental cross-section values. The results of the calculation are presented in Table 1. In these calculations, 50 000 events were generated for each target. For the ^{124}Sn target, Fig. 5 shows the results obtained by comparing the experimental cross-section values with the results of the calculations. We plot the ratio $\sigma_{\text{expt}}/\sigma_{\text{theor}}$ along the abscissa and the number of events along the ordinate. A sharp peak in the region of unity can be seen in this figure. In 25, 10, and 9 events of the set of 53 events considered in our study, the calculated values of cross sections differ from their experimental counterparts within 25, 50, and 75%, respectively. Although the agreement between the experimental and the calculated values of the cross sections is by and large satisfactory, we observed a considerable discrepancy for some residual nuclei (see Table 1). A clearer presentation of our results is given in Fig. 6, which displays the ratios of the experimental and theoretical values of the cross sections for the ^{112}Sn and ^{124}Sn targets versus $T_3 t_3/A$, where T_3 and t_3 are, respectively, the third projection of the target-nucleus isospin and the third projection of the isospin of the residual nucleus whose mass number is A. It can be seen that this ratio is close to unity for many residual nuclei; however, there are many cases where it is as large as 4 to 5. In the case of the ^{124}Sn target, the ratio $\sigma_{\text{expt}}/\sigma_{\text{theor}}$ is greater for nuclei undergoing β^+ decay (^{90}Nb, ^{90}Mo, ^{94}Ru, ^{86m,g}Y, etc.), while, in the case of the ^{112}Sn target, this ratio is greater primarily for nuclei undergoing β^- decay (^{103}Ru, ^{96}Nb, ^{95m,g}Nb, etc.). It is probable that, within the cascade–evaporation model, it is necessary to refine the dependence of the cross sections on the nucleonic content of the target and of residual nuclei.

ACKNOWLEDGMENTS

We are grateful to the personnel of the phasotron and of the synchrophasotron for providing good parameters of the beam during the irradiation of targets. A.S. Danagulyan thanks the directorate of the Laboratory of Nuclear Problems and of the JINR for the possibility to perform this experiment.

REFERENCES

1. A. S. Danagulyan, J. Adam, A. R. Balabekyan, *et al.*, Yad. Fiz. **63**, 204 (2000) [Phys. At. Nucl. **63**, 151 (2000)].
2. V. Alexandrian, J. Adam, *et al.*, Nucl. Phys. A **674**, 539 (2000).
3. V. S. Barashenkov and V. D. Toneev, *Interactions of High-Energy Particles and Nuclei with Nuclei* (Atomizdat, Moscow, 1972), pp. 51, 208.
4. A. S. Botvina, K. K. Gudima, A. S. Iljinov, and I. N. Mishustin, Yad. Fiz. **57**, 667 (1994) [Phys. At. Nucl. **57**, 628 (1994)]; J. P. Bondorf, A. S. Botvina, A. S. Iljinov, *et al.*, Phys. Rep. **257**, 133 (1995).
5. E. Hagebo and H. Ravn, J. Inorg. Nucl. Chem. **31**, 897 (1969).
6. N. T. Porile, G. D. Cole, and C. R. Rudy, Phys. Rev. C **19**, 2288 (1979).
7. P. Kozma, V. I. Ilyushchenko, and I. Ion, Yad. Fiz. **54**, 558 (1991) [Sov. J. Nucl. Phys. **54**, 338 (1991)].
8. V. E. Aleksandryan, G. S. Aivazyan, A. R. Balabekyan, *et al.*, Yad. Fiz. **59**, 592 (1996) [Phys. At. Nucl. **59**, 560 (1996)].
9. R. Michel *et al.*, Nucl. Instrum. Methods Phys. Res. B **103**, 183 (1995).
10. J. B. Cumming, Annu. Rev. Nucl. Sci. **13**, 261 (1963).
11. U. Reus and W. Westmeier, At. Data Nucl. Data Tables **29** (1), (1983); Nucl. Data Sheets **62** (1991); **64** (1991); **68** (1993); **70** (1993); **71** (1994); **73** (1994); **74** (1995); **79** (1996); **80** (1997); **82** (1997); **83** (1998).
12. J. Frana, Acta Polytech. – Nucleonika **38**,127 (1998).
13. A. S. Danagulyan, L. G. Martirosyan, N. S. Amelin, *et al.*, Yad. Fiz. **60**, 965 (1997) [Phys. At. Nucl. **60**, 863 (1997)].
14. N. S. Amelin, K. K. Gudima, and V. D. Toneev, Yad. Fiz. **51**, 1730 (1990) [Sov. J. Nucl. Phys. **51**, 1093 (1990)].
15. A. A. Arakelyan, A. R. Balabekyan, A. S. Danagulyan, and A. G. Khudaverdyan, Yad. Fiz. **45**, 609 (1987) [Sov. J. Nucl. Phys. **45**, 381 (1987)]; V. É. Aleksandryan, A. A. Arakelyan, and A. S. Danagulyan, Yad. Fiz. **56** (6), 1 (1993) [Phys. At. Nucl. **56**, 707 (1993)].
16. G. Musulmanbekov, in *Proceedings of XI International Symposium on High Energy Spin Physics, Bloomington, 1994* (American Inst. of Physics, New York, 1995), p. 428.

Translated by V. Bukhanov

Physics of Atomic Nuclei, Vol. 65, No. 5, 2002, pp. 785–794. Translated from Yadernaya Fizika, Vol. 65, No. 5, 2002, pp. 819–827.

NUCLEI
Experiment

Multipole Mixtures in γ Transitions Accompanying the $(n, n'\gamma)$ Reaction on ^{162}Dy

L. I. Govor, A. M. Demidov, and V. A. Kurkin*

Russian Research Centre Kurchatov Institute, pl. Kurchatova 1, Moscow, 123182 Russia

Received March 12, 2001; in final form, June 21, 2001

Abstract—By using a beam of fast reactor neutrons, the angular distributions of gamma radiation from the $(n,n'\gamma)$ reaction on ^{162}Dy are measured with respect to the axis of this beam. The values of the multipole-mixing parameter δ are found for many gamma transitions between levels whose spins and parities are known. © *2002 MAIK "Nauka/Interperiodica".*

For the ^{162}Dy nucleus, the last review of data on the energies of the levels and gamma transitions, as well as on their features, was given in [1]. The diagram of the levels and gamma transitions in ^{162}Dy is well established up to an excitation energy of 1.9 MeV; however, information about multipole mixtures in gamma transitions between these levels is scanty. The present study extends considerably our knowledge in this realm.

Simple regularities in the behavior of the multipole-mixing parameter δ as a function of the number of neutrons were revealed in [2] for gamma transitions from low-lying collective states in spherical even–even nuclei. For nonspherical nuclei, an attempt was made in [3] to associate a positive sign of δ with the contribution of the two-quasiparticle proton state $(p\mathrm{p}411\uparrow 411\downarrow)$ to the relevant collective state. However, a further accumulation of information about multipole mixtures in nonspherical nuclei is required for establishing reliable dependences of the sign of δ on the number of neutrons in such nuclei.

1. EXPERIMENTAL RESULTS

The spectra of gamma rays from the reaction $^{162}\mathrm{Dy}(n, n'\gamma)$ were measured in an extracted beam of fast neutrons from the IR-8 reactor installed at the Russian Research Centre Kurchatov Institute. A $^{162}\mathrm{Dy}_2\mathrm{O}_3$ sample of mass 10 g and thickness 0.96 g/cm^2 was enriched in ^{162}Dy to 95.2% (the content of the $A = 161$, 163, and 164 isotopes in the sample was 0.95, 3.12, and 0.73%, respectively). Gamma radiation was recorded by a germanium detector that had an efficiency of 10% and a resolution of 2.1 keV at $E_\gamma = 1.3$ MeV. In the measured γ spectra, we were able to single out 270 γ lines associated with ^{162}Dy. In order to find the angular distributions of gamma rays, their spectrum was measured at angles of $\theta = 90°$, 105°, 115°, 125°, 142°, and 150° with respect to the neutron-beam axis. The 1195.109-keV $(1^- - 2^+)$ transition, for which we adopted a theoretical angular distribution with $a_2 = -0.016$ and $a_4 = 0$, where a_2 and a_4 are the coefficients in the expansion of the angular distribution in Legendre polynomials, was used to normalize the intensities of the gamma radiation in question at various angles. A more detailed account of the procedure that we employ here is given in the review article [4].

For gamma transitions in ^{162}Dy, Table 1 presents the energies for the angle of $\theta = 90°$ and the data on the relative intensities for the angle of $\theta = 125°$. The energies (E_i) of the levels from which the above transitions proceed are given in the third column of Table 1. At a reactor in Riga, the spectrum of gamma rays from the reaction $^{162}\mathrm{Dy}\,(n, n'\gamma)$ induced by fast reactor neutrons was measured at 1.3 MeV with a resolution of 1.9 keV; the results of these measurements were reported in [5]. The data in Table 1 are sometimes at odds with those results. At energies below 1.5 MeV, the spectrum that was determined in our measurements shows almost all gamma lines that Berzins *et al.* [5] attributed to ^{162}Dy; however, these authors did not eliminate the background gamma lines from the interaction of fast neutrons with a germanium-detector material [for these background lines, they observed an enhanced intensity ratios in the reactions $^{162}\mathrm{Dy}(n, n'\gamma)$ and $^{161}\mathrm{Dy}(n, \gamma)^{162}\mathrm{Dy}$] and the gamma lines corresponding to the reactions $^{161,163,164}\mathrm{Dy}(n, n'\gamma)$ induced by fast neutrons and to the reaction $^{162}\mathrm{Dy}(n, \gamma)^{163}\mathrm{Dy}$ induced by intermediate-energy neutrons, which are present in the neutron beam used (the ^{162}Dy isotope

*e-mail: kurkin@polyn.kiae.su

is characterized by a very large resonance integral). In composing Table 1, we eliminated all of the aforementioned gamma lines using the results of measurements for a natural mixture of disprosium isotopes and the results for the reaction ^{164}Dy$(n, n'\gamma)$ that were reported in [6].

The spectrum of gamma rays from the $(n, n'\gamma)$ reaction on a natural mixture of isotopes receives a significant contribution from the $A = 161$ and 163 isotopes, and this facilitated the elimination of gamma lines of these isotopes from the spectrum measured with a ^{162}Dy sample containing admixtures of these isotopes. For some reasons that we do not understand, the gamma-ray spectrum that we measured for energies in excess of 2.3 MeV differs significantly from that presented in [5], but, as might have been expected, it agrees with the data for the reaction ^{161}Dy$(n, \gamma)^{162}$Dy [1] in what is concerned with the γ-line energy. In view of discrepancies with [5], we deemed it reasonable to present our data on the gamma-ray spectrum of ^{162}Dy in Table 1.

With the aid of our data, we composed the diagram of energy levels and gamma transitions in ^{162}Dy up to an energy of 1.9 MeV. The results are displayed in Table 2, which presents the values of the coefficients a_2 and a_4 and the values that we found for the multipole-mixing parameter δ or for the multipolarity ML, the errors in a_2, a_4, and δ corresponding to a 68% confidence level. The errors in the parameter δ and its signs are given according to the system adopted in the journal *Nuclear Data Sheets* [1]. In order to determine the populations of magnetic substates of levels, we used, as a rule, the angular distributions for pure $E2$ or $E1$ transitions proceeding from the same level (see [4]). In Table 2, the energies of the first three levels were taken from the review article of Helmer and Reich [1]; for higher levels, the energies are given according to the data of the present study. The features of the levels were also borrowed from the aforementioned review article [1].

The deexcitation of levels at energies above 1.9 MeV is reflected in Table 1. Here, we used levels found in the (d, p) and (d, t) reactions [5] and established the diagrams of their deexcitation. For this, it was assumed that the $E_\gamma > 1.9$ MeV γ lines found in the gamma-ray spectra of nonspherical even nuclei by studying the $(n, n'\gamma)$ reaction induced in these nuclei by fast reactor neutrons correspond, as a rule, to transitions proceeding to the 0^+, 2^+, and 4^+ levels of the rotational band built on the ground state. This statement is suggested by the dependence of the population of levels on their excitation energy [4].

2. DISCUSSION OF THE RESULTS

In Table 3, information about multipole mixtures in ^{162}Dy gamma transitions that was taken from various sources (see [7–10]) is contrasted against the results of our present study. In [7], the parameters $|\delta|$ were estimated on the basis of the internal-conversion coefficients for gamma transitions associated with the (n, γ) reaction. In [8], [9], and [10], the parameters δ were found from data on the $(n, \gamma\gamma(\theta))$, $(n, n'\gamma(\theta))$, and $(\alpha, 2n\gamma)$ reactions, respectively. The adapted values of δ from [1] are quoted in the penultimate column of Table 3, while our data are given in its last column.

Below, we comment on the values of δ for some individual gamma transitions.

807.502-keV transition from the 2^+ level at 888.156 keV. Indicating that $\delta < +\infty$ for this transition, we assume that the quantity δ may be very large, but that it remains positive within the errors.

882.272-keV transition from the 3^+ level at 962.932 keV. Data from [9], which are consistent with our results, were ignored in [1]. For the value of $\delta = +3.7$, which was indicated in [1], our experiment would have led to $+0.32$ for a_2 rather than to 0.095. Such a distortion of the angular distribution is not expected. The value of a_4 rules out the second, very small, value of δ.

795.315-keV transition from the 4^+ level at 1060.990 keV. The value of $\delta = -5.5$ must correspond to $a_2 = -0.28$; at the same time, the experiment yields $a_2 = -0.147(17)$. The second value of $\delta = -0.85(5)$ has been ruled out on the basis of data on the conversion coefficient found in [7].

917.089-keV transition from the 5^+ level at 1182.743 keV. The second, very small, value of δ is ruled out by a large value of a_4.

634.15-keV transition from the 5^+ level at 1182.743 keV. We discarded the second, small, value of $\delta = -0.06(6)$, adopting the estimate obtained in [7] for δ.

944.444-keV transition from the 3^- level at 1210.093-keV. An admixture of $M2$ radiation in this transition was revealed more reliably than in [8].

1319.65-keV transition from the 0^+ level at 1400.31 keV. In studying ^{162}Ho decay, which is characterized by the half-life of $T_{1/2} = 15$ min, the $J^\pi = 0^+$ level at 1400.2 keV was found on the basis of the 1319.6-keV gamma transition and of the 1400.3-keV $E0$ transition (see [1]). In [3] and, later on, in the review article of Helmer and Reich [1], the 1317.7-keV gamma transition was used for the deexcitation of this 0^+ level, while the level itself was assigned the energy of 1398.035 keV. We deem that this replacement is erroneous. The isotropic angular distribution of 1319.65-keV gamma rays and the population of the

Table 1. Energies and intensities of ^{162}Dy gamma rays

E_γ, keV	I_γ, arb. units	E_i, kev	E_γ, kev	I_γ, arb. units	E_i, keV
80.65(2)	62(3)	80.6	643.84(22)	0.29(5)	1826.6
114.0(4)	< 0.50(9)	1297.0	647.53(3)	3.03(16)	1535.7
149.26(3)	< 0.90(9)		652.1(3)	0.19(4)	
185.001(4)	100(5)	265.7	654.1(4)	0.18(5)	
212.96(6)	1.66(10)	1570.8	671.55(10)	0.83(6)	1634.5; 1886.8
220.08(24)	0.26(4)		678.05(13)	0.42(4)	1739.1; 1973.0
233.00(5)	0.18(6)	(1530.0)	681.0(5)	0.18(5)	
235.98(8)	1.41(9)	1297.0	684.8(2)	0.16(3)	1574.3; 2008.7
247.43(8)	0.60(10)	1210.1	694.19(16)	0.57(6)	
258.17(5)	1.5(2)	1895.5	697.29(2)	5.3(3)	962.9
260.08(2)	17.9(9)	1148.2	711.69(13)	0.60(6)	2008.7
282.88(2)	15.5(8)	548.5	714.5(3)	0.40(5)	
289.4(3)	0.16(4)		720.8(4)	0.09(3)	
295.05(3)	2.86(15)	1570.8	728.40(13)	0.82(6)	1691.4
311.22(5)	1.20(8)	1669.1	747.24(13)	0.51(5)	1895.5; 2071.7
321.96(4)	1.37(8)	1210.1	748.96(13)	0.58(5)	
329.7(3)	0.20(4)		765.3(4)	0.10(4)	1826.7
334.074(13)	5.97(30)	1297.0	770.96(22)	0.22(4)	2128.8
347.49(5)	< 1.1(2)	(1408.5)1530.0	775.93(6)	1.12(7)	1324.5
361.4(3)	0.19(4)	1570.8; 1637.3	779.57(19)	0.30(5)	1840.4
372.20(9)	1.65(10)	920.7	791.3(4)	0.29(4)	
391.71(22)	0.57(5)	1574.3	795.315(10)	9.6(5)	1061.0
411.4(11)	0.09(3)		801.3(6)	0.12(4)	
443.7(5)	0.17(5)		803.33(10)	< 1.0(7)	1766.4
451.99(22)	0.33(4)	1634.5	807.502(10)	27.1(14)	888.2
489.08(20)	0.16(4)		812.8(3)	0.17(3)	
523.5(3)	0.24(4)		815.8(5)	0.12(3)	
529.19(12)	0.80(6)	1739.1; 1826.6	819.76(13)	0.40(10)	1782.7
542.1(5)	0.19(5)		834.2(4)	0.15(4)	1895.5
543.54(10)	1.12(8)	1691.4; 1840.3	842.27(7)	1.41(9)	1390.6
551.1(6)	0.27(4)	1910.2	849.50(25)	0.41(5)	1739.1; 1910.2
556.33(19)	0.45(5)	1766.4	853.8(4)	0.09(3)	
565.77(22)	0.27(5)		857.54(6)	0.96(6)	1745.8
572.95(4)	2.03(11)	1634.5; 1535.7	863.77(13)	0.54(5)	1826.6
588.8(5)	0.12(5)	1863.8	867.93(13)	< 0.70(5)	
590.6(3)	0.28(5)	1739.1	872.7(4)	0.16(3)	
610.93(22)	< 0.39(5)		878.54(10)	0.84(6)	1766.4; 1840.6
616.2(5)	0.17(5)		882.272(10)	26.1(13)	962.9
618.3(3)	0.30(6)	1766.4	888.150(10)	24.4(12)	888.2
622.40(14)	0.38(4)	888.2	894.39(22)	0.35(5)	1782.8
630.48(22)	< 0.48(5)	1840.0	900.80(19)	0.44(5)	1863.8
632.4(4)	0.22(5)		911.86(22)	0.31(4)	1973.0
634.15(6)	1.49(9)	1182.7	917.089(15)	5.41(28)	1182.7

Table 1. (Contd.)

E_γ, keV	I_γ, arb. units	E_i, keV	E_γ, keV	I_γ, arb. units	E_i, keV
923.8(3)	0.13(3)	1886.8	1217.76(13)	0.69(6)	
932.5(3)	0.22(4)	1895.0	1219.94(4)	2.00(11)	1485.6
937.12(8)	0.80(6)	1485.6	1223.31(25)	0.26(5)	
942.12(11)	0.51(5)	1490.6	1227.8(6)	0.21(8)	
944.444(20)	3.94(20)	1210.1	1232.3(4)	0.11(3)	
947.35(16)	0.51(5)	1910.2	1252.79(6)	1.44(8)	1518.4
951.8(5)	0.065(26)	1840.6	1257.3(9)	0.09(4)	
956.0(3)	0.19(4)		1261.6(9)	0.09(4)	
957.3(6)	0.13(4)		1267.6(6)	0.14(4)	
969.74(10)	0.68(5)	1518.4	1276.56(2)	11.5(6)	1275.8; 1357.9
972.7(10)	0.056(28)		1284.6(5)	0.13(3)	
975.64(6)	1.26(8)	1863.8	1297.9(3)	0.18(3)	
980.352(20)	5.11(26)	1061.0	1308.64(6)	1.78(10)	1574.3
992.75(29)	0.15(4)	2053.5	1312.3(3)	0.28(4)	
1007.0(4)	0.27(4)	1895.5	1317.3(5)	0.24(5)	
1010.09(19)	0.51(5)	1973.0	1319.65(4)	2.44(14)	1400.3
1015.0(3)	$< 0.40(10)$		1330.0(3)	0.15(4)	
1017.7(3)	0.28(5)		1332.4(3)	0.20(4)	
1022.07(16)	0.38(5)	1910.2	1342.56(19)	0.33(4)	
1025.74(19)	0.39(5)	1574.3	1350.75(25)	0.23(4)	
1041.6(5)	0.24(5)		1355.5(3)	0.23(4)	
1047.0(3)	0.42(6)		1372.80(4)	3.50(18)	1453.4
1058.76(16)	0.59(5)	1324.4	1391.9(4)	0.21(5)	
1073.2(4)	0.30(4)		1394.5(4)	0.34(5)	
1079.1(5)	0.12(3)		1404.0(3)	0.31(4)	1669.1
1082.0(6)	0.07(3)		1428.1(5)	0.09(4)	
1088.40(19)	0.45(5)	1636.9	1438.6(3)	0.28(4)	
1092.23(2)	4.26(22)	1357.9	1462.92(13)	0.81(6)	1728.6
1107.8(4)	0.12(4)	2071.7	1464.7(5)	0.16(4)	
1109.9(3)	0.12(4)		1468.9(15)	0.10(5)	
1114.3(4)	0.23(4)		1473.40(19)	0.55(5)	1739.1
1124.95(3)	2.36(13)	1390.6	1483.2(5)	0.06(3)	
1129.424(15)	6.7(3)	1210.1	1489.5(4)	0.20(4)	
1134.2(3)	0.24(5)		1496.2(6)	0.10(4)	
1141.94(25)	0.42(4)		1501.5(4)	0.09(3)	1766.4
1152.9(6)	0.19(4)		1516.6(3)	0.14(4)	1782.7
1166.2(5)	0.15(4)		1556.67(10)	1.65(9)	1637.3
1169.2(5)	0.13(4)		1574.82(25)	0.22(4)	1840.4
1173.6(6)	0.16(4)		1585.62(10)	1.09(7)	1666.3; 1851.3
1178.4(6)	0.20(4)		1602.1(3)	0.33(4)	
1187.74(4)	2.52(13)	1453.4	1610.95(10)	0.99(7)	1691.4
1195.109(15)	9.0(4)	1275.8	1637.32(22)	0.40(4)	1637.3
1213.7(6)	0.07(3)		1647.90(10)	1.21(7)	1728.6

Table 1. (Contd.)

E_γ, keV	I_γ, arb. units	E_i, keV	E_γ, keV	I_γ, arb. units	E_i, keV
1658.5(3)	0.16(4)	1739.1	2361.7(8)	0.29(6)	2361.7
1665.29(10)	0.90(6)	1745.9; 1615.3	2369.4(6)	0.28(6)	2369.4
1684.1(5)	0.18(4)		2378.2(9)	0.22(7)	2458.9
1686.76(29)	0.35(5)	1951.6	2382.2(10)	0.21(7)	2382.2
1698.3(5)	0.057(27)		2394.8(10)	0.21(6)	2394.8
1702.08(19)	0.54(5)	1782.7; 1702.1	2399.4(6)	0.35(6)	2480.1
1708.3(10)	0.12(5)	1708.3	2406.8(7)	0.22(5)	2487.5
1710.4(13)	0.08(5)		2418.1(7)	0.16(6)	
1716.0(7)	0.17(5)	1983.0	2425.6(12)	0.20(7)	
1722.8(4)	0.20(5)		2429.6(10)	0.25(8)	2510.3
1728.58(19)	0.66(6)	1728.6	2438.4(6)	0.33(6)	2438.4
1735.7(4)	0.17(4)	1816.4	2442.4(10)	0.22(7)	2523.1
1757.3(6)	0.15(4)	1837.0	2448.4(6)	0.18(5)	2529.1
1759.63(26)	0.28(4)	1840.6; 1759.6	2455.3(10)	0.26(6)	2536.5
1767.9(7)	0.083(24)		2473.6(6)	0.53(7)	2554.3
1773.80(19)	0.46(5)	1773.8	2490.9(6)	0.43(6)	2571.6
1782.8(2)	0.61(6)	1782.7	2505.4(6)	0.44(6)	
1787.56(22)	0.41(5)	2053.5	2519.7(5)	0.47(6)	2519.7
1798.2(4)	0.20(4)	1798.2	2532.3(12)	0.19(6)	
1806.15(9)	1.29(8)	1886.8	2537.5(10)	0.23(7)	2536.5
1814.92(9)	1.22(8)	2080.6	2550.6(11)	0.21(7)	2550.6
1832.36(22)	0.19(5)	1832.4	2554.5(10)	0.25(7)	2554.3
1837.04(13)	0.31(4)	1837.0	2562.7(13)	0.14(5)	2643.4
1871.00(22)	0.31(4)	1951.6	2569.3(12)	0.16(6)	2569.3
1902.29(12)	1.09(7)	1983.0	2587.4(7)	0.30(5)	
1918.80(13)	1.00(7)	1999.2	2628.9(10)	0.08(3)	2709.6
1940.3(5)	0.17(5)		2644.7(7)	0.31(5)	
1943.7(6)	0.20(5)		2663.0(8)	0.13(4)	2663.0
1950.6(3)	0.38(4)	(1951.6)	2669.4(15)	0.14(5)	2750.1
1982.55(13)	1.08(7)	1983.0; ^{18}O	2674.5(14)	0.16(6)	
1992.0(10)	0.13(4)		2692.3(20)	0.11(6)	
1999.98(16)	1.00(7)	1999.2; 2080.6	2697.4(11)	0.21(7)	2778.1
2022.1(3)	0.38(4)	2022.1	2721.3(9)	0.13(5)	2801.9
2047.79(19)	0.50(5)	2128.6	2734.3(10)	0.23(5)	
2067.92(16)	0.56(5)		2745.0(12)	0.26(5)	
2111.3(4)	0.28(4)	2192.0	2756.9(11)	0.22(5)	
2124.1(4)	0.21(3)		2786.2(12)	0.12(5)	
2135.8(4)	0.12(4)	2216.4	2788.6(8)	0.19(6)	2788.6
2233.3(5)	0.30(5)	2314.0	2803.2(8)	0.26(5)	2801.9
2240.4(4)	0.35(5)	2240.4	2821.1(16)	0.15(6)	2901.8
2274.7(12)	0.23(8)	2355.4	2829.0(13)	0.20(7)	2909.6
2290.4(7)	0.27(7)	2290.4	2840.2(10)	0.23(5)	2960.9
2305.9(8)	0.38(7)	2386.6	2902.1(6)	0.27(5)	2901.8
2310.4(4)	0.90(9)	2310.4	2929.2(10)	0.12(4)	2929.2
2315.1(12)	0.29(9)	2314.0; 2394.8	2945.3(9)	0.13(4)	
2323.8(8)	0.22(6)	2323.8; 2404.5	2990.6(7)	0.23(4)	3071.3; 2990.6
2331.0(5)	0.33(6)		2999.1(14)	0.06(3)	
2339.6(8)	0.17(6)	2339.6	3014.0(9)	0.27(5)	3014.0
2345.7(7)	0.28(6)	2345.7	3148.2(9)	0.10(3)	
2349.7(7)	0.28(6)	2349.7			

Table 2. Diagram of levels and gamma transitions in ^{162}Dy that manifest themselves in the $(n, n'\gamma)$ reaction

E_i, keV	$J_i^\pi K - J_f^\pi K$	E_γ, keV	I_γ, arb. units	a_2	a_4	$\delta \pm \Delta\delta$; ML
80.6598	2^+0-0^+0	80.65	62			
265.6628	4^+0-2^+0	185.061	100	+0.33(11)	−0.19(11)	$E2$
548.5184	6^+0-4^+0	282.88	15.5	+0.44(4)	−0.07(6)	$E2$
888.156(7)	2^+2-0^+0	888.150	24.4	+0.225(10)	−0.043(15)	$E2$
	2^+2-^2+0	807.502	27.1	−0.035(12)	−0.010(16)	$+57\ +\infty - 33$
920.72(9)	8^+0-6^+0	372.20	1.65	+0.22(7)	−0.14(10)	$E2$
962.932(10)	3^+2-2^+0	882.272	26.1	+0.095(13)	+0.107(17)	$+41\ +34 - 13$
	3^+2-4^+0	697.29	5.3	−0.197(23)	+0.009(31)	$\lvert\delta\rvert > 45$
1060.990(8)	4^+2-2^+0	980.352	5.11	−0.340(29)	−0.056(35)	$E2$
	4^+2-4^+0	795.315	9.6	−0.147(17)	−0.097(24)	$+12\ +18 - 4$
1148.24(3)	2^-2-2^+0	260.08	17.9	+0.20(6)	−0.05(8)	$+0.04\ +16 - 11$
1182.743(15)	5^+2-4^+0	917.089	5.41	+0.039(24)	+0.21(3)	$+50\ +50 - 20$
	5^+2-6^+0	634.15	1.49	−0.05(8)	+0.01(10)	$-7\ +2 - 20$
1210.093(13)	3^-2-2^+0	1129.424	6.7	−0.16(3)	+0.05(4)	$+0.05 + 5 - 3$
	3^-2-4^+0	944.444	3.94	−0.007(34)	+0.015(42)	$-0.10 + 3 - 5$
	3^-2-2^+2	321.96	1.37	−0.215(30)	−0.006(41)	-0.01 ± 3
	3^-2-3^+2	247.43	0.60			
	3^-2-4^+2	149.26	< 0.90			
1275.769(15)	1^-0-0^+0	1276.56	< 11.5			
	1^-0-2^+0	1195.109	9.0	−0.016(7)	+0.002(11)	0.00 ± 4
1297.006(16)	4^-2-3^+2	334.074	5.97	−0.215(30)	−0.01(4)	-0.01 ± 3
	4^-2-4^+2	235.98	1.41			
	4^-2-5^+2	114.0	< 0.50			
1324.45(9)	6^+2-4^+0	1058.76	0.59			
	6^+2-6^+0	775.93	1.12			
1357.89(2)	3^-0-2^+0	1276.56	< 11.5			
	3^-0-4^+0	1092.23	4.26	−0.020(21)	−0.01(4)	-0.07 ± 4
1390.61(3)	5^-2-4^+0	1124.95	2.36	−0.14(4)	+0.03(6)	$+0.05 \pm 5$
	5^-2-6^+0	842.27	1.41			
1400.31(4)	0^+0-2^+0	1319.65	2.44	−0.006(33)	−0.016(40)	Isotropic
1408.48(5)?	-4^+0	1141.94	0.42			
	-4^+2	347.49	< 1.1			
1453.43(3)	2^+0-2^+0	1372.80	3.50	+0.34(3)	−0.06(5)	$+0.40 \pm 15$ or $+1.25 + 5 - 70$
	2^+0-4^+0	1187.74	2.52	+0.15(3)	+0.04(3)	$E2$
1485.60(4)	5^-5-4^+0	1219.94	2.00			
	5^-5-6^+0	937.12	0.80			
140.63(11)	7^+2-6^+0	942.12	0.51			
1518.43(6)	5^-0-4^+0	1252.79	1.44			
	5^-0-6^+0	969.74	0.67			
1530.01(5)	6^-2-5^+2	347.49	< 1.1			
	$6-2-4^-2$	233.00	0.18			
1535.69(3)	4^+4-2^+2	647.53	3.03	+0.36(5)	−0.08(7)	$E2$
	4^+4-3^+2	572.95	< 2.03			
1570.83(3)	3^-3-3^-2	361.4	0.19			
	3^-3-1^-0	295.05	2.86	−0.10(5)	−0.06(7)	$(E2 + M2)$
	3^-3-3^-0	212.96	1.66			
1574.30(6)	4^+0-4^+0	1308.64	1.78	+0.35(6)	+0.07(8)	$+0.04\ +8 - 10$
	4^+0-6^+0	1025.74	0.39			
	4^+0-2^+2	684.8	< 0.16			
	4^+0-5^+2	391.7	< 0.57			
1634.48(10)	5^+4-3^+2	671.55	0.83			
	5^+4-4^+2	572.95	< 2.03			
	5^+4-5^+2	451.99	0.33			

Table 2. (Contd.)

E_i, keV	$J_i^\pi K - J_f^\pi K$	E_γ, keV	I_γ, arb. units	a_2	a_4	$\delta \pm \Delta\delta$; ML
1636.92(19)	$7^-1 - 6^+0$	1088.40	0.45			
1637.33(10)	$1^-1 - 0^+0$	1637.32	0.40			
	$1^-1 - 2^+0$	1556.67	1.65	+0.05(5)	0.0	*E1*
1666.28(10)	$0^+0 - 2^+0$	1585.62	< 1.09			
1669.11(5)	$4^-3 - 4^+0$	1404.0	0.31			
	$4^-3 - 3^-0$	311.22	1.20			
1691.37(13)	$2^-1 - 2^+0$	1610.95	0.99	+0.20(14)	−0.02(16)	($E1$)
	$2^-1 - 3^+2$	728.40	0.82			
	$2^-1 - 2^-2$	543.30	< 1.12			
1728.56(10)	$2^+0 - 0^+0$	1728.58	0.66			
	$2^+0 - 2^+0$	1647.90	1.21	+0.07(8)	−0.08(10)	$-0.20\ +15\ -18$ or $+4.3\ +57\ -18$
	$2^+0 - 4^+0$	1462.92	0.81			
1739.06(19)	$3^-1 - 2^+0$	1658.5	0.16			
	$3^-1 - 4^+0$	1473.40	0.55			
	$3^-1 - 4^+2$	678.05	0.42			
	$3^-1 - 2^-2$	590.6	0.28			
	$3^-1 - 3^-2$	529.19	0.80			
1745.77(6)	$1^+1 - 2^+0$	1665.29	0.90	−0.03(6)	0.0	$E1$ or $M1$
	$1^+1 - 2^+2$	857.54	0.96	−0.09(7)	0.0	$E1$ or $M1$
1766.44(19)	$3^-3 - 4^+0$	1501.5	0.09			
	$3^-3 - 2^+2$	878.54	< 0.84	+0.20(15)	0.0	
	$3^-3 - 3^+2$	803.33	< 1.0			
	$3^-3 - 2^-2$	618.3	0.30			
	$3^-3 - 3^-2$	556.33	0.45			
1782.74(13)	$2^+1 - 0^+0$	1782.81	≤ 0.61			
	$2^+1 - 2^+0$	1702.08	0.54			
	$2^+1 - 4^+0$	1516.6	0.14			
	$2^+1 - 2^+0$	894.39	0.35			
	$2^+1 - 3^+0$	819.76	0.40			
1826.70(12)	$4^-3 - 3^+2$	863.77	0.54			
	$4^-3 - 4^+2$	765.3	0.10			
	$4^-3 - 5^+2$	643.84	0.29			
	$4^-3 - 4^-2$	529.19	< 0.80			
1840.56(19)	$3^+1 - 2^+0$ 1759.63	0.28				
	$3^+1 - 4^+0$	1574.82	0.22			
	$3^+1 - 3^+2$	878.54	< 0.84			
	$3^+1 - 4^+2$	779.57	0.30			
	$3^+1 - 3^-2$	630.48	< 0.48			
	$3^+1 - 4^-2$	543.54	< 1.12			
1851.3(5)	$4^-1 - 4^+0$	1585.62	< 1.09			
1863.80(7)	$3^-2 - 2^+0$	1782.81	< 0.61			
	$3^-2 - 2^+2$	975.64	1.25			
	$3^-2 - 3^+2$	900.80	0.44			
	$3^-2 - 1^-0$	588.8	0.12			
1886.81(9)	$4^+0 - 2^+0$	1806.15	1.29	+0.38(5)	+0.08(7)	$E2$
	$4^+0 - 3^+2$	923.8	0.13			
	$4^+0 - 3^-2$	671.55	< 0.83			
1895.50(10)	$2^+ - 2^+0$	1814.92	≤ 1.22			
	$2^+ - 2^+2$	1007.0	0.27			
	$2^+ - 4^+2$	834.2	0.15			
	$2^+ - 2^-2$	747.24	< 0.51			
	$2^+ - 1^-1$	258.17	1.5			

Note: The errors are given in units of the last digit.

level in the (n, n') reaction comply well with the $J^\pi = 0^+$ spin–parity assignment for the 1400.31-keV level.

1372.80-keV transition from the 2^+ level at 1453.43 keV. Two values of δ are quoted in Table 2. By using the experimental value of the conversion coefficient, $\alpha(\text{expt.}) = 0.0021(5)$ [1], it is impossible to choose unambiguously a value of δ, since a contribution from a $E0$ transition is expected here.

295.05-keV transition from the 3^- level at 1570.83 keV. In the case of $E2$ radiation, $a_2 \simeq +0.3$ is expected for the $(3^-3{-}1^-0)$ transition, but the observed value is $a_2 = -0.10(5)$. For this transition, the conversion coefficient found experimentally is $\alpha_K(\text{expt.}) = 0.014\ (20\%)$, with the theoretical value being $\alpha_K(E2, \text{theor.}) = 0.00492$ [5]. It follows that the 295.05-keV transition involves a mixture of $E2$ and $M1$ radiations and that the spin–parity of the 1570.83-keV level is not 3^- or that this is a mixture of $E2$ and $M3$ multipoles. The latter cannot be ruled out since it is assumed in [1] that $\Delta K = 3$ for this transition.

1308.64-keV transition from the 4^+ level at 1574.30 keV. The smaller value of δ that is presented in Table 2 was chosen because of the value of $a_4 = +0.07(8)$—for the second value of $\delta = +0.85(20)$, it is expected that $a_4 = -0.08$. The value of $\alpha(\text{expt.}) = 0.0023(6)$ [1] only makes it possible to suggest the presence of a small admixture of the $E0$ transition.

1585.62-keV from the 0^+ level at 1666.28 keV. The angular distribution of gamma rays of this energy is compatible with the $J^\pi = 0^+$ assignment for the initial state in this transition.

1665.29- and 857.54-keV transitions from the 1^+ level at 1745.77 keV. For both transitions, the angular distributions rule out the $J^\pi = 2^+$ and 3^- spin–parity assignments for the initial state, but they are compatible with $J = 1$. In Table 2, the value of a_2 is indicated for $a_4 = 0$.

Peak at 878.54 keV. This peak corresponds to two transitions from the levels at 1766.44 keV $(3^-{-}2^+)$ and at 1840.56 keV $(3^+{-}3^+)$. The $E1$ transition in the first case must correspond to $a_2 = -0.20$, while the $M1$ transition in the second case must have $a_2 = +0.26$. In all probability, this peak, which exhibits the value of $a_2 = +0.20(15)$, is associated predominantly with the deexcitation of the level at 1840.5 keV.

1806.15-keV transition from the 4^+ level at 1886.81 keV. For a reason that we do not understand, this transition was not observed in [5] in the $(n, n'\gamma)$ and (n, γ) reactions. For this, comparatively intense, transition, the angular distribution complies well with that which is expected for a $4^+{-}2^+$ transition.

1814.92-keV transition from the 2^+ level at 1895.50 keV. Two different versions of placement were used in [1] for this transition. The angular distribution for it is compatible with that for the $2^+{-}0^+$ transition.

Level at 1408.48 keV? A low population for this level in the (n, n') reaction induced by fast reactor neutrons rules out the $J = 3$, 4, and 5 assignments for it. If the 347.49-keV transition is of the $E1$ type [1], the spin value of $J = 6$ is ruled out as well. No strong arguments in favor of the existence of this level are given in the review article of [1].

3. COMPARISON OF THE VALUES OF δ FOR ^{160}Dy AND ^{162}Dy

Among nonspherical nuclei, the ^{160}Dy is a *rara avis* in the sense that multipole mixtures in gamma transitions between low-lying excited states have been thoroughly explored for it. This was due to the possibility of obtaining, upon neutron capture, radioactive ^{160}Tb, which has the half-life of $T_{1/2} = 72$ d and a well-ramified diagram of its beta decay into ^{160}Dy. The deexcitation of two isomers of ^{160}Ho furnishes additional information [11]. The multipole mixtures in gamma transitions between low-lying states in dysprosium isotopes other than ^{160}Dy and ^{162}Dy have received virtually no study.

Table 4 displays the values of δ for the deexcitation of some levels of γ- and β-rotational bands in ^{160,162}Dy. First of all, the higher absolute values of δ for the deexcitation of the γ-vibrational band in ^{162}Dy are worthy of note. This is due to the lower energies of the levels in this band and, hence, to a higher degree of its collectivization. That the signs of δ in the deexcitation of ^{160}Dy and ^{162}Dy levels of the same origin are opposite in the majority of the cases also attracts attention. At the same time, the two-quasiparticle structures of the 2^+ and 0^+ one-phonon excitations in these nuclei do not show drastic distinctions [12]. Yet, the contribution of the $(pp411\uparrow 411\downarrow)$ state is greater in ^{162}Dy than in ^{160}Dy (18% versus 15.9%). In considering the signs of δ for transitions from the levels of the β- and γ-rotational bands in even–even nuclei to the levels of the rotational band built on the ground state, it was previously found [3] that, as a rule, the signs of the multipole-mixing parameter are identical for $2^+_\gamma{-}2^+_g$ and $4^+_\gamma{-}4^+_g$ transitions and are opposite for $(2^+_\gamma{-}2^+_g)$ and $(2^+_\beta{-}2^+_g)$ transitions. The second rule, that of opposite signs in ^{160,162}Dy, may probably be due to a low degree of collectivization of the β-vibrational state. This feature of ^{162}Dy was previously indicated in [5]. It is conceivable that the reasons behind the distinctions between the signs of the multipole-mixture parameter for similar transitions in ^{160}Dy and ^{162}Dy could be established more

Table 3. Comparison of experimental data on the parameter δ in ^{162}Dy

E_γ, keV	E_i, keV	$J_i^\pi - J_f^\pi$	$\delta \pm \Delta\delta$; ML					
			(n,γ) [7]	$(n,\gamma\gamma(\theta))$ [8]	$(n,n'\gamma(\theta))$ [9]	$(\alpha,2n\gamma)$ [10]	NDS [1]	$(n,n'\gamma(\theta))$ Our study
807.5	888	2^+-2^+	>3	$-8.3>\delta>+41$	$-2.9>\delta>+11$	>1.7	>8.3	$+57+\infty-33$
882.3	963	3^+-2^+	>3	$+2.6+53-16$	$-6.3>\delta>+19$	>1.1	$+3.7+7-7$	$+41+34-13$
697.3	963	3^+-4^+	$E2$	>10.4	–	–	>10.4	>45
795.3	1061	4^+-4^+	>3.9	$-5.3+2-126$	$-0.4>\delta>+2.0$	>3.9	-5.5 ± 15	$+12+18-4$
260.1	1148	2^--2^+	$E1$	-0.03 ± 16	–	–	$E1$	$+0.04+16-11$
917.1	1183	5^+-4^+	>1	$-62>\delta>+4.8$	$-2.7>\delta>+14$	2 ± 1	>14	$+50+50-20$
634.2	1183	5^+-6^+	>0.8	$+3.9+41-15$	–	<1	$+4+4-2$	$-7+2-20$
1129.4	1210	3^--2^+	<0.22	–	–	$E1$	$E1$	$+0.05+5-3$
944.4	1210	3^--4^+	<0.26	$-0.19+14-15$	–	–	-0.19 ± 15	$-0.10+3-5$
322.0	1210	3^--2^+	<0.19	–	–	–	$E1$	-0.01 ± 3
1195.1	1276	1^--2^+	<0.17	–	–	–	$E1$	$+0.01\pm4$
334.1	1297	4^--3^+	$E1$	–	–	$+0.02\pm6$	$E1$	$+0.01\pm4$
1092.2	1358	3^--4^+	<0.27	-0.08 ± 12	$-0.2+5-6$	–	$E1$	-0.07 ± 4
1124.9	1391	5^--4^+	$E1$	–	–	$E1$	$E1$	$+0.05\pm5$
1308.6	1574	4^+-4^+	$E2+M1$	–	–	≤ 1.0	$M1+E2$	$+0.04+8-10$

Note: The values of δ that are given without a sign correspond to the absolute value $|\delta|$.
The errors are given in units of the last digit.

Table 4. Values of δ for ^{160}Dy and ^{162}Dy

Transition $J_i^\pi K - J_f^\pi K$	^{160}Dy			^{162}Dy		
	E_i, keV	E_γ, keV	$\delta \pm \Delta\delta$	E_i, keV	E_γ, keV	$\delta \pm \Delta\delta$
2^+2-2^+0	966.2	879.4	-16.6 ± 5	888.1	807.5	$+57+\infty-33$
3^+2-2^+0	1049.1	962.3	-13.8 ± 3	962.9	882.3	$+47+34-13$
3^+2-4^+0	1049.1	765.3	-13.8 ± 9	962.9	697.3	$\lvert\delta\rvert>45$
4^+2-4^+0	1155.8	872.0	-0.95 ± 11	1061.0	795.3	$+12+18-4$
5^+2-4^+0	1288.7	1004.7	$+7.1+8-10$	1182.7	917.1	$+50+50-20$
2^+0-2^+0	1349.6	1262.7	$-1.5+7-20$	1453.4	1372.8	$+0.40\pm15$ or $+1.25+5-70$

reliably by investigating multipole mixtures in gamma transitions for a longer chain of dysprosium isotopes.

REFERENCES

1. R. G. Helmer and C. W. Reich, Nucl. Data Sheets **87,** 317 (1999).
2. A. M. Demidov, L. I. Govor, V. A. Kurkin, and I. V. Mikhailov, Yad. Fiz. **60**, 581 (1997) [Phys. At. Nucl. **60**, 503 (1997)].
3. A. M. Demidov, L. I. Govor, V. A. Kurkin, and I. V. Mikhailov, Yad. Fiz. **62**, 1349 (1999) [Phys. At. Nucl. **62**, 1271 (1999)].
4. A. M. Demidov, L. I. Govor, and K. A. Baskova, *Study of Excited States of Nuclei* (Nauka, Alma-Ata, 1986).
5. J. Berzins, P. Prokofjevs, R. Georgii, *et al.*, Nucl. Phys. A **584**, 413 (1995).

6. A. M. Demidov, L. I. Govor, Yu. K. Cherepantsev, *et al.*, *Atlas of the Spectra of Gamma Rays from Inelastic Scattering of Fast Reactor Neutrons* (Atomizdat, Moscow, 1978).
7. B. P. K. Maier, U. Gruber, E. B. Shera, *et al.*, Phys. Rev. **160**, 1011 (1967).
8. P. Hungerford, W. D. Hamilton, S. M. Scott, and D. D. Warner, J. Phys. G **6**, 741 (1980).
9. H. R. Hooper, J. M. Davidson, P. W. Green, *et al.*, Phys. Rev. C **15**, 1665 (1977).
10. C. A. Fields, K. H. Hicks, R. A. Ristinen, *et al.*, Nucl. Phys. A **389**, 218 (1982).
11. R. G. Helmer, Nucl. Data Sheets **78**, 547 (1996).
12. E. P. Grigoriev and V. G. Soloviev, *Structure of Deformed Even–Even Nuclei* (Nauka, Moscow, 1974).

Translated by A. Isaakyan

Physics of Atomic Nuclei, Vol. 65, No. 5, 2002, pp. 795–798. From Yadernaya Fizika, Vol. 65, No. 5, 2002, pp. 828–831.

NUCLEI
Experiment

Detection of Neutron-Spin Rotation in Neutron Scattering by ^{204}Pb*

R. Golub[1], I. L. Karpikhin, P. A. Krupchitsky, S. Lamoreaux[2], and V. V. Vasiliev

Institute of Theoretical and Experimental Physics,
Bol'shaya Cheremushkinskaya ul. 25, Moscow, 117259 Russia

Received April 9, 2001

Abstract—The effect of neutron-spin rotation due to the parity-nonconserving interaction of neutrons with nuclei in a lead sample enriched in the ^{204}Pb isotope had been measured up to the end of 1999. The problem that initiated the experiment was the earlier observed effect of neutron-spin rotation in natural lead and futile attempts at discovering this effect in isotopes constituting natural lead. At present, the final data processing has been completed. A simple model of the experiment is proposed and considered. After a careful consideration, some possibility of evaluating the instrumental error is revealed and successfully used in the array of the data obtained. The result obtained for the neutron-spin-rotation angle in a lead sample is $(8 \pm 2) \times 10^{-5}$ rad/cm for lead containing 100% ^{204}Pb. This value corresponds to the proposition that the presence of ^{204}Pb is responsible for the observed effect of neutron-spin rotation in natural lead.

The idea to observe a parity-nonconservation (PNC) effect in neutron optics was first discussed by Michel in 1960 (see, for example, [1]). A coherent effect generated by PNC weak interaction might be revealed as neutron-spin rotation in a transversely polarized neutron beam due to the fact that neutron waves with different helicities $(\mathbf{s} \cdot \mathbf{p})$, where $\mathbf{s}$ is the neutron spin and $\mathbf{p}$ is the neutron momentum, have different refraction coefficients n_+ and n_-. This is so because the neutron–nucleus interaction has a weak component depending on the neutron-spin direction. Therefore, the spinor components receive different phases and the spinor behind the sample is written as

$$\frac{1}{\sqrt{2}} \exp(ikn_+l) \begin{pmatrix} 1 \\ \exp(-i\varphi) \end{pmatrix},$$

where $\varphi = kl\mathrm{Re}(n_+ - n_-)$, k is the neutron wave number, and l is the length of the sample. The resulting spinor corresponds to the spin rotated about the momentum through the angle φ. This angle can have a measurable value in elastic neutron scattering due to the effect of dynamical amplification of parity nonconservation in a nucleus if a P resonance is present whose energy is sufficiently close to the energy of the S resonance [2–4].

The preceding two measurements of spin rotation were performed with a sample of natural lead. In the first experiment [5], the rotation angle was found to be $\varphi = (2.24 \pm 0.33) \times 10^{-6}$ rad/cm. In the second one [6], the angle $\varphi = (3.53 \pm 0.79) \times 10^{-6}$ rad/cm was observed. A direct measurement of the same effect in a sample enriched in the ^{207}Pb isotope gave the spin-rotation angle in the region $\varphi < 4.3 \times 10^{-6}$ rad/cm at a 90% C.L. [6]. In the situation where no theory explaining the PNC effect in natural lead was suggested, only the ^{204}Pb isotope remained hopeful for the existence of the P-odd effect. In this nucleus, one may expect a mixture of opposite-parity nuclear states [7]. That is why an experiment with ^{204}Pb was started at the BENSC reactor (Berlin, Germany) in a polarized cold-neutron beam.

The experimental sample was enriched in ^{204}Pb to 36.6% and had a length of 1.56 cm and a diameter of 0.6 cm. The isotope content of the sample was by chance so successful, as compared to natural lead that, if an amplified parity-violating effect could be observed in the sample, the whole effect of natural lead would be attributed to ^{204}Pb. If the PNC effect in the sample is approximately the same, this means that ^{206}Pb is responsible for the effect of natural lead.

In the experiment, a horizontal neutron beam polarized along z axis enters the low-field region, where $B < 1$ mG, through a special inlet coil operating like a current sheet that ensures the nonadiabatic inlet of the neutron spin (see figure). A cylindrical box shields this region with a μ-metal double-layer wall. A so-called π coil occupies the central part of the low-field

*This article was submitted by the authors in English.

[1] Hahn-Meitner-Institut, Glienecker Strasse 100, 14109 Berlin, Germany.

[2] Los Alamos National Laboratory, PO Box 1663, Los Alamos, NM 87545 USA.

1063-7788/02/6505-0795$22.00

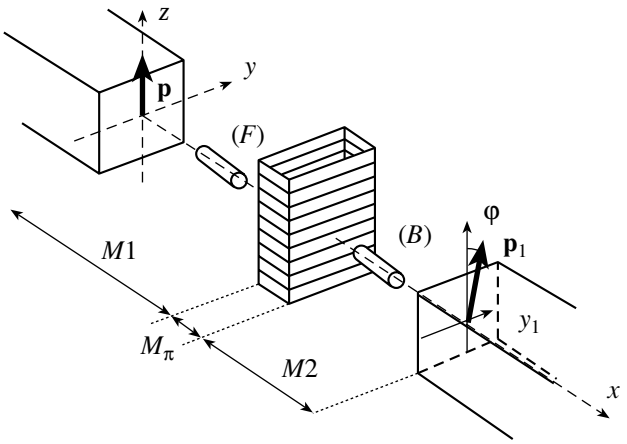

Simplified scheme of the experimental setup for neutron-spin-rotation measurements.

zone. Its magnetic field is directed along or against the z axis. The sample is placed on a holder. The holder can be moved by a system of strings and a special motor drive along channels in the supporting plate between the front position (F) and the back position (B) in the neutron beam around the π coil. If neutron transmission through the sample is dependent on the neutron helicity, an effect that is similar to neutron-spin rotation through some small angle about the beam axis will be observed. This means that, after neutron transmission through the sample, there appears a y component of the neutron polarization. The magnetic field of the π coil can rotate the horizontal neutron-spin component through 180° about the coil axis if its current is adjusted carefully. The exit of the low-field region is equipped with a rear outlet coil that is similar to the front coil, but which is rotated through 90° about the x axis to accept the y component of neutron polarization. The rear coil, together with an analyzer and a neutron counter, formed a device for detecting neutron-spin rotation. A detailed description of the setup was presented earlier in [5, 6]. But it is important here to emphasize that the residual magnetic fields before and behind the π coil can differ from each other. The effect of the distinction between scattering in the aforementioned two sample positions is taken into account as will be shown below.

To measure this spin-rotation angle, the current of the rear coil (spin flipper) is switched from $+I$ to $-I$ (I is the π-rotating value of the current) and from $-I$ to $+I$ with a period of 2 s. Thus, a relative effect of the well-known type can be measured as

$$\mathbf{A} = (N_+ - N_-)/(N_+ + N_-). \qquad (1)$$

Here, N_+ is the number of detector counts when the rear-coil field is parallel to the y polarization of the beam, while N_- is the number of detector counts when the rear-coil field is antiparallel to the y polarization of the beam. The sample position is changed from "front" to "back" and to "front" again with a period of about 140 s. It is very important to ensure conditions for measuring a spurious rotation effect caused by internal residual magnetic fields. In pursuing this objective, the current J of the π coil is changed during the measuring cycle, and three states of it are possible in the experiment: $J = +I$ ($P+$ state), $J = 0$ ($P0$ state), and $J = -I$ ($P-$ state). The order of switching was the following as a rule:

($P+$, $P0$, $P-$) for the sample in the front position (F);

($P-$, $P0$, $P+$) for the sample in the back position (B).

The developed computer code provides conditions to construct a measuring cycle where twelve average numbers represent the situation with spin rotation in the sample and in the residual magnetic field. They are

$$FN_+^{P+}, FN_-^{P+}, FN_+^{P0}, FN_-^{P0}, FN_+^{P-}, FN_-^{P-};$$
$$BN_+^{P+}, BN_-^{P+}, BN_+^{P0}, BN_-^{P0}, BN_+^{P-}, BN_-^{P-},$$

where F and B denote the front and back positions of the sample.

The relative entities like A (1) ("Angles," as is quite clear) are constructed from the numbers above:

$$\Psi_F^+ \equiv FA^{P+}, \Psi_B^+ \equiv BA^{P+},$$
$$\Psi_F^- \equiv FA^{P-}, \Psi_B^- \equiv BA^{P-}, \qquad (2)$$
$$\Psi_F^0 \equiv FA^{P0}, \Psi_B^0 \equiv BA^{P0}.$$

Taking into account the experimental scheme, one can show that the contributions of the PNC angle Φ_{PNC} and the angles of rotation by the residual magnetic fields and by the apparatus deviations must be included in the following way:

$$\Psi_F^+ = -\Phi_{\mathrm{PNC}} - \Phi_{M1} + \Phi_{M2} + \Phi_\pi, \qquad (3a)$$

$$\Psi_B^+ = +\Phi_{\mathrm{PNC}} - \Phi_{M1} + \Phi_{M2} + \Phi_\pi + 2(\delta_2 - \delta_1) + 2\delta_\pi, \qquad (3b)$$

$$\Psi_F^0 = +\Phi_{\mathrm{PNC}} + \Phi_{M1} + \Phi_{M2}, \qquad (4a)$$

$$\Psi_B^0 = +\Phi_{\mathrm{PNC}} + \Phi_{M1} + \Phi_{M2} + 2(\delta_1 + \delta_2), \qquad (4b)$$

$$\Psi_F^- = -\Phi_{\mathrm{PNC}} - \Phi_{M1} + \Phi_{M2} - \Phi_\pi, \qquad (5a)$$

$$\Psi_B^- = +\Phi_{\mathrm{PNC}} - \Phi_{M1} + \Phi_{M2} - \Phi_\pi + 2(\delta_2 - \delta_1) - 2\delta_\pi. \qquad (5b)$$

Here, Φ_{M1} and Φ_{M2} are the angles of rotation due to the residual magnetic fields before ($M1$) and behind ($M2$) the π coil, including (M_π) the possible inaccuracy in the relative orientation of the inlet and outlet

coils; Φ_π is the angle due to the effective longitudinal field of the π coil; $2\delta_1$ is the additional angle in the $M1$ zone due to the nonequivalence of the front and the rear position of the sample (effective neutron trajectories are different, and the effective magnetic fields in the front and in the back position are slightly different too); $2\delta_2$ is the additional angle in the $M2$ zone due to the same reason; and $2\delta_\pi$ is the additional angle in the π zone.

The well-known way to eliminate the direct contribution of the residual magnetic fields Φ_{M1} and Φ_{M2} is to introduce so-called π numbers:

$$\pi^+ = (\Psi_B^+ - \Psi_F^+)/2 = +\Phi_{\rm PNC} + (\delta_2 - \delta_1) + \delta_\pi, \tag{6a}$$

$$\pi^0 = (\Psi_B^0 - \Psi_F^0)/2 = (\delta_1 + \delta_2), \tag{6b}$$

$$\pi^- = (\Psi_B^- - \Psi_F^-)/2 = +\Phi_{\rm PNC} + (\delta_2 - \delta_1) - \delta_\pi. \tag{6c}$$

From (6a)–(6c), the quantity (PNC) is traditionally introduced as

$$({\rm PNC}) = (\pi^+ + \pi^-)/2 = \Phi_{\rm PNC} + (\delta_2 - \delta_1). \tag{7}$$

Thus, those six measured angles (2) are affected by seven variables. This means that it is impossible to determine $\Phi_{\rm PNC}$ exactly from Eqs. (3a)–(5b) without an additional measurement where $\Phi_{\rm PNC} = 0$ or where this angle is well known to a high precision. But this additional measurement was not foreseen by the experimental program and techniques and could not be performed.

Nevertheless, the difference $(\delta_2 - \delta_1)$ can be evaluated. As far as $\Phi_{\rm PNC} \ll (\Phi_{M1} + \Phi_{M2})$ (which is quite clear after a preliminary data processing), the ratio $\bar{k} = (\delta_2 + \delta_1)/(\Phi_{M1} + \Phi_{M2})$ can be determined from (4a) and (6b):

$$\bar{k} = \frac{(\delta_2 + \delta_1)}{\Phi_{M1} + \Phi_{M2}} \approx \frac{\pi^0}{\Psi_F^0} \approx \frac{\delta_1}{\Phi_{M1}} \approx \frac{\delta_2}{\Phi_{M2}}. \tag{8}$$

It is evident from (3a)–(5b) that the instrumental error $(\delta_2 - \delta_1)$ can be estimated as

$$\delta_2 - \delta_1 = \bar{k}[\Psi_F^0/2 + (\Psi_F^+ + \Psi_F^-)/4] - \frac{\bar{k}}{1 + 2\bar{k}}[\Psi_B^0/2 - (\Psi_B^+ + \Psi_B^-)/4]. \tag{9}$$

Thus, the difference $(\delta_2 - \delta_1)$ can be estimated [as is shown in Eqs. (8) and (9)] in each cycle. Therefore, the linear fit of (PNC) versus $(\delta_2 - \delta_1)$ will produce a result for $\Phi_{\rm PNC}$ [see (7)].

Two experimental runs (a summer run and an autumn run) were performed from the end of May to the middle of December 1999. In the final data processing, all cycles were combined into nine united runs or nine integrated so-called "big points" (BP).

Results for $\Phi_{\rm PNC}$ after a correlation analysis

Number of big points	Residual number of cycles	Angle of PNC rotation, $\Phi_{\rm PNC}$, 10^{-5} rad/cm	Standard error, 10^{-5} rad/cm
1	1239	7.2	7.3
2	3015	5.3	3.3
3	2236	1.4	4.0
4	2235	2.05	2.0
5	2138	6.5	1.9
6	631	3.76	3.6
7	1078	−2.35	5.4
8	450	15.2	8.6
9	3146	4.9	3.2

As a rule, each united run corresponds to a set of diurnal runs between succeeding readjustments of the setup. Those readjustments were initiated by repairs of the sample moving system when the strings were broken. The total numbers N of cycles at those BP before the final round of data processing were the following: $N = 5812$ for BP1, 8168 for (BP2 + BP3), 6532 for BP4, 6393 for BP5, 1592 for BP6, 2964 for BP7, 1349 for BP8, and 4383 for BP9.

Parameters like $M^+ = (\Psi_F^+ + \Psi_B^+)/2$, $M^0 = (\Psi_F^0 + \Psi_B^0)/2$, and $M^- = (\Psi_F^- + \Psi_B^-)/2$ were used to find "bad" cycles that differed from "good" cycles by more than three standard deviations from the mean value of each parameter. Sometimes, the reason for this was the malfunction of the sample moving system (most frequent situation). Sometimes, it was the malfunction of the π-coil power scheme or some perturbation of the outer magnetic field. All bad cycles that we revealed were excluded. The numbers of cycles shown above were obtained after the exclusion of preliminary bad points.

Note that, for all cycles taken into consideration, the averaging of (PNC) gave the weighted mean $(6 \pm 2) \times 10^{-5}$ rad for BP1, BP2, and BP3 and (PNC) = $(4 \pm 1) \times 10^{-5}$ rad for BP4–BP9. But these values are only upper limits on the PNC angle $\Phi_{\rm PNC}$ (7).

As is quite clear from expression (9), each cycle should be controlled in the parameter $\bar{k}$ for two reasons. The first is that $\bar{k} = -0.5$ is a singular point of (9). For the second reason, the definition of δ_1 and δ_2 means that $\delta_1 \ll \Phi_{M1}$ and $\delta_2 \ll \Phi_{M2}$, so that $\bar{k} \ll 1$. That is why only the cycles with $\bar{k} \leq 0.3$ were taken into consideration. This exclusion of cycles is quite natural if the presence of magnetic disturbances is taken into account.

After this procedure, the residual set of N cycles in each big run was subjected to a linear fit of the (PNC) quantity versus $(\delta_2 - \delta_1)$.

After all operations described above, an adequate set of the experimental data was selected and the values of Φ_{PNC} were calculated. The results are listed in the table. The weighted mean result is $(4 \pm 1) \times 10^{-5}$ rad with $\chi^2/(n-2) = 1.3$, $n = 9$. This number is the final result for the PNC effect in the sample of length 1.56 cm. Taking into account the length of the sample; the setup polarizing efficiency, which is equal to $P_1 P_2 = 0.92$; and the isotope content of the sample (36.6% of ^{204}Pb), we can show that, for a pure ^{204}Pb isotope sample, the final result for a specific rotation angle is $\Phi_{\mathrm{PNC}} = (8 \pm 2) \times 10^{-5}$ rad/cm.

Thus, the effect of neutron-spin rotation in a sample enriched in ^{204}Pb has been observed for the first time. Our final result differs from the preliminary value reported in [8]. It seems quite natural because we were able to suppress the instrumental error. The PNC angle of neutron-spin rotation in ^{204}Pb is many times greater than that in natural lead. Thus, it is possible to conclude that ^{204}Pb is responsible for the PNC effect in natural lead. The experimental result that we obtained here verified the prediction of [7] that a negative-parity nuclear state (P state) of energy close to the S resonance exists in the ^{204}Pb nucleus. It is important to emphasize that the accuracy in determining Φ_{PNC} can be improved after some modification of the experimental setup. This continuation of the work may be very productive for improving precision and, afterward, obtaining hints as to detecting a nuclear state of negative parity and energy in the ^{204}Pb nucleus by other methods.

A nuclear state of this kind has been revealed for the first time.

ACKNOWLEDGMENTS

We (especially the authors from ITEP) are indebted to O.N. Ermakov for numerous discussions on special experimental features and his constructive criticism at the stage of data processing and to G.A. Lobov for valuable advice and permanent attention.

This work was supported by the Russian Foundation for Basic Research (project no. 97-02-16184) and by the program "Fundamental Nuclear Physics" (grant no. 1.3.4-12u).

REFERENCES

1. F. C. Michel, Phys. Rev. B **133**, 329 (1964).
2. V. A. Karmanov and G. A. Lobov, Pis'ma Zh. Éksp. Teor. Fiz. **10**, 332 (1969) [JETP Lett. **10**, 212 (1969)]; G. A. Lobov, Izv. Akad. Nauk SSSR, Ser. Fiz. **34**, 1141 (1970).
3. I. S. Shapiro, Usp. Fiz. Nauk **95**, 647 (1968) [Sov. Phys. Usp. **11**, 582 (1968)].
4. O. O. Sushkov and V. V. Flambaum, Pis'ma Zh. Éksp. Teor. Fiz. **32**, 377 (1980) [JETP Lett. **32**, 352 (1980)].
5. B. R. Heckel, M. Forte, O. Schaerf, *et al.*, Phys. Rev. C **29**, 2389 (1984).
6. V. P. Bolotsky, O. N. Ermakov, R. Golub, *et al.*, Yad. Fiz. **59**, 1873 (1996) [Phys. At. Nucl. **59**, 1808 (1996)].
7. G. A. Lobov, Yad. Fiz. **63**, 1465 (2000) [Phys. At. Nucl. **63**, 1387 (2000)].
8. O. N. Ermakov, R. Golub, I. L. Karpikhin, P. A. Krupchitsky, and V. V. Vasiliev, in *Neutron Spectroscopy, Nuclear Structure, and Related Topics: Proceedings of the VIII International Seminar on Interaction of Neutrons with Nuclei, Dubna, 2000,* E3-2000-192, p. 377.

Physics of Atomic Nuclei, Vol. 65, No. 5, 2002, pp. 799–813. Translated from Yadernaya Fizika, Vol. 65, No. 5, 2002, pp. 832–846.

NUCLEI
Theory

Langevin Fission Dynamics of Hot Rotating Nuclei: Systematic Application to $Z^2/A = 34$–42 Heavy Nuclei

P. N. Nadtochy, A. V. Karpov, and G. D. Adeev

Omsk State University, pr. Mira 55A, Omsk, 644077 Russia

Received January 22, 2001; in final form, June 18, 2001

Abstract—A stochastic approach that treats fission dynamics on the basis of three-dimensional Langevin equations is used to calculate the mass–energy distributions of fragments originating from the fission of compound nuclei whose fissility parameter lies in the range $Z^2/A = 34$–42. In these calculations, use was made of the liquid-drop model allowing for finite-range nuclear forces and the diffuseness of the nuclear surface in calculating the potential energy and a modified one-body mechanism of viscosity in describing dissipation. The emission of light prescission particles is taken into account on the basis of the statistical model. The calculations performed within three-dimensional Langevin dynamics reproduce well all parameters of the experimental mass–energy distributions of fission fragments and all parameters of the prefission-neutron multiplicity for various parameters of the compound nucleus. The inclusion of the third collective coordinate in the Langevin equations leads to a considerable increase (by up to 40–50%) in the variances of mass–energy distributions in relation to what was previously obtained from two-dimensional Langevin calculations. For the parameters of the mass–energy distributions of fission fragments and the parameters of the prefission-neutron multiplicity to be reproduced simultaneously, the reduction coefficient k_s must be diminished at least by a factor of 2 ($0.2 \leq k_s \leq 0.5$) in relation to that in the case of total one-body viscosity ($k_s = 1$). © *2002 MAIK "Nauka/Interperiodica".*

1. INTRODUCTION

Over the past two decades, a stochastic approach [1–4] based on a multidimensional Fokker–Planck equation [5–8] or on the set of multidimensional Langevin equations [9], which is equivalent to it, has been successfully used to solve many problems of collective nuclear dynamics in reactions induced by heavy ions. In recent years, preference has been given in theoretical calculations to Langevin equations, since the Fokker–Planck equation is a partial differential equation, so that it can be solved only by applying cumbersome procedures and by invoking various assumptions [5–8]; at the same time, Langevin equations can be solved on the basis of conventional numerical methods without recourse to additional assumptions. However, the use of Langevin equations also involves difficulties. In order to describe as great a number of fission observables as is possible, one should ever increase the number of collective variables characterizing nuclear shapes. However, each new collective variable in Langevin equations renders relevant calculations more lengthy and cumbersome. For this reason, the calculations performed so far have been predominantly one- or two-dimensional (see [4, 10] or [11–17], respectively). One-dimensional calculations can yield only the fission probability and the multiplicities of evaporated particles. In addition to this, two-dimensional calculations make it possible to obtain the mass distribution corresponding to the most probable kinetic energy of fission fragments or the energy distribution corresponding to symmetric fission. Within one- or two-dimensional calculations, it is impossible to obtain the two-dimensional mass–energy distribution of fission fragments, which is observed experimentally and which is then used to deduce the one-dimensional mass and energy distributions. Not only does an analysis of two-dimensional mass–energy distributions provide the possibility of performing a full adequate comparison with experimental data, but it also enables one to unveil correlations between the masses and energies of fission fragments, these correlations carrying valuable information about scission configurations of a nucleus undergoing fission.

A rather comprehensive analysis of two-dimensional mass–energy distributions was first given by Nix and Swiatecki [18], who relied on the zero-viscosity dynamical model; later on, the problem was considered in [6, 19], where it was treated within the diffusion model based on the multidimensional Fokker–Planck equation. In the present article, we give an account of systematic calculations of mass–energy distributions within three-dimensional Langevin dynamics, where we also take into account the evaporation of light prescission particles. Qualitative and quantitative estimates of the effect of the third

1063-7788/02/6505-0799$22.00

collective coordinate (mass-asymmetry coordinate) on the parameters of the energy distribution were first presented in [3]. Our group also calculated the mass–energy distributions [20] for the reaction $^{12}C + {}^{194}Pt \to {}^{206}Po$ at $E_{lab} = 99$ MeV, but no systematic investigation of two-dimensional mass–energy distributions on the basis of three-dimensional models with allowance for the evaporation of light prescission particles has been performed so far.

For our analysis, we choose here reactions leading to the formation of highly excited heavy compound nuclei of temperature T in excess of 1.3 MeV. This choice of the object of investigation was motivated by the following considerations. For highly excited nuclei, we can disregard the effect of shell corrections in calculating the potential energy and the transport coefficients in the Langevin equations. For heavy nuclei characterized by values of the parameter Z^2/A in the region $Z^2/A > 32$, experiments revealed a considerable growth of the variances of the mass and energy distributions, which is not reproduced within the statistical model of Fong [21] or within the zero-viscosity dynamical model [18]. In the above region of the parameter Z^2/A, all highly excited nuclei promptly undergo fission with a probability close to unity; therefore, there is no need to consider a statistical branch in performing calculations within multidimensional Langevin dynamics [10, 22]. For lighter nuclei, it is necessary to consider a transition into this branch. The point is that, if the nuclear-fission process is simulated in terms of Langevin equations from the ground state, the nuclei being considered execute small vibrations about a spherical shape for a major part of the time, emitting light particles. In this case, dynamical calculations will be extremely time-consuming. In order to obtain a statistically significant result, a transition into the statistical branch is performed at the initial stage of the simulation; if it so happens that the nucleus does indeed undergo fission, one goes over to a dynamical simulation, beginning the calculation from the ridge that separates the ground state of the nucleus and the valley of separated fragments, the nucleus being forbidden to return to region of the ground state [10, 22].

This article is aimed at investigating nuclear-fission dynamics at the stage from the state of a statistically equilibrium nucleus formed to its separation into fragments and at computing two-dimensional mass–energy distributions and mean multiplicities of light prescission particles. The main objective of this study is to extract the nuclear viscosity from a comparison of the computed features of two-dimensional mass–energy distributions and of the multiplicity of prefission neutrons with experimental data.

2. DESCRIPTION OF THE MODEL USED

In our calculations, nuclear shapes were described in terms of a modified version of the well-known $\{c, h, \alpha\}$ parametrization [23, 24]. This parametrization was successfully used both in static and in dynamical calculations (see [23, 24] and [6, 13–15], respectively). In [23, 24], it was shown that, within the $\{c, h, \alpha\}$ parametrization, it is possible to reproduce accurately the features of the saddle-point nuclear configurations that were obtained on the basis of variational calculations [25] within the model representing a nucleus as a liquid drop with a sharp boundary, where no constraint is imposed on the nuclear shape.

The equation of the nuclear surface in cylindrical coordinates has the form [23, 26]

$$\rho_s^2(z) = \begin{cases} c^{-2}\left(c^2 - z^2\right)\left(A_s c^2 + Bz^2 + \dfrac{\alpha' z}{c^2}\right), & B \geq 0, \\ c^{-2}\left(c^2 - z^2\right)\left(A_s c^2 + \dfrac{\alpha' z}{c^2}\right)\exp(Bcz^2), & B < 0, \end{cases} \tag{1}$$

where z is the coordinate along the symmetry axis and ρ_s is the value of the coordinate ρ at the nuclear surface. The quantities B and A_s are expressed in terms of the nuclear-shape parameters (c, h) as

$$B = 2h + \frac{c-1}{2}, \tag{2}$$

$$A_s = \begin{cases} c^{-3} - \dfrac{B}{5}, & B \geq 0, \\ -\dfrac{4}{3}\dfrac{B}{\exp(Bc^3) + (1 + \dfrac{1}{2Bc^3})\sqrt{-\pi Bc^3}\,\mathrm{erf}(\sqrt{-Bc^3})}, & B < 0. \end{cases}$$

In Eqs. (1) and (2), c is the elongation parameter, h is a parameter that specifies the neck thickness at

a given elongation, and α' is the mass-asymmetry parameter. Shapes that are symmetric with respect to the $z = 0$ plane correspond to the case of $\alpha' = 0$.

The parametrization used in Eq. (1) differs from the original $\{c, h, \alpha\}$ parametrization in that it involves a new mass-asymmetry parameter related to α by the scale transformation

$$\alpha' = \alpha c^3. \tag{3}$$

The advantages of the parameter α' over α were indicated and discussed many years ago (see [27]). The problem of choosing collective coordinates was investigated in [14], and it was shown there, on the basis of two-dimensional calculations, that, in describing the fission process, the coordinates (R, h) are preferable to (c, h), where R is the distance between the centers of mass of nascent fragments. Strutinsky [28] proposed using, for a mass-asymmetry coordinate, the quantity η instead of α, where η is the ratio of the mass difference between the nascent fragments to the total mass of the compound nucleus, and proved that this choice is preferable. It should be noted that (R, η) are the first two collective coordinates in the scheme where the multipole moments of the nuclear density are used as a basis for introducing collective coordinates [29].

Although the coordinates (R, η) have a clear physical meaning, the use of these coordinates in three-dimensional Langevin calculations leads to serious computational problems, since it is impossible to find explicitly the dependence of the shape parameters (c, h, α') on (R, h, η). For this reason, we have chosen, for collective coordinates, the geometric parameters (c, h, α') of the nuclear shape. If, however, we assume that the nucleus being considered is split into fragments by the $z = 0$ plane, the parameter α' becomes proportional to η; that is,

$$\eta = \frac{3}{8}\alpha'. \tag{4}$$

The most important advantage of using the parameter α' instead of α is that the mesh suitable for dynamical calculations in the coordinates (h, α') can be considerably enlarged in relation to that for the original $\{c, h, \alpha\}$ parametrization.

The evolution of a nucleus undergoing fission was considered within the stochastic approach [1–9]. The evolution of the collective coordinates was treated by analogy with the motion of a Brownian particle placed in a heat bath formed by all other degrees of freedom of the nucleus. In the calculations, we used the set of coupled Langevin equations

$$\dot{q}_i = \mu_{ij} p_j, \tag{5}$$
$$\dot{p}_i = -\frac{1}{2} p_j p_k \frac{\partial \mu_{jk}}{\partial q_i} - \frac{\partial V}{\partial q_i} - \gamma_{ij}\mu_{jk} p_k + \theta_{ij}\xi_j,$$

where $\mathbf{q} = (c, h, \alpha')$ are collective coordinates; $\mathbf{p} = (p_c, p_h, p_{\alpha'})$ are the momenta conjugate to them; m_{ij} ($\|\mu_{ij}\| = \|m_{ij}\|^{-1}$) is the tensor of inertia; γ_{ij} is the friction tensor; V is the potential energy of the nucleus being considered; $\theta_{ij}\xi_j$ is a random force; θ_{ij} is its amplitude; and ξ_j is a random variable that possesses the following statistical properties:

$$\langle \xi_i \rangle = 0, \tag{6}$$
$$\langle \xi_i(t_1)\xi_j(t_2) \rangle = 2\delta_{ij}\delta(t_1 - t_2).$$

The angular brackets in Eq. (6) mean averaging over the statistical ensemble. Summation over dummy indices from 1 to 3 is implied in Eqs. (5) and (6) and below.

The random-force amplitudes are related to the diffusion tensor D_{ij} as

$$D_{ij} = \theta_{ik}\theta_{kj}. \tag{7}$$

The diffusion tensor in turn satisfies the Einstein relation

$$D_{ij} = T\gamma_{ij}. \tag{8}$$

The random-force amplitudes were found from Eqs. (7) and (8) by using the Jacobi method [30].

The heat-bath temperature T used in the calculations was determined within the Fermi gas model as

$$T = (E_{\rm int}/a(\mathbf{q}))^{1/2}, \tag{9}$$

where $E_{\rm int}$ is the excitation energy of single-particle degrees of freedom of the compound nucleus (internal energy) and $a(\mathbf{q})$ is the level-density parameter, which depends on the collective coordinates. Specifically, we take the level-density parameter in the form

$$a(\mathbf{q}) = a_v A + a_s A^{2/3} B_s(\mathbf{q}), \tag{10}$$

where A is the mass of the compound nucleus and $B_s(\mathbf{q})$ is the dimensionless surface-energy functional calculated in the model where a nucleus is represented as a liquid drop with a sharp boundary [23, 24]. The parameter values of $a_v = 0.073$ MeV^{-1} and $a_s = 0.095$ MeV^{-1} were borrowed from [31].

As the nucleus moved toward the scission surface, fulfillment of the energy-conservation law

$$E^* = E_{\rm int} + E_{\rm coll}(\mathbf{q}, \mathbf{p}) + V(\mathbf{q}) + E_{\rm evap}(t), \tag{11}$$

where E^* is the total excitation energy of the compound nucleus (it is determined in the input reaction channel from the energy of the projectile ion and the mass difference between colliding nuclei and the compound system), $E_{\rm coll}(\mathbf{q}, \mathbf{p}) = \frac{1}{2}\mu_{ij}(\mathbf{q})p_i p_j$ is the kinetic energy of the collective motion of the nucleus, and $E_{\rm evap}(t)$ is the nuclear excitation energy carried away by evaporated particles by the instant t, was

traced along the entire stochastic Langevin trajectory in the space of collective coordinates.

The tensor of inertia was calculated in the Werner–Wheeler approximation for the irrotational flow of an incompressible liquid (a description of the method can be found in [32]). In [33], it was shown that this method makes it possible to calculate accurately the components of the tensor of inertia for all shapes of the nucleus undergoing fission, with the exception of that which features a zero-thickness neck.

In order to describe the dissipation of the collective kinetic energy into the internal energy, we have used a modified version of one-body viscosity [34, 35], the so-called surface-plus-window mechanism of dissipation. In this case, the components of the friction tensor are given by

$$\gamma_{ij}^{\mathrm{sw}} = \frac{1}{2}\rho_m\bar{v}\left\{\frac{\partial R}{\partial q_i}\frac{\partial R}{\partial q_j}\Delta\sigma + \frac{32}{9}\frac{1}{\Delta\sigma}\frac{\partial V_1}{\partial q_i}\frac{\partial V_1}{\partial q_j}\right.$$
$$+ k_s\left[\pi\int\limits_{z_{\min}}^{z_N}\left(\frac{\partial\rho_s^2}{\partial q_i}+\frac{\partial\rho_s^2}{\partial z}\frac{\partial D_1}{\partial q_i}\right)\left(\frac{\partial\rho_s^2}{\partial q_j}+\frac{\partial\rho_s^2}{\partial z}\frac{\partial D_1}{\partial q_j}\right)\right.$$
$$\times\left(\rho_s^2+\left(\frac{1}{2}\frac{\partial\rho_s^2}{\partial z}\right)^2\right)^{-1/2}dz \qquad (12)$$
$$+\pi\int\limits_{z_N}^{z_{\max}}\left(\frac{\partial\rho_s^2}{\partial q_i}+\frac{\partial\rho_s^2}{\partial z}\frac{\partial D_2}{\partial q_i}\right)\left(\frac{\partial\rho_s^2}{\partial q_j}+\frac{\partial\rho_s^2}{\partial z}\frac{\partial D_2}{\partial q_j}\right)$$
$$\left.\left.\times\left(\rho_s^2+\left(\frac{1}{2}\frac{\partial\rho_s^2}{\partial z}\right)^2\right)^{-1/2}dz\right]\right\},$$

where ρ_m is the nuclear density; $\bar{v}$ is the mean velocity of intranuclear nucleons; $\Delta\sigma$ is the area of the window—that is, the neck between the two would-be fragments; D_1 and D_2 are the positions of their centers of mass with respect to the center of mass of the entire system; $z_{\min}$ and $z_{\max}$ are, respectively, the left and the right boundary of the nuclear surface; z_N is the coordinate of the neck, which was chosen at the minimum of the function $\rho_s^2(z)$; and V_1 is the volume of one of the would-be fragments.

A quantum analysis of one-body dissipation revealed [36] that the viscosity in a nucleus is only about 10% of the value computed by the wall formula [37, 38] [bracketed expression in (12)], but that the functional dependence of the viscosity on the nuclear shape is reproduced correctly by the wall formula. In view of this, Nix and Sierk proposed a modified version of one-body dissipation. In this version, referred to as the surface-plus-window one, the contribution of the wall formula to dissipation is reduced nearly by a factor of 4 (the value of the reduction coefficient k_s was determined from an analysis of the experimental widths of giant resonances; the result was $k_s = 0.27$). From a comparison of the calculated mean values of the kinetic energies of fission fragments with experimental data, it was found [35] that the reduction factor k_s lies in the range $0.2 < k_s < 0.5$. The value of $k_s = 1$ corresponds to the total one-body viscosity. In the following, we denote by γ_{ij}^w the friction-tensor components computed by the wall formula. In the present calculations, an additional term (second term in the braced expression) that takes into account dissipation associated with the change in the volumes of the would-be fragments that results from the exchange of nucleons between them [5, 39] is included in formula (12). For the analysis of the formation of the mass distribution to be adequate, the effect of this term must be taken into account in dynamical calculations.

For nuclear shapes featuring no neck, the friction tensor was calculated by the wall formula with the reduction coefficient k_s. As soon as a neck appeared in the nuclear shape, we began smoothly (in just the same way as was done in [40]) to switch on the surface-plus-window viscosity mechanism in such a way that there remained only the surface-plus-window viscosity mechanism at zero neck thickness; that is,

$$\gamma_{ij} = \begin{cases} k_s\gamma_{ij}^w \quad \text{for nuclear shapes featuring no neck,} \\ k_s\gamma_{ij}^w\sin^2(\pi R_N/(2R_L)) + \gamma_{ij}^{\mathrm{sw}}\cos^2(\pi R_N/(2R_L)) \\ \qquad \text{for nuclear shapes featuring a neck,} \end{cases} \qquad (13)$$

where R_N is the neck radius and R_L is the maximum value of the function $\rho_s(z)$ for the smaller fragment.

The potential energy of the nucleus was computed within the liquid-drop model taking into account finite-range nuclear forces and the diffuseness of the nuclear surface [41, 42]. The parameters of the model were set to the values used in [42]. The potential energy was reckoned from that in a spherical state of the nucleus with zero angular momentum.

As is well known [31, 43], it is a thermodynamic potential (free energy [2] or entropy [4]), rather than the potential energy, that must be used in calculating a conservative force in thermodynamic systems. For a long time, however, there had remained

an uncertainty in the temperature dependence of the parameters of the model representing a nucleus as a liquid drop with a sharp boundary [44–46]. Only quite recently did there appear the article of Krappe [47], who generalized the temperature dependence of the entropy in the liquid-drop model taking into account finite-range nuclear forces and the diffuseness of the nuclear surface. In our opinion, however, the first full-scale three-dimensional Langevin calculations should be performed with the potential energy in order that the results could be compared with the results of previous calculations based on two-dimensional models.

All transport coefficients appearing in the Langevin equations were computed on an equidistant cubic mesh containing $151 \times 101 \times 51$ nodes; the collective variables changed within the following ranges: $c \in [0.7, 3.7]$, $h \in [-0.6, 0.4]$, and $\alpha' \in [-1, 1]$. The interpolation between the nodes was performed by using the Lagrange formulas.

The initial conditions for the dynamical Eqs. (5) were chosen as follows. The initial shape of the nucleus was assumed to be spherical [$\mathbf{q}_0 = (c = 1, h = 0, \alpha' = 0)$], and the momentum distribution was taken to be equilibrium. The angular-momentum distribution was described by a function $F(l)$ whose explicit form was given in [4, 10]. Specifically, the function $F(l)$ represents the angular-momentum distribution of compound nuclei produced in the fusion process. The numerical procedure for fixing the initial conditions relied on the Neumann method involving the generating function

$$P(\mathbf{q}_0, \mathbf{p}_0, l, t = 0) \tag{14}$$
$$\sim \exp\left\{ -\frac{V(\mathbf{q}_0) + E_{\mathrm{coll}}(\mathbf{q}_0, \mathbf{p}_0)}{T} \right\} \delta(\mathbf{q} - \mathbf{q}_0) F(l).$$

This choice of initial conditions implies that we confine our consideration to the situation where the projectile particle and the target fuse completely, forming a compound nucleus in a state of statistical equilibrium. Therefore, this formalism is inappropriate for describing the quasifission process. It should be emphasized that, at high excitation energies and especially at high angular momenta, the traditional concept of a compound nucleus becomes a rough idealization of an intricate actual situation.

The evaporation of light prefission particles was simulated according to the following scheme. The Langevin equations were integrated with a time step τ by using the Hewn difference scheme [4, 12]. At each step of the integration, we determined the partial widths Γ_j ($j = n, p, d, t,\ ^3\mathrm{He}, \alpha, \gamma$) with respect to the decay of the compound nucleus through the corresponding channel [48]. After that, their sum was used to calculate the mean lifetime of the compound nucleus prior to the emission of some particle: $\tau_{\mathrm{tot}} = \hbar / \sum_j \Gamma_j$. Given the integration step τ, one can determine the probability of evaporation of one particle or another from the nucleus [49, 50]: for this, a uniformly distributed random number ξ was sampled over the segment $[0, 1]$ and was then compared with the ratio τ/τ_{tot}. Under the condition $\xi < \tau/\tau_{\mathrm{tot}}$, it was assumed that some light particle is emitted. The choice of particle type was implemented through a Monte Carlo procedure employing probabilities that are proportional to the decay widths Γ_j. This evaporation model makes it possible to describe discrete particle emission (in contrast to a continuous simulation of it in [11, 12]) and reproduces the law of radioactive decay. During the simulation of particle evaporation, the functionals representing the Coulomb, the nuclear, and the rotational energy and appearing in the expression for the potential energy were not rescaled. Only new values of relevant dimensional factors were determined on the basis of new values of A or Z (or both). Test calculations revealed that, even upon the emission of several particles, the difference of the precise value of the potential energy and its value found without rescaling the functionals does not exceed 1 MeV. In the calculations, it was assumed that the angular momentum of $l_j = 1, 1, 2, 1, 1, 2, 1$ (in $\hbar$ units) is carried away by the jth evaporated particle [22].

An important problem in performing calculations within multidimensional Langevin dynamics is that of choosing, in the space of collective coordinates, the scission surface upon the intersection of which the nucleus is thought to be split into fragments. This surface can be chosen on the basis of various scission criteria. The vanishing of the neck radius is one of the simplest criteria for this. If, however, use is made the model representing a nucleus as a liquid drop with a sharp boundary, this condition becomes meaningless as soon as the neck radius appears to be on the same order of magnitude as the internucleon spacing. The loss of stability of the nucleus to changes in the neck thickness seems a more justifiable criterion from the physical point of view. Within our problem, this criterion can be expressed in the following way: the nucleus loses stability once the relevant stochastic Langevin trajectory intersects the surface specified by the equation [6, 13, 23]

$$\left(\frac{\partial^2 V}{\partial h^2}\right)_{c=\mathrm{const}, \alpha'=\mathrm{const}} = 0. \tag{15}$$

Upon taking the average over the ensemble of Langevin trajectories, this condition corresponds to nuclear shapes for which the neck radius is $0.3R_0$ [14, 23, 25]. A different physically acceptable criterion of scission is based on the assumption that the nucleus

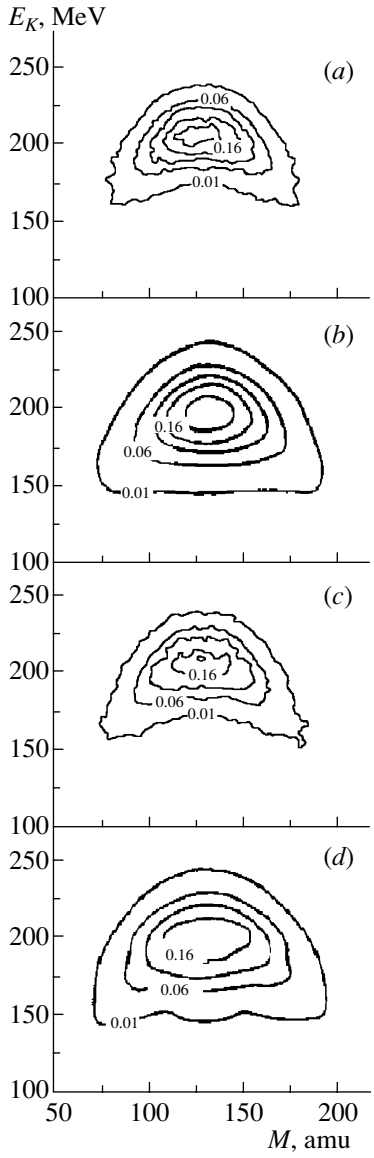

Fig. 1. Contour plots of the mass–energy distribution of fission fragments for the reaction $^{20}\mathrm{Ne} + {}^{240}\mathrm{Pu} \rightarrow {}^{260}\mathrm{Rf}$ at two values of the excitation energy: (a) results of our theoretical calculations with $k_s = 0.1$ at the excitation energy of $E_{\mathrm{lab}} = 142$ MeV, (b) experimental data from [52] at the excitation energy of $E_{\mathrm{lab}} = 142$ MeV, (c) results of our theoretical calculations with $k_s = 0.1$ at the excitation energy of $E_{\mathrm{lab}} = 174$ MeV, and (d) experimental data from [52] at the excitation energy of $E_{\mathrm{lab}} = 174$ MeV. The displayed distributions are normalized to 200%, and the numbers on the isolines indicate the yields of fission fragments (in percent).

becomes unstable to the rupture of the neck when the force of nuclear attraction between nascent fragments is equilibrated by the force of the Coulomb repulsion between them. It was shown in [51] that, in the region of actinides, this condition corresponds to nuclear shapes for which the neck radius is approximately equal to $0.3R_0$ as well. On the basis of the above, we assumed in our calculations that the nucleus is split into fragments as soon as the neck radius becomes equal to $0.3R_0$. This condition specifies the scission surface in the space of collective coordinates.

3. RESULTS OF THE CALCULATIONS AND DISCUSSION

The mass–energy distributions of fission fragments were calculated here for the following reactions:

$$^{12}\mathrm{C} + {}^{194}\mathrm{Pt} \rightarrow {}^{206}\mathrm{Po} \quad (E_{\mathrm{lab}} = 99\ \mathrm{MeV})\ [52],$$
$$^{18}\mathrm{O} + {}^{197}\mathrm{Au} \rightarrow {}^{215}\mathrm{Fr}$$
$$(E_{\mathrm{lab}} = 158.8\ \mathrm{MeV})\ [53],$$
$$^{16}\mathrm{O} + {}^{208}\mathrm{Pb} \rightarrow {}^{224}\mathrm{Th}$$
$$(E_{\mathrm{lab}} = 108\ \mathrm{MeV})\ [54, 55],$$
$$^{20}\mathrm{Ne} + {}^{209}\mathrm{Bi} \rightarrow {}^{229}\mathrm{Np} \quad (E_{\mathrm{lab}} = 149\ \mathrm{MeV})\ [56],$$
$$^{12}\mathrm{C} + {}^{232}\mathrm{Th} \rightarrow {}^{244}\mathrm{Cm} \quad (E_{\mathrm{lab}} = 97\ \mathrm{MeV})\ [57],$$
$$^{18}\mathrm{O} + {}^{238}\mathrm{U} \rightarrow {}^{256}\mathrm{Fm} \quad (E_{\mathrm{lab}} = 158.8\ \mathrm{MeV})\ [53],$$
$$^{20}\mathrm{Ne} + {}^{240}\mathrm{Pu} \rightarrow {}^{260}\mathrm{Rf}$$
$$(E_{\mathrm{lab}} = 142 \text{ and } 174\ \mathrm{MeV})\ [52].$$

Indicated above for each reaction are the references from which we borrowed experimental data. All these reactions lead to the production of highly excited heavy nuclei for which $Z^2/A = 34$–42. Typical contour plots of the mass–energy distribution $Y(E_K, M)$ are shown in Fig. 1 for the example of the compound nucleus $^{260}\mathrm{Rf}$ at two values of the excitation energy. First of all, it should be noted that the general character of the contour-plot chart of the distribution $Y(E_K, M)$ computed within three-dimensional Langevin dynamics closely resembles the pattern of the corresponding charts obtained from experimental data.

From Fig. 1, it can be seen that the shape of the contour lines is close to an ellipsoidal one near the maximum of $Y(E_K, M)$ and to triangles with smoothed angles at small values of $Y(E_K, M)$ and that the width of the mass–energy distributions increases with increasing excitation energy of the compound nucleus. These contour-line charts furnish compelling evidence in favor of the liquid-drop correlation between the masses and kinetic energies of fission fragments. It is also worthy of note that the contour-plot charts presented in Fig. 1 for the distribution $Y(E_K, M)$ are similar to those obtained in [18] on the basis of the zero-viscosity dynamical model proposed in that study and to those computed in [6, 19] on the basis of the diffusion model, although

the distribution $Y(E_K, M)$ was calculated by three different methods in the three cases in question.

The statistical uncertainty in the results presented here does not exceed 3–7%, the relevant calculations being performed in just the same way as in [58]. In order to avoid encumbering the figures displayed in this article, we therefore indicate here this uncertainty only in some cases.

In the following, the entire body of information about the characteristics of the distributions $Y(E_K, M)$ will be discussed in terms of the one-dimensional mass and energy distributions and their mean values and variances; also considered here are correlations between different parameters of $Y(E_K, M)$. The one-dimensional mass and energy distributions are obtained by integrating $Y(E_K, M)$ with respect to E_K and M, respectively.

3.1. One-Dimensional Mass and Energy Distributions

The one-dimensional mass and energy distributions calculated for the reaction

$$^{18}\mathrm{O} + {}^{197}\mathrm{Au} \to {}^{215}\mathrm{Fr} \quad (E_{\mathrm{lab}} = 158.8\ \mathrm{MeV})$$

are displayed in Figs. 2 and 3. For the sake of comparison, the experimental distributions of the corresponding quantities are also shown in these figures. From Fig. 3, it can be seen that the energy distribution computed here differs from a Gaussian distribution: it has a kurtosis approximately equal to unity and a nonzero negative value of the asymmetry factor. On the contrary, the mass distribution has a nearly Gaussian shape (the kurtosis and the asymmetry virtually vanish). The mean values and the variances of the one-dimensional mass and energy distributions are basic features of these distributions, and the discussion of our results is performed, as a rule, in terms of these quantities.

In the calculations presented in this article, it is assumed that the kinetic energy of fission fragments is the sum of the Coulomb repulsion energy V_{C}, the nuclear energy V_n of the attraction of the fragments, and the kinetic energy E_{ps} of their motion, all terms being calculated at the instant of scission. The expression for the mean kinetic energy of fission fragments has the form

$$\langle E_K \rangle = \langle V_{\mathrm{C}} \rangle + \langle V_n \rangle + \langle E_{\mathrm{ps}} \rangle; \qquad (16)$$

that is, it is assumed in our calculations that part of the Coulomb repulsion energy is expended into overcoming the force of nuclear attraction between the fragments. Simple estimates of this quantity as an additional surface energy appearing upon the rupture of the neck were obtained in [14, 59]. In the present study, V_n and V_{C} were computed within the liquid-drop model taking into account finite-range nuclear forces and the diffuseness of the nuclear surface. Numerical methods were employed in evaluating relevant integrals [60] and in calculating the potential energy.

Our calculations revealed that the first and the second moments of the mass and energy distributions are sensitive to the viscosity value used in the calculations and to the character of descent from the saddle to the scission point. The parameters of the energy distribution are also highly sensitive to the choice of scission condition [37, 51].

The parameters of the energy distributions for various nuclei were explored in a great number of both experimental and theoretical studies (see [57, 61, 62] and [11–14], respectively). From an analysis of experimental data, it was found that $\langle E_K \rangle$ is virtually independent either of the angular momentum or of the excitation energy [61]. In addition, it was shown in [57, 61] that $\langle E_K \rangle$ is not a linear function of the parameter $Z^2/A^{1/3}$, as is suggested by Viola's systematics [63]—if, in the entire body of experimental data, one selects only those for rather hot nuclei, eliminating low-energy fission and spontaneous fission, which are strongly affected by shell effects, and quasifission, there appears a break point at $Z^2/A^{1/3} \sim 1000$. From Fig. 4*a*, it can be seen that the $\langle E_K \rangle$ values obtained in our calculations agree well with experimental data and lie more closely to the systematics proposed in [54] than to Viola's systematics. It should be emphasized that the values of $\langle E_K \rangle$ that are obtained in our calculations decrease with increasing reduction factor k_s. A similar result was obtained in the two-dimensional calculations performed by Nix and Sierk [35], who took the vanishing of the neck radius for the scission condition and who achieved the best description of experimental data at k_s approximately equal to 0.3. In our calculations, the value of $\langle E_K \rangle$ is not very sensitive to changes in k_s; therefore, it is difficult to draw conclusions about the viscosity value on its basis. The fact that, in our calculations, $\langle E_K \rangle$ virtually ceases to be dependent on k_s is due to taking into account the evolution of the nucleus in the mass-asymmetry coordinate, in contrast to the two-dimensional calculations of Nix and Sierk [35], and to determining $\langle E_K \rangle$ by integrating $\langle E_K(M) \rangle$ with respect to M. In [3], it was shown that, for a large value of friction, in which case the descent from the saddle to the scission points proceeds slowly—that is, E_{ps} can be set to zero—$\langle E_K \rangle_{3D}$, the mean kinetic energy of fragments that is obtained in three-dimensional calculations, is related to $\langle E_K \rangle_{2D}$, the mean kinetic energy of fragments that is obtained in

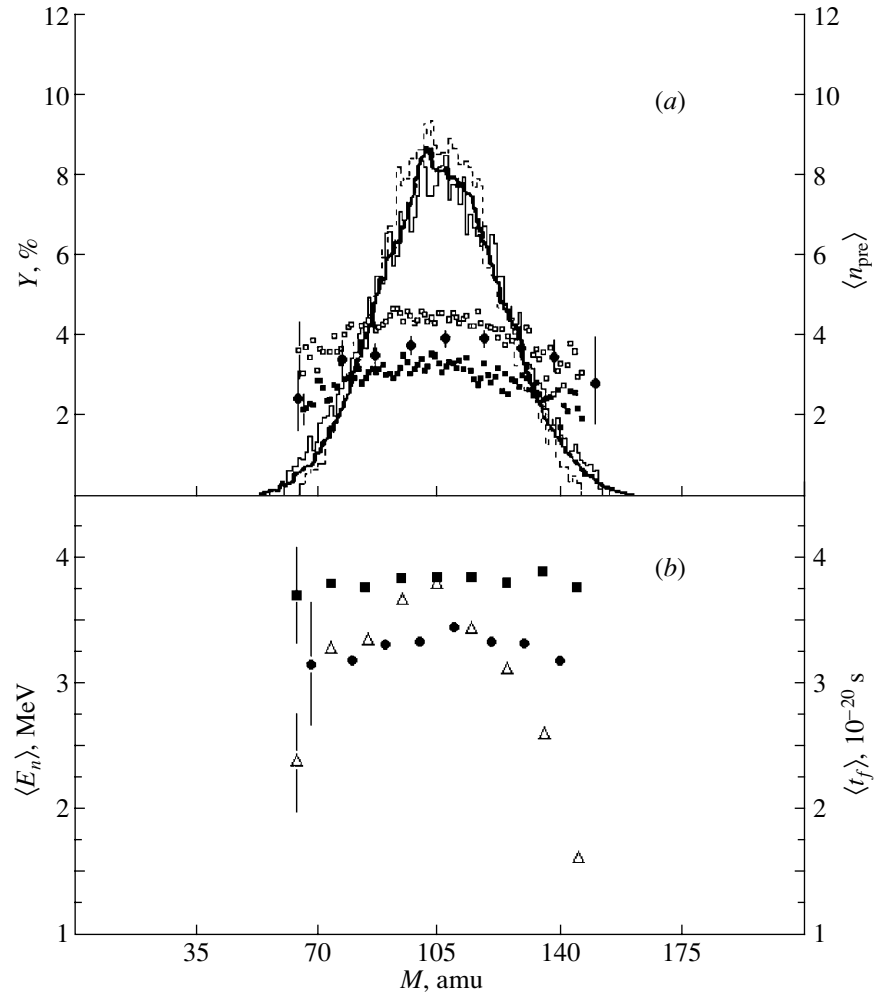

Fig. 2. Experimental data and results of the calculations for the reaction $^{18}O + {}^{197}Au \rightarrow {}^{215}Fr$ at $E_{lab} = 158.8$ MeV: (*a*) mass distribution {(thick solid line) experimental data from [53], (thin solid line) results of the calculations with $k_s = 0.25$, and (dashed line) results of the calculations with $k_s = 0.5$} and neutron multiplicity versus the fragment mass {(closed circles) experimental data from [53], (closed boxes) results of the calculations with $k_s = 0.25$, and (open boxes) results of the calculations with $k_s = 0.5$}; (*b*) neutron energy versus the fragment mass {(closed circles) experimental data from [53], (closed boxes) results of the calculations with $k_s = 0.25$, and (open triangles) calculated fission time versus the fragment mass}.

two-dimensional calculations, by the equation

$$\langle E_K \rangle_{3D} = (1 - \sigma_\eta^2)\langle E_K \rangle_{2D}, \qquad (17)$$

where σ_η^2 is the variance of the mass coordinate η. With increasing k_s, σ_η^2 decreases, which naturally leads to an increase in the parenthetical expression in Eq. (17); on the contrary, $\langle E_K \rangle_{2D}$ decreases. Upon the multiplication of these two factors, $\langle E_K \rangle_{3D}$ becomes less sensitive to k_s than $\langle E_K \rangle_{2D}$.

From Fig. 4*b*, it can be seen that the sharp growth of the experimental values of σ_M^2 in the region of heavy nuclei can also be reproduced fairly well within our stochastic approach. The results of our calculations with $k_s = 1$ virtually coincide with the results of the calculations performed within the statistical model used in [21]. The growth of σ_M^2 with decreasing k_s can be explained as follows: on one hand, the stiffness of the potential energy in the mass-asymmetry coordinate permanently increases as the nucleus descends from the saddle to the scission point; accordingly, the mass distribution becomes narrower. On the other hand, the system retains memory of the previous, larger, width of the distribution, since the descent proceeds within a finite time interval. Obviously, the faster the descent, the greater the values of the variance that are recalled. The velocity of the descent is controlled primarily by the viscosity, whose value is determined by the value of the coefficient k_s. This mechanism of formation of the mass distribution was discussed in greater detail elsewhere [6, 19].

The values of $\sigma_{E_K}^2$ that are calculated for various values of k_s are shown in Fig. 4*c*. From this fig-

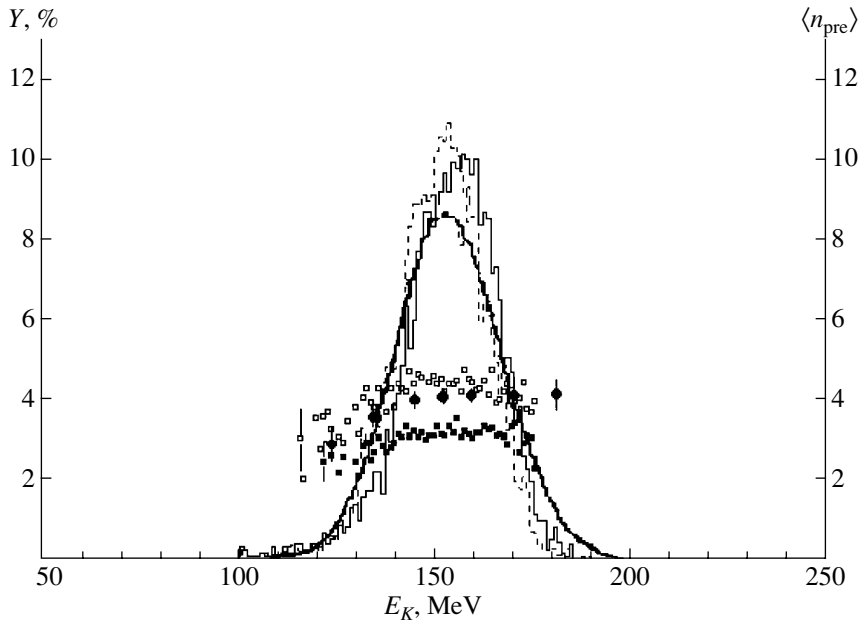

Fig. 3. Experimental data and results of the calculations for the reaction $^{18}O + {}^{197}Au \rightarrow {}^{215}Fr$ at $E_{lab} = 158.8$ MeV: energy distribution {(thick solid line) experimental data from [53], (thin solid line) results of the calculations with $k_s = 0.25$, and (dashed line) results of the calculations with $k_s = 0.5$} and neutron multiplicity versus the fragment kinetic energy {(closed circles) experimental data from [53], (closed boxes) results of the calculations with $k_s = 0.25$, and (open boxes) results of the calculations with $k_s = 0.5$}.

ure, we can see that the calculations within three-dimensional Langevin dynamics at $k_s \sim 0.1$–0.25 make it possible to reproduce fairly well the growth of the experimental values of the variances with increasing $Z^2/A^{1/3}$ at a quantitative level. The results of the calculations at $k_s = 1$ nearly coincide with the results of the calculations performed on the basis of the zero-viscosity dynamical model [18]. Our calculations revealed that the inclusion of the third collective coordinate (mass-asymmetry coordinate) leads to a considerable increase (by about 40%) in $\sigma^2_{E_K}$ in relation to the calculations within two-dimensional models [11–14] for symmetric fission. This result is in agreement with the qualitative estimates presented in [3], which predict that the width of the energy distribution obtained in two-dimensional calculations for symmetric fission increases upon taking into account fluctuations of the mass-asymmetry coordinate.

Thus, we see that, from a comparison of the variances computed for various values of k_s with experimental data, one can conclude that, in order to reproduce the experimental values of the variances in the region of the lightest nuclei considered here (^{206}Po, ^{215}Fr, ^{224}Th), it is necessary that the calculations be performed with value of $k_s \sim 0.5$; at the same time, values in the range $k_s \sim 0.1$–0.2 are appropriate for heavier nuclei.

At Z^2/A values in the range being considered, the sharp growth of the experimental values of $\sigma^2_{E_K}$ and σ^2_M with increasing mass of fissile nuclei cannot be described even qualitatively within the statistical model of fission [21] or within the zero-viscosity dynamical model [18]. Considerable advances in describing the fissility-parameter dependence of the variances $\sigma^2_{E_K}$ and σ^2_M have been made within the diffusion model [6, 19]; however, the calculations within the diffusion model were performed without taking into account the evaporation of light prescission particles. This effect has a strong impact on the parameters of the mass–energy distributions [12], since evaporated particles carry away a considerable part of the excitation energy; accordingly, the variances of the mass and energy distributions decrease.

3.2. Multiplicities of Prescission Neutrons and Fission Times

Among all particles evaporated from the nucleus, a special role is played by neutrons [64], because the number of neutrons evaporated in the fission process is much greater than the number of evaporated charged particles or photons. Moreover, the multiplicity of prefission neutrons, n_{pre}, appears to be a peculiar kind of clock measuring the fission time [53, 64].

The results of the calculations for the mean multiplicity of prefission neutrons, $\langle n_{pre} \rangle$, are presented in Fig. 5 for $k_s = 1$ and $k_s = 0.5$. From this figure,

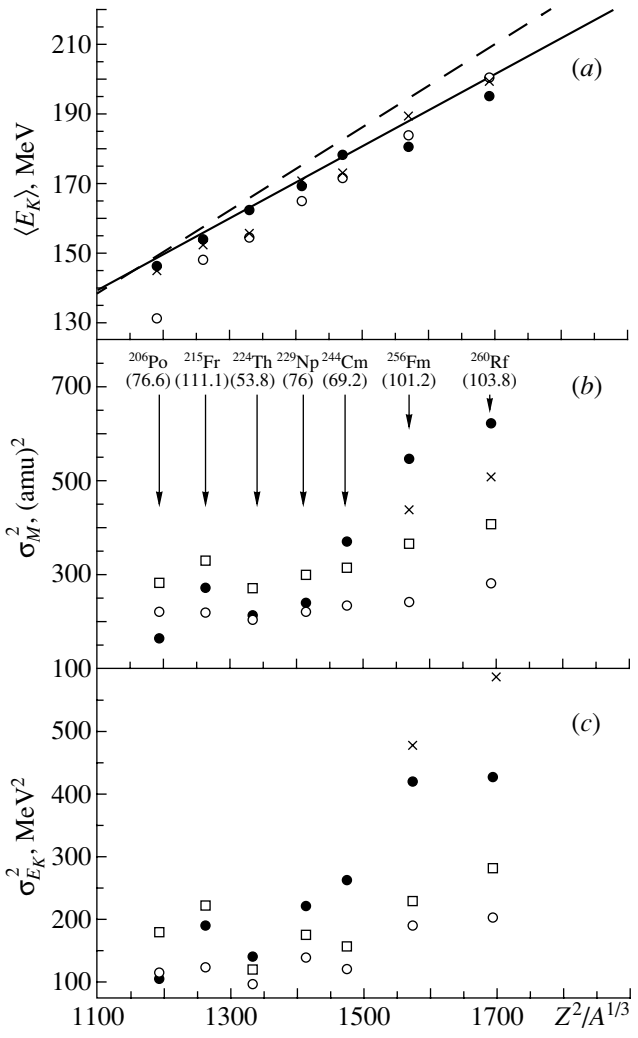

Fig. 4. (*a*) $\langle E_K \rangle$ as a function of the parameter $Z^2/A^{1/3}$: (closed circles) experimental data, (crosses) results of the calculations with $k_s = 0.1$, (open circles) results of the calculations with $k_s = 1.0$, (solid line) systematics from [54] [$\langle E_K \rangle = 0.104 Z^2/A^{1/3} + 24.3$ (MeV) in the range $Z^2/A^{1/3} = 900$–1800], and (dashed line) Viola's systematics [63] [$\langle E_K \rangle = 0.1189 Z^2/A^{1/3} + 7.3$ (MeV)]. (*b*, *c*) Computed variances of (*b*) the mass and (*c*) the energy distributions along with experimental data: (open squares) results of the calculations with $k_s = 0.25$; the rest of the notation is identical to that in Fig. 4*a*. The compound nuclei formed in the reactions considered here are displayed in Fig. 4*b* (below them, the corresponding initial excitation energies are indicated parenthetically). Arrows indicate the experimental and computed data for relevant nuclei.

it can be seen that, for all nuclei undergoing fission, with the exception of ^{260}Rf, the experimental values of $\langle n_{\rm pre} \rangle$ can be reproduced fairly well in the calculations with $k_s \sim 0.5$. For the ^{260}Rf nucleus, the calculations failed to reproduce the experimental values of $\langle n_{\rm pre} \rangle$ even at $k_s = 1$. A similar result was obtained in [65], where, on the basis of studying reactions leading to the production of heavy nuclei (whose mass numbers lie in the region $A_{\rm CN} > 260$), it was shown that the value of $k_s > 4$ is necessary for reproducing the experimental values of $\langle n_{\rm pre} \rangle$.

In the present study, we have explored the dependences of the multiplicities of prescission neutrons on the masses of fission fragments and their kinetic energies. These dependences are displayed in Figs. 2*a* and 3. In [53], it was shown that the number of evaporated neutrons is greater in events of symmetric fission than in events of asymmetric fission, the energies of evaporated neutrons being independent of the fragment masses. This trend proved to be virtually independent of the mass of the fissile compound nucleus. Three hypothesis were proposed in [53] for explaining this effect. The first relies on the fact that, at any instant of time, the ensemble of nuclei undergoing fission contains nuclei having different excitation energies since different numbers of particles can be evaporated from the nucleus in the course of the fission process. Thus, we conclude that, if the nucleus possesses a high excitation energy (a small number of particles have been evaporated from it), it can overcome a higher fission barrier at a higher mass asymmetry in relation to a nucleus that has evaporated a greater number of particles. Within the second hypothesis, it is assumed that, during the descent from the saddle to the scission point, the nucleus changes its mass asymmetry only slightly; that is, nuclei that split with a large mass asymmetry have fluctuated somewhere in the region of large mass asymmetries over the entire time of descent from the saddle to the scission point; therefore, they have had a lower temperature and evaporated a smaller number of particles in relation to the case of nuclei undergoing symmetric fission. Within the third hypothesis, it is assumed that the fission time decreases with increasing mass asymmetry; therefore, the nucleus evaporates a smaller number of neutrons in asymmetric fission than in symmetric fission. It should be emphasized that, in [53], it is implicitly assumed that, in the process of nuclear fission, neutrons are evaporated predominantly from the barrier top and during the descent from the saddle to the scission point. It follows that, if one of the first two hypotheses or their combination were correct, then, as was indicated in [53], the energy of evaporated neutrons, $\langle E_n(M) \rangle$, would decrease with increasing mass asymmetry. However, $\langle E_n(M) \rangle$ would increase with increasing mass asymmetry if the third hypothesis were correct. Therefore, the conclusion drawn in [53] was that, for explaining the dependence $\langle n_{\rm pre}(M) \rangle$, it is necessary to assume that all three hypotheses are correct.

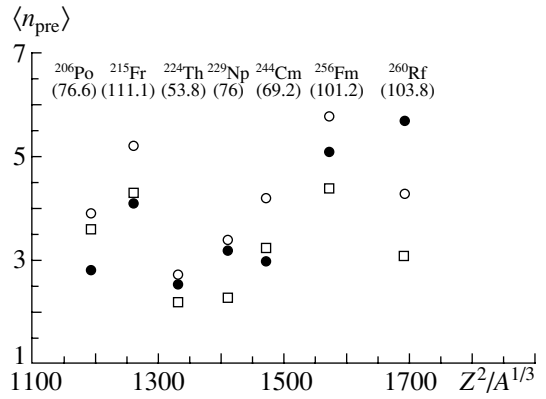

Fig. 5. Results of the calculations for $\langle n_{\rm pre}\rangle$ along with experimental data: (open circles) results of the calculations at $k_s = 1.0$, (open boxes) results of the calculations at $k_s = 0.5$, and (closed circles) experimental data. The compound nuclei formed are indicated in the figure; the initial excitation energies are quoted parenthetically below them.

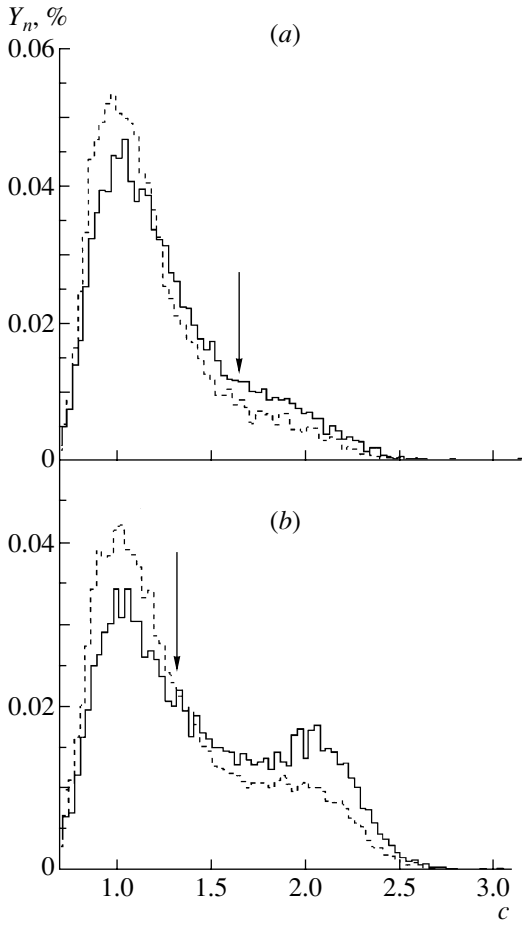

Fig. 6. Calculated yield of prescission neutrons (percentage of their total number) as a function of the elongation coordinate c for the fission of the compound nuclei (*a*) ^{215}Fr [(solid line) results of the calculations with $k_s = 0.25$ and (dashed line) results of the calculations with $k_s = 0.5$] and (*b*) ^{256}Fm [(solid line) results of the calculations with $k_s = 0.1$ and (dashed line) results of the calculations with $k_s = 0.25$]. Arrows indicate the positions of the saddle points.

The question of where neutrons are evaporated is of fundamental importance in explaining the character of the dependence $n_{\rm pre}(M)$. Our previous conclusion [17] that neutrons are predominantly evaporated from the ridge and in the course of descent from the saddle to the scission point was unfortunately incorrect because of the imperfections of the two-dimensional model. In the present study, this dependence has been explored in greater detail on the basis of our three-dimensional model. Figure 6 shows the mean multiplicity $\langle n_{\rm pre}\rangle$ as a function of the elongation coordinate c for the ^{215}Fr and ^{256}Fm nuclei. Our calculations reveal that a major part of neutrons, as well as other particles, are evaporated from the ground-state region: about 50 to 80% of the total number of evaporated particles are emitted before the saddle point, and about 10%, irrespective of the final mass asymmetry, are emitted upon passing saddle configurations. Of all nuclei considered in the present study, only ^{256}Fm and ^{260}Rf emit a considerable part of neutrons in the fission process at the stage of descent from the saddle to the scission point. Since the potential energy is weakly dependent on the collective coordinates h and α' in the ground-state region, Langevin trajectories can execute random walks for a long time over a nearly flat (in the coordinates h and α') potential-energy surface, emitting meanwhile light particles. The kinetic energies of particles that are evaporated from the ground-state region will not depend on the mass asymmetry in view of the weak dependence of the potential energy on the coordinates h and α' in the ground-state region. Since walks of Langevin trajectories in the space of collective coordinates are random, different trajectories reach the ridge surface within different time intervals. Trajectories that reached the region of saddle configurations within short times and, simultaneously, evaporated a small number of neutrons retain a major part of the excitation energy; therefore, they can reach fast the scission surface, having a large mass asymmetry. On the contrary, those trajectories whose evolution from the ground-state region involves the emission of a large number of neutrons lose a considerable part of the excitation energy; upon passing the ridge surface, they are therefore capable of only slowly descending along the bottom of the liquid-drop fission valley at a mass asymmetry approximately equal to zero, but they are incapable of climbing the potential energy surface in the region of large mass asymmetries. The calculated values of the mean time it takes for the

nuclei undergoing fission to reach the scission surface are displayed in Fig. 2*b* versus the fragment masses. As can be seen from this figure, the fission times for the cases of the symmetric and the asymmetric splitting of a nucleus differ by nearly a factor of 2. Thus, we can conclude that the final mass asymmetry and the time of the fission of a nucleus depend on its preceding evolution in the ground-state region. The smaller the number of particles that have been evaporated from the nucleus in the ground-state region, the higher the probability for the nucleus to reach fast the scission surface with a large mass asymmetry.

Within the two-dimensional model based on classical Euler–Lagrange equations, an attempt was made in [66] to describe theoretically the dependence $\langle n_{\rm pre}(M)\rangle$ observed experimentally. In their calculations, the authors of [66] used a combination of one-body and two-body viscosity and found that, for reproducing, in the calculations, the dependence $\langle n_{\rm pre}(M)\rangle$ observed experimentally, it is necessary to reduce considerably the viscosity (a specific value of this reduction depends of the mass-asymmetry coordinate) by multiplying the components of the friction tensor by $\exp(-K\times\alpha\times\alpha)$, where $K = 161\pm 3$. From Fig. 2*a*, it can be seen that our calculations reproduce fairly well, at a quantitative level, the dependence $\langle n_{\rm pre}(M)\rangle$ observed experimentally without including additional adjustable parameters in the model.

The dependence $\langle n_{\rm pre}(E_K)\rangle$ observed experimentally [67] exhibits a significant growth of $\langle n_{\rm pre}(E_K)\rangle$ with increasing E_K. However, $\langle n_{\rm pre}(E_K)\rangle$ appears to be virtually independent of E_K upon applying, to these results, the rescaling procedure that takes into account recoil effects [53]. In our calculations, $\langle n_{\rm pre}(E_K)\rangle$ proved to be virtually independent of E_K within the errors; only in the region of small E_K is there a modest falloff in the dependence $\langle n_{\rm pre}(E_K)\rangle$. This falloff can be explained by an ever increasing contribution of events featuring large mass asymmetry as E_K decreases—this follows from a general character of the two-dimensional mass–energy distribution.

In the present study, we have also calculated the fission time t_f. The results of these calculations are displayed in Figs. 2*b*, 7, and 8. Figure 7 shows the fission-time distribution of the trajectories versus k_s for the ^{215}Fr nucleus. Figure 8 presents the mean fission time $\langle t_f\rangle$ as a function of the parameter $Z^2/A^{1/3}$. In accord with the results of many previous calculations (see, for example, [6, 12, 65, 68]), it was found, for all reactions studied here, that the neutron multiplicities and the mean times it takes for nuclei undergoing fission to reach the scission surface grow with increasing viscosity, the fission time being the quantity in our calculations that exhibits the highest sensitivity to the value of viscosity. However, there are no direct experimental data on fission times, and their values are extracted from experimental data on $\langle n_{\rm pre}\rangle$ by invoking model concepts. Depending on the choice of model for neutron evaporation, fission times can vary within one order of magnitude [53, 69]. In what is concerned with the fission times obtained in the present calculations, we can only state that they are about 10^{-19}–10^{-20} s and that they decrease with increasing Z^2/A, which is in agreement with the results of experimental investigations.

3.3. Correlations between the Parameters of Two-Dimensional Mass–Energy Distributions

The correlation dependences $\langle E_K(M)\rangle$, $\sigma^2_{E_K}(M)$, and $\sigma^2_M(E_K)$ carry additional information about the scission configurations of nuclei undergoing fission. The dependence $\langle E_K(M)\rangle$ calculated in the present study for the ^{260}Rf nucleus is shown in Fig. 9. For a first approximation, this dependence can be approximated by the parabola [6, 62]

$$\langle E_K(M)\rangle = \langle E_K(A/2)\rangle\Big(1-\beta\Big(1-\frac{2M}{A}\Big)^2\Big). \quad (18)$$

This approximation reflects the dependence of the Coulomb energy of the repulsion of fission fragments on the distance between their centers of mass. The dependences $\langle E_K(M)\rangle$ observed experimentally for excitation energies E^* in excess of 20 MeV correspond to values in the region $\beta < 1$. It should be noted that β depends on the excitation energy and on the parameter Z^2/A as well. The dependences $\langle E_K(M)\rangle$ calculated in the present study correspond to β values varying from $\beta = 0.7$ for ^{206}Po to $\beta = 1.6$ for ^{260}Rf. At these values of β, the calculated dependences $\langle E_K(M)\rangle$ fall off with increasing M faster than in experimental data, as can be seen in Fig. 9 for the example of the ^{260}Rf nucleus. In all probability, this discrepancy is due to choosing a specific scission condition used in the present study.

The dependences $\sigma^2_{E_K}(M)$ and $\sigma^2_M(E_K)$ are not shown in the figures, because, in the Z^2/A range studied here, experimental data on these dependences are scanty; moreover, their dependence on the reduction coefficient k_s can be assessed on the basis of the behavior of the variances of the one-dimensional mass and the one-dimensional energy distribution. It should only be noted that the qualitative behavior of the dependences $\sigma^2_{E_K}(M)$ and $\sigma^2_M(E_K)$ computed in our study agrees well with the shapes of the experimental dependences for close fissile nuclei.

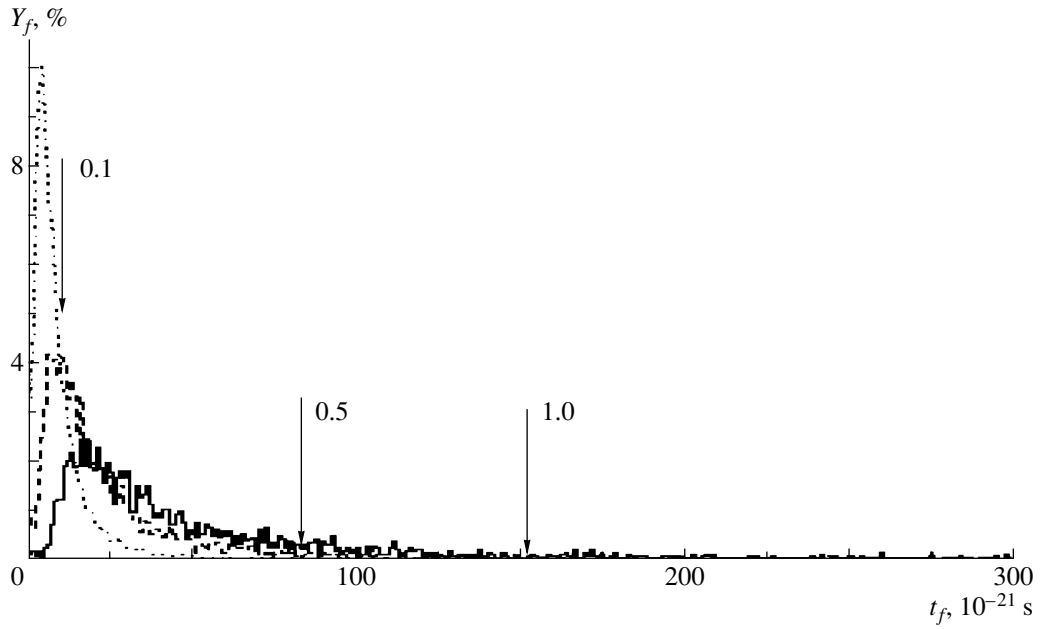

Fig. 7. Fission-time distributions of the trajectories for various values of k_s in the fission of the ^{215}Fr nuclei: (dotted curve) results of the calculations with $k_s = 0.1$, (solid line) results of the calculations with $k_s = 0.5$, and (dashed curve) results of the calculations with $k_s = 1.0$. Arrows indicate mean fission times, while the numbers near the arrows are the values of k_s at which these mean values were found.

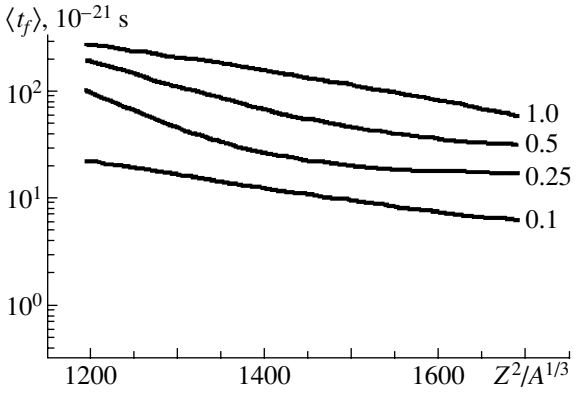

Fig. 8. Mean fission time as a function of the parameter $Z^2/A^{1/3}$ according to the calculations with various values of k_s that are indicated in the figure on the corresponding curves.

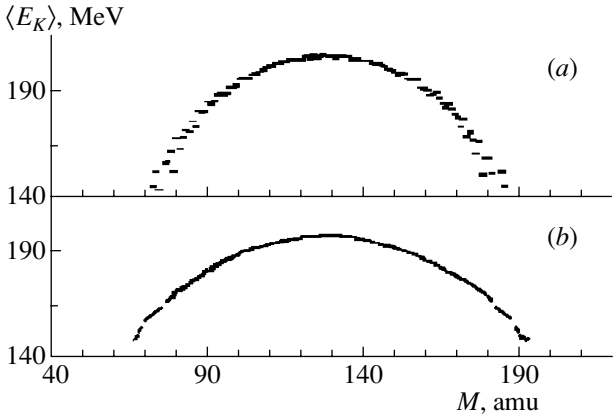

Fig. 9. Dependence $\langle E_K(M) \rangle$ for the reaction ^{20}Ne + ^{240}Pu $\rightarrow$ ^{260}Rf at $E_{\text{lab}} = 142$ MeV: (a) results of the calculations with $k_s = 0.1$ and (b) experimental data from [52].

4. CONCLUSION

We have performed systematic dynamical calculations of the two-dimensional mass–energy distributions of fragments originating from the fission of excited compound nuclei. For the same processes, we have also computed the multiplicities of light charged particles. Our calculations have been performed within three-dimensional Langevin dynamics by using a modified version of one-body dissipation. In order to calculate the potential energy, we have used a macroscopic model that takes into account the finite range of nuclear forces and the diffuseness of the nuclear surface. Our calculations have revealed that all features of the two-dimensional mass–energy distribution are sensitive to changes in nuclear viscosity. The data on $\sigma^2_{E_K}$ and σ^2_M can be employed, along with the traditionally used data on $\langle E_K \rangle$, to determine the magnitude and the mechanism of nuclear viscosity. From the analysis of all the computed features, we can draw the following conclusion: for all of the features of the mass–energy distributions studied here, the best agreement between the results of our theoretical

calculations and experimental data is attained at a value of $k_s \sim 0.5$ for the ^{206}Po, ^{215}Fr, and ^{224}Th nuclei; in dealing with heavier nuclei, a smaller value of $k_s \sim 0.2$ is preferable. It should be emphasized that k_s is the only adjustable parameter in our calculations, and the value of $k_s = 0.27$, which was found from an analysis of experimental giant-resonance widths [35] independently of fission, falls within the interval $k_s = 0.2$–0.5.

For the heaviest nuclei considered in our study (^{256}Fm and ^{260}Rf), the calculated values of the variances reproduce experimental data most closely at $k_s \sim 0.1$, but, at this value of k_s, the results of the calculations for the neutron multiplicity are far below the experimental multiplicities. The agreement between the theoretical results and experimental data on $\langle n_{\rm pre} \rangle$ for these nuclei is better at $k_s = 1.0$, but, at this value of k_s, the calculations are unable to reproduce even qualitatively the observed values of the variances. From our calculations, we can draw the conclusion that, for reactions involving the formation of ^{256}Fm and ^{260}Rf, it would be incorrect to begin calculations from the statistically equilibrium ground state of a nucleus—it is necessary to consider fission dynamics with allowance for the entrance channel of the fusion–fission reaction.

ACKNOWLEDGMENTS

We are grateful to A.Ya. Rusanov for enlightening discussions and for carefully reading the manuscript of this article and to D.V Vanin and M.V. Mebel for stimulating discussions and for placing some computational codes at our disposal.

REFERENCES

1. H. A. Kramers, Physica (Utrecht) **7**, 284 (1940).
2. H. J. Krappe, in *Proceedings of the International Workshop on Dynamical Aspects of Nuclear Fission, Smolenice, Slovakia, 1991,* Ed. by J. Kristiak and B. I. Pustylnik (Joint Inst. for Nuclear Research, Dubna, 1992), p. 51.
3. Y. Abe, S. Ayik, P.-G. Reinhard, and E. Suraud, Phys. Rep. **275**, 49 (1996).
4. P. Fröbrich and I. I. Gontchar, Phys. Rep. **292**, 131 (1998).
5. H. T. Feldmeier, Rep. Prog. Phys. **50**, 915 (1987).
6. G. D. Adeev and V. V. Pashkevich, Nucl. Phys. A **502**, 405c (1989); G. D. Adeev, I. I. Gonchar, V. V. Pashkevich, *et al.*, Fiz. Élem. Chastits At. Yadra **19**, 1229 (1988) [Sov. J. Part. Nucl. **19**, 529 (1988)].
7. H. A. Weidenmüller, Nucl. Phys. A **471**, 1c (1987); P. Grangé, J. O. Li, and H. A. Weidenmüller, Phys. Rev. C **27**, 2063 (1983).
8. F. Scheuter, C. Grégoire, H. Hofmann, and J. R. Nix, Phys. Lett. B **149B**, 303 (1984).
9. Y. Abe, C. Grégoire, and H. Delagrange, J. Phys. C **47**, 4 (1986); P. Fröbrich and S. Y. Xu, Nucl. Phys. A **477**, 143 (1988).
10. I. I. Gontchar, L. A. Litnevsky, and P. Fröbrich, Comput. Phys. Commun. **107**, 223 (1997).
11. T. Wada, N. Carjan, and Y. Abe, Nucl. Phys. A **538**, 283c (1992); T. Wada, Y. Abe, and N. Carjan, Phys. Rev. Lett. **70**, 3538 (1993).
12. G.-R. Tillack, R. Reif, A. Schülke, *et al.*, Phys. Lett. B **296**, 296 (1992); G.-R. Tillack, Phys. Lett. B **278**, 403 (1992).
13. G. I. Kosenko, I. I. Gonchar, O. I. Serdyuk, and N. I. Pischasov, Yad. Fiz. **55**, 920 (1992) [Sov. J. Nucl. Phys. **55**, 514 (1992)].
14. J. Bao, Y. Zhuo, and X. Wu, Z. Phys. A **352**, 321 (1995).
15. G. I. Kosenko, I. G. Kalyari, and G. D. Adeev, Yad. Fiz. **60**, 404 (1997) [Phys. At. Nucl. **60**, 334 (1997)]; G. I. Kosenko, D. V. Vanin, and G. D. Adeev, Yad. Fiz. **61**, 416 (1998) [Phys. At. Nucl. **61**, 356 (1998)].
16. D. V. Vanin, G. I. Kosenko, and G. D. Adeev, Phys. Rev. C **59**, 2114 (1999).
17. D. V. Vanin, P. N. Nadtochiĭ, G. I. Kosenko, and G. D. Adeev, Yad. Fiz. **63**, 1957 (2000) [Phys. At. Nucl. **63**, 1865 (2000)].
18. J. R. Nix and W. J. Swiatecki, Nucl. Phys. **71**, 1 (1965); J. R. Nix, Nucl. Phys. A **130**, 241 (1969).
19. O. I. Serdyuk, G. D. Adeev, I. I. Gonchar, *et al.*, Yad. Fiz. **46**, 710 (1987) [Sov. J. Nucl. Phys. **46**, 399 (1987)]; G. Saupe, O. I. Serdyuk, G. D. Adeev, and V. V. Pashkevich, Yad. Fiz. **48**, 42 (1988) [Sov. J. Nucl. Phys. **48**, 26 (1988)].
20. P. N. Nadtochiĭ, A. V. Karpov, D. V. Vanin, and G. D. Adeev, Yad. Fiz. **64**, 926 (2001) [Phys. At. Nucl. **64**, 861 (2001)].
21. P. Fong, *Statistical Theory of Nuclear Fission* (Gordon and Breach, New York, 1969).
22. I. I. Gonchar, Fiz. Élem. Chastits At. Yadra **26**, 932 (1995) [Phys. Part. Nucl. **26**, 394 (1995)].
23. M. Brack *et al.*, Rev. Mod. Phys. **44**, 320 (1972).
24. H. C. Pauli, Phys. Rep. **7**, 35 (1973).
25. V. M. Strutinsky, N. Ya. Lyashchenko, and N. A. Popov, Nucl. Phys. **46**, 639 (1963).
26. A. V. Karpov, P. N. Nadtochy, D. V. Vanin, and G. D. Adeev, Phys. Rev. C **63**, 054610 (2001).
27. H. C. Pauli, Nukleonika **20**, 601 (1975); T. Ledergerber and H. C. Pauli, Nucl. Phys. A **207**, 1 (1973).
28. V. M. Strutinskiĭ, Zh. Éksp. Teor. Fiz. **45**, 1900 (1963) [Sov. Phys. JETP **18**, 1305 (1963)].
29. T. Ledergerber, H. C. Pauli, and Y. Yariv, Nucl. Phys. A **280**, 241 (1977).
30. V. V. Voevodin and G. Kim, *Computational Methods and Programming* (Mosk. Gos. Univ., Moscow, 1962).
31. A. V. Ignatyuk, M. G. Itkis, V. N. Okolovich, *et al.*, Yad. Fiz. **21**, 1185 (1975) [Sov. J. Nucl. Phys. **21**, 612 (1975)].
32. K. T. R. Davies, A. J. Sierk, and J. R. Nix, Phys. Rev. C **13**, 2385 (1976); J. R. Nix and A. J. Sierk, Nucl. Phys. A **428**, 161c (1984).

33. A. A. Seregin, Yad. Fiz. **55**, 2639 (1992) [Sov. J. Nucl. Phys. **55**, 1473 (1992)].
34. J. R. Nix and A. J. Sierk, in *Proceedings of the International School–Seminar on Heavy Ion Physics, Dubna, 1986,* Ed. by M. I. Zarubina and E. V. Ivashkevich (Joint Inst. for Nuclear Research, Dubna, 1987), p. 453; J. R. Nix, Nucl. Phys. A **502**, 609 (1989).
35. J. R. Nix and A. J. Sierk, in *Proceedings of the 6th Adriatic Conference on Nuclear Physics: Frontiers of Heavy Ion Physics, Dubrovnik, Yugoslavia, 1987,* Ed. by N. Cindro, R. Caplar, and W. Greiner (World Sci., Singapore, 1990), p. 333.
36. J. J. Griffin and M. Dworzecka, Nucl. Phys. A **455**, 61 (1986).
37. A. J. Sierk and J. R. Nix, Phys. Rev. C **21**, 982 (1980).
38. J. Blocki *et al.*, Ann. Phys. (N.Y.) **113**, 330 (1978).
39. J. Randrup and W. J. Swiatecki, Nucl. Phys. A **429**, 105 (1984).
40. J. Blocki, H. T. Feldmeier, and W. J. Swiatecki, Nucl. Phys. A **459**, 145 (1986); J. Blocki, R. Planeta, J. Brzychczyk, and K. Grotowski, Z. Phys. A **341**, 307 (1992).
41. H. J. Krappe, J. R. Nix, and A. J. Sierk, Phys. Rev. C **20**, 992 (1979).
42. A. J. Sierk, Phys. Rev. C **33**, 2039 (1986).
43. A. Bohr and B. R. Mottelson, *Nuclear Structure* (Benjamin, New York, 1969, 1975; Mir, Moscow, 1971, 1977), Vols. 1, 2.
44. J. O. Newton, Fiz. Élem. Chastits At. Yadra **21**, 821 (1990) [Sov. J. Part. Nucl. **21**, 349 (1990)].
45. C. Guet, E. Strumberger, and M. Brack, Phys. Lett. B **205**, 427 (1988).
46. M. Brack, C. Guet, and H. B. Håkonsson, Phys. Rep. **123**, 275 (1985).
47. H. J. Krappe, Phys. Rev. C **59**, 2640 (1999).
48. V. Weisskopf, Phys. Rev. **52**, 295 (1937).
49. N. D. Mavlitov, P. Fröbrich, and I. I. Gontchar, Z. Phys. A **342**, 195 (1992).
50. C. Bhattacharya, S. Bhattacharya, and K. Krishan, Phys. Rev. C **53**, 1012 (1996).
51. K. T. R. Davies, R. A. Managan, J. R. Nix, and A. J. Sierk, Phys. Rev. C **16**, 1890 (1977).
52. G. G. Chubaryan, M. G. Itkis, S. M. Luk'yanov, *et al.*, Yad. Fiz. **56** (3), 3 (1993) [Phys. At. Nucl. **56**, 286 (1993)].
53. D. J. Hinde, D. Hilscher, H. Rossner, *et al.*, Phys. Rev. C **45**, 1229 (1992).
54. A. Ya. Rusanov, M. G. Itkis, and V. N. Okolovich, Yad. Fiz. **60**, 773 (1997) [Phys. At. Nucl. **60**, 683 (1997)].
55. M. G. Itkis, Yu. Ts. Oganessian, G. G. Chubarian, *et al.*, in *Proceedings of the XV EPS Conference on Low Energy Nuclear Dynamics (LEND-95), St. Petersburg, Russia, 1995,* Ed. by Yu. Ts. Oganessian, R. Kalpakchieva, and W. von Oertzen (World Sci., Singapore, 1995), p. 177.
56. D. J. Hinde *et al.*, Phys. Rev. C **39**, 2268 (1989).
57. M. G. Itkis, S. M. Luk'yanov, V. N. Okolovich, *et al.*, Yad. Fiz. **52**, 23 (1990) [Sov. J. Nucl. Phys. **52**, 15 (1990)].
58. G. Kendall and A. Stuart, *The Advanced Theory of Statistics, Distribution Theory* (Griffin, London, 1958), Vol. 1.
59. S. K. Samaddar, D. Sperber, M. Zielińska-Pfabé, and M. I. Sobel, Phys. Scr. **25**, 517 (1982).
60. K. T. R. Davies and J. R. Nix, Phys. Rev. C **14**, 1977 (1976).
61. M. G. Itkis and A. Ya. Rusanov, Fiz. Élem. Chastits At. Yadra **29**, 389 (1998) [Phys. Part. Nucl. **29**, 160 (1998)].
62. M. G. Itkis, V. N. Okolovich, and G. N. Smirenkin, Nucl. Phys. A **502**, 243c (1989).
63. V. E. Viola, K. Kwiatkowski, and M. Walker, Phys. Rev. C **31**, 1550 (1985).
64. D. Hilscher and H. Rossner, Ann. Phys. (Paris) **17**, 471 (1992); D. J. Hinde, D. Hilscher, and H. Rossner, Nucl. Phys. A **502**, 497c (1989).
65. J. Wilczyński, K. Siwek-Wilczyńska, and H. W. Wilschut, Phys. Rev. C **54**, 325 (1996).
66. A. K. Dhara, K. Krishan, C. Bhattacharya, *et al.*, Phys. Rev. C **57**, 2453 (1998).
67. H. Rossner, D. Hilsher, D. J. Hinde, *et al.*, Phys. Rev. C **40**, 2629 (1989).
68. P. Fröbrich and I. I. Gontchar, Nucl. Phys. A **563**, 326 (1993).
69. K. Siwek-Wilczyńska, J. Wilczyński, R. H. Siemssen, and H. W. Wilschut, Phys. Rev. C **51**, 2054 (1995).

Translated by A. Isaakyan

Physics of Atomic Nuclei, Vol. 65, No. 5, 2002, pp. 814–823. Translated from Yadernaya Fizika, Vol. 65, No. 5, 2002, pp. 847–855.

NUCLEI
Theory

Binding Energies of Nuclei and Their Density Distributions in a Nonlocal Extended Thomas–Fermi Approximation

V. Yu. Denisov* **and V. A. Nesterov**

Institute for Nuclear Research, National Academy of Sciences of Ukraine, pr. Nauki 47, 03680 Kiev, Ukraine

Received April 12, 2000; in final form, May 10, 2001

Abstract—Basic properties of the ground states of spherical nuclei are investigated in a nonlocal extended Thomas–Fermi approximation under the assumption of Skyrme forces. It is shown that, for nuclei occurring near the β-stability line, the binding energies, the root-mean-square radii, and the density distributions found on this basis agree well with experimental data. Binding energies, root-mean-square radii, and density distributions are also calculated for the ground states of nuclei lying far off the β-stability line and for superheavy elements. For the proton, the neutron, and the total particle density, the thickness of the diffuse layer is investigated as a function of the number of neutrons in tin isotopes.

1. INTRODUCTION

A description of the properties of nuclei in their ground states and low-lying excited states is one of the most important problems in nuclear physics. Over the past decades, theoretical investigations aimed at this have gained a new momentum in connection with the development of phenomenological effective nucleon–nucleon potentials that are expressed in a simple mathematical form [1]. The use of effective Skyrme forces [1] in investigating the properties of nuclear systems facilitates relevant calculations considerably. For the Skyrme forces, a few successful parametrizations were constructed in [2–8], which ensure a description of many nuclear properties to a high precision.

The Hartree–Fock method underlies one of the fundamental approaches to calculating the properties of complex nuclei [2, 3, 5, 6, 8–12]. This quantum-mechanical approach, combined with Skyrme forces, makes it possible to describe well the properties of the ground states of nuclei almost over the entire periodic table of elements [2, 3, 5, 6, 8–10, 12]. Many properties of nuclei were successfully described within Fermi liquid theory [13, 14]. However, an implementation of the Hartree–Fock method and of calculations within Fermi liquid theory in practice involves considerable difficulties. In view of this, use is frequently made of a semiclassical approach that is referred to as the extended Thomas–Fermi approximation [15]. This method is simple, conceptually clear, and rather accurate, which makes it possible to apply it successfully to describing various physical systems [16]. There is yet another point in favor of using the Thomas–Fermi approximation in calculating basic properties of nuclei: although various modern modifications of the Hartree–Fock approximation are quite fundamental conceptually and elaborate, the most precise description of experimental nuclear masses is provided by simple macroscopic–microscopic approximations [11, 12], which often employ the Thomas–Fermi approximation to calculate the macroscopic part of the binding energy [12].

The extended Thomas–Fermi approximation has been successfully used in atomic and nuclear physics and, since more recent times, in investigations of the properties of metal clusters [17]. Results obtained with the aid of the variational extended Thomas–Fermi approximation for proton-density distributions in nuclei agree well with experimental data, showing slight deviations from them only in the diffuse region [15]. We note that, previously, many properties of nuclei were studied in the local extended Thomas–Fermi approximation [18]; in the nonlocal approximation, this was done by Brack *et al.* [15], whose analysis also involved variations of the parameters in trial functions for nucleon-density distributions.

Under the assumption of Skyrme forces, the nonlocal extended Thomas–Fermi approximation implemented to second-order terms in $\hbar$ [15] is used in the present study to describe the properties of the ground states of medium-mass and heavy spherical nuclei. More specifically, this investigation is performed both for nuclei occurring near the β-stability line and for nuclei lying far off it, as well as for nuclei of superheavy elements. An investigation of nuclei in the

*e-mail: denisov@kinr.kiev.ua

vicinity of the presumed stability island around $Z = 114$, $N = 182$ [11, 19] is an especially topical issue, since there have recently appeared reports on the observation of the $Z = 114$–116 and the $Z = 104$–112 nuclei (see [20] and [21], respectively). The equations of the nonlocal extended Thomas–Fermi approximation for the case of Skyrme forces considered in the present study are solved here numerically.

2. EXTENDED THOMAS–FERMI APPROXIMATION

The equations

$$\frac{\delta\mathcal{E}(\rho_n,\rho_p)}{\delta\rho_p} - \lambda_p = 0, \tag{1}$$

$$\frac{\delta\mathcal{E}(\rho_n,\rho_p)}{\delta\rho_n} - \lambda_n = 0 \tag{2}$$

of the extended Thomas–Fermi approximation [15, 16] can be obtained from the variational principle where the total energy of a nucleus is considered as a functional $\mathcal{E}(\rho_n,\rho_p)$ of the neutron density ρ_n and the proton density ρ_p. The possibility of constructing such a functional follows from the Hohenberg–Kohn theorem [22], which is valid for any multicomponent system. The total-energy functional for a nucleus has the form

$$\mathcal{E}(\rho_n,\rho_p) = \int d\mathbf{r}(\tau + \varepsilon_{\rm pot} + \varepsilon_{\rm Coul}), \tag{3}$$

where τ, $\varepsilon_{\rm pot}$, and $\varepsilon_{\rm Coul}$ are the densities of, respectively, the kinetic, the potential, and the Coulomb energy. In Eqs. (1) and (2), λ_n and λ_p are Lagrange multipliers that are chemical potentials for neutrons and protons, respectively, and which are associated with the conservation of the number of neutrons (N) and the number of protons (Z) in a nucleus:

$$\int d\mathbf{r}\rho_{n(p)}(\mathbf{r}) = N(Z). \tag{4}$$

Knowing the expressions for the kinetic, the potential, and the Coulomb energy in (3), one can solve the set of Eqs. (1) and (2) and find the distributions of the neutron and the proton density.

To terms of second order in $\hbar$ [15], the kinetic-energy density is given by

$$\tau = \tau_{\rm TF} + \tau_2 \tag{5}$$

(the sum of the densities of the kinetic energies of protons and neutrons, $\tau = \tau_p + \tau_n$), where

$$\tau_{{\rm TF},n(p)} = k\rho_{n(p)}^{5/3} \tag{6}$$

is the density of the kinetic energy of neutrons (protons) in the Thomas–Fermi approximation ($k = (5/3)(3\pi^2)^{2/3}$) and $\tau_{2n(p)}$ is the second-order gradient correction in $\hbar$ in the nonlocal case [15]. It has the form

$$\tau_{2q} = b_1\frac{(\nabla\rho_q)^2}{\rho_q} + b_2\nabla^2\rho_q + b_3\frac{(\nabla f_q\nabla\rho_q)}{f_q} + b_4\rho_q\frac{\nabla^2 f_q}{f_q} + b_5\rho_q\left(\frac{\nabla f_q}{f_q}\right)^2 + b_6h_m^2\rho_q\left(\frac{W_q}{f_q}\right)^2, \tag{7}$$

where $q = p$ or n; $b_1 = 1/36$, $b_2 = 1/3$, $b_3 = 1/6$, $b_4 = 1/6$, $b_5 = -1/12$, and $b_6 = 1/2$ are numerical coefficients; and $h_m = \hbar^2/(2m)$. The explicit expressions for the functions f_q and W_q are presented in the Appendix. The last term in Eq. (7) takes into account spin–orbit interaction.

In the case of Skyrme forces, the potential-energy density has the form [1, 2, 10, 15]

$$\begin{aligned}\varepsilon_{\rm pot} = {}& \frac{1}{2}t_0\left[\left(1+\frac{1}{2}x_0\right)\rho^2 - \left(x_0+\frac{1}{2}\right)\right.\\ &\left.\times(\rho_n^2+\rho_p^2)\right] + \frac{1}{12}t_3\rho^\alpha\left[\left(1+\frac{1}{2}x_3\right)\rho^2\right.\\ &\left.-\left(x_3+\frac{1}{2}\right)(\rho_n^2+\rho_p^2)\right] + \frac{1}{4}\left[t_1\left(1+\frac{1}{2}x_1\right)\right.\\ &\left.+t_2\left(1+\frac{1}{2}x_2\right)\right]\tau\rho + \frac{1}{4}\left[t_2\left(x_2+\frac{1}{2}\right)\right.\\ &\left.-t_1\left(x_1+\frac{1}{2}\right)\right](\tau_n\rho_n+\tau_p\rho_p)\\ &+\frac{1}{16}\left[3t_1\left(1+\frac{1}{2}x_1\right)-t_2\left(1+\frac{1}{2}x_2\right)\right](\nabla\rho)^2\\ &-\frac{1}{16}\left[3t_1\left(x_1+\frac{1}{2}\right)+t_2\left(x_2+\frac{1}{2}\right)\right]\\ &\times((\nabla\rho_p)^2+(\nabla\rho_n)^2)\\ &+\frac{1}{2}W_0[\mathbf{J}\nabla\rho+\mathbf{J}_n\nabla\rho_n+\mathbf{J}_p\nabla\rho_p],\end{aligned} \tag{8}$$

where t_0, t_1, t_2, t_3, x_0, x_1, x_2, x_3, α, and W_0 are the parameters of the Skyrme potential; $\rho = \rho_n + \rho_p$; $\tau = \tau_n + \tau_p$; $\mathbf{J} = \mathbf{J}_n + \mathbf{J}_p$; and

$$\mathbf{J}_{n(p)} = -\frac{h_m}{f_{n(p)}}\rho_{n(p)}\mathbf{W}_{n(p)}. \tag{9}$$

With allowance for the exchange term, the Coulomb energy density is given by [15, 17]

$$\varepsilon_{\rm Coul} = \frac{1}{2}e^2\rho_p(\mathbf{r})\int d\mathbf{r}'\frac{\rho_p(\mathbf{r}')}{|\mathbf{r}-\mathbf{r}'|} - \frac{3}{4}e^2\left(\frac{3}{\pi}\right)^{1/3}\rho_p^{4/3}(\mathbf{r}). \tag{10}$$

Table 1. Binding energies E, root-mean-square radii $\langle r\rangle$, and chemical potentials λ of β-stable nuclei (experimental values E_{expt} and $\langle r_p\rangle_{\text{expt}}$ were borrowed from [24])

Nucleus	E_{expt}, MeV	E, MeV	$\langle r_p\rangle_{\text{expt}}$, fm	$\langle r_p\rangle$, fm	$\langle r_n\rangle$, fm	λ_n, MeV	λ_p, MeV
^{40}Ca	342.1	340.7	3.450	3.186	3.230	−12.12	−10.61
^{48}Ca	416.1	418.1	3.451	3.322	3.499	−6.14	−18.86
^{58}Ni	506.45	506.1	3.769	3.560	3.617	−11.23	−11.53
^{90}Zr	783.9	790.2	4.258	4.069	4.170	−8.62	−14.53
^{114}Sn	971.6	982.6	4.602	4.389	4.491	−8.34	−14.41
^{140}Ce	1172.7	1182.8	–	4.681	4.817	−6.59	−16.63
^{208}Pb	1636.5	1639.8	5.503	5.330	5.486	−5.27	−17.45

Taking into account (3)–(10) and considering the spherically symmetric case, we can recast Eqs. (1) and (2) into the form

$$A_{nn}\nabla^2\rho_n + A_{np}\nabla^2\rho_p + B_{nn}(\nabla\rho_n)^2 \quad (11)$$
$$+ B_{np}(\nabla\rho_p)^2 + D_{np}(\nabla\rho_n\nabla\rho_p) + F_n + \lambda_n = 0,$$

$$A_{pp}\nabla^2\rho_p + A_{pn}\nabla^2\rho_n + B_{pp}(\nabla\rho_p)^2 \quad (12)$$
$$+ B_{pn}(\nabla\rho_n)^2 + D_{pn}(\nabla\rho_p\nabla\rho_n) + F_p + C + \lambda_p = 0,$$

where A, B, C, D, and F are functions of the variable r. The explicit expressions for them are presented in the Appendix. The coefficient C in Eq. (12) stems from taking into account the Coulomb interaction between intranuclear protons.

The set of Eqs. (11) and (12) is a set of nonlinear integro-differential equations in partial derivatives. In order to solve it in a spherically symmetric case, we make use of the method of successive approximations. The iterative process is continued until the change in the chemical potential upon going over from one iteration to the subsequent one becomes small (specifically, $\delta\lambda_q/\lambda_q \le 10^{-4}$).

For a zero approximation to the density distribution in the spherically symmetric case, we take the form

$$\rho_q(r) = \rho_{0q}/[1 + \exp((r-R)/a)], \quad (13)$$

where $R = 1.2A^{1/3}$ fm, $a = 0.6$ fm, and ρ_{0q} is the normalization constant determined with the aid of Eq. (4). If we assume that the proton and the neutron density decrease at infinity according to the same law, the large-r asymptotic behavior of the densities is given by

$$\rho_q(r)|_{r\to\infty} = r^{-2}\exp\left(-\sqrt{|\lambda_q|/(h_m b_1)}\,r\right). \quad (14)$$

At the point $r = 0$, the proton and the neutron density must be bounded.

Prior to proceeding to solve the set of Eqs. (11) and (12) numerically, it is convenient to make the change of variables $\rho_q = y_q/r$, which simplifies these equations somewhat. Since ρ_q is bounded at the point $r = 0$, the function $y_q(r)$ satisfies the condition

$$y_q(0) = 0. \quad (15)$$

In order to solve the set of Eqs. (11) and (12) numerically, use was made of the Numerov method in the summed form [23], whereby the computational scheme was stabilized to the maximum possible extent.

3. DISCUSSION OF NUMERICAL RESULTS

We begin the discussion of our numerical results by considering the binding energies of spherical nuclei occurring in the β-stability valley, such as ^{40}Ca, ^{48}Ca, ^{58}Ni, ^{90}Zr, ^{114}Sn, ^{140}Ce, and ^{208}Pb. In computing the binding energies, we employed the *SIII* [3], *SkM** [5], *T6* [7], *SkP* [6], and *SLy4* [8] parametrizations of the Skyrme forces. Figure 1 shows the relative deviations $(E - E_{\text{expt}})/E_{\text{expt}}$ of the computed binding energies E from their experimental counterparts E_{expt} versus the number of nucleons in the nuclei being considered. The experimental values of the nuclear binding energies were borrowed from [24]. As can be seen from Fig. 1, the calculations with the *SkP* potential reproduce the experimental binding energies most closely. For this reason, the computed binding energies, root-mean-square radii, and chemical potentials are presented in Table 1 only for the *SkP* parametrization.

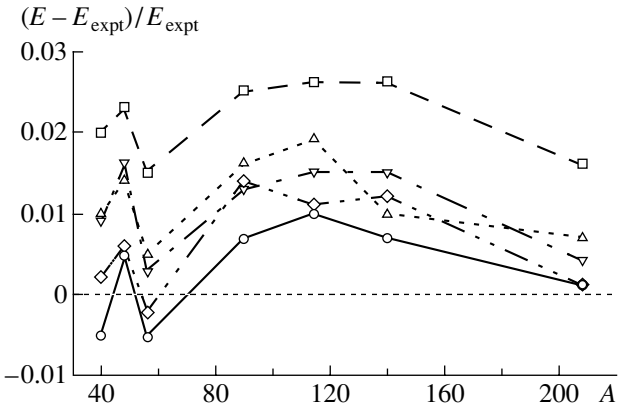

Fig. 1. Relative deviations $(E - E_{expt})/E_{expt}$ of the computed nuclear binding energies from their experimental counterparts for the (boxes) *SIII*, (inverted triangles) *SkM**, (triangles) *T6*, (circles) *SkP*, and (diamonds) *SLy4* parametrizations of the Skyrme forces.

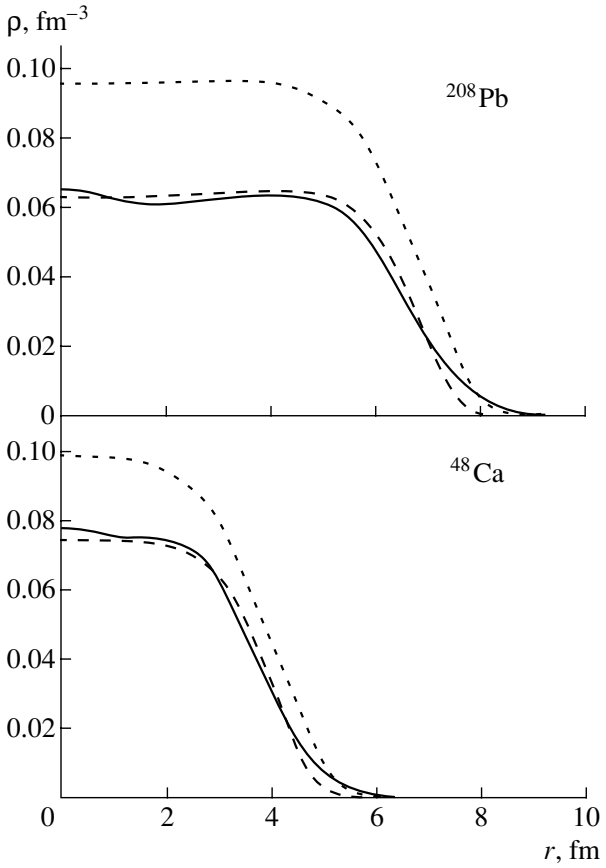

Fig. 2. Radial distributions of (dashed curves) the proton $[\rho_p(r)]$ and (dotted curves) the neutron $[\rho_n(r)]$ density according to the calculations within the extended Thomas–Fermi approximation and (solid curves) experimental proton densities in ^{48}Ca and ^{208}Pb. The experimental charge densities were borrowed from [26].

It should be noted that, for the majority of the nuclei quoted in Fig. 1, the computed binding energies are slightly in excess of their experimental counterparts. As a rule, the inclusion of shell corrections [11] enhances this effect since, for the majority of the spherical models considered in the present study, the shell correction either increases the binding energy or is close to zero [25]. It follows that, for the majority of the nuclei quoted in Fig. 1, the results that the extended Thomas–Fermi approximation with the *SkP* potential yields for the binding energies with allowance for shell corrections will also be close to the corresponding experimental values.

The values calculated here within the extended version of the Thomas–Fermi approximation for the binding energies and the root-mean-square radii agree well with available experimental data (see Table 1).

The binding energies, root-mean-square radii, and chemical potentials computed here were obtained in the nonlocal approximation. In the local approximation, the coefficients b_2, b_3, and b_4 in Eq. (7) vanish; that is, three gradient terms are discarded, which leads to an additional contribution to the nuclear binding energy. As a result, the nuclear binding energy computed in the nonlocal approximation differs from that which was obtained in the local approximation by a few tenths of a megaelectronvolt in light nuclei and by about 1 MeV in heavy nuclei.

In Fig. 2, the proton densities computed for ^{48}Ca and ^{208}Pb are contrasted against their experimental counterparts. Here and below, the experimental radial distributions of the charge density in nuclei were taken from the analysis of inelastic electron scattering on nuclei as given in [26]. From the results presented in Fig. 2, it follows that the computed proton densities agree well with the experimental densities in the interior of the nuclei, but that there are slight distinctions in the diffuse region, especially in the region of the distribution tail. These distinctions can be removed by replacing the value of $b_1 = 1/36$ by a greater value—for example, by the quantum-mechanical value of $b_1 = 1/9$ [15]. This replacement improves considerably the density profile, but it reduces significantly the binding energy [15]. The fact that the description of the proton-density profile within the nonlocal extended Thomas–Fermi approximation, which takes into account $\hbar^2$ terms in the kinetic-energy functional, is insufficiently accurate affects the root-mean-square radii as well, which appear to be slightly underestimated (see Table 1).

Having demonstrated that, for spherical nuclei from the region around the β-stability line, the extended Thomas–Fermi approximation provides an accurate description of their gross properties, we now proceed to consider nuclei lying far off the stability

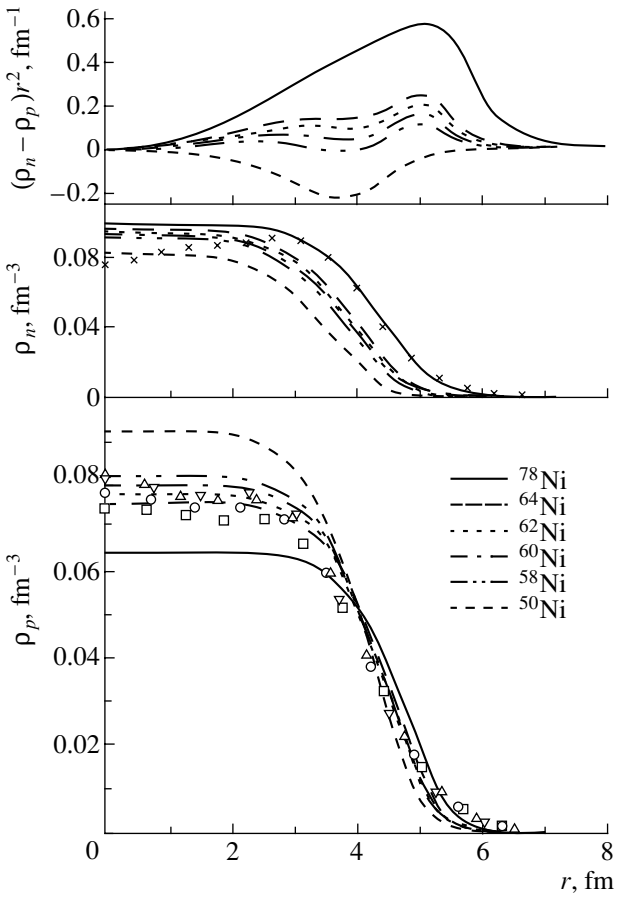

Fig. 3. Radial distributions of the proton $[\rho_p(r)]$ and the neutron $[\rho_n(r)]$ density according to the calculations within the extended Thomas–Fermi approximation, $(\rho_n(r) - \rho_p(r))r^2$, and experimental proton densities for nickel isotopes (data for ^{64}Ni, ^{62}Ni, ^{60}Ni, and ^{58}Ni are represented by boxes, circles, triangles, and inverted triangles, respectively). The experimental charge densities were borrowed from [26]. The radial distribution of neutrons in ^{78}Ni according to the calculations within the relativistic Hartree–Bogolyubov approximation (crosses) was taken from [30].

line, such as ^{32,56}Ca, ^{48,78}Ni, and ^{100,132}Sn. The binding energies, root-mean-square radii, and chemical potentials computed for these nuclei within the extended Thomas–Fermi approximation are quoted in Table 2. The experimental value of the binding energy of the ^{100}Sn isotope was taken from [27]; for the remaining isotopes, the binding energies were borrowed from [24]. We note that the ^{40,48}Ca, ^{48,78}Ni, and ^{100,132}Sn nuclei, for which some features are presented in Tables 1 and 2 and in Figs. 1–4, are doubly magic. The doubly magic nucleus ^{48}Ni was synthesized quite recently [28]. Our computed value of 346.8 MeV for the binding energy of this nucleus agrees well with the result (349.0 MeV) obtained in [29] from a systematics of binding energies.

As can be seen from Table 2, the binding energies calculated within the extended Thomas–Fermi approximation for nuclei lying far off the β-stability line agree well with their experimental counterparts. This indicates that the extended Thomas–Fermi approximation is a highly accurate method for computing the ground-state properties of spherical nuclei.

For the nickel isotopes, the results of the calculations for the density distributions are displayed in Fig. 3, where we can see that, in the interior of the ^{50}Ni and ^{78}Ni nuclei, the proton and neutron densities differ considerably. In the surface layer, there is an excess of proton density (proton skin) in ^{50}Ni; on the contrary, ^{78}Ni has a neutron skin. We note that the proton and the neutron density in the interior of nuclei change considerably upon going over from neutron-deficient to neutron-rich isotopes, the total particle density at the center of a nucleus remaining virtually unchanged. The results that we obtained for the proton-density distributions agree well with experimental data from [26], while our result for the neutron-density distribution in the ^{78}Ni nucleus comply with the results of microscopic calculations performed within the relativistic Hartree–Bogolyubov approximation [30].

For tin isotopes, the radial dependences of the proton and neutron densities are displayed in Fig. 4. The shapes of the densities for neutron-deficient and neutron-rich tin isotopes are identical to those for nickel isotopes.

From Figs. 3 and 4, it can be seen that the radial proton-density distributions computed in the extended Thomas–Fermi approximation comply well with experimental data (for the Ni and Sn isotopes presented in these figures) in the interior of the nuclei and slightly differ from them in their surface regions.

Within the extended Thomas–Fermi approximation, it is possible to assess the position of the line of neutron stability of the elements. As can be seen from Fig. 5, the chemical potentials computed within the extended Thomas–Fermi approximation for Ni and Sn isotopes change smoothly in response to variations in the number of neutrons. The neutron number at which the chemical potential changes sign from a negative to a positive one corresponds to the boundary of neutron stability of an element. The extended Thomas–Fermi approximation is a macroscopic approach taking no account of either the shell structure of the nucleus or pairing effects; therefore, it can yield only an approximate position for the boundary of neutron stability of the elements. Nonetheless, the value computed here on this basis for tin isotopes ($A = 162$) is in satisfactory agreement with the value found within the model proposed in [25] ($A = 157$). Moreover, our curves comply well with the results of calculations within the relativistic Hartree–Bogolyubov

Table 2. Binding energies E, root-mean-square radii $\langle r\rangle$, and chemical potentials λ of neutron-rich and neutron-deficient nuclei (the experimental values E_{expt} were taken from [27] for ^{100}Sn and from [24] for the remaining isotopes)

Nucleus	E_{expt}, MeV	E, MeV	$\langle r_p\rangle$, fm	$\langle r_n\rangle$, fm	λ_n, MeV	λ_p, MeV
^{32}Ca	–	201.5	3.100	2.922	−22.470	−0.590
^{56}Ca	449.6	456.0	3.447	3.754	−2.440	−25.248
^{48}Ni	–	346.8	3.433	3.328	−19.707	−2.521
^{50}Ni	385.5	385.7	4.453	4.389	−17.643	−4.431
^{60}Ni	526.9	528.9	3.589	3.670	−9.991	−13.153
^{62}Ni	545.3	549.4	3.618	3.723	−8.854	−14.694
^{64}Ni	561.8	567.6	3.646	3.774	−7.825	−16.184
^{78}Ni	641.4	646.8	3.833	4.124	−2.572	−24.853
^{100}Sn	825.8	819.7	4.243	4.247	−13.37	−7.84
^{124}Sn	1049.4	1060.0	4.491	4.655	−5.702	−18.480
^{132}Sn	1102.7	1104.0	4.568	4.783	−3.981	−21.352

Table 3. Binding energies E, root-mean-square radii $\langle r\rangle$, and chemical potentials λ computed for superheavy nuclei within the extended Thomas–Fermi approximation and binding energies E_{TF} obtained in the Thomas–Fermi approximation [32]

Z	N	E, MeV	E_{TF}, MeV	$\langle r_p\rangle$, fm	$\langle r_n\rangle$, fm	λ_n, MeV	λ_p, MeV
114	182	2121.6	2099.8	6.006	6.536	−4.777	−16.640
118	182	2132.1	2109.9	6.040	6.176	−5.418	−15.347
120	182	2134.9	2112.7	6.061	6.210	−6.064	−13.711
126	182	2134.2	2112.32	6.107	6.209	−6.692	−11.855
126	184	2149.4	2127.50	6.119	6.225	−6.482	−13.190
164	272	2667.9	–	6.686	7.012	−4.303	−15.003
164	318	2847.6	–	7.080	7.315	−1.716	−19.907

approximation [30] (see Fig. 5). For Ni isotopes, the computed value of $A = 90$ agrees well with the value obtained within the relativistic Hartree–Bogolyubov approximation ($A = 94$) [30] and with the value found in the three-dimensional Hartree–Fock–Bogolyubov approximation [31].

Let us now proceed to investigate the ground-state properties of superheavy elements in the region of the possible stability island around $Z = 114$, $N = 184$. We will also consider the $Z = 164$, $N = 272$, 318 nuclei. It should be noted that the magic number of $Z = 114$ was obtained within various models [11, 19]. The $Z \approx 114$ and $N \approx 182$ nuclei have a spherical shape or a shape close to it [19].

The stability of superheavy nuclei is associated with the shell correction, owing to which there is a fission barrier in these nuclei [11, 19, 21]. However, the effect of the shell correction on the density distributions in nuclei occurring close to the β-stability line is insignificant. Moreover, it is necessary to know the macroscopic binding energy in order to calculate the total binding energy of nuclei by the shell-correction method. Therefore, it is of great interest to investigate, within the extended Thomas–Fermi approximation, the density distributions in superheavy nuclei and their macroscopic binding energies.

For the ground-state properties of the nuclei of superheavy elements, the results of the calculations

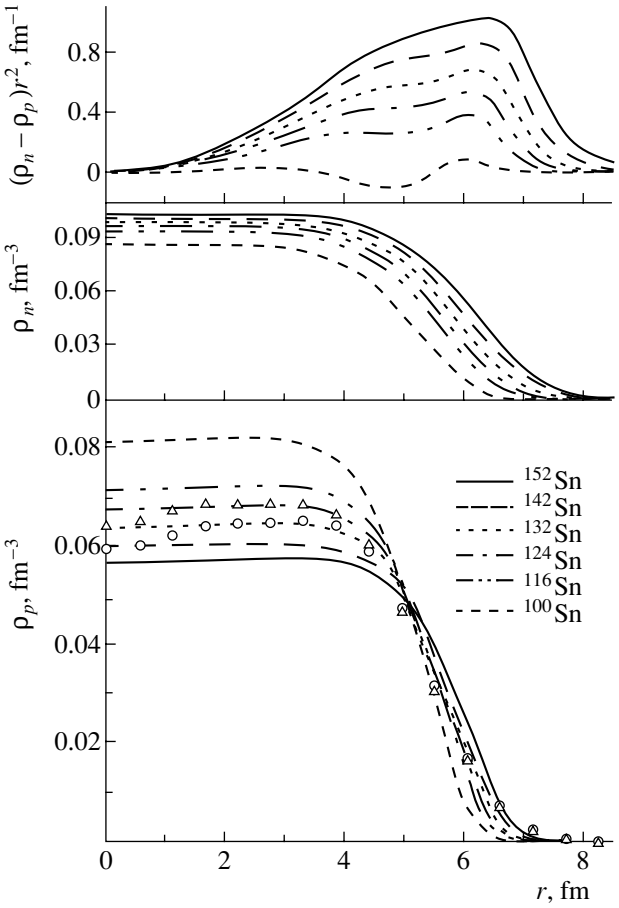

Fig. 4. Radial distributions of the proton $[\rho_p(r)]$ and the neutron $[\rho_n(r)]$ density according to the calculation within the extended Thomas–Fermi approximation, $(\rho_n(r) - \rho_p(r))r^2$, and experimental proton densities for tin isotopes (data for ^{124}Sn and ^{116}Sn are represented by circles and triangles, respectively). The experimental charge densities were borrowed from [26].

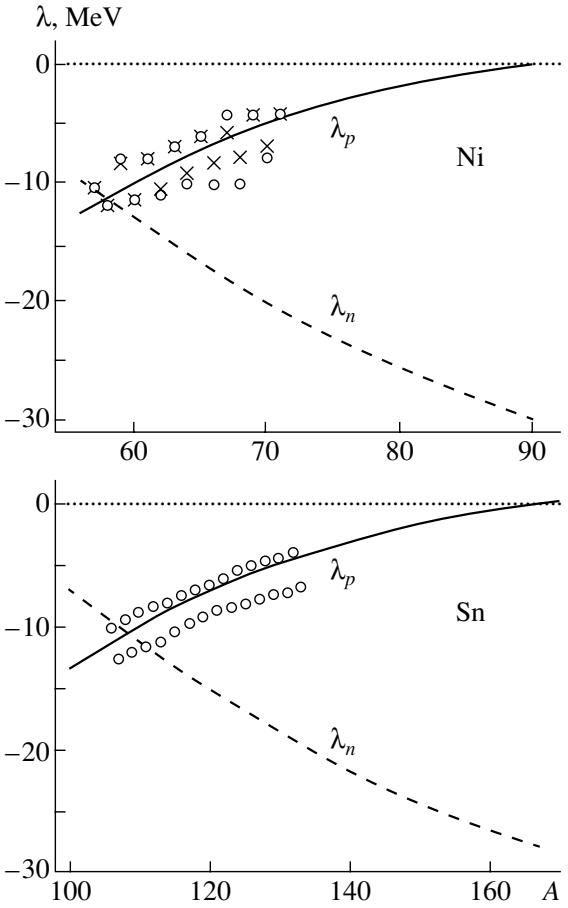

Fig. 5. Proton and neutron chemical potentials versus the number of neutrons for nickel and tin isotopes. The results of the calculations within the relativistic Hartree–Bogolyubov approximation [30] (circles) and the experimental values of the neutron-separation energies [24] (crosses) are also presented here for the sake of comparison.

with the *SkP* potential are presented in Table 3. The results of the calculations with the *SkM** and *SLy4* potentials agree within 1% with the results quoted in this table. In the region of the nuclei being considered, the Coulomb repulsion is so strong that the binding energy of the nuclei changes only slightly in response to an increase in the number of protons at a fixed number of neutrons ($N = 182$). From the values of λ_n quoted in Table 3, it can be seen that the superheavy nuclei must be stable with respect to neutron emission. For superheavy nuclei, Table 3 also gives the binding energies that were obtained in the Thomas–Fermi approximation for the case of finite-range forces [32]. The parameters of these forces were chosen in [32] in such a way as to reproduce the experimental nuclear masses. From Table 3, it can be seen that the binding energies computed for superheavy nuclei in the extended Thomas–Fermi approximation with the *SkP* forces are greater than those found in [32], this difference significantly exceeding the typical value of the shell correction for these nuclei [19, 21, 25, 32].

Figure 6 displays the distributions of the proton and the neutron density for the $^{292,300}_{120}$X and $^{482}_{168}$X nuclei. As can be seen from Fig. 6, the Coulomb repulsion leads to a significant displacement of the intranuclear protons to the periphery of the nuclei. The proton density in the interior of the nuclei is lower than at their surfaces and in the intermediate region between the periphery and the interior.

We define the thickness of the diffuse layer, t, for a density distribution as the distance over which the density changes from 90 to 10% of its maximum value. Figure 7 displays the thicknesses of the diffuse layer for the proton (t_p), the neutron (t_n), and the total particle (t_{tot}) density versus the number of neutrons

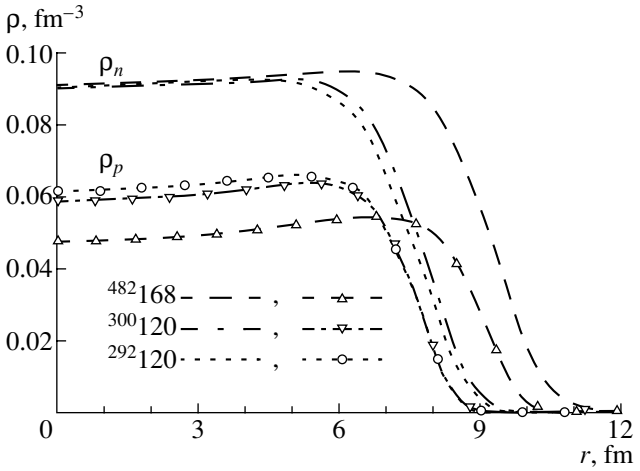

Fig. 6. Radial distributions of the proton and the neutron density in the nuclei of superheavy elements according to the calculations within the extended Thomas–Fermi approximation.

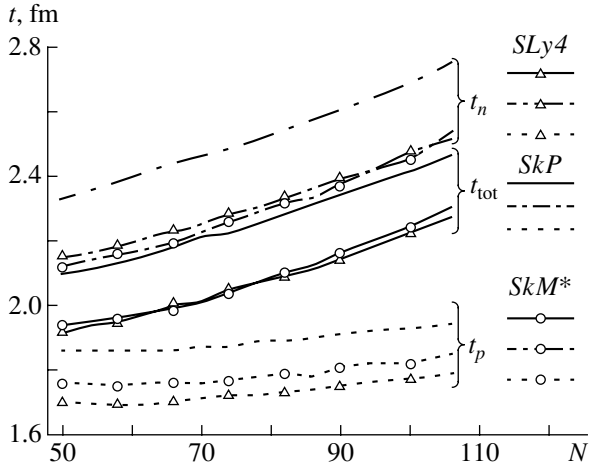

Fig. 7. Thicknesses of the diffuse layer for the proton (t_p), the neutron (t_n), and the total particle ($t_{\rm tot}$) density in tin isotopes versus the number of neutrons (N) according to the calculations with the *SLy4*, the *SkP*, and the *SkM** parametrization.

in tin isotopes. The thicknesses of the diffuse layer that are presented in Fig. 7 were computed within the extended Thomas–Fermi approximation by using the *SLy4*, *SkP*, and *SkM** parametrizations of the Skyrme forces. From Fig. 7, it can be seen that the thickness of the diffuse layer increases with increasing number of neutrons. A similar type of behavior of the diffuse layer in these nuclei was also found within microscopic calculations [33]. At the same time, the quantity t_p remains virtually unchanged, the growth of $t_{\rm tot}$ with increasing number of neutrons being due to the growth of t_n. This behavior of the neutron density in various tin isotopes is expected to manifest itself in nuclear reactions that are sensitive to the distribution of neutrons.

4. CONCLUSION

It has been shown that the nonlocal extended Thomas–Fermi approximation implemented for the case of Skyrme forces appears to be a simple, fairly accurate, and efficient means for studying the ground-state properties of medium-mass and heavy nuclei, both those occurring near the β-stability line and those lying far off it. The calculated binding energies of stable and unstable nuclei closely reproduce experimental data. A good description of the root-mean-square charge radii has also been obtained. The results of the calculations within the extended Thomas–Fermi approximation for the radial distributions of the proton densities agree well with the experimental distributions in the interior of nuclei and slightly deviate from them in the diffuse region. The ground states of superheavy nuclei have been considered. It has been found that, in the $Z \approx 114$–120 superheavy nuclei, there is a modest decrease in the density at the center of a nucleus. The thicknesses of the diffuse layer for the total particle density and for the neutron density have been shown to increase with increasing number of neutrons in nuclei.

ACKNOWLEDGEMENTS

We are grateful to Prof. D. Vretenar for kindly placing at our disposal the results of numerical calculations within the relativistic Hartree–Bogolyubov method.

APPENDIX

The functions $f_{p(n)}$ and $\mathbf{W}_{n(p)}$ introduced in (7) are given by

$$f_{n(p)} = 1 + h_m[(\gamma+\beta)\rho_{n(p)} + \gamma\rho_{p(n)}],$$
$$f'_{np(pn)} = h_m\gamma, \quad f'_{nn(pp)} = h_m(\gamma+\beta),$$
$$\mathbf{W}_{n(p)} = \frac{W_0}{2}[2\nabla\rho_{n(p)} + \nabla\rho_{p(n)}],$$

where

$$\gamma = \frac{1}{4}\left[t_1\left(1+\frac{1}{2}x_1\right) + t_2\left(1+\frac{1}{2}x_2\right)\right],$$
$$\beta = \frac{1}{4}\left[t_2\left(x_2+\frac{1}{2}\right) - t_1\left(x_1+\frac{1}{2}\right)\right].$$

The coefficients in Eqs. (11) and (12) can be represented as

$$A_{pp} = \frac{2}{h_m}\left(f'_{pp}(b_2 - b_3 + b_4) - b_1\frac{f_p}{\rho_p} - C_{pp}\frac{\rho_p}{f_p}\right.$$

$$-\bar{C}_{np}\frac{\rho_n}{f_n}\Big) + 2h_m a_9^2\left(4\frac{\rho_p}{f_p}+\frac{\rho_n}{f_n}\right) - 2(a_7+a_8),$$

$$A_{pn} = \frac{2}{h_m}\left(f'_{pn}(b_2-b_3+b_4) - C_{pn}\left(\frac{\rho_p}{f_p}+\frac{\rho_n}{f_n}\right)\right)$$
$$- 2a_7 + 4h_m a_9^2\left(\frac{\rho_p}{f_p}+\frac{\rho_n}{f_n}\right),$$

$$B_{pp} = \frac{1}{h_m}\left(b_1\frac{f_p}{\rho_p^2}F_{pp} - C_{pp}\frac{F_{pp}}{f_p} + \bar{C}_{np}f'_{np}\frac{\rho_n}{f_n^2}\right)$$
$$+ h_m a_9^2\left(4\frac{F_{pp}}{f_p} - f'_{np}\frac{\rho_n}{f_n^2}\right),$$

$$B_{pn} = \frac{1}{h_m}\left(\bar{C}_{pn}\frac{F_{pp}}{f_p} + b_1\frac{f'_{np}}{\rho_n} - C_{nn}\frac{f'_{np}}{f_n^2}\rho_n\right.$$
$$\left. + 2C_{pn}f'_{pn}\frac{\rho_p}{f_p^2} - 2C_{pn}\frac{F_{nn}}{f_n}\right)$$
$$+ h_m a_9^2\left(-\frac{F_{pp}}{f_p} + 4\frac{F_{nn}}{f_n} - 4f'_{pn}\frac{\rho_p}{f_p^2} + 4f'_{np}\frac{\rho_n}{f_n^2}\right),$$

$$D_{pn} = \frac{2}{h_m}\left(-f'_{pn}\frac{b_1}{\rho_p} + C_{pp}f'_{pn}\frac{\rho_p}{f_p^2} - \bar{C}_{np}\frac{F_{nn}}{f_n}\right)$$
$$+ 2h_m a_9^2\left(\frac{F_{nn}}{f_n} - 4f'_{pn}\frac{\rho_p}{f_p^2}\right),$$

$$F_p = \frac{k}{h_m}\left(f'_{pp}\rho_p^{5/3} + \frac{5}{3}f_p\rho_p^{2/3} + f'_{np}\rho_n^{5/3}\right)$$
$$+ 2a_1(\rho_n+\rho_p) + 2a_2\rho_p + (\alpha+2)a_3(\rho_n+\rho_p)^{\alpha+1}$$
$$+ \alpha a_4(\rho_n+\rho_p)^{\alpha-1}(\rho_n^2+\rho_p^2) + 2a_4\rho_p(\rho_n+\rho_p)^{\alpha},$$

$$C = 2\pi e^2\left(\frac{1}{r}\int_0^r r'^2\rho_p(r')dr' + \int_r^\infty r'\rho_p(r')dr'\right)$$
$$- e^2\left(\frac{3\rho_p(r)}{\pi}\right)^{1/3},$$

where we have introduced the following notation:

$$F_{nn(pp)} = 1 - \rho_{n(p)}f'_{nn(pp)}/f_{n(p)},$$
$$C_{nn(pp)} = b_5 f'^2_{nn(pp)} + 4b_6 h_m^2 a_9^2,$$
$$C_{np(pn)} = b_5 f'_{nn(pp)}f'_{np(pn)} + 2b_6 h_m^2 a_9^2,$$
$$\bar{C}_{np(pn)} = b_5 f'^2_{np(pn)} + b_6 h_m^2 a_9^2,$$
$$C_{nn} = C_{pp}, \quad C_{np} = C_{pn}, \quad \bar{C}_{np} = \bar{C}_{pn},$$
$$a_1 = 0.5t_0(1+0.5x_0), \quad a_2 = -0.5t_0(x_0+0.5),$$
$$a_3 = t_3(1+0.5x_3)/12, \quad a_4 = -t_3(x_3+0.5)/12,$$
$$a_7 = (3t_1(1+0.5x_1) - t_2(1+0.5x_2))/16,$$
$$a_8 = -(3t_1(0.5+x_1) + t_2(0.5+x_2))/16,$$
$$a_9 = 0.5W_0.$$

The corresponding coefficients for Eq. (12) are obtained upon the interchange of n and p.

REFERENCES

1. T. H. R. Skyrme, Nucl. Phys. **9**, 635 (1959).
2. D. Vatherin and D. Brink, Phys. Rev. C **5**, 626 (1972).
3. M. Beiner, H. Flocard, N. V. Giai, and P. Quentin, Nucl. Phys. A **238**, 29 (1975).
4. Nguyen Van Giai and N. Sagawa, Nucl. Phys. A **371**, 1 (1981).
5. J. Bartel, P. Quentin, M. Brack, *et al.*, Nucl. Phys. A **386**, 79 (1982).
6. J. Dobaczewski, H. Flocard, and J. Treiner, Nucl. Phys. A **422**, 103 (1984).
7. F. Tondeur, M. Brack, M. Farine, and J. M. Pearson, Nucl. Phys. A **420**, 297 (1984).
8. E. Chabanat, PhD Thesis (Lyon, 1995); E. Chabanat, P. Bonche, P. Haensel, *et al.*, Nucl. Phys. A **635**, 231 (1998).
9. B. I. Barts, Yu. L. Bolotin, E. V. Inopin, and V. Yu. Gonchar, *Hartree-Fock Method in Nuclear Theory* (Naukova Dumka, Kiev, 1982).
10. P.-G. Reinhard, D. J. Dean, W. Nazarewicz, *et al.*, Phys. Rev. C **60**, 014316 (1999).
11. V. M. Strutinsky, Nucl. Phys. A **95**, 420 (1967); **122**, 1 (1968).
12. Z. Patyk, A. Baran, J. F. Berger, *et al.*, Phys. Rev. C **59**, 704 (1999).
13. A. B. Migdal, *Theory of Finite Fermi Systems and Applications to Atomic Nuclei* (Nauka, Moscow, 1983, 2nd ed.; Interscience, New York, 1967).
14. É. E. Sapershteĭn and V. A. Khodel', Izv. Akad. Nauk SSSR, Ser. Fiz. **47**, 907 (1983).
15. M. Brack, C. Guet, and H.-B. Hakanson, Phys. Rep. **123**, 275 (1985).
16. M. Brack and R. K. Bhaduri, *Semiclassical Physics* (Addison-Wesley, Reading, 1997).
17. M. Brack, Rev. Mod. Phys. **65**, 677 (1993).
18. V. M. Kolomiets, *Local-Density Approximation in Atomic and Nuclear Physics* (Naukova Dumka, Kiev, 1990).
19. R. Smolanczuk, J. Skalski, and A. Sobiczewski, Phys. Rev. C **52**, 1871 (1995); R. Smolanczuk, Phys. Rev. C **56**, 812 (1997).
20. Yu. Ts. Oganessian *et al.*, Phys. Rev. Lett. **83**, 3154 (1999); Yad. Fiz. **63**, 1769 (2000) [Phys. At. Nucl. **63**, 1679 (2000)]; Yad. Fiz. **64**, 1427 (2001) [Phys. At. Nucl. **64**, 1349 (2001)].
21. G. Münzenberg, Rep. Prog. Phys. **51**, 57 (1988); S. Hofmann, Rep. Prog. Phys. **61**, 373 (1998); G. N. Flerov, I. Zvara, G. M. Ter-Akopyan, *et al.*, Fiz. Élem. Chastits At. Yadra **22**, 931 (1991) [Sov. J. Part. Nucl. **22**, 453 (1991)].
22. P. Hohenberg and W. Kohn, Phys. Rev. **136**, B864 (1964).
23. Liviu Gr. Iharu, *Numerical Methods for Differential Equations and Applications* (Editura Academiei, Bucharest, 1984).

24. G. Audi, O. Bersillon, J. Blachot, and A. H. Wapstra, Nucl. Phys. A **624**, 1 (1997); G. Audi and A. H. Wapstra, Nucl. Phys. A **595**, 409 (1995).
25. P. Moller, J. R. Nix, and K.-L. Kratz, At. Data Nucl. Data Tables **66**, 131 (1997); P. Möller, J. R. Nix, W. D. Myers, and W. J. Swiatecki, At. Data Nucl. Data Tables **59**, 185 (1995).
26. H. De Vries, C.W. De Jager, and C. De Vries, At. Data Nucl. Data Tables **36**, 495 (1987).
27. M. Chartier *et al.*, Phys. Rev. Lett. **77**, 2400 (1996).
28. B. Blank *et al.*, Phys. Rev. Lett. **84**, 1116 (2000).
29. B. A. Brown, Phys. Rev. C **58**, 220 (1998).
30. G. A. Lalazissis, D. Vretenar, and P. Ring, Phys. Rev. C **57**, 2294 (1998).
31. J. Terasaki, P.-H. Heenen, H. Flocard, and P. Bonche, Nucl. Phys. A **600**, 371 (1996).
32. W. D. Myers and W. J. Swiatecki, Nucl. Phys. A **601**, 141 (1996).
33. J. Dobaczewski *et al.*, Phys. Rev. C **53**, 2809 (1996).

Translated by A. Isaakyan

Physics of Atomic Nuclei, Vol. 65, No. 5, 2002, pp. 824–830. From Yadernaya Fizika, Vol. 65, No. 5, 2002, pp. 856–862.

NUCLEI
Theory

Fission Dynamics of Excited Nuclei within the Liquid-Drop Model*

S. V. Radionov, F. A. Ivanyuk, V. M. Kolomietz, and A. G. Magner

Institute for Nuclear Research, National Academy of Sciences of Ukraine, pr. Nauki 47, Kiev, 03680 Ukraine

Received August 24, 2000; in final form, May 11, 2001

Abstract—We evaluate the temperature $T_{\rm scis}$ at the scission point and the saddle-to-scission time $\tau_{\rm scis}$ for the fission of heated nuclei. We use classical Lagrange-like equations of motion within the liquid-drop model. The nuclear surface is parameterized by a two-parameter family of the Lawrence shapes. Conservative forces are defined through the free energy of the nucleus at finite temperatures. We use the friction tensor that is derived from the Navier–Stokes momentum-flux tensor and which takes into account the boundary conditions at the nuclear surface. The scission line is determined from the instability condition of the nuclear shape with respect to variations of the neck radius. A numerical solution to the dynamical equations is obtained for the ^{236}U nucleus. The viscosity coefficient μ is deduced from a comparison of experimental data on the kinetic energy of fission fragments with the computed one. It is found that μ obtained by using our approach deviates significantly from μ of the standard hydrodynamic model. © *2002 MAIK "Nauka/Interperiodica".*

1. INTRODUCTION

Many general features of nuclear dynamics can be described on the basis of macroscopic models in terms of collective variables. A few important degrees of freedom are usually used to simplify a complex dynamical problem of large-amplitude motion like nuclear fission. An available approach to such large-amplitude-motion problems is based on the standard liquid-drop model (LDM). Up to now, the LDM has been widely used to describe the main macroscopic (that is, averaged over many quantum states) characteristics of nuclear fission [1]. Within this model, one starts with the classical equations of motion for collective variables that describe the shape of the nuclear surface. The conservative forces and the mass coefficients are derived from the LDM under the assumption of the irrotational motion and incompressibility of a nuclear liquid. The friction tensor is derived by using the well-known Rayleigh function in the same way as for infinite viscous matter.

In [2], the nuclear liquid-drop model was introduced by combining the initial Navier–Stokes problem inside a nucleus and the boundary conditions at the nuclear surface. The friction tensor was modified by taking into account the finite size of the liquid drop. In the present study, we solve the macroscopic equations of motion with the friction tensor of [2] and compare the results of numerical calculations with those obtained within the standard hydrodynamic model.

2. MACROSCOPIC EQUATION OF MOTION

The motion of incompressible viscous and uniformly charged liquid can be described by the Navier–Stokes equation

$$m\rho_{\rm eq}\frac{\partial}{\partial t}u_\alpha = -\frac{\partial}{\partial r_\beta}\Pi_{\alpha\beta} - \rho_{p,{\rm eq}}\frac{\partial}{\partial r_\alpha}\varphi, \qquad (1)$$

where $\rho_{\rm eq}(\mathbf{r})$ is the equilibrium particle density, $\rho_{p,{\rm eq}}(\mathbf{r})$ is the equilibrium charge density, m is the nucleon mass, $\mathbf{u}(\mathbf{r},t)$ is the velocity field, and $\varphi(\mathbf{r},t) = \int \rho_{p,{\rm eq}}(\mathbf{r}')|\mathbf{r}-\mathbf{r}'|^{-1}d\mathbf{r}'$ is the Coulomb potential (here, φ is time-dependent because of the time dependence of the nuclear surface S). In Eq. (1) and in the following expressions, summation is implied over dummy Greek indices. The momentum-flux tensor $\Pi_{\alpha\beta}(\mathbf{r},t)$ contains conservative and dissipative parts. Below, we assume the potential motion of fluid. Taking into account Eq. (1), one obtains the momentum-flux tensor in the form (see also § 62 of [3])

$$\Pi_{\alpha\beta} = \left[-m\rho_{\rm eq}\frac{\partial\chi}{\partial t} - \frac{\mathcal{Z}e}{A}\rho_{\rm eq}\varphi\right]\delta_{\alpha\beta} - 2\mu\frac{\partial^2\chi}{\partial r_\alpha \partial r_\beta}, \qquad (2)$$

where $\chi(\mathbf{r},t)$ is the potential of the velocity field ($\mathbf{u} = \nabla\chi$), $\mathcal{Z}$ is the number of protons, e is the electron charge, A is the number of nucleons in the nucleus, and μ is the viscosity coefficient.

The potential $\chi(\mathbf{r},t)$ can be obtained from the continuity equation

$$\Delta\chi = 0. \qquad (3)$$

*This article was submitted by the authors in English.

1063-7788/02/6505-0824$22.00

The equations of motion (1) and (3) must be completed with the boundary conditions. Under the assumption of the sharp surface of a nucleus, the boundary conditions at the moving surface are given by (see § 61 of [3])

$$(\mathbf{n}\cdot\mathbf{u})|_S = (\mathbf{n}\cdot\nabla\chi)|_S = u_S, \tag{4}$$

$$\Pi_{nn}(\mathbf{r},t)|_S = P_S, \tag{5}$$

where $\mathbf{n}$ is a unit vector normal to the surface S, $\Pi_{nn}(\mathbf{r},t)$ is the normal–normal component of the momentum-flux tensor $\Pi_{\alpha\beta}$, u_S is the velocity of the surface S, and P_S is the surface-tension pressure. We indicate that the tensor $\Pi_{\alpha\beta}$ contains both time-reversible and viscous contributions [see Eq. (2)].

Let us introduce the displacement field $\mathbf{w}(\mathbf{r},t)$ given by $\mathbf{u}(\mathbf{r},t) = \partial\mathbf{w}(\mathbf{r},t)/\partial t$. It is convenient to rewrite the boundary condition (5) in the form of the variational problem (see [4], p. 195)

$$\int_{t_0}^{t_1} dt \oint_S dS\delta w_n[\Pi_{nn} - P_S] = 0, \tag{6}$$

where $\delta w_n(\mathbf{r},t_0) = \delta w_n(\mathbf{r},t_1) = 0$ for any variations of the normal component w_n of the displacement field $\mathbf{w}(\mathbf{r},t)$. The variational problem (6) can be simplified [2] by parametrizing the liquid-drop surface S in terms of the collective variables $q(t) = q_1,\ldots,q_N$,

$$\delta w_n|_S = \bar{u}_i\delta q_i, \quad u_S = \bar{u}_i\dot{q}_i, \quad \chi = \bar{\chi}_i\dot{q}_i. \tag{7}$$

We will assume that the nuclear surface is created by rotation of a certain profile function $\rho = Y(z,t)$ about the z axis in the cylindrical coordinates ρ, z, and ϕ. The quantity $\bar{u}_i$ in Eq. (7) is then given by [2]

$$\bar{u}_i = \frac{1}{\Lambda}\frac{\partial Y}{\partial q_i}, \quad \Lambda = \sqrt{1+\left(\frac{\partial Y}{\partial z}\right)^2}. \tag{8}$$

In order to define the quantity $\bar{\chi}_i$ in Eq. (7), we substitute Eq. (7) into Eqs. (3) and (4) and use Eq. (8). We obtain

$$\Delta\bar{\chi}_i = 0, \quad (\mathbf{n}\cdot\nabla\bar{\chi}_i)|_S = \frac{1}{\Lambda}\frac{\partial Y}{\partial q_i}. \tag{9}$$

After substitution of Eqs. (2) and (6) into Eq. (7), we finally obtain the basic macroscopic equations of motion for the collective variables $q_i(t)$; that is,

$$M_{ij}\ddot{q}_j + \frac{\partial M_{ij}}{\partial q_k}\dot{q}_j\dot{q}_k = K_i - Z_{ij}\dot{q}_j, \qquad i = 1,2,\ldots,N, \tag{10}$$

where

$$M_{ij} = m\rho_{\mathrm{eq}}\oint_S dS\bar{u}_i\bar{\chi}_j \tag{11}$$

is the inertia tensor determining the collective kinetic energy E_{kin}. Namely, we have

$$E_{\mathrm{kin}} = \frac{1}{2}m\rho_{\mathrm{eq}}\int_V u^2 dV \tag{12}$$

$$= \frac{1}{2}m\rho_{\mathrm{eq}}\oint_S dS\chi(\mathbf{n}\cdot\nabla\chi) = \frac{1}{2}M_{ij}(q)\dot{q}_i\dot{q}_j.$$

In Eq. (10), Z_{ij} is the friction tensor [2],

$$Z_{ij} = 2\mu\oint_S dS\bar{u}_i\frac{\partial^2\bar{\chi}_j}{\partial r_\alpha\partial r_\beta}n_\alpha n_\beta. \tag{13}$$

We indicate that the friction tensor (13) differs from the friction tensor of the standard hydrodynamic model [1] (see Appendix 1). In the case of a heated system, the conservative forces K_i in Eq. (10) are related to the free energy F as (see Appendix 2)

$$K_i = -\left(\frac{\partial F}{\partial q_i}\right)_{V,T,\dot{q}}, \tag{14}$$

where T is the temperature of the system and $\dot{q} \equiv \dot{q}_1,\dot{q}_2,\ldots,\dot{q}_N$ stands for N collective velocities.

The free energy of the nucleus at a finite temperature is given by

$$F = E_{\mathrm{kin}} + F_S + F_{\mathrm{C}} + F^*. \tag{15}$$

Here, F_S and F_{C} are the free surface and Coulomb energies, respectively, and F^* is the internal free energy. The energies F_S and F_{C} are given by [5]

$$F_S = \sigma(T)B_S(q)\gamma A^{2/3}, \quad \gamma = 1 - 1.78\left[\frac{\mathcal{N}-\mathcal{Z}}{A}\right]^2, \tag{16}$$

$$F_{\mathrm{C}} = \alpha(T)B_{\mathrm{C}}(q)\frac{\mathcal{Z}^2}{A^{1/3}},$$

where $B_S(q)$ and $B_{\mathrm{C}}(q)$ are the deformation form factors defined in [1] and $\mathcal{N}$ is the number of neutrons. For numerical calculations, we assume here that the surface and Coulomb parameters in Eq. (16) depend on temperature as [6, 7]

$$\sigma(T) = 17.94\left(1 - \frac{5}{2}\frac{T^2}{T_{\mathrm{C}}^2}\right)\ (\mathrm{MeV}), \tag{17}$$

$$\alpha(T) = 0.7(1 - x_{\mathrm{C}}T^2)\ (\mathrm{MeV}),$$

where the parameter x_{C} was chosen to be $x_{\mathrm{C}} = 0.76\times10^{-3}\,\mathrm{MeV}^{-2}$ [6], and $T_{\mathrm{C}} = 18$ MeV is taken as the critical temperature for the infinite nuclear Fermi liquid ($T \ll T_{\mathrm{C}}$) [7]. The internal free energy F^* in Eq. (15) has the form

$$F^* = -a_V T^2, \tag{18}$$

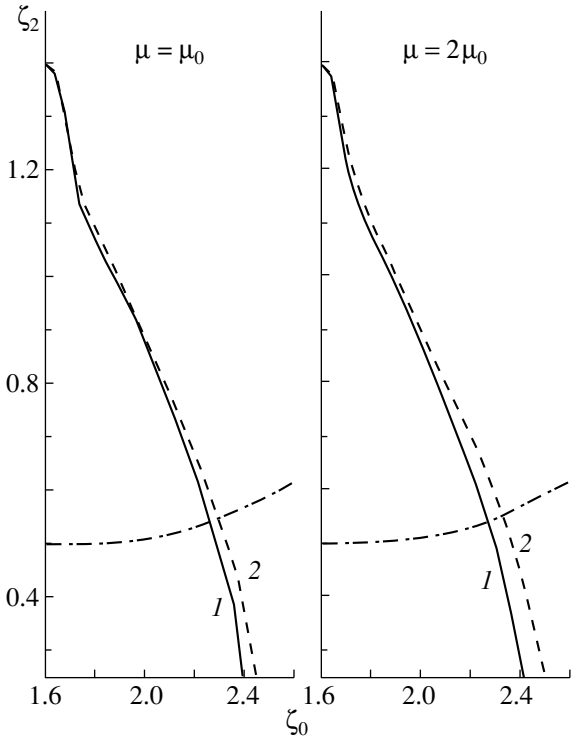

Fig. 1. Trajectories of descent from the saddle point of the ^{236}U nucleus in the ζ_0–ζ_2 plane. Two parts of the figure are given for two different values of the viscosity coefficient, $\mu = \mu_0$ and $\mu = 2\mu_0$ ($\mu_0 = 10^{-23}$ MeV s fm^{-3}). The initial kinetic energy $E_{\mathrm{kin},0}$ and the initial temperature T_0 were taken to be $E_{\mathrm{kin},0} = 1$ MeV and $T_0 = 2$ MeV. Curve *1* was obtained by using the friction tensor (13) and the theory of potential for evaluating $\bar{\chi}_i$ (see [2]). Curve *2* was obtained with the friction tensor of the standard hydrodynamic model (A.7) within the Werner–Wheeler method [1]. The dash-dotted curve is the scission line derived from the condition (29).

where $a_V = \pi^2 A/4\varepsilon_{\mathrm{F}}$ is the volume contribution to the level-density parameter and $\varepsilon_{\mathrm{F}} = 40$ MeV is the Fermi energy.

Using Eqs. (17) and (18), we can recast the free energy (15) into the form

$$F = E_{\mathrm{kin}} + U(q) - aT^2, \tag{19}$$

where $U(q)$ is the potential energy of the cold nucleus,

$$U(q) = 17.94 B_S(q)\gamma A^{2/3} + 0.7 B_{\mathrm{C}}(q)\mathcal{Z}^2/A^{1/3}\,(\mathrm{MeV}), \tag{20}$$

and the level-density parameter a is given by

$$a(q) = a_V + a_S + a_{\mathrm{C}} \tag{21}$$

with

$$a_S(q) = 17.94\frac{5}{2T_{\mathrm{C}}^2} B_S(q)\gamma A^{2/3}, \tag{22}$$

$$a_{\mathrm{C}}(q) = 0.7 x_{\mathrm{C}} B_{\mathrm{C}}(q)\frac{\mathcal{Z}^2}{A^{1/3}}.$$

The deformation form factors $B_S(q)$ and $B_{\mathrm{C}}(q)$ in Eqs. (20) and (22) are normalized as $B_S(q) = B_{\mathrm{C}}(q) = 1$ for the spherical shape of the nucleus. The system of macroscopic Eqs. (10) with the conservative forces K_i (14) should be completed with the condition for determining the temperature T along the dynamical trajectory. In order to obtain this condition, we consider the entropy $\mathcal{S}$:

$$\mathcal{S} = -\left(\frac{\partial F}{\partial T}\right)_{V,q,\dot{q}} = 2a(q)T. \tag{23}$$

The entropy $\mathcal{S}$ changes owing to the work of friction forces,

$$T d\mathcal{S} = Z_{ij}(q)\dot{q}_i\dot{q}_j dt. \tag{24}$$

Using Eq. (23), we have

$$d\mathcal{S} = 2\frac{da(q)}{dq_i} dq_i T + 2a(q) dT. \tag{25}$$

By comparing Eqs. (24) and (25), one obtains the equation for the temperature:

$$\dot{T} = \frac{1}{2aT}\left[Z_{ij}(q)\dot{q}_i\dot{q}_j - 2\frac{da(q)}{dq_i}\dot{q}_i T^2\right]. \tag{26}$$

We indicate that the same equation of motion for the temperature can be obtained from the conservation law for the total energy $E = F + T\mathcal{S}$.

Thus, the closed system of equations for the variables q and T consists of Eq. (26) and the equation

$$M_{ij}\ddot{q}_j + \frac{\partial M_{ij}}{\partial q_k}\dot{q}_j\dot{q}_k = -\left(\frac{\partial F}{\partial q_i}\right)_{V,T,\dot{q}} - Z_{ij}\dot{q}_j, \quad i = 1, 2, \ldots, N. \tag{27}$$

3. NUMERICAL RESULTS

We consider the symmetric fission of an excited nucleus ^{236}U. We will neglect the q dependence of the level-density parameter $a(q)$, assuming the empirical value $a(q) = A/8$ MeV^{-1}.

We solved Eqs. (26) and (27) numerically using the two-parameter shape family in the Lawrence parametrization [8]

$$Y^2(z) = \frac{(\zeta_0^2 - z^2)(\zeta_2^2 + z^2)}{\zeta_0^3(\zeta_0^2/5 + \zeta_2^2)}. \tag{28}$$

Here and below, all quantities having dimensions of length are expressed in units of the radius R_0 of the equivalent spherical shape. The parameter ζ_0 in (28) determines the general elongation of the figure, and ζ_2 is related to the neck radius. In our numerical calculations, we used the deformation form factors $B_S(q)$ and $B_{\mathrm{C}}(q)$ from [5, 8]. We derived the scission line from the condition of instability of the nuclear

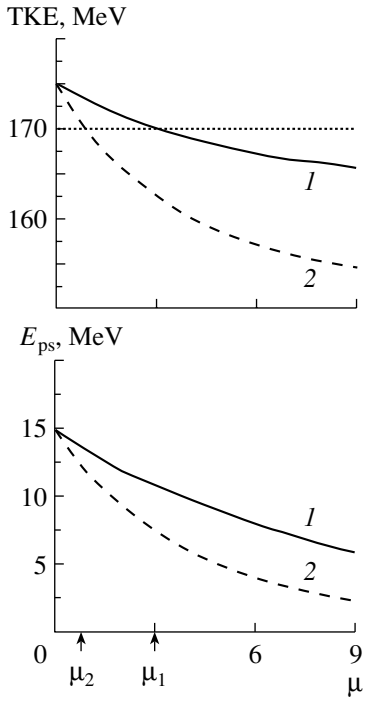

Fig. 2. Fission-fragment kinetic energy TKE and kinetic energy E_{ps} of a fissioning nucleus at the scission point as functions of the viscosity coefficient μ (in units of μ_0). The calculation was performed under the same conditions as in Fig. 1. The dotted line is the empirical TKE [see Eq. (30)] used to analyze experimental data.

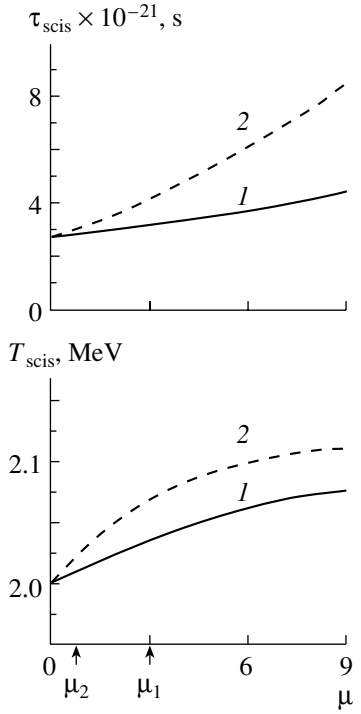

Fig. 3. Time τ_{scis} of descent from the saddle to the scission point and scission temperature T_{scis} versus the viscosity coefficient μ (in units of μ_0). The calculation was performed under the same conditions as in Fig. 1.

shape with respect to variations of the neck radius; that is,

$$\frac{\partial^2 U(q)}{\partial \rho_{neck}^2} = 0, \qquad (29)$$

where $\rho_{neck} = \zeta_2/\sqrt{\zeta_0(\zeta_0^2/5 + \zeta_2^2)}$ is the neck radius (in units of R_0) [8].

The macroscopic equations of motion (26) and (27) were solved for the initial conditions corresponding to the saddle-point deformation, the initial kinetic energy of $E_{kin,0} = 1$ MeV (initial neck velocity $\dot{\zeta}_2 = 0$), and the initial temperature of $T_0 = 2$ MeV. To solve the Neumann problem (9) for the velocity-field potential, we have used the method based on potential theory [9]. For comparison, we have solved the dynamical Eqs. (26) and (27) with the friction tensor of the standard hydrodynamic model computed within the Werner–Wheeler method [1] [see Appendix 1, Eq. (A.7)].

The dynamical trajectories for various values of the viscosity coefficient μ (in units of $\mu_0 = 10^{-23}$ MeV s fm^{-3}) are presented in Fig. 1, which also shows the dependence of the neck parameter ζ_2 on the elongation ζ_0 for a fissioning nucleus ^{236}U at two different values of the viscosity coefficient μ. Curve *1* was obtained by using the friction tensor of Eq. (13) and theory of potential for the evaluation of the fields $\bar{\chi}_i(\mathbf{r}, q)$ (see [2]). Curve *2* corresponds to the calculations with the friction tensor of the standard liquid-drop model [see Eq. (A.7)] [1]. For zero viscosity, curves *1* and *2* coincide. The scission line (dash-dotted curve in Fig. 1) was obtained as a solution to Eq. (29). We define the scission point as the intersection point of the dynamical trajectory with the scission line. As can be seen from Fig. 1, viscosity hinders neck formation and leads to a more elongated scission configuration. As the viscosity coefficient μ grows, the difference between curves *1* and *2* increases. This demonstrates a high sensitivity of dynamical calculations to the choice of friction tensor.

To illustrate the effect of viscosity on observables, we evaluated the translation kinetic energy (TKE) of fission fragments at infinity and the prescission kinetic energy E_{ps}. The value of TKE is the sum of the Coulomb interaction energy at the scission point, $V_{C,scis}$, and the prescission kinetic energy. Namely, we have

$$\mathrm{TKE} = V_{C,scis} + E_{ps}. \qquad (30)$$

After scission, fission fragments were described in terms of two equal-mass spheroids (see [10]). We

assumed that the distance between the centers of mass, d, of two spheroids is equal to the distance between the two halves of the fissioning nucleus at the scission point:

$$d = \frac{5}{4}\zeta_0 \frac{\zeta_0^2 + 3\zeta_2^2}{\zeta_0^2 + 5\zeta_2^2}\bigg|_{\rm scis}. \qquad (31)$$

The corresponding velocity $\dot{d}$ was obtained by differentiating Eq. (31) with respect to time. The elongation c of both separated spheroids is defined by the condition

$$2c + d = 2\zeta_{0,\rm scis}, \qquad (32)$$

where $\zeta_{0,\rm scis}$ is the elongation of the nucleus at the scission point. The collective parameters c and d and the velocity $\dot{d}$ were then used to evaluate the Coulomb energy $V_{\rm C,scis}$ (see [8], p. 121) and the prescission kinetic energy $E_{\rm ps}$ in Eq. (30).

Figure 2 shows the effect of viscosity on the fission-fragment kinetic energy TKE and on the prescission kinetic energy $E_{\rm ps}$. The dotted line in Fig. 2 presents a fit to the experimental data for the TKE from [1] in terms of the formula (see also [11])

$$\mathrm{TKE} = 0.108\frac{\mathcal{Z}^2}{A^{1/3}} + 21.9\,(\mathrm{MeV}). \qquad (33)$$

The viscosity coefficients μ_1 and μ_2 are given by the intersection of curves *1* and *2* with the dotted line. The viscosity coefficient μ_1 derived within our approach (see Fig. 2) is 3×10^{-23} MeV s fm^{-3}. The value of $\mu_2 \approx 1 \times 10^{-23}$ MeV s fm^{-3} corresponds to the calculation with the friction tensor of the standard liquid-drop model within the Werner–Wheeler method [1]. Note that the improved value obtained in [12] for the viscosity coefficient, $\mu \approx 1.9 \times 10^{-23}$ MeV s fm^{-3}, is smaller than our result by a factor of about 1.5. We indicate, however, that the use of our approach to describing the width of the isoscalar giant multipole resonances (see [13]) leads to better agreement with experimental data than the analogous calculations within the Werner–Wheeler method that are presented in [14].

Figure 3 illustrates the effect of viscosity on the saddle-to-scission time $\tau_{\rm scis}$ and on the temperature of the nucleus at the scission point $T_{\rm scis}$. The difference of our $T_{\rm scis}$ and $\tau_{\rm scis}$ (see curve *1*) from those within the traditional Werner–Wheeler model (curve *2*) increases with growing viscosity.

4. SUMMARY

We have derived macroscopic equations of motion for collective degrees of freedom from the variational approach to macroscopic nuclear dynamics. In the case of the heated nuclei, the conservative forces in these equations are defined through the free energy of the nucleus. We have used the friction tensor (13), which is presented in [2] and which takes into account the boundary conditions at the nuclear surface. Instead of applying the traditional Werner–Wheeler method, we have solved the exact Neumann problem for the incompressible, irrotational velocity field using the theory of potential. The scission line has been determined from the instability condition of the nuclear shape with respect to variations of the neck radius.

Our numerical calculations have been performed for the ^{236}U nucleus. We obtained the viscosity dependence of the fission-fragment kinetic energy TKE and the prescission kinetic energy $E_{\rm ps}$. Also, the effect of viscosity on the saddle-to-scission time $\tau_{\rm scis}$ and on the scission temperature $T_{\rm scis}$ has been studied. We have found a significant deviation of the results obtained for $T_{\rm scis}$ and $\tau_{\rm scis}$ with the friction tensor (13) from the analogous results obtained with the friction tensor of the standard hydrodynamic model [1].

APPENDIX 1

Friction Tensor

To clarify the origin of the friction tensor Z_{ij} (13), we will evaluate the rate of change in the collective liquid-drop energy. Multiplying Eq. (1) by $\mathbf{u}$, integrating it over the nuclear volume, and using Eqs. (4) and (5), we derive the rate of change in the collective energy $E_{\rm coll} = E_{\rm kin} + E_{\rm C} + E_S$ of the nuclear liquid drop as

$$\frac{dE_{\rm coll}}{dt} = \frac{d}{dt}(E_{\rm kin} + E_{\rm C} + E_S) = -Z_{ij}\dot{q}_i\dot{q}_j. \quad (A.1)$$

Here, $E_{\rm C}$ and E_S are the Coulomb and the surface energy, respectively, and we have used the following expression for the rate of change in the surface energy (see [4], p. 195):

$$\frac{dE_S}{dt} = \oint_S dS\,\Pi_{nn}u_n. \qquad (A.2)$$

The friction tensor Z_{ij} in Eq. (10) is given by Eq. (13) and can be recast into the form

$$Z_{ij} = \mu \oint_S dS \frac{\partial}{\partial n}(u_n^{(i)}u_n^{(j)}), \qquad (A.3)$$

where $\mathbf{u}^{(i)} = \nabla\bar{\chi}_i$.

Expression (A.3) for the friction tensor Z_{ij} can also be obtained from the Rayleigh function [2]

$$R = -\frac{1}{2}\oint_S dS\,u_n\Pi_{nn}^{(\rm dis)} = -\frac{1}{2}Z_{ij}\dot{q}_i\dot{q}_j, \qquad (A.4)$$

where $\Pi^{(\mathrm{dis})}_{\alpha\beta}$ is the dissipative part of the momentum-flux tensor (2)

$$\Pi^{(\mathrm{dis})}_{\alpha\beta} = -2\mu\frac{\partial^2\chi}{\partial r_\alpha \partial r_\beta}. \qquad (A.5)$$

We indicate that the Rayleigh function R (A.4) differs from that of infinite matter, which is used in the standard hydrodynamic model [1]:

$$2R^{(\mathrm{stand})} = \mu\int d^3r \triangle u^2 \qquad (A.6)$$

$$= -\oint\limits_S dS u_n \Pi^{(\mathrm{dis})}_{nn} - \oint\limits_S dS u_\tau \Pi^{(\mathrm{dis})}_{n\tau}.$$

Here, the index τ labels the tangential component.

The friction tensor $Z^{(\mathrm{stand})}_{ij}$ corresponding to the Rayleigh function $R^{(\mathrm{stand})}$ is written as

$$Z^{(\mathrm{stand})}_{ij} = 2\mu\oint\limits_S dS\bar{u}^{(i)}_\alpha \frac{\partial^2\bar{\chi}_j}{\partial r_\alpha \partial r_\beta} n_\beta \qquad (A.7)$$

$$= \mu\oint\limits_S dS\frac{\partial(\mathbf{u}^{(i)}\cdot\mathbf{u}^{(j)})}{\partial n},$$

where

$$u_\alpha = \bar{u}^{(i)}_\alpha \dot{q}_i, \quad \bar{u}^{(i)}_\alpha = \frac{\partial\bar{\chi}_i}{\partial r_\alpha}. \qquad (A.8)$$

It should be noted that the deviation of the Rayleigh function R from that of the standard hydrodynamic model, $R^{(\mathrm{stand})}$, is due to the fact that R of Eq. (A.4) was obtained by using the boundary conditions (4) and (5). In general, the Rayleigh functions (A.4) and (A.6), as well as the friction tensors (A.3) and (A.7), are different because the normal–tangential component of the pressure tensor $\Pi^{(\mathrm{dis})}_{\alpha\beta}$ does not vanish at the nuclear surface.

APPENDIX 2

Conservative Forces and Variational Principle

Here, we will prove expression (14) for the conservative forces K_i in the case of a heated system. We start with the first law of thermodynamics. In addition to the volume and entropy, the generalized coordinates and velocities, q_i and $\dot{q}_i$, determine the thermodynamic state of a heated system. The first law of thermodynamics takes the form (see [15], §15)

$$dE = Td\mathcal{S} - PdV - K_i dq_i - Q_i d\dot{q}_i, \qquad (A.9)$$

where $P = -(\partial E/\partial V)_{\mathcal{S},q,\dot{q}}$ is the pressure and

$$K_i = -\left(\frac{\partial E}{\partial q_i}\right)_{V,\mathcal{S},\dot{q}}, \quad Q_i = -\left(\frac{\partial E}{\partial \dot{q}_i}\right)_{V,\mathcal{S},q} \qquad (A.10)$$

are the generalized forces and the generalized momenta, respectively. In many cases, it is more convenient to use the temperature T instead of the entropy $\mathcal{S}$. Using the thermodynamic definition of the free energy $F = E - T\mathcal{S}$, we can write the generalized forces K_i in the form (14) (see [15], §15); i.e., the conservative forces K_i in equations of motion (27) should be defined through the derivation of the energy E or of the free energy F with respect to the shape parameters q_i at fixed entropy $\mathcal{S}$ or temperature T, respectively.

Below, we will also demonstrate the method that allows us to derive the macroscopic equations of motion (26) and (27) from the minimal-action principle.

Let us write the minimal-action principle in the form (see [4], p. 20)

$$\delta\int\limits_{t_1}^{t_2}[E_{\mathrm{kin}} + \lambda(E_{\mathrm{kin}} + U + E^* - E_0)]dt = 0, \quad (A.11)$$

where U is the potential energy of the cold nucleus as given by (20), E_0 is the initial total energy, λ is the Lagrange multiplier taking into account the conservation of the total energy $E = E_{\mathrm{kin}} + U + E^*$, and E^* is the internal energy of the nuclear thermal excitation [$E^* = E^*(\mathcal{S})$]. We calculate the variation in (A.11), assuming that, at the initial time instant t_1,

$$\delta q_i(t_1) = 0, \quad \delta\dot{q}_i(t_1) = 0 \qquad (A.12)$$

and that, at the final time instant t_2, the quantities δq_i and $\delta\dot{q}_i$ are arbitrary.

It should be noted that the minimal-action principle (A.11) is written for the kinetic energy E_{kin}, provided that the total energy of the system (which includes both the mechanical and thermal energies) is constant. This form of the minimal-action principle allows one to take into account friction forces in the dynamical equation through the condition in (24).

We will consider the entropy $\mathcal{S}$ as a collective variable that, together with the q and $\dot{q}$, determines the dynamical behavior of the system. From Eq. (A.11), one obtains

$$\int\limits_{t_1}^{t_2}\left(\frac{\partial\mathcal{F}}{\partial q_i}\delta q_i + \frac{\partial\mathcal{F}}{\partial\dot{q}_i}\delta\dot{q}_i + \frac{\partial\mathcal{F}}{\partial\mathcal{S}}\delta\mathcal{S}\right)dt + \mathcal{F}|_{t_2}\delta t_2 = 0, \qquad (A.13)$$

where $\mathcal{F} = E_{\mathrm{kin}} + \lambda(E_{\mathrm{kin}} + U + E^* - E_0)$.

Using the thermodynamic definition of the temperature, $T = (\partial E/\partial\mathcal{S})_{V,q,\dot{q}}$, we have

$$\left(\frac{\partial\mathcal{F}}{\partial\mathcal{S}}\right)_{V,q,\dot{q}}\delta\mathcal{S} = \lambda\left(\frac{\partial E}{\partial\mathcal{S}}\right)_{V,q,\dot{q}}\delta\mathcal{S} = \lambda T\delta\mathcal{S}, \quad (A.14)$$

where [see Eq. (24)]

$$T\delta\mathcal{S} = Z_{ij}\dot{q}_i\dot{q}_j\delta t = Z_{ij}\dot{q}_j\delta q_i. \qquad \text{(A.15)}$$

After substituting Eqs. (A.14) and (A.15) into Eq. (A.13), we obtain

$$\int_{t_1}^{t_2}\left[\frac{\partial\mathcal{F}}{\partial q_i} - \frac{d}{dt}\Big(\frac{\partial\mathcal{F}}{\partial\dot{q}_i}\Big) + \lambda Z_{ij}\dot{q}_j\right]\delta q_i dt \qquad \text{(A.16)}$$

$$+\left[-(2\lambda+1)E_{\rm kin}+\lambda(E_{\rm kin}+U+E^*-E_0)\right]\delta t_2 = 0.$$

The variations δq_i and δt_2 are independent, and Eq. (A.16) takes the form

$$\frac{\partial\mathcal{F}}{\partial q_i} - \frac{d}{dt}\Big(\frac{\partial\mathcal{F}}{\partial\dot{q}_i}\Big) + \lambda Z_{ij}\dot{q}_j = 0, \qquad \text{(A.17)}$$
$$i = 1, 2, \ldots, N,$$

$$-(2\lambda+1)E_{\rm kin} + \lambda(E_{\rm kin}+U+E^*-E_0) = 0. \qquad \text{(A.18)}$$

Using the condition $E_{\rm kin}+U+E^* = E_0$, we obtain

$$\lambda = -1/2, \quad \mathcal{F} = \frac{1}{2}(E_{\rm kin}-U-E^*), \qquad \text{(A.19)}$$

and Eq. (A.17) leads to Lagrange equations of motion in the form

$$\frac{\partial\mathcal{L}}{\partial q_i} - \frac{d}{dt}\left(\frac{\partial\mathcal{L}}{\partial\dot{q}_i}\right) - Z_{ij}\dot{q}_j = 0 \qquad \text{(A.20)}$$

with the Lagrange function $\mathcal{L} = E_{\rm kin} - U - E^*$.

The Lagrange Eq. (A.20) can be rewritten as

$$M_{ij}\ddot{q}_j + \frac{\partial M_{ij}}{\partial q_k}\dot{q}_j\dot{q}_k = K_i - Z_{ij}\dot{q}_j, \qquad \text{(A.21)}$$
$$i = 1, 2, \ldots, N,$$

where

$$K_i = -\left(\frac{\partial E}{\partial q_i}\right)_{V,\mathcal{S},\dot{q}} = -\left(\frac{\partial F}{\partial q_i}\right)_{V,T,\dot{q}}. \qquad \text{(A.22)}$$

The change in the temperature T with the time is found from Eq. (26).

REFERENCES

1. K. T. R. Davies, A. J. Sierk, and J. R. Nix, Phys. Rev. C **13**, 2385 (1976).
2. F. A. Ivanyuk, V. M. Kolomietz, and A. G. Magner, Phys. Rev. C **52**, 678 (1995).
3. L. D. Landau and E. M. Lifshitz, *Course of Theoretical Physics,* Vol. 6: *Fluid Mechanics* (Nauka, Moscow, 1986; Pergamon, New York, 1959).
4. V. L. Berdichevskiĭ, *Variational Principle for Continuum Mechanics* (Nauka, Moscow, 1983).
5. W. D. Myers and W. J. Swiatecki, Ark. Fys. **36**, 343 (1967).
6. C. Guet, E. Strumberger, and M. Brack, Phys. Lett. B **205**, 427 (1988).
7. D. G. Ravenhall, C. J. Pethick, and J. M. Lattimer, Nucl. Phys. A **407**, 571 (1983).
8. R. W. Hasse and W. D. Myers, *Geometrical Relationships of Macroscopic Nuclear Physics* (Springer-Verlag, Berlin, 1988).
9. H. Jeffreys and B. Swirles, *Methods of Mathematical Physics* (Cambridge Univ. Press, Cambridge, 1966).
10. J. R. Nix and W. J. Swiatecki, Nucl. Phys. **71**, 1 (1965).
11. U. Brosa, S. Grossmann, A. Müller, and E. Becker, Nucl. Phys. A **502**, 423c (1989).
12. A. J. Sierk, S. E. Koonin, and J. R. Nix, Phys. Rev. C **17**, 646 (1978).
13. A. G. Magner, V. M. Kolomietz, H. Hofmann, and S. Shlomo, Phys. Rev. C **51**, 2457 (1995).
14. J. R. Nix and A. J. Sierk, Phys. Rev. C **21**, 396 (1980).
15. L. D. Landau and E. M. Lifshitz, *Course of Theoretical Physics,* Vol. 5: *Statistical Physics* (Nauka, Moscow, 1995; Pergamon, Oxford, 1958).

Physics of Atomic Nuclei, Vol. 65, No. 5, 2002, pp. 831–840. Translated from Yadernaya Fizika, Vol. 65, No. 5, 2002, pp. 863–872.

NUCLEI
Theory

Protonic Decay of Oriented Nuclei

S. G. Kadmensky

Voronezh State University, Universitetskaya pl. 1, Voronezh, 394693 Russia

Received February 22, 2001; in final form, July 18, 2001

Abstract—On the basis of the multiparticle theory of protonic decay, the angular distributions of protons emitted by oriented spherical and deformed nuclei in the laboratory frame and in the internal coordinate frame of deformed parent nuclei are constructed with allowance for symmetry with respect to time inversion. It is shown that, because of the deep-subbarrier character of protonic decay, the adiabatic approximation is not applicable to describing the angular distributions of protons emitted by oriented deformed nuclei and that the angular distribution of protons in the laboratory frame does not coincide with that in the internal coordinate frame. It is demonstrated that these angular distributions coincide only if the adiabatic and the semiclassical approximation are simultaneously valid. © *2002 MAIK "Nauka/Interperiodica"*.

1. INTRODUCTION

Considerable advances [1–3] in evolving experimental procedures for investigating the angular distributions of alpha particles emitted by nuclei oriented in strong magnetic fields at ultralow temperatures give reasons to hope that methods that would make it possible to explore the protonic decay of oriented nuclei will be developed in the near future.

From the experimental point of view, the problem of investigating the angular distributions of protons emitted by an oriented nucleus is extremely difficult. These difficulties are associated with the following circumstances [4]: (i) Proton emitters are synthesized in the fusion of multiply charged ions, which is followed by the evaporation of several (up to six) nucleons and which is characterized by small cross sections (about 1 μb or even smaller). (ii) The lifetimes of these emitters are rather short (from a few seconds to a few microseconds). (iii) The most efficient procedures for proton detection, which employ strip detectors, are poorly suited to analyzing angular distributions of protons. At the same time, it seems that such problems can be solved since ^{189}Bi, which is one of the explored oriented alpha-decaying nuclei [3], differs in composition only by four neutrons from the ^{185}Bi nucleus, which is capable of undergoing protonic decay. That the aforementioned experiments are feasible is additionally supported by recent measurements [5] of the angular distributions of delayed protons associated with the beta decay of oriented nuclei.

The multiparticle theory of protonic decay—it was developed in [6–10] for spherical nuclei and in [10–13] for deformed nuclei—made it possible to solve successfully the problem of calculating the protonic partial widths for transitions from ground and isomeric states of odd–even and odd–odd parent nuclei to ground and excited states of daughter nuclei (the existence of transitions to ground and excited states of daughter nuclei leads to the emergence of a fine structure in the proton spectra, which was first investigated in [14]). In view of this, the angular distributions of protons emitted by oriented nuclei were analyzed in the laboratory frame [15] on the basis of the theory in question, and it was demonstrated that the shape of the above distributions is sensitive to the structural features of parent and daughter nuclei.

Previously, the angular distributions of protons emitted in the decay of a single-proton quasistationary state in a deformed potential were investigated in the intrinsic coordinate frame of this potential [16, 17]. More recently, these angular distributions were identified with the angular distributions of protons emitted by oriented deformed nuclei in the laboratory frame.

The objective of the present study is to investigate in detail the angular distributions of protons emitted by oriented spherical and deformed nuclei in the laboratory frame and to compare them with the analogous distributions in the internal coordinate frame of nuclei for the protonic decay of deformed nuclei. Special attention will be given to the analysis of the conditions ensuring the applicability of the adiabatic approximation [18, 19] and to a comparison of this approximation with nonadiabatic approaches [11, 20, 21] to describing the angular distributions of protons emitted by oriented deformed nuclei.

1063-7788/02/6505-0831$22.00

2. ANGULAR DISTRIBUTIONS OF PROTONS EMITTED BY ORIENTED NUCLEUS

Our further analysis will be based on the methods of the multiparticle theory of protonic decay [6, 7, 10, 11]. The wave function ψ_σ^{JM} for a parent nucleus of atomic weight A and charge Z in a quasistationary state characterized by a spin J and its projection M onto the laboratory axis z and other quantum numbers σ satisfies the Schrödinger equation

$$H_A\psi_\sigma^{JM} = E_\sigma^J\psi_\sigma^{JM}, \tag{1}$$

where H_A is the Hamiltonian of the A nucleus in its c.m. frame and $E_\sigma^J = (\mathrm{Re}E_\sigma^J - i\Gamma_\sigma^J/2)$ is a complex energy; here, Γ_σ^J is the total decay width of the above state of the A nucleus (this width is determined by the sum of the partial widths with respect to decays through all open channels). For the parent nucleus, we will consider only decays through protonic channels; specifying a final state in such channels as that which involves a daughter nucleus $(A-1)$ with a spin J_1, its projection M_1, and other quantum numbers σ_1 and a proton with an orbital angular momentum l with respect to the daughter nucleus and a total spin j $(j = l \pm 1/2)$, we denote the channels in question by the symbols $cjl = \sigma_1 J_1 jl$. The wave function for the daughter nucleus, $\psi_{\sigma_1}^{J_1M_1}$, satisfies the Schrödinger Eq. (1), where the Hamiltonian H_{A-1} and the energy $E_{\sigma_1}^{J_1}$ are substituted for H_A and E_σ^J, respectively. The energy Q_c, the velocity v_c, and the wave vector k_c of the relative motion of the proton and the daughter nucleus can be determined as

$$Q_c = \mathrm{Re}E_\sigma^J - \mathrm{Re}E_{\sigma_1}^{J_1} = \frac{m_c v_c^2}{2} = \frac{\hbar^2 k_c^2}{2m_c}, \tag{2}$$

where $m_c = (m_p M_{A-1})/M_A$ is the reduced mass. Let us introduce the orthonormalized channel function U_{cjl}^{JM} that, by construction, possesses correct transformation properties with respect to time inversion [22] (just as the wave functions for the parent and the daughter nucleus do):

$$U_{cjl}^{JM} = \{\psi_{\sigma_1}^{J_1M_1} i^l \Phi_{jlm}(\Omega,\alpha)\}_{JM}. \tag{3}$$

Here, braces denote the vector coupling of the angular momenta, and the function $\Phi_{jlm}(\Omega,\alpha)$ is the proton spin–orbit function, with α being the relevant spin variable. We have

$$\Phi_{jlm}(\Omega,\alpha) = \{Y_{lm_l}(\Omega)\chi_{\frac{1}{2}m_s}(\alpha)\}_{jm}, \tag{4}$$

where the spherical harmonic $Y_{lm_l}(\Omega)$ corresponds to the orbital motion of the proton and depends on the solid angle Ω, which determines the direction of the radius vector $\mathbf{R} = \mathbf{R}_p - \mathbf{R}_{A-1}$ in the laboratory frame, $\mathbf{R}_p$ and $\mathbf{R}_{A-1}$ being the coordinates of, respectively, the proton and the center of mass of the daughter nucleus.

The wave function ψ_σ^{JM} for the parent nucleus satisfies the Gamow boundary condition in the external region $R \geq R_{cjl}$ (R_{cjl} is the radius of the channel cjl) [10], where the proton and the daughter nucleus interact only through the long-range Coulomb potential $(Z-1)e^2/R$; that is,

$$\psi_\sigma^{JM} \to \sum_{cjl} U_{cjl}^{JM}\left(\frac{G_{cl}(R) + iF_{cl}(R)}{R}\right)\sqrt{\frac{\Gamma_{cjl}^J}{\hbar v_c}}. \tag{5}$$

Here $F_{cl}(R)$ and $G_{cl}(R)$ are, respectively, the regular and the nonregular radial Coulomb functions, whose asymptotic expressions for $R \to \infty$ are

$$F_{cl}(R) \to \sin\left[k_c - l\pi/2 + \delta_{cl}^{\mathrm{Coul}}\right], \tag{6}$$

$$G_{cl}(R) \to \cos\left[k_c - l\pi/2 + \delta_{cl}^{\mathrm{Coul}}\right], \tag{7}$$

with $\delta_{cl}^{\mathrm{Coul}}$ being the Coulomb phase shift for elastic scattering.

Since the wave functions for the parent and the daughter nucleus and the channel functions (3) possess correct transformation properties under time inversion, the amplitude $\sqrt{\Gamma_{\sigma cjl}^J}$ of the partial width with respect to the protonic decay of the parent nucleus through the channel jl is invariant under time inversion and is a real-valued quantity independent of the projection M of the parent-nucleus spin J. Further, it follows from the parity-conservation law that the partial-width amplitude does not vanish, provided that

$$\pi = \pi_1(-1)^l, \tag{8}$$

where π and π_1 are the parities of the parent and the daughter nucleus, respectively.

Let us now consider the multiparticle density j_σ^{JM} of the flux of decay fragments in the direction of the radius vector $\mathbf{R}$:

$$j_\sigma^{JM} = \frac{i\hbar}{2m_c}\left[\psi_\sigma^{JM}\frac{d}{dR}\left(\psi_\sigma^{JM}\right)^* - \left(\psi_\sigma^{JM}\right)^*\frac{d}{dR}\psi_\sigma^{JM}\right]. \tag{9}$$

Further, we make use of the boundary condition in (5) for $R \to \infty$ and integrate j_σ^{JM} with respect to all coordinates of the nucleus A, with the exception of the radius vector $\mathbf{R}$, considering that the functions $\psi_{\sigma_1}^{J_1M_1}$

and $\chi_{1/2m_s}(\alpha)$ are orthonormalized. As a result, we find that the proton-flux density $j_\sigma^{JM}(\mathbf{R})$ is given by

$$j_\sigma^{JM}(\mathbf{R}) = \frac{1}{R^2}\sum_c A_{\sigma c}^{JM}(\Omega), \qquad (10)$$

where

$$A_{\sigma c}^{JM}(\Omega) \qquad (11)$$
$$= \sum_{M_1 m_s}\left|\sum_{jl} C_{J_1 j M_1 m}^{JM} C_{\frac{1}{2} l m_s m_l}^{jm} Y_{lm_l}(\Omega) e^{i\delta_{cl}^{\mathrm{Coul}}} \frac{\sqrt{\Gamma_{\sigma cjl}^J}}{\hbar}\right|^2.$$

Let us now average expression (10) over the values of the projection M of the nuclear spin J by using the distribution function $S(M)$. Suppose that protons are recorded by a detector that is arranged orthogonally to the radius vector $\mathbf{R}$ in the direction of the solid angle Ω in the laboratory frame and that the area covered by the detector is $R^2 d\Omega$. The number dN_σ^J of protons that this detector records per unit time is then given by

$$dN_\sigma^J = \sum_M S(M)\sum_c A_{\sigma c}^{JM}(\Omega)d\Omega. \qquad (12)$$

By integrating formula (12) over all directions of the solid angle Ω, we find, as might have been expected, that the total number N_σ^J of protons emitted by the decaying nucleus per unit time is

$$N_\sigma^J = \frac{1}{\hbar}\sum_{cjl}\Gamma_{\sigma cjl}^J = \frac{1}{\hbar}\sum_c \Gamma_{\sigma c}^J = \frac{1}{\hbar}\Gamma_\sigma^J, \qquad (13)$$

where $\Gamma_{\sigma c}^J = \sum_{jl}\Gamma_{\sigma cjl}^J$. The angular distribution of protons that is normalized to unity, $dP_\sigma^J(\Omega)/d\Omega$, will then have the form

$$dP_\sigma^J(\Omega)/d\Omega = \frac{1}{\Gamma_\sigma^J}\sum_M S(M)\sum_c A_{\sigma c}^{JM}(\Omega). \qquad (14)$$

It can be seen from (10) and (14) that, in the laboratory frame, the interference between the groups of protons corresponding to decay channels that produce daughter nuclei in states where c and M_1 take different values and protons in states where the spin projections m_s are different is not observed even if the resolution of the detectors used is insufficient for separating the above groups of protons in the energy Q_c. The angular distribution in (14) can be represented in the form

$$\frac{dP_\sigma^J(\Omega)}{d\Omega} = \sum_c \frac{\Gamma_{\sigma c}^J}{\Gamma_\sigma^J}\frac{dP_{\sigma c}^J(\Omega)}{d\Omega}, \qquad (15)$$

where, in the channel c, the angular distribution of protons that is normalized to unity is given by

$$\frac{dP_{\sigma c}^J(\Omega)}{d\Omega} = \frac{1}{\Gamma_{\sigma c}^J}\sum_M S(M)A_{\sigma c}^{JM}(\Omega). \qquad (16)$$

Distributions of the form (16) will be observed if the energy resolution of the detectors makes it possible to separate well the groups of protons having different energies Q_c.

By using, instead of the functions U_{cjl}^{JM} (3), the new channel functions U_{cIl}^{JM},

$$U_{cIl}^{JM} = \left\{\left\{\psi_{\sigma_1}^{J_1 M_1}\chi_{\frac{1}{2}m_s}\right\}_{IM_I} i^l Y_{lm_l}(\Omega)\right\}_{JM}, \qquad (17)$$

formula (11) can be considerably simplified. Since the functions in (17) differ from the functions in (3) only by the order in which the angular momenta are coupled, these functions are related by the Racah transformation [22]

$$U_{cIl}^J = \sum_j U_{cjl}^J\sqrt{(2j+1)(2I+1)} \qquad (18)$$
$$\times W(J_1\tfrac{1}{2}Jl;Ij),$$

where $W(J_1\frac{1}{2}Jl;Ij)$ are Racah coefficients. We can now specify the new partial-width amplitudes $\sqrt{\Gamma_{\sigma cIl}^J}$ that are related to the amplitudes $\sqrt{\Gamma_{\sigma cjl}^J}$ introduced above by the equation

$$\sqrt{\Gamma_{\sigma cIl}^J} = \sum_j \sqrt{(2j+1)(2I+1)} \qquad (19)$$
$$\times W(J_1\frac{1}{2}Jl;Ij)\sqrt{\Gamma_{\sigma cjl}^J},$$

which follows from the invariance of formula (5) under the substitution of the channel functions (17) and the amplitudes $\sqrt{\Gamma_{\sigma cIl}^J}$ for the channel functions (3) and the amplitudes $\sqrt{\Gamma_{\sigma cjl}^J}$, respectively. By virtue of the fact that the Racah transformations are orthonormalized [22], the following relation holds:

$$\sum_I \Gamma_{\sigma cIl}^J = \sum_j \Gamma_{\sigma cjl}^J. \qquad (20)$$

The formula in (11) can then be recast into the form

$$A_{\sigma c}^{JM}(\Omega) \qquad (21)$$
$$= \sum_{M_1 m_s}\left|\sum_{Il} C_{J_1\frac{1}{2}M_1 m_s}^{IM_I} C_{IlM_I m_l}^{JM} Y_{lm_l}(\Omega) e^{i\delta_{cl}^{\mathrm{Coul}}}\sqrt{\Gamma_{\sigma cIl}^J}\right|^2.$$

By performing summation over M_1 and m_s and by using the orthonormalization condition for the Clebsch–Gordan coefficients, we can represent expression (21) as

$$A_{\sigma c}^{JM}(\Omega) \qquad (22)$$

$$= \sum_{IM_I} \left| \sum_l C^{JM}_{IlM_Im_l} Y_{lm_l}(\Omega) e^{i\delta^{\mathrm{Coul}}_{cl}} \sqrt{\Gamma^J_{\sigma cIl}} \right|^2 .$$

By using now the multiplication theorem for spherical harmonics [22],

$$Y_{lm_l}(\Omega) Y_{l'm_l}(\Omega) = \frac{(-1)^{m_l}}{4\pi} \times \sqrt{(2l+1)(2l'+1)} \sum_L C^{L0}_{ll'm_l-m_l} C^{L0}_{ll'00} P_L(\cos\theta), \quad (23)$$

where $P_L(\cos\theta)$ is a Legendre polynomial, and the technique of Racah coefficients, we can recast (22) into the form

$$A^{JM}_{\sigma c}(\Omega) = \frac{1}{4\pi} \sum_{LIll'} P_L(\cos\theta) C^{JM}_{JLM0} \times C^{L0}_{ll'00} \cos(\delta^{\mathrm{Coul}}_{cl} - \delta^{\mathrm{Coul}}_{cl'}) (-1)^{J-I} \times \sqrt{(2L+1)(2J+1)(2l+1)(2l'+1)} \times W(JlJl'; IL) \sqrt{\Gamma^J_{\sigma cIl}} \sqrt{\Gamma^J_{\sigma cIl'}}. \quad (24)$$

From the fact that the orbital angular momenta l and l' have the same parity in (24) by virtue of relation (8) and from the properties of the coefficient $C^{L0}_{ll'00}$, it follows that L takes only even values: $L = 0, 2, \ldots$. Since the contribution to the integral of the angular distribution (16) over the solid angle Ω comes only from the $L = 0$ term in the sum over L in formula (24), the value $\Gamma^J_{\sigma c}/(4\pi)$ of this term is consistent with the condition in (13). If the spin of the parent nucleus is $J = 0$ or $J = 1/2$, the Clebsch–Gordan coefficient C^{JM}_{JLM0} in (24) does not vanish only for $L = 0$; therefore, the angular distribution (24) is isotropic and is equal to $1/(4\pi)$.

In the case of an unoriented parent nucleus whose spin J is greater than $1/2$, in which case spin projections M are equiprobable and the distribution function has the form $S(M) = 1/(2J+1)$, we have $\sum_M S(M) A^{JM}_{\sigma c}(\Omega) = \Gamma^J_{\sigma c}/(4\pi)$, so that the angular distributions in (14) and (16) are also isotropic and equal to $1/(4\pi)$. If the parent nucleus is completely oriented by an external magnetic field directed along the z axis in the laboratory frame, the distribution function $S(M)$ is equal to $S(M) = \delta_{M,J}$ or $S(M) = \delta_{M,-J}$ for, respectively, positive or negative values of the gyromagnetic ratio for this nucleus. Since the Clebsch–Gordan coefficient C^{JM}_{JLM0} in formula (24) does not change under the substitution of $-M$ for M at even values of L, we have $A^{JJ}_{\sigma c}(\Omega) = A^{J-J}_{\sigma c}(\Omega)$; as a result, the proton angular distributions (16) for oriented nuclei are independent of the sign of the gyromagnetic ratio for the parent nucleus and are given by

$$\frac{dP^J_{\sigma c}(\Omega)}{d\Omega} = \frac{1}{\Gamma^J_{\sigma c}(\Omega)} A^{JJ}_{\sigma c}. \quad (25)$$

We note that, for the protonic decay of oriented nuclei, the proton angular distributions (25) have the same mathematical form both for spherical and for deformed parent nuclei. Distinctions between the above angular distributions arise only because of the different structures of the amplitudes of the protonic partial decay widths for these nuclei.

In the case where the protonic decay of an oriented odd–even parent nucleus leads to the production of an even–even daughter nucleus in the $J_1 = 0$ ground state (the index σ_1 can then be replaced by 0), the only partial width that is nonzero is the protonic one $\Gamma^J_{\sigma 00 j_0 l_0}$, for which $j_0 = J$ and the value of l_0 is determined from the conditions $l_0 = j_0 \pm 1/2$ and $(-1)^{l_0} = \pi$. In this case, the proton angular distribution (25) becomes independent of the protonic widths, acquiring a universal character for spherical and deformed nuclei [15]. By using formula (11) for $M = J$, the distribution in question can be represented as

$$\frac{dP^J_{\sigma 00}(\Omega)}{d\Omega} = \sum_{m_s m_l} \left| C^{JJ}_{\frac{1}{2} l_0 m_s m_l} Y_{l_0 m_l}(\Omega) \right|^2 . \quad (26)$$

As was shown in [15], this distribution does not depend on the parity of the parent nucleus or on the orbital angular momentum l_0 and has the form

$$\frac{dP^J_{\sigma 00}(\Omega)}{d\Omega} = \left| Y_{J-1/2, J-1/2}(\Omega) \right|^2 = \frac{(2J)!}{\pi \cdot 4^{J+1/2} [(J-1/2)!]^2} (\sin\theta)^{2J-1}. \quad (27)$$

This distribution is symmetric with respect to the angle $\theta = \pi/2$; is zero at $\theta = 0$ and $\theta = \pi$; and has a maximum at $\theta = \pi/2$, the amplitude of this maximum increasing fast with increasing J [15]. This means that, by measuring the angular distribution (26), we can determine the parent-nucleus spin J. Since the spin J of the ground state of an odd–even nucleus is equal to the spin j_p of the odd proton for a spherical nucleus or to the projection of the spin K_p of the odd proton onto the symmetry axis of a deformed nucleus, the known value of the spin J makes it possible to obtain information about the deformation parameters β_λ and to establish thereby the shape of the decaying nucleus. For transitions of oriented parent nuclei from $J > 1/2$ states to $J \neq 0$ states of daughter nuclei, the proton angular distribution (25) becomes sensitive to the structural features of the parent nucleus and daughter nuclei. This was demonstrated in [15] by

considering the example of the angular distribution of protons for the protonic transition of the oriented deformed odd–even nucleus ^{131}Eu ($\beta_2 = +0,3$) to the excited $J_1^{\pi_1} = 2^+$ state of the deformed even–even daughter nucleus ^{130}Sm. As the subject for investigating the angular distributions of protons emitted by oriented nuclei, I can propose the spherical nucleus ^{53m}Co, where the protonic decay from the high-spin ($J = 19/2^-$) isomeric state to the $J_1^{\pi_1} = 0^+$ ground state of the spherical daughter nucleus ^{52}Fe was observed in [23], the half-life of this final state being rather long (16 s). The protonic decay of this nucleus was successfully described on the basis of the multiparticle theory of protonic decay in [7] as an example of an off-diagonal protonic transition. For the transition under investigation, the ratio of the values of the angular distribution (27) of protons emitted by the oriented parent nucleus at angles of $\theta = 75°$ and $90°$ is 0.54. That this value differs significantly from zero gives sufficient grounds to hope for a successful experimental measurement of this angular distribution.

3. PARTIAL WIDTHS WITH RESPECT TO PROTONIC DECAYS OF ORIENTED SPHERICAL NUCLEI AND ANGULAR DISTRIBUTIONS OF PROTONS FROM SUCH DECAYS

Within the multiparticle theory of deep-subbarier protonic decay [6, 10], the amplitude of the protonic partial width can be generally represented as

$$\sqrt{\Gamma^J_{\sigma cjl}} = \sqrt{2\pi} \times \left\langle \hat{A} \left\{ U^{JM}_{\sigma cjl} \frac{\tilde{F}_l(R)}{R} \left| \left(V_{A-1,p} - \frac{(Z-1)e^2}{R} \right) \right| \right\} \psi^{JM}_{\sigma} \right\rangle, \quad (28)$$

where $\hat{A}$ is the operator executing the antisymmetrization of the emitted proton and the nucleons of the daughter nucleus, $V_{A-1,p}$ is the total potential describing the interaction of the proton and the daughter nucleus, and $\tilde{F}_l(R)$ is the regular radial Coulomb function normalized to the δ function of energy.

Let us consider the case of diagonal protonic transitions [6, 10], for which, in the spherical parent nucleus, the structure of the state of all nucleons, with the exception of the emitted one, is close to the structure of the state of the nucleons of the spherical daughter nucleus. Such protonic transitions are similar to favored alpha transitions in the theory of alpha decay. The amplitude in (28) can then be recast into the form

$$\sqrt{\Gamma^J_{\sigma cjl}} = \sqrt{2\pi} \int \tilde{F}_l(R) \times \left(V_p(R) - \frac{(Z-1)e^2}{R} \right) \chi^J_{\sigma cjl}(R) dR, \quad (29)$$

where $V_p(R)$ is the spherical shell potential for a proton in the parent nucleus and $\chi^J_{\sigma cjl}(R)$ is the proton form factor for the transition under investigation. This form factor is introduced as

$$\chi^J_{\sigma cjl}(R) = R \left\langle \hat{A} \left\{ U^{JM}_{\sigma cjl} \delta(R - R') \right\} |\psi^{JM}_{\sigma} \right\rangle, \quad (30)$$

where the integral is taken with respect to all coordinates of the nucleus A, including the radius R'. For diagonal transitions, this form factor can be approximated to a fairly high precision as [10]

$$\chi^J_{\sigma cjl}(R) = \varphi_{nj_0l_0}(R) S^J_{\sigma cnj_0l_0} \delta_{j,j_0} \delta_{l,l_0}, \quad (31)$$

where $\varphi_{nj_0l_0}(R)$ is the radial wave function for the proton shell state nj_0l_0 in the parent nucleus and $S^J_{\sigma cnj_0l_0}$ is the amplitude of the spectroscopic factor for the transition being considered. From expression (31), it then follows that, for diagonal protonic transitions in spherical nuclei, only the partial protonic width $\Gamma^J_{\sigma cj_0l_0}$ is nonvanishing, in which case the proton angular distributions determined by formulas (16) and (11) become, for the decay of oriented nuclei, independent of the protonic partial width and take the form

$$\frac{dP^J_{\sigma c}(\Omega)}{d\Omega} = \sum_{M_1 m_s} \left| C^{JJ}_{J_1 j_0 M_1 m} C^{j_0 m}_{1/2 l_0 m_s m_l} Y_{l_0 m_l}(\Omega) \right|^2$$
$$= \frac{1}{4\pi} \sum_{I=|J_1-1/2|}^{J_1+1/2} \sum_L P_L(\cos\theta)(-1)^{J-I} C^{JJ}_{JLJ0} C^{L0}_{l_0 l_0 00}$$
$$\times \sqrt{(2L+1)(2J+1)(2l_0+1)^2} W(Jl_0Jl_0; IL)$$
$$\times (2j_0+1)(2I+1) \left[W(J_1 1/2 J l_0 | I j_0) \right]^2. \quad (32)$$

In the decay of the ground and single-particle proton isomeric states of spherical odd–even nuclei, a diagonal transition is realized for the ground states of daughter nuclei, in which case $J_1 = 0$ and σ_1 is denoted as 0. The distribution in (32) then reduces to the distribution in (26). In the decay of the ground and single-particle proton isomeric states of odd–odd parent nuclei, a diagonal transition is realized for the states of the even–odd daughter nucleus whose neutron subsystem has the spin J_1 coinciding with the spin of the neutron subsystem of the parent nucleus and whose proton subsystem has zero spin. By experimentally investigating the angular distributions (32), we can in principle determine the angular momenta J, J_1, j_0, and l_0; this is very important for obtaining deeper insight into the structure of spherical odd–odd nuclei.

4. PARTIAL WIDTHS WITH RESPECT TO PROTONIC DECAYS OF ORIENTED DEFORMED NUCLEI AND ANGULAR DISTRIBUTIONS OF PROTONS FROM THESE DECAYS

Let us investigate protonic decay for the case where the parent and the daughter nucleus have identical axially symmetric deformed shapes. In the strong-coupling approximation [22], the wave function $\psi^{JM}_{K_i}$ for the parent nucleus can then be represented as

$$\psi^{JM}_{K_i} = \sqrt{\frac{(2J+1)}{16\pi^2(\delta_{K_i,0}+1)}} \tag{33}$$
$$\times\Big\{D^J_{MK_i}(\omega)\chi_{K_i}(q)+(-1)^{J+K_i}D^J_{M-K_i}(\omega)\chi_{\bar{K}_i}(q)\Big\},$$

where $D^J_{MK_i}(\omega)$ is a generalized Wigner spherical function [22] depending on the Euler angles $(\alpha\beta\gamma)=\omega$, while $\chi_{K_i}(q)$ and $\chi_{\bar{K}_i}(q)$ are, respectively, the internal wave function for the parent nucleus having the spin projection $K_i>0$ onto the z axis in its internal coordinate frame and its time conjugate. The wave function $\psi^{J_1M_1}_{K_1}$ for the daughter nucleus takes the analogous form upon substituting, in (33), J_1 and K_1 for the variables J and K_i, respectively, and the set of $(3A-9)$ internal coordinates q_1 of the daughter nucleus for the set of $(3A-6)$ internal coordinates q of the parent nucleus.

For the sake of simplicity, our further consideration will be performed for the example of the diagonal protonic decay of the ground or a single-particle proton isomeric state of an odd–even parent nucleus whose spin is $J=K_i$ and whose proton and neutron subsystems have the spin projections of $K^{(p)}_i=K_i$ and $K^{(n)}=0$, respectively. In this case, diagonal protonic transitions occur to the $K_1=0$, even-J_1 levels of the ground-state rotational band of the even–even daughter nucleus. In the spin–orbit wave function for the proton, $\Phi_{jlm}(\Omega,\alpha)$, we further go over to the intrinsic coordinate frame of the parent nucleus by means of the Wigner transformation [22]

$$\Phi_{jlm}(\Omega,\alpha)=\sum_{k_j}D^j_{mk_j}(\omega)\Phi_{jlk_j}(\Omega',\alpha') \tag{34}$$

and employ the multiplication theorem for D functions [22]. As a result, we reduce the channel functions (3) to the form

$$U^{JM}_{K_i0J_1jl}=\sqrt{\frac{2J+1}{8\pi^2}} \tag{35}$$
$$\times\sum_K D^J_{MK}(\omega)C^{JK}_{J_1j0K}\Phi_{jlK}(\Omega',\alpha')\chi^{(1)}_0(q_1)\,i^l,$$

where, instead of the indices σ and σ_1 for the deformed parent and daughter nuclei, use is made of the projections of their spins, K_i and $K_1=0$. Just like the original functions in (3), the channel functions are orthonormalized in the space spanned by the coordinates ω, Ω', α', and q_1. In the case of diagonal transitions, the internal wave functions χ_{K_i} and $\chi^{(1)}_0$ treated within the superfluid model of the nucleus [24] for both the parent and the daughter nucleus satisfy the relation [11]

$$\Big\langle\chi^{(1)}_0|\chi_{K_i}\Big\rangle=f_{K_i}(\mathbf{R}',\alpha')u^{(1)}_{K_i}, \tag{36}$$

where the function $f_{K_i}(\mathbf{R}',\alpha')$ can be considered, to a good approximation, as the shell wave function for the proton in the nonspherical shell potential $V_p(\mathbf{R}',\alpha')$, the quantity K_i being a multi-index that includes, in addition to the spin projection K_i, the Nilsson asymptotic quantum numbers [24], while the quantity $u^{(1)}_{K_i}$ coincides with a coefficient in the u–v Bogolyubov transformation for an even–even daughter nucleus. By substituting expressions (33)–(36) into formula (28) for the amplitude of the protonic partial width, we obtain

$$\sqrt{\Gamma^J_{K_i0J_1jl}}=u^{(1)}_{K_i}\sqrt{\frac{(2J_1+1)}{2(2J+1)}}C^{JK_i}_{J_1j0K_i} \tag{37}$$
$$\times\left[\sqrt{\Gamma_{K_ijl}}+(-1)^{j+K_i}\sqrt{\Gamma_{\bar{K}_ijl}}\;\right],$$

where $\sqrt{\Gamma_{K_ijl}}$ is the amplitude of the partial width with respect to the decay of the single-particle shell state f_{K_i} (36) through the decay channel described by the function $\Phi_{jlK_i}(\Omega',\alpha')$,

$$\sqrt{\Gamma_{K_ijl}}=\sqrt{2\pi}\Big\langle\Phi_{jlK_i}(\Omega',\alpha') \tag{38}$$
$$\times\,i^l\,\frac{\tilde{F}_l(R)}{R}\left|\left(V_p(\mathbf{R}',\alpha')-\frac{(Z-1)e^2}{R}\right)\right|f_{K_i}\Big\rangle.$$

The amplitude $\sqrt{\Gamma_{\bar{K}_ijl}}$ is given by (38) with the substitution of the functions $\Phi_{jl\bar{K}_i}$ and $f_{\bar{K}_i}$ for Φ_{jlK_i} and f_{K_i}, respectively. By using the relation between the function f_{K_i} and its time conjugate $f_{\bar{K}_i}$, one can obtain

$$\sqrt{\Gamma_{\bar{K}_ijl}}=(-1)^{j+K_i}\sqrt{\Gamma_{K_ijl}}, \tag{39}$$

so that formula (37) takes the form [11]

$$\sqrt{\Gamma^J_{K_i0J_1jl}}=u^{(1)}_{K_i}\sqrt{\frac{2(2J_1+1)}{(2J+1)}} \tag{40}$$
$$\times\,C^{JK_i}_{J_1j0K_i}\sqrt{\Gamma_{K_ijl}(Q_c)},$$

where the dependence of the partial-width amplitude $\sqrt{\Gamma_{K_i jl}}$ on the energy Q_c (2) is indicated explicitly. By substituting the partial-width amplitude (37) into (14) and using (11), we find that, in the laboratory frame, the angular distribution of protons emitted by the oriented parent nucleus has the form

$$\frac{P^J_{K_i}(\Omega)}{d\Omega} = \frac{1}{\Gamma^J_{K_i}} \sum_{J_1 M_1 m_s} \left| \sum_{jl} C^{JJ}_{J_1 j M_1 m} \right. \tag{41}$$

$$\left. \times C^{jm}_{\frac{1}{2} l m_s m_l} Y_{l m_l}(\Omega) C^{J_1 0}_{Jj-K_i K_i} (-1)^{j+K_i} \sqrt{\Gamma^J_{K_i jl}(Q_c)} \right|^2 .$$

5. ANGULAR DISTRIBUTIONS OF PROTONS FROM THE DECAY OF ORIENTED DEFORMED NUCLEI IN THE INTERNAL COORDINATE FRAME OF THE PARENT NUCLEUS

By using the channel function in the form (35), we represent the asymptotic expression (5) for the wave function describing an oriented deformed parent nucleus in the form

$$\psi^{JJ}_{K_i} = \sum_{J_1 K k_s jl} \sqrt{\frac{2J+1}{8\pi^2}} D^J_{JK}(\omega) C^{JK}_{J_1 j 0 K} \tag{42}$$

$$\times C^{jK}_{\frac{1}{2} l k_s k_l} Y_{l k_l}(\Omega') i^l \chi^{(1)}_0(q_1) \chi_{\frac{1}{2} k_s}(\alpha')$$

$$\times \frac{G_{cl}(R) + iF_{cl}(R)}{R} \sqrt{\frac{\Gamma^J_{K_i 0 J_1 jl}}{\hbar v_c}},$$

where the solid angle $\Omega'(\Omega, \omega)$ is a function of the solid angle Ω and the Euler angles ω. In order to obtain the angular distribution of protons in the internal coordinate frame of the parent nucleus, we place a proton detector in this coordinate frame and use it to measure the angular distribution of protons directly as a function of the angle Ω'. In this case, the variables ω and Ω' in expression (42) can be considered to be independent. Further, we employ the multiparticle flux density (9), together with the asymptotic expression (42) for the wave function describing the parent nucleus, and integrate it with respect to the variables ω, q_1, and α', taking into account the conditions of ortonormality of the functions D [22]. For the single-particle proton-flux density $\tilde{j}^J_{K_i}(\Omega')$ in the intrinsic coordinate frame of the parent nucleus, this yields

$$\tilde{j}^J_{K_i}(\Omega') = \frac{1}{R^2} \sum_{K k_s} \left| \sum_{J_1 jl} C^{J_1 0}_{Jj-KK} \right. \tag{43}$$

$$\left. \times C^{jK}_{\frac{1}{2} l k_s k_l} Y_{l k_l}(\Omega') (-1)^{j+K} \sqrt{\Gamma^J_{K_i 0 J_1 jl}}\, e^{i\delta^{\mathrm{Coul}}_{lc}} \right|^2 .$$

The number of protons recorded per unit time by a detector of area $R^2 d\Omega'$ arranged orthogonally to the radius vector $\mathbf{R}'$ is then determined by the product $R^2 \tilde{j}^J_{K_i}(\Omega') d\Omega'$. The total number $\tilde{N}^J_{K_i}$ of protons recorded by the detector over the total solid angle Ω' is given by the integral $\int R^2 \tilde{j}^J_{K_i}(\Omega') d\Omega'$, which, upon the use of Eq. (43), becomes

$$\frac{1}{\hbar} \sum_{J_1 jl} \Gamma^J_{K_i 0 J_1 jl} = \frac{1}{\hbar} \sum_{J_1} \Gamma^J_{K_i 0 J_1} = \frac{1}{\hbar} \Gamma^J_{K_i}.$$

This result coincides with the analogous result (13) in the laboratory frame and corroborates the correctness of formula (43). In the internal coordinate frame of the parent nucleus, the angular distribution of protons that is normalized to unity can be represented in the form

$$\frac{d\tilde{P}^J_{K_i}(\Omega')}{d\Omega'} = \frac{1}{\Gamma^J_{K_i}} \sum_{K} \left| \sum_{J_1 jl} C^{J_1 0}_{Jj-KK} \right. \tag{44}$$

$$\left. \times C^{jK}_{\frac{1}{2} l k_s k_l} Y_{l k_l}(\Omega') (-1)^{j+K} \sqrt{\Gamma^J_{K_i 0 J_1 jl}}\, e^{i\delta^{\mathrm{Coul}}_{cl}} \right|^2 .$$

A comparison of this distribution with the angular distribution (41) of protons in the laboratory frame shows that, if the energy resolution of the detectors used is fairly high, these distributions are totally different. In the particular case where it is legitimate to take into account, in (41) and (44), only the protonic transition to the $J_1 = 0$ ground state of the daughter nucleus, formula (41) reduces to formula (25), which gives an anisotropic angular distribution in the laboratory frame (it has a maximum in the direction of the angle $\theta = \pi/2$), while formula (44) leads to an isotropic angular distribution of protons in the intrinsic coordinate frame [it is equal to $1/(4\pi)$].

6. ADIABATIC APPROXIMATION

In order to describe the structure of deformed nuclei in their interior, use is often made of the adiabatic approximation, which is based on the fact that the characteristic times of nucleon motion within the nucleus are much shorter than the characteristic times associated with the rotation of nuclei. This means that the characteristic energy spacing ΔE_N between the single-nucleon levels having identical values of the good quantum numbers is considerably greater than the characteristic energy spacing between neighboring rotational levels, which is $\Delta E_r \approx \hbar^2/2I_0$, where I_0 is the nuclear moment of inertia. In this approximation, the strong-coupling model is realized, and the wave functions for deformed nuclei are constructed on its basis.

In the case of the deep-subbarrier protonic decay of nuclei, the adiabatic approximation is not applicable because the protonic partial widths with respect to transitions to excited states of daughter nuclei decrease sharply. This is the reason why it is so difficult to reveal the fine structure of proton spectra—so far, it has been found only for one strongly deformed nucleus ^{131}Eu [14]. Nevertheless, the angular distributions of protons from the protonic decay of oriented deformed odd–even nuclei will be investigated here in the adiabatic approximation with the aim of exploring the situation arising in the adiabatic limit. For the adiabatic approximation to be applicable, two conditions must be satisfied. First, one has to require that the excitation energy $(E_0^{J_1})^*$ of the $J_1 > 0$ states belonging to the ground-state rotational band of the deformed even–even daughter nucleus be much lower than the proton-separation energy Q_{00} for the transition to the ground state ($J_1 = 0$) of the daughter nucleus, so that one could neglect the effects of the energies $(E_0^{J_1})^*$ on the penetrability of the potential barrier and also on the Coulomb phase shifts $\delta_{cl}^{\mathrm{Coul}}$ (this condition is more lenient); this would make it possible to take, in the angular distributions (41) and (44), all partial widths and Coulomb phase shifts at a single energy value Q_{00}. Second, the detectors used must not distinguish in energy the groups of protons corresponding to different spins J_1 of the daughter nucleus, in which case the interference between the wave functions for these groups of protons arises in the angular distribution (44). By taking into account formula (40) and the relation

$$\sum_{J_1} C^{J_1 0}_{Jj-KK} C^{J_1 0}_{Jj-K_iK_i} = \delta_{K,K_i}, \tag{45}$$

we can then recast the angular distributions (44) into the form

$$\frac{d\tilde{P}^J_{K_i}(\Omega')}{d\Omega'} = \frac{1}{\sum\limits_{jl}\Gamma_{K_ijl}} \tag{46}$$

$$\times \sum_{k_s}\left|\sum_{jl} C^{jK_i}_{\frac{1}{2}lk_sk_l} Y_{lk_l}(\Omega')\sqrt{\Gamma_{K_ijl}}\, e^{i\delta_{cl}^{\mathrm{Coul}}}\right|^2,$$

where the energy Q_{00} has been employed for all terms in the sums over j and l.

This distribution coincides with the angular distribution of protons in the internal coordinate frame of the parent nucleus in the decay of a single-proton shell state f_{K_i} in a nonspherical shell potential. It is this distribution that was investigated in [16, 17] and that was proposed for consideration as the angular distribution of protons emitted by $J = K_i$ oriented nuclei in the laboratory frame. The argument behind this statement is based on the fact that the projection K_i of the spin J of a nucleus onto the z axis in its internal coordinate frame coincides with J for the ground or a single-particle isomeric state of this nucleus. At the same time, the projection M of the spin J of the oriented nucleus onto the z axis of the laboratory frame is also equal to J. This could seems to imply the coincidence of the z axes in the laboratory frame and in the intrinsic coordinate frame, with the result that the angular distributions in these coordinate frames would also coincide. It is obvious, however, that this statement is of a semiclassical character. In order to prove this, we go over, in the asymptotic expression for the wave function ψ^{JJ}_J describing the parent nucleus [formula (42)], to the adiabatic limit. We have

$$\psi^{JJ}_J \to \sqrt{\frac{2J+1}{16\pi^2}} \tag{47}$$

$$\times \sum_{k_sjl}\left[D^J_{JJ}(\omega)C^{jJ}_{\frac{1}{2}lk_sk_l} + (-1)^{j-J}D^J_{J-J}(\omega)C^{j-J}_{\frac{1}{2}lk_sk_l}\right]$$

$$\times Y_{lk_l}(\Omega')\chi^{(1)}_0(q_1)\chi_{\frac{1}{2}k_s}(\alpha')$$

$$\times\sqrt{\frac{\Gamma_{Jjl}}{\hbar\upsilon}}\,\frac{G_l(R)+iF_l(R)}{R}\,i^l.$$

The normalized (to unity) angular distribution of protons in the laboratory frame can then be represented in the form

$$\frac{dP^J_J(\Omega)}{d\Omega} = \frac{1}{\sum\limits_{jl}\Gamma_{Jjl}}\frac{(2J+1)}{16\pi^2} \tag{48}$$

$$\times\sum_{k_s}\int\left|\sum_{jl}\left[D^J_{JJ}(\omega)C^{jJ}_{\frac{1}{2}lk_sk_l} + (-1)^{j-J}\right.\right.$$

$$\left.\left.\times D^J_{J-J}(\omega)C^{j-J}_{\frac{1}{2}lk_sk_l}\right]Y_{lk_l}\left[\Omega'(\Omega,\omega)\right]\sqrt{\Gamma_{Jjl}}e^{i\delta_{cl}^{\mathrm{Coul}}}\right|^2 d\omega,$$

where we have taken into account the dependence of the angles Ω' on the angles Ω and ω and where $d\omega = \sin\beta d\beta d\alpha d\gamma$. Since the integrand on the right-hand side of (48) is a function of only the angle θ', which is independent of the Euler angle γ, we can perform integration with respect to the angle γ in this formula, taking into account the explicit form of the functions D,

$$D^J_{JJ}(\omega) = e^{iJ\alpha}(\cos(\beta/2))^{2J}e^{iJ\gamma}, \tag{49}$$
$$D^J_{J-J}(\omega) = e^{iJ\alpha}(\sin(\beta/2))^{2J}e^{-iJ\gamma},$$

and using the orthogonality of the functions $D^J_{JJ}(\omega)$ and $D^J_{J-J}(\omega)$ in the angle γ and formula (46). This

yields

$$\frac{dP_J^J(\Omega)}{d\Omega} = \frac{(2J+1)}{16\pi^2} \times \int d\omega \left[\left|D_{JJ}^J(\omega)\right|^2 + \left|D_{J-J}^J(\omega)\right|^2\right] \frac{d\tilde{P}_J^J(\theta'(\Omega,\omega))}{d\Omega'}. \quad (50)$$

According to formulas (49), the functions $\left|D_{JJ}^J(\omega)\right|^2$ and $\left|D_{J-J}^J(\omega)\right|^2$ can be written as $(\cos(\beta/2))^{4J}$ and as $(\sin(\beta/2))^{4J}$, respectively; for $J \gg 1$, they become close to $\delta(\xi-1)$ and $\delta(\xi+1)$, respectively, where $\xi = \cos\beta$. This indicates that the orientation of the z axis of the intrinsic coordinate frame of the parent nucleus is parallel or antiparallel to the z axis of the laboratory frame. It then follows that $\theta' = \theta$ or $\theta' = \pi - \theta$. Since the angular distribution $d\tilde{P}_J^J(\theta)/d\Omega'$ does not change upon the substitution of $(\pi - \theta')$ for θ', we can take this distribution outside the sign of the integral with respect to ω in (50), replacing the angle θ' by θ, whereupon the integration of the resulting expression with respect to ω yields

$$\frac{dP_J^{JJ}(\theta)}{d\Omega} = \frac{d\tilde{P}_J^J(\theta')}{d\Omega'}. \quad (51)$$

This means that, if use is made of the adiabatic approximation, only in the semiclassical limit $J \gg 1$ does the angular distribution of protons emitted in the decay of an oriented nucleus in the laboratory frame coincide with that in the internal coordinate frame of the parent nucleus.

Let us consider yet another particular case, that which cannot be realized in the protonic decay of oriented deformed nuclei, but which can be of use for obtaining deeper insights into different forms of nuclear decays—for example, in investigating the nuclear-fission process. Suppose that the angular distribution of protons, $d\tilde{P}_J^J(\Omega')/d\Omega'$ (46), in the internal coordinate frame of the parent nucleus has the form $[\delta(\xi'-1) + \delta(\xi'+1)]/4\pi$, where $\xi' = \cos\theta'$—that is, it is oriented along or against the z axis in this coordinate frame. This means that the radius vector $\mathbf{R}'$ is parallel or antiparallel to the z axis in this coordinate frame; that is, the angle θ in the laboratory frame coincides with the Euler angle β or with $\pi - \beta$. We can then replace $[\delta(\xi'-1) + \delta(\xi'+1)]$ by $[\delta(\theta-\beta) + \delta(\theta-\pi+\beta)]$ and perform integration with respect to the Euler angles in (50). The result is

$$\frac{dP_J^J(\Omega)}{d\Omega} = \frac{(2J+1)}{8\pi} \times \left[\left|D_{JJ}^J(\omega)\right|^2 + \left|D_{J-J}^J(\omega)\right|^2\right]_{\beta=\theta,\alpha=0,\gamma=0}. \quad (52)$$

This formula is analogous to the formula proposed by A. Bohr [22] for describing the angular distributions of fragments originating from the fission of oriented nuclei. From (49), it follows that, for $J = 1/2$, the angular distribution (52) is isotropic and is equal to $1/(4\pi)$ and that, for $J = 3/2$, it has the form

$$\frac{dP_J^J(\Omega)}{d\Omega} = \frac{1}{2}\pi\left[[\sin(\theta/2)]^6 + [\cos(\theta/2)]^6\right]$$

and has the maximum value of $1/2\pi$ at $\theta = 0$ and $\theta = \pi$ and the minimum value of $(1/2\pi \cdot 1/4)$ at $\theta = \pi/2$. For spin values of $J \gg 1$, this distribution takes the delta-function form in the directions specified by the angles of $\theta = 0$ and $\theta = \pi$.

7. CONCLUSION

The results obtained in this study make it possible to describe the angular distributions of protons in the protonic decay of oriented nuclei, both spherical and deformed ones. Owing to the sensitivity of these distributions to the features of parent and daughter nuclei, their investigation is, in some cases, a unique method for determining the shape and the structure of nuclei lying off the proton drip line and, consequently, near the boundary of the existence of nuclei in nature. Hence, one can hope that experimentalists will be able to develop procedures for obtaining the aforementioned distributions in the near future.

Although the adiabatic approximation is unacceptable in the case of deep-subbarier protonic decay, this approximation and the mathematical scheme developed here in order to apply it to describing nuclear decays seem very useful for understanding the features of the spontaneous and the low-energy induced fission of nuclei.

ACKNOWLEDGMENTS

This work was supported by INTAS (grant no. 99-0229).

REFERENCES

1. J. Wouters *et al.*, Phys. Rev. Lett. **56**, 1901 (1986).
2. P. Schuurmans *et al.*, Phys. Rev. Lett. **77**, 4720 (1996).
3. J. Krause *et al.*, Phys. Rev. C **58**, 3181 (1998).
4. P. J. Woods and C. N. Davids, Annu. Rev. Nucl. Part. Sci. **47**, 541 (1997).
5. J. Rikovska, N. J. Stone, and A. Wohl, in *Proceedings of International Symposium on Proton-Emitting Nuclei,* Ed. by J. C. Batchelder, AIP Conf. Proc. **518**, 316 (2000).
6. V. P. Bugrov, S. G. Kadmenskiĭ, V. I. Furman, and V. G. Khlebostroev, Yad. Fiz. **41**, 1123 (1985) [Sov. J. Nucl. Phys. **41**, 717 (1985)].

7. V. P. Bugrov, V. E. Bunakov, S. G. Kadmenskiĭ, and V. I. Furman, Yad. Fiz. **42**, 57 (1985) [Sov. J. Nucl. Phys. **42**, 34 (1985)].
8. S. Aberg, P. B. Semmes, and W. Nazarewich, Phys. Rev. C **56**, 1762 (1997); **58**, 3011 (1998).
9. C. N. Davids and H. Esbensen, Phys. Rev. C **61**, 054302 (2000).
10. S. G. Kadmensky, Yad. Fiz. **63**, 613 (2000) [Phys. At. Nucl. **63**, 551 (2000)].
11. V. P. Bugrov and S. G. Kadmenskiĭ, Yad. Fiz. **49**, 1562 (1989) [Sov. J. Nucl. Phys. **49**, 967 (1989)].
12. D. D. Bogdanov, V. P. Bugrov, and S. G. Kadmenskiĭ, Yad. Fiz. **52**, 358 (1990) [Sov. J. Nucl. Phys. **52**, 229 (1990)].
13. S. G. Kadmensky and V. P. Bugrov, Yad. Fiz. **59**, 424 (1996) [Phys. At. Nucl. **59**, 399 (1996)].
14. A. A. Sanzogni, C. N. Davids, P. J. Woods, *et al.*, Phys. Rev. Lett. **83**, 1116 (1999).
15. S. G. Kadmensky and A. A. Sanzogni, Phys. Rev. C **62**, 054601 (2000).
16. P. Talou, N. Carjan, and D. Strottman, Phys. Rev. C **58**, 3280 (1998).
17. D. Strottman, P. Talou, and N. Carjan, Phys. Scr. **88**, 148 (2000).
18. L. S. Ferreira, E. Magleone, and R. J. Liotta, Phys. Rev. Lett. **78**, 1640 (1997).
19. E. Magleone and L. S. Ferreira, Phys. Rev. C **61**, 047307 (2000).
20. H. Esbensen and C. N. Davids, Preprint PHY-9590-TH-2000 (Argonne National Laboratory, 2000).
21. A. T. Kruppa, B. Barmore, W. Nazarewicz, *et al.*, Phys. Rev. Lett. **84**, 4549 (2000).
22. A. Bohr and B. R. Mottelson, *Nuclear Structure* (Benjamin, New York, 1969, 1975; Mir, Moscow, 1971, 1977), Vols. 1, 2.
23. J. Cerny *et al.*, Phys. Lett. B **33B**, 281 (1970).
24. V. G. Solov'ev, *Theory of Atomic Nuclei* (Énergoatomizdat, Moscow, 1989; Institute of Physics, Bristol, 1992).

Translated by A. Isaakyan

Physics of Atomic Nuclei, Vol. 65, No. 5, 2002, pp. 841–842. Translated from Yadernaya Fizika, Vol. 65, No. 5, 2002, pp. 873–874.

NUCLEI
Theory

Turbulence in Nuclear Reactions

B. A. Rumyantsev[*] [†]

Budker Institute of Nuclear Physics, Siberian Division, Russian Academy of Sciences, pr. Akademika Lavrent'eva 11, Novosibirsk, 630090 Russia

Received June 9, 2000

Abstract—An explanation of the emergence of turbulence in nuclear collisions is proposed on the basis of the assumption that, in an excited nucleus, there arise nonequilibrium steady-state distributions $n(\varepsilon)$ of occupation numbers. © *2002 MAIK "Nauka/Interperiodica".*

Popular models of preequilibrium emission study predominantly the hard ("nonevaporative") part of the energy spectrum of secondary particles, $N(\varepsilon)$, where there are strong deviations from the Maxwell distribution. Under the assumption that statistical relaxation is due exclusively to binary collisions of on-shell nucleons, the time evolution of the occupation numbers $n(\varepsilon)$ was considered in [1–3]. Here, we propose a competing mechanism of formation of a power-law component of $n(\varepsilon)$, assuming that nonequilibrium steady-state distributions of $n(\varepsilon)$ that admit the existence of fluxes along the spectrum appear in an excited nucleus. Such distributions are intensively studied in the physics of weakly turbulent plasma [4–6].

The decay of an input resonance (energy-containing region), which is the initial stage of the reactions being considered, results in the population of single-particle states of energies about ε (inertial interval in terms of turbulence theory). The smallness of the occupation numbers in the inertial interval makes it possible to describe kinetics in this region on the basis of the Boltzmann equation

$$\frac{\partial n_1}{\partial t} = -\pi \sum_{234} |\langle 12|V|34\rangle|^2 \qquad (1)$$
$$\times\, \delta(\varepsilon_1 + \varepsilon_2 - \varepsilon_3 - \varepsilon_4)(n_1 n_2 - n_3 n_4) = I(n),$$

where $I(n)$ is the collision integral.

Multiplying this equation by the density of single-particle states $\rho(\varepsilon_1)$ and summing it over the angular quantum numbers m and l (averaging over these numbers selects isotropic solutions that depend only on energy ε), we recast Eq. (1) into the form

$$\rho(\varepsilon)\frac{\partial n(\varepsilon)}{\partial t} \qquad (2)$$
$$= -\pi \int\int_{\varepsilon'+\varepsilon''>\varepsilon} d\varepsilon' d\varepsilon'' T(\varepsilon, \varepsilon', \varepsilon'', \varepsilon' + \varepsilon'' - \varepsilon)$$
$$\times \left(n(\varepsilon) n(\varepsilon' + \varepsilon'' - \varepsilon) - n(\varepsilon') n(\varepsilon'')\right),$$

where $T(\{\varepsilon\})$ is the result of averaging, over the angular variables, the product of the squared modulus of the matrix element $\langle 12|V|34\rangle$ of the pair interaction V and single-particle densities $\rho(\varepsilon)$; here, $T_{1234} = T_{2134} = T_{4321}$.

By making a linear-fractional transformation of the variables ε' and ε'' in (2) [6], we can find power-law solutions to the time-independent Boltzmann equation ($\partial n_1/\partial t = 0$) that are additional to the Maxwell solution $n(\varepsilon) \sim \exp((\varepsilon - \mu)/T)$. If $T(\{\varepsilon\})$ is a homogeneous function whose homogeneity exponent is r [that is, $T(\lambda\varepsilon_1, \lambda\varepsilon_2, \lambda\varepsilon_3, \lambda\varepsilon_4) = \lambda^r T(\varepsilon_1, \varepsilon_2, \varepsilon_3, \varepsilon_4)$], then

$$n(\varepsilon) \sim \varepsilon^{s_i}, \qquad s_0 = -\frac{r+3}{2}, \qquad (3)$$
$$s_1 = -\frac{r+4}{2}.$$

If $|\langle 12|V|34\rangle|^2$ is independent of energy and if the level density is $\rho(\varepsilon) \sim \sqrt{\varepsilon}$, we arrive at $r = 2$. For the spectrum of the emitted nucleons, $N(\varepsilon)$, we then obtain

$$\frac{dN(\varepsilon)}{d\varepsilon} \sim n(\varepsilon)\varepsilon \sim \begin{cases} \varepsilon^{-3/2} \text{ for} & s = s_0 \\ \varepsilon^{-2} \text{ for} & s = s_1. \end{cases} \qquad (4)$$

These expressions are valid if the decrease in the fluxes along the spectrum because of particle emission is disregarded. We note that our expression (4)

[†] Deceased.

[*] Boris Alekseevich Rumyantsev (1944–1977) was one of the most brilliant and talented theoretical nuclear physicists. The editorial board of our journal has got one of his last articles not published during his life. We deem it still interesting. The article was prepared for publication by V.A. Khodel.

differs from the analogous expressions in the preequilibrium-emission model, which are dominated by the term $dN(\varepsilon)/d\varepsilon \sim (\varepsilon - \varepsilon_0)^{n_0-2}$, where ε_0 is the kinematical limit and $n_0 \geq 3$.

The physical meaning of power-law solutions to Eq. (2) was analyzed in [5, 6]. In order to supplement the definition of the solutions in (3), which are singular (at zero or at infinity, depending on the sign of s_i), it is necessary to introduce an external source of particles and energy, as well as the region of their removal that would ensure a steady-state character of solutions featuring fluxes along the spectrum. The decay of the input configuration and processes due to the relaxation-induced rearrangement of the self-consistent field [7] play the role of the above source. The absorption is provided by particle emission and by the heating of nucleons in the vicinity of the Fermi sphere.

In contrast to a Maxwell distribution, which depends on two parameters, T and μ, the solutions in (3) are one-parameter solutions and are characterized by one constant, the source power. Let us estimate the parameter A in the solution $n(\varepsilon) = A\varepsilon^{s_1}$. Solutions of this type are expected in deep-inelastic processes [8], where a strong dissipation creates an intense source of the energy flux P_1. In the inertial interval, we use dimensional considerations for P_1, which lead, in the case being considered, to the exact exponent in $n(\varepsilon)$. As a result, we obtain

$$P_1 = \int \varepsilon \frac{\partial n(\varepsilon)}{\partial t} d\varepsilon \sim \frac{\varepsilon^2 n(\varepsilon)}{\tau}, \tag{5}$$

where

$$\frac{n(\varepsilon)}{\tau} \sim \int\int d\varepsilon_1 d\varepsilon_2 T(\{\varepsilon\}) n^2(\varepsilon) \sim T(\varepsilon)\varepsilon^2 n^2(\varepsilon), \tag{6}$$

whence it follows that

$$n(\varepsilon) \sim \sqrt{\frac{P_1}{T}}\varepsilon^{-2}. \tag{7}$$

The parameter P_1 can be related to physical quantities by calculating the flux P_1 in the energy-containing region ($\varepsilon_{\max} = \omega$). We have

$$P_1 = \int_0^\omega n(\varepsilon)\rho(\varepsilon)\gamma(\varepsilon)\varepsilon d\varepsilon \sim \omega n_\omega \rho(\omega)\gamma(\omega)\Delta\varepsilon, \tag{8}$$

where γ is the rate of population of single-particle states and $\Delta\varepsilon \leq \gamma(\omega)$ is the width of the energy-containing region. Combining (7) and (8), we finally arrive at the expression

$$n(\varepsilon) \sim \varepsilon^{-2}\gamma(\omega)\left(\frac{n_\omega \omega \rho(\omega)}{T(\{\varepsilon\})}\right)^{1/2}, \tag{9}$$

which, at $r = 2$, is consistent with (4). In a similar way, we can estimate the constant in the solution $n(\varepsilon) = \varepsilon^{s_0}$, which corresponds to the particle flux

$$P_0 = \int \rho(\varepsilon)\frac{\partial n(\varepsilon)}{\partial t} d\varepsilon.$$

An important property of power-law distributions like (3) is that they are local. Formally, this ensures convergence of the integrals in Eq. (2). In our case, the physical criterion of locality is that the contributions from collisions of nucleons from the inertial interval, where all energies are on the same order of magnitude, with particles in the vicinity of the Fermi sphere must be small. This ensures stability of the power-law solution (3). In the region of low energies ($\omega = 10$–20 MeV), where we can neglect the energy dependence of $|\langle 12|V|34\rangle|^2$, the distributions in (3) are nonlocal. Therefore, it is difficult to identify the contribution in (4) against the background of the ordinary preequilibrium spectrum. With increasing energy of emitted particles ($\geq$100 MeV), the inertial interval and the validity range of the Boltzmann Eq. (1) both become wider. Assuming that the momentum $\mathbf{p}$ is a good quantum number and isolating $\delta(\mathbf{p}_1 + \mathbf{p}_2 - \mathbf{p}_3 - \mathbf{p}_4)$ in the matrix element $\langle 12|V|34\rangle$, we find for the exponent r in (3) that $r = 1/2 + q$, where q is the exponent that determines the energy dependence of $d\sigma/d\theta$.

ACKNOWLEDGMENTS

I an grateful to S.T. Belyaev for critical comments and to E.A. Kuznetsov for enlightening discussions.

REFERENCES

1. J. J. Griffin, Phys. Rev. Lett. **17**, 478 (1966).
2. C. K. Cline and M. Blann, Nucl. Phys. A **172**, 225 (1971).
3. K. Seidel, D. Seeliger, R. Reif, and V. D. Toneev, Fiz. Élem. Chastits At. Yadra **7**, 499 (1976) [Sov. J. Part. Nucl. **7**, 192 (1976)].
4. V. E. Zakharov, Zh. Éksp. Teor. Fiz. **51**, 668 (1966) [Sov. Phys. JETP **24**, 443 (1966)].
5. A. V. Kats *et al.*, Zh. Éksp. Teor. Fiz. **71**, 177 (1976) [Sov. Phys. JETP **44**, 93 (1976)].
6. V. I. Karas', S. S. Moiseev, and V. E. Novikov, Zh. Éksp. Teor. Fiz. **71**, 1421 (1976) [Sov. Phys. JETP **44**, 744 (1976)].
7. S. T. Belyaev and B. A. Rumyantsev, Phys. Lett. B **53B**, 6 (1974).
8. V. V. Volkov, Fiz. Élem. Chastits At. Yadra **6**, 1040 (1975) [Sov. J. Part. Nucl. **6**, 420 (1975)].

Translated by M. Kobrinsky

Physics of Atomic Nuclei, Vol. 65, No. 5, 2002, pp. 843–848. Translated from Yadernaya Fizika, Vol. 65, No. 5, 2002, pp. 875–880.

ELEMENTARY PARTICLES AND FIELDS
Experiment

Effect of Radon on SAGE Results

V. N. Gavrin, V. V. Gorbachev, and I. N. Mirmov

Institute for Nuclear Research, Russian Academy of Sciences, pr. Shestidesyatiletiya Oktyabrya 7a, Moscow, 117312 Russia

Received March 22, 2001

Abstract—A method for estimating the systematic uncertainty associated with radon in the SAGE experiment[1)] aimed at observing the solar-neutrino flux is described. For the gallium target used in this experiment, the systematic uncertainty in the measured neutrino-capture rate of 75 SNU[2)] is below 0.3 SNU. © *2002 MAIK "Nauka/Interperiodica".*

1. INTRODUCTION

Radon and products of its decay appear to be one of the main sources of background in experiments aimed at detecting solar neutrinos and double β decay and at seeking dark matter and events of other rare processes. Radon, a gaseous element of the chain of ^{238}U and ^{226}Ra decays, can find its way into a detector, and its decays mimic sought events.

Since 1990, the SAGE Russian–American experiment has been measuring the rate of solar-neutrino capture in 50 t of liquid metal gallium. Neutrinos interact with the target ^{71}Ga isotope via the reaction of inverse β decay: $^{71}\mathrm{Ga}\ (\nu, e^-)\ ^{71}\mathrm{Ge}$. With the aid of a special chemical procedure, the product ^{71}Ge atoms are extracted from the target at the end of each exposure period (1–1.5 months); are converted into the gaseous state of GeH_4 (germane); and are placed into the proportional counter, where the decays of these atoms [$T_{1/2}(^{71}\mathrm{Ge}) = 11.4$ d] are observed over a period of 5 to 6 months. A detailed description of the experiment, including the description of the chemical procedures for extracting germanium from the gallium target and procedures for counting ^{71}Ge decays and for analyzing the resulting data, is given in [1, 2].

We subdivide radon into external and internal portions according to the type of its effect. External radon is outside the counter in ambient air and is recorded in the counter owing primarily to γ rays from β-decay elements. External radon is displaced from the environment of the counters by means of a blow through with evaporating liquid nitrogen. The residual activity of external radon is monitored by the active-shield system. It is constant in time; therefore, external radon affects only the background counting rate, increasing the statistical uncertainty of the measurements—there is no systematic bias of the measurement results in this case.

Internal radon, admixed to the counter gas during counter filling, has a totally different effect on measurements. Here, the detection efficiency is considerably higher than for external radon—almost all decays of radon and of elements of its decay chain are recorded. It is important to note that radon decays occur at the beginning of the exposure [$T_{1/2}(^{222}\mathrm{Rn}) = 3.8$ d], increasing the measured number of ^{71}Ge decays. Thus, radon decays result in overestimating the measured flux of solar neutrinos. In this article, we assess this overestimation and indicate a possible way to reduce the systematic uncertainty caused by internal radon. The method used to estimate the systematic uncertainty is the following. Special features of the formation of pulses from the decays of radon and its daughter elements in the counter are determined on the basis of measurements. Further, the spectra of pulses for the decay of each radon-chain element are simulated. Taking into account the data obtained in solar-neutrino-run measurements and using the SAGE method for determining radon decays, we obtain the sought systematic uncertainty.

2. PROPORTIONAL COUNTERS AND COUNTING SYSTEM

Quartz cylindrical proportional counters are used in the SAGE experiment to detect ^{71}Ge decays. The

[1)] The SAGE experiment is being performed with the aid of the gallium–germanium neutrino telescope (GGNT) at the underground laboratory of the Baksan Neutrino Observatory of the Institute for Nuclear Research (Russian Academy of Sciences) in the Republic of Kabardino-Balkaria (near Elbrus). This underground laboratory is located at a distance of 3.5 km from the entrance of the adit excavated into the Mount Andyrchi. The rock thickness provides shielding from cosmic muons corresponding to 4700 mwe.

[2)] 1 SNU corresponds to one event of neutrino capture per second in a target that contains 10^{36} atoms.

1063-7788/02/6505-0843$22.00

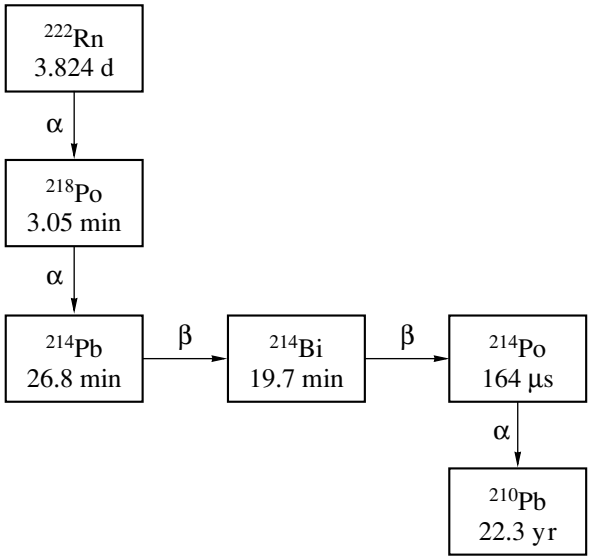

Fig. 1. ^{222}Rn decay chain.

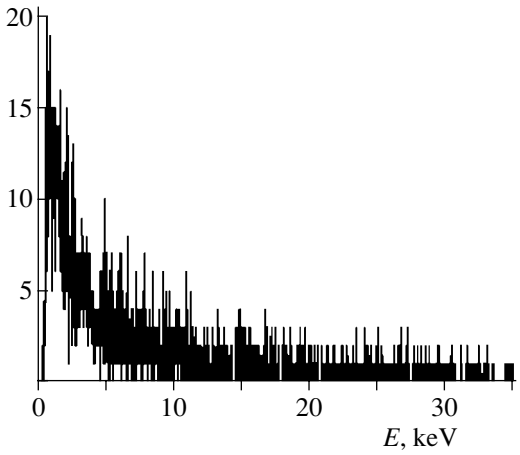

Fig. 2. Spectrum of pulses coincident with signals from NaI.

counter cathode manufactured from iron has an inner diameter of 0.4 cm and a length of 5 cm, while the anode is a tungsten wire of diameter 10–12 μm. The counter gas is a mixture of xenon and germane (GeH_4) at a pressure of about 1 atm. Germane constitutes up to 30% of the gas in volume and plays the role of a quencher. The range of the pulse-height measurement is 0.3–16 keV. The energy scale is linear over the entire range of measurements. The detecting facility includes a system of anticoincidences that is based on a NaI crystal and which plays the role of an active shield. A digital oscilloscope is used in the detecting facility to record the pulse shape; the oscilloscope-frame duration is 1 μs, with the time resolution being 1 ns. On the basis of the pulse shape, the pulse rise time is determined, which permits subdividing pulses into "pointlike" and "extended" ones with respect to the track length of an ionizing particle in the counter gas. The decay of ^{71}Ge proceeds through electron capture followed by the emission of 10.4-, 1.2-, and 0.1-keV Auger electrons (K, L, and M modes, respectively). The energy range of the detecting facility makes it possible to observe only the K and L decays of ^{71}Ge. The Auger electrons lose energy in the gas near the production vertex and are recorded as pointlike events—that is, as events characterized by a short pulse rise time (T_N). Gamma rays are not emitted in ^{71}Ge decay. In order to reduce the background counting rate, each pulse is tested for complying with specific requirements on the detection of germanium decays (1) in the amplitude, (2) in the rise time, and (3) in the coincidence with pulses from NaI. The pulse amplitude must be within the intervals (windows) of the K and L peaks of ^{71}Ge. The width of the windows is $\pm 2.36\sigma$ (σ is the standard deviation) around the peak mean value and covers 98% events under the peak.

3. MEASUREMENTS

Figure 1 displays the ^{222}Rn decay chain. Its three elements decay through the emission of α particles, and two of them undergo β decay. The chain ends in the ^{210}Pb isotope, whose half-life ($T_{1/2} = 22.3$ yr) exceeds considerably the counting time of an individual run. The total lifetime of all chain elements, with the exception of the first one, is about 1 h.

In order to choose a correct model for describing processes occurring in the counter upon radon decay, measurements were performed with a large amount of radon (about 3200 atoms) placed into the counter gas. In processing the pulses, use was made of a special procedure that relies on the method of reconstruction of primary-ionization tracks [3, 4] and which makes it possible to study pulses in detail and to determine the pulse amplitude on the basis of the initial portion of the pulse [5]. In our case, the application of this method enabled us to extend the range of the energy measurement up to about 35 keV and to reveal some special features of the radon-decay spectra. Two spectra were obtained in the measurements: (1) the spectrum of events coinciding with signals from NaI (Fig. 2) and (2) the spectrum of events that do not coincide with signals from NaI (Fig. 3). The first is formed by ^{214}Pb and ^{214}Bi β decays, which are accompanied by γ radiation. Here, the measurements yield a descending spectrum without clear-cut structures. The spectrum of events that do not coincide with signals from NaI is more complicated: a peak with a resolution of about 41% is observed in

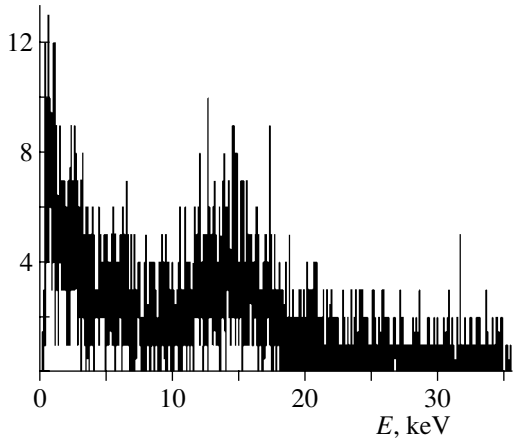

Fig. 3. Spectrum of pulses that do not coincide with signals from NaI.

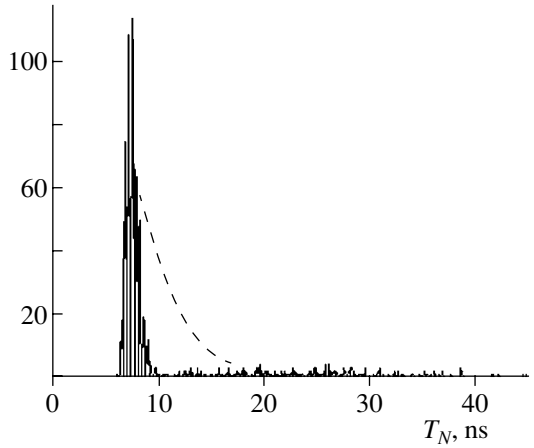

Fig. 4. Distribution of events from the 14-keV peak versus the pulse rise time T_N (1250 events). The analogous distribution for events from the K peak of ^{71}Ge is given for the sake of comparison (dashed curve).

the region around 14.2 keV (the counter resolution is 20% for the 5.9-keV line).

The pulses that form this spectrum are due to α decays of the radon-chain elements in the cases where β decays are not accompanied by signals from NaI inclusive (the efficiency of NaI in detecting γ rays produced in the counter is on average about 80%). Since there is no indication of this peak in the first spectrum, it can be attributed to α decays exclusively. We associate this peak with the detection of recoil nuclei produced in the α decays in question.

The energy transferred to recoil nuclei in the α decays is 100–150 keV, about 10% of it going into ionizing molecules of the counter gas. That the distribution of events versus the pulse rise times (Fig. 4) that corresponds to pointlike events is narrow—that is, the particles involved have a very small range—is another piece of evidence for believing recoil nuclei to be responsible for the events of this peak. Figure 4 shows that this distribution is even narrower than that for the K peak of ^{71}Ge. The peak in the vicinity of 14 keV is of importance for us, since part of it overlaps the region corresponding to the K peak of ^{71}Ge.

4. SIMULATION OF EVENT SPECTRA FOR COUNTERS

In order to calculate the number of pulses originating from each element of the radon chain and mimicking ^{71}Ge decays, we determined the spectra of pulses associated with the decays of these elements in the counter using the Monte Carlo method. In doing this, we took into account the geometric parameters of the counters and the properties of the counter gas. We assumed that radon decays in the counter gas and that the remaining elements of the chain have sufficiently long lifetimes to be deposited on the counter walls. It should be noted that they are deposited predominantly on the cathode, because some atomic electrons are stripped off their shells in the α-decay process, so that the daughter element arises in the form of a positively charged ion [6], which is attracted to the cathode. This is also suggested by the fact that the peak due to recoil nuclei has a rather high resolution—if recoil nuclei were produced in the vicinity of the anode, there would arise considerable fluctuations of gas amplification. In the case of ^{222}Rn α decay, the emitted α particle and the resulting recoil nucleus are both recorded. In the α decay of ^{218}Po and ^{214}Po, either the α particle or the recoil nucleus is recorded (the latter occurs if the α particle goes away toward the counter wall). Because of a high ionizing power of α particles, α decays are recorded predominantly as saturated events—that is, events corresponding to energy losses beyond the measurement range (16 keV). Only an insignificant fraction of α decays is recorded as "ordinary" events, in which case the α-particle path in the gas is sufficiently short for the ionization losses not to exceed 16 keV and the recoil nucleus falls onto the wall. From our simulation, it follows that the pulse spectrum of these events is uniform and that their number does not exceed 5% of the total number of α decays at the cathode. In the case of ^{222}Rn α decays in the counter gas, the number of events that do not lead to results beyond the scale is close to zero (their probability is below 10^{-4}). Thus, the number of pulses from the α decays that mimic ^{71}Ge decays is proportional to the widths of the energy windows of the L and K peaks of ^{71}Ge. Additionally, the K peak of ^{71}Ge comprises α-decay events in which the α particle goes away to the wall and one records the pulse from the recoil nucleus.

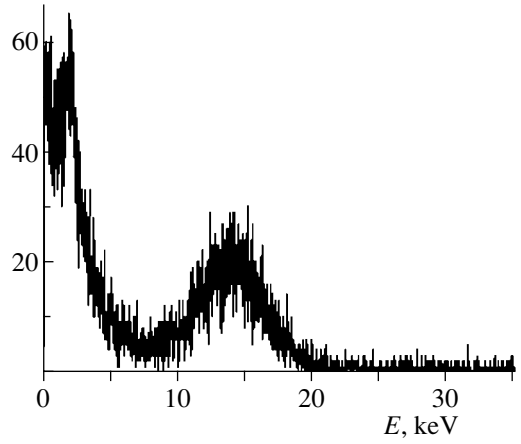

Fig. 5. Result of a Monte Carlo simulation for the integrated spectrum of pulses from the decays of all elements of the radon chain.

Since the α-particle range in the gas is too short (below 0.35 mm) to produce a pulse that does not go beyond the scale, these events can be considered as pointlike ones; hence, the parameter T_N (pulse rise time) cannot be used as a selection criterion for these pulses. A selection according to coincidences with pulses from NaI is also impossible, because γ radiation is not generated in α decays.

It is more difficult to simulate β than α decays. Here, it is necessary to take additionally into account the complex shape of the β-particle spectrum [7], the energy losses of electrons by bremsstrahlung, and changes in the direction of electron motion, as well as nonuniform energy losses of electrons. Moreover, part of the electrons that have gone away to the counter wall return to the gas volume, increasing the pulse energy [8, 9]. In β decay, a pulse in the counter is formed owing to the ionization losses of the β particle, which are calculated by the well-known Bethe formula (see, for example, [8]). It is difficult to take directly into account changes in the direction of electron motion and nonuniformity of the energy losses by bremsstrahlung. Under our conditions (the geometry of the counter and the working gas mixture as described above), it is possible, however, to use straight electron trajectories and the continuous energy losses. The pulse spectra underwent virtually no change upon applying a refined method for assessing electron energy losses that employs information about electron ranges and various versions of taking into account changes in the direction of electron motion. (The change in the number of events that fell within the K- and L-peak regions was always below 50%.) In view of this, we abandoned complicated models and present here the results of the simulation where the trajectories of the β particles in the gas are straight and where their energy losses are continuous. The fraction of the β particles that are reflected from the wall of the iron cathode back into the counter-gas volume is taken to be independent of the angle of incidence and equal to 0.3. For the β particles, the change in the energy due to reflection from the wall is also taken into account [8].

Figure 5 shows the integrated spectrum of simulated events associated with all elements of the radon chain. Its shape reproduces that of the pulse spectrum obtained in the measurements.

Given the spectra of the pulses in the counter that are due to the decays of each element of the radon chain, one can determine the probability for the pulses from specific decays to fall within the energy region of the L and K peaks of ^{71}Ge. Additional selections that are based on the pulse rise time T_N and on the coincidence with signals from NaI can be applied to the pulses from the β decays. We use the intensity of each γ line of ^{214}Pb and ^{214}Bi [10] and take into account their detection efficiency in the NaI crystal to obtain the probabilities of coincidences between β decays and NaI signals. In our case, the β decays of ^{214}Pb are accompanied by signals from NaI in 50% of cases. For ^{214}Bi, this value is greater (75%). Thus, the measured spectrum of pulses coinciding with signals from NaI (see Section 2) is the corresponding sum of ^{214}Pb and ^{214}Bi decays. On the basis of this spectrum, we determine the probability that an event falling within the energy intervals of the L and K peaks will be characterized by a value of T_N that corresponds to pointlike events ($T_N < 10$ ns and $T_N < 18.4$ ns for the L and the K peak, respectively). These probabilities are $w_L(T_N < 10\ \text{ns}) = 0.17$ and $w_K(T_N < 18.4\ \text{ns}) = 0.40$.

We can apply only a selection in energy to the pulses from α decays. These α decays are not accompanied by γ rays, and short tracks of the α particles with pulses that do not go beyond the scale ensure the pointlike character of these pulses.

The table gives the resulting values of the probability that, upon the decay of each element of the radon chain, there appears an event mimicking ^{71}Ge decay. Here, it is considered that the α decay of ^{214}Po can be detected only if the preceding β decay of ^{214}Bi was not detected (the β particle falls onto the wall and is not reflected from it). This is because the dead time of the detecting facility (about 0.9 s) exceeds significantly the half-life of ^{214}Po ($T_{1/2} = 164\ \mu$s).

The radon decay chain begins with ^{222}Rn α decay in the counter gas, the corresponding pulse almost always leading to results beyond the scale. This is taken into account within the standard procedure adopted by SAGE for analyzing detected pulses. Around each saturated event that is not accompanied by a signal

Probabilities of detecting the decays of the radon-chain elements at the L and K peaks of ^{71}Ge

	^{222}Rn (α)	^{218}Po (α)	^{214}Pb (β)	^{214}Bi (β)	^{214}Po (α)	$\sum$
L peak	0	4.2×10^{-3}	1.1×10^{-2}	7.2×10^{-3}	1.6×10^{-3}	0.024
K peak	4×10^{-5}	4.9×10^{-2}	6.1×10^{-3}	1.8×10^{-3}	1.86×10^{-2}	0.076

from NaI, the time interval from 15 min before detecting this event to 3 h after it is declared to be a dead time. The pulses that arrived from the counter within this interval and the interval itself are eliminated from the determination of the event-detection rate. In the case where it is not radon decay but the decay of ^{218}Po that generates a saturated pulse, the above 15-min period before this pulse must quench the contribution to the probability of mimicking germanium decay by the α particle from radon. As can be seen from the table, it is very difficult to ensure fulfillment of this condition; in all probability, it will not be used in the future for this reason. In order to determine the probability that ^{71}Ge decay is mimicked by radon, it is therefore necessary to find the number of the decays of the radon-chain elements within 3 h after the beginning of the initial α decay. This was done with the aid of the Monte Carlo method. Only the β decays of ^{214}Pb and ^{214}Bi and the α decays of ^{214}Po are of importance here: 1.1% of ^{214}Pb decays and 3.5% of ^{214}Bi and ^{214}Po decays occur within the interval of 3 h. By increasing the time interval that is reckoned from a saturated pulse and which is eliminated from the analysis, it is possible to achieve a more pronounced reduction of the radon systematic uncertainty: each additional hour reduces the systematic uncertainty about 3 times.

5. RESULTS

Considering that the time intervals associated with detecting pulses yielding results beyond the scale are removed from the analysis (see Section 4), we have determined the probability of recording an event that mimics ^{71}Ge decay per event of the decay of one radon atom in the counter gas. This has yielded 4.3×10^{-4} and 7.8×10^{-4} for the L and the K peak, respectively.

In an individual run of SAGE measurements, we record, on average, 2.1 and 2.5 events of ^{71}Ge decay at the L and at the K peak, respectively, and 7.7 saturated pulses attributed to radon decays. This number of radon-decay events causes the appearance of an additional signal: on average, 3.2×10^{-3} and 6.0×10^{-3} pulses at the L and at the K peak, respectively, per individual run. This corresponds to the relative uncertainty of 0.2% for both peaks and to the uncertainty of 0.1 SNU at the measured solar-neutrino-capture rate of 75 SNU.

It should be noted here that some counters used in the solar-neutrino runs had a resolution lower than that for which the spectra were calculated in Section 3. A poorer resolution increases the width of the time intervals in which amplitudes of the recorded pulses were selected. In the case of the L peak, the probability increases linearly despite the descending character of the spectrum of the β pulses within this range of amplitudes. In the case of the K peak, the change in the probability of the detection of mimicking events from radon is nonlinear because of the overlap of the amplitude intervals for recording the K peak and the peak associated with recoil nuclei. As a rule, the resolution of the counters used in the runs of solar-neutrino measurements was below 25% for the 5.9-keV line. This resolution is used to calculate the eventual uncertainty. As a result, the uncertainty increases by a factor of 1.3 at the L peak and by a factor of 1.5 at the K peak. Finally, we find that the systematic uncertainty is 0.2% (0.2 SNU) at the L peak and 0.4% (0.3 SNU) at the K peak. The value obtained for the K peak should be treated as the integrated uncertainty, because SAGE statistics were based primarily on ^{71}Ge decays measured precisely at the K peak [1].

The value of 0.3 SNU obtained here is an upper limit on the systematic uncertainty associated with radon. Its small value indicates that radon does not contribute noticeably to the SAGE results.

ACKNOWLEDGMENTS

We are grateful to J.N. Abdurashitov, A.V. Kalikhov, and V.E. Yants for enlightening comments and to all the members of the SAGE collaboration for stimulating discussion.

REFERENCES

1. J. N. Abdurashitov *et al.*, Phys. Rev. C **60**, 055801 (1999).
2. V. N. Gavrin, Nucl. Phys. B (Proc. Suppl.) **91**, 36 (2001).
3. J. N. Abdurashitov, T. V. Ibragimova, and A. V. Kalikhov, http://xxx.lanl.gov/physics/9908023.

4. J. N. Abdurashitov, T. V. Ibragimova, and A. V. Kalikhov, in *Proceedings of the X International School "Particles and Cosmology," Baksan, Russia, 1999,* p. 77.
5. V. V. Gorbachev, T. V. Ibragimova, and A. V. Kalikhov, in *Proceedings of the X International School "Particles and Cosmology," Baksan, Russia, 1999,* p. 81.
6. T. A. Carlson, *Photoelectron and Auger Spectroscopy* (Plenum, New York, 1975; Mashinostroenie, Leningrad, 1981).
7. *Beta Rays of Decay Products: A Handbook* (Énergoatomizdat, Moscow, 1978).
8. S. V. Starodubtsev and A. M. Romanov, *Propagation of Charged Particles through Matter* (Tashkent, 1962).
9. A. A. Vorob'ev and B. A. Kononov, *Propagation of Electrons through Matter* (Tomsk, 1966).
10. *Table of Isotopes,* Ed. by C. M. Lederer and V. S. Shirley (Wiley, New York, 1978, 7th ed.).

Translated by E. Kozlovskiĭ

Physics of Atomic Nuclei, Vol. 65, No. 5, 2002, pp. 849–851. Translated from Yadernaya Fizika, Vol. 65, No. 5, 2002, pp. 881–883.

ELEMENTARY PARTICLES AND FIELDS
Experiment

Experimental Estimate of the Diffractive-Dissociation Phenomenon Following Neutrino Interaction with Photoemulsion Nuclei

O. K. Egorov*

Institute of Theoretical and Experimental Physics,
Bol'shaya Cheremushkinskaya ul. 25, Moscow, 117259 Russia

Received February 21, 2001; in final form, August 23, 2001

Abstract—The first experimental estimate of the diffractive-dissociation (DD) cross section for muon-neutrino interaction with nuclei is presented. Eleven events that satisfy the DD criteria ($x_B < 0.1$, $\Delta\eta > 2$) are found among 207 events induced by neutrino interactions with Ag and Br nuclei of nuclear photoemulsion and borrowed from the database of the E-564 experiment (FNAL). The ratio of the DD cross section to the total deep-inelastic cross section for the charged current is 0.29 ± 0.09. Four of the 11 events proved to be candidates for events of coherent DD. © *2002 MAIK "Nauka/Interperiodica".*

It was predicted theoretically in [1] that the cross section for coherent diffractive dissociation (DD) in neutrino interaction with a heavy nucleus can amount to half the total deep-inelastic cross section for a collision between a neutrino and a heavy nucleus. Earlier, it was shown in [2] that DD effects are significant in photoproduction as well.

The experimental study of the DD phenomenon in photoproduction became possible only upon the commissioning of the HERA electron–proton collider. In particular, a comprehensive investigation of this phenomenon by the H1 and ZEUS collaborations was presented in [3, 4].

By using the database of the E-564 experiment (FNAL) [5], we estimate here the DD cross section for muon-neutrino interactions with Ag and Br nuclei of photoemulsion. Of the total of 207 neutrino–nucleus collisions involving silver and bromine, 179 were events associated with the charged current. The distribution of these events with respect to the Bjorken variable x_B is displayed in Fig. 1, where the number of events is plotted along the ordinate. An analysis of data in terms of this variable is used in [1, 2] to separate the DD effect. The quantity x_B is defined as

$$x_B = Q^2/(2m\nu),$$

where ν is the neutrino energy in the laboratory frame; m is the nucleon mass; and $Q^2 = -q^2$, q being the 4-momentum transfer to hadrons.

Of the aforementioned 179 events, 76 have a gap in the pseudorapidity ($\Delta\eta > 2$), which is defined as

$$\eta \approx -\ln(\tan(\theta/2)),$$

where θ is the hadron emission angle.

Figure 2 presents the distribution of these 76 events with respect to the Bjorken variable x_B. It is clear from Fig. 2 that the range $x_B = 0$–0.1 contains 11 events. Those are the same events from the range 0–0.1 in Fig. 1. As can be seen from the figures, both criteria select the same events. According to various calculations, including those that were performed in our laboratory [6], it is the range $x_B = 0$–0.1 that contains all DD events.

Figure 3 shows the distribution of the selected 11 events with respect to x_B in the interval 0–0.1, with the mean value being $\langle x_B \rangle = 0.048$. At this mean value of x_B, the calculations performed on the basis of the procedure described in [7] (the results of these calculations are illustrated in Fig. 4) predict 65 events. Quark–lepton interactions were generated by the LEPTO code, version 4.3 [7]. However, the code was adjusted to the kinematical conditions of the experiment being studied; in particular, the cuts on Q^2 and W (W is the mass of the hadron final state) were lowered down to 0.1 $(\mathrm{GeV}/c)^2$ and 1 GeV/c^2,

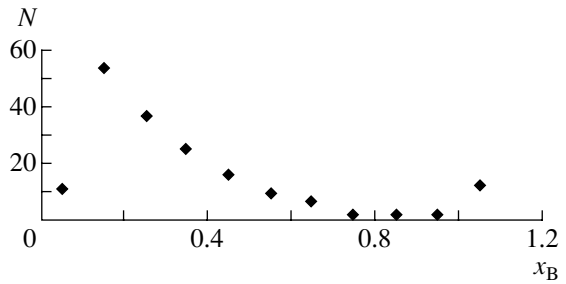

Fig. 1. Distribution of 179 charged-current events with respect to x_B for Ag and Br nuclei of photoemulsion.

*e-mail: egorov_o@vitep.itep.ru

1063-7788/02/6505-0849$22.00

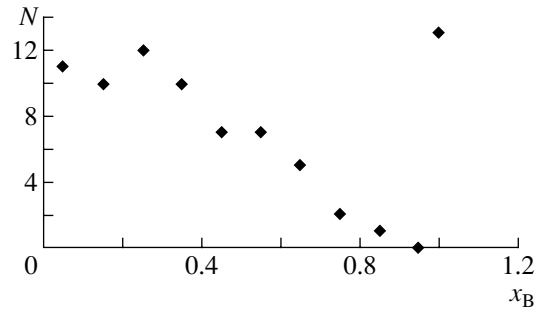

Fig. 2. Distribution of 76 charged-current events with $\eta > 2$ in x_B.

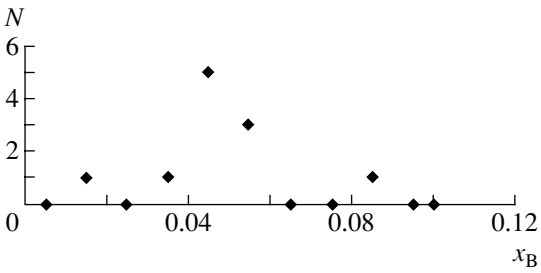

Fig. 3. Distribution of 11 charged-current events with $\eta > 2$ in the range $x_B = 0$–0.1. The mean value is $\langle x_B \rangle = 0.048$.

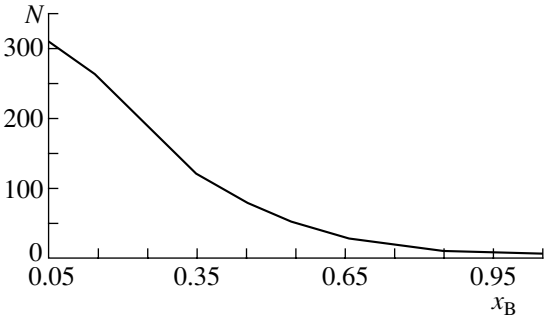

Fig. 4. Results of a Monte Carlo simulation of charged-current events (distribution with respect to the Bjorken variable).

respectively. According to the data of the E-531 experiment [8, 9], which employed the same neutrino beam as the E-564 experiment, these cuts left 98% of the total number of events, events of cumulative production being eliminated.

In order to estimate experimentally the ratio of the DD cross section to the total deep-inelastic cross section for neutrino interaction with a heavy nucleus of photoemulsion, we must take into account the efficiency of event detection in the photoemulsion chamber. In order to accomplish this, we applied the following procedure. In the E-564 experiment, the efficiency of event detection is known as a function of the multiplicity of black and gray tracks in an event. Assuming that the detection efficiency is the same for detected and for undetected events, we can determine it for each of the 11 detected events according to the corresponding track multiplicity. We weighted all these events in accordance with their efficiencies. (By way of example, we indicate that, if the detection efficiency for events featuring one black track is 1/2, these events have a weight of 2.) The procedure yielded 40 ± 8 events; for the cross-section ratio, this leads to 0.22 ± 0.06. In all probability, this is a lower bound on the cross-section ratio, because the efficiency of event detection decreases fast with decreasing particle multiplicity in an event.

A more reliable estimate of the efficiency can be obtained by extracting, from the database of neutrino–nucleus interactions, events found by tracing along a track. Eighty-two events of this type were among 179 charged-current events; of these, ten events passed the DD criteria. The correction for the efficiency of finding events by means of tracing along the track versus x_B can be taken from the data of the E-531 experiment (see [9]). By formally applying this criterion, we obtain the value of 0.19. If, however, we take into account the distinction between the efficiencies of finding low-multiplicity events in the E-531 and E-564 experiments, the result for the ratio of the cross sections becomes $\sigma_{DD}/\sigma_{tot} = 0.29 \pm 0.09$.

Of 11 DD events found in the experiment, four events can be considered as candidates for coherent DD—that is, as events that do not involve either the decay of the nucleus or the emission of any of its constituents. In nuclear photoemulsion, such events look like white stars (that is, stars not containing gray or black tracks).

Among 79 white stars in the database of the E-564 experiment, we found only four events that pass the DD criteria. These events are presented in the degree works by Moskvin [10] and Marikhin [11] performed at the Institute of Theoretical and Experimental Physics (ITEP, Moscow) under the supervision of the present author. By way of example, we indicate that one event has $\Delta\eta = 2.2$ and involves a muon and a "jet" of four π mesons and that another event is characterized by a rapidity gap of 3.0 and by the presence of a muon and a "jet" of two π mesons. It is such events that are considered here as events of coherent DD in muon-neutrino interaction with a heavy nucleus of photoemulsion. These events correspond to nuclear excitation energy below 5 keV. The relative DD cross section estimated on the basis of these four events is 0.18 ± 0.09. This estimate takes into account the additional inefficiency associated with finding white stars at low multiplicities of relativistic particles in an event. However, this definition of coherent DD is open to criticism, if for no other reason

than the fact that, according to the model of free nucleons, the proton momentum in a heavy nucleus exceeds 250 MeV/c.

We consider the remaining seven events as events of incoherent DD. These events have a pseudorapidity gap in excess of 2 and Bjorken variable values in the region $x_B < 0.1$, but they involve black or gray tracks of particles emitted from the nucleus; that is, these events are characterized by a significant excitation energy of the nucleus involved.

ACKNOWLEDGMENTS

I am grateful to the participants of the E-564 experiment (FNAL) and especially to E.D. Kolganova, O.M. Kuznetsov, Z.V. Minervina, P.V. Pitukhin, and V.V. Shamanov, who were the creators of the database of neutrino–nucleus interactions. I would also like to thank A.E. Asratyan, A.G. Dolgolenko, V.R. Zoller, A.B. Kaidalov, and K.A. Ter-Martirosyan for stimulating discussions and advice. I am indebted to Yu.D. Aleshin, who prepared the database for an analysis with a PC; to my graduate students N.Yu. Marikhin and R.R. Moskvin, who found events that passed the DD criteria in the database; and to Seren Frederiksen, who placed the data of the E-531 experiment (FNAL) at my disposal.

This work was supported by the Russian Foundation for Basic Research (project no. 96-02-18564).

REFERENCES

1. N. N. Nikolaev, B. G. Zakharov, and V. R. Zoller, Z. Phys. A **351**, 435 (1995).
2. N. N. Nikolaev and B. G. Zakharov, Z. Phys. C **49**, 607 (1991).
3. C. Adloff, S. Aid, M. Anderson, *et al.*, Preprint No. 97-009, DESY (Hamburg, 1997).
4. J. Breitweg, M. Derrick, D. Krakauer, *et al.*, Phys. Lett. B **421**, 368 (1998).
5. Yu. Batusov, S. Bunyatov, O. Kuznetsov, *et al.*, Z. Phys. C **45**, 557 (1990).
6. R. R. Moskvin, Preprint No. 48-94, ITÉF (Inst. of Theoretical and Experimental Physics, Moscow, 1994).
7. B. Andersson, G. Gustafsson, G. Ingelman, *et al.*, Phys. Rep. **97**, 31 (1983).
8. N. Usida, T. Kondo, F. Fujioka, *et al.*, Nucl. Instrum. Methods Phys. Res. A **224**, 50 (1984).
9. S. G. Frederiksen, PhD Thesis in Physics (Univ. of Ottawa, Ottawa, 1987).
10. R. R. Moskvin, Degree Thesis (Mosk. Fiz.-Tekhnol. Inst., Moscow, 1994).
11. N. Yu. Marikhin, Degree Thesis (Mosk. Fiz.-Tekhnol. Inst., Moscow, 1998).

Translated by M. Kobrinsky

Physics of Atomic Nuclei, Vol. 65, No. 5, 2002, pp. 852–860. Translated from Yadernaya Fizika, Vol. 65, No. 5, 2002, pp. 884–892.

ELEMENTARY PARTICLES AND FIELDS
Experiment

New Method for Determining Energies of Cosmic-Ray Nuclei

N. A. Korotkova, D. M. Podorozhnyi, E. B. Postnikov, T. M. Roganova, L. G. Sveshnikova, and A. N. Turundaevsky

Institute of Nuclear Physics, Moscow State University, Vorob'evy gory, Moscow, 119899 Russia

Received February 13, 2001; in final form, September 14, 2001

Abstract—A new procedure for determining the energies of particles of primary cosmic radiation is described. The procedure is based on measuring the spatial density of the flux of secondary particles originating from the first event of nuclear interaction that have traversed a thin-converter layer. The use of the proposed method makes it possible to create equipment of comparatively small mass and high sensitivity. The procedure can be applied in balloon- and satellite-borne cosmic-ray experiments with cosmic nuclei for all types of nuclei over a wide energy range between 10^{11} and 10^{16} eV per particle. Physical foundations of the method, results of a simulation, and the applicability range are described.

INTRODUCTION

Investigation of primary cosmic rays has been of interest for astrophysics since the discovery of cosmic rays. Processes occurring in the Milky Way Galaxy and maybe beyond it are reflected in the chemical composition of cosmic rays, in the energy spectra of cosmic-ray components, and in their possible anisotropy. The spectrum and the composition of primary cosmic rays have been explored with the aim of obtaining answers to the fundamental questions of the origin of primary cosmic radiation, the mechanisms of their acceleration, and their propagation in the Milky Way Galaxy.

In the energy range 10^{11}–10^{16} eV, which is usually of prime interest, the energy spectrum of cosmic rays behaves as follows. For $10^{11} < E < 3 \times 10^{15}$ eV, it can be approximated by a power-law function proportional to $E^{-\gamma}$ with $\gamma \sim 1.7$; at $E \sim 3 \times 10^{15}$ eV, the spectrum has a knee, becoming steeper, which is described by a value of $\gamma \sim 2.2$. There are a few different interpretations of the knee phenomenon in the spectrum of cosmic rays, but none of these has been corroborated experimentally. This is because there are no data from a direct investigation of the chemical composition of primary cosmic rays in the region $E > 10^{15}$ eV; as to data in the energy region immediately below the knee ($E = 10^{14}$–10^{15} eV), their statistical significance is insufficient. The knee phenomenon was discovered by means of an indirect procedure that employs extensive air showers and which makes it possible to determine, to a rather high degree of precision, the energy spectrum of the sum of all cosmic-ray components over a wide energy region ($E > 10^{15}$ eV), but which cannot pinpoint the type of a primary particle. Results obtained by this method for the chemical composition of primary cosmic radiation are still hotly debated [1]. In order to explore the energy range $E = 10^{14}$–10^{16} eV, which is of crucial importance for the astrophysics of high-energy cosmic rays, it is necessary to study directly the composition of cosmic rays beyond the atmosphere, which fully transforms the primary flux. This requires deployment of large-area arrays and long exposure times.

The main difficulty in directly investigating cosmic rays over the aforementioned energy range is that, of the entire toolkit of procedures that contemporary experimental physics provides for simultaneously measuring the energies of all types of $Z = 1$–26 nuclei (this is of paramount importance for determining the relationship between the intensities of different nuclei), only two can be applied in the case being discussed. These are the magnetic-spectrometer and the ionization-calorimeter procedure. However, the potential of the first procedure is severely constrained by the need for generating magnetic fields of enormous strength beyond the atmosphere. In view of the current state of the art in superconducting technologies, such investigations into the energy range above 1 TeV will become possible only in the future. Over the past 30 years, the ionization-calorimeter procedure has been the main tool in experiments with high-energy cosmic rays. It furnished unique results in experiments like PROTON [2] and SOKOL [3] and in experiments where a modified ionization-calorimeter procedure is implemented with the aid of a facility that employs x-ray emulsion chambers (JACEE [4], MUBEE [5], RUNJOB [6]). Over the past two

1063-7788/02/6505-0852$22.00

decades, however, the experimental astrophysics of cosmic rays has run into considerable difficulties, since arrays having a weight of a few tons must be placed beyond the atmosphere for a long time in order extend investigations with ionization calorimeters to energies in excess of 10^{14} eV. This obviously makes such investigations extremely expensive. There are also limitations on the use of the procedure based on x-ray emulsion chambers: first, long-term exposures (of duration in excess of 250 h) of nuclear emulsions and x-ray films is impossible; second, treatment of primary data requires painstaking efforts.

For performing investigations in the vicinity of the knee in the spectrum of primary cosmic radiation, it is crucial to create detecting equipment having a relatively low weight and a high sensitivity and providing the possibilities for long-term exposures and for explorations of cosmic rays by a single procedure over a wide energy range (of a few orders of magnitude). For this, it is necessary to develop new approaches that would make it possible to determine the energies of ultrahigh-energy particles without employing thick absorbers.

A procedure that is a development of the well-known and extensively used method for determining the primary-particle energy from the mean angle of divergence of secondaries originating from an inelastic-interaction event (Castagnoli's method [8]) was proposed in [7] on the basis of experience gained in previous investigations. This procedure, in contrast to that based on ionization calorimetry, does not require a thick absorber of energy—a thin target of depth about a few centimeters is sufficient. In the following, we describe the physical foundations of the method and present results obtained from a simulation of it.

1. METHOD FOR DETERMINING THE ENERGIES OF NUCLEI FROM THE LATERAL DISTRIBUTION OF THE DENSITY OF THE SECONDARY-PARTICLE FLUX

The method due to Castagnoli [8] is based on the assumption that secondary pions originating from proton interactions are emitted isotropically in the c.m. frame. By virtue of Lorentz transformations, the mean value of $\ln\tan\theta_i$ in the laboratory frame (θ_i is the emission angle of a secondary particle) is then proportional to the logarithm of the primary energy of the incident particle; that is, the lateral distribution of secondaries, which is usually analyzed in terms of the pseudorapidity $\eta = -\ln\tan(\theta/2)$, $dN/d\eta$, is sensitive, under certain conditions, to the primary energy. This method was applied in experiments where nuclear emulsions and spark chambers were employed for detectors and where secondary photons from neutral-pion decays could not therefore be detected, which resulted in the violation of the condition of isotropy of charged-particle emission in the c.m. frame of colliding protons, since these secondary photons carry away an uncontrollable momentum fraction. This is not the whole story, however: in nucleon–nucleus interactions, the left wing of the distribution $dN/d\eta$ is distorted by the contribution of slow particles produced in the subsequent interactions of the incident nucleon with target nucleons; this leads to the growth of fluctuations of $\langle\eta\rangle$ in individual events and, as a consequence, to an increase in the error in determining the energy. The aforementioned factors and experimental difficulties in detecting all slow particles traveling within the backward cone were the main reasons for a very large error in determining the energy by Castagnoli's method in individual events: 100–200% for energies in the range 0.1–1 TeV. Methods for determining the energy that are based on computing the maximum value of η, which is also proportional to the logarithm of the primary-particle energy, were developed in the RUNJOB experiment [6], whereby the effect of slow particles was eliminated [9]. For technical reasons, however, that experiment measured only secondary photons rather than charged particles.

Prior to demonstrating how the aforementioned problems were sidestepped, we will dwell upon general criteria for choosing the method. For a nuclear interaction, it is necessary to find a parameter S (or a set of parameters) that can easily be measured with a specific array and which depends on the primary-particle energy. Upon plotting the mean calibration dependence $\langle S\rangle(E)$, an energy value E_{meas} can be associated with each individual event. The basic requirements are the following: first, the mean calibration dependence must be linear or must be close to a linear one, $\langle S\rangle \approx kE$ (if the energy dependence of $\langle S\rangle$ is much weaker than a linear dependence, small fluctuations in the measured parameter S would lead to large errors in determining the energy); second, the error in determining the energy, $\delta(E_{\text{meas}}/E)$, must be independent of energy—otherwise, the measured spectra of particles would differ considerably from the true spectra [10].

Taking into account special features of the determination of energies from the emission angles of secondary particles and the aforementioned difficulties in this determination, we propose using a combined method that relies on a measurement of the emission angles both for charged and for the fastest neutral particles, on one hand, and which employs information about the energies of secondaries, on the other

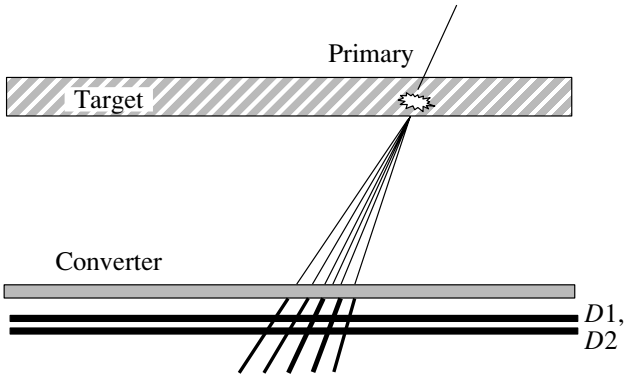

Fig. 1. Layout of the proposed array ($D1$ and $D2$ denote layers of coordinate-sensitive detectors).

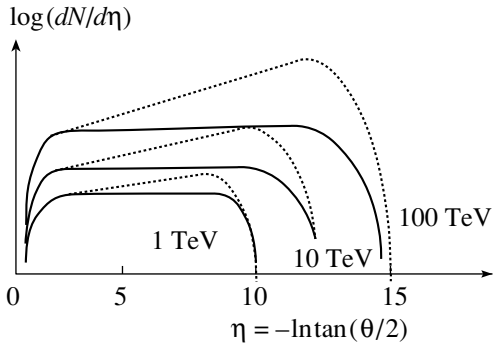

Fig. 2. Schematic representation of the emission-angle distribution of secondary particles (solid curves) before and (dotted curves) after the converter for 1-, 10-, and 100-TeV protons.

hand. The layout of the proposed array is displayed in Fig. 1.

The array in question consists of a target and a converter of photons in the form of a thin lead layer ($h \sim 1$–2 cm) placed at a certain distance from the primary-interaction vertex ($H \sim 20$ cm). A layer of coordinate-sensitive detectors that are capable of recording the number and the coordinates of charged particles (silicon microstrip detectors, which will be discussed below, can be used for such detectors) is proposed to be arranged underneath the converter.

A primary particle interacts in the target, where there arise secondary photons (from the decays of π^0 and η mesons) and singly charged particles of energy E^i. The converter transforms almost all secondary photons incident on this layer of matter into a narrow electron beam owing to a cascade multiplication in lead. The number of product electrons is proportional to $(E^i)^s$ (where s is the shower age, which is a function of the depth h and the energy E^i; $s = 0.1$–0.2 for $h = 1$–2 cm). Some of the charged particles incident on the converter interact within a thin lead layer, the multiplicity of secondaries from these interactions being logarithmically dependent on the energy E^i. As a result, the total number of singly charged particles (electrons, pions, kaons) below the converter, N_{after}, appears to be considerably greater than the number of particles before the converter, N_{before} ($N_{\text{after}} \sim N_{\text{before}}\, M(E^i, E, R)$). The coefficient of multiplication, $M(E^i, E, R)$ proves to be dependent on the primary-particle energy E and on the energies E^i of secondary particles; it is also dependent on the distance R from the shower axis, because the most energetic secondaries travel near the shower axis. The multiplication of particles is more intense at the center of a shower than at its periphery, with the result that the spatial density of particles changes upon traversing the converter. The mean value of M increases from 3.5 at 100 GeV to 20 at 1000 TeV. Figure 2 shows schematically the variation of the spatial density of secondaries, $dN/d\eta$, where $\eta_i = -\ln\tan(\theta_i/2)$. The fastest particles, which carry the bulk of the interaction energy and which, on the pseudorapidity scale, occur on the right wing of the distribution depicted in Fig. 2, have the largest coefficient of multiplication. The contribution of fast particles is emphasized by the converter, the shape of the distribution $dN/d\eta$ beginning to depend more sharply on energy.

The parameter S characterizing the pseudorapidity distribution of the density of the secondary-particle flux was introduced as

$$S(E_0) = \sum \eta_i^2 N_i,$$

where $\eta_i = -\ln\tan(\theta_i/2) \approx -\ln(r_i/(H/2))$; here, r_i is the distance between the shower axis and the ith coordinate-sensitive detector, which recorded N_i particles, while H is the distance between the plane of the coordinates of the coordinate-sensitive detectors and the particle-interaction vertex in the target. The shower axis is found by determining the maximum of the particle density. The parameter S suppresses sizably the contribution of slow particles (owing to the fact that the function in question is quadratic in pseudorapidity) formed as the result of a cascade process in the target nucleus, thereby remedying one of the flaws in Castagnoli's method.

Alternatively, S can be represented in the form

$$S = \sum \eta_i^2 N_i = \langle\eta^2\rangle N,$$

where N is the total multiplicity and $\langle\eta^2\rangle$ is related, by definition, to the variance of the distribution as $\sigma_\eta^2 = \langle\eta^2\rangle - \langle\eta\rangle^2$. The following features of the pseudorapidity distribution $dN/d\eta$ before the converter are known: the mean value $\langle\eta\rangle$ and the maximal value

$\eta_{\max}$ (which is proportional to the distribution width σ_η) grow logarithmically with increasing interaction energy [9]. The value of S above the converter must then depend on energy rather weakly, as $\ln^3 E$. However, the converter changes considerably the shapes of the functions $\langle\eta^2\rangle(E)$ and $\langle N\rangle(E)$ and, as a consequence, the shape of $\langle S\rangle(E)$. For primary protons of energy in the range between 100 GeV and 1 PeV, Fig. 3 shows the parameter S and the the total particle multiplicity N versus energy before and after the converter. It can be seen that, after the converter, the parameter S depends on the primary energy as a power-law function over the entire energy range under investigation, the exponent in this dependence being 0.7 to 0.8. The errors in Fig. 3 represent the root-mean-square deviation in determining the energy of an individual event. As can be seen from Fig. 3 (and as will be demonstrated below), it is virtually independent of energy, amounting to about 60%. Attempts at determining the energy by using only the energy dependence of the total multiplicity $N(E)$ yielded a poorer result—the error proved to be about 100%.

It should be noted that the functions $\langle S\rangle(E)$ and $\langle N\rangle(E)$ are much more gently sloping before than after the converter—it is the application of the converter that radically improves the result. Therefore, the proposed method can be considered as a combination of the kinematical and the burst method.

The method can be used to determine the energies of nuclei. In doing this, it is necessary to take into account some special features of nucleus–nucleus collisions. In the interactions of an incident nucleus having an atomic number A and an energy E_A with a target nucleus (carbon), only part of the nucleons of the incident nucleus , N_w, are involved in the interaction. The pseudorapidity distribution of secondary pions in the forward cone can be represented as the sum of the distributions for independent pC interactions at energy E_A/A (in accordance with the superposition model). The parameter $S(E_A/A)$ for primary nuclei will then differ from $S(E)$ for primary protons at a fixed energy per nucleon only by the factor N_w; that is,

$$S_A(E_A/A) = N_w S_p(E_p = E_A/A).$$

However, part of the noninteracted nucleons of the incident nucleus A, N_w, will be emitted in the form of light fragments and spectator nucleons whose transverse momenta are much lower than those of secondary pions. The spectator nucleons make a significant contribution to the right wing in the pseudorapidity distribution, but they cause virtually no change in the energy dependence of S. It is more difficult to estimate the contribution of fragments that have not suffered interactions in the converter, since the response of a microstrip detector is proportional to the square of the charge of a particle that traverses the detector. These effects can be taken into a account through a Monte Carlo simulation. Relevant calculations will be described in the next section.

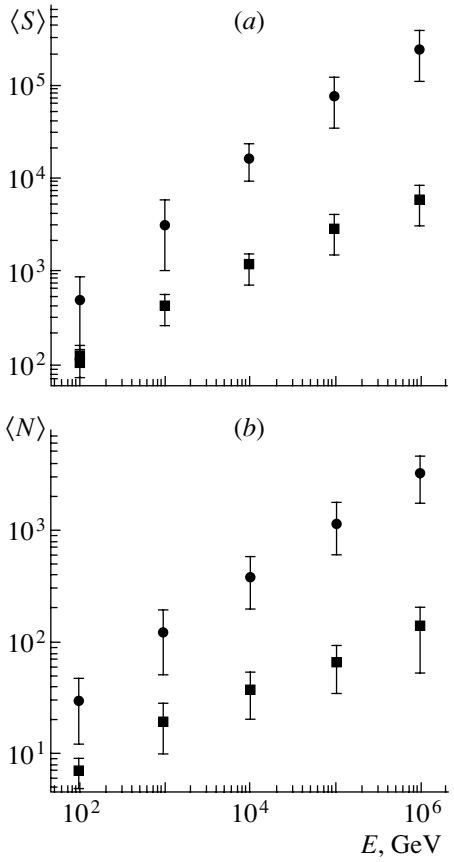

Fig. 3. (a) Parameter $\langle S\rangle(E) = \sum \eta_i^2 N_i$ and (b) total multiplicity $\langle N\rangle(E)$ versus the primary-proton energy (closed boxes) before and (closed circles) after the converter.

2. SIMULATION OF THE METHOD

The planned experiment was simulated with the aid of the GEANT package, which includes codes describing electromagnetic processes. Various generators were applied to treat hadron interactions. Originally, the FLUKA model was used a basic generator. Later on, this model was invoked only in describing hadron–nucleus interactions for energies below 50 GeV. High-energy hadron–nucleus and all kinds of nucleus–nucleus interactions were treated on the basis of the QGSJET model [11]. This code is tested by contrasting its predictions against collider data at laboratory energies up to about 500 TeV (the fragmentation region being excluded from this comparison) and is widely used in describing extensive atmospheric showers. It should be noted that QGSJET

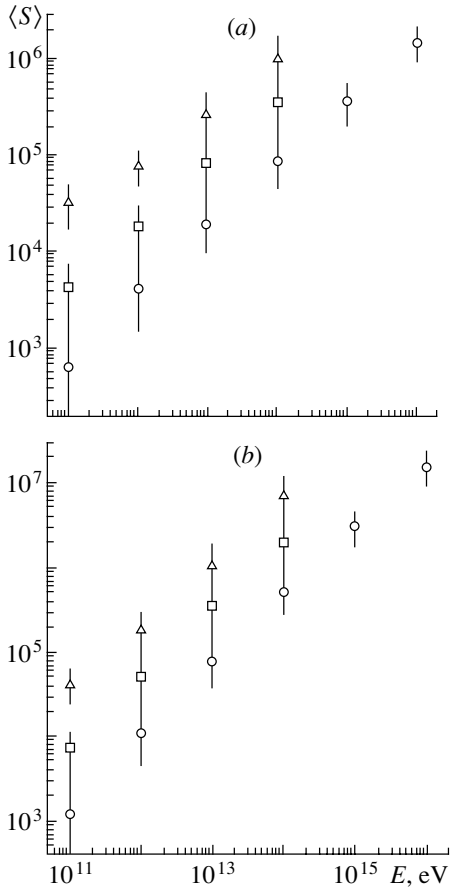

Fig. 4. Calibration dependences $\langle S\rangle(E)$ for (open circles) primary protons, (open boxes) carbon nuclei, and (open triangles) iron nuclei at the converter-thickness values of (*a*) 1 and (*b*) 2 cm.

reproduces fairly well the experimental pseudorapidity distributions of secondaries produced by colliding proton and antiproton beams of energies up to $\sim 10^{15}$ eV, this energy value being rescaled to the laboratory frame.

The QGSJET generator includes the production of nuclear fragments having various masses. The transverse momenta of these fragments were generated according to an exponential distribution, as was proposed in [12]. This is consistent with modern model concepts and available experimental data. In performing our simulation, we traced the tracks of electrons and photons whose energies were in excess of 10 keV, the threshold for other particles being 60 keV. In the version of the calculations that is described here, we chose the following values for the parameters of the array: the thickness of the graphite target was 10 cm, the converter thickness was 1 to 2 cm of lead, and the air gap between the target and the converter was 20 cm. The calculation was performed for the cases where protons, C nuclei, and Fe nuclei were vertically incident on the target. For a trigger, we took the requirement that more than four charged particles be produced between the target and the converter. The coordinates and the charges of particles at the upper plane of the converter and at the depths of 1 and 2 cm of lead were recorded in a database. In all, we obtained 15 groups, each containing, on average, 400 events: six groups of events for primary protons of energy ranging between 10^{11} and 10^{16} eV (one group per one order of magnitude of energy and analogously for other primary-nucleus species), five groups of events for carbon nuclei of energy 10^{11} to 10^{15} eV/nucleon, and four groups of events for iron nuclei of energy 10^{11} to 10^{14} eV/nucleon.

As was indicated above, the parameter $S(E) = \sum \eta_i^2 N_i$ was proposed for determining the energy. In this section, we consider a more general form of it, $S(E) = \sum \eta_i^k$, where k is varied from 1 to 4 and η_i is the pseudorapidity of the ith secondary particle at the level of detection; that is, we disregard the spatial resolution of detectors in analyzing the potential of the method. The calculations performed for various values of k revealed that, in the energy range being considered, an optimum reconstruction of energy on the basis of the parameter S for all types of nuclei simultaneously is accomplished at $k = 2$, provided that the converter thickness is 1 or 2 cm of lead. The dependences $S(E)$ are displayed in Figs. 4*a* and 4*b* for the converter thicknesses of 1 and 2 cm, respectively.

The accuracy of energy reconstruction is determined by the fluctuations of the parameter S used and by the slope of its dependence. For the power-law dependence $\langle S\rangle \sim E^\beta$, the relative error of the energy measurements is $\delta E = (1/\beta)\delta S$. At the converter thickness of 2 cm, the slope exponent β proved to be 0.80, 0.77, and 0.75 for incident protons, carbon nuclei, and iron nuclei, respectively. At the converter thickness of 1 cm, it appeared to be less by 0.1–0.15 for all species of incident nuclei. The resulting errors in determining the energy, $\delta(E_{\rm meas}/E)$, in an individual event are given in Table 1 for two versions of the converter. They are close, on average, to 60% for all nuclear species under investigation and are virtually independent of energy in the range 10^{11}–10^{16} eV per particle. No pronounced difference of these values between the cases of $h = 1$ and 2 cm has been revealed. The disintegration of heavy nuclear fragments in the converter upon their interaction with matter reduces fluctuations of the signal. In this respect, a converter of thickness $h = 2$ cm is preferable. For $h >$ 2 cm, however, the rate of photon multiplication in lead is much greater than the rate of charged-particle multiplication, in which case fluctuations associated with masking the contribution of charged particles may increase. In an actual array, we propose using a

Table 1. Errors in determining the energy, $\delta(E_{\text{meas}}/E)$, versus the type of the primary nucleus, the energy, and the converter thickness h

h, cm	Type of nucleus	Energy of the primary nucleus, eV/nucleon					
		10^{11}	10^{12}	10^{13}	10^{14}	10^{15}	10^{16}
1	p	0.67	0.70	0.63	0.57	0.57	0.61
1	C	0.73	0.68	0.71	0.72		
1	Fe	0.51	0.40	0.52	0.62		
2	p	0.72	0.69	0.61	0.55	0.56	0.60
2	C	0.69	0.70	0.67	0.69		
2	Fe	0.42	0.52	0.62	0.65		

converter of thickness 1 cm; for particles arriving at large angles, the effective thickness will then be about 2 cm.

An example of the distribution of events with respect to the reconstructed energy, $W(\log(E_{\text{meas}}/E))$, is given in Figs. 5*a* and 5*b* for primary protons and iron nuclei.

A feature peculiar to the method is that the distributions in question exhibit a pronounced asymmetry. A significant contribution to the fluctuations comes from the tail in the region of underestimated values of E_{meas}. The distributions displayed in Fig. 5 were obtained at a fixed primary energy; that is, they represent the probability $W(E, E_{\text{meas}})$ of assigning a particle of energy E the energy E_{meas}. In this case, the mean error in determining the energy on a logarithmic scale is $\delta(\log(E_{\text{meas}}/E)) = 0.46$, 0.49, and 0.54 for

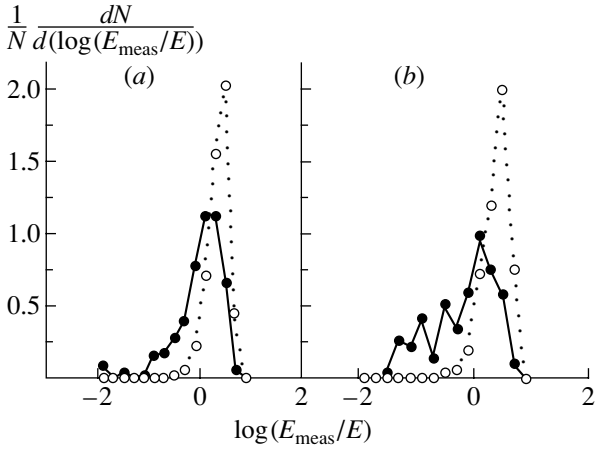

Fig. 5. Distribution of events with respect to $\log(E_{\text{meas}}/E)$ for (*a*) primary protons and (*b*) iron nuclei at a converter thickness of 2 cm. The closed and the open circles represent, respectively, the direct distribution function W and the inverse distribution function W^* that takes into account the a priori spectrum of particles.

protons, carbon nuclei, and iron nuclei, respectively. In measuring power-law spectra of particles, the inverse distribution function $W^*(E_{\text{meas}}, E)$ defined as the probability that, at a fixed measured energy E_{meas}, the true particle energy is E is of importance. According to the Bayes theorem, the direct and the inverse distribution function are related by the equation

$$W^*(E_{\text{meas}}, E) = W(E, E_{\text{meas}})F(E) \Big/ \int W(E, E_{\text{meas}})F(E)dE,$$

where $F(E)$ is the a priori spectrum of hadrons. If this a priori spectrum has a power-law form, $F(E) = E^{-\gamma}$, the contribution of small values of E_{meas}/E is suppressed in proportion to $(E_{\text{meas}}/E)^{\gamma-1}$. The inverse distribution function W^* is represented by the dotted curve in Fig. 5. It is much narrower than the direct distribution function W. The calculation by the above formula at $\gamma = 2.7$ yields $\delta(\log(E_{\text{meas}}/E)) =$ 0.22, 0.23, and 0.25 for protons, carbon nuclei, and iron nuclei, respectively.

In measuring monotonic power-law spectra of particles, the absolute error is not very important—the energy independence of the errors is quite sufficient [10]. In the case of uniform distribution functions depending only on the ratio E_{meas}/E, the measured spectrum is related to the true spectrum by the equation $F(E_{\text{meas}}) = \langle(E_{\text{meas}}/E)^{\gamma-1}\rangle F(E)$ [10]. If $\langle E_{\text{meas}}/E\rangle \sim 1$, the intensity of the measured spectrum is always higher than the intensity of the true spectrum.

A small error in determining the energy is necessary if some structures are presumed in the measured spectrum. In order to demonstrate measurements of a peak in the particle spectrum and of the knee region in the spectrum, the true particle spectra and the spectra that are measured by our method are presented in Figs. 6*a* and 6*b* with these features. For the sake of visual convenience, the spectra are multiplied by

Table 2. Errors in determining the energy, $\delta(E_{\text{meas}}/E)$, versus the type and the energy of the primary nucleus with allowance for the process of detection by strip detectors

Type of nucleus	Energy of the primary nucleus, eV/nucleon					
	10^{11}	10^{12}	10^{13}	10^{14}	10^{15}	10^{16}
p	0.77	0.71	0.62	0.62	0.54	0.54
C	0.75	0.69	0.72	0.78		
Fe	0.45	0.77	0.78	0.81		

$E^{2.7}$. As can be seen from Fig. 6, the structures of the spectra are reconstructed rather well. That the intensity of the measured spectrum of particles is higher by the factor $\langle(E_{\text{meas}}/E)^{\gamma-1}\rangle$ leads to a shift of the knee region and of the peak region—these effects, which are associated with the presence of fluctuations, can easily be taken into account in analyzing experimental data.

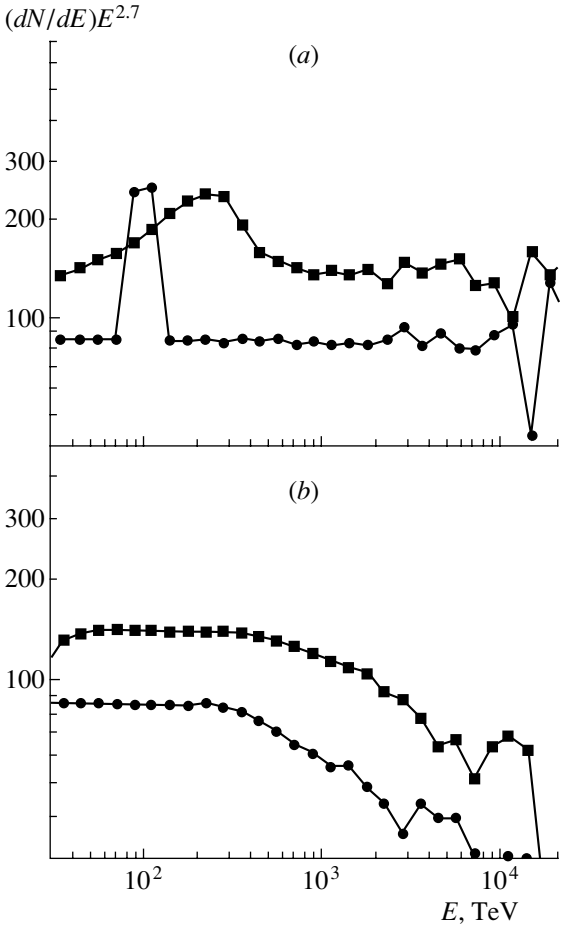

Fig. 6. Presumed spectra of primary cosmic rays with (*a*) a peak and (*b*) a knee (curves passing through closed circles) along with corresponding particle spectra measured by the method proposed here (curves passing through closed boxes).

3. POTENTIAL OF THE METHOD WITH ALLOWANCE FOR DETECTION PROCESSES

The above results refer to the case of an ideal instrument that can measure the coordinates of all secondary particles to as high a precision as is desired. There is, however, the question of whether the method is applicable in the case of actual instruments, where the detection procedure has a finite spatial resolution. The first question to be answered here is that of how the calibration dependence and the error in determining the energy change in this case. In order to avoid technical details, we performed a calculation for the case where the lateral distribution of secondaries is roughened to a considerable extent. We assumed that, under the converter, there are two layers of coordinate-sensitive detectors; that these layers are oriented orthogonally to each other in space; and that each of these consists of strips that have a thickness of 50 μm and a length equal to that of the entire array. The signal is read off each strip. Thus, the total ionization is fixed in each strip (as a matter of fact, it determines the number of secondaries that fall within this strip); that is, the lateral distribution of secondaries is integrated with respect to x and y. On average, the distributions of secondaries with respect to x and y are symmetric; therefore, two detector layers yield two independent measurements of the transverse density, whereby the accuracy in determining the energy is improved.

For the case being considered, the parameter S was modified: instead of the emission angle of

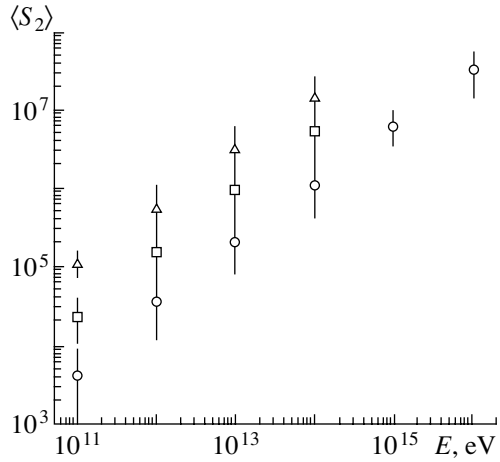

Fig. 7. Dependence $\langle S_2\rangle$ (E) for primary (open circles) protons, (open boxes) carbon nuclei, and (open triangles) iron nuclei that was obtained with allowance for the process of detection by coordinate-sensitive detectors.

a secondary particle, we took its projection onto the observation plane. Since $\eta_i = -\ln(\tan(\theta_i/2)) = \ln(2H/r_i)$, where H is the distance from the primary-interaction vertex to the detector plane and r_i is the distance between the secondary particle and the shower axis, the quantities $\phi_i^x = \ln(2H/x_i)$ and $\phi_i^y = \ln(2H/y_i)$, where x_i and y_i stand for the distance from the strip center to the shower axis along the respective coordinate, were chosen for new variables. For the analog of S, we can then take the parameter

$$S_2 = frac12\left(\sum \phi_i^x N_i + \phi_i^y N_i\right),$$

where N_i^x and N_i^y represent the number of particles that hit the strip (for each coordinate axis, the shower axis is found as the line that breaks down the number of particles into two equal parts). For the coordinate, we used the position of the midpoint of the relevant strip.

It turned out that the modified parameter S_2 averaged over the coordinates x and y is also a power-law function of energy, $\langle S_2\rangle(E) \sim E^\beta$. It is displayed in Fig. 7 for various types of primary nuclei. The exponents β in this power-law dependence proved to be very close ($\beta = 0.78$ for protons, $\beta = 0.79$ for carbon nuclei, and $\beta = 0.71$ for iron nuclei) to those obtained previously for the case where the coordinates of each secondary are recorded ($\beta = 0.80$ for protons, $\beta = 0.77$ for carbon nuclei, and $\beta = 0.75$ for iron nuclei). The direct distributions with respect to the energy reconstructed with the aid of the parameter S_2, $W(E_{\text{meas}}/E)$, also differ insignificantly from the distributions in Fig. 5, which were obtained without taking into account processes of detection by coordinate-sensitive detectors. A characteristic tail in the region of underestimated energies is present in this case as well, but, as was shown in the preceding section, it has only a modest effect on the actual accuracy of the method. The resulting values of the errors in determining the energy through the parameter S_2 are quoted in Table 2. On the logarithmic scale, they are (for the case where the exponent of the a priori spectrum is $\gamma = 2.7$) $\delta(\log(E_{\text{meas}}/E)) = 0.22$, 0.219, and 0.265 for protons, carbon nuclei, and iron nuclei. This indicates that, within the method being discussed the most pronounced fluctuations are associated with the physical fluctuations of the production of secondary particles in a nuclear interaction rather than with the method of detection.

The effect that errors introduced by microstrip detectors exert on the accuracy in determining the primary-particle energy was investigated here by using part of the statistics presented in [13]. It turned out that the calibration dependences $\langle S_2\rangle(E)$ and the errors in determining the energy have undergone virtually no changes. This can easily be understood by comparing the errors of the measurements with fluctuations of the multiplicities of secondary particles. The fraction of nonrelativistic particles after 2 cm of lead is still very small, so that the fluctuations that they introduce in the total ionization are insignificant. The fluctuations of the ionization for relativistic secondary particles can be estimated at 10 to 15%. Fluctuations that are introduced by electronics and detector noises are on the same order of magnitude. Therefore, the total contribution of all fluctuations of measurements does not exceed 20%; that is, it is negligibly small in relation to multiplicity fluctuations that are greater than 100% per strip.

4. APPLICABILITY RANGE OF THE METHOD

The proposed method for determining the primary-particle energy and the possible design of the respective array possess a fairly high potential for studying primary cosmic radiation in space-vehicle-borne experiments. Such an implementation of this procedure could solve many topical problems of astrophysics that have hitherto defied any attempt at tackling them by means of modern technologies. The dependence of a geometric factor on the weight of equipment that we have described is much more favorable than that in burst detectors of similar energy resolution. By way of example, we indicate that (see [14]) an array of weight 500 kg can have a geometric factor of about 3, whereas a burst detector of the same weight has a geometric factor that is approximately ten times smaller than that. With respect to the weight–aperture–dimension relationship, the equipment constructed on the basis of the ideas developed here would possess unique properties—none of the facilities known to date would be able to compete with it in what is concerned with detecting cosmic rays of energy in excess of 10^{12} eV. Moreover, the structure of the proposed equipment may admit its design in the form of separate modules; that is, one could construct a basic module of dimensions, say, $30 \times 30 \times 30$ cm^3 and weight about 40 to 50 kg and take this module beyond the atmosphere, whereupon the experiment in question would begin. Further, advancements toward higher energies are accomplished along with a gradual increase in the number of such modules in the orbit used. This principle of designing equipment would make it possible to take into account, to a maximum possible degree, the structural features of the space vehicle used and to facilitate the implementation of the respective cosmic experiments as a whole.

To conclude this section, we address the question of what the detectors of the proposed array would record if multiparticle-production events undergo an

abrupt change in the energy range 10^{15}–10^{16} eV (this hypothesis, which was put forth by S.I. Nikolsky, has been discussed for many years in cosmic-ray physics as the possible explanation of the knee in the spectrum of extensive air showers with respect to the number of electrons). As was suggested in [15], the emergence of a considerable number (about 50%) of proton interactions in which the multiplicity of charged secondary pions is 10^2 to 10^3 times greater than the mean multiplicities predicted by currently available models may be one of the possible scenarios of the above changes in multiparticle-production events. It is foreseen that the charge of a primary particle would be determined, to a very high precision, by silicon detectors positioned at the upper plane of the target (see Fig. 1). In relation to what is observed for heavy nuclei, which also generate events characterized by a very high multiplicity, the lateral distribution of low-energy secondary pions produced in proton interactions must be much narrower because of the difference in the energy per nucleon. This class of high-multiplicity events generated by a primary particle of small charge is easily identifiable. If an additional plane of strip detectors is arranged above the converter, the fraction of neutral pions produced in an anomalous nuclear-interaction event can be assessed on the basis of the relation between the multiplicity of secondaries above the converter and the multiplicity of secondaries below it.

CONCLUSION

The proposed method for determining the energy of particles of primary cosmic radiation on the basis of the lateral distribution of the secondary-particle-flux density makes it possible to construct arrays of large area and high sensitivity at a comparatively small weight of the array. The method is applicable to all nuclei of primary cosmic rays over a wide energy range (from 10^{11} to 10^{16} eV per particle). A fairly small error in determining the energy in an individual event [$\delta(\log(E_{\text{meas}}/E)) \sim 0.2$–$0.25$ for a measurement of power-law spectra of primary cosmic rays with a slope exponent of $\gamma \sim 2.5$–3.3] enables one to resolve some features of the spectra of primary cosmic rays (such as the presence of a knee in the spectrum and the existence of peaks). The proposed design of the detector will make it possible to single out the class of events that are characterized by an anomalously high multiplicity.

ACLNOWLEDGMENTS

This work was supported by the Russian Foundation for Basic Research (project nos. 99-02-17772 and 01-02-16611).

REFERENCES

1. T. Stanev, in *Proceedings of the 26th International Cosmic Ray Conference (ICRC), Salt Lake City, 1999* (American Inst. of Physics, Melville, 2000), p. 247.
2. N. L. Grigorov, G. P. Kakhidze, V. E. Nesterov, *et al.*, Kosm. Issled. **5** (3), 383 (1967).
3. I. P. Ivanenko, V. Ja. Shestoperov, *et al.*, in *Proceedings of the 23rd International Cosmic Ray Conference (ICRC), Calgary, Canada, 1993* (World Sci., New York, 1994), Vol. 2, p. 17.
4. K. Asakimory, T. H. Burnett, M. Cherry, *et al.*, Astrophys. J. **502**, 278 (1998).
5. V. I. Zatsepin, T. V. Lazareva, G. P. Sazhina, and N. V. Sokol'skaya, Yad. Fiz. **57**, 684 (1994) [Phys. At. Nucl. **57**, 645 (1994)].
6. RUNJOB Collab. (A.V. Apanasenko *et al.*), Izv. Akad. Nauk, Ser. Fiz. **65**, 433 (2001).
7. G. L. Bashindzhagyan, N. A. Korotkova, M. I. Panasuk, *et al.*, Preprint No. 99013/571, NIIYaF MGU (Institute of Nuclear Physics, Moscow State University, Moscow, 1999).
8. C. Castagnoli, Nuovo Cimento **10**, 1261 (1953).
9. V. S. Murzin and L. I. Sarycheva, *Multiple Processes at High Energies* (Atomizdat, Moskow, 1974).
10. V. S. Murzin, Yad. Fiz. **1**, 835 (1965) [Sov. J. Nucl. Phys. **1**, 599 (1965)].
11. N. N. Kalmykov, S. S. Ostapchenko, and A. I. Pavlov, Izv. Akad. Nauk, Ser. Fiz. **58** (12), 21 (1994).
12. J. Bellandi *et al.*, Prog. Theor. Phys. **83**, 58 (1990).
13. G. L. Bashindzhagyan *et al.*, Preprint No. 99-15/573, NIIYaF MGU (Institute of Nuclear Physics, Moscow State University, Moscow, 1999).
14. P. G. Bashindzhagyan *et al.*, Preprint No. 01-2/642, NIIYaF MGU (Institute of Nuclear Physics, Moscow State University, Moscow, 2001).
15. A. L. Shchepetov, F. P. Chubenko, and S. I. Nikol'skiĭ, in *Proceedings of the XXVI All-Russia Conference on Cosmic Rays, Dubna, 2000*.

Translated by A. Isaakyan

Physics of Atomic Nuclei, Vol. 65, No. 5, 2002, pp. 861–865. Translated from Yadernaya Fizika, Vol. 65, No. 5, 2002, pp. 893–897.

ELEMENTARY PARTICLES AND FIELDS
Experiment

Determination of Energies of Cosmic-Ray Nuclei in the Region above 1 TeV

I. D. Rapoport, A. N. Turundaevsky*, and V. Ya. Shestoperov

Institute of Nuclear Physics, Moscow State University, Vorob'evy gory, Moscow, 119899 Russia

Received March 5, 2001; in final form, July 16, 2001

Abstract—A method is proposed for measuring energies of particles in the region above 1 TeV. The method is based on detecting the greatest specific energy deposition in hadronic cascades propagating in dense matter. This makes it possible to improve accuracy in measuring energy by thin calorimeters in studying the energy spectra of high-energy cosmic rays at high altitudes. Attainable accuracies in measuring energy are considered for protons and He nuclei. The results of a relevant simulation are compared with the results of a satellite-borne experiment with Kosmos-1713 . © *2002 MAIK "Nauka/Interperiodica"*.

In the region of high energies (above 1 TeV), ionization calorimetry is the main method for determining the energies of particles [1]. Since the method requires large masses of absorbing substance, its application in high-altitude and space experiments is hindered. A common way to overcome this limitation has become the use of thin calorimeters, where only part of the hadronic cascade initiated by a primary particle is detected within an absorber of moderate dimensions [2]. In connection with advancements of balloon- and satellite-borne experiments toward ever higher energies, the problem of optimizing and refining the method remains important [3, 4].

A traditional approach to reconstructing the primary particle energy consists in measuring the energy E_b deposited in an absorber and in taking into account, on the basis of model concepts, its ratio to the primary energy, $K_b = E_b/E$. With allowance for fluctuations, this makes it possible to relate the required characteristics of the energy spectrum of particles to the detected spectrum of energy depositions. There is, however, every reason to believe that, if the quantity E_b, which is expressed as an integral of specific energy depositions detected in the absorber, is strongly correlated with the extremal value of the specific energy deposition, $K_m = (dE/dX)_{\max}$, the latter can serve as a rather sensitive alternative measure of the primary energy E.

Let us give a more precise definition of K_m for some particular cases. If the absorber thickness is sufficiently large, the cascade curve of specific energy depositions may have a few maxima owing to multiple inelastic particle interactions [5], which occur more frequently in the case of heavier primary nuclei, with a greater energy fraction being carried away by spectator nucleons. By choosing the maximum corresponding to the highest specific energy deposition in the case of cascade curves featuring many peaks, one can reduce fluctuations in relation to fluctuations of the inelasticity factor. If the absorber thickness is limited, the greatest of the specific-energy-deposition values realized in the absorber is taken for K_m.

In order to investigate the energy deposition at the cascade maximum and the possibility of employing this quantity in measuring energies, we performed a mathematical simulation of hadronic cascades initiated by protons and He nuclei in an iron and a lead absorber, relying on the GEANT package [6]. A comparative analysis of the results obtained with different codes generating inelastic hadron interactions (GHEISHA [6, 7], FLUKA [6, 8, 9], and QGSM [10, 11]) made it possible to assess the sensitivity of the calculations to model concepts. The maximum energy deposition is determined predominantly by the electromagnetic component generated in an inelastic interaction; the mean depth of the extremum in a cascade increases slowly with increasing primary-particle energy. In our analysis of cascade curves, a segment of 17 cascade units after the first inelastic interaction was traced in order to determine the maximum energy deposition. In studying the dependence of accuracy in measuring energies on the cascade depth, the segment under study was varied.

The mean values $\langle K_m \rangle$ obtained as the result of our simulation are displayed in Fig. 1 versus the energy of particles [(a) protons and (b) He nuclei] for an iron and a lead absorber. For the case of an iron absorber, the data calculated on the basis of a satellite-borne experiment that was implemented at Kosmos-1713 with the Sokol-2 equipment [12,

*e-mail: ant@eas.npi.msu.ru

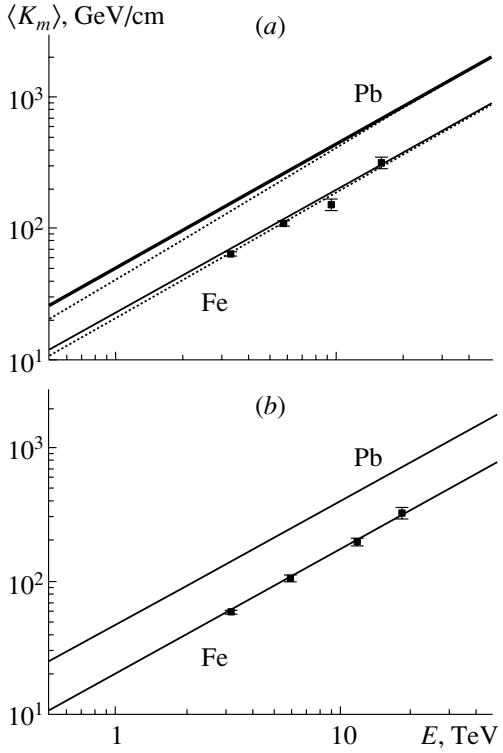

Fig. 1. Mean specific energy deposition at the maximum of the hadronic cascade, $\langle K_m\rangle = \langle (dE/dX)_{\max}\rangle$, versus the primary-particle energy E for (*a*) protons and (*b*) He nuclei in an iron and a lead absorber according to the calculations on the basis of (solid lines) the FLUKA and (dotted lines) the GHEISHA model (on the scale of the figure, the QGSM data are indistinguishable from the dependence computed with the aid of FLUKA). The displayed experimental points were obtained by processing the data reported in [12, 13].

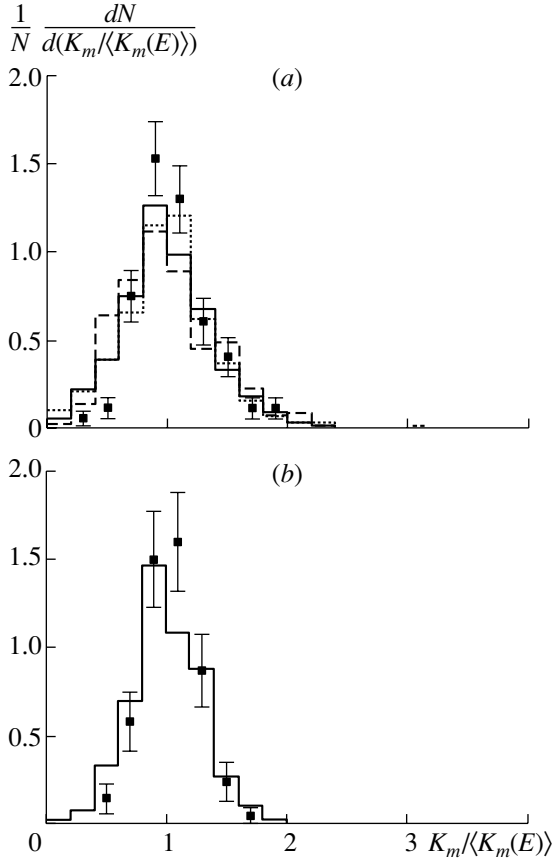

Fig. 2. Distribution of events with respect to the specific energy release $K_m/\langle K_m(E)\rangle$ at the maximum of a cascade initiated by (*a*) protons and (*b*) He nuclei according to the calculations based on (solid-line histrograms) the FLUKA, (dashed-line histogram) the GHEISHA, and (dotted-line histogram) the QGSM generators. The experimental points were obtained by processing the data reported in [12, 13].

13], transition effects [14] caused by the structure of the absorber being taken into account in this calculation, are also given in this figure for the sake of comparison. As can be seen from the data presented in Fig. 1, the different model concepts used in the calculations lead to close results, which agree with the experimental data within the statistical errors of the measurements. The dependence of $(dE/dX)_{\max}$ on the primary energy E for protons and He nuclei can be approximated by a linear ($\langle K_m\rangle = CE + c$) or a power-law ($\langle K_m\rangle = AE^a$) form, the fitted parameter values being quoted in Table 1. The parameter values were obtained for energies in the range 0.5–32 TeV. These approximations can be used to determine the primary energy by the formula $E = (K_m/A)^{1/a}$ or by the formula $E = (K_m - c)/C$.

Table 2 presents the values of the relative fluctuation $D(K_m) = \langle (K_m - \langle K_m\rangle)^2\rangle^{1/2}/\langle K_m\rangle$. They are weakly dependent on energy, and this makes it possible to compare K_m distributions computed at a fixed energy with generalized experimental data for a comparatively broad energy range. For an iron absorber, Fig. 2 displays the $K_m/\langle K_m(E)\rangle$ distribution for (a) primary protons or (*b*) primary He nuclei that was obtained with the aid of experimental data reported in [12, 13] and approximated by the expression $\langle K_m(E)\rangle = AE^a$ for $E > 2.5$ TeV. For the sake of comparison, the relevant results of a simulation at an energy of 8 TeV are displayed in the same figure.

From the data presented in Fig. 2, it follows that the energy deposition at the cascade maximum exhibits stronger fluctuations in lead than in iron. While the mean inelasticity factors differ by not more than 10% (see Table 3), the fluctuations of the partial inelasticity factor K_γ show more pronounced distinctions, which are due to a greater number of deep-inelastic interactions in the case of heavier nuclei [8] (a great many nucleons are involved, and the inelasticity factor is much larger than the mean value).

Table 1. Fitted values of the parameters in the approximation $\langle K_m \rangle = AE^a$ or $\langle K_m \rangle = CE + c$ of the mean energy deposition at the cascade maximum [$K_m = (dE/dX)_{\max}$, where E and K_m are given in TeV and GeV/cm, respectively; A is the mean energy deposition at $E = 1$ TeV]

Reaction	Model	A	a	C	c
pFe	FLUKA	22.9	0.941	19.4	2.7
	GHEISHA	20.9	0.961	18.9	1.5
	QGSM	23.6	0.938	19.9	2.8
	Experiment	19.7	0.949	16.1	13.3
HeFe	QGSM + FLUKA	20.4	0.937	17.1	2.4
	Experiment	18.7	0.948	13.5	22.7
pPb	FLUKA	49.6	0.952	43.5	4.5
	GHEISHA	41.3	1.008	42.1	−0.5
	QGSM	53.4	0.948	46.3	5.3
HePb	QGSM + FLUKA	47.5	0.933	39.7	5.7

Table 2. Relative fluctuation of the energy deposition at the cascade maximum, $D(K_m)$

Reaction	Model	E, TeV			
		0.5	2	8	32
pFe	FLUKA	0.37	0.36	0.38	0.38
	GHEISHA	0.41	0.40	0.40	0.39
	QGSM	0.38	0.38	0.39	0.38
HeFe	QGSM + FLUKA	0.30	0.30	0.30	0.29
pPb	FLUKA	0.48	0.49	0.48	0.52
	GHEISHA	0.56	0.62	0.63	0.63
	QGSM	0.46	0.52	0.52	0.62
HePb	QGSM + FLUKA	0.44	0.39	0.43	0.53

Table 3. Partial inelasticity factor K_γ

Reaction	Model	E, TeV				
		0.125	0.5	2	8	32
pC	FLUKA	0.182	0.182	0.179	0.194	0.194
	GHEISHA	0.127	0.143	0.159	0.183	0.179
	QGSM	0.166	0.173	0.175	0.175	0.178
pFe	FLUKA	0.201	0.201	0.199	0.203	0.202
	GHEISHA	0.140	0.152	0.178	0.187	0.196
	QGSM	0.197	0.200	0.196	0.209	0.201
pPb	FLUKA	0.207	0.203	0.203	0.209	0.214
	GHEISHA	0.163	0.173	0.182	0.205	0.210
	QGSM	0.226	0.233	0.226	0.230	0.233

In developing new ionization calorimeters, preference should therefore be given to a combination of a light target and a heavy absorber.

From Table 1, where the coefficients in the approximation of the quantity $\langle K_m(E) \rangle$ that were obtained on the basis of experimental data reported in [12, 13] are contrasted against the calculated values, we can see that the distinctions between the respective results are 15% for primary protons and 7% for primary He nuclei. These distinctions are commensurate with the errors in the experimental data from [13], which are used here.

For primary protons and He nuclei, Fig. 3 shows the energy spectra that were obtained from the data of the Sokol-2 experiment both by the traditional method on the basis of the total energy deposition in an iron absorber of thickness 85 cm and by the

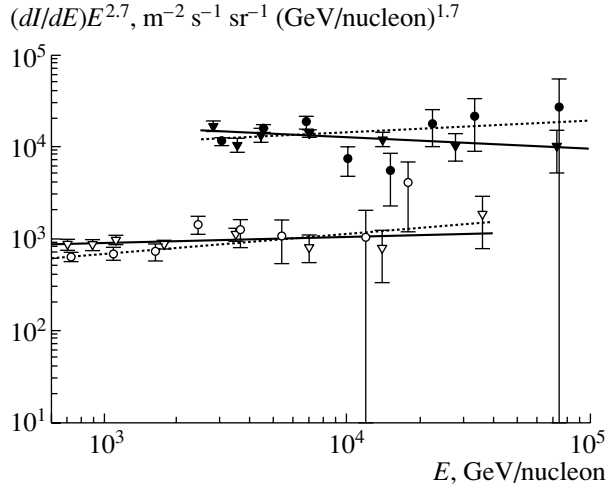

Fig. 3. Energy spectra of (closed symbols) protons and (open symbols) He nuclei as obtained by processing data from [12, 13] on the total energy deposition (the triangles and the solid line represent the experimental points and their power-law approximation) and on the specific energy deposition at the cascade maximum (the circles and the dashed line represent the experimental points and their power-law approximation).

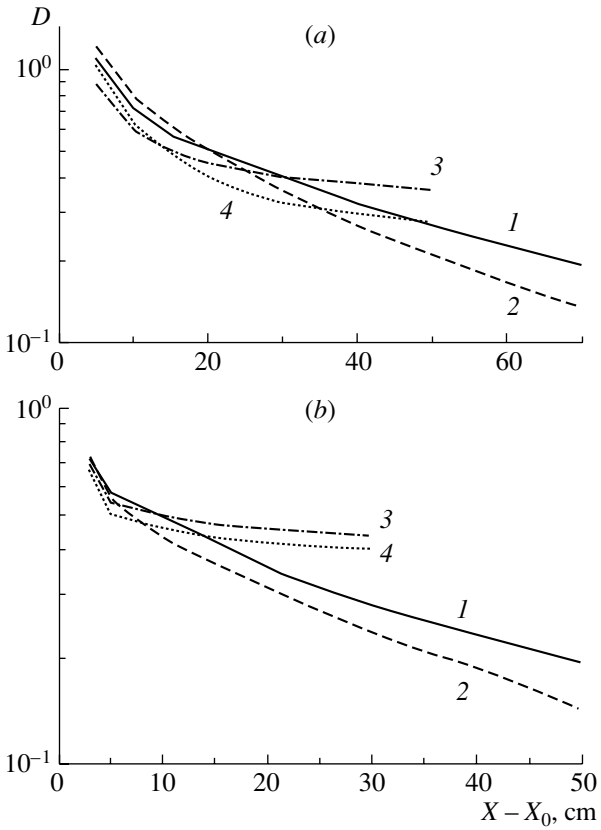

Fig. 4. Relative error in determining energy, $D(E)$, versus the depth of cascade development according to the total energy deposition [(*1*) protons and (*2*) He nuclei] and according to the maximum specific energy deposition [(*3*) protons and (*4*) He nuclei] at $E = 8$ TeV in (*a*) an iron and (*b*) a lead absorber.

proposed method on the basis of the specific energy deposition at a maximum (the maximum was determined over a segment of length 30 cm from the primary-interaction vertex). An analysis reveals that, within the statistical experimental errors, the two methods yield close results.

It is advisable to compare the relative root-mean-square deviation $D(E)$ for the case where the energy E was determined from the maximum energy deposition K_m with that for the case where this energy was determined from the total energy deposition E_b in an absorber. Such a comparison is illustrated in Fig. 4, where the quantities $D(E)$ are displayed versus the depth of a cascade initiated by protons or He nuclei of energy 8 TeV in (*a*) an iron or (*b*) a lead absorber. We can see that a determination of the energy E on the basis of the quantity K_m provides a higher accuracy at small depths of the cascade, where it grows, while its determination on the basis of the total energy release E_b is more accurate at large cascade depths. In the intermediate region, the methodological errors for the case of primary protons become equal at the depth of $L_{\mathrm{Fe}} = 30$ cm (16.8 cascade units from the proton-interaction vertex) in an iron absorber and at the depth of $L_{\mathrm{Pb}} = 10$ cm (17.7 cascade units) in a lead absorber. The relative errors of $D_{\mathrm{Fe}}(E) = 0.40$ and $D_{\mathrm{Pb}}(E) = 0.50$ in determining energy correspond to these depths. For primary He nuclei, the corresponding values are $L_{\mathrm{Fe}} = 35$ cm (19.6 cascade units) and $L_{\mathrm{Pb}} = 8$ cm (14.2 cascade units), with the relative errors being $D_{\mathrm{Fe}}(E) = 0.30$ and $D_{\mathrm{Pb}}(E) = 0.43$. The above intermediate region corresponds to the depth of the cascade maximum and is weakly dependent on the energy E.

The above description of the specific energy deposition at the maximum of a hadronic cascade initiated by high-energy particles, the results being slightly dependent on the model of inelastic interaction and being close (FLUKA, QGSM) to experimental data, makes it possible to use this quantity as a basis in a method for determining the energy of a primary particle in the region above 1 TeV to a precision higher than that of the traditional method at a cascade depth less than L_{Fe}. Owing to this, there arises the possibility of employing absorbers of smaller thickness (and, hence, of smaller mass) at a given accuracy in reconstructing the primary energy E. Another advantage of the proposed method for reconstructing the primary energy is that, in the case where the absorber is thin, the maximum specific energy release can be determined with one ionization detector arranged below the absorber, provided that the interaction vertex

is determined, for example, in a thin target above the absorber.

REFERENCES

1. N. L. Grigorov, V. S. Murzin, and I. D. Rapoport, Zh. Éksp. Teor. Fiz. **34** 506 (1958) [Sov. Phys. JETP **7**, 348 (1958)].
2. I. P. Ivanenko, D. M. Podorozhnyĭ, I. D. Rapoport, *et al.*, *Shower Theory* (Mosk. Gos. Univ., Moscow, 1996), p. 102.
3. T. G. Guzik, J. Adams, J. Ampe, *et al.*, in *Proceedings of 26th International Cosmic Ray Conference (ICRC 99), Salt Lake City, 1999* (American Inst. of Physics, Melville, 2000), Vol. 5, p. 9.
4. J. W. Watts, J. Lee, L. W. Howell, *et al.*, in *Proceedings of 26th International Cosmic Ray Conference (ICRC 99), Salt Lake City, 1999* (American Inst. of Physics, Melville, 2000), Vol. 5, p. 457.
5. A. I. Dem'yanov, V. S. Murzin, and L. I. Sarycheva, *Nuclear Cascade Process in Dense Matter* (Atomizdat, Moscow, 1977).
6. *GEANT User's Guide*, CERN DD/EE/83/1 (1983).
7. H. C. Fesefeldt, Technical Report PITHA 85-02 (III Physikalisches Institut, RWTH Aachen Physikzentrum, 1985).
8. J. Ranft and S. Ritter, Z. Phys. C **20**, 347 (1983).
9. A. Fasso, A. Ferrari, J. Ranft, *et al.*, Nucl. Instrum. Methods Phys. Res. A **332**, 459 (1993).
10. N. S. Amelin, K. K. Gudima, S. Yu. Sivoklokov, and V. D. Toneev, Yad. Fiz. **52**, 272 (1990) [Sov. J. Nucl. Phys. **52**, 172 (1990)].
11. N. S. Amelin, K. K. Gudima, and V. D. Toneev, Yad. Fiz. **51**, 512 (1990) [Sov. J. Nucl. Phys. **51**, 327 (1990)].
12. I. P. Ivanenko, I. D. Rapoport, V. Ya. Shestoperov, *et al.*, Preprint No. 89-29/106, NIIYaF MGU (Institute of Nuclear Physics, Moscow State University, Moscow, 1989).
13. I. P. Ivanenko, I. D. Rapoport, V. Ya. Shestoperov, *et al.*, Preprint No. 88-6/83, NIIYaF MGU (Institute of Nuclear Physics, Moscow State University, Moscow, 1988).
14. A. M. Kolchuzkin and V. I. Bespalov, in *Proceedings of 16th International Cosmic Ray Conference (ICRC), Kyoto, Japan, 1979,* Vol. 9, p. 222.

Translated by A. Isaakyan

Physics of Atomic Nuclei, Vol. 65, No. 5, 2002, pp. 866–876. Translated from Yadernaya Fizika, Vol. 65, No. 5, 2002, pp. 898–908.

ELEMENTARY PARTICLES AND FIELDS
Theory

Yang Effect in Multiparticle Hadron Production at the HERA Collider

A. V. Kisselev* **and V. A. Petrov****

Institute for High Energy Physics, Protvino, Moscow oblast, 142284 Russia

Received November 29, 2000; in final form, May 28, 2001

Abstract—It is argued that the mean multiplicities in a deep-inelastic process that are measured at the HERA collider grow with increasing photon virtuality at a fixed invariant mass of final hadron states. This is yet another piece of experimental evidence in favor of the qualitative hypothesis put forth by C.N. Yang and his colleagues and of the quantitative predictions obtained by the present authors on the basis of QCD.

1. INTRODUCTION

At present, the multiparticle production of hadrons in so-called hard scattering processes featuring one or two leptons in the initial state is being intensively investigated at modern colliders. The process of e^+e^- annihilation into hadrons is the simplest of such interactions. The total energy of colliding leptons, $\sqrt{s}$, simultaneously specifies the hardness (mass scale) of this collision, $Q = \sqrt{s}$. Therefore, the dependence of the features of final hadrons on the interaction-region dimension, which is proportional to $1/Q$, cannot be deduced unambiguously from the experimental observation that, in e^+e^- annihilation, the hadron multiplicities and the height of the hadron spectra grow with increasing $\sqrt{s}$.

Deep-inelastic lepton–nucleon scattering is characterized not only by the total energy W of the final hadron system but also by the square of the 4-momentum transfer, Q^2, from the lepton to this hadron system. By changing Q^2 at fixed W, one can study the effect of the dimensions of the hard-interaction region (in deep-inelastic scattering, they are also specified by $1/Q$) on the efficiency of hadron production. The mean multiplicity of charged hadrons in deep-inelastic scattering is the simplest and, at the same time, an important feature here.

In 1969, Yang and his collaborators (see [1]), who proceeded from the fragmentation pattern of high-energy multiparticle hadron production, made the following qualitative prediction concerning the particle yield (at fixed values of the energy W): "for larger values of the momentum transfer t, the breakup process favors larger multiplicities of hadrons."

For the first time, a quantitative theoretical description supporting this hypothesis[1)] was presented in [3, 4]. It was shown later that the calculations within QCD that were performed in [5] are in good agreement with the EMC experimental data from [6].

The objective of the present study is to apply the theoretical formulas that we derived previously to describing new data obtained by the H1 and ZEUS collaborations at the HERA collider for the mean multiplicities of charged hadrons in the current-fragmentation region [7–9]. Among other things, it will be demonstrated that these experimental data are in accord with the Yang hypothesis [1] and with our previous predictions for the dependence of the number of hadrons in deep-inelastic scattering on the momentum transfer (see the review article in [10]).

This article is organized as follows. In Section 2, we give a survey of the measurements of the Q^2 dependence of the mean multiplicity of charged hadrons by various groups of experimentalists and analyze the properties of the spectra and multiplicities in various reference frames. In Section 3, we present formulas that relate the hadron multiplicity in deep-inelastic scattering to the multiplicity of particles in e^+e^- annihilation and which reflect the fact that the mechanism of multiparticle hadron production is common to these two hard processes. Section 4 is devoted to describing quantitatively high-energy data from the HERA collider in terms of QCD formulas. In the Conclusion, we discuss our results.

* e-mail: kisselev@mx.ihep.su
** e-mail: petrov@mx.ihep.su

[1)] Considering that the ideas underlying this hypothesis were developed in various studies where Yang was always among the authors (see, for example, [2]), we deemed it appropriate to introduce the term "Yang effect."

2. Q DEPENDENCE OF THE MEAN MULTIPLICITY OF HADRONS (EXPERIMENT)

The first measurements of the mean number of charged hadrons, $\langle n\rangle^{\rm ch}$, in deep-inelastic e^-p collisions were performed 25 years ago by a group from Cornell University [11], who discovered a modest decrease in $\langle n\rangle^{\rm ch}$ with increasing Q^2. We note, however, that the energy W and the square of the momentum transfer, Q^2, were low ($3 < W^2 < 14$ GeV^2, $1.4 < Q^2 < 8$ GeV^2) in that experiment.

Later, the quantity $\langle n\rangle^{\rm ch}$ as a function of two variables W and Q^2 was measured in a number of neutrino experiments [12]. Rather large errors gave no way to draw definitive conclusions on whether there is a growth of the mean multiplicity of hadrons in deep-inelastic scattering (or there is no such growth).

A statistically significant effect of the growth of the mean multiplicity of charged hadrons, $\langle n\rangle^{\rm ch}(W, Q^2)$, in the variable Q^2 at fixed values of W was established in $\nu(\bar\nu)p$ and μ^+p deep-inelastic processes (see [13] and [6], respectively). By fitting their data in terms of a logarithmic dependence of the form

$$\langle n\rangle^{\rm ch}(W, Q^2) = a + b\ln W^2 + c\ln Q^2, \qquad (1)$$

the EMC collaboration obtained the following results [6] (with $\chi^2/{\rm NDF} = 26.0/22$):

$$a = -0.30 \pm 0.16, \quad b = 1.22 \pm 0.03, \qquad (2)$$
$$c = 0.22 \pm 0.06.$$

The growth with increasing Q^2 at fixed energy values from the interval $4 < W < 20$ GeV was observed for the total multiplicity—that is, for the multiplicity of hadrons emitted into the forward and into the backward hemisphere in the c.m. frame of the final hadron system:

$$\mathbf{p} + \mathbf{q} = 0. \qquad (3)$$

Here, $\mathbf{p}$ is the momentum of the target proton, while $\mathbf{q}$ is the momentum of a virtual photon (Z^0 boson).

A weak Q^2 dependence of the mean multiplicity of charged hadrons in deep-inelastic scattering that travel along the current direction in the c.m. frame was recently discovered in the energy range $7.5 < W < 30$ GeV at momentum-transfer-squared values in the intermediate region $0.15 < Q^2 < 20$ GeV^2 [14].

At energies of the HERA collider, the hadron multiplicity $\langle n\rangle_F^{\rm ch}(W, Q^2)$ in the current-fragmentation region in the c.m. frame [see Eq. (3)] was measured by the H1 collaboration [7]. The authors of [7] themselves indicated that, for the first time, they observed a fast growth of the mean multiplicity of charged hadrons traveling along the current direction. This effect is similar to the growth of the hadron multiplicity in a quark jet from e^+e^- annihilation, whence one can conclude that multiparticle hadron production in the different hard processes is governed by similar mechanisms.

That the H1 collaboration was the first, after the aforementioned EMC experiments, who measured the mean multiplicity of charged particles as a function of two variables is yet another important result of [7]. Figure 1, borrowed from that study, demonstrates the Q^2 dependence of $\langle n\rangle_F^{\rm ch}(W, Q^2)$ as obtained by integrating the spectrum with respect to the pseudorapidity η^* ($-5 < \eta^* < -1$) for four intervals of W.

The authors of [7] concluded that the multiplicity of particles in deep-inelastic scattering is independent of Q^2 at fixed W and presented fits to these data in terms of constants. By using, however, the more general phenomenological formula (1) to fit the H1 data, we obtained

$$a = -7.47, \quad b = 1.44, \quad c = 0.25. \qquad (4)$$

In this case, the value of $\chi^2/{\rm NDF}$ was as small as $2.72/13$. The fit with the fixed value of $c = 0$ led to a value that is about two times greater ($\chi^2/{\rm NDF} = 6.10/14$).

We note that the value in (4) for the coefficient c, which is a factor in front of $\ln Q^2$ in (1), appears to be very close to that which was obtained previously by the EMC collaboration at lower energies [see (2)]. The results of our fitting are shown in Fig. 1 by solid curves. In this fit, we used the data from Table 1, which were kindly placed at our disposal by the H1 collaboration.

In recent years, the results obtained by measuring, in deep-inelastic scattering, the mean number of hadrons in the current-fragmentation region are commonly given in the Breit frame [8, 9, 15] (see also the earlier studies in [16, 17]). In this frame, the proton and virtual-photon 4-momenta can be represented as (the positive direction of the z axis coincides with the direction of the target momentum p)

$$p = (Q/2x + M^2x/Q,\ 0,\ 0,\ Q/2x), \qquad (5)$$
$$q = (0,\ 0,\ 0,\ -Q),$$

where M is the proton mass and $x = Q^2/(W^2 + Q^2 - M^2)$ is the Bjorken variable. Hereafter, we use the notation $Q \equiv \sqrt{Q^2}$.

As we can see, the knock-on quark has the momentum $-Q/2$ in the Breit frame; that is, it moves in the direction of the current. At the same time, target fragments travel in the same direction as the proton

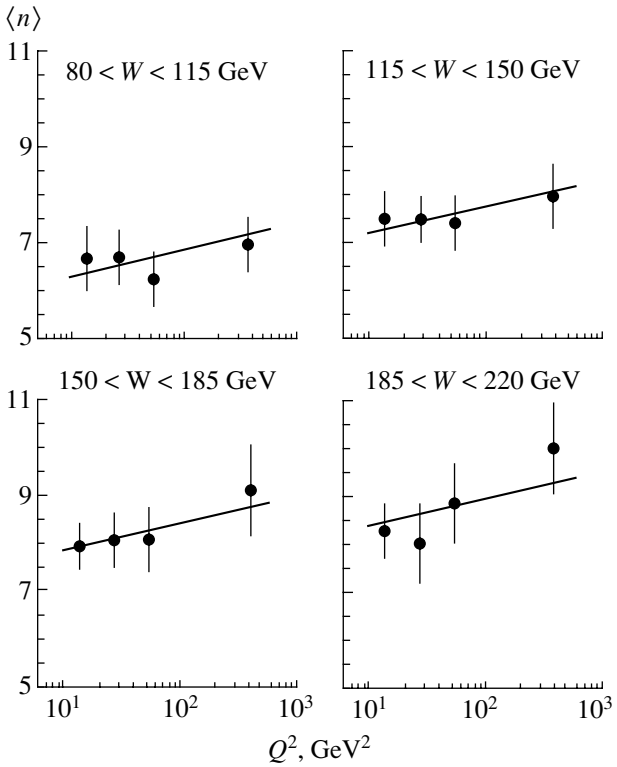

Fig. 1. Mean multiplicity of charged hadrons as a function of Q^2 for various intervals of W in the c.m. frame for pseudorapidities in the region $-5 < \eta^* < -1$: (points) data of the H1 collaboration [7] and (straight lines) results of fitting in terms of the function in (1).

with momenta up to $p_{z>0}^{\max} = Q(1-x)/2x$. However, the cut $p_{z>0}^{\max} = Q/2$ [8, 9] is applied in experiments.

In the following, we analyze the c.m. spectra of hadrons with respect to the rapidity, which we denote henceforth by y^*. In the c.m. frame, the current region for a particle of mass m_h is

$$-Y < y^* < 0, \tag{6}$$

where $Y = \ln(W/m_h)$ is the maximum magnitude of the rapidity. In the Breit frame, the current region is specified by the inequalities

$$-Y < y^* < -y_{\mathrm{B}}. \tag{7}$$

The quantity

$$y_{\mathrm{B}} = \frac{1}{2}\ln\left(\frac{1+v}{1-v}\right) \tag{8}$$

is defined in terms of the velocity v at which the Breit frame moves with respect to the c.m. frame:

$$v = |1-2x|. \tag{9}$$

At low x typical of the H1 and ZEUS experiments that measured the hadron spectra and multiplicities in deep-inelastic scattering, we can set

$$y_{\mathrm{B}} \simeq \frac{1}{2}\ln\left(\frac{1}{x}\right). \tag{10}$$

Thus, we can see that, in the Breit frame, the current region lies entirely in the domain of negative values of y^* and, as follows from (7) and (10), occupies the rapidity interval $\Delta y = \ln(Q/m_h)$.

As was noted above, the results on the mean multiplicity of charged hadrons from deep-inelastic scattering in the current region, $\langle n\rangle_F^{\mathrm{DIS}}$, at HERA energies are predominantly presented in the Breit frame versus the variable Q, often without indicating the value of x, another kinematical variable, since the dependence on it is assumed to be weak [8, 9]. The resulting growth of the mean multiplicity $\langle n\rangle_F^{\mathrm{DIS}}$ with Q is compared with the growth of half the mean multiplicity of charged hadrons from e^+e^- annihilation, $(1/2)\langle n\rangle^{e^+e^-}$, with increasing $\sqrt{s}$.

In such a comparison, it is implicitly assumed that the Q dependence of $\langle n\rangle_F^{\mathrm{DIS}}$ in the Breit frame is analogous to the W dependence of $\langle n\rangle_F^{\mathrm{DIS}}$ in the c.m. frame, whence it would follow that such a growth of the mean multiplicity of charged hadrons in the current region reflects the growth of the number of hadrons with energy in deep-inelastic scattering.

In this connection, we note that, if the spectrum of hadrons from deep-inelastic scattering had the form of a perfect plateau of height h, the mean "current"

multiplicity of hadrons would be equal to $h\ln(W/m_h)$ in the c.m. frame and to $h\ln(Q/m_h)$ in the Breit frame; that is, it would be given by the same expression apart from the substitution of Q for W (or vice versa) . However, the actual spectrum has a more complicated form. Moreover, both the position of its maximum with respect to the point $y^* = 0$ (see Section 3) and the boundary of the current region in the Breit frame, y_B (7), depend on the kinematical variables.

In Fig. 2, borrowed from [9], new ZEUS data on the mean multiplicity of charged hadrons in the current-fragmentation region are presented in the Breit frame. For the sake of comparison, the results of similar measurements in e^+e^- annihilation [18] (divided by two) and the results obtained in deep-inelastic scattering on a fixed target [19] are also given in this figure. The data are corrected in such a way as to take into account the contribution to the multiplicity from the products of K^0_S and Λ decays [9].

In the region $Q^2 > 80$ GeV^2, there is reasonably good agreement between the ZEUS data and data obtained in e^+e^- annihilation. At lower values of Q^2, the hadron multiplicity measured by the ZEUS collaboration is lower than the multiplicity in e^+e^- annihilation and the multiplicity in deep-inelastic scattering on the fixed target. We note that the data in Fig. 2 correspond to different values of the variable x.

Similar results were obtained by the H1 collaboration [8]. They are presented in Fig. 3, along with the ZEUS data of 1993 [17]. The values of the variable x that correspond to the experimental points in question were not indicated in the original study. The solid curve in Fig. 3 represents a fit to a vast body of e^+e^- data. Data on the number of hadrons in deep-inelastic scattering and those in e^+e^- annihilation disagree in the region $Q^2 < 100$ GeV^2. This disagreement cannot be attributed to the different flavor compositions in the two processes being considered—according to the estimates presented by the H1 collaboration [8], effects associated with a higher multiplicity in b-quark jets do not exceed 3%, while, according to [17], the contributions of heavy flavors lead to effects within the measurement errors.

The above disagreement stems from the fact that, in the process of e^+e^- annihilation into hadrons, the growth of $(1/2)\langle n\rangle^{e^+e^-}$ with increasing $\sqrt{s}$ is a dynamical effect (energy dependence of the particle yield), while, in deep-inelastic scattering, the growth of $\langle n\rangle_F^{\rm DIS}$ with Q in the Breit frame has both a dynamical and a kinematical origin (see above). Because of this, a direct comparison of these two physical quantities is not quite correct in our opinion.

Table 1. Mean multiplicity of charged hadrons as a function of Q^2 for various regions of W in the c.m. frame at η^* values from the interval $-5 < \eta^* < -1$ (H1 data)

W, GeV	$\langle W\rangle$, GeV	Q^2, GeV^2	$\langle Q^2\rangle$, GeV^2	$\langle n\rangle \pm$ stat. $\pm$ syst.
80–115	96.9	10–12	13.9	$6.63 \pm 0.10 \pm 0.53$
		20–40	27.6	$6.68 \pm 0.11 \pm 0.40$
		40–80	55.0	$6.24 \pm 0.13 \pm 0.46$
		200–1000	385.0	$7.02 \pm 0.22 \pm 0.37$
115–150	132.0	10–12	13.9	$7.49 \pm 0.09 \pm 0.48$
		20–40	27.6	$7.46 \pm 0.11 \pm 0.38$
		40–80	55.0	$7.42 \pm 0.15 \pm 0.41$
		200–1000	385.0	$8.00 \pm 0.23 \pm 0.46$
150–185	166.8	10–12	13.9	$7.92 \pm 0.09 \pm 0.43$
		20–40	27.6	$8.05 \pm 0.10 \pm 0.53$
		40–80	55.0	$8.08 \pm 0.17 \pm 0.56$
		200–1000	385.0	$9.12 \pm 0.33 \pm 0.51$
185–220	201.9	10–12	13.9	$8.29 \pm 0.11 \pm 0.47$
		20–40	27.6	$8.03 \pm 0.15 \pm 0.71$
		40–80	55.0	$8.84 \pm 0.22 \pm 0.60$
		200–1000	385.0	$10.04 \pm 0.36 \pm 0.59$

In order to verify the universality of multiparticle hadron production, it is necessary to measure the multiplicity $\langle n\rangle_F^{\rm DIS}(W, Q^2)$ in the c.m. frame as a function of two variables (at HERA energies, this was done in [7]) and to compare $(1/2)\langle n\rangle^{e^+e^-}(\sqrt{s})$ and $\langle n\rangle_F^{\rm DIS}(W, Q^2)$ at $W^2 = s$ for fixed values of Q^2. It is the quantity $W(\sqrt{s})$ that constrains the phase space of the final states (at the same time, Q^2 can have any value in deep-inelastic scattering).

3. SPECTRUM AND MULTIPLICITY OF HADRONS IN QCD

According to the theorem of the factorization of the inclusive spectrum in deep-inelastic scattering, the spectrum of hadrons can be represented in the form

$$\frac{dn^{\rm DIS}}{dy}(W, Q^2, y) \tag{11}$$
$$= \int_{x_0}^{1} \frac{dz}{z} w(x, z, Q^2) \frac{d\hat{n}}{dy}(W_{\rm eff}, y - y_0) + \frac{dn_0}{dy},$$

where $x_0 = x + (1 - x)(m_h/W)\exp(-y)$, y is the rapidity of the detected hadron, $d\hat{n}/dy$ is the hadron

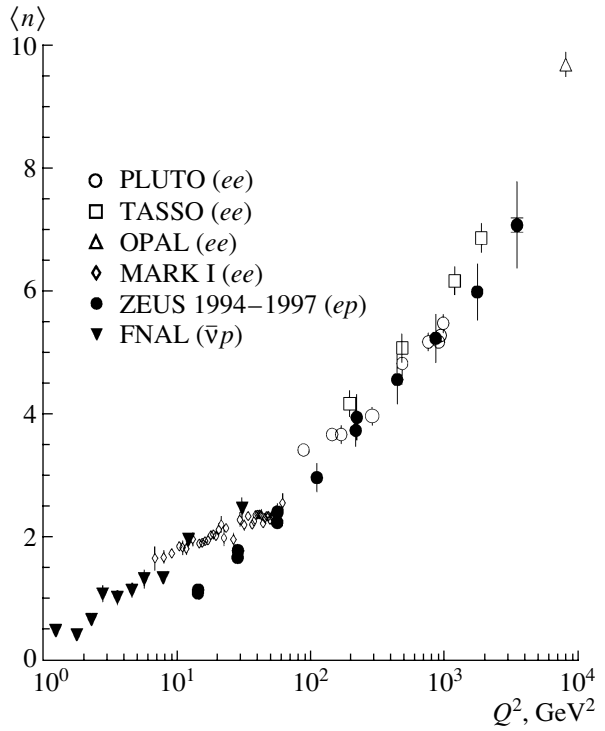

Fig. 2. Mean multiplicity of charged hadrons in the current-fragmentation region in the Breit frame [9]. Open symbols represent the results obtained in e^+e^- experiments [18] and divided by two; also shown are data on deep-inelastic scattering occurring on a fixed target (▼).

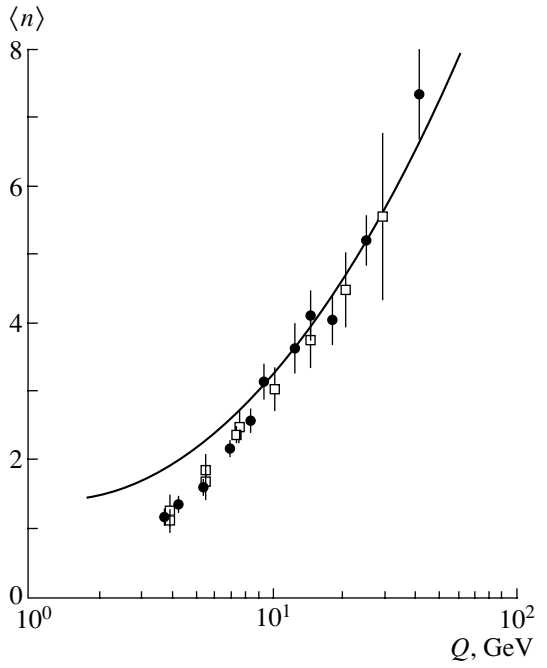

Fig. 3. Mean multiplicity of charged hadrons in the current-fragmentation region in the Breit frame: data from (closed circles) [8] and (open boxes) [17]. The curve represents a global fit to the entire body of e^+e^- data.

spectrum in the parton subprocesses, and dn_0/dy is the spectrum of the fragments of the proton target. At HERA energies, these fragments do not contribute to the multiplicity in the current region. Hereafter, the caret symbol "^" labels quantities referring to the parton subprocess. The quantities y_0 and $W_{\rm eff}$ will be defined and discussed in detail below [see Eqs. (15), (17)].

Accordingly, the mean multiplicity can be represented in the form

$$\langle n\rangle^{\rm DIS}(W,Q^2) \tag{12}$$
$$= \int\limits_{x_0}^{1} \frac{dz}{z} w(x,z,Q^2)\langle\hat{n}\rangle(W_{\rm eff}+\langle n_0\rangle).$$

At small values of x that are considered here, the weight function $w(x,z,Q^2)$ appearing in (11) and (12) has the form

$$w(x,z,Q^2) = D_g^q\left(\frac{x}{z},Q^2,Q_0^2\right) f_g(z,Q_0^2) \tag{13}$$
$$\times\left(\int\limits_{x_0}^{1}\frac{dz}{z}D_g^q\left(\frac{x}{z},Q^2,Q_0^2\right) f_g(z,Q_0^2)\right)^{-1}.$$

In (13), D_g^q denotes the distribution of the quark of virtuality Q^2 in the qluon of initial virtuality Q_0^2, while f_g is the distribution of this gluon (it plays the role of a target for the parton subprocess at low values of x) in the proton (the relevant details can be found in [10]).

For hadrons produced in the parton subprocess, the inclusive rapidity spectrum is symmetric in the c.m. frame of this subprocess; that is,

$$z\mathbf{p}+\mathbf{q}=0, \tag{14}$$

where z is the target-proton-momentum fraction carried away by the initial gluon (of virtuality Q_0^2). This is additionally corroborated by recent measurements of final hadron states in diffractive deep-inelastic scattering [20] versus the invariant mass of the diffracting system in its c.m. frame.

The reference frame specified by Eq. (14) moves at the rapidity

$$y_0 = -\frac{1}{2}\ln\left(\frac{1-x}{1-z}\right) \tag{15}$$

with respect to the reference frame specified by Eq. (3). In the c.m. frame of deep-inelastic scattering [see Eq. (3)], the rapidities of the hadrons produced in the parton subprocess therefore fall within the interval

$$-\hat{Y} < y^* - y_0 < \hat{Y}, \tag{16}$$

where $\hat{Y} = \ln(W_{\text{eff}}/m_h)$ and the quantity

$$W_{\text{eff}}^2 = \frac{z-x}{1-x}W^2 \qquad (17)$$

determines the square of the invariant mass available for particle production in the parton subprocess.

Thus, the position of the maximum of the inclusive rapidity spectrum of hadrons is controlled by the mean value of y_0. In turn, the quantity $\langle y_0\rangle = \langle y_0\rangle(Q^2)$ is determined both by perturbative effects associated with the emission of massive gluon jets from the target parton before the hard interaction with the photon and by nonperturbative effects associated with the distribution of low-virtuality partons in the nucleon [4].

At asymptotically high values of Q^2, we have [4]

$$\langle y_0\rangle(Q^2 \gg \Lambda^2) \sim -\frac{1}{\ln(\ln Q^2)}. \qquad (18)$$

Such a weak dependence of $\langle y_0\rangle$ on Q^2 is directly related to a slow growth of the QCD evolution parameter

$$\xi = \frac{2}{\beta_0}\ln\left(\frac{\alpha_s(Q_0^2)}{\alpha_s(Q^2)}\right), \qquad (19)$$

since the quantity $\langle y_0\rangle$ [4] is expressed in terms of this parameter [in (19), $\beta_0 = 11 - 2N_f/3$, where N_f is the number of flavors, is the β function in the lowest order in the coupling constant]. In the asymptotic regime, we have $\xi \sim \ln(\ln Q^2)$.

At moderate values of Q^2, the Q^2 dependence of $\langle y_0\rangle$ is steeper. These circumstances are of importance for understanding the qualitative features of the behavior of the mean multiplicity of hadrons emitted into the backward hemisphere in the Breit frame (see Figs. 2, 3).

As can be seen from (11) and (12), the inclusive spectrum and multiplicity in the parton subprocess depend on the effective energy W_{eff} (17) but not on W (the total energy of the final hadron system, which includes the products of target disintegration). According to the estimates presented in [3, 4],

$$\langle W_{\text{eff}}^2 \simeq \kappa(Q^2)W^2. \qquad (20)$$

At available values of Q^2, the factor $\kappa(Q^2)$ in (20) is much smaller than unity; it increases slowly with Q^2, approaching unity only in the asymptotic limit.

That $\langle W_{\text{eff}}^2\rangle$ (20) depends on Q^2 at a fixed value of the energy W is an important circumstance, which eventually leads to the aforementioned Q^2 dependence of the mean hadron multiplicity in the c.m. frame of deep-inelastic scattering. Thereby, the hypothesis of Yang *et al.* [1] that the particle yield grows with increasing momentum transfer (at a fixed energy of the process) is confirmed by QCD calculations [3–5, 10].

The relationship between the total multiplicities in the two hard processes was established in [3, 4, 21]—namely, the mean number of hadrons in deep-inelastic scattering is given by the expression for the mean number of hadrons in e^+e^- annihilation (apart from corrections decreasing with Q^2):

$$\langle\hat{n}\rangle(\hat{W}, Q^2) \simeq \langle n\rangle^{e^+e^-}(\sqrt{s} = \hat{W}). \qquad (21)$$

Formulas (12) and (21), which were obtained on the basis of QCD, proved to be in perfect agreement with data that the EMC collaboration presented shortly afterward for the Q^2 dependence of the mean multiplicity of charged hadrons [6] and made it possible to describe successfully these data [5].

Concurrently, we made the following predictions for the behavior of $\langle n\rangle^{\text{DIS}}(W, Q^2)$ at high energies [10]:

(i) The growth of the mean multiplicity of hadrons with W has the same physical nature as in e^+e^- annihilation.

(ii) Owing to the smallness of the ratio W_{eff}/W, the mean multiplicity in deep-inelastic scattering is expected to vary in proportion to $\ln W^2$ up to energies of $W \sim 40$–45 GeV. At higher energies, the mean multiplicity $\langle n\rangle^{\text{DIS}}$ will begin to grow fast, precisely in the same way as $\langle n\rangle^{e^+e^-}$ does at energies in the region $W > 10$ GeV.

(iii) The Q^2 dependence of the mean multiplicity $\langle n\rangle^{\text{DIS}}$ will remain numerically weak at high energies inclusive.

The predictions in items (i) and (ii) were recently corroborated by the data obtained at the HERA collider. In the experimental study reported in [7], it was indicated that "the HERA data confirm, for the first time in DIS lepton–proton scattering, the faster than linear growth of $\langle n\rangle$ with $\ln W$, a feature already well-known from e^+e^- annihilation ... and expected in perturbative QCD."

As to the Q^2 dependence of the hadron yield in deep-inelastic scattering, it was discussed in detail in the preceding section. Although the authors of [7] themselves assumed that their data can be described in terms of constants, the results of fitting in (4) are indicative of a slow growth of $\langle n\rangle_F^{\text{DIS}}$ with increasing momentum transfer; numerically, this growth is very close to that which was obtained by the EMC collaboration [formulas (1), (2)].

In the next section, we will demonstrate that our theoretical formulas also make it possible to describe the set of high-energy data presented by H1 [7] and ZEUS [9].

Table 2. Mean multiplicity of charged hadrons in the current-fragmentation region in the Breit frame (ZEUS data)

No.	$\langle Q^2\rangle$, GeV^2	x	$\langle n\rangle \pm$ stat. $\pm$ syst.
1	14.0	$(6.0–12.0)\times10^{-4}$	$1.13\pm0.01\pm0.05$
2	14.1	$(1.2–2.4)\times10^{-3}$	$1.18\pm0.01\pm0.04$
3	27.9		$1.70\pm0.01\pm0.07$
4	55.3		$2.27\pm0.01\pm0.07$
5	28.0	$(2.4–10.0)\times10^{-3}$	$1.81\pm0.01\pm0.06$
6	55.9		$2.44\pm0.01\pm0.14$
7	110.0		$3.00\pm0.01\pm0.23$
8	216.0		$3.77\pm0.02\pm0.26$
9	221.0	$(1.0–5.0)\times10^{-2}$	$3.98\pm0.02\pm0.37$
10	443.0		$4.59\pm0.03\pm0.40$
11	863.0		$5.26\pm0.05\pm0.39$
12	1766.0	0.025–0.15	$6.01\pm0.05\pm0.46$
13	3507.0	0.05–0.25	$7.10\pm0.11\pm0.69$

4. HADRON MULTIPLICITY IN THE CURRENT-FRAGMENTATION REGION

In the parton subprocess, the parton spectrum $\bar{D}^h$ with respect to the variable

$$\zeta = \ln\left(\frac{W}{E_h}\right), \tag{22}$$

where E_h is the energy of the detected particle, was calculated with allowance for nonleading corrections in [22]. The result was

$$\bar{D}^h(W,\zeta) = \frac{N}{\sigma\sqrt{2\pi}}\exp\left[\frac{1}{8}k + \frac{1}{2}s\delta - \frac{1}{4}(2+k)\delta^2 + \frac{1}{6}s\delta^3 + \frac{1}{24}k\delta^4\right]. \tag{23}$$

The quantity N in (23) is the normalization factor in the variable ζ.

The mean value of ζ and its variance (which we denote by ζ_0 and σ, respectively) are given by [22]

$$\zeta_0 = \frac{1}{2}\tau\left(1+\frac{\rho}{24}\sqrt{\frac{48}{\beta_0\tau}}\right)\left(1-\frac{\omega}{6\tau}\right), \tag{24}$$

$$\sigma = \sqrt{\frac{\tau}{3}}\left(\frac{\beta_0\tau}{48}\right)^{1/4}\left(1-\frac{\beta_0}{64}\sqrt{\frac{48}{\beta_0\tau}}\right)\left(1+\frac{\omega}{8\tau}\right),$$

where $\tau = \ln(W/\Lambda)$ (Λ is the QCD parameter); we also have

$$s = -\frac{\rho}{16}\sqrt{\frac{3}{\tau}}\left(\frac{48}{\beta_0\tau}\right)^{1/4}\left(1+\frac{\omega}{4\tau}\right), \tag{25}$$

$$k = -\frac{27}{5\tau}\left(\sqrt{\frac{\beta_0\tau}{48}}-\frac{\beta_0}{24}\right)\left(1+\frac{5\omega}{12\tau}\right),$$

$$\delta = \frac{\zeta-\zeta_0}{\sigma}.$$

In (24) and (25), we have introduced the following notation: $\rho = 11 + 2N_f/27$ and $\omega = 1 + N_f/27$.

At $\zeta \ll Y$, the variable ζ and the rapidity in the c.m. frame are related as

$$y^* \simeq Y - \zeta. \tag{26}$$

Relying on the hypothesis of local parton–hadron duality [23]—it was well justified by experiments—and taking into account the aforesaid (see Section 3), we find that the spectrum of hadrons in the parton subprocess with respect to the rapidity in the c.m. frame can be represented in the form

$$\frac{d\hat{n}}{dy^*}(W_{\rm eff}, y^*) = n^{e^+e^-}(W_{\rm eff})\bar{D}^h(W_{\rm eff}), y^* - y_0), \tag{27}$$

where y_0 and $W_{\rm eff}$ are given by (15) and (17), respectively. The spectrum in (27) is normalized to the multiplicity of hadrons in e^+e^- annihilation according to Eq. (21), which relates the hadron multiplicities in the two hard processes.

Let us try to find out which qualitative predictions for the Q and x dependences of the mean multiplicity in the current region in the Breit frame can be made without resort to specific expressions for the spectrum on the right-hand side of (27).

We first fix x and assume that $Q_2 > Q_1$, in which case $W_2 > W_1$; hence, the height of the spectrum is greater in the first than in the second case. On the other hand, the position of the center of the rapidity spectrum is shifted, as was indicated in Section 3, toward the point $y^* = 0$. At high values of Q, this effect is negligible [see (18)], and we have a growth of the mean hadron multiplicity with Q because of an increase in the energy W, this being in perfect analogy with the growth of $n^{e^+e^-}(Q)$.

At moderate values of Q, the shift of the spectrum with respect to the point $y^* = 0$ is more pronounced. Since the boundary of the current region in the Breit frame as given by (7) depends only on x [see Eq. (10)] and is identical in the two cases, we conclude that, in the second case, the shift of the spectrum reduces the multiplicity (as if the spectrum moves upon the point $-y_{\rm B}$). As a result, it is natural to expect a faster decrease in the multiplicity $n_F^{\rm DIS}$ in relation to the behavior of $n^{e^+e^-}$ in the region of intermediate and low values of Q, and this is confirmed by the data obtained at the HERA collider (see Figs. 2, 3).

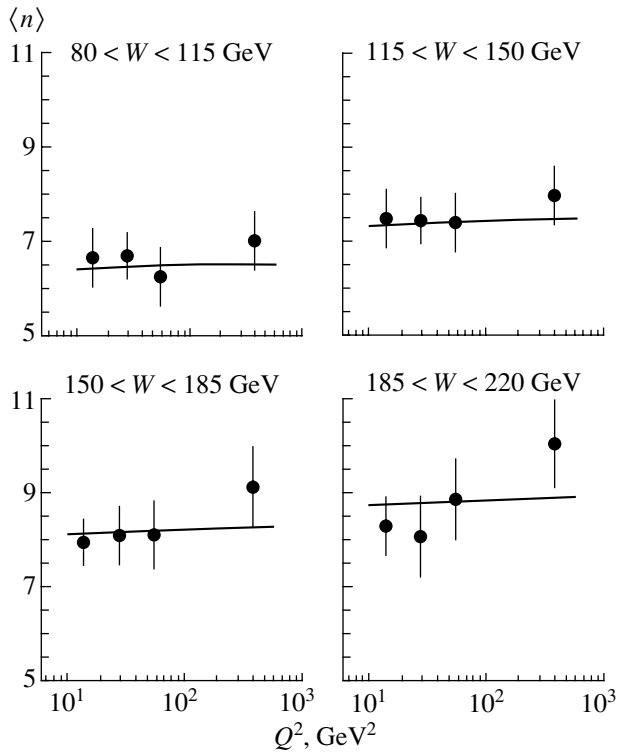

Fig. 4. Mean multiplicity of charged hadrons in the current region in the c.m. frame as a function of Q^2 for various intervals of the energy W. The H1 data (closed circles) were taken from Table 1. The curves were obtained with the aid of the formulas presented in the main body of the text.

We now fix Q and assume that $x_2 > x_1$, in which case $W_2 < W_1$. This leads to a decrease in n_F^{DIS} in the second case. The position of the spectrum does not change since it is determined by the variable Q^2. Further, it follows from (10) that $y_{\mathrm{B}}^2 < y_{\mathrm{B}}^1$. In other words, the current region (that is, the rapidity region over which we must integrate the spectrum in order to determine n_F^{DIS}) becomes broader, which yields an increase in the multiplicity.

Thus, there are two mechanisms affecting, at fixed values of Q, the x dependence of the mean number of hadrons in opposite directions. We can predict a mutual compensation of these effects and, as a consequence, a numerically weak growth of n_F^{DIS} as the kinematical variable x increases.

Experimental data confirm this. In Table 2, we display the ZEUS data borrowed from Tables 1 and 2 of [9]. It is sufficient to compare, in a pairwise manner, the following data sets characterized by nearly identical Q^2 but different x: $(1,2)$, $(3,5)$, $(4,6)$, and $(8,9)$. We can see that, at fixed Q^2, the possible decrease in the multiplicity with increasing x (that is, with decreasing W) is almost completely compensated by its growth owing to the broadening of the current region in the Breit frame.

In order to describe quantitatively the experimental data, we need, in addition to relation (27), a specific expression for the hadron multiplicity $n^{e^+e^-}(\sqrt{s})$, as

Table 3. Mean multiplicity of charged hadrons in the current-fragmentation region in the Breit frame (the ZEUS data from Table 2 are grouped according to the intervals of the energy W)

No.	W, GeV	$\langle W\rangle$, GeV	$\langle Q^2\rangle$, GeV^2	$\langle n\rangle \pm$ stat. $\pm$ syst.
2	67.2–95.0	84.1	14.1	$1.18 \pm 0.01 \pm 0.04$
5			28.0	$1.81 \pm 0.01 \pm 0.06$
6			55.9	$2.44 \pm 0.01 \pm 0.14$
9			221.0	$3.98 \pm 0.02 \pm 0.37$
1	121.5–141.0	131.3	14.0	$1.13 \pm 0.01 \pm 0.05$
3			27.9	$1.70 \pm 0.01 \pm 0.07$
7			110.0	$3.00 \pm 0.01 \pm 0.23$
10			443.0	$4.59 \pm 0.03 \pm 0.40$
12			1766.0	$6.01 \pm 0.05 \pm 0.46$
13			3507.0	$7.10 \pm 0.11 \pm 0.69$
4	169.6–186.7	177.2	55.3	$2.27 \pm 0.01 \pm 0.07$
8			216.0	$3.77 \pm 0.02 \pm 0.26$
11			863.0	$5.26 \pm 0.05 \pm 0.39$

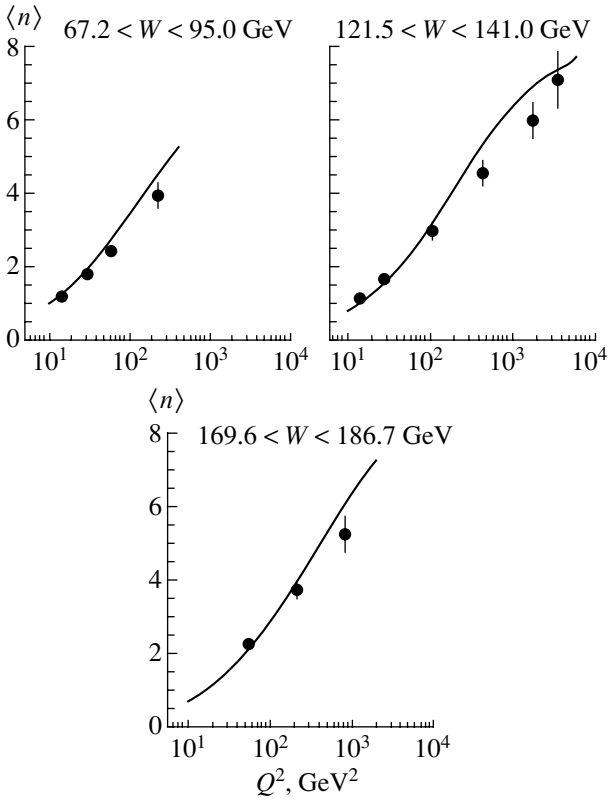

Fig. 5. Mean multiplicity of charged hadrons in the current-fragmentation region in the Breit frame as a function of Q^2. The experimental points displayed here were borrowed from [9]. The curves represent our predictions based on the formulas given in the main body of the text.

well as the quark distribution at low x and the distribution $f_g(z, Q_0^2)$ of a gluon of initial virtuality Q_0^2 in the proton [more precisely, the behavior of $f_g(z, Q_0^2)$ for $z \to 1$ is of importance for our calculations].

For the quark distribution, it is convenient to choose the analytic expression obtained in [24]; that is,

$$D_g^a(z, Q^2) \sim rI_1(t)\exp(-d\xi/2), \qquad (28)$$

where I_1 is a modified Bessel function of the first kind and where the variable t is defined in terms of the QCD evolution parameter ξ (19) as

$$t = 2\sqrt{6\xi \ln\left(\frac{1}{z}\right)}. \qquad (29)$$

We have also introduced the following notation: $r = -t/(2\ln z)$ and $d = \beta_0 + 20N_f/27$.

The parton distributions calculated in [24] satisfy the ordinary evolution equations [25] and describe well experimental data at low values of x over a broad interval of Q^2.

For the initial gluon distribution in the proton for $z \to 1$, we choose the commonly accepted power-law behavior; that is,

$$f_g(z, Q_0^2)|_{z\to 1} = A(1-z)^{n_g}, \qquad (30)$$

where A is an insignificant constant, which drops out from the expression for the multiplicity.

For the mean multiplicity of charged hadrons originating from e^+e^- annihilation, we use different expressions in the low- and the high-energy region. This is because the mean value of the effective energy W_{eff} (20) can be small despite high values of the total energy W. From early experiments that measured the hadron multiplicity in e^+e^- annihilation, it is well known that, for $\sqrt{s} < 7$–10 GeV, the multiplicity $\langle n\rangle^{e^+e^-}(\sqrt{s})$ grows logarithmically with $\sqrt{s}$. For $\sqrt{s} < 10$ GeV, we therefore choose the fit from [26]:

$$\langle n\rangle^{e^+e^-}(\sqrt{s}) = 2.67 + 0.48\ln s. \qquad (31)$$

For $\sqrt{s} > 10$ GeV, we use the expression

$$\langle n\rangle^{e^+e^-}(\sqrt{s}) = -1.66 + 0.866\exp(1.047\sqrt{\ln s}), \qquad (32)$$

which was presented in [27] and which is based on QCD calculations, because it describes well e^+e^- data up to LEP energies.

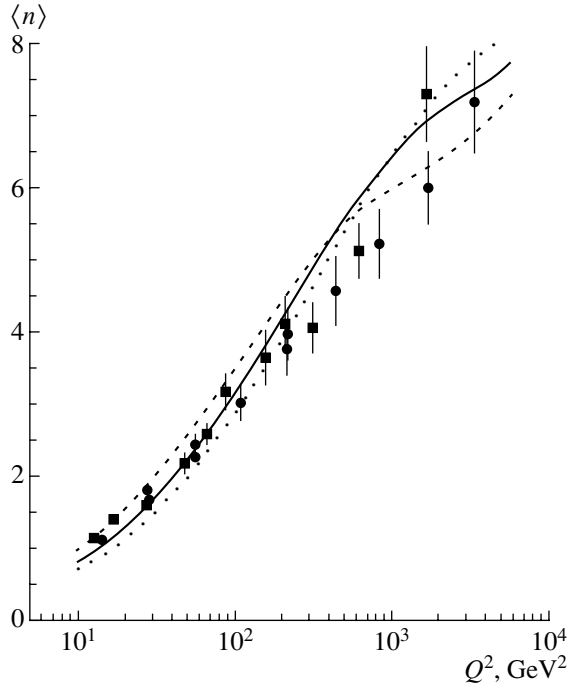

Fig. 6. Mean multiplicity of charged hadrons in the current-fragmentation region in the Breit frame. Experimental data are represented by points: (closed circles) ZEUS data [9] and (closed boxes) H1 data [8]. The dashed, the solid, and the dotted curve depict the results of our calculations at the energies of $W = 84.1$, 131.3, and 177.2 GeV, respectively.

In our calculations, we corrected formula (31) by taking into account the contribution from the products of the decays of short-lived particles K_S^0 and Λ. Expression (32) was obtained with a correction for such a contribution to the multiplicity.

In Fig. 4, our predictions for the Q^2 dependence of the mean multiplicity of charged hadrons in the current region in the c.m. frame of deep-inelastic scattering are shown by solid curves. These predictions were obtained at the following parameter values (see our recent study in [28]):

$$\Lambda = 0.25 \text{ GeV}, \quad Q_0^2 = 0.96 \text{ GeV}^2, \quad n_g = 6.1. \tag{33}$$

The parameter value of $n_g = 6.1$, which controls the behavior of the input distribution for $z \to 1$ [see Eq. (30)], is close to the value of the analogous exponent for one of the sets of the MRST parton distributions taken at $Q_0^2 = 1$ [29].

The formulas presented in this article make it possible to describe data in the Breit frame as well. We mean here the ZEUS data [9], where (in contrast to the H1 data [8]) not only the mean values of Q^2 but also the intervals of x values at which they were measured are known (see Table 2). In Table 3, the experimental data are partitioned into three groups corresponding to three intervals of energy of the final hadron system.

In Fig. 5, the results of our calculations with the same phenomenological parameters as those in (33) are shown by solid curves. Finally, Fig. 6 displays the entire set of experimental points obtained at the HERA collider. These data describe the Q^2 dependence of the mean multiplicity of charged hadrons in the current-fragmentation region in the Breit frame [8, 9]. In Fig. 6, we also depicted the theoretical curves for three midpoints of the intervals of the energy W from Table 3 because different points correspond to different values of the variable x (or W) (some averaged values of x for the H1 data).

5. CONCLUSION

The above phenomenological and theoretical analysis based on QCD has revealed that the latest experimental data confirm the qualitative hypothesis of Yang and his coauthors in [1] that the "productivity" of multiparticle-production processes grows with increasing momentum transfer and make it possible to estimate this growth quantitatively. The weakness of this effect is due to the composite (nonperturbative) structure of the nucleon and to the slow Q^2 dependence of the QCD evolution parameter. However, the effect in question is quite significant statistically.

REFERENCES

1. J. Beneke, T. T. Chou, C. N. Yang, and E. Yen, Phys. Rev. **188**, 2159 (1969).
2. T. T. Wu and C. N. Yang, Phys. Rev. B **137**, 708 (1965).
3. G. Sh. Dzhaparidze, A. V. Kiselev, and V. A. Petrov, in *Proceedings of the IV International Workshop on High Energy Physics and Theory of Field, Protvino, 1981,* Vol. 1, p. 12; Yad. Fiz. **35**, 1627 (1982) [Sov. J. Nucl. Phys. **35**, 951 (1982)].
4. A. V. Kisselev and V. A. Petrov, Phys. Lett. B **131B**, 468 (1983).
5. V. A. Petrov, A. V. Kisselev, and O. P. Yushchenko, Phys. Lett. B **193**, 357 (1987).
6. EMC Collab. (M. Arneodo *et al.*), Phys. Lett. B **165B**, 222 (1985); **165B**, 357 (1985); Z. Phys. C **31**, 1 (1986).
7. H1 Collab. (S. Aid *et al.*), Z. Phys. C **72**, 573 (1996).
8. H1 Collab. (C. Adolf *et al.*), Nucl. Phys. B **504**, 3 (1997).
9. ZEUS Collab. (J. Breitweg *et al.*), Eur. Phys. J. C **11**, 251 (1999).
10. A. V. Kiselev and V. A. Petrov, Fiz. Élem. Chastits At. Yadra **19**, 51 (1988) [Sov. J. Part. Nucl. **19**, 21 (1988)].
11. B. Gibbard *et al.*, Phys. Rev. D **11**, 2367 (1975).

12. M. Derrick *et al.*, Phys. Lett. B **91B**, 470 (1980); V. V. Amossov *et al.*, Nucl. Phys. B **203**, 1 (1982); H. Gräsler *et al.*, Nucl. Phys. B **223**, 269 (1983).
13. WA25 Collab. (D. Allasia *et al.*), Z. Phys. C **24**, 119 (1984); WA21 Collab. (C. T. Jones *et al.*), Z. Phys. C **52**, 11 (1991).
14. E665 Collab. (M. R. Adams *et al.*), Z. Phys. C **76**, 441 (1997).
15. NOMAD Collab. (J. Altegoer *et al.*), Phys. Lett. B **445**, 439 (1999).
16. H1 Collab. (S. Aid *et al.*), Nucl. Phys. B **445**, 3 (1995).
17. ZEUS Collab. (M. Derrick *et al.*), Z. Phys. C **67**, 93 (1995).
18. TASSO Collab. (W. Braunschweig *et al.*), Z. Phys. C **45**, 193 (1989); PLUTO Collab. (Ch. Berger *et al.*), Phys. Lett. B **95B**, 313 (1980); OPAL Collab. (P. D. Acton *et al.*), Z. Phys. C **53**, 539 (1992); HRS Collab. (M. Derrick *et al.*), Phys. Rev. D **34**, 3304 (1986); MARKI Collab. (J. L. Siegrist *et al.*), Phys. Rev. D **26**, 969 (1982).
19. M. Derrick *et al.*, Phys. Lett. B **91B**, 470 (1980).
20. H1 Collab. (C. Adloff *et al.*), Eur. Phys. J. C **5**, 439 (1998).
21. A. Bassetto, Nucl. Phys. B **202**, 493 (1982).
22. C. P. Fong and B. R. Webber, Phys. Lett. B **229**, 289 (1989); Nucl. Phys. B **355**, 54 (1991).
23. Ya. I. Azimov *et al.*, Z. Phys. C **27**, 65 (1985); **31**, 213 (1986).
24. A. V. Kotikov and G. Parente, Nucl. Phys. B **549**, 242 (1999).
25. V. N. Gribov and L. N. Lipatov, Yad. Fiz. **15**, 781 (1972) [Sov. J. Nucl. Phys. **15**, 438 (1972)]; L. N. Lipatov, Yad. Fiz. **20**, 181 (1974) [Sov. J. Nucl. Phys. **20**, 95 (1974)]; G. Altarelli and G. Parisi, Nucl. Phys. B **126**, 298 (1977); Yu. L. Dokshitzer, Sov. Phys. JETP **46**, 691 (1977).
26. R. Brandelik *et al.*, Phys. Lett. B **89B**, 418 (1980).
27. P. V. Chiliapnikov and V. A. Uvarov, Phys. Lett. B **251**, 192 (1990).
28. A. V. Kisselev and V. A. Petrov, Eur. Phys. J. C **19**, 373 (2001); hep-ph/0003083.
29. A. D. Martin *et al.*, Eur. Phys. J. C **4**, 463 (1998).

Translated by A. Isaakyan

Physics of Atomic Nuclei, Vol. 65, No. 5, 2002, pp. 877–878. Translated from Yadernaya Fizika, Vol. 65, No. 5, 2002, pp. 909–910.

ELEMENTARY PARTICLES AND FIELDS
Theory

Froissart–Martin Bound in Spaces of Compact Dimensions

V. A. Petrov*

Institute for High Energy Physics, Protvino, Moscow oblast, 142284 Russia

Received April 2, 2001

Abstract—By considering the example of five-dimensional spacetime, it is shown that the presence of extra spacelike compact dimensions (in addition to common Minkowski space) does not lead to any changes in the prerequisites for proving the Froissart–Martin bound. © *2002 MAIK "Nauka/Interperiodica".*

Interest in the possible existence of rather large spacelike compact extra dimensions (as large as 1 mm according to some estimations!) furnishes a strong motivation for considering the problem of extending the axiomatic approach within quantum field theory to this case. There is also practical interest associated with cosmic rays of ultrahigh energy [1]. A cursory heuristic derivation of such an extension for the Froissart–Martin theorem was given in [2]. In this study, we analyze this problem more thoroughly.

We consider a free neutral scalar field $\Phi(X)$ of mass m in five-dimensional Minkowski spacetime,

$$\Phi(X) = \int \frac{\prod_{i=1}^{4} dK_i}{(2\pi)^4 \cdot 2E(\mathbf{K})} \times \left[e^{iKX} A^+(\mathbf{K}) + e^{-iKX} A(\mathbf{K})\right],$$

$$\left[A(K), A^+(K')\right] = (2\pi)^4 \cdot 2E(\mathbf{K})\delta^{(4)}(\mathbf{K}-\mathbf{K}'),$$

$$K_0 = E(\mathbf{K}) = \sqrt{m^2 + \mathbf{K}^2}.$$

We perform a conventional compactification of the fourth spacelike dimension onto a circle of radius R. As a result, the field $\Phi(X) \equiv \Phi(x, y)$ [$x = (x_0, \mathbf{x}), y \equiv X_4$] appears to be periodic in y,

$$\Phi(x, y + 2\pi R) = \Phi(x, y),$$

and integration with respect to the fifth component of the 5-momentum reduces to a sum,

$$\int \frac{dK_4}{2\pi} \to \sum_{n=-\infty}^{\infty} \frac{1}{2\pi R}, \quad K_4 \to \frac{n}{R}.$$

We then have

$$\Phi(x, y) = \sum_{n=-\infty}^{\infty} \frac{1}{\sqrt{2\pi R}} e^{iyn/R} \times \int \frac{d^3k}{(2\pi)^3 \cdot 2E_n(\mathbf{k})} \left[e^{ikx} b_n^+(\mathbf{k}) + e^{-ikx} a_n(\mathbf{k})\right] = \sum_n \frac{1}{\sqrt{2\pi R}} e^{iyn/R} \Phi_n(x),$$

where $E_n = \sqrt{m^2 + \mathbf{k}^2 + n^2/R^2}$;

$$a_n(\mathbf{k}) = A\left(\mathbf{k}, \frac{n}{R}\right)/\sqrt{2\pi R},$$

$$b_n^+(\mathbf{k}) = A^+\left(\mathbf{k}, -\frac{n}{R}\right)/\sqrt{2\pi R};$$

$$\left[a_n(\mathbf{k}), a_{n'}^+(\mathbf{k}')\right] = \delta_{nn'}(2\pi)^3 \cdot 2E_n\delta(\mathbf{k}-\mathbf{k}'),$$

$$\left[b_n(\mathbf{k}), b_{n'}^+(\mathbf{k}')\right] = \delta_{nn'}(2\pi)^3 \cdot 2E_n\delta(\mathbf{k}-\mathbf{k}'),$$

the remaining commutators being zero. Thus, we can see that a free neutral scalar field in five-dimensional spacetime with one compact spacelike dimension is equivalent to an infinite set of complex scalar fields featuring a conserved Kaluza–Klein quantum number $n = (0, \pm 1, \ldots)$ and the masses $m_n^2 = m^2 + n^2/R^2$ in a conventional four-dimensional Minkowski spacetime. As far as the quantum number n is concerned, it should be noted that, in those cases where only one (gravitational) field can propagate through the whole multidimensional space, with the other fields being associated with four-dimensional Minkowski space, so that translation symmetry in extra dimensions is violated, the Kaluza–Klein quantum number is not conserved.

Considering $\Phi(x)$ as an asymptotic field in five-dimensional space, we obtain, after compactification, an infinite set of asymptotic fields in four-dimensional space.

From the standpoint of the axiomatic approach formulated in [3], the S matrix in five-dimensional space with a compact dimension,

$$S = \sum_N \frac{1}{N!} \int (d^4x_1 dy_1) \ldots (d^4x_N dy_N) \times S(x_1y_1, \ldots, x_Ny_N) : \Phi(x_1, y_1) \ldots \Phi(x_N, y_N) :, \quad (1)$$

*e-mail: petrov@mx.ihep.su

1063-7788/02/6505-0877$22.00

can be recast into the ordinary four-dimensional form

$$S = \sum_N \sum_{n_1 \ldots n_N} \int d^4x_1 \ldots d^4x_N \times S_{n_1 \ldots n_N}(x_1, \ldots, x_N) : \Phi_{n_1}(x_1) \ldots \Phi_{n_N}(x_N) : .$$

Suppose that the Bogolyubov microcausality principle holds in five-dimensional space; that is,

$$\frac{\delta J(x,y)}{\delta \Phi(x',y')} = 0,$$
$$(x_0 - x_0') < \sqrt{(\mathbf{x}-\mathbf{x}')^2 + (y-y')^2}.$$

By virtue of the spacelike character of the compact dimension, it follows from this principle that, for any n and n',

$$\frac{\delta J_n(x)}{\delta \Phi_{n'}(x')} = 0 \quad \text{for} \quad (x_0 - x_0') < |\mathbf{x} - \mathbf{x}'|.$$

Thus, we have all conditions for the ordinary axiomatic approach. Here, all "five-dimensional" amplitudes $\hat{T}_{MN}$ for an arbitrary $M \to N$ reaction and the amplitude T_{MN} observed in four dimensions are related by the equation

$$T_{MN} = \hat{T}_{MN}/(2\pi R)^{\frac{M+N}{2}-1}.$$

For binary processes ($M = N = 2$), this equation reduces to

$$T_{22} = \hat{T}_{22}/2\pi R.$$

Thus, we can employ well-known methods (see, for example, [4]) and, for the amplitude of any $1+2 \to 3+4$ process, obtain a bound of the Froissart–Martin type,

$$|T_{n_1,n_2;n_3,n_4}(s,t)|_{n_1+n_2=n_3+n_4} \le \frac{\pi s}{t_{(n_1-n_3)}} \ln^2(s/s_0),$$

where $t_{(n_1-n_3)}$ is the nearest singularity t in the channel featuring the quantum number $n_1 - n_3$. In the case of $n_1 = n_3$, we have

$$|T_{n_1,n_2;n_1,n_2}(s,t)| \le \frac{\pi s}{t_0} \ln^2(s/s_0), \quad t_0 = 4m^2,$$

$$s \gg 4m^2 + \frac{(n_1+n_2)^2}{R^2}.$$

If $n_1 \ne n_3$, then

$$|T_{n_1,n_2;n_3,n_4}(s,t)| \le \pi s \frac{R^2}{R^2 t_0 + (n_1-n_3)^2} \times \ln^2(s/s_0) \approx \pi s \frac{R^2}{(n_1-n_3)^2} \ln^2(s/s_0), \quad R^2 t_0 \ll 1.$$

At $n_1 = n_2 = n_3 = n_4 = 0$, we have the ordinary Froissart–Martine bound

$$|T_{00;00}(s,t)| \le \frac{\pi s}{t_0} \ln^2(s/s_0).$$

It is worth noting that, for $R \to 0$, all amplitudes involving a nonzero transfer of the quantum number n vanish. From crossing symmetry, it follows that, for $R \to 0$, all amplitudes with the exception of the neutral one, $T_{00;00}$, vanish.

Thus, we have shown that, for $R \to 0$, the theory transforms continuously into that of a neutral scalar field in four-dimensional Minkowski spacetime. In this study, we have assumed that there is a nonzero lower bound on the masses involved. In the absence of this "mass gap," bounds for elastic scattering are trivial; it is likely, however, that, even in this case, nontrivial bounds can be derived for total inelastic cross sections. This is so within the Regge eikonal approach, but a rigorous proof has yet to be obtained.

In the future, I am going to consider this problem for the case of compact multidimensional manifolds of various topologies.

ACKNOWLEDGMENTS

I am grateful to Yu.S. Vernov, G.G. Volkov, A.A. Logunov, A. Martin, and N.E. Tyurin for interest in this study and stimulating discussions.

REFERENCES

1. M. Kachelriess and M. Plumacher, Phys. Rev. D **62**, 103006 (2000).
2. V. A. Petrov, Mod. Phys. Lett. A **16**, 151 (2001).
3. N. N. Bogolyubov, B. V. Medvedev, and M. K. Polivanov, *Problems in Theory of Dispersion Relations* (GIFML, Moscow, 1958).
4. *General Principles of Quantum Field Theory and Their Implications,* Ed. by V. A. Meshcheryakov (Nauka, Moscow, 1977).

Translated by O. Chernavskaya

Physics of Atomic Nuclei, Vol. 65, No. 5, 2002, pp. 879–885. From Yadernaya Fizika, Vol. 65, No. 5, 2002, pp. 911–917.

ELEMENTARY PARTICLES AND FIELDS
Theory

Flavor Correlations in B_s- and B_c-Meson Production at Hadron Colliders*

S. P. Baranov**

Lebedev Institute of Physics, Russian Academy of Sciences, Leninskiĭ pr. 53, Moscow, 117924 Russia

Received February 7, 2001; in final form, September 4, 2001

Abstract—We present a comparative analysis of three different theoretical approaches to the production of B_s and B_c mesons in high-energy hadron collisions. Our attention focuses on the azimuthal and pseudorapidity correlations between B_s or B_c mesons and accompanying strange or charmed particles. The corresponding kinematical distributions are found to exhibit a high sensitivity to details of the production mechanism and can therefore serve as indicators of interaction dynamics. © *2002 MAIK "Nauka/Interperiodica".*

1. INTRODUCTION

Heavy-flavor-production processes are rightfully regarded as important tests of perturbative QCD. A typical example of this kind is the production of beauty hadrons. The production of b-flavored hadrons containing another heavy flavor, such as B_s or B_c mesons, may constitute an even more sensitive test because these reactions are related to higher orders of perturbation theory. At the same time, the intermediate position of s and c quarks on the mass scale opens a wide field for theoretical models where various perturbative and nonperturbative approaches compete with one another.

The objective of this study is to compare the predictions of three commonly used popular models. One of them [1–4], hereafter referred to as fixed-order QCD, considers both quark pairs as those that are produced perturbatively in a fourth-order hard gluon–gluon interaction

$$g + g \to B_q + b + \bar{q}, \qquad q = s, c \qquad (1)$$

(examples of the corresponding Feynman diagrams are shown in Fig. 1). The formation of heavy-quark bound states is treated here within the nonrelativistic approximation [5–8].

In a somewhat different scheme known as the flavor-excitation mechanism [9–11], a certain part of the relevant partonic subprocess is factored out, so that b-flavored quarks are considered as sea partons. They are excited from the sea via a hard interaction, with an external gluon producing at the same time a pair of additional quarks $q\bar{q}$ (see Fig. 2),

$$g + \bar{b} \to B_q + \bar{q}, \qquad q = s, c. \qquad (2)$$

Also possible is the excitation of lighter flavors $g + q \to B_q + b$, though it was found [11] to be of minor importance compared to the excitation of beauty. The formation of final-state double-heavy hadrons is treated within the same nonrelativistic approximation as above.

As the consequence of the factorization hypothesis, some interference terms are neglected here, which are present in full $O(\alpha_s^4)$ calculations of subprocess (1). On the other hand, the flavor-excitation approach efficiently includes higher order contributions, which are absorbed in the sea-quark evolution equations.

The third approach to the production of B_s mesons is given by the Lund model [12] as implemented in the event-generator PYTHIA [13]. This approach contains an essentially nonperturbative ingredient, an algorithm of color string fragmentation. Here, only a single $b\bar{b}$ pair is thought to be produced perturbatively in a hard parton interaction, while the pair of lighter quarks originates from the color-string breakup.

Since the string stretched between the b quark and a lighter quark also represents a kind of soft gluon-exchange process, PYTHIA's production mechanism possesses some similarity to the fragmentation approach of [14, 15]. Note, however, that the fragmentation functions in [14, 15] depend only on the longitudinal momentum fraction z; therefore, the B_s or B_c meson and the accompanying strange or charm particle both move exactly along the direction of the parent b quark. On the contrary, the nonperturbative string fragmentation in PYTHIA may cause the particles to deviate significantly from that direction.

From a numerical comparison of all models, we wish to see how large the effects due to different theoretical approximations can be. A comparison with

*This article was submitted by the author in English.

** e-mail: baranov@sci.lebedev.ru

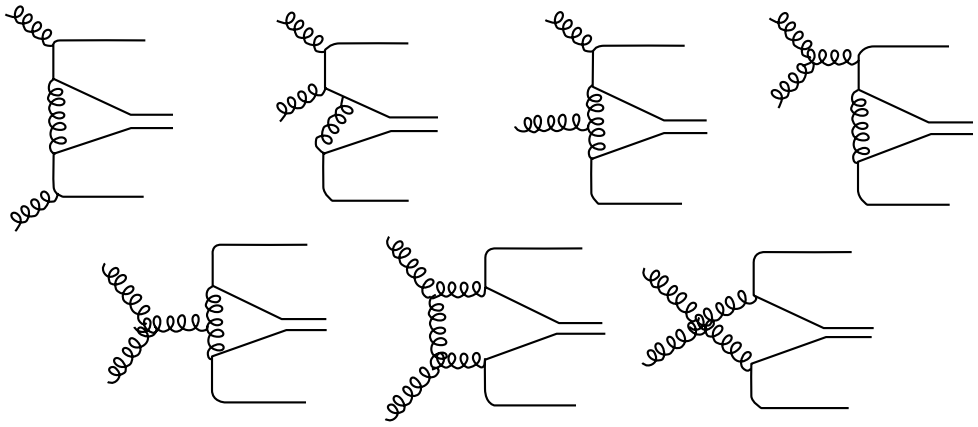

Fig. 1. Examples of fourth-order Feynman diagrams representing the production of $B_{c,s}$ mesons in the gluon–gluon fusion subprocess.

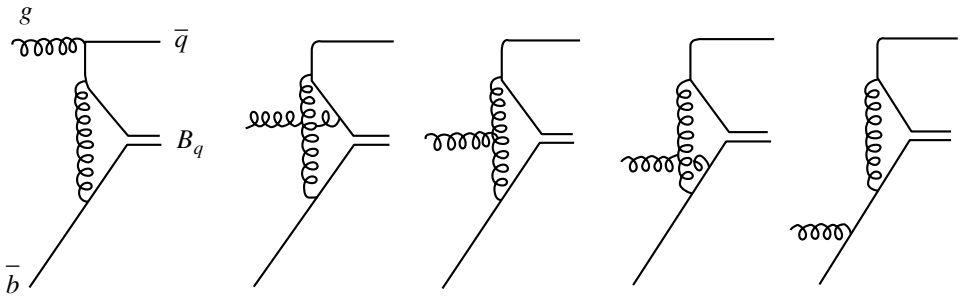

Fig. 2. Feynman diagrams representing the production of $B_{c,s}$ mesons in the flavor-excitation subprocess.

(the future) experimental measurements will be helpful in assessing the quality of the underlying theoretical assumptions. Previously, a comparison between full $O(\alpha_s^4)$ calculations and the factorization approach was performed by other authors [16, 17]. The latter was, however, restricted to the inclusive B_c distributions. A consideration of various kinds of correlations is promising for revealing new interesting details.

2. DETAILS OF THE CALCULATIONS

Let us first consider the partonic subprocess (1). We denote by k_1 and k_2 the 4-momenta of the incoming gluons; by p_b, p_q, and P_B the momenta of the b quark, the lighter antiquark, and the B_q meson; and by m_b, m_q, and M_B their respective masses. The partonic cross section can then be parametrized in the form [18]

$$\frac{d\hat{\sigma}(g+g\to B_q+b+\bar{q})}{dt_1 ds_2 d\cos\theta d\phi} = \frac{\alpha_s^4\lambda^{1/2}(s_2,m_q^2,m_b^2)}{4\hat{s}^2 s_2} \times \frac{|\Psi(0)|^2}{M_B}\frac{1}{4}\frac{1}{64}\sum_{\text{spin color}}\sum|\mathcal{M}|^2, \quad (3)$$

where $\hat{s}=(k_1+k_2)^2$, $t_1=(k_1-P_B)^2$, $s_2=(p_q+p_b)^2$, $\lambda(x,y,z)=x^2+y^2+z^2-2xy-2yz-2zx$, and the angles θ and ϕ are the polar and azimuthal angles of $\mathbf{p}_q$ in the $\bar{q}b$-pair rest frame ($\mathbf{p}_q+\mathbf{p}_b=0$). Averaging over the initial gluon spins and colors is represented by the factors $1/4$ and $1/64$, respectively. The full gauge-invariant set of matrix elements collected in $|\mathcal{M}|^2$ comprises 36 Feynman diagrams. The evaluation of these diagrams is performed by means of the orthogonal-amplitude technique explained in detail in [1].[1)]

For subprocess (2), we similarly have

$$\frac{d\hat{\sigma}(g+\bar{b}\to B_q+\bar{q})}{d\cos\theta} = \frac{2\pi^2\alpha_s^3\lambda^{1/2}(\hat{s},m_q^2,M_B^2)}{\hat{s}^2} \times \frac{|\Psi(0)|^2}{M_B}\frac{1}{4}\frac{1}{12}\sum_{\text{spin color}}\sum|\mathcal{M}|^2, \quad (4)$$

where, now, $\hat{s}=(k+p_b)^2$, with k and p_b being the 4-momenta of the initial gluon and the b antiquark, respectively, and θ is the B_q meson azimuthal angle

[1)] A somewhat different computational method was used in [2–4], although all articles present consistent numerical results.

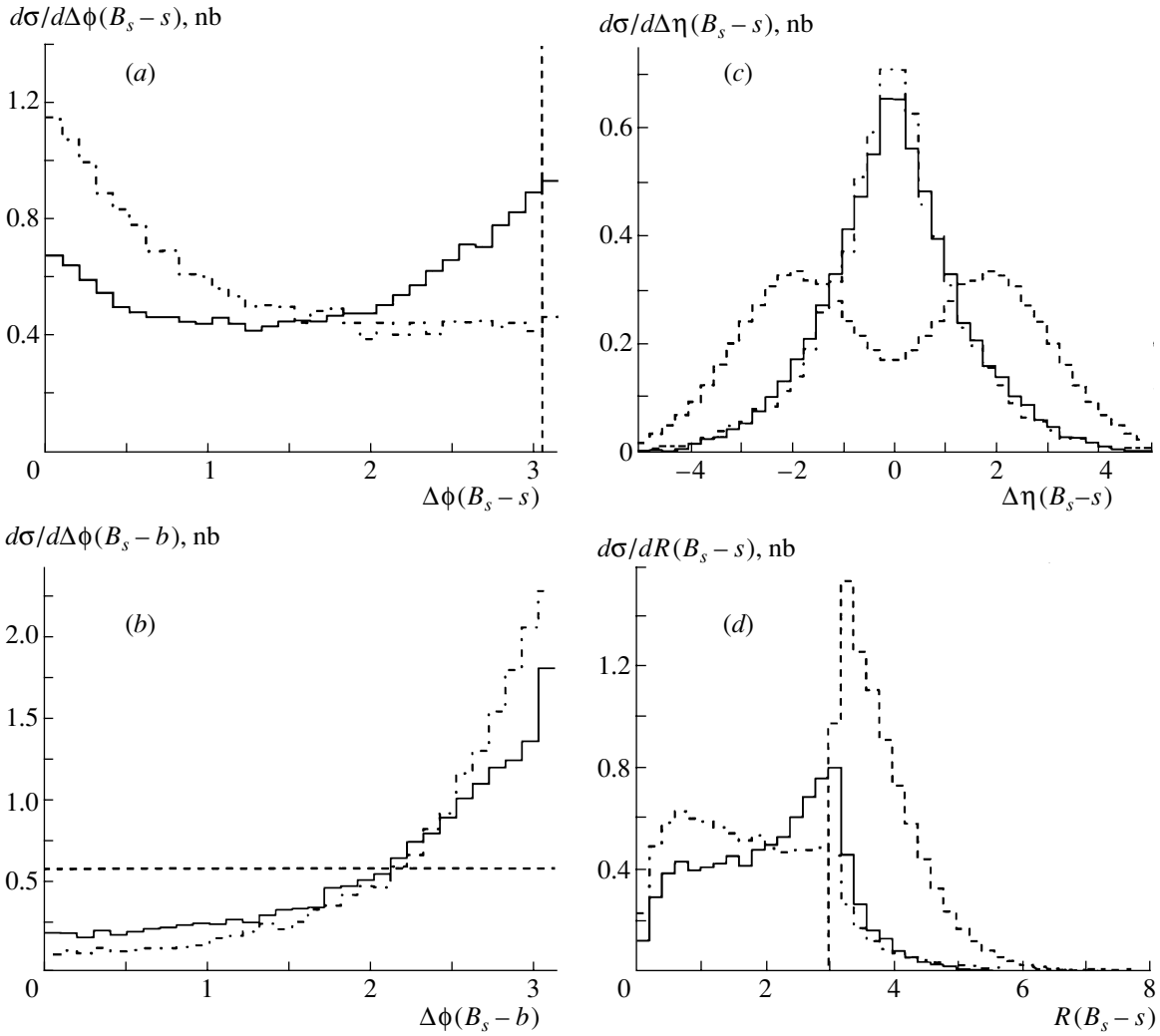

Fig. 3. Kinematical correlations in the production of B_s mesons under Tevatron conditions: (a) distributions in the azimuthal-angle difference $\Delta\phi(B_s - s)$, (b) distributions in the azimuthal-angle difference $\Delta\phi(B_s - b)$, (c) distributions in the pseudorapidity difference $\Delta\eta(B_s - s)$, and (d) distributions in the variable $R = [\Delta\phi(B_s - s)^2 + \Delta\eta(B_s - s)^2]^{1/2}$. Solid, dashed, and dash-dotted histograms represent the results obtained on the basis of, respectively, fixed-order $O(\alpha_s^4)$ calculations, the flavor-excitation model, and the string-fragmentation model.

in the rest frame of colliding partons. The analytic expressions for $|\mathcal{M}|^2$ in (3) and (4) are too cumbersome to be presented in this article.[2)]

According to the nonrelativistic formalism [5–8], the probability of forming a bound quark system is determined by the hadron wave function, which, in the leading approximation, reduces to the single parameter $|\Psi(0)|^2$, the value of the wave function at the origin of coordinate space. In the present calculations, we use $|\Psi_{B_s}(0)|^2 = 0.012$ GeV^3 and $|\Psi_{B_c}(0)|^2 = 0.12$ GeV^3. Both estimates were obtained from a simple power-law interpolation between the known wave functions of Υ, J/ψ, and ϕ mesons. We are not interested in more accurate estimates because the values of the wave functions are important only for the total production rates, but they are not important for the shape of kinematical correlations, which is the purpose of the present study. Also, we set $\alpha_s = \text{const} = 0.25$ for the sake of simplicity. For the quark and meson masses, we adopt the values of $m_s = 0.5$ GeV, $m_c = 1.5$ GeV, $m_b = 4.8$ GeV, $M_{B_s} = m_b + m_s = 5.3$ GeV, and $M_{B_c} = m_b + m_c = 6.3$ GeV.

To obtain the fully differential cross sections for hadron–hadron collisions, expressions (3) and (4) must be convoluted with proper parton distribution

[2)]The FORTRAN codes both for fixed-order and for flavor-excitation calculations are available from the present author on request.

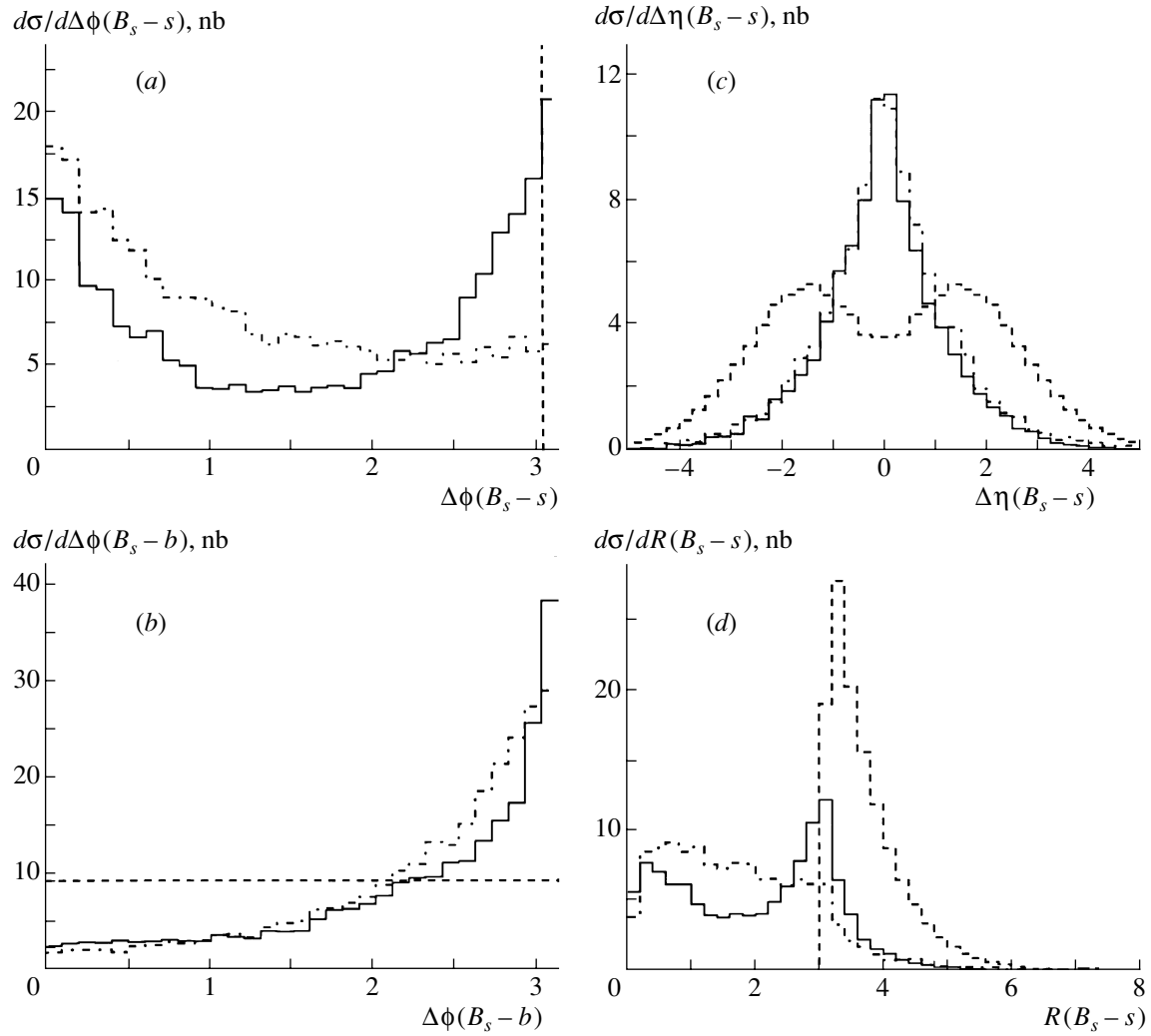

Fig. 4. Kinematical correlations in the production of B_s mesons under LHC conditions: (*a*) distributions in the azimuthal-angle difference $\Delta\phi(B_s - s)$, (*b*) distributions in the azimuthal-angle difference $\Delta\phi(B_s - b)$, (*c*) distributions in the pseudorapidity difference $\Delta\eta(B_s - s)$, and (*d*) distributions in the variable $R = [\Delta\phi(B_s - s)^2 + \Delta\eta(B_s - s)^2]^{1/2}$. Solid, dashed, and dash-dotted histograms represent the results obtained on the basis of fixed-order $O(\alpha_s^4)$ calculations, the flavor-excitation model, and the string-fragmentation model.

functions:

$$d\sigma(AB \to X) = \int F_{a/A}(x_1)F_{b/B}(x_2)d\hat{\sigma}(ab \to X)dx_1dx_2. \quad (5)$$

The GRV LO set [19] was used for all gluon and quark distributions. Integration with respect to the longitudinal-momentum variables x_1 and x_2 and over the multidimensional phase space in (3) and (4) was performed by means of the Monte Carlo technique by using the VEGAS routine [20]. For the strange- and charmed-quark fragmentation functions, we used the parametrization due to Field and Feynman [21] with $a = 0.77$ and the parametrization due to Peterson *et al.* [22] with $\epsilon = 0.06$, respectively.

3. NUMERICAL RESULTS

We start with the production properties of B_s mesons under Tevatron conditions. Of various kinematical distributions, we concentrate on those that show the highest sensitivity to details of the production mechanism. The quantities of interest are the azimuthal-angle difference between the momenta of the B_s meson and the accompanying strange particle, $\Delta\phi(B_s - s)$; the azimuthal-angle difference between the momenta of the B_s meson and the accompanying b-flavored particle, $\Delta\phi(B_s - b)$; the pseudorapidity difference $\Delta\eta(B_s - s)$; and the variable $R = [\Delta\phi(B_s - s)^2 + \Delta\eta(B_s - s)^2]^{1/2}$. It is worth mentioning that the corresponding kinematical distributions are rather insensitive to the b- and

s-quark fragmentation functions. The reason may be understood from the fact the above kinematical variables are related only to the directions of the particle momenta and are therefore assumed to remain intact in the fragmentation process. In order to make perturbative calculations more credible, we applied extra cuts on the B_s-meson and s-quark transverse momenta: $p_T(B_s) > 3$ GeV and $p_T(s) > 3$ GeV. These cuts are also helpful in avoiding the ambiguous kinematical region, where the presence of beam remnants may lead to unwanted contaminations and induce serious distortions in event topology.

The calculations corresponding to the fixed-order and flavor-excitation approaches were performed with the model parameters specified in Section 2. The event generator PYTHIA was run with its default setting, except for the quark masses, which were taken to be equal to those used in perturbative calculations. The numerical results are shown in Fig. 3.

The models considered here exhibit clearly different types of behavior in azimuthal correlations. In fixed-order perturbation theory, the events tend to concentrate at $\Delta\phi(B_s - s) \approx \pi$, as can be seen in Fig. 3*a*; a smaller maximum is also seen at $\Delta\phi(B_s - s) \approx 0$. The contribution from the flavor-excitation mechanism forms a delta function at $\Delta\phi(B_s - s) = \pi$, which is a direct consequence of momentum conservation in two-body kinematics. One can expect that, in a more realistic consideration taking into account the initial-parton transverse momenta, this delta function would transform into a smooth distribution localized in the vicinity of $\Delta\phi(B_s - s) \approx \pi$. The nonperturbative string fragmentation predicts a rather flat spectrum increasing toward $\Delta\phi(B_s - s) = 0$.

The distributions in the azimuthal-angle difference $\Delta\phi(B_s - b)$ (Fig. 3*b*) look more or less similar in the fixed-order calculations and in the fragmentation approach. In both cases, the distributions decrease from $\Delta\phi(B_s - b) = \pi$ to $\Delta\phi(B_s - b) = 0$, thus demonstrating the tendency to preserve back-to-back kinematics for the heaviest product particles. This contrasts with the flavor-excitation model, where the spectator sea b quark is considered to be totally disconnected from the hard subprocess, and no correlation is therefore possible between this quark and other particles.

The sensible difference in the pseudorapidity correlations seen in Fig. 3*c* is closely connected with the forward-backward asymmetry of the flavor excitation (2): the B_s meson produced in this partonic subprocess tends to follow the direction of the parent $\bar{b}$ antiquark. The two maxima seen in Fig. 3*c* are due to the two possible configurations of parton collisions: the initial $\bar{b}$ antiquark can be picked up

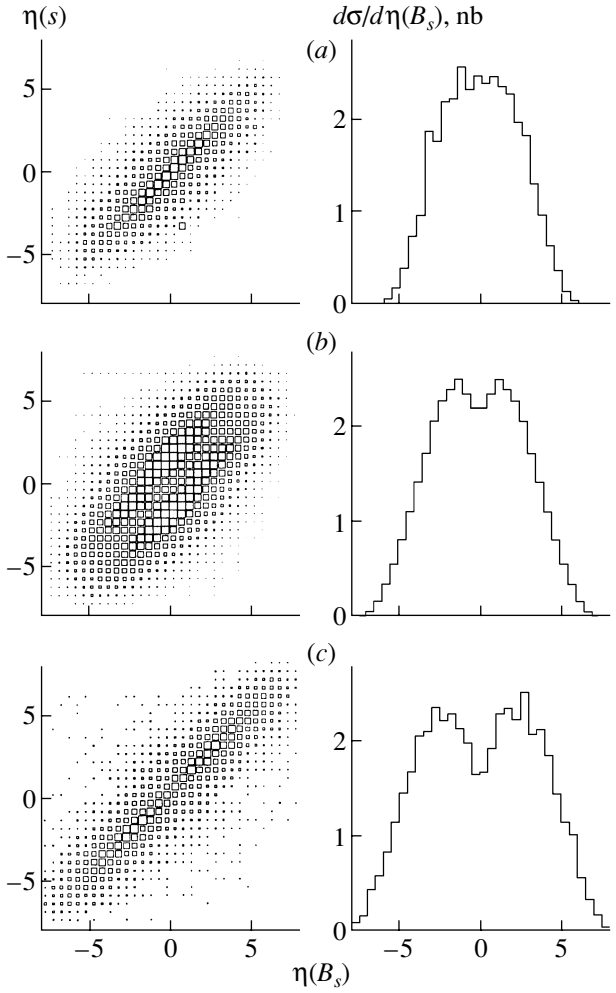

Fig. 5. Pseudorapidity correlations in $B_s + \bar{s}$ production under LHC conditions for (left column) the double differential distributions $d^2\sigma/d\eta(B_s)d\eta(s)$ and (right column) for the inclusive distributions $d\sigma/d\eta(B_s)$: (*a*) fixed-order $O(\alpha_s^4)$ calculations, (*b*) flavor-excitation model, and (*c*) string-fragmentation model.

from either of the two protons (i.e., be moving forward or backward), and the gluon comes from the other proton. On the contrary, the other two production mechanisms are connected with the gluon–gluon fusion subprocess, and therefore possess no forward–backward asymmetry. The distribution in the variable $R = [\Delta\phi(B_s - s)^2 + \Delta\eta(B_s - s)^2]^{1/2}$ accumulates the differences seen in the azimuthal and pseudorapidity correlations.

At higher energies, typical of planned LHC experiments, the kinematical distributions (see Fig. 4) generally reproduce the pattern that we have already discussed for the Tevatron conditions. One can only indicate that the peaks in the $\Delta\phi(B_s - s)$ spectrum predicted by perturbation theory become sharper. The perturbatively calculated $\Delta\phi(B_s - b)$ distribu-

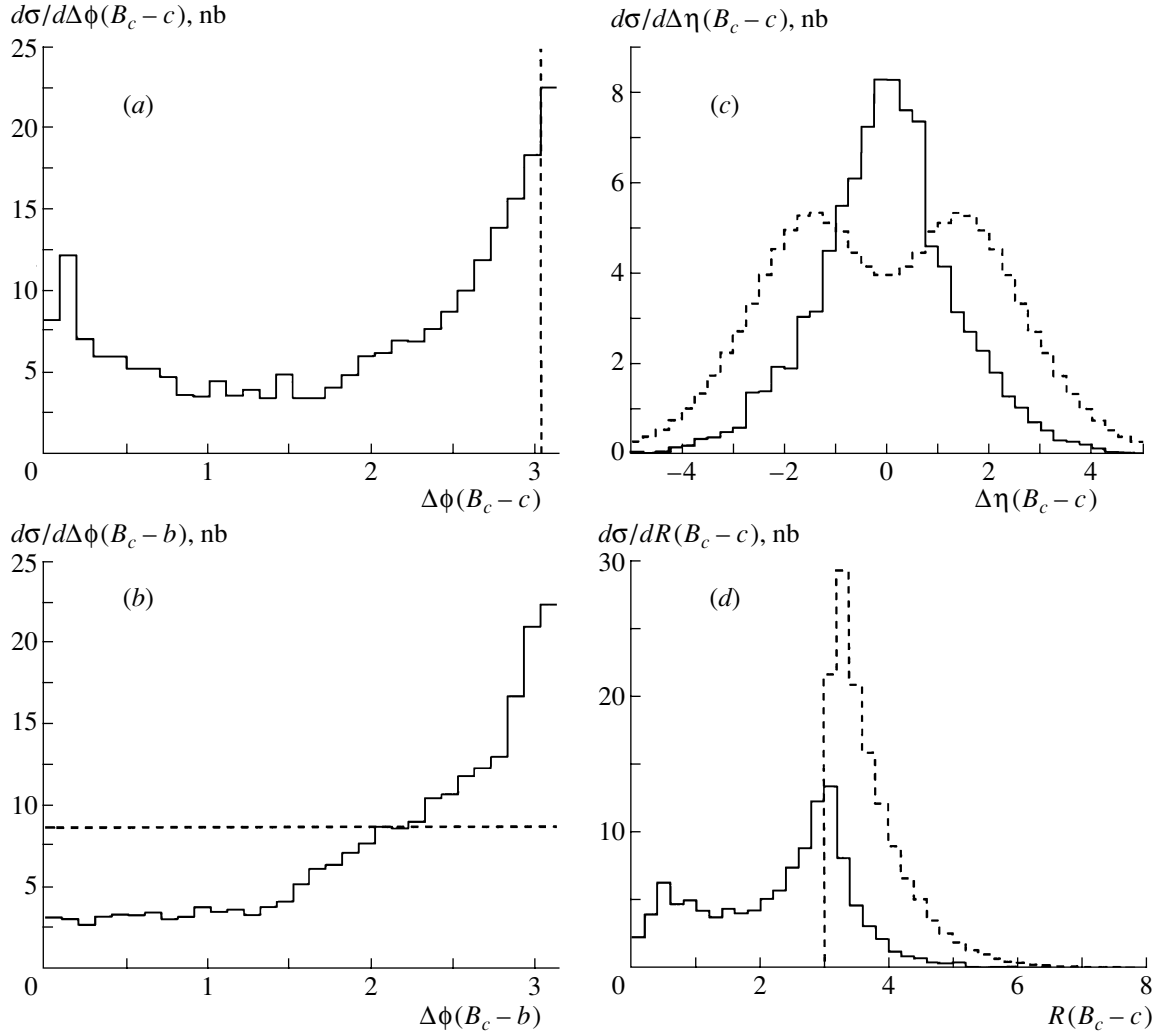

Fig. 6. Kinematical correlations in the production of B_c mesons under LHC conditions: (a) distributions in the azimuthal-angle difference $\Delta\phi(B_c - c)$, (b) distributions in the azimuthal-angle difference $\Delta\phi(B_c - b)$, (c) distributions in the pseudorapidity difference $\Delta\eta(B_c - c)$, and (d) distributions in the variable $R = [\Delta\phi(B_c - c)^2 + \Delta\eta(B_c - c)^2]^{1/2}$. Solid and dashed histograms represent the results obtained on the basis of fixed-order $O(\alpha_s^4)$ calculations and the flavor-excitation model.

tion also sharpens, though remains similar to the predictions of the string-fragmentation model.

Some interesting features can be observed in the double-differential pseudorapidity distributions $d^2\sigma/d\eta(B_s)d\eta(s)$ displayed in Fig. 5 (for the LHC conditions as well). In fixed-order perturbation theory, events fill up an elongated ellipse oriented along the principal diagonal of the plot. In the flavor-excitation approach, the distribution shows two overlapping off-diagonal maxima (each being connected with one of the two initial parton configurations, as explained earlier). Finally, in the string-fragmentation model, events are again arranged along the principal diagonal. However, in fixed-order perturbation theory, they tend to concentrate in the middle area around $\eta(B_s) = \eta(s) = 0$, while, in the case of the fragmentation approach, the distribution shows two separate maxima at approximately $\eta(B_s) = \eta(s) \approx \pm 3$. This difference is also seen in the projections onto the $\eta(B_s)$ or $\eta(s)$ axes, so that even the inclusive single-particle pseudorapidity distributions demonstrate different shapes.

The regularities being considered apply to the production of B_c mesons as well (see Fig. 6). Here, we restrict ourselves to the LHC conditions, because, at Tevatron energies, the production rate is too low to obtain necessary experimental statistics. Since PYTHIA does not produce charmed quarks in fragmenting strings, one can use only the factorization approach of [14, 15]. In the latter case, the B_c meson and the accompanying charmed quark move strictly along the direction of the parent b quark.

Since the corresponding kinematical correlations become rather trivial [$\Delta\phi(B_c - c) = 0$, $\Delta\eta(B_c - c) = 0$, $\Delta\phi(B_c - b) \approx \pi$], they are not shown in the figures.

4. DISCUSSIONS AND CONCLUSIONS

A number of conclusions can be drawn from the results shown in the preceding section. First, one can see the importance of nonfragmentation contributions. The difference between the predictions of full $O(\alpha_s^4)$ calculations and the flavor-excitation approach shows that, even at LHC energies, the production conditions are far from those assumed by the factorization hypothesis. The reason may be understood from the fact that the production cross section is dominated by processes occurring at moderate p_T, where the mass of b-flavored particles is not negligible in relation to a typical momentum transfer. A similar conclusion was drawn in [16, 17], where the authors considered the inclusive distributions in the B_c transverse momentum and in the energy-fraction variable $z = 2E_{B_c}/\sqrt{s}$.

Nonperturbative effects associated with the string-fragmentation algorithm in PYTHIA can mimic, to some extent, the presence of interference terms contributing to the intermediate region of azimuthal angles [i.e., where the $\Delta\phi(B_q-)$ and $\Delta\phi(B_q - b)$ values are not close to π or to zero]. However, the character of the pseudorapidity correlations shows that full $O(\alpha_s^4)$ calculations and the (nonperturbative) fragmentation approach do not yet predict identical event topologies.

At the same time, the absolute size of the production cross sections obtained within the flavor-excitation approach shows the importance of higher order contributions emerging from the evolution of the sea-quark densities. In fact, there were no reasons to expect that the perturbation expansion should just terminate at the Born approximation. The very last conclusion that we can draw on this topic is that the theory of double heavy-flavor production is by far not complete and that more efforts are needed from both theoretical and experimental sides.

REFERENCES

1. S. P. Baranov, Yad. Fiz. **60**, 1459 (1997) [Phys. At. Nucl. **60**, 1322 (1997)].
2. C.-H. Chang, Y.-Q. Chen, G.-P. Han, and H.-T. Jiang, Phys. Lett. B **364**, 78 (1995).
3. K. Kolodziej, A. Leike, and R. Rückl, Phys. Lett. B **355**, 337 (1995).
4. A. V. Berezhnoy, A. K. Likhoded, and O. P. Yushchenko, Yad. Fiz. **59**, 742 (1996) [Phys. At. Nucl. **59**, 709 (1996)]; A. V. Berezhnoy, V. V. Kiselev, and A. K. Likhoded, Z. Phys. A **356**, 79 (1996); Yad. Fiz. **60**, 108 (1997) [Phys. At. Nucl. **60**, 100 (1997)]; A. V. Berezhnoy, V. V. Kiselev, A. K. Likhoded, and A. I. Onishchenko, Yad. Fiz. **60**, 1889 (1997) [Phys. At. Nucl. **60**, 1729 (1997)].
5. H. Krasemann, Z. Phys. C **1**, 189 (1979).
6. G. Guberina, J. Kühn, R. Peccei, and R. Rückl, Nucl. Phys. B **174**, 317 (1980).
7. R. Baier and R. Rückl, Phys. Lett. B **102B**, 364 (1981); Z. Phys. C **19**, 251 (1983).
8. E. L. Berger and D. Jones, Phys. Rev. D **23**, 1521 (1981).
9. A. P. Martynenko and V. A. Saleev, Phys. Lett. B **343**, 381 (1995).
10. A. P. Martynenko and V. A. Saleev, Phys. Rev. D **54**, 1891 (1996).
11. S. P. Baranov, Phys. Rev. D **56**, 3046 (1997).
12. B. Andersson, G. Gustafson, G. Ingelman, and T. Sjöstrand, Phys. Rep. **97**, 31 (1983); B. Andersson, *The Lund Model* (Cambridge Univ. Press, Cambridge, 1998).
13. T. Sjöstrand, Comput. Phys. Commun. **82**, 74 (1994).
14. E. Braaten, K. Cheung, and T. C. Yuan, Phys. Rev. D **48**, 5049 (1993).
15. A. F. Falk, M. Luke, M. Savage, and M. Wise, Phys. Rev. D **49**, 555 (1994).
16. C.-H. Chang, Y.-Q. Chen, and R. J. Oakes, Phys. Rev. D **54**, 4344 (1996).
17. A. V. Berezhnoy, V. V. Kiselev, and A. K. Likhoded, Yad. Fiz. **60**, 353 (1997) [Phys. At. Nucl. **60**, 289 (1997)].
18. E. Bycling and K. Kajantie, *Particle Kinematics* (Wiley, New York, 1973; Mir, Moscow, 1975).
19. M. Glück, E. Reya, and A. Vogt, Z. Phys. C **67**, 433 (1995).
20. G. P. Lepage, J. Comput. Phys. **27**, 192 (1978).
21. R. D. Field and R. P. Feynman, Nucl. Phys. B **136**, 1 (1978).
22. C. Peterson, D. Schlatter, I. Schmitt, and P. Zerwas, Phys. Rev. D **27**, 105 (1983).

Physics of Atomic Nuclei, Vol. 65, No. 5, 2002, pp. 886–897. From Yadernaya Fizika, Vol. 65, No. 5, 2002, pp. 918–929.

ELEMENTARY PARTICLES AND FIELDS
Theory

Angular Pattern of Minijet Transverse Energy Flow in Hadron and Nuclear Collisions*

A. V. Leonidov and D. M. Ostrovsky

Lebedev Institute of Physics, Russian Academy of Sciences, Leninskiĭ pr. 53, Moscow, 117924 Russia

Received January 25, 2000; in final form, April 19, 2000

Abstract—The azimuthal asymmetry of a minijet system produced at the early stage of nucleon–nucleon and nuclear collisions in a central rapidity window is studied. We show that, in *pp* collisions, the minijet-transverse-energy production in a central rapidity window is essentially unbalanced in azimuth because of asymmetric contributions in which only one minijet hits the acceptance window. We further study the angular pattern of the transverse-energy flow generated by semihard degrees of freedom at the early stage of high-energy nuclear collisions and its dependence on the number of semihard collisions in the models either including or neglecting soft contributions to the inelastic cross section at RHIC and LHC energies, as well as on the choice of infrared cutoff. © *2002 MAIK "Nauka/Interperiodica".*

1. INTRODUCTION

Minijet physics is one of the most promising applications of perturbative QCD to the analysis of processes involving multiparticle production. It addresses a crucial question of how many (semi)hard degrees of freedom can be available in a given event. The approach is based on the idea that some portion of transverse energy is produced in a semihard form, i.e., is perturbatively calculable because of relatively high transverse momenta involved in the scattering process, but, due to parametrically strong hadronization effects, cannot be observed in the form of customary well-collimated hard jets distinctly separable from the soft background. This mechanism operates at the early stage of the collision and, when relevant, determines the characteristics of the primordial transverse-energy flow.

The creation of many (semi)hard degrees of freedom corresponds to a new physical situation characterized by nontrivial, possibly kinetic or even hydrodynamic, phenomena occurring at the parton level at the early stages of a high-energy collision. Of special relevance here are ultrarelativistic heavy-ion collisions, where one would expect that a dense system of (semi)hard degrees of freedom in the volume much larger than, e.g., the proton one can arise, which makes natural the application of concepts borrowed from macroscopic physics. A recent critical discussion of this field can be found in [1].

Minijet physics is an actively developing field. Reviews on the subject containing a large number of references can be found, e.g., in [2–4]. Several approaches have been considered with an aim of providing a quantitative description of the primordial parton system produced at the earliest stage of, e.g., high-energy heavy-ion collisions. The conceptually simplest one is based on the standard formalism of collinearly factorized QCD at small parton densities (see [5–9]). Here, one operates with a single hard parton–parton scattering in a given hadron–hadron collision, so that standard QCD structure functions can be used in computing the probability of generating a pair of partons with specific kinematical characteristics.

This approach has a natural generalization in which multiple binary parton–parton collisions in the given hadron–hadron one are considered, provided some ad hoc distribution in the number of these collisions is chosen (see, e.g., [10]). This also allows one to construct a geometrically motivated scheme for unitarizing the semihard contribution to the inelastic cross section for hadron scattering as described, e.g., in [3].

Starting from [11], nonlinear QCD effects in relation to describing the early stages of heavy-ion collisions drew progressively more and more attention. New results were obtained within the approach to minijet production based on the semiclassical treatment of nuclear gluon distributions within the McLerran–Venugopalan model [12] (see [13–17]). First nonperturbative results on gluon production are now available [18] (see also [19, 20]). Recently, a nonperturbative model for gluon production in heavy-ion collisions based on the physical concepts of the

*This article was submitted by the authors in English.

1063-7788/02/6505-0886$22.00

McLerran–Venugopalan model and a corresponding kinetic equation describing the evolution of the primordial gluon system were discussed in [21]. For pedagogical introduction to this rapidly developing field, the reader is referred to the lectures in [22] and in [23].

A notable feature of the physical phenomena related to the collective behavior of multiparton systems is their genuine event-by-event nature, so that many usual tools used in high-energy physics, such as inclusive distributions, become less helpful. Thus, the analysis of event-by-event variations of the quantities sensitive to the collective dynamics is very important (see, e.g., [24–27] and references therein).

The description of the primordial parton configuration should provide information on the event-by-event pattern of the parton system—in particular, on the number of perturbative parton-producing interactions, which, to a large extent, determines the initial parton density and other kinematical characteristics. In particular, the discrete nature of parton production in phase space, as described by finite-order QCD calculations, can give rise to primordial event-by-event angular asymmetries of the parton flow. The fate of the primordial angular asymmetries depends on relevant dynamics. (Is the evolution of the product system long enough to wash them out? Can they be frozen and directly relevant to the observed hadronic flow? There are also some other related questions.) In any case, the first problem to look at is to study the primordial parton system before the reinteraction of partons sets in.

The aim of this study is to analyze the characteristics of the initial minijet-induced transverse-energy flow in nucleon–nucleon and nucleus–nucleus collisions within the minijet-production scenario based on collinearly factorized QCD [5, 6]. In particular, we will analyze the fluctuational azimuthal imbalance in the minijet transverse-energy flow due to a discrete nature of transverse-energy production through basic QCD hard scattering. We can expect that the effect will be essentially sensitive to the number of semihard scatterings. In what follows, we will see that this is indeed the case.

Below, we study event-by-event inhomogeneities in the azimuthal distribution of minijets following from the basic asymmetry of minijet transverse-energy production into a finite rapidity window in pp collisions. Nuclear collisions are described by a geometric model [6] in which they are considered as a superposition of basic nucleon–nucleon ones. The azimuthal asymmetry of the minijet system will be specified in terms of (transverse) momenta exclusively, as calculated in the conventional S-matrix field-theory formalism without referring to the coordinates of partons and without making assumptions on the structure of the contributions of higher order in the QCD coupling constant in describing the transverse-energy production in an elementary nucleon–nucleon collision. This analysis can be extended to the next-to-leading order (e.g., along the lines of [28]) due to the infrared stability of the distributions being considered, which are of the energy–energy correlation type.

The analysis of the event-by-event pattern of the initial minijet-generated transverse-energy flow was first presented in [29], where the list of partons that was generated on the basis of HIJING [30] and which possesses specified coordinates and momenta was used to compute a coarse-grained energy density and velocity field at the RHIC of energy $\sqrt{s} = 200$ GeV. The resulting distributions proved to be highly irregular and similar to those occurring in turbulent flows. Note that, besides the parton–parton scattering described by collinearly factorized QCD considered in the present study, HIJING makes explicit assumptions on the structure of higher order contributions (unitarization), the contributions from initial- and final-state radiation, and the structure of the parton system in coordinate space (thus going beyond standard S-matrix formalism). The existence of asymmetry due to unbalanced particle production from minijets into a finite acceptance was mentioned in [3].

This article is organized as follows.

In Section 2, we analyze the basic mechanism for producing azimuthally symmetric and asymmetric configurations in the restricted phase-space domain, which, in the case considered here, will be a unit central rapidity window, in pp collisions. In the leading-twist (lowest order in parton density) and leading-order collinear factorization scheme, we calculate the relative weights for symmetric (two-jet) and asymmetric (one-jet) contributions to the transverse-energy-production cross section for RHIC ($\sqrt{s} =$ 200 GeV) and LHC ($\sqrt{s} = 5500$ GeV) for underlying nucleon–nucleon collisions.

In Section 3, the computed contributions to azimuthally symmetric and asymmetric components of the pp minijet-transverse-energy production into a unit central rapidity window are used in calculating the asymmetry of transverse-energy production in heavy-ion collisions, where a nuclear collision is described as a superposition of nucleon–nucleon ones in the geometric approach of [6]. We study the azimuthal asymmetry at RHIC and LHC energies for central collisions within two dynamical scenarios. In the first scenario, transverse-energy production is assumed to occur through two physically different mechanisms, the soft one and the (semi)hard one. Since our aim is to study the transverse-energy flow at the early collision stage related to the semihard

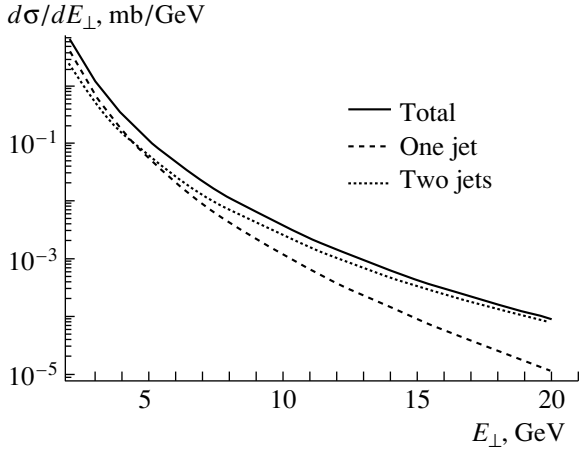

Fig. 1. One- and two-jet contributions to transverse-energy production in pp collisions in a unit central rapidity window at the RHIC energy of $\sqrt{s} = 200$ GeV.

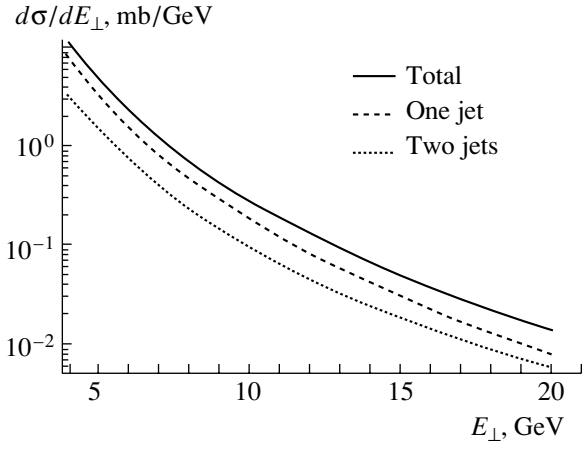

Fig. 2. One- and two-jet contributions to transverse-energy production in pp collisions in a unit central rapidity window at the LHC energy of $\sqrt{s} = 5500$ GeV.

degrees of freedom, the contribution of soft interactions will be taken into account only in determining the relative yield of the semihard contribution. In the second scenario, which can become realistic at LHC energies, all primordial transverse-energy production is assumed to occur through the semihard mechanism.

In the last section, we discuss the results and formulate the conclusions.

2. AZIMUTHAL PATTERN OF MINIJET PRODUCTION IN pp COLLISIONS

The mechanism responsible for transverse-energy production in the leading order in perturbative QCD is an elastic two-to-two parton–parton scattering. Its cross section is given by the standard collinearly factorized expression

$$\frac{d\sigma}{dp_\perp^2\, dy_1 dy_2} = x_1 f(x_1, p_\perp^2)\frac{d\hat{\sigma}}{dp_\perp^2} x_2 f(x_2, p_\perp^2), \quad (1)$$

where $xf(x, p_\perp^2)$ is the parton structure function, $x_{1,2} = p_\perp(e^{\pm y_1} + e^{\pm y_2})/\sqrt{s}$ are the fractional longitudinal momenta of the product partons, and $d\hat{\sigma}/dp_\perp^2$ is the differential cross section for elastic parton–parton scattering. In the following, we will be specifically interested in transverse-energy production into some given (central) rapidity interval $y_{\min} < y_1, y_2 < y_{\max}$. Operationally, the transverse energy $E_\perp$ deposited in this window by the two scattered partons is defined as[1)]

$$E_\perp = p_1\theta(y_{\min} \le y_1 \le y_{\max}) + p_2\theta(y_{\min} \le y_2 \le y_{\max}). \quad (2)$$

[1)]In Eq. (2) and below, $p_i = |\mathbf{p}_{\perp i}|$.

Let us emphasize that, while the expression for the transverse energy in Eq. (2) is specifically taken to be of the lowest order in α_s, the quantity $E_\perp$ refers to the total transverse energy produced in a particular rapidity interval in a semihard collision. In the following, we will confine ourselves to considering the central rapidity interval $y_{\min} = -0.5 < y < y_{\max} = 0.5$ and stay at the leading-order (Born elastic scattering) level, so that, in each collision, the transverse momenta of the two product partons are equal, $p_{\perp 1} = p_{\perp 2} = p$. This does not mean that these transverse momenta will be balanced in the rapidity window under consideration; therefore, the event space for transverse-energy deposition can be summarized by

$$E_\perp = \begin{cases} 0 & \text{if no particle gets into the gap} \\ p & \text{if one particle gets into the gap} \\ 2p & \text{if two particles get into the gap.} \end{cases} \quad (3)$$

In considering the transverse-energy production into a given rapidity window in pp collisions, only the second and third possibilities are relevant. To quantify the computation of the contribution corresponding to the second and third cases in (3), it is convenient to introduce the integral operators

$$S_1 = \int dy_1 dy_2 (\theta(y_1) + \theta(y_2) - 2\theta(y_1)\theta(y_2)) \cdot (\dots), \quad (4)$$

$$S_2 = \int dy_1 dy_2 (\theta(y_1)\theta(y_2)) \cdot (\dots), \quad (5)$$

where $\theta(y_{1,2}) = \theta(y_{\min} < y_{1,2} < y_{\max})$. Applying these operators to the differential cross section (1), we get the decomposition of the transverse-energy-production cross section in a given rapidity window into the separate one-jet and two-jet contributions

[second and third entries in the event list in Eq. (3)]; that is,

$$\frac{d\sigma}{dE_\perp} = \frac{d\sigma_1}{dE_\perp} + \frac{d\sigma_2}{dE_\perp}, \tag{6}$$

where

$$\frac{d\sigma_1}{dE_\perp} = S_1 \cdot \left(\frac{d\sigma}{dp}\right)\Big|_{p=E_\perp}, \tag{7}$$

$$\frac{d\sigma_2}{dE_\perp} = 2S_2 \cdot \left(\frac{d\sigma}{dp}\right)\Big|_{p=E_\perp/2}. \tag{8}$$

On the event-by-event basis, these contributions correspond to completely distinct possibilities of having the azimuthally balanced symmetric or unbalanced asymmetric transverse-energy flow in the rapidity window under consideration.

We emphasize that the cross section in Eq. (2) is an exclusive and infrared-stable quantity because $E_\perp$ is the total transverse energy deposited in a given rapidity interval.

In Figs. 1 and 2, we plot the transverse-energy-production cross sections (7) and (8) associated both with gluon and with quark (with $n_f = 5$) minijets for the RHIC and LHC energies of $\sqrt{s} = 200$ GeV and $\sqrt{s} = 5500$ GeV, where, for LHC, we have chosen the energy to be available for protons in lead beams and where we used the MRSG structure functions [31].

In Fig. 3, we also present the differential cross sections for transverse-energy production into full rapidity intervals available at RHIC and LHC energies, which will be used in the next section to normalize the differential cross sections for transverse-energy production in *pp* collisions.

Information contained in Figs. 1 and 2 is summarized in Table 1, where we show the fitted parameters for the one-jet and two-jet spectra in Eqs. (7) and (8) having the functional form $c(E_\perp/1\ \text{GeV})^{-\alpha}$.

We see that, at RHIC energies, the one-jet asymmetric contribution dominates at low transverse energies and that the two-jet symmetric contribution takes over at $E_\perp \sim 4.5$ GeV. At LHC energies, the asymmetric contribution is clearly dominant in the entire minijet-transverse-energy range.

3. AZIMUTHAL ASYMMETRY OF MINIJET-TRANSVERSE-ENERGY FLOW IN NUCLEAR COLLISIONS

In this section, we proceed to analyze the angular asymmetry of minijet-produced transverse-energy flow in nuclear collisions induced by the fundamental asymmetry in *pp* collisions described in the preceding section. The translation of the features characterizing

Table 1

$\sqrt{s}$, GeV	α_1	α_2	c, mb/GeV	
	1 jet	2 jets	1 jet	2 jets
200	5.09	4.53	173	77
5500	4.25	3.93	3099	819

particle production in *pp* collisions to those characterizing nuclear ones is possible, e.g., in a geometric model, where a nucleus–nucleus collision is considered as a superposition of the proton–proton ones (see, e.g., [5, 6]). At each value of the impact parameter b, where b is the distance in the transverse plane between the centers of the colliding nuclei, a nucleus–nucleus collision is described as a Poisson superposition of nucleon–nucleon collisions such that the probability of n *pp* collisions is given by

$$w_n(b) = \frac{1}{n!}\bar{N}_{AB}^n(b)e^{-\bar{N}_{AB}(b)}, \tag{9}$$

where $\bar{N}_{AB}(b)$ is the average number of *pp* collisions in the nucleus–nucleus one, which is thus described as a specific superposition of multiple independent *pp* collisions occurring with the weight given by Eq. (9). Elementary *pp* collisions occur between some nucleon belonging to the nucleus A located at the transverse distance b_1 from its center with the probability given by the probability density $\rho_A(b_1)$ with the normalization

$$\int d^2b_1\rho_A(b_1) = 1 \tag{10}$$

and the nucleon from nucleus B located at the transverse distance b_2 from its center with the probability given by the probability density $\rho_B(b_2)$ with the collision probability $P\left(\bar{b} - \bar{b}_1 + \bar{b}_2\right)$. Thus, the average

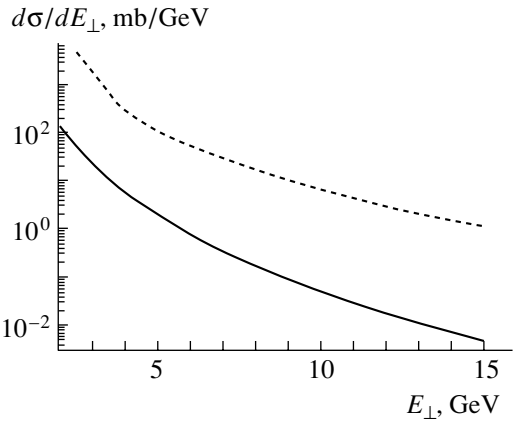

Fig. 3. Transverse-energy production in *pp* collisions in the entire rapidity interval at RHIC ($\sqrt{s} = 200$ GeV, solid curve) and LHC ($\sqrt{s} = 5.5$ TeV, dashed curve) energies.

number of pp collisions characterizing the basic Poisson process [Eq. (9)] is given by

$$\bar{N}_{AB}(b) = AB \int d^2b_1 d^2b_2 P\left(\bar{b} - \bar{b}_1 + \bar{b}_2\right) \times \rho_A(b_1)\rho_B(b_2), \quad (11)$$

where $P(b)$ is a probability of an inelastic collision of two nucleons initially separated by the transverse distance $\bar{b} - \bar{b}_1 + \bar{b}_2$. For practical calculations, we use the Woods–Saxon nuclear probability density [32]. The physical meaning of the collision probability $P(b)$ depends on the underlying physical mechanism responsible for inelastic transverse-energy production in binary nucleon–nucleon collisions. Our discussion is confined to minijets as providing such a source; therefore, in our case, $P(b)$ is the probability of a minijet-producing inelastic nucleon–nucleon collision occurring at fixed impact parameter b. Let us emphasize that the differential probability of minijet-induced transverse-energy production depends on the rapidity window under consideration. The usual assumption about the impact-parameter dependence of the probability $P(b)$ of nucleon–nucleon collisions is that the collisions are local in the impact-parameter plane; i.e.,

$$P(b) = \sigma_{pp}^{\text{minijet}}(|\Delta y| \le y_0)\delta^{(2)}(b). \quad (12)$$

Let us now discuss in some detail the normalization of the Poisson process (9) provided by the overall cross section for minijet production into the rapidity window $|\Delta y| \le y_0$, $\sigma_{pp}^{\text{minijet}}(|\Delta y| \le y_0)$. The overall minijet contribution to the transverse-energy-production cross section is given by the integral with respect to $E_\perp$ of the differential cross section (6). Because of the singular behavior of the perturbative transverse-energy-production cross section at low $E_\perp$, the very definition of the overall contribution of the minijet mechanism to transverse-energy production requires introducing a cutoff at low transverse energies,

$$\sigma_{pp}^{\text{minijet}}(|\Delta y| \le y_0 | E_0) = \int\limits_{E_0} dE_\perp \frac{d\sigma}{dE_\perp}(\Delta y). \quad (13)$$

We note that, for any rapidity interval,

$$\int\limits_{E_0} dE_\perp \frac{d\sigma}{dE_\perp}(\Delta y) \le \sigma^{\text{inel}}(\Delta y), \quad (14)$$

where $\sigma^{\text{inel}}(\Delta y)$ is the (experimental) inelastic cross section in a given rapidity window Δy. This shows that the cutoff E_0 is physically a function of the rapidity interval being considered.

Another important issue related to the choice of this cutoff is the possible contribution to the overall inelastic cross section for other mechanisms of transverse-energy production—e.g., for soft particle production due to the decay of hadronic strings. The restriction in Eq. (14) clearly refers only to that part of the inelastic cross section which corresponds to hard inelasticity—i.e., transverse-energy production through semihard processes. The other part of the inelastic cross section corresponds to soft mechanisms of transverse-energy production, which do not involve high momentum transfers. It is important to note that the characteristic time scale of semihard transverse-energy production is shorter than that for the soft nonperturbative mechanism. At the early stages of the collision process, the hard-parton skeleton is formed, which is then dressed by soft particle production due to strings stretched between partons originating from primordial processes characterized by a high momentum transfer. This shows, in particular, that soft processes do not have, generally speaking, an independent share of the overall inelasticity; therefore, the naive additivity

$$\frac{d\sigma}{dE_\perp} = \frac{d\sigma^{\text{minijet}}}{dE_\perp} + \frac{d\sigma^{\text{soft}}}{dE_\perp} \quad (15)$$

is not valid in general. It could happen, e.g., that, with growing collision energy, the yield of events with hard initial inelasticity would be dominant or even cover the whole event space (here, we refer to nondiffractive contribution). In this extreme scenario, the only function of the soft mechanism is to stretch strings between the hard initial partons. Here, it is important to recall that the cross section for transverse-energy production [see Eq. (6)] as computed within perturbative QCD is a so-called infrared-safe quantity and is thus entirely determined by its early quark–gluon stage—it does not depend on the late stages of the process, including string formation between the separated partons.

Let us emphasize once again that, in the present study, we confine our consideration to analyzing the angular pattern of the primordial transverse-energy flow generated at the early stages of collisions by semihard degrees of freedom (minijets). The analysis of the effects related to the subsequent redistribution of primordial transverse energy by soft interactions at longer times will be discussed in the future publications [33].

The yield of the perturbative contribution as a function of the c.m. energy is a crucial characteristic of the inelastic cross section. Unfortunately, very little can currently be said about its magnitude; this results in the uncertainty in fixing the cutoff for the perturbative contribution.

In view of this, we will fix the cutoff value E_0 at a given collision energy as follows. To explore the possible "window of opportunities" for the hard minijet contribution as determined by the yield of

Table 2

$\sqrt{s}$, GeV	$\sigma^{\rm soft}$, mb	$\sigma^{\rm hard}$, mb	E_0, GeV	p_1	$\sigma_{pp}^{\rm minijet}$, mb	$\sigma_{\rm PbPb}^{\rm minijet}$, mb
200	0	41.8	2.4	0.54	2.4	5336
	32	9.8	3.5	0.48	0.54	4102
5500	0	66.3	6.9	0.65	2.8	5443
	32	34.3	8.4	0.64	1.5	4970

independent soft particle production, we will discuss two model scenarios—namely, in considering inelastic particle production at all rapidities, we will either assume the constant soft contribution $\sigma^{\rm soft}(pp) = 32$ mb, the inelastic cross section for pp scattering at intermediate energies universally present at all c.m. energies (mixed scenario), or assume that, in all collisions, the transverse energy is produced via the early perturbative minijet stage—i.e., set $\sigma^{\rm soft}(pp) = 0$ (hard scenario). The cutoff E_0 is thus determined from the relation[2)]

$$\int\limits_{E_0} dE_\perp \frac{d\sigma_{pp}^{\rm minijet}}{dE_\perp} = \sigma^{\rm hard} \qquad (16)$$

$$= \begin{cases} \sigma_{\rm exp}^{\rm inel}, & \text{no soft contribution,} \\ \sigma_{\rm exp}^{\rm inel} - 32\ \text{mb}, & \text{a soft contribution of 32 mb,} \end{cases}$$

where the transverse spectrum in Eq. (16) refers to the full kinematic interval [see Fig. (3)]. Let us emphasize that the differential cross section for transverse-energy production that we use in Eq. (16) is the result of the lowest order calculation from the preceding section; the higher order effects, which can phenomenologically be included within the geometric unitarization scheme (see, e.g., [3]), are not included. The numerical values of the cutoff that were found by integrating the spectra shown in Fig. (3) are given in Table 2. In the fifth column, we show the overall probability of asymmetric one-jet contribution $p_1(E_0)$ calculated by using the differential transverse-energy-production spectra in (6)–(8):

$$p_1(E_0) = \left(\int\limits_{E_0}^{\infty} dE_\perp \frac{d\sigma_1}{dE_\perp}\right) \Bigg/ \left(\int\limits_{E_0}^{\infty} dE_\perp \frac{d\sigma}{dE_\perp}\right). \qquad (17)$$

It was mentioned above that, although the differential spectra describe transverse-energy production into some given rapidity window, the value of the cutoff E_0 will be determined below from Eq. (14) considered for the full rapidity window kinematically available for inelastic energy production at a given collision energy. For a more accurate determination of the cutoff E_0, one would need experimental data on inelastic cross sections in, e.g., the central rapidity window. Different quantities have different sensitivities to the choice of cutoff; in particular, the E_0 dependence of $p_1(E_0)$ in Eq. (17) is quite weak. In the last column of Table 2, we show the cross section for the production of at least one minijet in lead–lead collisions, $\sigma_{\rm PbPb}^{\rm minijet}$:

$$\sigma_{\rm PbPb}^{\rm minijet} = \int d^2b(1 - w_0(b)) \qquad (18)$$

$$= \int d^2b(1 - e^{-\bar{N}_{AB}(b)}).$$

Here, $w_0(b)$ is the probability of having no minijet-producing nucleon–nucleon collisions [cf. Eq. (9)].

Transverse-energy production in nucleus–nucleus collisions is then described by the convolution of the distribution in the number of pp collisions obtained from Eq. (9) at a given impact parameter with the distributions characterizing transverse-energy production in pp collisions in Eqs. (7) and (8).

In practice, this convolution was realized by a Monte Carlo procedure, where a large number (10^7) of nucleus–nucleus collisions were generated, with the number of pp collisions N being distributed according to Eq. (9); the weight of one-jet asymmetric (two-jet symmetric) pp collisions is equal to the probability $p_1\,(1 - p_1)$, with p_1 being taken from Table 2. More explicitly, this corresponds to a binomial distribution in the number of asymmetric collisions N_a

$$w(N_a) = C_N^{N_a} p_1^{N_a} (1 - p_1)^{N - N_a}; \qquad (19)$$

the weight for $E_\perp$ itself was in turn determined by Eqs. (7) and (8) for asymmetric and symmetric contributions, respectively. The azimuthal orientation of jet(s) was determined at random in accordance with a flat distribution in the azimuthal angle. For two-jet events, the jets travel in opposite directions, so that their azimuths differ by π.

Let us now perform a quantitative analysis of the event-by-event asymmetry of the minijet-generated transverse-energy flow. This will be done by using a

[2)]The inelastic cross section is computed by using the parametrization $\sigma^{\rm inel}(s) = \sigma_0(s/s_0)^{0.0845}(0.96 - 0.03\log(s/s_0))$, where $s_0 = 1$ GeV and $\sigma_0 = 21.4$ mb, which provides a good description of the existing experimental data [34] (see also the compilation in [3]).

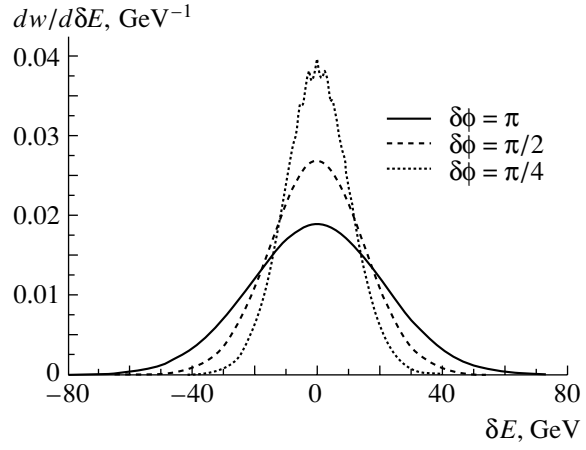

Fig. 4. Probability distribution of the azimuthal asymmetry δE in a unit central rapidity window at the RHIC energy of $\sqrt{s} = 200$ GeV for central PbPb collisions, $\sigma^{\rm soft} = 0$.

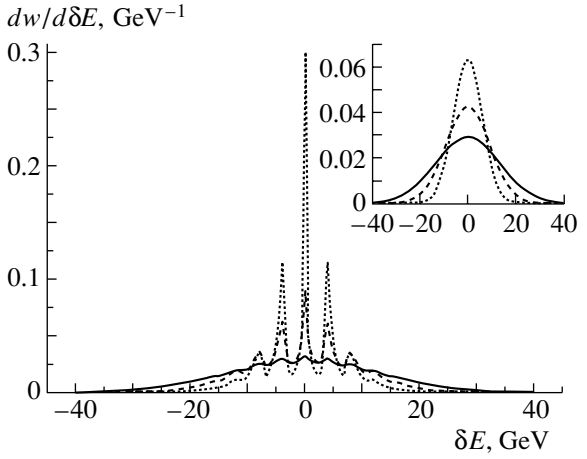

Fig. 5. As in Fig. 4, but for $\sigma^{\rm soft} = 32$ mb. The result of smoothing appears as a Gaussian distribution shown in the inset.

(normalized) difference of the transverse-energy flows into the sectors that are characterized by opposite azimuthal orientations and which have a specified angular opening $\delta\varphi$ each and the rapidity window $|y| < 0.5$. Let us note that this quantity has an important advantage of admitting a future next-to-leading order analysis. For the sake of convenience, one can think of the directions of these cones as being "up" and "down," which corresponds to some specific choice of orientation of the system of coordinates in the transverse plane. All our results are of course insensitive to a particular choice. Let us denote by $E_\uparrow(\delta\varphi)$ and $E_\downarrow(\delta\varphi)$ the transverse energies going into, respectively, the "upper" and the "lower" cones in a given event. The magnitude of the asymmetry in transverse-energy production can then be quantified by introducing the variable

$$\delta E = E_\uparrow(\delta\varphi) - E_\downarrow(\delta\varphi). \qquad (20)$$

Using the distribution in the number of asymmetric collisions [see Eq. (19)] and considering that the event space of asymmetric collisions is further subdivided into two sets corresponding to nonzero energies $E_\uparrow$ and $E_\downarrow$ going into the upper and lower cone, we can calculate the squared mean of $\delta E(\delta\phi)$ for the azimuthal openings $\delta\phi = \pi/2^n$ being considered ($n = 0, 1, 2$):[3)]

$$\sqrt{\langle\delta E^2\rangle} = \frac{1}{2^{n/2}} E_0 \sqrt{p_1 \bar{N} \frac{\alpha_1 - 1}{\alpha_1 - 3}}. \qquad (21)$$

The values of α_1 are given in Table 1. The quantity $\delta E(\delta\phi)$ in Eq. (21) characterizes the magnitude of the disbalance in the minijet-generated transverse-energy flow. Note that δE is highly sensitive to the overall magnitude of the semihard (minijet-generated) transverse-energy flow. In Eq. (21), this is clearly seen from $\langle\delta E^2\rangle \propto E_0^2 \bar{N}$. The numerical values of $\sqrt{\langle\delta E^2\rangle}$ are given below. From now on, we confine our discussion to central PbPb collisions.

Figures 4–7 show the probability distribution of δE in central PbPb collisions for two values of the c.m. energy (200 GeV and 5.5 TeV) and two choices of E_0 corresponding to the mixed and the hard scenario. The angular apertures were chosen to be π, $\pi/2$, and $\pi/4$. From these figures, we see that, for all types of collisions (except for Fig. 6), there appear peaks in the probability distribution at $\delta E = nE_0$. This is a reflection of a sharp cutoff adopted in the model and of a fast decrease in the minijet cross section with increasing $E_\perp$. In the majority of cases, this effect is seen only for small values of the angular opening. A crucial parameter related to the appearance of the peaks is in fact $\bar{N}$. The smaller $\bar{N}$, the more pronounced the peaks. One could expect that hadronization and soft processes accompanying minijet production smoothed out these peaks. Curves that were initially smooth undergo the Gaussian law with the variance $\langle\delta E^2\rangle$. Therefore, we can imagine the appearance of curves with peaks that have, after smoothing, a Gaussian shape with variances given by Eq. (21). For Fig. 5, the result of such smoothing is shown in the inset.

Another useful quantity is a normalized asymmetry, on the contrary, which is insensitive to the absolute magnitude of transverse energy flow,

$$r(\delta\varphi) = \frac{E_\uparrow(\delta\varphi) - E_\downarrow(\delta\varphi)}{E_\uparrow(\delta\varphi) + E_\downarrow(\delta\varphi)}, \qquad (22)$$

[3)] It is easy to see that the distribution of δE is a so-called multi-Poisson one.

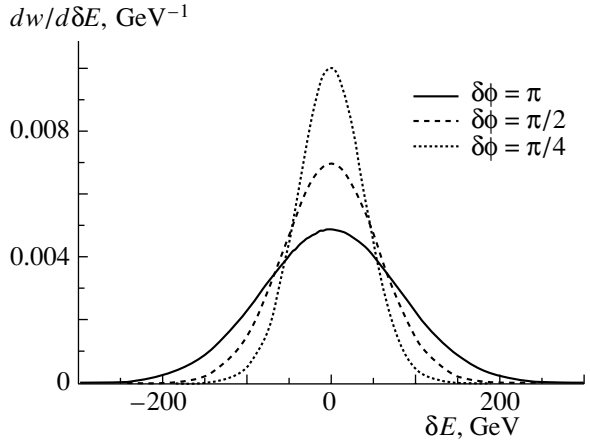

Fig. 6. Probability distribution of the azimuthal asymmetry δE in a unit central rapidity window at the LHC energy of $\sqrt{s} = 5.5$ TeV for central PbPb collisions, $\sigma^{\text{soft}} = 0$.

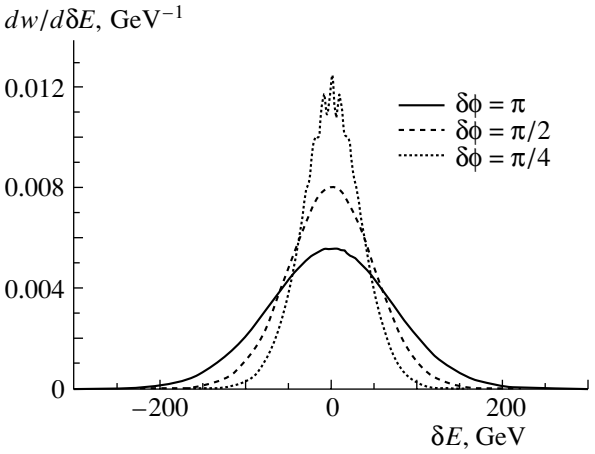

Fig. 7. As in Fig. 6, but for $\sigma^{\text{soft}} = 32$ mb.

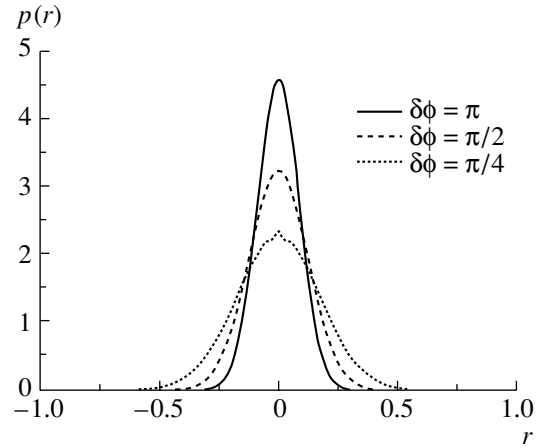

Fig. 8. Probability distribution of the normalized azimuthal asymmetry, $p(r)$, in a unit central rapidity window at the RHIC energy of $\sqrt{s} = 200$ GeV for central PbPb collisions, $\sigma^{\text{soft}} = 0$.

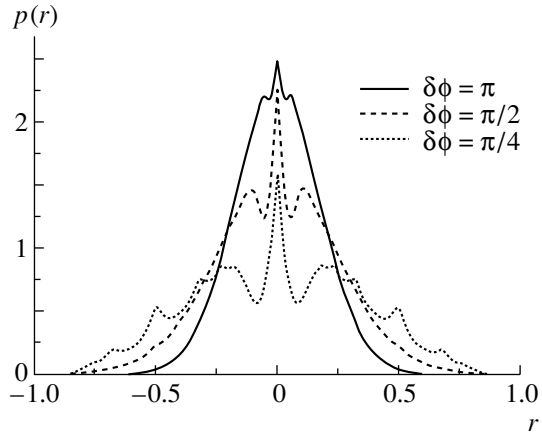

Fig. 9. As in Fig. 8, but for $\sigma^{\text{soft}} = 32$ mb.

where $r \in [-1, 1]$. In particular, the normalized asymmetry r simplifies a comparison of the asymmetries at different c.m. energies. The values of $r(\delta\varphi)$ in different collisions are characterized by the normalized probability distribution

$$p(r)|_{\delta\varphi} = \frac{1}{\sigma}\frac{d\sigma}{dr}\bigg|_{\delta\varphi}. \qquad (23)$$

To evaluate $p(r)$, we use a Monte Carlo simulation of the nuclear-scattering process as described above for a generated ensemble of 10^7 PbPb collisions at RHIC and at LHC energies. We have calculated the asymmetry distributions $p(r)$ for the central (zero impact parameter, $b = 0$) collisions and cone apertures of $\pi, \pi/2$, and $\pi/4$. The resulting probability distributions are illustrated in Figs. 8–11 for the mixed ($\sigma^{\text{soft}} = 32$ mb) and the hard ($\sigma^{\text{soft}} = 0$) scenario at RHIC and LHC energies. Let us note that, in the cases where the number of contributing collisions is not large (RHIC), one encounters "singular" configurations for which $r = -1, 1$ and $r = 0$ correspond to absolutely asymmetric and absolutely symmetric events in PbPb collisions. These are events in which only one one-jet event contributes to the given aperture during the collision ($r = -1, 1$) or one two-jet event contributes to $r = 0$. Their probabilistic weight can be described by a δ-functional contribution to $p(r)$ at the "singular" points. Their yield in the minijet event ensemble is given in Table 3 for the mixed ($\sigma^{\text{soft}} = 32$ mb) scenario at the RHIC energy (other values are negligible).

In Fig. 9, these contributions would correspond to infinitely narrow peaks; therefore, they are not shown.

The angular pattern of transverse-energy production as characterized by the energy–energy azimuthal

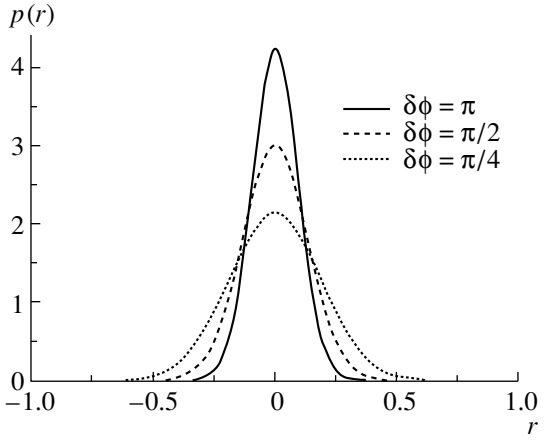

Fig. 10. Probability distribution of the normalized azimuthal asymmetry, $p(r)$, in a unit central rapidity window at the LHC energy of $\sqrt{s} = 5.5$ TeV for central PbPb collisions; $\sigma^{\rm soft} = 0$.

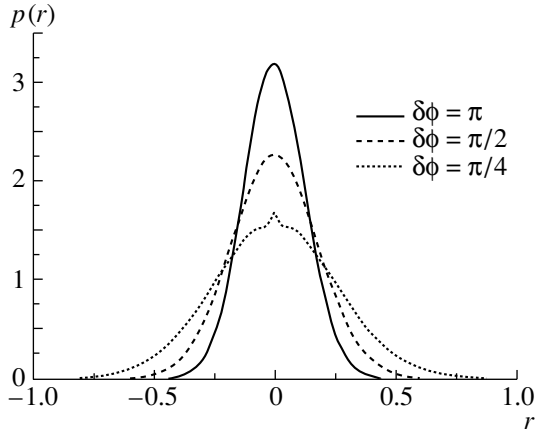

Fig. 11. As in Fig. 10, but for $\sigma^{\rm soft} = 32$ mb.

correlation probability distribution being considered is conveniently described by the lowest moments of $p(r)$. In Table 4, we present, together with the numerical values of the root-mean-square value $\sqrt{\langle \delta E^2 \rangle}$ [cf. Eqs. (20) and (21)], the values of the standard deviation a defined as

$$a^2 = \int dr (r - \bar{r})^2 p(r), \qquad (24)$$

where $\langle r \rangle = 0$ in our case.

Table 3

$\delta\varphi$	$r = -1$	$r = 0$	$r = 1$
$\pi/2$	1.3×10^{-3}	1.6×10^{-2}	1.3×10^{-3}
$\pi/4$	2.5×10^{-2}	1.2×10^{-1}	2.5×10^{-2}

Note that all the data presented in Table 4 include contributions from the singular points $r = -1, 0, 1$.

Let us now proceed to analyze the results presented in Figs. 4–11 and in Tables 3 and 4. The main goal is to understand the dependence of the angular pattern of the transverse-energy flow on basic parameters such as the infrared cutoff E_0, the total number $\bar{N}$ of minijet-generating collisions, the yield p_1 of asymmetric pp collisions, and c.m. energy $\sqrt{s}$.

In the fourth column of Table 4, we show the mean-square value $\langle \delta E^2 \rangle$ for the azimuthal opening of $\delta\phi = \pi$. The results agree with Eq. (21), so that the average disbalance in the transverse energy is indeed essentially determined by E_0 and $\bar{N}$.

To understand the results for the normalized asymmetry $p(r)$, it is advisable to consider a simplified model where elementary pp collisions can produce only some given amount of transverse energy,

$$\left(\frac{d\sigma}{dE_\perp}\right)^{pp} = \sigma^{\rm hard}(\sqrt{s})\delta(E_\perp - E_0(\sqrt{s})), \qquad (25)$$

so that all transverse energy is assumed to be produced exactly at the cutoff E_0. Note that, except for ascribing energy production to elementary pp collisions, this model is very similar to the expected pattern of transverse-energy production in the semiclassical approach based on the McLerran–Venugopalan model (cf. [21]). For the azimuthal apertures of $\delta\phi = \pi/2^n (n = 0, 1, 2)$ considered here, we find for the standard deviation a defined in Eq. (24) that[4)]

$$a\left(\delta\phi = \frac{\pi}{2^n}\right) \approx \sqrt{\frac{1}{2^n}\frac{p_1}{\bar{N}}}\left(1 + O\left(\frac{1}{\bar{N}}\right)\right). \qquad (26)$$

This shows that the width of the distribution $p(r)$ is determined by the ratio of the relative yield p_1 of asymmetric collisions to the mean number of collisions. In Table 4, we compare the predictions of this simple model with the values of standard deviation a computed by using the differential spectra plotted in Figs. 1 and 2 (for the reasons of space, only the results for $\delta\phi = \pi$ are given in the fifth column) and observe only a 10% difference. This shows that the results obtained by using the continuous spectra in Figs. 1 and 2 are essentially determined by the contribution at the cutoff energy E_0.

From Fig. 9, we can see that, for a small number of asymmetric collisions, the shape of $p(r)$ has peculiar sharp peaks at certain values of r. The origin of this is in fact the growth of the differential cross section for transverse-energy production at low $E_\perp$ in pp collisions (cf. Figs. 1 and 2). Indeed, we assume,

[4)] The details of this calculation can be found in the Appendix.

Table 4

σ^{soft}, mb	$\sqrt{s}$, GeV	$\bar{N}_{\mathrm{PbPb}}$	$\sqrt{\langle\delta E^2\rangle}$, GeV	$\sqrt{p_1/N}$	a		
					$\delta\phi=\pi$	$\delta\phi=\pi/2$	$\delta\phi=\pi/4$
0	200	75.7	21	0.084	0.088	0.124	0.178
	5500	87.4	84	0.086	0.094	0.133	0.189
32	200	17.1	14	0.168	0.177	0.259	0.387
	5500	47.1	74	0.117	0.127	0.180	0.257

for simplicity, that each pp collision in the restricted minijet ensemble can produce transverse energy only exactly at the cutoff $E_\perp = E_0$ [cf. Eq. (25)]. In this case, we will have, in addition to the "true" singular points $r = -1, 0, 1$, "semisingular" ones, so that, for a particular event containing n minijets, with $n_{1\uparrow}$ being the number of "up-coming" one-jet events, $n_{1\downarrow}$ being the number of "down-coming" one-jet events, and $n_2 = n - n_{1\uparrow} - n_{1\downarrow}$ being the number of two-jet events, the following exact relation holds:

$$r = \frac{n_{1\uparrow} - n_{1\downarrow}}{n}. \qquad (27)$$

Thus, the values of r belong to a set of rational numbers in the interval $[-1, 1]$ that are called here "semisingular" points. Of course, the most spectacular "semisingular" points are those with small numerators and denominators, both due to a higher frequency of events having a small number of minijets and due to a smaller distribution width (deviation from $E_\perp = nE_0$) for events with a small number of asymmetric collisions.

Let us note that the appearance of the singular points -1, 0, and 1 is a consequence of calculating the cross sections for transverse-energy production in the elementary hard block in the lowest order of perturbation theory. In the next-to-leading order, where transverse energy can be shared among three (mini)jets, these singular points will become milder singularities of $p(r)$ at $r = -1, 0, 1$. This shows that the calculation of the true shape of $p(r)$ near the singular points requires, as usual, resumming all orders of the perturbative contributions.

Physically, within the scheme adopted in this study, the number of semihard collisions depends on sharing inelasticity among the soft and hard mechanisms of transverse-energy production. In the mixed scenario, we assumed that 32 mb of the inelastic cross section for pp collisions corresponds to the soft production mechanism, while the rest of the inelastic cross section is due to semihard production. In the hard scenario, it is assumed that semihard transverse-energy production saturates all available inelasticity. It is expected that the distributions $p(r)$ characterizing the azimuthal asymmetry of transverse-energy production defined in Eq. (23) will be wider in the mixed than in the hard scenario. From Table 4, we can see that this is indeed so. At RHIC energies, the standard deviation for the mixed scenario is larger than that in the hard one, their ratio being $a^{\mathrm{mixed}}_{\mathrm{RHIC}}/a^{\mathrm{hard}}_{\mathrm{RHIC}} \simeq 2.0$–$2.1$. At LHC energies, the effect is less pronounced; here, $a^{\mathrm{mixed}}_{\mathrm{LHC}}/a^{\mathrm{hard}}_{\mathrm{LHC}} \simeq 1.3$–$1.4$. We see that, with increasing c.m. energy, the angular pattern of the minijet-generated transverse-energy flow becomes less sensitive to the relative weight of the perturbative and nonperturbative contributions to the inelastic cross section.

The dependence of the standard deviation a on the aperture remains essentially the same for both c.m. energies and values of the impact parameter considered here and is inversely proportional to the angular opening:

$$a_{\pi/2n} \simeq 2^{n/2} a_\pi. \qquad (28)$$

This is consistent with the prediction of the simple model of transverse-energy production as given by Eq. (26) and corresponds to a purely statistical change in the standard deviation, where the shrinking of the angular aperture by a factor of 2 enlarges the standard deviation by a factor of $\sqrt{2}$.

4. CONCLUSIONS

The main results of our analysis can be formulated as follows.

We have first discussed a basic asymmetry in minijet-transverse-energy production in a restricted rapidity window in pp collisions due to different probabilities of having a "symmetric" two-jet or an "asymmetric" one-jet contribution in the rapidity interval under consideration. The cross sections for symmetric and asymmetric contributions in pp collisions for RHIC and LHC energies show that, while, at the RHIC energy, the weights of the two configurations are approximately equal, at the LHC energy, the asymmetric contribution is clearly dominant.

We have further considered a geometric model for nuclear collisions in which they are described as an incoherent superposition of nucleon–nucleon ones. We have discussed two possible partitions of the inelastic cross section in terms of the soft and semihard contributions and analyzed the angular pattern of the minijet-generated energy flow for central and peripheral nuclear collisions at RHIC and LHC energies. Specifically, we have considered the probability distributions for transverse-energy–transverse-energy correlations in cones having opposite azimuthal orientations and a varying aperture. We have shown that the resulting distributions are highly sensitive to the number of semihard collisions, which is in turn dependent on the above-mentioned partition of the inelastic cross section into contributions of different types and on the (related) choice of infrared cutoff. We have also shown that the results are very close to the predictions of the simple model where all the transverse energy is produced directly at the infrared cutoff.

The approach developed in this study could be further generalized to the analysis of the minijet-generated background-oriented flow [35] (for the definition of the oriented flow and a comprehensive discussion, see, e.g., [36]). In particular, since the importance of the minijet contribution is expected to grow with energy, the presence of the background-oriented flow of a purely fluctuational origin could increasingly affect corresponding hadronic observables.

Another crucial issue is the dynamical evolution of primordial partonic inhomogeneities in the course of parton–hadron conversion. In [37], it was shown, that the seed inhomogeneity in the initial condition of the elliptic-flow type for the hadronic RQMD code survives the freeze-out and is visible in final azimuthal distributions. This question is surely the most important and will be discussed in the forthcoming publication [33].

ACKNOWLEDGMENTS

We are grateful to K. Kajantie, G. Zinovjev, J. Schukraft, K. Eskola, I.M. Dremin, I.V. Andreev, J.-P. Blaizot, J.-Y. Ollitrault, L. McLerran, and P. Jacobs for stimulating discussions. A. Leonidov is grateful for the kind hospitality and support at CERN Theory Division, where this work was started, and at Service de Physique Theorique de Saclay, where a major part of it was done. We are grateful to the referee of the first version of this article for constructive comments and suggestions.

This work was supported in part by the Russian Foundation for Basic Research (project no. 96-02-16347). The work of D. Ostrovsky was supported in part by INTAS (grant no. 96-0457) within the ICFPM program.

APPENDIX

In this appendix, we present a derivation of the formula for the standard deviation a (26). Let n be the number of minijet-producing hadron–hadron collisions in a given nucleus–nucleus collision characterized by a Poisson distribution (9). Let us further denote by n_1 the number of those minijet-producing hadron collisions in which only one minijet hits the rapidity window under consideration (asymmetric contribution) and by $n_{1\uparrow}$ and $n_{2\downarrow}$ the numbers of such single minijets propagating into, respectively, the upper and the lower of the two oppositely oriented cones. In this appendix, we employ the model where the minijet transverse energy hitting the acceptance window in a single hadron–hadron collision is fixed at the cutoff value E_0 [cf. Eq. (25)]. Averaging over the event ensemble must be performed in the order opposite to that adopted in the Monte Carlo procedure. First, we average over $n_{1\uparrow}$ at fixed $n_1 = n_{1\uparrow} + n_{1\downarrow}$:

$$\langle r^2 \rangle_{n_1} = \sum_{n_{1\uparrow}=0}^{n_1} \frac{1}{2^{n_1}} C_{n_1}^{n_{1\uparrow}} \frac{(n_{1\uparrow} - n_{1\downarrow})^2}{n^2} = \frac{n_1}{n^2}. \quad \text{(A.1)}$$

Next, we average over n_1 at fixed n according to the binomial probability distribution (19):

$$\langle r^2 \rangle_n = \frac{p_1}{n}. \quad \text{(A.2)}$$

Finally, we must average over the Poisson distribution (9). This yields

$$a^2 = \langle r^2 \rangle = e^{-\bar{N}} \sum_{n=1}^{\infty} \frac{p_1}{n} \frac{\bar{N}^n}{n!} \quad \text{(A.3)}$$

$$= p_1 \bar{N} e^{-\bar{N}} F(1,1;2,2;\bar{N}) \approx \frac{p_1}{\bar{N}} \left(1 + O\left(\frac{1}{\bar{N}}\right)\right),$$

where $F(1,1;2,2;\bar{N})$ is a generalized hypergeometric function.

REFERENCES

1. S. A. Baas, M. Gyulassy, H. Stöcker, and W. Greiner, hep-ph/9810281.
2. E. M. Levin and M. G. Ryskin, Phys. Rep. **189**, 267 (1990).
3. X.-N. Wang, Phys. Rep. **280**, 287 (1997).
4. K. J. Eskola, Comments Nucl. Part. Phys. **22**, 185 (1998); nucl-th/9705027.
5. K. Kajantie, P. V. Landshoff, and J. Lindfors, Phys. Rev. Lett. **59**, 2527 (1987).
6. K. J. Eskola, K. Kajantie, and J. Lindfors, Nucl. Phys. B **323**, 37 (1989).
7. K. J. Eskola, K. Kajantie, and V. Ruuskanen, Eur. Phys. J. C **1**, 627 (1998).
8. K. J. Eskola and K. Kajantie, Z. Phys. C **75**, 515 (1997).

9. K. J. Eskola, K. Kajantie, P. V. Ruuskanen, and K. Tuominen, hep-ph/9909456.
10. T. Sjostrand and M. van der Zijl, Phys. Rev. D **36**, 2019 (1987).
11. J. P. Blaizot and A. H. Mueller, Nucl. Phys. B **289**, 847 (1987).
12. L. McLerran and R. Venugopalan, Phys. Rev. D **50**, 2225 (1994); **49**, 2233 (1994).
13. A. Kovner, L. McLerran, and H. Weigert, Phys. Rev. D **52**, 3809, 6231 (1995).
14. Yu. V. Kovchegov and D. H. Rischke, Phys. Rev. C **56**, 1084 (1997).
15. S. G. Matinyan, B. Mueller, and D. H. Rischke, Phys. Rev. C **56**, 2197 (1997); **57**, 1927 (1998).
16. M. Gyulassy and L. McLerran, Phys. Rev. C **56**, 2219 (1997).
17. Yu. Kovchegov and A. Mueller, Nucl. Phys. B **529**, 451 (1998).
18. A. Krasnitz and R. Venugopalan, hep-ph/9808332; hep-ph/9809433; hep-ph/9905319; hep-ph/9909203.
19. S. A. Bass, B. Mueller, and W. Poeschl, nucl-th/9808011.
20. W. Poeschl and B. Mueller, nucl-th/9808031; hep-ph/9811441; nucl-th/9903050.
21. A. H. Mueller, hep-ph/9906322; hep-ph/9909388.
22. L. McLerran, hep-ph/9903536.
23. A. H. Mueller, hep-ph/9911289.
24. R. Stock, in *Proceedings of the Pre-Conference Workshop Quark Matter'95,* UCRL-TD-121571.
25. E. Shuryak and C. M. Hung, Phys. Rev. C **56**, 453 (1997).
26. M. Gazdzicki, A. Leonidov, and G. Roland, Eur. Phys. J. C **6**, 365 (1999).
27. M. Stephanov, K. Rajagopal, and E. Shuryak, hep-ph/9903292.
28. A. Leonidov and D. Ostrovsky, hep-ph/9811417.
29. M. Gyulassy, D. Rischke, and B. Zhang, Nucl. Phys. A **613**, 397 (1997).
30. X.-N. Wang and M. Gyulassy, Phys. Rev. D **44**, 3501 (1991); **45**, 844 (1992); Comput. Phys. Commun. **83**, 307 (1994).
31. A. D. Martin, R. G. Roberts, and W. J. Stirling, Phys. Lett. B **354**, 155 (1995).
32. A. Bohr and B. R. Mottelson, *Nuclear Structure,* Vol. 1: *Single-Particle Motion* (Benjamin, New York, 1969; Mir, Moscow, 1971), pp. 160, 223.
33. A. Leonidov and D. Ostrovsky, in preparation.
34. UA4 Collab. (M. Bozzo *et al.*), Phys. Lett. B **147B**, 392 (1984); UA5 Collab. (G. J. Alner *et al.*), Z. Phys. C **32**, 153 (1986); Fermilab E710 Collab. (N. Amos *et al.*), Phys. Rev. Lett. **63**, 2784 (1989); R. M. Baltrusaitis *et al.*, Phys. Rev. Lett. **52**, 1380 (1984).
35. A. Leonidov, J.-Y. Ollitrault, and D. Ostrovsky, in preparation.
36. J.-Y. Ollitrault, nucl-ex/9802005.
37. F. Wang and H. Sorge, nucl-th/9811006.

Physics of Atomic Nuclei, Vol. 65, No. 5, 2002, pp. 898–905. Translated from Yadernaya Fizika, Vol. 65, No. 5, 2002, pp. 930–937.

ELEMENTARY PARTICLES AND FIELDS
Theory

Renormalization of the Casimir Energy in the $(1+1)$-Dimensional Fermion-Bag Models

I. O. Cherednikov[1)*]

Institute for Theoretical Problems of Microphysics, Moscow State University, Vorob'evy gory, Moscow, 119899 Russia

Received August 18, 2000; in final form, July 3, 2001

Abstract—The ground-state energy in the two-phase hybrid chiral fermion-bag model involving boson–fermion interaction is studied in $(1+1)$-dimensional spacetime. A procedure for renormalizing the divergent energy of the fermion sea is proposed. The procedure is based on the isolation of singular terms and the subsequent absorption of these divergences in the redefined parameters of the input Lagrangian. © *2002 MAIK "Nauka/Interperiodica".*

1. INTRODUCTION

At present, a few methods have been developed for calculating the Casimir energy of a system of quantized fields satisfying nontrivial boundary conditions [1–3]. The methods employed most extensively are those of Green's functions [2–5], ζ-function regularization [6–11], contour integration [2, 12, 13], multiple scattering [1, 14], and straightforward summation over modes by using a temperature regularization [15–17]. These methods are often applied to computing the ground-state energy in models of the quark-bag type [1, 5, 8, 15, 18–22], where it is necessary to take into account one-loop corrections from the filled Dirac sea. Quantum corrections are known to play a significant role in such models, ensuring self-consistency of the theory; therefore, they must be properly taken into account [23, 24]. However, the results of calculations along these lines depend crucially on the number of spacetime dimensions, on boundary conditions, and on the geometry of the system [7, 25, 26]. Moreover, one cannot rule out the possibility that different methods applied to the same systems would yield different results [3, 4, 27]. A commonly recognized approach to computing the Casimir energy has yet to be developed.

From the physical point of view, summation over modes with a temperature cutoff [15–17] is the most natural method for computing the Casimir energy problems of this type. However, a straightforward application of this method is possible only if all eigenvalues ω_n of the Hamiltonian are known exactly, but this is so only for a rather narrow class of systems. In the present study, the method for computing the fermion-sea energy by means of summation over modes is adapted to cases where the exact spectrum ω_n of the Hamiltonian is not known. However, the use of an asymptotic expansion for ω_n for $n \geq 1$ [19] makes it possible to isolate divergent terms unambiguously as poles at the physical value of the regularization parameter [28] (this procedure is similar to the minimal-subtraction scheme in quantum field theory), whereupon the energy is renormalized via the absorption of divergences in the bare coupling constants of the input Lagrangian [5, 15, 20, 21]. An advantage of this renormalization method over, for example, that where, in order to determine the ground-state energy of some configuration, one subtracts, from an infinite sum corresponding to this energy, an infinitely large energy of some other configuration is that our method can be used to renormalize not only the energy but also other observables of the theory.

The implementation of the proposed renormalization procedure requires that some contact terms that depend on the geometric parameters of the system in the same way as the isolated divergent terms be included in the "classical" expression for the energy [8, 18, 21]. By considering the example of the $(3+1)$-dimensional fermion-bag model, it was shown [18], among other things, that, upon the removal of regularization, there inevitably remain singular terms proportional to various powers of the bag radius. These terms can be compensated only by redefining the coupling constants that are defined as the coefficients of the respective contact terms introduced in the classical expression for energy in an ad hoc manner. However, all such coupling constants do not have a clear physical meaning—only the bag constant (vacuum

[1)]Joint Institute for Nuclear Research, Dubna, Moscow oblast, 141980 Russia.

[*]e-mail: igorch@goa.bog.msu.ru;igorch@thsun1.jinr.ru

pressure), the constant of surface tension, and the coefficient of the term independent of the geometric parameters of the model admit a reasonable interpretation. The values of these three constants must be determined from experimental data [8, 18]. We can avoid introducing these contact terms, assuming that there are some additional external modes [21, 29] (as in chiral bag models). In this case, it turns out that the majority of the divergent terms are canceled. However, there is no rigorous proof of the statement that such cancellations occur for any system. Moreover, the existence of external modes cannot be justified in many cases (the introduction of external modes in the bag model is based on the hypothesis that quark–gluon plasma exists, but the concept of a bag essentially implies a perfect confinement). For this reason, the inclusion of contact terms for implementing a self-consistent renormalization procedure seems inevitable. It should be noted that, in the simple problems considered here, all contact terms introduced have a clear physical meaning.

In this study, we develop a method for isolating divergences and finite parts in a divergent sum over the eigenenergies ω_n in the case of unknown values of ω_n, employing the exponential cutoff $\sum\omega_n \to \sum\omega_n e^{-\tau\omega_n}$ or the ζ-function regularization $\sum\omega_n \to \mu^{1+s}\sum\omega_n^{-s}$. We demonstrate that both these methods yield identical results. By way of example, we consider the $(1+1)$-dimensional MIT bag model involving massive fermions and find an analytic expression for the ground-state energy. Next, we apply the developed approach to the analysis of the ground-state energy in the two-phase hybrid bag model featuring chiral boson–fermion interaction in the interior domain [19, 30, 31]. Making use of the self-consistent solution found previously for a similar system [19], we compute the Casimir energy to the leading terms of the expansion in powers of the chiral coupling constant m_F. The total energy in this model with allowance for the contribution of the scalar field is analyzed as a function of the bag size.

2. COMPARISON OF TWO REGULARIZATION METHODS

The ground-state energy of the fermion field is defined as the vacuum expectation value of the Hamiltonian:

$$\langle 0|H|0\rangle \equiv E_0 = -\frac{1}{2}\left(\sum_{\omega_n>0}\omega_n - \sum_{\omega_k<0}\omega_k\right). \quad (1)$$

If the eigenvalues ω_n are invariant under sign reversal, $\omega_n \to -\omega_n$, then the vacuum expectation value of the Hamiltonian has the form

$$E_0 = -\sum_{\omega_n>0}\omega_n. \quad (2)$$

This sum is divergent, but it can be regularized, for example, by applying an exponential cutoff, whereupon the regularized expression for the vacuum energy becomes

$$E_0^{\exp} = \lim_{\tau\to 0}\left(-\sum_{\omega_n>0}\omega_n e^{-\tau\omega_n}\right) \quad (3)$$
$$= \lim_{\tau\to 0}\frac{d}{d\tau}\sum_{\omega_n>0}e^{-\tau\omega_n},$$

where $\tau \sim \mu^{-1}$ and μ has dimensions of mass. This method was in fact used to compute the Casimir energy in some simple cases [1, 15–17], but it is workable only when the eigenvalues ω_n are known. Let us now assume that, for $n \geq 1$, the eigenvalues ω_n can be approximated by the asymptotic series [19]

$$\omega_n = \sum_{i=1}^{-\infty}\Omega_i n^i = \Omega_1 n + \Omega_0 + \frac{\Omega_{-1}}{n} + O\left(\frac{1}{n^2}\right). \quad (4)$$

It is obvious that the first three terms in (4) specify the divergences in the sum in (2). First, we consider the auxiliary case where the expansion in (4) contains only the first two terms (for example, this is the case of a free massless field in a bag):

$$\omega_n^{(1)} = \Omega_1 n + \Omega_0. \quad (5)$$

The regularized energy then takes the form [15]

$$E_1^{\exp} = \lim_{\tau\to 0}\frac{d}{d\tau}\sum_{n=1}e^{-\tau(\Omega_1 n+\Omega_0)} - \omega_0 \quad (6)$$
$$= \lim_{\tau\to 0}\frac{d}{d\tau}\left(e^{-\tau\Omega_0}\sigma_1(\tau)\right) - \omega_0,$$

where

$$\sigma_1(\tau) = \sum_{n=1}e^{-\tau\Omega_1 n} = \frac{1}{e^{\tau\Omega_1}-1}. \quad (7)$$

The term ω_0 in (6) has been isolated because the expansion in (4) does not apply to it. In what follows, it will convenient to begin summation from $n = 1$. Since

$$\frac{1}{e^x-1} = \sum_{k=0}\frac{B_k}{k!}x^{k-1}, \quad (8)$$

where B_k are Bernoulli numbers, we obtain

$$E_1^{\exp} = -\lim_{\tau\to 0}\frac{1}{\tau^2\Omega_1} + \frac{\Omega_1}{12} + \frac{\Omega_0}{2} + \frac{\Omega_0^2}{2\Omega_1} - \omega_0. \quad (9)$$

This expression involves the quadratic divergence

$$E^{\mathrm{quad}}(\tau) = -\frac{1}{\tau^2\Omega_1},$$

which depends on an arbitrary mass μ and on the geometric parameters that enter into Ω_1.

Let us now consider the case where

$$\omega_n^{(2)} = \Omega_1 n + \Omega_0 + \frac{\Omega_{-1}}{n}. \tag{10}$$

The regularized energy then has the form

$$E_2^{\exp} = \lim_{\tau\to 0} \frac{d}{d\tau}\sigma_2(\tau) - \omega_0, \tag{11}$$

where

$$\sigma_2(\tau) = \sum_{n=1} e^{-\tau\left(\Omega_1 n+\Omega_0+\frac{\Omega_{-1}}{n}\right)} \tag{12}$$
$$= e^{-\tau\Omega_0}\sum_{n=1} e^{-\tau\Omega_1 n}e^{-\tau\Omega_{-1}/n}.$$

It can be seen that only the first and the second term in the expansion of $e^{-\tau\Omega_{-1}/n}$ in powers of τ make a nonvanishing contribution to $E_2^{\exp}$ in the limit $\tau \to 0$. Thus, we arrive at

$$\sigma_2(\tau) = e^{-\tau\Omega_0}\sum_{n=1} e^{-\tau\Omega_1 n}\left(1 - \frac{\tau\Omega_{-1}}{n}\right) \tag{13}$$
$$+ O(\tau^2) = e^{-\tau\Omega_0}\sigma_1(\tau) - \tau\Omega_{-1}e^{-\tau\Omega_0}$$
$$\times \sum_{n=1}\frac{1}{n}e^{-\tau\Omega_1 n} + O(\tau^2),$$

where $\sigma_1(\tau)$ is defined in (7). Using the relation

$$\sum_{n=1}\frac{1}{n}e^{-\alpha n} = -\ln(1-e^{-\alpha}),$$

we obtain

$$\sigma_2(\tau) = \sigma_1(\tau) \tag{14}$$
$$+ \tau\Omega_{-1}e^{-\tau\Omega_0}\left(\ln\tau\Omega_1 - \frac{\tau\Omega_1}{2}\right) + O(\tau^2).$$

Thus, the regularized energy takes the form

$$E_2^{\exp} = \lim_{\tau\to 0}\left(-\frac{1}{\tau^2\Omega_1} + \Omega_{-1}\ln\tau\mu\right) \tag{15}$$
$$+ \Omega_{-1}\ln\frac{\Omega_1}{\mu} + \frac{\Omega_1}{12} + \frac{\Omega_0}{2} + \frac{\Omega_0^2}{2\Omega_1} + \Omega_{-1} - \omega_0.$$

The contribution of the $O(1/n^2)$ terms (E^{fin}) is finite and can be found in each specific case. The divergent parts

$$E^{\text{quad}}(\tau) = -\frac{1}{\tau^2\Omega_1}, \quad E^{\log}(\tau) = \Omega_{-1}\ln\tau\mu$$

must be removed by means of a relevant renormalization procedure, but we will not construct this procedure at this point.

We now consider another version of regularization, that employing a ζ function. In this case, the regularized expression for the energy has the form

$$E_1^\zeta = -\sum_n \omega_n \to -\lim_{s\to -1}\mu^{1+s}\sum_n \omega_n^{-s}, \tag{16}$$

where an arbitrary mass μ is introduced on the basis of dimensional considerations. Without loss of generality, the value of μ in (16) can be set to that in the preceding case. For $\omega_n^{(1)} = \Omega_1 n + \Omega_0$, we obtain

$$E_1^\zeta = -\lim_{s\to -1}\mu^{s+1}\sum_{n=1}(\Omega_1 n + \Omega_0)^{-s} - \omega_0 \tag{17}$$
$$= -\lim_{s\to -1} z_1(s|\mu) - \omega_0,$$

where

$$z_1(s|\mu) = \mu^{s+1}\sum_{n=1}(\Omega_1 n + \Omega_0)^{-s} \tag{18}$$
$$= \mu^{s+1}\sum_{n=1}\frac{1}{(\Omega_1 n)^s}\left(1 - \frac{s\Omega_0}{\Omega_1 n}\right.$$
$$\left. + \frac{s(s+1)}{2!}\left(\frac{\Omega_0}{\Omega_1 n}\right)^2 + O(1/n^3)\right).$$

In the limit $s \to -1$, the contribution of the $O(1/n^3)$ terms vanishes; therefore, the regularized sum E_1^ζ is completely determined by the first three terms of the expansion in (18). We arrive at

$$z_1(s|\mu) = \mu^{s+1}\left(\Omega_1^{-s}\zeta(s) - \frac{s\Omega_0}{\Omega_1^{s+1}}\zeta(s+1)\right. \tag{19}$$
$$\left. + \frac{\Omega_0^2}{2\Omega_1^{s+2}}s(s+1)\zeta(s+2)\right).$$

The values of the $\zeta(z)$ function continued to the analytically entire real axis are known to be [32]

$$\zeta(0) = -\frac{1}{2}, \quad \zeta(-1) = -\frac{B_2}{2} = -\frac{1}{12}. \tag{20}$$

In the vicinity of unity, the function $\zeta(z)$ can be approximated as

$$\lim_{z\to 1}\zeta(z) = \frac{1}{z-1} + C, \tag{21}$$

where $C = 0.5772156649\ldots$ is the Euler constant. In the limit $s \to -1$, we obtain

$$E_1^\zeta = \frac{\Omega_1}{12} + \frac{\Omega_0}{2} + \frac{\Omega_0^2}{2\Omega_1} - \omega_0. \tag{22}$$

This expression coincides with the finite part of expression (9). The absense of a divergent term is due to the use of the analytic continuation of the function $\zeta(z)$. Now, we address the case where ω_n involves the next term of the expansion in powers of $1/n$ [see Eq. (10)]. We then have

$$E_2^\zeta = -\lim_{s\to -1}\mu^{s+1}\sum_{n=1}\left(\Omega_1 n + \Omega_0 + \frac{\Omega_{-1}}{n}\right)^{-s} \tag{23}$$
$$- \omega_0 = -\lim_{s\to -1} z_2(s|\mu) - \omega_0,$$

where

$$z_2(s|\mu) = z_1(s|\mu) - \frac{s\Omega_{-1}\mu^{s+1}}{\Omega_1^{s+1}}\zeta(s+2) \qquad (24)$$

(here, we retain only the terms that do not vanish in the limit mentioned above). The second term in expression (24) can be calculated by using the property in (21) and the expansion $x^\varepsilon = 1 + \varepsilon \ln x + O(\varepsilon^2)$, $\varepsilon = s+1$, $\varepsilon \to 0$. The result is

$$\lim_{s\to -1} s\Omega_{-1}\left(\frac{\mu}{\Omega_1}\right)^{s+1}\zeta(s+2) \qquad (25)$$
$$= \Omega_{-1}\lim_{\varepsilon\to 0}(-1+\varepsilon)\left(1-\varepsilon\ln\frac{\Omega_1}{\mu}\right)\left(\frac{1}{\varepsilon}+C\right)$$
$$= -\Omega_{-1}\left(\lim_{\varepsilon\to 0}\frac{1}{\varepsilon} - 1 + C - \ln\frac{\Omega_1}{\mu}\right).$$

Thus, the regularized expression for the energy takes the form

$$E_2^\zeta = \frac{\Omega_1}{12} + \frac{\Omega_0}{2} + \frac{\Omega_0^2}{2\Omega_1} - \omega_0 \qquad (26)$$
$$+ \Omega_{-1}\left(\ln\frac{\Omega_1}{\mu} + 1\right) - \Omega_{-1}\left(\lim_{\varepsilon\to 0}\frac{1}{\varepsilon} + C\right),$$

which coincides with (15) (apart from the quadratic divergence E_2^{quad}), provided that

$$\frac{1}{\tau} = \mu\gamma e^{1/\varepsilon}, \quad \ln\gamma = C. \qquad (27)$$

In order to take into account the contribution of the $O\left(1/n^2\right)$ terms in the expansion in (4), which do not involve singularities after the removal of the regularization, it is necessary to subtract their sum E^{fin} from expressions (15) and (26). It can be concluded that the Casimir energy computed for the $(1+1)$-dimensional fermion bag by using the regularization with an exponential cutoff coincides with that computed on the basis of the ζ-function regularization. This result is in fact more general, because it holds for all cases where ω_n can be represented in the form (4), which is always true for a quasidiscrete spectrum.

Expressions (15) and (26) involve terms that are divergent upon going over to the physical values of the respective regularization parameters. For the sake of definiteness, we will henceforth use formula (15), because the absence of the quadratic divergence in (26) is an artifact of the analytic continuation of the ζ function—it is not related to the physical content of the problem under consideration. The singular terms then have the form

$$E^{\mathrm{div}}(\tau) = -\frac{1}{\tau^2\Omega_1} + \Omega_{-1}\ln\tau\mu. \qquad (28)$$

These divergences can be eliminated by redefining the bare coupling constants in the input Lagrangian. By way of example, we perform a renormalization in the $(1+1)$-dimensional MIT bag model involving massive fermions [33, 34]. The Lagrangian of the model has the form

$$\mathcal{L}_{\mathrm{MIT}} = \theta(|x|<R)(i\bar\psi\hat\partial\psi - m_F\bar\psi\psi - B) \qquad (29)$$
$$+ \theta(|x|>R)(i\bar\psi\hat\partial\psi - M_F\bar\psi\psi),$$

where $2R$ is the length of a segment of the real axis, $m_F(M_F)$ is the mass of an elementary fermion within (outside) the bag, and B is the bag constant characterizing the excess of the vacuum energy density within the hadron in relation to the energy density of the nonperturbative vacuum outside of the hadron (the bag model is based on the assumption that there exists such an excess). In the limit of an infinitely large fermion mass outside of the bag, $M_F \to \infty$ (the production of free fermions in the region $|x| > R$ is suppressed in this case), we arrive at a "bag" in the form of the segment $[-R, R]$ of the real axis. The boundary conditions

$$(\pm i\gamma^1 + 1)\psi(\pm R) = 0 \qquad (30)$$

lead to the exact eigenvalues

$$\omega_n = \sqrt{\left(\frac{\pi}{2R}n + \frac{\pi}{4R}\right)^2 + m_F^2}. \qquad (31)$$

We assume that the elementary-fermion mass m_F is much smaller than the characteristic energy scale of the problem, the mass parameter μ appearing in the denominator of the argument of the cutoff exponential function (3). This assumption is plausible because bag models are constructed as effective theories of the hadronic structure and can be applied only to studying low-energy processes. To $O(m_F^4)$ terms, we then obtain

$$\omega_n = (\Omega_1 n + \Omega_0) + \frac{m_F^2}{2(\Omega_1 n + \Omega_0)} + O(m_F^4), \qquad (32)$$

where $\Omega_1 = \pi/2R$ and $\Omega_0 = \pi/4R$. For $n \geq 1$, we use the expansion in (4), where

$$\Omega_{-1} = \frac{m_F^2}{2\Omega_1} = \frac{m_F^2 R}{\pi}, \qquad (33)$$

whereas, at $n = 0$, we have

$$\omega_0 = \Omega_0 + \frac{m_F^2}{2\Omega_0} = \Omega_0 + 2\Omega_{-1}. \qquad (34)$$

The divergent part of the sea contribution (28) is

$$E^{\mathrm{div}}(\tau|R) \qquad (35)$$
$$= \left(-\frac{1}{\tau^2\pi} + \frac{m_F^2}{2\pi}\ln\tau\mu\right)\cdot 2R = 2B'(\tau)R.$$

The renormalization procedure proposed in [5, 6, 8] involves redefining the bag constant B, which enters into the Lagrangian in (29):

$$B = B_0 - B'(\tau). \tag{36}$$

All the remaining parts of the energy in (15) converge and can be found explicitly. The contribution of the $O\left(n^{-2}\right)$ terms in expansion (4) is determined by the expression

$$E^{\text{fin}}(R) = -\frac{m_F^2}{2}\sum_{n=1}\left(\frac{1}{\Omega_1 n + \Omega_0} - \frac{1}{\Omega_1 n}\right) \tag{37}$$
$$= \frac{m_F^2}{2\Omega_1}\sum_{n=1}\frac{1}{n(2n+1)} = \frac{2m_F^2 R}{\pi}(1-\ln 2).$$

Thus, the renormalized energy of the fermion sea in the $(1+1)$-dimensional massive MIT bag model as a function of the bag size R, the elementary-fermion mass m_F within the bag, and the "running" bag constant $B_0(\mu)$ has the form [to $O(m_F^4)$ terms of the expansion in powers of m_F^2]

$$E_{\text{MIT}}(R) = 2B_0(\mu)R - \frac{\pi}{48R} \tag{38}$$
$$+ \frac{m_F^2 R}{\pi}\left(1 - 2\ln 2 + \ln\frac{\pi}{2R\mu}\right) + O(m_F^4).$$

The logarithmic dependence of the bag constant on μ implies that the renormalized total energy is independent of μ. In the limit of vanishing fermion mass, $m_F \to 0$, formula (38) reproduces the well-known result obtained in [34]. This configuration is unstable, collapsing for $R \to 0$. It can be stabilized, for example, by adding one valence fermion occupying the lowest level corresponding to $n = 0$. The energy is then given by

$$\tilde{E}_{\text{MIT}}(R) = 2B_0 R + \frac{11}{48}\frac{\pi}{R} \tag{39}$$
$$+ \frac{m_F^2 R}{\pi}\left(3 - 2\ln 2 + \ln\frac{\pi}{2R\mu}\right) + O(m_F^4).$$

3. TWO-PHASE HYBRID BAG MODEL

Here, we consider yet another version of the hybrid bag model, that where the fermion ("quark") field $\psi(x)$ interacts with the boson ("meson") scalar field $\varphi(x)$. In contrast to the three-phase model investigated in [19], our version does not contain the domain of massless quarks; therefore, it is referred to as a two-phase model. The respective Lagrangian has the form

$$\mathcal{L} = i\bar{\psi}\hat{\partial}\psi + \frac{1}{2}\partial_\mu\varphi\partial^\mu\varphi \tag{40}$$
$$- \theta(|x| < R)\left(\frac{1}{2}m_F[\bar{\psi}, e^{i\gamma_5\varphi}\psi] - B\right)$$
$$-\theta(|x| > R)\left(V(\varphi) + \frac{1}{2}M_F[\bar{\psi}, e^{i\gamma_5\varphi}\psi]\right),$$

where $V(\varphi)$ describes the nonlinear interaction of the scalar field outside the bag. The commutator is used in the terms bilinear in the fermion fields in order to ensure charge-conjugation invariance. The key distinction between the model specified by this Lagrangian and the standard fermion–soliton bag models [35–38] is that, here, the boson field $\varphi(x)$, which is responsible for the generation of the effective fermion mass, differs from the field $\theta(x)$ forming the bag.

For the sake of simplicity, we will use the mean-field approximation (MFA) [30] for the scalar field $\varphi(x,t)$; that is, it is treated as a c function of the spacetime coordinates. Moreover, we assume that it is independent of time: $\varphi(x,t) = \varphi(x)$.

One possible way to investigate theories involving boson–fermion coupling is to employ an expansion in the chiral coupling constant [39]. Here, we assume that the fermion mass m_F within the segment $|x| < R$ is small and that the mass M_F outside the bag ($|x| > R$) is infinitely large. The fermion field for $|x| > R$ then disappears for dynamical reasons, and the set of equations of motion for $|x| < R$ takes the form

$$(i\hat{\partial} - m_F e^{i\gamma_5\varphi})\psi(x,t) = 0, \tag{41}$$

$$\varphi'' = i\frac{m_F}{2}\langle[\bar{\psi}, \gamma_5 e^{i\gamma_5\varphi}\psi]\rangle_{\text{sea}}, \tag{42}$$

where the vacuum expectation value of the axial current on the right-hand side of (42) is evaluated in the MFA. The behavior of the scalar field for $|x| > R$ is governed by the nonlinear equation

$$-\varphi''(x) = V'_\varphi(\varphi). \tag{43}$$

We assume that the scalar field is an odd function and that its behavior outside the bag (that is, for $|x| > R$) has the form of the "Yukawa tail,"

$$\varphi(x) = \pi\left(1 - Ae^{-mx}\right), \quad x > 0, \tag{44}$$

where m is the meson mass; the behavior of the field $\varphi(x)$ at $x < 0$ is readily determined by its oddness. The formulation of the problem must be supplemented with the boundary conditions for the fields:

$$(\pm i\gamma^1 + e^{i\gamma_5\varphi(x)})\psi(\pm R) = 0, \tag{45}$$
$$\varphi(\pm R \pm 0) = \varphi(\pm R \mp 0),$$
$$\varphi'(\pm R \pm 0) = \varphi'(\pm R \mp 0).$$

The fermion spectrum is invariant under the transformation $\nu \to -\nu$, $\nu = \omega - \lambda$, which is associated with the unitary transformations of the wave function, $\chi \to i\gamma_1\chi$ ($\chi = e^{i\gamma_5\varphi/2}\psi$). For this reason, the vacuum expectation value of the axial current on the

right-hand side of Eq. (42) vanishes and the linear function $\varphi(x) = 2\lambda x$ is a solution to Eq. (42) (a self-consistent solution for this system is considered in detail in [19, 39]). The eigenvalues ω_n are determined from the equation

$$\left(1 - e^{2ikR}\frac{m_F + i(\nu + k)}{m_F + i(\nu - k)}\right) \times \left(1 - e^{-2ikR}\left(\frac{\nu - k}{\nu + k}\right)\frac{m_F - i(\nu + k)}{m_F - i(\nu - k)}\right) = \left(1 - e^{2ikR}\frac{m_F - i(\nu + k)}{m_F - i(\nu - k)}\right) \times \left(1 - e^{-2ikR}\left(\frac{\nu - k}{\nu + k}\right)\frac{m_F + i(\nu + k)}{m_F + i(\nu - k)}\right), \quad (46)$$

where $k^2 = m_F^2 - \nu^2$. With the proviso that the signs of ω_n and ν_n are identical at all n, the energy of the filled sea of negative-energy states, $\omega_n < 0$, is determined by expression (2) with the substitution $\omega_n \to \nu_n$. For the sake of definiteness, we regularize this expression using the exponential cutoff (3):

$$E_0^{\exp} = \lim_{\tau\to 0}\left(-\sum_{\nu_n>0}\nu_n e^{-\tau\nu_n}\right) = \lim_{\tau\to 0}\frac{d}{d\tau}\sum_{\nu_n>0}e^{-\tau\nu_n}.$$

Equation (46) can be recast into the form

$$m_F \sin 2Rk + k\cos 2Rk = 0. \quad (47)$$

Expanding k in powers of m_F,

$$k = \tilde{k}_0 + m_F\tilde{k}_1 + m_F^2\tilde{k}_2 + O(m_F^3), \quad (48)$$

we arrive at

$$\nu = \tilde{k}_0 + m_F\tilde{k}_1 + m_F^2\left(\tilde{k}_2 + \frac{1}{2\tilde{k}_0}\right) + O(m_F^3). \quad (49)$$

Next, we solve Eq. (47) in each order of the expansion. Neglecting $O\left(m_F^3\right)$ terms, we obtain

$$m_F(\sin 2R\tilde{k}_0 + 2Rm_F\tilde{k}_1\cos 2R\tilde{k}_0) + (\tilde{k}_0 + m_F\tilde{k}_1 + m_F^2\tilde{k}_2)\left(\left[1 - \frac{1}{2}(2R\tilde{k}_1 m_F)^2\right] \times \cos 2R\tilde{k}_0 - 2R(m_F\tilde{k}_1 + m_F^2\tilde{k}_2)\sin 2R\tilde{k}_0\right) = 0, \quad (50)$$

whence it follows that

$$\nu_n = \frac{\pi}{2R}n + \frac{\pi}{4R} + \frac{2}{\pi}m_F(1 + m_F R) \times \frac{1}{(2n+1)} - \frac{16Rm_F^2}{\pi^3(2n+1)^3} + O(m_F^3). \quad (51)$$

Further, we expand ν_n in powers of $1/n$; that is,

$$\nu_n = \Omega_1 n + \Omega_0 + \frac{\Omega_{-1}}{n} + O\left(\frac{1}{n^2}\right), \quad (52)$$

where

$$\Omega_1 = \frac{\pi}{2R}, \quad \Omega_0 = \frac{\pi}{4R}, \quad \Omega_{-1} = \frac{m_F}{\pi}(1 + m_F R). \quad (53)$$

This formula differs from that in the massive MIT bag model by the term m_F/π в Ω_{-1}, which is independent of the bag size R. For $n = 0$, we obtain

$$\nu_0 = \Omega_0 + 2\Omega_{-1} - \frac{16Rm_F^2}{\pi^3}. \quad (54)$$

Now, we can use the regularized expression (15) for the energy. In order to perform a renormalization, we must redefine the bag constant B (36) and the overall factor Λ, which is independent of R and which does not appear in (29) explicitly:

$$\Lambda = \Lambda_0 - \frac{m_F}{\pi}\ln\tau\mu. \quad (55)$$

It only remains to find the contribution E^{fin} from $O\left(1/n^2\right)$ nonsingular terms. The result is

$$E^{\text{fin}} = \Omega_{-1}\sum_{n=1}\frac{1}{n(2n+1)} + \frac{16Rm_F^2}{\pi^3} \times \sum_{n=0}\frac{1}{(2n+1)^3} = \Omega_{-1}\cdot 2(1 - \ln 2) + \frac{16Rm_F^2}{\pi^3}A, \quad (56)$$

where $A = 1.051799\ldots$. Thus, the renormalized energy of the fermion sea as a function of the bag size R has the form (it is assumed that $\Lambda_0 = 0$)

$$E(R) = 2B_0 R - \frac{\pi}{48R} + \frac{m_F}{\pi}(1 + m_F R) \times \left[\ln\frac{\pi}{2\mu R} + 1 - 2\ln 2\right] + \frac{16Rm_F^2}{\pi^3}A. \quad (57)$$

The total energy of the system also involves the contribution of the scalar field. In order to find it we make use of the boundary conditions for the field φ and its derivative (45). This yields

$$2\lambda = \frac{\pi m}{mR + 1}. \quad (58)$$

Employing the virial theorem in the external domain $\frac{1}{2}\varphi'^2(x) = V(\varphi)$, we obtain the scalar-field energy in the form

$$E_\varphi(R) = \frac{1}{2}\int_{-R}^{R} dx\varphi'^2(x) \quad (59)$$

$$+\left(\int_{-\infty}^{-R}+\int_{R}^{\infty}\right)dx\varphi'^2(x)=\frac{\pi^2 m}{mR+1}.$$

It should be recalled that the representation of the scalar field in the form (44) is appropriate only at distances far exceeding the soliton size (which is about m^{-1}). The point is that the effective chiral Lagrangian adequately describes the behavior of the meson (pion) field and its interaction with baryons only at distances much longer than the baryon radius R. At distances shorter than R, the pion field cannot be treated as a local field, but the interactions of the pion field can be described in terms of the chiral Lagrangian only under the condition of locality. Thus, the internal structure of the pion can be neglected only in the case of long-wave fields whose wavelength λ is much greater than R [40]. Within the bag model, this gives rise to the following constraint on the meson mass m and the bag radius:

$$mR = K_\pi, K_\pi \geq 1.$$

The behavior of the field $\varphi(x)$ within the region $|x| < R$ does not affect the topological charge of a given configuration—it is completely determined by the asymptotic behavior of $\varphi(x)$ at infinity. It is natural to assume that the "meson" mass m outside the bag is not a free parameter, but that it is determined by the bag size. The contribution of the scalar field to the energy of the bag is then given by

$$E_\varphi(R)=\frac{\pi^2 K_\pi}{(1+K_\pi)R}, \tag{60}$$

while the total energy of this configuration is

$$E_{\rm tot}(m,R)=E(R)+E_\varphi(R). \tag{61}$$

Thus, the quantity obtained by renormalizing the total energy in this model according to the above prescription has a unique minimum. This indicates that there is a stable state at some value of the parameter R.

Let us now clarify the role of the parameter μ in this situation. The emergence of an arbitrary mass parameter upon renormalizing one-loop diagrams is well known [18]. In the case being considered, however, the parameter μ has also a different meaning. Since the models under study are effective low-energy models, they are applicable to phenomena occurring at energies lower than some specified value. Within both regularization schemes used in the present study, the main contribution to the sum over ω_n comes from $\omega_n < \mu$ terms, the contribution of other terms being suppressed by the cutoff. Because of this, the mass parameter μ can be interpreted, in either case, as the energy scale specifying the domain of validity of the method used. One can either introduce the running bag constant $B_0(\mu)$ in such a way that the total energy would be independent of μ or consider μ as a measurable quantity that determines the validity range of our approach [18]. The former possibility was realized in the present study.

4. CONCLUSION

It has been demonstrated directly that, in order to calculate the finite energy of the filled sea of negative-energy fermion states (Casimir energy), one can use a renormalization procedure based on an analytic regularization of divergent sums (such as a temperature regularization or a ζ-function regularization), the isolation of singular terms in the form of poles at the physical value of the regularization parameter, and the absorption of divergences in the redefined bare constants of the input Lagrangian. The singular terms can be unambiguously isolated by using a scheme that is similar to the minimal-subtraction scheme in quantum field theory. Upon the removal of regularization, the remaining terms are finite and have a nontrivial dependence on the geometric parameters of the model (bag size). That all computations have been performed analytically makes it possible to trace thoroughly the emergence of singular and regular contributions in regularized sums. Unfortunately, many attractive features of the proposed renormalization scheme are peculiar only to the $(1+1)$-dimensional case [41] and can hardly be extended to the four-dimensional case. Nevertheless, problems associated with such an extension will be discussed elsewhere.

ACKNOWLEDGMENTS

I am grateful to K.A. Sveshnikov for discussions and constructive criticism, to O.V. Pavlovsky for numerous discussions and enlightening comments, and to the referee for some valuable remarks. I gratefully acknowledge the Abdus Salam International Centre for Theoretical Physics and the Isaac Newton Institute for Mathematical Sciences, where a large part of this work was performed.

This work was supported in part by the Russian Foundation for Basic Research (RFBR, project no. 01-02-16431), by the RFBR program of Support of Leading Scientific Schools (project no. 00-15-96577), and by a scholarship from the Council of Young Scientists at the Institute of Nuclear Physics (Moscow State University).

REFERENCES

1. G. Plumien, B. Müller, and W. Greiner, Phys. Rep. **134**, 87 (1986).
2. *The Casimir Effect 50 Years Later*, Ed. by M. Bordag (World Sci., Singapore, 1999).
3. K. Milton, hep-th/9901011.

4. D. Deutsch and P. Candelas, Phys. Rev. D **20**, 3063 (1979).
5. K. Milton, Phys. Rev. D **22**, 1441 (1980).
6. K. Milton, Phys. Rev. D **27**, 439 (1983).
7. E. Elizalde *et al.*, *Zeta Regularization Techniques with Application* (World Sci., Singapore, 1994).
8. E. Elizalde, M. Bordag, and K. Kirsten, J. Phys. A **31**, 1743 (1998).
9. M. Bordag, E. Elizalde, and K. Kirsten, J. Math. Phys. (N.Y.) **37**, 895 (1996).
10. M. Bordag, E. Elizalde, K. Kirsten, and S. Leseduarte, hep-th/9608071.
11. E. Elizalde, J. Phys. A **30**, 2735 (1997).
12. G. Lambiase and V. Nesterenko, Phys. Rev. D **54**, 6387 (1996).
13. V. Nesterenko and I. Pirogenko, Phys. Rev. D **57**, 1284 (1998).
14. R. Balian and B. Duplautier, Ann. Phys. (N.Y.) **112**, 165 (1978).
15. K. Johnson, Acta Phys. Pol. B **6**, 865 (1975).
16. W. Lukosz, Physica (Amsterdam) **56**, 109 (1971).
17. J. A. Ruggiero, A. Villani, and A. H. Zimmermann, J. Phys. A **13**, 761 (1980).
18. S. K. Blau, M. Visser, and A. Wipf, Nucl. Phys. B **310**, 163 (1988).
19. K. A. Sveshnikov and P. K. Silaev, Teor. Mat. Fiz. **117**, 263 (1998).
20. C. M. Bender and P. Hays, Phys. Rev. D **14**, 2622 (1976).
21. K. Milton, Ann. Phys. (N.Y.) **150**, 432 (1983).
22. R. Hofmann, M. Schumann, and R. D. Viollier, Eur. Phys. J. C **11**, 153 (1999).
23. M. Rho, Phys. Rep. **240**, 1 (1994).
24. H. Hosaka and O. Toki, Phys. Rep. **277**, 65 (1996).
25. K. Milton, Phys. Rev. D **55**, 4940 (1997).
26. C. M. Bender and K. Milton, Phys. Rev. D **50**, 6547 (1994).
27. L. G. de Albuquerque, hep-th/9803223.
28. C. J. Bollini, J. J. Giambiagi, and A. Gonzales Domingues, Nuovo Cimento **31**, 550 (1964).
29. L. Vepstas and A. D. Jackson, Phys. Rep. **187**, 109 (1990).
30. M. Birse, Prog. Part. Nucl. Phys. **25**, 1 (1990).
31. *Chiral Solitons: A Review Volume*, Ed. by Ken-Fei Liu (World Sci., Singapore, 1987).
32. E. T. Whittaker and G. N. Watson, *A Course of Modern Analysis* (Cambridge, 1927), Vol. II.
33. A. Chodos, R. L. Jaffe, K. Johnson, *et al.*, Phys. Rev. D **9**, 3471 (1974).
34. R. J. Perry and M. Rho, Phys. Rev. D **34**, 1169 (1986).
35. D. Diakonov, hep-th/9802298.
36. T. Hatsuda and T. Kunihiro, Phys. Rep. **247**, 221 (1994).
37. T. Watabe and H. Toki, Prog. Theor. Phys. **87**, 651 (1992).
38. A. W. Thomas, Adv. Nucl. Phys. **13**, 1 (1984); A. W. Thomas, S. Théberge, and G. A. Miller, Phys. Rev. D **24**, 2539 (1981).
39. I. Cherednikov, S. Fedorov, M. Khalili, and K. Sveshnikov, Nucl. Phys. A **676**, 339 (2000); hep-th/9912237.
40. A. B. Migdal, D. N. Voskresenskiĭ, É. E. Sapershteĭn, and M. A. Troitskiĭ, *Pionic Degrees of Freedom in Nuclear Matter* (Nauka, Moscow, 1991).
41. I. Cherednikov, Phys. Lett. B **498**, 40 (2001); hep-th/0009044.

Translated by R. Rogalyov

Physics of Atomic Nuclei, Vol. 65, No. 5, 2002, pp. 906–916. Translated from Yadernaya Fizika, Vol. 65, No. 5, 2002, pp. 938–948.

ELEMENTARY PARTICLES AND FIELDS
Theory

Instability of the *Y* String Baryon Model within Classical Dynamics

G. S. Sharov

Tver State University, per. Sadovyi 35, Tver, 170002 Russia

Received February 5, 2001; in final form, June 20, 2001

Abstract—For the three-string baryon model (Y configuration), the known exact solution to the classical equations of motion that describes the rotational motion of the system at a constant speed is investigated for stability. In the spectrum of small perturbations of this solution, modes growing exponentially with time are found, whereby the instability of rotational motion is proven for the Y configuration. This result is confirmed within an alternative approach that makes it possible to determine the classical motion of the system from a specific initial position and initial velocities of string points. A comparison of the Y configuration with the model of a relativistic string with massive ends, in which case rotational motion is stable in the linear approximation, aids in revealing the most adequate string model from the point of view of describing baryon excitations on Regge trajectories. © *2002 MAIK "Nauka/Interperiodica"*.

INTRODUCTION

String models of baryons differ by the geometric character of connection of three matter points representing quarks by relativistic strings. Four possible configurations proposed for the first time in [1] are shown in Fig. 1. These are (*a*) the quark–diquark model q–qq [2], which coincides, at the classical level, with the meson model of a relativistic string featuring masses at its ends [3]; (*b*) the linear configuration q–q–q [4]; (*c*) the three-string (star or Y) configuration [5–9]; and (*d*) the triangle model (Δ configuration) [10, 11].

These string baryon configurations have not attracted the attention of researchers to the same extent (the greatest number of studies have been devoted to the q–qq and Y models); however, the question of which model is preferable remains open. In tackling this problem, it is desirable to take into account some considerations. In particular, the justifiability of one configuration or another from the point of view of QCD is of paramount importance. Within various approaches, a validation of this type has been conducted by various authors (who preliminarily chose, as a rule, a baryon configuration they preferred) for the quark–diquark model of baryons [12] (see also the review articles quoted in [13]), as well as for the three-string and triangle models. By way of example, it can be recalled that, in [14], the lattice formulation of QCD in the strong-coupling limit led to the Y configuration for baryons. Moreover, the method of vacuum correlation functions [15] lends additional support to this model within QCD, the baryon Wilson loop having the Y configuration [16, 17]. At the same time, Cornwall [18] argues that the Δ configuration for the baryon Wilson loop should be preferred to the Y configuration.

In order to choose the most adequate string model of baryons, it is nevertheless necessary to compare the predictions of the models being considered with data of baryon spectroscopy. An analysis of this problem reveals [19, 20] that, in terms of rotational motions, one can describe, under specific assumptions, orbital excitations of baryons on Regge trajectories within each of the models specified in Fig. 1. Classical rotational motion is a rotation of the system in a plane at a constant speed, in which case relativistic-string segments are rectilinear for the q–qq, q–q–q, and Y configurations, but they appear to be hypocycloid segments for the Δ configuration [10, 11]. For all of the aforementioned string models, the relationship between the energy E and the angular momentum J of rotational motion leads, within any methods for taking into account spin corrections, to quasilinear Regge trajectories whose high-J asymptotic behavior is given by [19]

$$J \simeq \alpha' E^2 - \nu E^{1/2} \sum_i m_i^{3/2}, \quad J, E \to \infty, \qquad (1)$$

where m_i are the masses of the matter points simulating quarks. In the different models, the relation between the slope α' of the trajectory (and the coefficient ν) and the string tension γ has different forms: $\alpha' = (2\pi\gamma)^{-1}$ for the q–$\overline{q}$, q–qq, and q–q–q configurations; $\alpha' = 2/3(2\pi\gamma)^{-1}$ for the three-string model; and $\alpha' = 3/8(2\pi\gamma)^{-1}$ for so-called simple rotational states of the Δ configuration. It follows that only under the assumption [19] that the effective string tension γ for the last two models differs from the corresponding fundamental constant in the q–$\overline{q}$ and q–qq

1063-7788/02/6505-0906$22.00

models can the three-string and triangle configurations be considered as candidates for describing leading Regge trajectories with slope $\alpha' \simeq 0.9\ \mathrm{GeV}^{-2}$.

The problem of stability of rotational motion within the models depicted in Fig. 1 is yet another important aspect that affects the choice of model. It should be noted in this connection that, until recently, the linear q–q–q configuration received virtually no study since it was assumed in [2], on the basis of clear physical ideas, that it is unstable with respect to a transition into the quark–diquark (q–qq) configuration via a displacement of the central quark. This assumption was examined in [4], where it was shown that the rotational motion of the q–q–q system is indeed unstable, but that, at the classical level, this system does not undergo a transition into the quark–diquark configuration.

The question of whether the rotational motions of the other string configurations are stable (or not) is equally important. Here, this question is investigated in detail at the classical level for the three-string model, both in the case where there are massive points at the string ends and in the massless case. An unexpected result of this analysis would be of importance not only from the point of view of choosing an adequate string model of baryons but also for further advances in quantizing the systems being considered. Difficulties involved in quantizing string configurations with masses at the ends stem from the fact that the boundary conditions on the world lines of massive points are essentially nonlinear [3, 21]. These difficulties were usually sidestepped by significantly constraining the class of motions being considered—for example, via quantization of specific motions of the three-string system [22] or within the extensively used rectilinear-string ansatz [16, 17, 23, 24], which leads to an almost complete elimination of string degrees of freedom. In this connection, it should be noted that the spectrum of small oscillatory perturbations for a rotating string with massive ends was investigated in [25] without introducing constraints of the above types. This opens the possibility for developing a quantum description of a sufficiently broad class of states of the system in a linear vicinity of rotational motion, provided that the motion in question is stable.

The ensuing exposition is organized as follows. The question concerning the character of analogous (quasirotational) perturbations for the Y configuration, which is a more complicated string model of baryons—this question is closely related to that of stability of its rotational motion—is analyzed in Section 2, a comparison with the case of the q–$\overline{q}$ or the q–qq configuration being drawn in the course of this analysis. This is preceded by a description of the dynamics of the three-string system in Section 1. In order to analyze the character of instability and to include all physical motions in the proposed description, a method is developed for solving the initial- and boundary-value problem for the Y configuration (Section 3)—that is, for determining the classical motion from the initial positions and initial velocities of the points of the system. This approach makes it possible to establish, among other things, that, in order to describe all motions of the Y configuration, it is necessary to parametrize the three-sheet world surface in a form that is more general than that in [6, 7, 9], where only a narrow class of motions was considered.

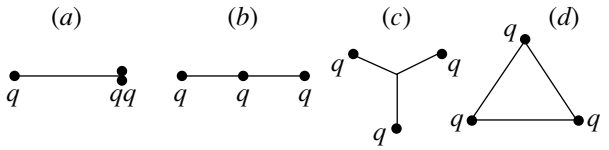

Fig. 1. String baryon models.

1. DYNAMICS OF THE Y CONFIGURATION

In the three-string model (Y configuration), three world sheets swept out by three segments of the relativistic string in D-dimensional Minkowski space are parametrized by three functions $X_i^\mu(\tau_i, \sigma)$, in which it is convenient to use different symbols τ_1, τ_2, and τ_3 for the time parameter [5]. As to space coordinates, they will be denoted by a single symbol σ. The three world sheets are connected along the node world line, which, as will be demonstrated below, can be specified, without loss of generality, in the form $\sigma = 0$ on each of the sheets.

In this notation, the action functional for the Y configuration featuring matter points with masses m_i at the string ends has the form

$$S = -\sum_{i=1}^{3} \int d\tau_i \left[\gamma \int_0^{\sigma_i(\tau_i)} \sqrt{-g_i}\, d\sigma + m_i \sqrt{\dot{x}_i^2(\tau_i)} \right], \quad (2)$$

where γ is the string tension, $-g_i = (\dot{X}_i, X_i')^2 - \dot{X}_i^2 X_i'^2$, $\sigma = \sigma_i(\tau_i)$, and $\dot{x}_i^\mu(\tau_i) = \frac{d}{d\tau_i} X^\mu(\tau_i, \sigma_i(\tau_i))$ is a vector tangential to the trajectory of the ith matter point; here, $\dot{X}_i^\mu = \partial_{\tau_i} X_i^\mu$, $X_i'^\mu = \partial_\sigma X_i^\mu$, and $(a, b) = a_\mu b^\mu$. We use here the system of units where the speed of light is set to unity ($c = 1$).

The action functional (2), which employs the parametrization involving different τ_i, is a generalization of the analogous expressions in [5, 6, 9] and in [7], where the analyses were performed for, respectively, the case of $m_i = 0$ and the case of a constrained class of motions of the system with $m_i \neq 0$.

The matching of the three sheets of the world surface $X_i^\mu(\tau_i, \sigma)$ on the node world line leads, at each point of this line, to a relationship between the parameters τ_i, which is specified here in the general form

$$\tau_2 = \tau_2(\tau), \quad \tau_3 = \tau_3(\tau), \quad \tau_1 \equiv \tau.$$

The matching condition for the three strings at the node is then given by

$$X_1^\mu(\tau, 0) = X_2^\mu\big(\tau_2(\tau), 0\big) = X_3^\mu\big(\tau_3(\tau), 0\big). \quad (3)$$

Varying the above action functional, we obtain the equations of motion

$$\frac{\partial}{\partial\tau_i}\frac{\partial\sqrt{-g_i}}{\partial\dot X_i^\mu} + \frac{\partial}{\partial\sigma}\frac{\partial\sqrt{-g_i}}{\partial X_i'^\mu} = 0, \quad i = 1, 2, 3, \quad (4)$$

and the boundary conditions on the trajectories of the quarks[1)] and the node.

By using nondegenerate changes of parameters, $\tau_i, \sigma \to \tilde\tau_i, \tilde\sigma$, and taking into account the invariance of the action functional (2) under these changes [21], we introduce, on each of the three sheets of the world surface, coordinates (as before, we denote them by τ_i, σ) in such a way as to ensure fulfillment of the orthonormality conditions

$$\dot X_i^2 + X_i'^2 = 0, \quad (\dot X_i, X_i') = 0, \quad i = 1, 2, 3. \quad (5)$$

The matching condition (3), in contrast to the more stringent condition $\tau_1 = \tau_2 = \tau_3$ on the node line [6, 9], makes it possible to implement these reparametrizations on each of the three sheets independently. However, the intrinsic equations of the node line then take the form $\sigma = \sigma_{0i}(\tau_i)$, which is more general than that of $\sigma = 0$.

In terms of the coordinates satisfying the conditions in (5), the equations of motion are linear; that is,

$$\ddot X_i^\mu - X_i''^\mu = 0. \quad (6)$$

Concurrently, the boundary conditions at the node and on the quark trajectories $\sigma = \sigma_i(\tau_i)$ take the form

$$\sum_{i=1}^{3}\Big[X_i'^\mu\big(\tau_i(\tau), \sigma_{0i}(\tau_i)\big) + \sigma_{0i}'(\tau_i)\dot X_i^\mu\big(\tau_i, \sigma_{0i}(\tau_i)\big)\Big]\tau_i'(\tau) = 0, \quad (7)$$

$$m_i\frac{d}{d\tau_i}U_i^\mu(\tau_i) + \gamma\big[X_i'^\mu + \sigma_i'(\tau_i)\dot X_i^\mu\big]\Big|_{\sigma=\sigma_i(\tau_i)} = 0, \quad i = 1, 2, 3, \quad (8)$$

where $U_i^\mu(\tau_i) = \dot x_i^\mu(\tau_i)\big/\sqrt{\dot x_i^2(\tau_i)}$ is the unit vector along the velocity of the ith quark. In the notation σ_{0i}', σ_i', and τ_i', the prime on a function of one variable hereafter denotes the derivative with respect to its argument—for example, $\sigma_i'(\tau_i) = \dfrac{d}{d\tau_i}\sigma_i$.

The orthonormality conditions (5) and, hence, Eqs. (6), together with the corresponding boundary conditions, remain invariant under reparametrizations of the class

$$\tilde\tau_i \pm \tilde\sigma = f_{i\pm}(\tau_i \pm \sigma), \quad i = 1, 2, 3, \quad (9)$$

where $f_{i\pm}$ are arbitrary smooth monotonic functions [21]. By appropriately choosing the functions $f_{i\pm}$, we can fix, on all sheets of the world surface of the Y configuration, the equations for the trajectories of the node and the strings ends in the form

$$\sigma_{0i}(\tau_i) = 0, \quad \sigma_i(\tau) = \pi, \quad 0 \le \sigma \le \pi, \quad i = 1, 2, 3. \quad (10)$$

On each sheet individually, we can ensure fulfillment of the node-line condition $\sigma = 0$ by choosing the functions $f_{i+}(\xi)$ in (9) and fulfillment of the condition $\sigma_i = \text{const}$ by making the additional substitution $f_{i+} = f_{i-}$, which leaves the equation $\sigma = 0$ invariant. The constants σ_i are not bound to be equal to π—the transformation in (9) with $f_{i\pm}(\xi) = \xi \cdot \text{const}$ changes their values.

In this study, we use a parametrization that satisfies the conditions in (10) and (5). An alternative approach is possible where the requirement $\tau_1 = \tau_2 = \tau_3$ on the node line (3) is introduced along with the condition $\sigma_{0i} = 0$ (or $\sigma_{0i} = \text{const}$). As was shown in [5], however, the functions $\sigma_i(\tau)$ in the equations for the quark trajectories are not equal to constants in this case.

But if we require fulfillment of both the conditions in (10) and the relations $\tau_1 = \tau_2 = \tau_3$ on the node line (3), simultaneously preserving the orthonormalized gauge (5)—this was done in [6, 7, 9]—the class of motions of the system that are described by the model will be constrained, since all physically possible motions will not meet the above conditions. In order to prove this, we note that, upon imposing the constraints in (5) and (10), there remains a class of reparametrizations (9) such that they do not disturb these constraints [26] and that the functions $f_{i+}(\xi) = f_{i-}(\xi) = f_i(\xi)$ in (9) obey the requirements

$$f_i(\xi + 2\pi) = f_i(\xi) + 2\pi, \quad f_i'(\xi) > 0. \quad (11)$$

Functions belonging to this class can be represented in the form $f(\xi) = \xi + \phi(\xi)$, where $\phi(\xi + 2\pi) = \phi(\xi)$ and $\phi'(\xi) > -1$ [26], and possess, as can easily be verified, the following properties: if $f(\xi)$

[1)] For the sake of brevity, we will henceforth refer to the matter point at the ends of the strings as quarks, bearing in mind, however, that the spin and other quantum characteristics of quarks cannot be described at the classical level.

and $g(\xi)$ satisfy the conditions in (11), the inverse function $f^{-1}(\xi)$ and the superposition $f\big(g(\xi)\big)$ also satisfy (11).

We require that the equalities $\tilde{\tau}_2 = \tilde{\tau}_3 = \tilde{\tau}_1$ on the node line $\sigma = 0$ be the result of the transformations specified by Eqs. (9) and (11). This leads to the relations

$$f_2\big(\tau_2(\tau)\big) = f_3\big(\tau_3(\tau)\big) = f_1(\tau),$$

which mean that, under the conditions in (5) and (10), only in the case where the functions $\tau_2(\tau)$ and $\tau_3(\tau)$ meet the conditions in (11) can the equalities $\tilde{\tau}_2 = \tilde{\tau}_3 = \tilde{\tau}_1$ be satisfied at all values of $\tilde{\tau}$. The class of motions that is constrained by this requirement is very narrow—it does not exhaust all physically possible motions. In Section 3 below, an arbitrary motion of the three-string system is described in such a way that unknown functions $\tau_i(\tau)$ are determined from the dynamical equations; also presented there is an example of the evolution of the system where the functions $\tau_i(\tau)$ do not satisfy the conditions in (11).

Let us recast the boundary conditions (3), (7), and (8) into a form that is convenient for the ensuing analysis. We substitute the general solution

$$X_i^\mu(\tau_i,\sigma) = \frac{1}{2}\big[\Psi_{i+}^\mu(\tau_i+\sigma) + \Psi_{i-}^\mu(\tau_i-\sigma)\big], \quad i = 1,2,3, \tag{12}$$

to Eqs. (6) on the world sheets into the boundary conditions (8) on the trajectories of the string ends; by using expressions (10), these boundary conditions can be reduced to the form [4, 27]

$$\frac{dU_i^\mu}{d\tau_i} = \frac{\gamma}{m_i}\big[\delta_\nu^\mu - U_i^\mu(\tau_i)U_{i\nu}(\tau_i)\big]\Psi_{i-}'^\nu(\tau_i-\pi), \tag{13}$$

$$\Psi_{i+}'^\mu(\tau_i+\pi) = \Psi_{i-}'^\mu(\tau_i-\pi) - 2m_i\gamma^{-1}U_i'^\mu(\tau_i), \tag{14}$$

where $\delta_\nu^\mu = \begin{cases} 1, & \mu = \nu, \\ 0, & \mu \neq \nu. \end{cases}$ The substitution of the solution specified by (12) into the boundary conditions (3) and (7) on the node line yields

$$\frac{d}{d\tau}\begin{pmatrix} \Psi_{1-}^\mu(\tau) \\ \Psi_{2-}^\mu\big(\tau_2(\tau)\big) \\ \Psi_{3-}^\mu\big(\tau_3(\tau)\big) \end{pmatrix} = \frac{1}{3}\begin{pmatrix} -1 & 2 & 2 \\ 2 & -1 & 2 \\ 2 & 2 & -1 \end{pmatrix}\frac{d}{d\tau}\begin{pmatrix} \Psi_{1+}^\mu(\tau) \\ \Psi_{2+}^\mu\big(\tau_2(\tau)\big) \\ \Psi_{3+}^\mu\big(\tau_3(\tau)\big) \end{pmatrix}. \tag{15}$$

The formulation of the boundary conditions in terms of Eqs. (13)–(15) is convenient for solving the initial- and boundary-value problem in question (see Section 3 below) and for analyzing the stability of the rotational motion of the Y configuration.

For the three-string model, the best known example of an exact solution is that which corresponds to the case where three rectangular segments connected at the node at angles of 120° execute a rotational motion at a constant speed [5–9]. This solution can be parametrized as

$$X_i^\mu = X_{i(\mathrm{rot})}^\mu(\tau_i,\sigma) = \Omega^{-1}\big[\theta\tau_i e_0^\mu + \sin(\theta\sigma)e^\mu(\tau_i+\Delta_i)\big], \quad \sigma \in [0,\sigma_i], \tag{16}$$

where $\tau_1 = \tau_2 = \tau_3$; e_0^μ is a vector directed along the center-of-mass velocity and subjected to the condition $e_0^2 = 1$; the rotating vector

$$e^\mu(\tau) = e_1^\mu\cos(\theta\tau) + e_2^\mu\sin(\theta\tau) \tag{17}$$

is aligned with the first segment of the string, $e^2 = -1$ and $(e_0, e) = 0$; e_0, e_1, e_2, and e_3 is the orthonormalized vierbein in $(3+1)$-dimensional Minkowski space; and θ, σ_i, and $\Delta_i = 2\pi(i-1)/(3\theta)$ are constants ($i = 1, 2, 3$). The parametrization in (16) satisfies Eq. (6) and the conditions in (3), (5), (7), and (8) if the angular frequency Ω of rotation, the parameters θ and σ_i, and the constant velocities v_i of the string ends are related by equations [2, 19]

$$v_i = \sin(\theta\sigma_i) = \Big[\Big(\frac{\Omega m_i}{2\gamma}\Big)^2 + 1\Big]^{1/2} - \frac{\Omega m_i}{2\gamma}, \quad i = 1,2,3. \tag{18}$$

In order to analyze the stability of the motion specified by Eq. (16), we consider, in the next section, small perturbations of this solution and of an analogous solution in the string model of mesons.

2. QUASIROTATIONAL MOTIONS AND ANALYSIS OF STABILITY

Before proceeding to analyze quasirotational states of the three-string system—that is, small perturbations of the motion described by Eq. (16)—we consider similar states of a relativistic string with massive ends [3]. In this simpler model, the string part of the action functional is equivalent to one term in expression (2). A rotation of a rectangular string at a constant velocity is a well-known rotational motion of this system. It is widely used to describe orbital excitations of mesons and, within the q–qq model, baryons [2, 19, 20, 24] and can be parametrized in the form

$$X^\mu = X_{\mathrm{rot}}^\mu(\tau,\sigma) = \Omega^{-1}\big[\theta\tau e_0^\mu + \cos(\theta\sigma+\phi_0)e^\mu(\tau)\big], \quad \sigma \in [0,\pi], \tag{19}$$

which is similar to that of (16). This solution to Eqs. (6) satisfies the conditions in (5) and boundary conditions of the form (8) for this model [3, 21] (naturally, we suppress here the index i on X^μ) at $v_1 = \cos\phi_0$, $v_2 = -\cos(\pi\theta + \phi_0)$, and $m_i\gamma^{-1}\Omega = (1 - v_i^2)/v_i$; here, m_1 and m_2 are the masses at the string ends.

The question concerning small perturbations of the motions described by Eq. (19) has long since aroused interest [28] in connection with the need for describing, within this model, hadron states interpreted as higher radial excitations in potential models [20]. One of the recent attempts of this type in [29] does not seem successful because of an inappropriate choice of gauge beyond (5)—this led to the complicated nonlinear equations of the general form (4)—and because of the disregard of the boundary conditions (8) and resort to unjustifiable simplifying assumptions. Not only were these drawbacks analyzed in [25], but also an adequate method was proposed there for describing arbitrary small perturbations of the rotational motion given by (19). This method is based on the fact that, if the orthonormality conditions (5) are satisfied, the substitution of the general solution $X^\mu(\tau,\sigma) = \frac{1}{2}\left[\Psi_+^\mu(\tau+\sigma) + \Psi_-^\mu(\tau-\sigma)\right]$ to the equations of motion (12) into the boundary conditions reduces them to the form [26]

$$\Psi_\pm'^\mu(\tau \pm \sigma_i) = m_i\gamma^{-1}\left[\sqrt{-U_i'^2(\tau)}U_i^\mu(\tau) \mp (-1)^i U_i'^\mu(\tau)\right], \quad i = 1, 2, \tag{20}$$

which makes it possible to determine $\Psi_\pm^\mu$ and, hence, the world surface $X^\mu(\tau,\sigma)$ by using the preset vector function $U_1^\mu(\tau)$ or $U_2^\mu(\tau)$ (the unit vector of the velocity of a string end). Upon the substitution of expressions (20) into the boundary conditions, there arises a set of ordinary differential equations with a deviating argument [26, 27]. In the particular case of $m_2 \to \infty$ (which is of importance for a comparison with the Y configuration), this set of equations assumes the form [25, 26]

$$U_1'^\mu(\tau) = \left[\delta_\nu^\mu - U_1^\mu(\tau)U_{1\nu}(\tau)\right](2e_0^\nu e_{0\kappa} - \delta_\kappa^\nu) \times \left[\sqrt{-U_1'^2(-)}U_1^\kappa(-) - U_1'^\kappa(-)\right], \tag{21}$$

where $(-) \equiv (\tau - 2\pi)$. In this case, the infinitely heavy second end of the string is at rest: $v_2 = 0$ and $U_2^\mu(\tau) = e_0^\mu = \text{const}$.

The vector function

$$U_{1(\text{rot})}^\mu(\tau) = (1 - v_1^2)^{-1/2}\left[e_0^\mu + v_1\acute{e}^\mu(\tau)\right], \quad \acute{e}^\mu(\tau) = \theta^{-1}\frac{d}{d\tau}e^\mu(\tau), \tag{22}$$

which corresponds to the rotational motion described in (19), satisfies Eq. (21). In order to describe an arbitrary motion close to a rotational one, we specify a vector function $U_1^\mu(\tau)$ close to $U_{1(\text{rot})}^\mu$ in the form [25]

$$U_1^\mu(\tau) = U_{1(\text{rot})}^\mu(\tau) + u^\mu(\tau), \qquad |u^\mu| \ll 1, \tag{23}$$

and substitute this expression into (21), omitting second-order terms in the small perturbation $u^\mu(\tau)$. For the resulting linearized set of equations, we seek solutions in the form $u^\mu = A^\mu e^{-i\omega\tau}$, which exist only in the case where $\omega = \omega_n$ is an eigenvalue of some boundary-value problem [25]. An arbitrary perturbation can be expanded in a series as [25, 26]

$$u^\mu(\tau) = \sum_n A_n^\mu \exp(-i\omega_n\tau). \tag{24}$$

Upon the substitution into Eqs. (23) and (20), this leads to the Fourier series

$$X^\mu(\tau,\sigma) = X_{\text{rot}}^\mu(\tau,\sigma) + \sum_{n=-\infty}^{\infty}\Big\{e_3^\mu\alpha_n\cos(\omega_n\sigma + \phi_n)\exp(-i\omega_n\tau) + \beta_n\left[e_0^\mu f_0(\sigma) + \acute{e}^\mu(\tau)f_\perp(\sigma) + ie^\mu(\tau)f_r(\sigma)\right]\exp(-i\tilde{\omega}_n\tau)\Big\}, \tag{25}$$

which describes an arbitrary small perturbation of the motion (19) (quasirotational motion) of a string with massive ends. Each term of this series corresponds to a vibration of a rotating string in the form of a standing wave that belongs to one of two types. This is either a vibration in the direction of the vector e_3^μ orthogonal to the plane of rotation, the frequency of this vibration being proportional to the root ω_n of the equation[2)]

$$(\omega^2 - Q_1Q_2)/\left[(Q_1 + Q_2)\omega\right] = \cot\pi\omega, \tag{26}$$

or a vibration in the plane of rotation spanned by the vectors e_1 and e_2, its dimensionless frequency $\tilde{\omega}_n$ satisfying the equation

$$\frac{(\tilde{\omega}^2 - q_1)(\tilde{\omega}^2 - q_2) - 4Q_1Q_2\tilde{\omega}^2}{2\tilde{\omega}\left[Q_1(\tilde{\omega}^2 - q_2) + Q_2(\tilde{\omega}^2 - q_1)\right]} = \cot\pi\tilde{\omega}, \tag{27}$$

where $Q_i = \theta v_i/\sqrt{1 - v_i^2}$, $q_i = Q_i^2(1 + v_i^{-2})$, and the root $\omega_1 \in (0,1)$ of Eq. (26) is equal to θ.

Expressions (25)–(27) are presented here for the case of arbitrary masses m_1 and m_2. For $m_2 \to \infty$,

[2)] It is interesting to note that the same Eq. (26) describes the spectrum of states of this string model for the case of linearized boundary conditions [26].

the transcendental Eqs. (26) and (27) and the functions appearing in series (25) become

$$\frac{\omega}{Q_1} = \cot\pi\omega, \quad \frac{\tilde{\omega}^2 - q_1}{2Q_1\tilde{\omega}} = \cot\pi\tilde{\omega}, \qquad (28)$$

$f_0 = 2(\theta^2 - \tilde{\omega}_n^2)\cos(\tilde{\omega}_n\tilde{\sigma})$; $f_\perp = (\tilde{\omega}_n + \theta)^2\sin(\tilde{\omega}_n - \theta)\tilde{\sigma} - (\tilde{\omega}_n - \theta)^2\sin(\tilde{\omega}_n + \theta)\tilde{\sigma}$; $f_r = (\tilde{\omega}_n + \theta)^2 \times \sin(\theta - \tilde{\omega}_n)\tilde{\sigma} - (\tilde{\omega}_n - \theta)^2\sin(\tilde{\omega}_n + \theta)\tilde{\sigma}$, where $\tilde{\sigma} = \pi - \sigma$.

All the quantities ω_n and $\tilde{\omega}_n$ satisfying Eqs. (26), (27) or (28) and appearing in expression (25) are real-valued; therefore, the rotational motion (19) of a string with massive ends is stable in the linear approximation.

Following the scheme outlined above, we will now analyze stability of the rotational motion (16) of the three-string model. We will consider that, as in the case of the q–$\overline{q}$ model, the three world surfaces $X_i^\mu(\tau_i, \sigma)$ of the Y configuration can be expressed in terms of the unit vectors $U_i^\mu(\tau_i)$ of the velocity of the massive string ends by using formulas of the type in (20) that are derived from the conditions in (13) and (14). Specifically, we have

$$\Psi'^\mu_{i\pm}(\tau_i \pm \sigma_i) = m_i\gamma^{-1}\Big[\sqrt{-U_i'^2(\tau_i)}U_i^\mu(\tau_i) \mp U_i'^\mu(\tau_i)\Big]. \qquad (29)$$

By analogy with (22), we further represent the above unit vectors U_i^μ and the functions $\Psi'^\mu_{i\pm}$ for the rotational motion (16) as

$$U^\mu_{i(\mathrm{rot})}(\tau_i) = \Gamma_i\big[e_0^\mu + v_i\acute{e}^\mu(\tau_i + \Delta_i)\big], \qquad (30)$$

$$\Psi'^\mu_{i\pm(\mathrm{rot})}(\tau_i) = m_i\gamma^{-1}Q_i\big[\Gamma_i e_0^\mu + \Gamma_i v_i\acute{e}^\mu(\tau_i + \Delta_i \mp \sigma_i) \pm e^\mu(\tau_i + \Delta_i \mp \sigma_i)\big], \qquad (31)$$

where $\Gamma_i = (1 - v_i^2)^{-1/2}$, $Q_i = \theta\Gamma_i v_i$, and $\acute{e}^\mu(\tau) = \theta^{-1}\frac{d}{d\tau}e^\mu(\tau) = e^\mu\big(\tau + \pi/(2\theta)\big)$. The orthogonal vectors e^μ and $\acute{e}^\mu$ (17) form a movable basis in the plane of rotation of the Y configuration. Below, we will consider the case of $m_1 = m_2 = m_3$, in which $v_i = v_1$, $\Gamma_i = \Gamma_1$, and $Q_i = Q_1$ for $i = 2, 3$, and choose the constants σ_i in the form (10), $\sigma_i = \pi$.

If an arbitrary motion of the system is close to the rotational motion given by Eq. (16), we will describe it in terms of the unit vectors $U_i^\mu(\tau)$ specified in the form

$$U_i^\mu(\tau_i) = U^\mu_{i(\mathrm{rot})}(\tau_i) + u_i^\mu(\tau_i), \qquad (32)$$

which is similar to that in (23). The perturbations $u_i^\mu(\tau_i)$ are assumed to be small ($|u_i^\mu| \ll 1$), which makes it possible to neglect second-order terms in u_i. Thereupon, we arrive at the conditions

$$\big(U_{i(\mathrm{rot})}(\tau_i), u_i(\tau_i)\big) = 0, \qquad (33)$$

which follow from the fact that U_i^μ and $U^\mu_{i(\mathrm{rot})}$ in (32) are unit vectors.

By virtue of expressions (29), small perturbations of the form (32) determine, in the linear approximation, the corresponding corrections for the functions $\Psi'^\mu_{i\pm}$ (31); that is,

$$\Psi'^\mu_{i\pm}(\tau_i) = \Psi'^\mu_{i\pm(\mathrm{rot})}(\tau_i) + m_i\gamma^{-1}\big[Q_i u_i^\mu(\tau_i \mp \pi) \mp u_i'^\mu(\tau_i \mp \pi) + U^\mu_{i(\mathrm{rot})}(\tau_i \mp \pi)\big(e(\tau_i + \Delta_i \mp \pi), u_i'(\tau_i \mp \pi)\big)\big]. \qquad (34)$$

Considering that an arbitrary perturbation u^μ for a string with massive ends can be expanded in the Fourier series (24), we will seek quasirotational motions in the form (32), where perturbations are represented as the harmonics

$$u_i^\mu(\tau_i) = \big[A_i^0 e_0^\mu + A_i e^\mu(\tau_i + \Delta_i) + v_i^{-1}A_i^0\acute{e}^\mu(\tau_i + \Delta_i) + A_i^z e_3^\mu\big]\exp(-i\omega\tau_i). \qquad (35)$$

The complex amplitudes A_i^0, A_i, and A_i^z are assumed to be small. The factor $v_i^{-1}A_i^0$ in front of $\acute{e}^\mu$ is determined by condition (33).

The dependence $\tau_i(\tau)$ in the conditions given by (3) is sought in the form

$$\tau_i(\tau) = \tau + \delta_i\exp(-i\omega\tau), \quad |\delta_i| \ll 1, \quad i = 2, 3. \qquad (36)$$

This leads to the expansions $e^\mu(\tau_i) \simeq e^\mu(\tau) + \theta\delta_i\acute{e}^\mu(\tau)e^{-i\omega\tau}$ in (30), (31), and (34).

We now substitute expressions (34), (35), and (36) into the boundary conditions (15) at the node. For the functions $\Psi'^\mu_{i\pm(\mathrm{rot})}(\tau)$ (31), they are satisfied identically; in the first-order (linear) approximation in the amplitudes A_i^0, A_i, A_i^z, and δ_i, we obtain a set of three vector equations. We further consider their projections onto the basis vectors e_0^μ, $e^\mu(\tau - \pi)$, $\acute{e}^\mu(\tau - \pi)$, and e_3^μ.

The projections of these equations onto the normal e_3^μ to the plane of rotation reduce to the form

$$(\omega C_\omega + Q_1)(A_1^z + A_2^z + A_3^z) = 0, \quad (Q_1C_\omega - \omega)(A_1^z - A_i^z) = 0, \quad i = 2, 3, \qquad (37)$$

where $C_\omega = \cot\pi\omega$. These three equations, which involve only the amplitudes A_i^z, form a closed subset in the set of twelve projections being considered; therefore, orthogonal perturbations described by these equations are independent of vibrations in the plane of rotation, which are characterized by the amplitudes A_i^0 and A_i. The set of Eqs. (37) has nontrivial

solutions only in the case where the dimensionless frequency ω satisfies one of the two equations

$$\omega/Q_1 = \cot\pi\omega, \qquad \omega/Q_1 = -\tan\pi\omega. \tag{38}$$

Perturbations of the rotational motion (16) that have the form

$$X_i^\mu(\tau_i,\sigma) = X_{i(\mathrm{rot})}^\mu(\tau_i,\sigma) \tag{39}$$
$$+ |A_i^z|\sqrt{1+Q_1^2/\omega_n^2}\,e_3^\mu \sin(\omega_n\sigma)\cos(\omega_n\tau+\phi_n),$$

where $\tau_i = \tau$ and where the amplitudes A_i^z are related by the equation $A_1^z + A_2^z + A_3^z = 0$, correspond to the roots $\omega = \omega_n$ $(n = 1, 2, \ldots)$ of the first of the above two equations, which coincides with the first equation in (28). Expression (39) describes small perturbations of the rotating Y configuration whose node is at rest in the c.m. frame that have the form of standing waves with n antinodes and which are similar to quasirotational states of a string with a fixed end [25], which appears in the series in (25) with the factor e_3^μ. The frequencies of vibrations in these waves are $\Omega_n = \Omega\omega_n/\theta$ (the minimum positive root ω_1 is equal to θ).

For the standing waves corresponding to the roots of the second equation in (38), the amplitudes satisfy the equalities $A_1^z = A_2^z = A_3^z$ (the vibrations of the three segments of the string are synchronous and identical) and expression (39) is valid upon the substitution of $\cos(\omega_n\sigma)$ for $\sin(\omega_n\sigma)$. Thus, the node of the Y configuration is involved in such vibrations in the direction of e_3^μ.

All roots of Eqs. (38) are real-valued; therefore, the motion specified by Eq. (16) is stable with respect to orthogonal perturbations in the linear approximation.

The pattern of perturbations in the plane of rotation is of a different character. It is described by the remaining nine linear equations of the aforementioned set of twelve equations in eight unknown complex-valued amplitudes A_i^0, A_i, and δ_i. Upon rather cumbersome transformations, these equations, which include eight independent equations, can be represented as

$$i\tilde\omega\Gamma_1\big[Q_1(C_{\tilde\omega}+i)\delta_i + C_{\tilde\omega}(A_1 - A_i)\big] \tag{40}$$
$$+ (Q_1^{-1}q_1C_{\tilde\omega} - \tilde\omega)(A_1^0 - A_i^0) = 0,$$
$$\epsilon_i v_1\Gamma_1^2(\tilde\omega^2-\theta^2)A_i + 2K_1A_1^0 + (K_1 - i\epsilon_iK_2)A_i^0 = 0,$$
$$2K_1A_1 + (K_1 + i\epsilon_iK_2)A_i + \epsilon_iK_3A_i^0 = 0,$$
$$i\tilde\omega\Gamma_1(A_1+A_2+A_3) + (Q_1^{-1}q_1 + \tilde\omega C_{\tilde\omega})$$
$$\times (A_1^0 + A_2^0 + A_3^0) = 0,$$
$$K_4\big[2\tilde\omega A_1^0 - (\tilde\omega - i\sqrt{3}\theta)A_2^0 - (\tilde\omega + i\sqrt{3}\theta)A_3^0\big] = 0,$$
$$\big[K_4(\tilde\omega^2-\theta^2) + 2iK_1(\tilde\omega^2+\theta^2)\big](A_2^0 - A_3^0) = 0,$$

where $q_1 = Q_1^2(1+v_1^{-2})$; $\epsilon_i = (-1)^i\sqrt{3}$; in the first three equations, the subscript i takes the values of 2 and 3; $K_1 = q_1 - \tilde\omega^2 + 2Q_1\tilde\omega C_{\tilde\omega}$; $K_2 = \Gamma_1 v_1\big[(\tilde\omega^2 + \theta^2)C_{\tilde\omega} + 2Q_1\tilde\omega\big]$; $K_3v_1\Gamma_1^2(\tilde\omega^2-\theta^2) = K_2^2 - K_1^2$; and $K_4 = (q_1 - \tilde\omega^2)C_{\tilde\omega} - 2Q_1\tilde\omega$.

Nontrivial solutions to this set of equations correspond to the frequencies $\tilde\omega$ obtained as the roots of the characteristic equation

$$K_1K_4\big[K_4(\tilde\omega^2-\theta^2) + 2iK_1(\tilde\omega^2+\theta^2)\big] = 0. \tag{41}$$

These solutions can be broken down into three classes. Two of them are described by the equations $K_1 = 0$ and $K_4 = 0$ or

$$\frac{\tilde\omega^2 - q_1}{2Q_1\tilde\omega} = \cot\pi\tilde\omega, \quad \frac{\tilde\omega^2 - q_1}{2Q_1\tilde\omega} = -\tan\pi\tilde\omega, \tag{42}$$

which are similar to relations (38) and (28). The roots of Eqs. (27) are real-valued, and the corresponding vibrations of the segments of the strings in the plane of rotation have the form of standing waves of constant amplitude. The waves corresponding to the first equation in (42) are symmetric since they are determined by the equal amplitudes $A_1 = A_2 = A_3$ and $A_1^0 = A_2^0 = A_3^0$ and coincide with analogous vibrations of a string with a fixed end, which are characterized by $\tilde\omega_n$ obtained as the roots of the second equation in (28).

However, the frequencies that are characteristic of the third of the aforementioned classes and which annihilate the third factor on the left-hand side of (41), so that they are the roots of the equation

$$2\frac{Q_1\tilde\omega(\theta^2-\tilde\omega^2) - i(\tilde\omega^2-q_1)(\tilde\omega^2+\theta^2)}{(\tilde\omega^2-q_1)(\tilde\omega^2-\theta^2) - 4iQ_1\tilde\omega(\tilde\omega^2+\theta^2)} = \cot\pi\tilde\omega, \tag{43}$$

are complex-valued (with the exception of the roots $\tilde\omega = \pm\theta$). After the substitution $\tilde\omega = \mathrm{Re}\tilde\omega + i\mathrm{Im}\tilde\omega$ and some transformations, an analysis of Eq. (43) reveals that its roots form a countable set, $\tilde\omega = \tilde\omega_n$. The behavior of the real parts of these roots is similar to the behavior of the roots of Eqs. (38) and (42)—that is, $\mathrm{Re}\tilde\omega_n \in (n-1, n)$ for the corresponding numbering; at the same time, the imaginary parts $\vartheta_n = \mathrm{Im}\tilde\omega_n$ possess the property $\vartheta_{-n} = \vartheta_n$ and, for $n \geq 1$, form an increasing sequence, its limit being given by $\lim_{n\to\infty}\vartheta_n = \pi^{-1}\mathrm{arctanh}(1/2) \simeq 0.1748$. It is the most important that the imaginary parts of the complex-valued roots of Eq. (43) are positive. This leads to an increase in the amplitude of these perturbations owing to the presence of the factor

$$\exp(-i\tilde\omega_n\tau) = \exp(-i\mathrm{Re}\tilde\omega_n\tau + \mathrm{Im}\tilde\omega_n\tau), \tag{44}$$
$$\mathrm{Im}\tilde\omega_n > 0.$$

Exponentially growing modes are also present in the spectrum of quasirotational states of the massless version of the three-string model [1, 5, 6, 9]. If, in the case of $m_i = 0$ (which is equivalent to $v_i = 1$ or $q_i, Q_i \to \infty$), Eqs. (38) and (42) lead to known integral and half-integer eigenfrequencies ω_n and $\tilde{\omega}_n$ [9], Eq. (43) takes the form

$$-2i(4\tilde{\omega}^2 + 1)/(4\tilde{\omega}^2 - 1) = \cot\pi\tilde{\omega}, \quad m_i = 0.$$

The complex-valued roots of this equation behave in the same way as in the general case of (43).

An arbitrary perturbation of the form (16) imposed on rotational motion in the three-string model can be expanded in a Fourier series in harmonics of all the above classes with frequencies determined by Eqs. (38), (42), and (43) that is similar to that in (24). Only in the case where all coefficients of the harmonics belonging to the last class are zero (this is realized only if there exist some special symmetries of a perturbation that are peculiar to the remaining classes) does the amplitude of this perturbation not grow exponentially according to (44). Thus, we have proven that, for the Y configuration, the classical rotational motion specified by Eq. (16) is unstable; this is so even in the linear approximation.

In order to explore the evolution of this instability in the case where perturbations are not small, we consider the initial- and boundary-value problem for this model.

3. INITIAL- AND BOUNDARY-VALUE PROBLEM FOR THE Y MODEL

The general formulation of the initial- and boundary-value problem for the three-string system consist in determining the motion of the system for preset initial conditions—that is, in constructing the solution $X_i^\mu(\tau_i, \sigma)$ to Eq. (6) that satisfies the orthonormality conditions (5) and the boundary conditions (3), (7), and (8). The initial conditions imply the preassignment of the initial position of the Y configuration as three curves (initial curves) connected at the node that are parametrized in the form $\rho_i^\mu(\lambda)$ with $\lambda \in [0, \lambda_i]$ $(i = 1, 2, 3)$ such that $\rho_1^\mu(0) = \rho_2^\mu(0) = \rho_3^\mu(0)$ and $\rho_i'^2 < 0$ and the preassignment of initial velocities $V_i^\mu(\lambda)$. The timelike vector $V_i^\mu(\lambda)$ is defined apart from an arbitrary positive scalar factor $\chi(\lambda)$.

In this study, the method developed for solving the initial- and boundary-value problem within the model of a relativistic string with massive ends [27] and within the q–q–q model [4] is taken as a basis and is applied to the more complicated system considered here.

Let us specify the intrinsic equations of the initial curves on the world sheets,[3)]

$$\tau_i = \tau_i^*(\lambda), \quad \sigma = \sigma_i^*(\lambda),$$

and the initial position of the Y configuration in the form [27]

$$X_i^\mu\big(\tau_i^*(\lambda), \sigma_i^*(\lambda)\big) = \rho_i^\mu(\lambda), \quad \lambda \in [0, \lambda_i], \quad i = 1, 2, 3, \tag{45}$$

where $|\tau_i^{*\prime}| < \sigma_i^{*\prime}$, $\tau_i^*(0) = \sigma_i^*(0) = 0$, and $\sigma_i^*(\lambda_i) = \pi$. By using the initial data, we determine the functions $\Psi_{i\pm}^\mu$ appearing in (12) by the formulas [27]

$$\frac{d}{d\lambda}\Psi_{i\pm}^\mu\big(\tau_i^*(\lambda) \pm \sigma_i^*(\lambda)\big) = \big[1 \pm (V_i, \rho_i')G_i\big]\rho_i'^\mu \mp G_i\rho_i'^2 V_i^\mu, \tag{46}$$

where $G_i(\lambda) = \big[(V_i, \rho_i')^2 - V_i^2\rho_i'^2\big]^{-1/2}$. Expressions (46) make it possible to find the functions Ψ_{i+}^μ within the initial segments $I_{i+} = \big[0, \tau_i^*(\lambda_i) + \pi\big]$ and the functions Ψ_{i-}^μ within the segments $I_{i-} = \big[\tau_i^*(\lambda_i) - \pi, 0\big]$. The constant of integration in (46) is determined from the initial condition (45).

A continuation of the functions $\Psi_{i\pm}^\mu$ as their arguments grow indefinitely can be uniquely performed with the aid of the boundary conditions (3), (7), and (8), which were reduced above, for this purpose, to the form (13)–(15). The set of Eqs. (13) must be supplemented with the initial conditions $U_i^\mu\big(\tau^*(\lambda_i)\big) = V_i^\mu(\lambda_i)/\sqrt{V_i^2(\lambda_i)}$ $(i = 1, 2, 3)$. Expressing the functions Ψ_{i-}^μ in terms of Ψ_{i+}^μ with the aid of Eqs. (15) (initially within the segments I_{i+}), integrating Eqs. (13) with the above initial conditions, and using expressions (14) to determine the functions Ψ_{i+}^μ off the segments I_{i+}, we can continue infinitely the functions $\Psi_{i\pm}^\mu$ beyond the initial segments $I_{i\pm}$, provided that the functions $\tau_2(\tau)$ and $\tau_3(\tau)$ are known. In order to find them, we use the isotropy conditions $\Psi_{i\pm}'^2 = 0$, which follow from (5), and the relations

$$[\tau_i'(\tau)]^2\big(\Psi_{i+}'(\tau_i), \Psi_{i-}'(\tau_i)\big) = \big(\Psi_{1+}'(\tau), \Psi_{1-}'(\tau)\big), \quad i = 2, 3, \tag{47}$$

which were obtained with the aid of equalities (3) and (12). Only if the conditions in (47) are satisfied does the isotropy of the vector functions $\Psi_{i-}'^\mu$ on the left-hand side of (15) follow from the isotropy of the vector functions $\Psi_{i+}'^\mu$ on the right-hand side of this equation.

[3)] There is arbitrariness in choosing the functions $\tau_i^*(\lambda)$ and $\sigma_i^*(\lambda)$ that is associated with the freedom in choosing the functions f_i in (11).

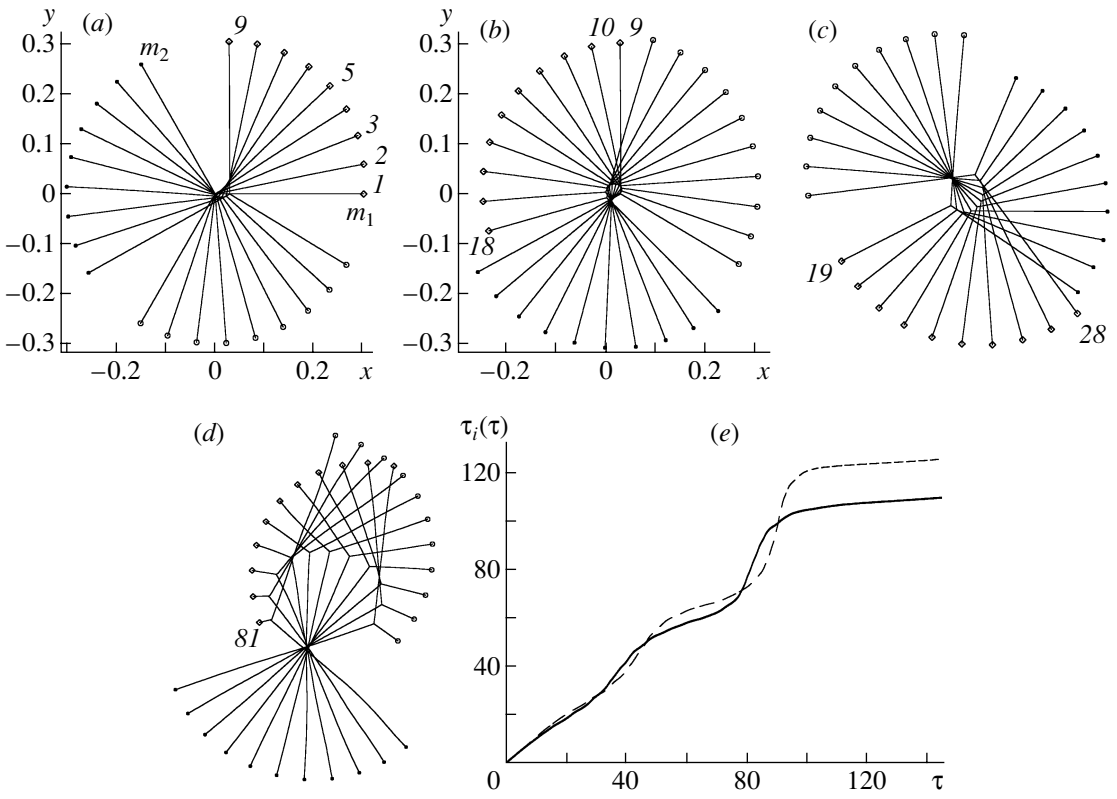

Fig. 2. Example of the quasirotational motion of the Y configuration.

By substituting Ψ'^{μ}_{i-} from (15) into (47), we obtain the expressions

$$\tau'_2(\tau) = \frac{\left(\Psi'_{1+}(\tau), \Psi'_{3+}(\tau_3)\right)}{\left(\Psi'_{2+}(\tau_2), \Psi'_{3+}(\tau_3)\right)}, \qquad (48)$$

$$\tau'_3(\tau) = \frac{\left(\Psi'_{1+}(\tau), \Psi'_{2+}(\tau_2)\right)}{\left(\Psi'_{2+}(\tau_2), \Psi'_{3+}(\tau_3)\right)},$$

which make it possible to find $\tau_2(\tau)$ and $\tau_3(\tau)$ if the functions Ψ'^{μ}_{i+} have been determined first within the segments I_{i+} by formulas (46) and then, in the course of implementing the above procedure of their continuation, beyond the segments I_{i+}.

Examples of solving the initial- and boundary-value problem according to this scheme for the Y string configuration were given in [25, 30], where numerical methods were applied since analytic solutions exist only for a bounded class of motions at $m_i = 0$ [9] and $m_i \neq 0$ [7].

For the system with $m_1 = m_2 = m_3 = 1$ and $\gamma = 1$, Fig. 2 presents an example of a motion that is close to a rotational motion and which was obtained as a solution to the initial- and boundary-value problem with the initial position of the three string segments $\rho^{\mu}_i(\lambda)$ having the same length $R_i = v_i/\Omega = 0.3$ and forming angles of 120° (position *1* in Fig. 2*a*) and the initial velocities $\mathbf{V}_i(\lambda) = \left[\mathbf{\Omega} \times \rho_i\right] + \delta\mathbf{V}_i(\lambda)$, where Ω satisfies relations (18). The exact solution (16) in the form of rotational motion corresponds to case of $\delta\mathbf{V}_i = 0$. For the motion in Fig. 2, the only nonvanishing component of the perturbation is that which is associated with e^{μ}_1 on the first segment of the string, $\delta V^1_1(\lambda) = 0.05\lambda$ $(0 < \lambda < \lambda_1 = 1)$. Figures 2*a*–2*d* show the successive positions of the system on the xy or $(e^{\mu}_1 e^{\mu}_2)$ plane (sections $t = \text{const}$ of the world surface) at regular time intervals of $\Delta t = 0.15$. The numbers of these sections in the order of increasing t are indicated near the position of the first massive point.

An asymmetric distribution of the initial velocities results in that, at some instant (position *5* in Fig. 2*a*), the node begins to move. The distance from the node to the center of rotation increases with time, while the lengths of the string segments quasiperiodically change in turn (Figs. 2*b*, 2*c*) until one of these lengths vanishes (Fig. 2*d*).

In Fig. 2, the development of the instability at the initial stage is consistent with the results of the analysis performed in Section 2. According to expression (44), the increment of the growth of perturbations is determined by the imaginary parts of the roots $\tilde{\omega}_n$ of Eq. (43). For the parameters of

the motion illustrated in Fig. 2, these roots are $\tilde{\omega}_1 \simeq 0.276 + 0.0297i$, $\tilde{\omega}_2 \simeq 1.05 + 0.157i$, $\tilde{\omega}_3 \simeq 2.027 + 0.17i$, $\tilde{\omega}_4 \simeq 3.0183 + 0.173i, \ldots$. It can be seen that the relevant increment is determined predominantly by $\mathrm{Im}\tilde{\omega}_1 \simeq 0.0297$ (recall that the frequencies normalized to t are $\Omega_n = \Omega\tilde{\omega}_n/\theta$; in the present case, $\theta \simeq 0.1595$ and $\Omega \simeq 1.6$).

In Fig. 2*e*, the dependences (solid curve) $\tau_2(\tau)$ and (dashed curve) $\tau_3(\tau)$ are shown for the motion in question. The rate of passage of the time τ_i increases as the corresponding segment of the string decreases. The horizontal asymptotes of the curves in Fig. 2*e* can be explained by the vanishing of the length of the first string segment. As can be seen, the functions $\tau_2(\tau)$ and $\tau_3(\tau)$ do not satisfy the periodicity conditions in (11). This gives no way to describe this motion (and an arbitrary motion in the general case) within the parametrization [6, 9] with $\tau_1 = \tau_2 = \tau_3$. Along with the justification of the last statement, it was shown in [30] that this result of the development of instability of the rotational motion specified by Eq. (16) is a feature peculiar to the dynamics of the Y baryon configuration. The amplitude of any asymmetric planar [$\delta\rho_i$, $\delta\mathbf{V}_i$ in the (xy) plane] initial perturbation grows with time, which inevitably leads to the fusion of one of the massive points with the node.

CONCLUSION

It has been shown that the rotational motion (16) in the three-string baryon model is unstable at the classical level. In order to do this, two approaches have been employed: that which is based on an analysis of the spectrum of small perturbations of the motion being considered (Section 2) and that which is based on the method proposed for solving the initial- and boundary-value problem with general initial conditions for the Y string configuration (Section 3). Within the second approach, it has been established that, because of the development of instability, an arbitrary small asymmetric perturbation of a rotating three-string configuration inevitably leads to the fusion of the node and the massive point at the end of one of three strings.

In Section 2, the fact that this instability is realized for the three-string model with equal masses at the ends has been proven by analyzing, in the linear approximation, small perturbations of the motion described by Eq. (16). The exponentially growing modes (44), which are associated with the complex roots $\tilde{\omega}_n$ of Eq. (43)—they are the frequencies of these modes—have been found in the spectrum of these perturbations. Their presence leads to the growth of arbitrary asymmetric perturbations of the rotational motion.

It is useful to compare this behavior of the three-string system with the result of a similar analysis of quasirotational motions of a string with massive ends in [25]. These motions can be represented in the form of the series (25), which represents a superposition of vibrational motions of a rotating string that have the form of standing waves. Their frequencies that are obtained as the roots of Eqs. (26) and (27) are real-valued; therefore, the rotational motion (19) of a string with massive ends is stable in the linear approximation.

Expression (25) makes it possible to quantize quasirotational states of a string with masses at its ends in the linear vicinity of the stable solution (19). We recall that the quantization method commonly used in string theory [21] cannot be applied to the system in question because of the nonlinearity of the boundary conditions (8), which prevents a representation of a general solution to the equations of motion in the form of a series. Because of these difficulties, approaches were developed to quantizing such a system by constraining its dynamics by the condition requiring that the string be rectilinear [23, 24, 28], whereby the majority of string degrees of freedom were eliminated (in some cases, this reduced to the introduction of a string term in the potential).

It should be noted in this connection that a quantum description of the series in (25), which was obtained without introducing the above constraint and which takes into account all quasirotational states of the string, does not lead to analogs of the Virasoro conditions, since, by construction, this series satisfies the orthonormality condition (5) in the linear approximation. The objective of this approach (its elaboration is beyond the scope of the present study devoted to the three-string model) is to describe not only orbital but also other excitations of hadrons within the $q\text{–}\overline{q}$ and $q\text{–}qq$ string models.

As to the three-string model specified by the action functional (2), the instability of its classical rotational motion given by Eq. (16) presents difficulties in applying the above approach to quantizing its quasirotational states because this is possible only in the linear vicinity of a stable solution. The same is true for the $q\text{–}q\text{–}q$ string baryon configuration [4]; at the same time, so-called simple rotational motions in the triangle model are stable [25].

The results of this study are of importance for choosing the most adequate string configuration both for describing baryon excitations on the Regge trajectories (1) [19, 20] and for constructing more elaborate baryon models on the basis of QCD.

ACKNOWLEDGMENTS

This study was supported by the Russian Foundation for Basic Research (project no. 00-02-17359).

REFERENCES

1. X. Artru, Nucl. Phys. B **85**, 442 (1975).
2. I. Yu. Kobzarev, L. A. Kondratyuk, B. V. Martem'yanov, and M. G. Shchepkin, Yad. Fiz. **45**, 526 (1987) [Sov. J. Nucl. Phys. **45**, 330 (1987)]; I. Yu. Kobzarev, B. V. Martem'yanov, and M. G. Shchepkin, Usp. Fiz. Nauk **162** (4), 1 (1992) [Sov. Phys. Usp. **35**, 257 (1992)].
3. A. Chodos and C. B. Thorn, Nucl. Phys. B **72**, 509 (1974); B. M. Barbashov and V. V. Nesterenko, Teor. Mat. Fiz. **31**, 291 (1977).
4. V. P. Petrov and G. S. Sharov, Mat. Model. **11**, 39 (1999); hep-ph/9812527.
5. P. A. Collins, J. L. Hopkinson, and R. W. Tucker, Nucl. Phys. B **100**, 157 (1975).
6. K. Sundermeyer and A. de la Torre, Phys. Rev. D **15**, 1745 (1977).
7. A. L. Koshkarov, Preprint No. P2-11104, OIYaI (Joint Inst. for Nuclear Research, Dubna, 1977).
8. K. Kamimura, Prog. Theor. Phys. **62**, 508 (1979).
9. M. S. Plyushchaĭ, G. P. Pron'ko, and A. V. Razumov, Teor. Mat. Fiz. **63**, 97 (1985); S. V. Klimenko, V. R. Kochin, M. S. Plyushchaĭ, *et al.*, Teor. Mat. Fiz. **64**, 245 (1985).
10. G. S. Sharov, Teor. Mat. Fiz. **113**, 68 (1997).
11. G. S. Sharov, Phys. Rev. D **58**, 114009 (1998); hep-th/9808099.
12. D. B. Leinweber, Phys. Rev. D **47**, 5096 (1993); hep-ph/9302266; Yu. Novozhilov, A. Pronko, and D. Vassilevich, Phys. Lett. B **343**, 358 (1995); hep-ph/9411421.
13. M. Szczekowski, Int. J. Mod. Phys. A **4**, 3985 (1989); M. Anselmino, E. Predazzi, S. Ekelin, *et al.*, Rev. Mod. Phys. **65**, 1199 (1993).
14. N. Isgur and J. Paton, Phys. Rev. D **31**, 2910 (1985); S. Capstick and N. Isgur, Phys. Rev. D **34**, 2809 (1986); S. Capstick and P. R. Page, Phys. Rev. D **60**, 111501 (1999); nucl-th/9904041.
15. Yu. A. Simonov, Nucl. Phys. B **307**, 512 (1988); Yad. Fiz. **54**, 224 (1991) [Sov. J. Nucl. Phys. **54**, 133 (1991)].
16. Yu. S. Kalashnikova and A. V. Nefediev, Yad. Fiz. **60**, 1470 (1997) [Phys. At. Nucl. **60**, 1333 (1997)].
17. D. S. Kuzmenko and Yu. A. Simonov, Phys. Lett. B **494**, 81 (2000); hep-ph/0006192; hep-ph/0010114.
18. J. M. Cornwall, Nucl. Phys. B **128**, 75 (1977); Phys. Rev. D **54**, 6527 (1996).
19. G. S. Sharov, Yad. Fiz. **62**, 1831 (1999) [Phys. At. Nucl. **62**, 1705 (1999)].
20. A. Inopin and G. S. Sharov, Phys. Rev. D **63**, 054023 (2001); hep-ph/9905499.
21. B. M. Barbashov and V. V. Nesterenko, *Introduction to the Relativistic String Theory* (Énergoatomizdat, Moscow, 1987; World Sci., Singapore, 1990).
22. M. S. Plyushchaĭ, G. P. Pron'ko, and A. V. Razumov, Teor. Mat. Fiz. **67**, 396 (1986).
23. A. Y. Dubin, A. B. Kaidalov, and Yu. A. Simonov, Phys. Lett. B **323**, 41 (1994); Yu. S. Kalashnikova and A. V. Nefediev, Yad. Fiz. **61**, 871 (1998) [Phys. At. Nucl. **61**, 785 (1998)].
24. L. D. Solov'ev, Yad. Fiz. **62**, 534 (1999) [Phys. At. Nucl. **62**, 491 (1999)]; hep-ph/9803483; Phys. Rev. D **58**, 035005 (1998); **61**, 015009 (2000); hep-ph/9907486.
25. G. S. Sharov, Phys. Rev. D **62**, 094015 (2000); hep-ph/0004003.
26. G. S. Sharov, Teor. Mat. Fiz. **107**, 86 (1996); V. P. Petrov and G. S. Sharov, Teor. Mat. Fiz. **109**, 187 (1996).
27. B. M. Barbashov and G. S. Sharov, Teor. Mat. Fiz. **101**, 253 (1994).
28. M. Ida, Prog. Theor. Phys. **59**, 1661 (1978); D. LaCourse and M. G. Olsson, Phys. Rev. D **39**, 2751 (1989); V. V. Nesterenko, Z. Phys. C **47**, 111 (1990).
29. T. J. Allen, M. G. Olsson, and S. Veseli, Phys. Rev. D **59**, 094011 (1999); **60**, 074026 (1999); hep-ph/9903222.
30. G. S. Sharov, hep-ph/0001154.

Translated by A. Isaakyan

Physics of Atomic Nuclei, Vol. 65, No. 5, 2002, pp. 917–924. From Yadernaya Fizika, Vol. 65, No. 5, 2002, pp. 949–955.

ELEMENTARY PARTICLES AND FIELDS
Theory

Heavy Baryons in the Nonperturbative String Approach*

I. M. Narodetskii and M. A. Trusov

Institute of Theoretical and Experimental Physics,
Bol'shaya Cheremushkinskaya ul. 25, Moscow, 117259 Russia

Received April 12, 2001

Abstract—We present some piloting calculations of the short-range correlation coefficients for light and heavy baryons and of the masses of the doubly heavy baryons $\Xi_{QQ'}$ and $\Omega_{QQ'}$ $(Q, Q' = c, b)$ on the basis of a simple approximation within nonperturbative QCD. © *2002 MAIK "Nauka/Interperiodica".*

1. INTRODUCTION

The observation of the B_c^+ meson by the CDF collaboration [1] opens a new direction in the physics of hadrons containing two heavy quarks. Presently, at the LHC, B factories, and the Tevatron with high luminosity, several experiments have been proposed in which it is possible to identify and study hadrons containing two heavy quarks, like doubly charmed baryons (ccq) or baryons (bcq) with charm and beauty.[1)] In the more distant future, next-generation experiments with a high bottom-quark-production rate will provide excellent possibilities for studying bottom baryons and their decays. In view of this project, it is important to have safe theoretical predictions for heavy-baryon masses as a guide to experimental searches for these hadrons.

A number of authors [2–12] have already considered baryons containing two heavy quarks in anticipation of future experiments that may discover these particles. In the majority of those studies, however, theoretical predictions are somewhat biased by the introduction of additional dynamical assumptions and supplementary dynamical parameters, like constituent quark masses, in addition to the only one parameter really pertinent to QCD—the overall scale $\Lambda_{\rm QCD}$ of the theory.

The purpose of this study is to calculate the masses of heavy baryons in a simple approximation within nonperturbative QCD developed in [13–16]. This method has already been applied to studying baryon Regge trajectories [15] and, very recently, to computing the magnetic moments of light baryons [17]. The key point of this study is that it is very reasonable that the same method should also hold for hadrons containing heavy quarks. Here, we concentrate on the masses of doubly heavy baryons. As in [17], we take, as the universal parameter, the QCD string tension σ, fixed experimentally by the meson and baryon Regge slopes. We also include the perturbative Coulomb interaction with the frozen coupling $\alpha_s(1\ {\rm GeV}) = 0.39$. The basic feature of this approach is the dynamical calculation of the quark constituent masses m_i in terms of the quark current masses $m_i^{(0)}$. This is done by using the einbein (auxiliary-field) formalism, which is proven to be rather accurate in various calculations for relativistic systems. The einbeine are treated as variational parameters that are to be found from the condition requiring that the baryon eigenenergies be minimal [18].

2. DESCRIPTION OF FORMALISM

The starting point of the approach is the Feynman–Schwinger representation of the $3q$ Green's function, where the role of "time" parameter along a quark path is played by the Fock–Schwinger proper time. The final step is the derivation of the c.m. effective Hamiltonian (EH) containing the dynamical quark masses as parameters. For many details, the reader is referred to the original studies reported in [13–16].

Let us consider a baryon consisting of three quarks of arbitrary masses m_i, $i = 1, 2, 3$. In what follows, we confine ourselves to a consideration of the ground-state baryons without radial and orbital excitations, in which case tensor and spin–orbit forces do not contribute perturbatively. Then, only the spin–spin interaction survives in the perturbative approximation. The EH has the form

$$H = \sum_{i=1}^{3}\left(\frac{m_i^{(0)2}}{2m_i} + \frac{m_i}{2}\right) + H_0 + V, \qquad (1)$$

*This article was submitted by the authors in English.

[1)]Here, and throughout this paper, q denotes a light quark u or d.

1063-7788/02/6505-0917$22.00

where $m_i^{(0)}$ are the current quark masses and m_i are the dynamical quark masses to be found from the minimum condition [see Eq. (2) below]. Since $m_i \gg m_i^{(0)}$ for light quarks, but $m_i \sim m_i^{(0)}$ for heavy quarks, each light quark contributes to the baryon mass an additional mass $\sim m_i/2$ (not m_i as in the ordinary nonrelativistic quark model), whereas each heavy quark contributes an additional mass of about m_i. The dynamical quark masses are evaluated from the equations defining the stationary points of the baryon mass M_B as a function of m_i:

$$\frac{\partial M_B(m_i)}{\partial m_i} = 0. \tag{2}$$

Let $\boldsymbol{r}_i$ be the quark coordinates. The kinetic-energy operator H_0 in Eq. (1) takes the familiar form

$$H_0 = -\frac{1}{2m_1}\frac{\partial^2}{\partial \boldsymbol{r}_1^2} - \frac{1}{2m_2}\frac{\partial^2}{\partial \boldsymbol{r}_2^2} - \frac{1}{2m_3}\frac{\partial^2}{\partial \boldsymbol{r}_3^2}. \tag{3}$$

The quantity V is the sum of the perturbative Coulomb-like one-gluon-exchange potential and the string potential. The Coulomb-like potential is given by

$$V_{\mathrm{C}} = -\frac{2\alpha_s}{3}\sum_{i<j}\frac{1}{|\boldsymbol{r}_{ij}|}, \tag{4}$$

where the factor $2/3$ is the value of the quadratic Casimir operator for the group $SU_c(3)$. The string potential was calculated in [15] as the static energy of the three heavy quarks,

$$V_{\mathrm{string}}(\boldsymbol{r}_1, \boldsymbol{r}_2, \boldsymbol{r}_3) = \sigma R_{\mathrm{min}}, \tag{5}$$

where R_{min} is the sum of the three distances $|\boldsymbol{r}_i|$ from the string junction point, which, for the sake of simplicity, is chosen to coincide with the center-of-mass coordinate $\mathbf{R}_{\mathrm{c.m.}}$.

3. HYPERRADIAL APPROXIMATION

We use the hyperspherical-formalism approach (for details, see the original studies in [19]). In the hyperradial approximation (HRA) corresponding to the truncation of the wave function $\psi(\{\boldsymbol{r}_i\})$ by the component with grand-orbital momentum $K = 0$, the three-quark wave function depends only on the hyperradius $R^2 = \boldsymbol{\rho}^2 + \boldsymbol{\lambda}^2$, where $\boldsymbol{\rho}$ and $\boldsymbol{\lambda}$ are the three-body Jacobi variables,[2)] and does not depend on angular variables. The confining potential (5) has a specific three-body character. However, this potential, as well as the Coulomb potential in Eq. (4), is smooth in the sense that the HRA (where only that part of the potential which is invariant under rotations in the six-dimensional space spanned by the Jacobi coordinates is taken into account) is already an excellent approximation. The HRA neglects the mixed-symmetry components of the three-quark wave function, which appear in the higher approximations of the hyperspherical formalism [19]. Introducing the reduced function[3)] $\chi(R) = R^{5/2}\psi(R)$ and averaging $V = V_{\mathrm{C}} + V_{\mathrm{string}}$ over the six-dimensional sphere, one obtains the Schrödinger equation

$$\frac{d^2\chi(R)}{dR^2} + 2\mu\left[E - W(R) - \frac{15}{8\mu R^2}\right]\chi(R) = 0, \tag{6}$$

where μ is an arbitrary parameter that has dimensions of mass and which drops out of the final expressions. The last term in (6) represents the three-body centrifugal barrier, and $W(R)$ is the average of the three-quark potentials over the six-dimensional sphere,

$$W(R) = \langle V \rangle = -\frac{a}{R} + bR \tag{7}$$

with

$$a = \frac{2\alpha_s}{3}\frac{16}{3\pi}\sum_{i<j}\alpha_{ij}, \quad b = \sigma\frac{32}{15\pi}\sum_{i,j}\gamma_{ij}. \tag{8}$$

The mass-depending constants α_{ij} and γ_{ij} are defined by Eqs. (A.2) and (A.13) in the Appendix.

It is convenient to introduce the variable $x = R\sqrt{\mu}$ and to eliminate an artificial dependence of Eq. (6) on μ, whereupon Eq. (6) becomes

$$\chi''(x) + 2\left(E - U(x) - \frac{15}{8x^2}\right)\chi(x) = 0, \tag{9}$$

where

$$U(x) = -\frac{a\sqrt{\mu}}{x} + \frac{b}{\sqrt{\mu}}x. \tag{10}$$

Since $a \sim 1/\sqrt{\mu}$ and $b \sim \sqrt{\mu}$ [see Eqs. (A.2) and (A.13)], the eigenvalue E in (6) does not depend on μ.

4. QUARK DYNAMICAL MASSES

Equation (9) when applied to the nucleon ($m_q^{(0)} \sim 0$) yields the dynamical mass m_q of the light quark and when applied to strange hyperons yields the strange-quark mass m_s. In the same manner, the application of this equation to charm and beauty baryons yields the constituent masses of the c and b quarks. In our calculations, we use the same parameters as in [20], namely, $\sigma = 0.17$ GeV, $\alpha_s = 0.4$, $m_q^{(0)} =$

[2)] For their definition, see the Appendix.

[3)] In what follows, we omit the value of $K = 0$ to avoid subscripts. Note that the radially symmetric component with $K = 0$ is a dominant one in the three-quark wave function.

Table 1. Constituent quark masses m_i and ground-state eigenenergies E_0 (in GeV) for various baryon states (the results obtained from the semiclassical and from the variational solution virtually coincide)

Baryon	m_1	m_2	m_3	E_0
(qqq)	0.446	0.446	0.446	1.438
(qqs)	0.451	0.451	0.485	1.414
(qss)	0.457	0.490	0.490	1.392
(sss)	0.495	0.495	0.495	1.370
(qqc)	0.519	0.519	1.502	1.176
(qsc)	0.522	0.555	1.505	1.157
(ssc)	0.589	0.589	1.507	1.138
(qqb)	0.564	0.564	4.836	1.057
(qsb)	0.567	0.601	4.837	1.038
(ssb)	0.604	0.604	4.838	1.019
(qcc)	0.569	1.555	1.555	0.926
(scc)	0.604	1.557	1.557	0.908
(qcb)	0.606	1.616	4.866	0.783
(scb)	0.642	1.618	4.867	0.765
(qbb)	0.636	4.931	4.931	0.582
(sbb)	0.673	4.931	4.931	0.565

Table 2. Dynamical quark masses for the ground-state (qc), (sc), (qb), and (sb) mesons [20] and for the corresponding ground-state baryons

State	m_q	m_s	m_c	m_b
(qc)	0.529		1.497	
(sc)		0.569	1.501	
(qqc)	0.519		1.502	
(qsc)	0.522	0.555	1.505	
(qb)	0.619			4.84
(sb)		0.658		4.842
(qqb)	0.564			4.836
(qsb)	0.567	0.601		4.838

0.009 GeV, $m_s^{(0)} = 0.17$ GeV, $m_c^{(0)} = 1.4$ GeV, and $m_b^{(0)} = 4.8$ GeV.

We solve Eq. (9) using both semiclassical and variational solutions. The first approach is based on the well-known fact that the interplay between the centrifugal term and the confining potential produces a minimum of the effective potential specific to the three-body problem. The numerical solution to Eq. (9) for the ground-state eigenenergy can be reproduced at a percent level of accuracy by using the parabolic approximation for the effective potential [21, 22]. This approximation provides an analytic expression for the eigenenergy. The potential $\tilde{U}(x) = U(x) + 15/8x^2$ has the minimum at the point $x = x_0$ that is defined by the condition $\tilde{U}'(x_0) = 0$; that is,

$$\frac{b}{\sqrt{\mu}}x_0^3 + (a\sqrt{\mu})x_0 - 15/4 = 0. \qquad (11)$$

Expanding $\tilde{U}(x)$ in the vicinity of $x = x_0$, one obtains

$$\tilde{U}(x) \approx \tilde{U}(x_0) + \frac{1}{2}\tilde{U}''(x_0)(x - x_0)^2,$$

which is the potential of a harmonic oscillator with frequency $\omega = \sqrt{\tilde{U}''(x_0)}$. Therefore, the energy eigenvalue is

$$E_0 \approx \tilde{U}(x_0) + \frac{1}{2}\omega. \qquad (12)$$

Table 1 presents the dynamical masses m_i and the ground-state eigenvalues E_0 for various baryons according to the calculations based on the procedure described above. Our values of the light-quark mass m_q agree qualitatively with the results obtained in [20] from the analysis of the heavy–light meson ground states, but they are about 60 MeV higher than those of [15, 17]. This difference is due to the different treatment of the Coulomb and spin–spin interactions. In [15], neither interaction was included and the light-quark mass was calculated from a fit to the mass of $\Delta(1232)$, where the Coulomb-like potential and the spin–spin interaction seem to balance each other. In [17], the smeared spin–spin interaction for the light quarks was included into Eq. (2) defining the dynamical mass of the light quark. In our calculation, as in [20], we include the Coulomb-like term, but we neglect the spin–spin interaction.

There is no good theoretical reason for the dynamical quark masses to take identical values in different mesons and baryons. From the results given in Table 1, we conclude that the dynamical masses of the light quarks (u, d, or s) increased by about 100–150 MeV upon going over from light to heavy baryons. For the heavy quarks (c and b), the variation in the values of their dynamical masses is marginal. In Table 2, we compare the quark masses in the Λ_Q and Ξ_Q baryons with those calculated in [20] in the D and B mesons. One observes that the masses of the light quarks in baryons are slightly smaller than those in the mesons. Small variations in the values of m_c and m_b are within the accuracy of our calculations.

Table 3. R_{ijk} in units of GeV^3 and $\bar{r}_{ij} = \sqrt{\langle \boldsymbol{r}_{ij}^2 \rangle}$ in units of fm (the results were obtained from the trial functions (13) with the variational parameters p_0 given in units of $\mathrm{GeV}^{1/2}$ in the first column; the results for light baryons are presented for the sake of completeness)

Baryon	p_0	R_{123}	R_{231}	R_{312}	$\bar{r}_{12}$	$\bar{r}_{23}$	$\bar{r}_{31}$
(qqq)	0.472	0.00564	0.00564	0.00564	0.777	0.777	0.777
(qqs)	0.470	0.00567	0.00598	0.00598	0.775	0.762	0.762
(qss)	0.469	0.00600	0.00633	0.00600	0.760	0.747	0.760
(sss)	0.467	0.00636	0.00636	0.00636	0.746	0.746	0.746
(qqc)	0.454	0.00626	0.0113	0.0113	0.750	0.615	0.615
(qsc)	0.452	0.00656	0.0121	0.0113	0.738	0.601	0.615
(ssc)	0.451	0.00688	0.0121	0.0121	0.727	0.602	0.602
(qqb)	0.447	0.00681	0.0163	0.0163	0.729	0.545	0.545
(qsb)	0.446	0.00711	0.0176	0.0163	0.719	0.531	0.545
(ssb)	0.445	0.00742	0.0176	0.0176	0.708	0.531	0.531
(qcc)	0.439	0.0116	0.0296	0.0116	0.611	0.447	0.611
(scc)	0.438	0.0123	0.0294	0.0123	0.599	0.448	0.599
(qcb)	0.436	0.0123	0.0562	0.0166	0.599	0.361	0.541
(scb)	0.435	0.0130	0.0559	0.0178	0.587	0.361	0.529
(qbb)	0.438	0.0181	0.165	0.0181	0.527	0.252	0.527
(sbb)	0.437	0.0194	0.165	0.0194	0.515	0.252	0.515

5. CORRELATION FUNCTIONS FOR BARYONS

For many applications, one needs the quantities $\langle\psi|\delta^{(3)}(\boldsymbol{r}_j - \boldsymbol{r}_i)|\psi\rangle$. To estimate effects associated with the baryon wave function, we solve Eq. (9) by the variational method. We introduce a simple variational ansatz for $\chi(x)$,

$$\chi(x) = 2\sqrt{2}p^3 x^{5/2} e^{-p^2x^2}, \tag{13}$$

where p is the variational parameter, and the numerical factor is chosen in such a way that $\int \chi^2(x)dx = 1$. The trial three-quark Hamiltonian admits explicit solutions for the energy, the wave function, and the density matrix; that is,

$$E_0 \approx \min_p E(p), \tag{14}$$

where

$$E(p) = \langle\chi|H|\chi\rangle = 3p^2 - (a\sqrt{\mu})\frac{3}{4}\sqrt{\frac{\pi}{2}}p \tag{15}$$
$$+ (b/\sqrt{\mu})\frac{15}{16}\sqrt{\frac{\pi}{2}}p^{-1}.$$

The density matrix (correlation function) $f_{ijk}(\boldsymbol{r}_{ij})$ in a baryon $\{ijk\}$ is defined as

$$f_{ijk}(\boldsymbol{r}_{ij}) = \alpha_{ij}^3 \int |\psi(\alpha_{ij}\boldsymbol{r}_{ij}, \boldsymbol{\lambda}_{ij})|^2 d\boldsymbol{\lambda}_{ij}, \tag{16}$$

so that

$$\int f_{ijk}(\boldsymbol{r}_{ij})d\boldsymbol{r}_{ij} \tag{17}$$
$$= \iint |\psi(\boldsymbol{\rho}_{ij}, \boldsymbol{\lambda}_{ij})|^2 d\boldsymbol{\lambda}_{ij} d^3\boldsymbol{\rho}_{ij} = 1.$$

For the trial function (13), $f_{ijk}(\boldsymbol{r}_{ij})$ can be evaluated explicitly. The result is

$$f_{ijk}(\boldsymbol{r}_{ij}) = \left(\frac{\xi_{ij}}{\pi}\right)^{3/2} e^{-\xi_{ij}|\boldsymbol{r}_{ij}|^2}, \tag{18}$$

where

$$\xi_{ij} = 2p_0^2\mu_{ij}. \tag{19}$$

Here, μ_{ij} is the reduced mass of the quarks i and j and p_0 must be found from the condition

$$\left.\frac{dE}{dp}\right|_{p=p_0} = 0.$$

Table 4. Ratios of the squares of the wave functions determining the probability of finding a light quark at the location of the heavy quark inside a heavy baryon and the corresponding meson (the meson wave functions are taken from [20])

R_{ucd}/R_{uc}	R_{scu}/R_{sc}	$R_{ubd}/R_{\bar{b}d}$	R_{sbu}/R_{sb}
0.436	0.405	0.373	0.340

Table 5. Short-range correlation coefficients R_{ijk} (shown parenthetically are the corresponding quantities calculated by using the power-law potential from [7]; in brackets, we present the correlation coefficients calculated on the basis of the nonrelativistic model featuring the Buchmüller–Tye potential)

State	R_{123}	R_{231}	R_{312}
(ccq)	0.030 (0.039) [0.022]	0.012 (0.009)	0.012 (0.009)
(ccs)	0.030 (0.042) [0.022]	0.012 (0.019)	0.012 (0.019)
(bbq)	0.165 (0.152) [0.144]	0.018 (0.012)	0.018 (0.012)
(bbs)	0.165 (0.162) [0.144]	0.019 (0.028)	0.019 (0.028)
(bcq)	0.056 (0.065) [0.042]	0.012 (0.010)	0.017 (0.011)
(bcs)	0.056 (0.071) [0.042]	0.013 (0.021)	0.018 (0.025)

The expectation values $f_{ijk}(\boldsymbol{r}_{ij})$ depend on the third or spectator quark through the three-quark wave function.

Let us define the quantities

$$R_{ijk} = f_{ijk}(0) = \left(\frac{\xi_{ij}}{\pi}\right)^{3/2}. \qquad (20)$$

The corresponding quantity for a meson is denoted by R_{ij}. The results of the variational calculations are given in Table 3, where, for each baryon, we show the variational parameters p_0, the quantities R_{ijk} (in units of GeV^3), and the average distances $\bar{r}_{ij} = \sqrt{\langle \boldsymbol{r}_{ij}^2 \rangle}$ (in fm). The variational estimates of E_0 and quark dynamical masses do not differ from those in Table 1.

Comparing the results given in Table 3 with those from [20], we obtain (see Table 4)[4)]

$$R_{ijk} < \frac{1}{2} R_{ij}, \qquad (21)$$

$$R_{ijk} \gtrsim R_{ijl} \quad \text{if} \quad m_k \le m_l. \qquad (22)$$

Note, however, that, if i and j are the light quarks and if the quarks k and l are heavy, then $R_{ijk} \approx R_{ijl}$ (e.g., $R_{qqc} \approx R_{qqb}$), which is in agreement with the limit of heavy-quark effective theory.

Our estimates for the ratios R_{ijk}/R_{ij} agree with the results obtained by using the nonrelativistic quark model, the bag model [24–26], or QCD sum rules [27], which are typically in the range 0.1–0.5. On the other hand, our result for Λ_b disagrees with that obtained by Rosner [28], who estimated the heavy–light diquark density at zero separation in Λ_b from the ratio of hyperfine splittings between the Σ_b and Σ_b^* baryons and the B and B^* mesons and found $R_{qbu}/R_{\bar{b}d} \sim 0.9 \pm 0.1$ if the baryon splitting is taken to be $m^2_{\Sigma_b^*} - m^2_{\Sigma_b} \sim m^2_{\Sigma_c^*} - m^2_{\Sigma_c} = (0.384 \pm 0.035)\ \mathrm{GeV}^2$ or even $R_{ubd}/R_{\bar{b}d} \sim 1.8 \pm 0.5$ if the surprisingly small DELPHI result $m_{\Sigma_b^*} - m_{\Sigma_b} = (56 \pm 16)$ MeV, which has not yet been confirmed, is used.

From the results of Table 3, it follows that the correlation between two quarks depends on the third one. It should also be noted that the wave function calculated in HRA shows marginal diquark clustering in the doubly heavy baryons. This is basically a kinematical effect related to the fact that, in the HRA, the difference between the different $\bar{r}_{ij}$ in a baryon is due to the factor $\sqrt{1/\mu_{ij}}$, which varies between $\sqrt{2/m_i}$ for $m_i = m_j$ and $\sqrt{1/m_i}$ for $m_i \ll m_j$.

In Table 5, we compare the short-range correlation coefficients in doubly heavy baryons with those calculated in [7] by using the pairwise quark interaction represented by a power-law potential and in [9] by using the nonrelativistic model involving the Buchmüller–Tye potential.

6. MASSES OF DOUBLY HEAVY BARYONS

To calculate hadron masses we, as in [15], first renormalize the string potential as

$$V_{\text{string}} \to V_{\text{string}} + \sum_i C_i, \qquad (23)$$

where the constants C_i take into account the residual self-energy (RSE) of quarks. In principle, these constants can be expressed in terms of two scalar functions entering into covariant expansion of the bilocal cumulants of gluonic fields in the QCD vacuum [14, 15]. In the present study, we treat them phenomenologically. To find C_i in (23), we assume, first, that the spin splittings of hadrons with a given quark content arise from the color-magnetic interaction in QCD. Indeed, for ground-state hadrons, the hadron wave functions have no orbital angular momentum; therefore, tensor and spin–orbit forces do not contribute.

[4)] Inequalities (21) and (22) were first suggested in [23] from the observed mass splitting in mesons and baryons.

Table 6. Masses of baryons containing two heavy quarks

State	Present study	[7][(a)]	[8][(b)]	[10][(c)]	[11]	[12][(d)]
$\Xi\{qcc\}$	3.69	3.70	3.71	3.66	3.61	3.48
$\Omega\{scc\}$	3.86	3.80	3.76	3.74	3.71	3.58
$\Xi\{qcb\}$	6.96	6.99	6.95	7.04		6.82
$\Omega\{scb\}$	7.13	7.07	7.05	7.09		6.92
$\Xi\{qbb\}$	10.16	10.24	10.23	10.24		10.09
$\Omega\{sbb\}$	10.34	10.30	10.32	10.37		10.19

[(a)] The additive nonrelativistic quark model with a power-law potential.
[(b)] Relativistic quasipotential quark model.
[(c)] The Feynman–Hellmann theorem.
[(d)] Approximation of doubly heavy diquark.

The second assumption is that the color-magnetic interaction can be treated perturbatively [29, 30]:

$$\Delta E_{\rm spin} = \frac{16\pi\alpha_s}{9}\sum_{i<j}\frac{\mathbf{s}_i\cdot\mathbf{s}_j}{m_i m_j}R_{ijk}. \qquad (24)$$

Because the color-magnetic interaction between two quarks is in inverse proportion to the product of their masses, the perturbative approximation is improved with increasing quark mass. However, this approximation may not be good for baryons containing light quarks.[5)] In what follows, we adjust the RSE constants C_i to reproduce the center of gravity for baryons with a given flavor. To this end, we consider the spin-averaged masses, such as

$$\frac{M_N + M_\Delta}{2} = 1.085\ \text{GeV}, \qquad (25)$$
$$\frac{M_\Lambda + M_\Sigma + 2M_{\Sigma^*}}{4} = 1.267\ \text{GeV},$$

and analogous combinations for qqc and qqb states. Then, we obtain

$$C_q = 0.34\ \text{GeV}, \quad C_s = 0.19\ \text{GeV}, \qquad (26)$$
$$C_c \sim C_b \sim 0.$$

We keep these parameters fixed to calculate the masses given in Table 6, namely, the spin-averaged masses (computed without the spin–spin term) of the lowest doubly heavy baryons. Our results are very similar to those obtained in [7] by using the pairwise power-law potential.

[5)]Note that the $1/m_i m_j$ dependence in Eq. (24), if treated literally in the EH method, results in a collapse both in the pseudoscalar $q\bar{q}$ channel and in the proton. That may be a signal of the Nambu–Goldstone phenomenon.

7. CONCLUSION

We have employed the general formalism for baryons that is based on nonperturbative QCD and where the only inputs are the string tension σ, the strong coupling constant α_s, and two additive constants C_q and C_s (residual self-energies of light quarks). We have presented some piloting calculations of the dynamical quark masses for various baryons (see Table 1). The masses have been computed solely in terms of σ and α_s and depend on a baryon.

The second important point of our investigation is the calculation of the correlation functions for baryons. They are given, among other things, in Table 3. We have also calculated the spin-averaged masses of baryons containing two heavy quarks. One can see from Table 6 that our predictions are especially close to those obtained in [7] by using a version of the power-law potential adjusted to fit ground-state baryons.

An evaluation of spin–spin interactions requires the inclusion of the $K = 2$ hyperspherical components and/or a more sophisticated treatment of the color-magnetic interaction. We will present these calculations in a forthcoming publication.

ACKNOWLEDGMENTS

We are grateful to Yu.S. Kalashnikova and Yu.A. Simonov for stimulating discussions. We also thank K.A. Ter-Martirosian for his interest in this work.

This work was supported in part by Russian Foundation for Basic Research (project nos. 00-02-16363 and 00-15-96786).

APPENDIX

Let us consider three quarks of arbitrary masses m_i, $i = 1, 2, 3$, with coordinates $\boldsymbol{r}_i$. The problem is conveniently treated by using the Jacobi coordinates $\boldsymbol{\rho}_{ij}$ and $\boldsymbol{\lambda}_{ij}$,

$$\boldsymbol{\rho}_{ij} = \alpha_{ij}(\boldsymbol{r}_i - \boldsymbol{r}_j), \qquad (A.1)$$
$$\boldsymbol{\lambda}_{ij} = \beta_{ij}\left(\frac{m_i\boldsymbol{r}_i + m_j\boldsymbol{r}_j}{m_i + m_j} - \boldsymbol{r}_k\right),$$

where

$$\alpha_{ij} = \sqrt{\frac{\mu_{ij}}{\mu}}, \quad \beta_{ij} = \sqrt{\frac{\mu_{ij,k}}{\mu}}. \qquad (A.2)$$

Here, μ_{ij} and $\mu_{ij,k}$ are the reduced masses:

$$\mu_{ij} = \frac{m_i m_j}{m_i + m_j}, \quad \mu_{ij,k} = \frac{(m_i + m_j)m_k}{m_i + m_j + m_k}. \qquad (A.3)$$

Together with the center-of-mass coordinate $\mathbf{R}_{\text{c.m.}}$, the Jacobi coordinates determine completely the position of the system. The Jacobian of the transformation for the differential volume elements is equal to unity; i.e.,

$$d\boldsymbol{\rho}_{12}d\boldsymbol{\lambda}_{12} = d\boldsymbol{\rho}_{32}d\boldsymbol{\lambda}_{32} = d\boldsymbol{\rho}_{13}d\boldsymbol{\lambda}_{13}. \quad (A.4)$$

The inverse transformations for the relative coordinates $\boldsymbol{r}_{ij} = \boldsymbol{r}_i - \boldsymbol{r}_j$ and $\boldsymbol{r}_k - \mathbf{R}_{\text{c.m.}}$ are

$$\boldsymbol{r}_{ij} = \frac{1}{\alpha_{ij}}\boldsymbol{\rho}_{ij}, \quad (A.5)$$

$$\boldsymbol{r}_k - \mathbf{R}_{\text{c.m.}} = -\sqrt{\frac{\mu(m_i+m_j)}{m_k(m_1+m_2+m_3)}}\boldsymbol{\lambda}_{ij}.$$

The hyperradius R^2 is defined as $R^2 = \boldsymbol{\rho}_{ij}^2 + \boldsymbol{\lambda}_{ij}^2$ and is independent of the order of quark numbering:

$$R^2 = \boldsymbol{\rho}_{12}^2 + \boldsymbol{\lambda}_{12}^2 = \boldsymbol{\rho}_{32}^2 + \boldsymbol{\lambda}_{32}^2 = \boldsymbol{\rho}_{13}^2 + \boldsymbol{\lambda}_{13}^2. \quad (A.6)$$

Written in terms of $\boldsymbol{r}_{ij}$, Eq. (A.6) reads

$$R^2 = \sum_{i<j}\frac{m_i m_j}{\mu(m_1+m_2+m_3)}\boldsymbol{r}_{ij}^2. \quad (A.7)$$

In the center-of-mass frame ($\mathbf{R}_{\text{c.m.}} = 0$), the invariant-kinetic-energy operator (3) is written in terms of the Jacobi coordinates (A.1) as

$$H_0 = -\frac{1}{2\mu}\left(\frac{\partial^2}{\partial\boldsymbol{\rho}^2} + \frac{\partial^2}{\partial\boldsymbol{\lambda}^2}\right) \quad (A.8)$$

$$= -\frac{1}{2\mu}\left(\frac{\partial^2}{\partial R^2} + \frac{5}{R}\frac{\partial}{\partial R} + \frac{K^2(\Omega)}{R^2}\right),$$

where $K^2(\Omega)$ is angular-momentum operator, whose eigenfunctions (hyperspherical harmonics) are

$$K^2(\Omega)Y_{[K]} = -K(K+4)Y_{[K]}, \quad (A.9)$$

with K being the grand-orbital momentum. In terms of $Y_{[K]}$, the wave function $\psi(\boldsymbol{\rho},\boldsymbol{\lambda})$ can be written symbolically as

$$\psi(\boldsymbol{\rho},\boldsymbol{\lambda}) = \sum_K \psi_K(R)Y_{[K]}(\Omega).$$

In the HRA, we have $K = 0$ and $\psi = \psi(R)$. Note that the centrifugal potential in the Schrödinger equation for the radial function $\psi_K(R)$ with a given K,

$$\frac{(K+2)^2 - 1/4}{R^2},$$

is not zero even for $K = 0$. For the reduced function $\chi(R) = R^{5/2}\psi(R)$, one obtains, after averaging the interaction over the six-dimensional sphere, Eq. (6) with

$$W(R) = \langle V(\boldsymbol{\rho},\boldsymbol{\lambda})\rangle = \int (V_{\text{C}} + V_{\text{string}})\frac{d\Omega}{\pi^3}. \quad (A.10)$$

One can easily see that the definition of $\langle V(\boldsymbol{\rho},\boldsymbol{\lambda})\rangle$ does not depend on the order of quark numbering.

In terms of the Jacobi coordinates, the Coulomb and string potentials read

$$V_{\text{C}} = -\frac{2}{3}\alpha_s\sum_{i<j}\frac{\alpha_{ij}}{|\boldsymbol{\rho}_{ij}|}, \quad (A.11)$$

$$V_{\text{string}} = \sigma\sum_{i<j}\gamma_{ij}|\boldsymbol{\lambda}_{ij}|, \quad (A.12)$$

where

$$\gamma_{ij} = \sqrt{\frac{\mu(m_i+m_j)}{m_k(m_1+m_2+m_3)}}. \quad (A.13)$$

Using the relations [20]

$$\left\langle\frac{1}{|\boldsymbol{\rho}_{ij}|}\right\rangle = \frac{16}{3\pi}\frac{1}{R}, \quad \langle|\boldsymbol{\lambda}_{ij}|\rangle = \frac{32}{15\pi}R,$$

which are valid for any pair (ij), one obtains Eqs. (8).

REFERENCES

1. CDF Collab. (F. Abe *et al.*), Phys. Rev. Lett. **81**, 2432 (1998).
2. S. Capstick and N. Isgur, Phys. Rev. D **34**, 2809 (1986).
3. M. J. Savage and M. Wise, Phys. Lett. B **248**, 177 (1990).
4. P. L. White and M. J. Savage, Phys. Lett. B **271**, 410 (1991).
5. E. Bagan, M. Chabab, and S. Narison, Phys. Lett. B **306**, 350 (1993).
6. A. F. Falk, M. Luke, and M. J. Savage, Phys. Rev. D **49**, 555 (1994).
7. E. Bagan, H. G. Dosch, P. Godzinsky, *et al.*, Z. Phys. C **64**, 57 (1994).
8. D. Ebert, R. N. Faustov, V. O. Galkin, *et al.*, Z. Phys. C **76**, 111 (1997).
9. S. S. Gershtein, V. V. Kiselev, A. K. Likhoded, and A. I. Onishchenko, Mod. Phys. Lett. A **14**, 135 (1999); Heavy Ion Phys. **9**, 133 (1999).
10. R. Roncaglia, D. B. Lichtenberg, and E. Predazzi, Phys. Rev. D **51**, 1248 (1995).
11. J. G. Körner, M. Krämer, and D. Pirjol, Prog. Part. Nucl. Phys. **33**, 787 (1994).
12. A. K. Likhoded and A. I. Onishchenko, hep-ph/9912425.
13. Yu. A. Simonov, Nucl. Phys. B **307**, 512 (1988); Phys. Lett. B **226**, 151 (1989); **228**, 413 (1989).
14. Yu. A. Simonov, Nucl. Phys. B **324**, 67 (1989).
15. M. Fabre de la Ripelle and Yu. A. Simonov, Ann. Phys. (N.Y.) **212**, 235 (1991).
16. A. Yu. Dubin, A. B. Kaidalov, and Yu. A. Simonov, Phys. Lett. B **323**, 41 (1994).
17. B. O. Kerbikov and Yu. A. Simonov, hep-ph/0001243.
18. Yu. S. Kalashnikova, A. V. Nefediev, and Yu. A. Simonov, hep-ph/0103274.

19. Yu. A. Simonov, Yad. Fiz. **3**, 630 (1966) [Sov. J. Nucl. Phys. **3**, 461 (1966)]; A. M. Badalyan and Yu. A. Simonov, Yad. Fiz. **3**, 1032 (1966) [Sov. J. Nucl. Phys. **3**, 755 (1966)]; F. Calogero and Yu. A. Simonov, Phys. Rev. **183**, 869 (1969).
20. Yu. S. Kalashnikova and A. Nefediev, Phys. Lett. B **492**, 91 (2000).
21. Yu. S. Kalashnikova, I. M. Narodetskiĭ, and Yu. A. Simonov, Yad. Fiz. **46**, 1181 (1987) [Sov. J. Nucl. Phys. **46**, 689 (1987)].
22. B. O. Kerbikov, M. I. Polikarpov, and L. S. Shevchenko, Nucl. Phys. B **331**, 19 (1990).
23. D. B. Lichtenberg, Phys. Rev. D **54**, 5887 (1996).
24. M. B. Voloshin and M. A. Shifman, Yad. Fiz. **41**, 187 (1985) [Sov. J. Nucl. Phys. **41**, 120 (1985)]; Zh. Éksp. Teor. Fiz. **91**, 1180 (1986) [Sov. Phys. JETP **64**, 698 (1986)].
25. B. Guberina, S. Nussinov, R. Peccei, and R. Rückl, Phys. Lett. B **89B**, 111 (1979); N. Bilić, B. Guberina, and J. Trampetić, Nucl. Phys. B **248**, 261 (1984); B. Guberina, R. Rückl, and J. Trampetić, Z. Phys. C **33**, 297 (1986).
26. I. Bigi *et al.*, in *B-decays,* Ed. by S. Stone (World Sci., Singapore, 1994, 2nd ed.), p. 134; I. Bigi, hep-ph/9508408.
27. P. Conangelo and F. De Fazio, Phys. Lett. B **387**, 371 (1996).
28. J. L. Rosner, Phys. Lett. B **379**, 267 (1996).
29. A. De Rújula, H. Georgi, and S. L. Glashow, Phys. Rev. D **12**, 147 (1975).
30. W. Kwong, J. L. Rosner, and C. Quigg, Annu. Rev. Nucl. Part. Sci. **37**, 325 (1987).

Physics of Atomic Nuclei, Vol. 65, No. 5, 2002, pp. 925–928. Translated from Yadernaya Fizika, Vol. 65, No. 5, 2002, pp. 956–960.

ELEMENTARY PARTICLES AND FIELDS
Theory

Effect of Hadronization on the Form of Correlation Moments for Instanton Processes and Possibility of Discovering Them Experimentally

V. I. Kashkan*, V. I. Kuvshinov, and R. G. Shulyakovsky*****

Institute of Physics, National Academy of Sciences of Belarus, Minsk, Belarus

Received February 22, 2001; in final form, June 29, 2001

Abstract—The possibility of discovering QCD instantons in deep-inelastic scattering by analyzing correlations in final states is studied. The correlation moments F_q and H_q for instanton processes are calculated at the parton and at the hadron level. Hadronization is taken into account by the Monte Carlo method. The moments for instanton and for usual processes are found to behave differently, which can be used to identify experimentally instantons. © *2002 MAIK "Nauka/Interperiodica".*

Within four-dimensional non-Abelian gauge theories, degeneracy of the vacuum state at the classical level is one of the most important theoretical predictions [1]. Various minima of the potential energy correspond to Chern–Simons integral numbers in the gauge $A_0^a = 0$:

$$N_{\rm cs} = \frac{g^2}{16\pi^2} \times \int d^3x\, \varepsilon_{ijk}\Big(A_i^a \partial_j A_k^a + \frac{g}{3}\varepsilon^{abc} A_i^a A_j^b A_k^c\Big). \quad (1)$$

Here, g is a coupling constant and A_i^a are gauge fields (the superscripts and the subscripts contain, respectively, the group and the Lorentz indices). The classical vacua are separated by potential barriers. Instantons, which are topologically nontrivial finite-action solutions to the classical field equations in Euclidian space, can describe subbarrier tunneling [2]. Allowances made for tunnel transitions (or instantons) lead to new implications. By way of example, we indicate that, in the Standard Model of electroweak interactions, instantons induce processes in which the baryon and lepton numbers [3] are not conserved and which can be responsible for matter–antimatter asymmetry in the visible part of the Universe [4]. Chiral-symmetry breaking is a similar effect in QCD. It is worth noting that such phenomena are impossible within usual perturbation theory, which is constructed with respect to the classical vacuum, where $N_{\rm cs} = 0$, and which completely ignores tunneling. Therefore, an experimental corroboration of the existence of instantons would be of importance for the physics of fundamental interactions.

It is well known that the cross section for a spontaneous vacuum–vacuum instanton transition is very small [3]:

$$\sigma^{\rm inst}_{|{\rm vac}\rangle\to|{\rm vac}\rangle} \sim \exp\left(-\frac{16\pi^2}{g^2}\right). \quad (2)$$

This quantity is about 10^{-160} for electroweak interactions and about 10^{-10} for QCD. This rules out the possibility of experimentally observing the effect.

It was shown in the early 1990s [5] that the probability of instanton transitions can increase significantly in collisions of particles whose total energy $\sqrt{s}$ is high; that is,

$$\sigma^{\rm inst}(\varepsilon) \sim \exp\left(\frac{16\pi^2}{g^2}F(\varepsilon)\right), \qquad \varepsilon = \frac{\sqrt{s}}{E_{\rm sp}}, \quad (3)$$
$$F(\varepsilon) = -1 + \frac{9}{8}\varepsilon^{4/3} - \frac{9}{16}\varepsilon^2 + \ldots,$$

where $\varepsilon < 1$, $E_{\rm sp}$ is the so-called sphaleron energy (the height of the energy barrier between the vacua), and $F(\varepsilon)$ is the "Holy Grail" function.

In 1993, Balitsky and Braun [6] showed that QCD instantons can appear in deep-inelastic scattering as a new channel (Fig. 1) and actually be identified at the HERA accelerator (DESY, Hamburg). In this case, it is convenient to use, in addition to the ordinary kinematical variables $Q^2 = -q^2$ and $x = Q^2/(2Pq)$, the quantities $Q'^2 = -q'^2$ and $x' = Q'^2/(2pq')$, which characterize the instanton subprocess (a quark–gluon collision producing secondary partons).

At the parton level, the instanton process is characterized by the following specific features:

*e-mail: kashkan@dragon.bas-net.by
**e-mail: kuvshino@dragon.bas-net.by
***e-mail: shul@dragon.bas-net.by

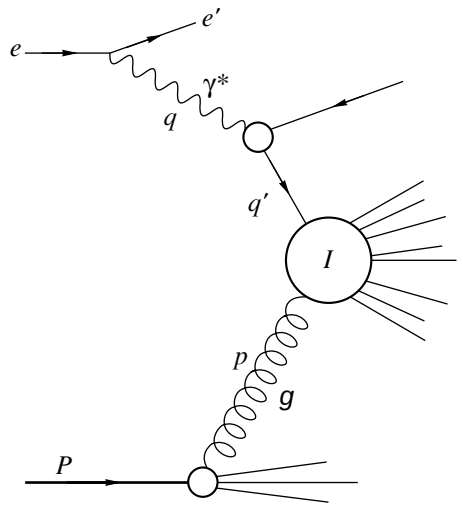

Fig. 1. Instanton channel of deep-inelastic scattering. The following notation is used in the figure: e and e' are, respectively, the initial and the final electron; P, q, q', and p are the 4-momenta of the initial proton, the virtual photon γ^*, the quark, and the gluon g, respectively; and the letter I enclosed by a circle stands for the process of instanton formation in a quark–gluon collision.

(i) a high multiplicity of secondary partons (about ten [6, 7]); (ii) the isotropic "decay" of an instanton in its rest frame [7]; (iii) the appearance of at least one quark and one antiquark of each of the three flavors u, d, and s in the chiral limit [3] in any instanton event; and (iv) the presence of specific gluon correlations [8, 9].

There are also some signatures of instanton-induced processes at the hadron level [7, 10], which include special features of the final-particle spectra, a high transverse momentum, and behavior of the structure function $F_2(x, Q^2)$.

According to theoretical estimates, the relative fraction of instanton events at HERA for $x \geq 10^{-3}$, $x' \geq 0.35$, and $Q' \geq 8$ GeV [7, 10] can amount to about 1%. The number of instanton events accumulated over 1996 and 1997 is $N = \sigma^{\text{inst}}_{\text{HERA}} L \sim O(10^4)$, where the integrated luminosity is $L \approx 30$ pb^{-1} and the total cross section for instanton processes is $\sigma^{\text{inst}}_{\text{HERA}} \approx 130$ pb (at $\Lambda_{\text{QCD}} = 234$ MeV).

Despite this, the question of whether it is possible to identify instantons at HERA is open, in particular, owing to the uncertainty in $\Lambda_{\text{QCD}} = 234 \pm 65$ MeV; this uncertainty leads to the uncertainty in the cross section $\sigma^{\text{inst}}_{\text{HERA}} \sim 0$–300 pb.

In this study, we propose employing the normalized factorial moments and the moments H_q as additional criteria for QCD instantons at HERA, along with already known criteria.

We recall that the well-known definitions of the moments are [11]

$$F_q = \frac{1}{\bar{n}^q} \left.\frac{d^q Q(z)}{dz^q}\right|_{z=1}, \tag{4}$$

$$K_q = \frac{1}{\bar{n}^q} \left.\frac{d^q \ln Q(z)}{dz^q}\right|_{z=1}, \quad Q(z) = \sum_{n=1}^{\infty} P_n z^n,$$

$$\bar{n} = \sum_{n=1}^{\infty} n P_n, \quad H_q = \frac{K_q}{F_q},$$

where $Q(z)$ is the generation function, $\bar{n}$ is the mean multiplicity of secondaries, and P_n is the multiplicity distribution.

The distribution with respect to the number of gluons in instanton processes is given by

$$P_n^{(g)} = \frac{\sigma_{\text{tot}}^{-1}}{n!} \int d^4k_1 \ldots d^4k_n \left|T(k_1, \ldots, k_n)\right|^2, \tag{5}$$

where σ_{tot} is the total cross section and $T(k_1, \ldots, k_n)$ is the amplitude for the production of gluons with 4-momenta $k_1, \ldots, k_n$. The amplitude $T(k_1, \ldots, k_n)$ can be calculated by applying the Lehmann–Symanzik–Zimmermann procedure to the Euclidian n-particle Green's function. In the semiclassical approximation, this Green's function takes the form of the path integral

$$\int DA e^{-S^e[A]} A^{I\,a_1}_{\mu_1}(x_1) \ldots A^{I\,a_n}_{\mu_n}(x_n), \tag{6}$$

where integration is performed only over field configurations that link nonequivalent classical vacua, DA is the integration measure, $S^e[A]$ is the Euclidian QCD action functional, and $A^{I\,a}_{\mu}(x)$ are instanton solutions [2]. In the Gaussian approximation, the Green's function in (6) reduces to a known calculable integral. Factorization in (6) leads to the Poisson multiplicity distribution of gluons [7, 9]:

$$P_n^{(g)} = e^{-\bar{n}_g} \frac{\bar{n}_g^n}{n!}, \quad \bar{n}_g = \frac{16\pi^2}{g^2}\left(\frac{1-x'}{x'}\right)^2, \tag{7}$$

$$0.5 < x' < 1.$$

In the chiral limit, the distribution with a fixed multiplicity describes the quark multiplicity (only zero quark modes are taken into account in the instanton field) [3]; that is

$$P_n^{(q)} = \delta_{2n_f, n}, \tag{8}$$

where n_f is the number of flavors of quarks that can be considered to be massless (we assume that $m_u \approx m_d \approx m_s \approx 0$).

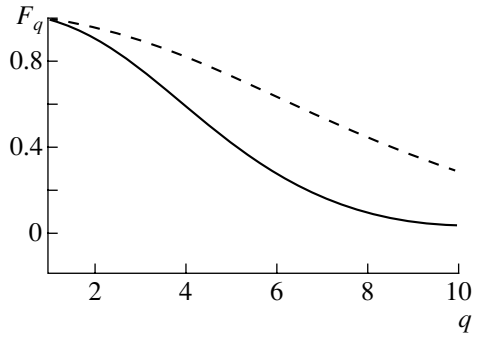

Fig. 2. Normalized factorial moments for instanton-induced parton processes at the mean gluon multiplicities of $\bar{n}_g =$ (solid curve) 2 and (dashed curve) 8. The moments in (4) are defined only for integral q (here and in the figures that follow, the points are connected by curves just to guide the eye).

Taking into account both the quark and the gluon multiplicity, we finally find, within the above approximations, that

$$P_n^{\text{part}} = \begin{cases} e^{-\bar{n}_g} \dfrac{\bar{n}_g^{n-2n_f}}{(n-2n_f)!} \text{ for} & n \geq 2n_f \\ 0 \text{ for} & n < 2n_f. \end{cases} \qquad (9)$$

The generating function for instanton processes at the parton level and the mean number of partons are [12]

$$Q^{\text{part}}(z) = \sum_{n=2n_f}^{\infty} e^{-\bar{n}_g} \frac{\bar{n}_g^{n-2n_f} z^n}{(n-2n_f)!} \qquad (10)$$
$$= z^{2n_f} e^{\bar{n}_g[z-1]}, \qquad \bar{n} = \bar{n}_g + 2n_f.$$

The factorial moments F_q calculated for instanton processes according to the definition in (4) with the generating function (10) decrease with increasing q, and satisfy the inequality $F_q < 1$ for $q = 2, 3, \ldots$ (see Fig. 2). At the same time, perturbative QCD predicts a strong increase in F_q with q, the resulting values satisfying the inequality $F_q > 1$ for $q = 2, 3, \ldots$ [11]. The moments H_q also behave very differently in instanton and in ordinary (perturbative) processes. The instanton distribution features a pronounced first minimum of H_q at $q = 2$ and oscillations (see Fig. 3). It is worth noting that, as was found earlier in [9], the inclusion of the first quantum correction to the gluon distribution in the instanton field also leads to the appearance of the first minimum of H_q at $q = 2$. In contrast to this, perturbative QCD predicts low-frequency oscillations, the first minimum occurring at q values between about 5 and 6 [11].

Let us now consider variations in the correlations for ordinary and for instanton processes upon taking

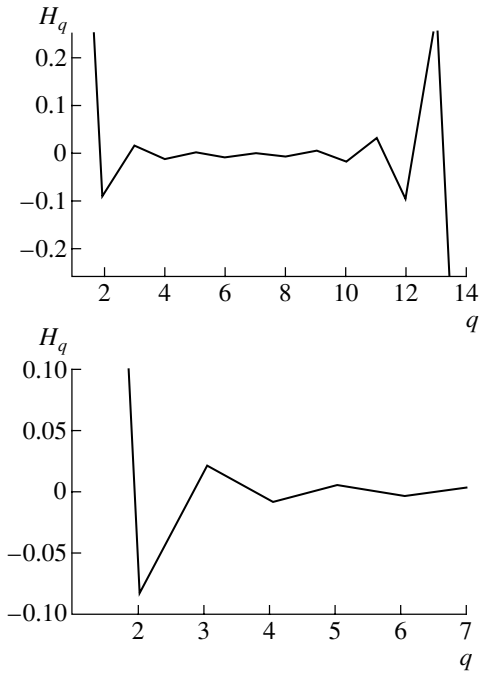

Fig. 3. Moments H_q of the instanton parton distributions ($\bar{n}_g = 2$).

into account hadronization. Usual channels of deep-inelastic scattering are characterized by a strong increase in F_q (see Fig. 4) and by an oscillating form of H_q with a pronounced minimum at q values of about 6 to 7 (see Fig. 5). It can easily be seen that hadronization does not lead to any significant qualitative changes in the behavior of the correlation moments for usual channels of deep-inelastic scattering. For the instanton channel, the effect of the hadronization stage is more significant: the moments F_q exhibit a slow increase (see Fig. 4), while the moments H_q oscillate with a lower frequency (see Fig. 5); however, the main qualitative properties of the moments do not change.

We used the QSDINS 2.0 package [10] to calculate the correlation moments for the instanton channels. In these calculations, we used the distribution in (9) as a starting point in this generator. For the hadronization model, we used JETSET [13] or HERWIG [14]. We found that the values of the moments for instanton processes are virtually independent of the choice of hadronization model. This confirms that our results are quite reliable. The moments for ordinary (one- and two-jet) deep-inelastic scattering at HERA were calculated by means of the HERWIG code.

Nontrivial hadron correlations in the instanton channels are associated with large numbers of soft quarks and gluons (about 10) produced upon the "decay" of instantons. The perturbative cascade

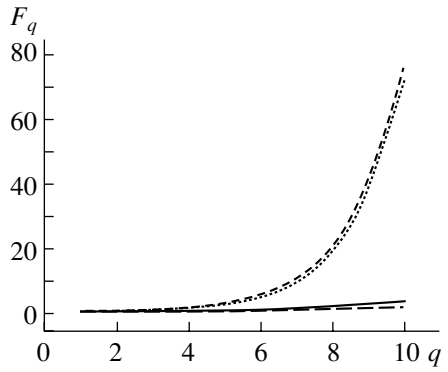

Fig. 4. Moments F_q for (short-dashed curve) one-jet, (dotted curve) two-jet, and (solid and long-dashed curves corresponding to the HERWIG and JETSET hadronization models, respectively) instanton channels of deep-inelastic scattering.

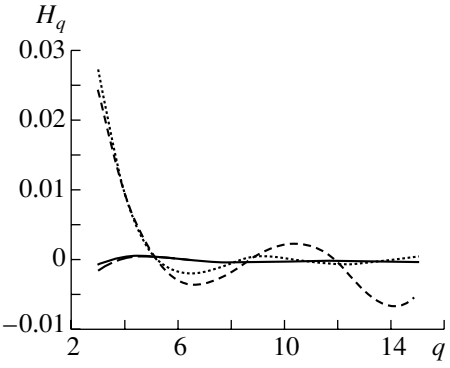

Fig. 5. As in Fig. 4, but for the moments H_q.

terminates very fast, so that it does not have time to distort significantly the initial parton-multiplicity distribution (9). The hadronization stage does not lead to significant variations in the behavior of moments (for example, Dremin *et al.* [11] showed that the moments H_q calculated on the basis of perturbative QCD describe experimental data satisfactorily even without invoking any model of hadronization). The contribution of the instanton subprocess can be mixed with the contribution of the initial-proton remnant, with the result that the moments for instanton processes are somewhat distorted. Despite this, the moments differ significantly from those for ordinary processes and can therefore be used to identify instanton processes experimentally.

It is worth noting that the cross sections for instanton processes, their structure functions, and other quantities used to identify instantons in [7, 10] have a significant uncertainty in the low-x' region. At the same time, the correlation moments proposed here as new identification criteria for QCD instantons depend only on the multiplicity distribution, which is determined primarily by a large fixed multiplicity of quarks in final states. The quark multiplicity is completely independent of x', which makes it possible to expect that our results are highly reliable in the entire region of x'. In view of this property, we can propose the following scenario for identifying QCD instantons at HERA: six criteria developed by Ringwald, Schrempp *et al.* [7] are used to select instanton events presumably, whereupon the moments F_q and H_q are calculated for them. Should the calculated moments agree with the theoretical predictions, this would furnish stronger evidence than previously that the instanton channel of deep-inelastic scattering exists.

REFERENCES

1. R. Jackiw and C. Rebbi, Phys. Rev. Lett. **37**, 172 (1976).
2. A. Belavin, A. Polyakov, A. Schwarz, and Yu. Tyupkin, Phys. Lett. B **59B**, 85 (1975).
3. G. 't Hooft, Phys. Rev. Lett. **37**, 8 (1976); Phys. Rev. D **14**, 3432 (1976).
4. A. D. Sakharov, Pis'ma Zh. Éksp. Teor. Fiz. **5**, 32 (1967) [JETP Lett. **5**, 24 (1967)].
5. A. Ringwald, Nucl. Phys. B **330**, 1 (1990); D. D'yakonov and V. Petrov, in *Proceedings of the XXVI Winter School of Leningrad Institute of Nuclear Physics "Nuclear and Elementary Particle Physics," Leningrad, 1991,* p. 8.
6. I. Balitsky and V. Braun, Phys. Lett. B **314**, 237 (1993); Phys. Rev. D **47**, 1879 (1993).
7. M. Gibbs, A. Ringwald, and F. Schrempp, in *Proceedings of the Workshop on Deep Inelastic Scattering and QCD, Paris, 1995,* Ed. by J.-F. Laporte and Y. Sirois, p. 341; hep-ph/9506392; S. Moch, A. Ringwald, and F. Schrempp, Nucl. Phys. B **507**, 134 (1997); A. Ringwald and F. Schrempp, Phys. Lett. B **438**, 217 (1998); **495**, 249 (1999); J. Phys. G **25**, 1297 (1999).
8. V. Kuvshinov and R. Shulyakovsky, Acta Phys. Pol. B **28**, 1629 (1997).
9. V. Kuvshinov and R. Shulyakovsky, Acta Phys. Pol. B **30**, 69 (1999).
10. T. Carli, J. Gerigk, A. Ringwald, and F. Schrempp, in *Proceedings of the Workshop on Monte Carlo Generators for HERA Physics,* Ed. by A. T. Doyle *et al.* (DESY, Hamburg, 1998), p. 329.
11. I. M. Dremin, E. De Wolf, and W. Kittel, Usp. Fiz. Nauk **163** (1), 3 (1993); I. Dremin, Phys. Lett. B **313**, 209 (1993); in *Proceedings of the 7th Workshop on Multiparticle Production "Correlations and Fluctuations," Nijmegen, 1996* (World Sci., Singapore, 1997), p. 313.
12. V. Kuvshinov and R. Shulyakovsky, Nonlinear Phenomenon in Complex Systems **2**, 8 (1999).
13. T. Sjostrand, Comput. Phys. Commun. **82**, 74 (1994).
14. G. Marchesini *et al.*, Comput. Phys. Commun. **67**, 465 (1992).

Translated by M. Kobrinsky

Physics of Atomic Nuclei, Vol. 65, No. 5, 2002, pp. 929–942. Translated from Yadernaya Fizika, Vol. 65, No. 5, 2002, pp. 961–973.

ELEMENTARY PARTICLES AND FIELDS
Theory

Quark Interaction with an Instanton Liquid

G. M. Zinovjev[1)], S. V. Molodtsov, and A. M. Snigirev[2)]

Institute of Experimental and Theoretical Physics,
Bol'shaya Cheremushkinskaya ul. 25, Moscow, 117259 Russia

Received March 5, 2001

Abstract—The effect of quarks on an instanton liquid through the excitation of adiabatic phonon-like modes in it is considered. An effective Lagrangian that includes a scalar color-singlet field interacting with quarks is derived, and the relevant generating functional is estimated in the tadpole approximation. The nature of this dynamical field as a mediator of interaction at soft momenta and its possible relationship with unusual properties of the sigma meson are discussed. © *2002 MAIK "Nauka/Interperiodica".*

1. INTRODUCTION

It seems that there is presently every reason to believe that the instanton-liquid model [1, 2] and the chiral-symmetry-breaking mechanism based on it [2] correctly describe light-quark physics at low energies and serve as an appropriate basis for the phenomenology of the QCD vacuum. This model provides quantitatively correct results for the gluon and the quark condensate, which are expressed in terms of the instanton-medium parameters and, eventually—as is well known—in terms of the renormalization constant $\Lambda_{\rm QCD}$. In particular, the resulting quark condensate is in accord with the well-established phenomenological value of $-i\langle\psi^\dagger\psi\rangle \sim -(250\ \text{MeV})^3$; also, correct results are obtained for the energy scale of the dynamical light-quark mass (about 350 MeV) and for the pion-decay constant ($F_\pi \sim 100$ MeV). Concurrently, a closed description of the generating functional for the emerging effective theory can be achieved via quite justifiable and consistent simplifications in the original QCD functional. Within this approach, the generating functional of the theory reduces to the factorized form

$$\mathcal{Z} = \mathcal{Z}_g \cdot \mathcal{Z}_\psi,$$

where the first and the second factor represent, respectively, a gluon and a quark component. The former provides a nontrivial gluon condensate, while the latter (fermion) component describes a chiral condensate in an instanton medium and its excitations. It is assumed that, in $\mathcal{Z}_g$, there is a dominant vacuum configuration saturating the relevant path integral and that this configuration is represented as a superposition of pseudoparticle fields obtained as solutions to the Yang–Mills equations and referred to as (anti)instantons. Specifically, they are given by

$$A_\mu(x) = \sum_{i=1}^{N} A_\mu(x;\gamma_i), \tag{1}$$

where $A_\mu(x;\gamma_i)$ stands for the field of an individual (anti)instanton in a singular gauge. For the $SU(N_c)$ group, it depends on $4N_c$ coordinates $\gamma = (\rho, z, U)$, where ρ is its size, z is the position of its center, and U is its color orientation that appears in a nontrivial block of the $N_c \times N_c$ color matrix for the field

$$A_\mu(x;\gamma) = \frac{\bar\eta_{a\mu\nu}}{g}\frac{y_\nu}{y^2}\frac{\rho^2}{y^2+\rho^2}U^\dagger\tau_a U, \tag{2}$$
$$y = x - z, \quad a = 1, 2, 3.$$

Here, τ_a are the Pauli matrices, η is the 't Hooft symbol [3], and g is the coupling constant; for an (anti)instantanton, we have $\bar\eta \to \eta$. In order to avoid encumbering the presentation, we do not introduce separate symbols for instantons (N_+) and for anti-instantons (N_-), always considering a topologically neutral instanton liquid ($N_+ = N_- = N/2$). With the aid of the variational maximum principle [2], the gluon component can be estimated as $\mathcal{Z}_g \simeq e^{-\langle S\rangle}$, the instanton-liquid action $\langle S\rangle$ having the form of the

[1)]Bogolyubov Institute for Theoretical Physics, National Academy of Sciences of Ukraine, Metrologicheskaya 14b, 03143 Kiev-143, Ukraine.
[2)]Institute of Nuclear Physics, Moscow State University, Vorob'evy gory, Moscow 119899 Russia.

1063-7788/02/6505-0929$22.00

additive functional[3)]

$$\langle S\rangle = \int dz \int d\rho n(\rho) s(\rho). \tag{3}$$

Integration is performed here over the volume V occupied by the liquid, the action functional per instanton,

$$s(\rho) = \beta(\rho) + 5\ln(\Lambda\rho) - \ln\widetilde{\beta}^{2N_c} + \beta\xi^2\rho^2 \int d\rho_1 n(\rho_1)\rho_1^2, \tag{4}$$

being averaged with the equilibrium size distribution of instantons, which is given by

$$n(\rho) = Ce^{-s(\rho)} = C\rho^{-5}\widetilde{\beta}^{2N_c} e^{-\beta(\rho)-\nu\rho^2/\overline{\rho^2}}, \tag{5}$$

where $\overline{\rho^2} = \int d\rho\rho^2 n(\rho)/n = \left(\dfrac{\nu}{\beta\xi^2 n}\right)^{1/2}$, $n = \int d\rho n(\rho) = \dfrac{N}{V}$, $\nu = \dfrac{b-4}{2}$, $b = \dfrac{11N_c - 2N_f}{3}$, and N_f is the number of flavors. The constant C is determined self-consistently from the variational maximum principle, while $\beta(\rho) = 8\pi^2/g^2 = -\ln C_{N_c} - b\ln(\Lambda\rho)$ ($\Lambda = \Lambda_{\overline{MS}} = 0.92\Lambda_{\rm PV}$), with C_{N_c} being dependent on the normalization scale:

$$C_{N_c} \approx \frac{4.66\exp(-1.68N_c)}{\pi^2(N_c-1)!(N_c-2)!}.$$

The parameters $\beta = \beta(\bar\rho)$ and $\widetilde{\beta} = \beta + \ln C_{N_c}$ are fixed at the characteristic scale $\bar\rho$ (the mean size of a pseudoparticle). The parameter $\xi^2 = \dfrac{27}{4}\dfrac{N_c}{N_c^2-1}\pi^2$ characterizes pseudoparticle interaction. The equilibrium state of the instanton liquid is described by Eqs. (3)–(5). A slight modification of the variational maximum principle (see Appendix) leads to an explicit formula to the mean pseudoparticle size, $\bar\rho\Lambda = \exp\{-2N_c/(2\nu-1)\}$ and, hence, to a direct determination of the parameters of the instanton liquid, in contrast to what is done within the original variational principle [2], where its parameters are determined by numerically solving a transcendental equation.

[3)]We recall that the property of additivity is due to the presumed uniformity of the vacuum wave function in coordinate space. Although formula (3) has a form that it could have within classical physics, it describes, in fact, the ground state of a quantum ensemble of instantons. Intuitively, it is clear that this formula will also remain valid in the case where the wave function for the ensemble in question features inhomogeneities of scale much larger than the mean instanton size—more precisely, larger than or on the order of the mean size of the characteristic saturating configuration (see below). In this case, each instanton-liquid fragment that has the aforementioned characteristic size will make a partial contribution dependent on the current state of the instanton liquid.

In evaluating the quark determinant $\mathcal{Z}_\psi$, the quark fields are considered to be affected by a preset stochastic ensemble of pseudoparticles as given by (1), the inverse effect of quarks on the instantons being disregarded; that is,

$$\mathcal{Z}_\psi \simeq \int D\psi^\dagger D\psi \langle\langle e^{S(\psi,\psi^\dagger,A)}\rangle\rangle_A,$$

where $S(\psi,\psi^\dagger,A)$ is the QCD action functional for massless quarks. Since the instanton liquid is dilute (the characteristic packing parameter $n\bar\rho^4$ is small), correlations between pseudoparticles is usually disregarded. Moreover, it is common practice to restrict the analysis to the approximation of $N_c \to \infty$, in which case it is sufficient to take into account only planar graphs in evaluating the path integral, and to consider the action functional for fermion fields in the approximation of zero modes $\Phi_\pm(x-z)$, which are solutions to the Dirac equation $(i[\hat D(A_\pm) + m]\Phi_\pm = 0)$ in the (anti)instanton field $A_\pm$,

$$[\Phi_\pm(x)]_{ic} = \frac{\rho}{\sqrt{2}\pi|x|(x^2+\rho^2)^{3/2}}\left[\hat x\frac{1\pm\gamma_5}{2}\right]_{ij}\varepsilon_{jd}U_{dc}.$$

Here, c and d are color indices, i and j are Lorentz indices, ε is an antisymmetric tensor, and $\hat x = x_\mu\gamma_\mu$ (this notation is further used for all quantities contracted with the Dirac γ matrices γ_μ, $\mu = 1$–4). For the particular case of $N_f = 1$, the quark determinant has the form [2]

$$\mathcal{Z}_\psi \simeq \int D\psi^\dagger D\psi \exp\left\{\int dx\psi^\dagger(x)i\hat\partial\psi(x)\right\} \times \left(\frac{Y^+}{VR}\right)^{N_+}\left(\frac{Y^-}{VR}\right)^{N_-}, \tag{6}$$

$$Y^\pm = i\int dzdUd\rho n(\rho)/n \times \int dxdy\psi^\dagger(x)i\hat\partial_x\Phi_\pm(x-z)\Phi_\pm^\dagger(y-z)i\hat\partial_y\psi(y),$$

where R is a factor reducing the result to a dimensionless form (it is determined by the method of steepest descent) and where averaging over color orientations is given by integration with respect to U. On the basis of the exact Green's function for quarks in the ensemble of pseudoparticles [4, 5], a correct extension of the generating functional beyond the chiral limit was obtained in [6]; in doing this, it turned out that, for low-energy phenomenology of light quarks to be reproduced correctly at a quantitative level, it is sufficient to take into account the contribution of zero modes.

Thus, we see that the instanton-liquid model where the inverse effect of quarks on the instanton

ensemble is disregarded is by and large reasonable—it leads to a right form of the generating function and correctly determines the functional dependence on the parameters of the instanton liquid. In view of this, we believe that the inverse effect of quarks on the instanton liquid is rather weak and must be treated by means of perturbation theory in terms of small variations of the instanton-liquid parameters δn and $\delta\rho$ in the vicinity of the equilibrium values n and $\bar{\rho}$. This can be done in a way similar to that used to describe excitations of the chiral condensate. We recall that a nontrivial evaluation of the path integral in (6) (this evaluation takes into account the physics content of zero modes in the quark determinant) results in that the state of the instanton liquid is encoded in this path integral only in terms of the above two parameters, the instanton-liquid density appearing in the theory in a combination like the packing parameter $n\bar{\rho}^4$ (this is also suggested by a dimensional analysis); that is, the pseudoparticle size remains the only free parameter. The present article, which reports on a continuation of the studies begun in [7], where it was shown that an instanton liquid has phonon-like excitations associated with adiabatic changes in the instanton size, is devoted to a more detailed investigation into quark interaction with an instanton liquid. Considering here only the simplest case of a topologically neutral liquid, we will demonstrate that it is natural to describe the inverse effect of quarks on the instanton liquid in terms of deformable field configurations that are similar to those specified by Eq. (2) and which have the size ρ dependent on x and z: $\rho \to \rho(x, z)$.

The ensuing exposition is organized as follows. In Section 2, we will discuss changes in evaluating the quark determinant (at the minimum number of flavors) that are introduced by deformable modes. On the basis of an approximate calculation of the path integral (in the tadpole approximation), we find, in Section 3, the relevant equation within the saddle-point method; in the same section, we further construct an iterative procedure that makes it possible to take into account the effect of quarks on the instanton ensemble. After that, we generalize these results to the case of many flavors in Section 4 and analyze qualitatively the possible new physical implications of the proposed approach in Section 5. In addition, the article contains an Appendix, where we describe the procedure that we use to determine the parameters of the instanton liquid.

2. INCLUSION OF PHONON-LIKE EXCITATIONS

Our personal view on the essence of the approach proposed here is the following. An evaluation of the path integral by the saddle-point method implies the use of the extremals of the action functional (solutions to the classical field equations)—in the case being considered, the action functional $S[A, \psi^\dagger, \psi]$ constructed from the gluon fields A and the quark fields $\psi^\dagger$ and ψ—and of the extremals that are obtained by simultaneously solving the set of the Yang–Mills and Dirac equations. In the theory of an instanton liquid, a superposition of (anti)instantons that is a solution to only the Yang–Mills equations (without taking into account the effect of quark fields) and which is simultaneously an external field for the Dirac equation is taken for a trial configuration. In our opinion, it is advisable to choose saturating configurations in the form of deformable (easily crumpled) (anti)instantons $A_\pm(x; \gamma(x))$, in which case there is the possibility of varying the parameters $\gamma(x)$ of the solutions to the Yang–Mills equations with the aim of describing the effect of the quark fields in terms of those variables natural for the quark determinant that appear in the final expression for it (in the case being considered, in terms of the pseudoparticle size). Choosing the action functional in the form $S[A_\pm(x, \gamma(x)), \psi^\dagger, \psi]$, one can obtain, for the deformation field $\gamma(x)$, the corresponding variational equation that provides the best (in the sense of an extremum of the action functional) description of an (anti)instanton in nontrivial external quark fields. In field theory, the scattering of monopoles [8] and Abrikosov vortices [9] is described in a similar way.

In the case of an instanton liquid, it turns out that, if we restrict our consideration to long-wave perturbations—that is, perturbations whose wavelength λ is much greater than the characteristic instanton size $\bar{\rho}$—the problem is radically simplified, since it reduces to finding the kinetic energy of the deformation fields[4)] (single-particle contributions) and to taking into account the pair interaction of pseudoparticles, which, in the adiabatic regime, assumes the form of a contact interaction [7].

We now recall changes that arise in evaluating the path integral. In deriving expression (3), averaging is performed over the positions of the instanton in metric space. Obviously, it is necessary that the characteristic linear size L of the domain that must be taken into consideration in doing this be greater than the mean instanton size $\bar{\rho}$. At the same time, this size must not be indefinitely large, since there is no causal coupling between widely spaced fragments of the instanton liquid. At this scale $L \geq \bar{R}$ ($\bar{R}$ is the mean distance between pseudoparticles),

[4)] In calculating the action functional for a deformed instanton, it is then legitimate to take the slowly varying deformation field outside the integral sign.

it is assumed that the ensemble wave function is uniform (each pseudoparticle enters into the path integral with a weight that is proportional to $1/V$, where $V = L^4$). A characteristic configuration that saturates the path integral is chosen in the form of a superposition of (anti)instantons that is specified by Eq. (1), with N being equal to the number of pseudoparticles in the volume V. It can easily be seen that, owing to the additivity of the action functional, expression (3) describes correctly even nonequilibrium states of the instanton liquid, in which case the distribution $n(\rho)$ does not coincide with the vacuum distribution in (5); moreover, it admits a generalization to the case of an inhomogeneous liquid, provided that the size λ of the inhomogeneity satisfies the obvious requirement $\lambda \geq L > \bar{\rho}$. In particular, this consideration is applicable to a saturating ensemble that is formed by deformable pseudoparticles, the deformation-field corrections $g_{\mu\nu}$ to the original instanton fields $G_{\mu\nu}$ being small ($g_{\mu\nu} \ll G_{\mu\nu}$) for long-wave excitations (at the instanton-size scale $\bar{\rho}$), $|\partial\rho(x,z)/\partial x| \ll O(1)$. This condition, which ensures the smoothness of changes suffered by the instanton size, makes it possible to introduce yet another important simplification and to use everywhere, for a characteristic deformation field, the field at the instanton center, $\dfrac{\partial\rho(x,z)}{\partial x} \sim \left.\dfrac{\partial\rho(x,z)}{\partial x}\right|_{x=z}$. In general, the instanton-field correction taking into account the effect of quarks can be obtained with the aid of the Green's function for gluons in an instanton medium; that is,

$$a^a_\mu(x,z) = \int d\xi D^{ab}_{\mu\nu}(x-z,\xi-z)J^b_\nu(\xi-z_\psi), \quad (7)$$

where J^b_ν is the current associated with the external (quark) source, z_ψ lies in the region where the long-wave perturbation is localized, and $D^{ab}_{\mu\nu}(x-z,\xi-z)$ is the Green's function for a pseudoparticle in an instanton medium. Formally, the gluon Green's function in the field of an individual instanton is poorly defined [4]. In the approach developed here, one may expect that, for this Green's function, there is a regular expression, a nonsingular behavior of the propagator in the region of soft momenta being controlled by the mass gap in the spectrum of phonon-like excitations. A more detailed treatment of these issues will be given elsewhere, since the explicit form of the Green's function is immaterial for the present purposes. Within the the nonperturbative region, the Green's function is concentrated at the scale of the mean pseudoparticle size; therefore, the integral in (7) can be estimated as

$$a^a_\mu(x,z) \simeq \bar{D}^{ab}_{\mu\nu}(x-z)\bar{J}^b_\nu(z-z_\psi). \quad (8)$$

Here, the notation on the right-hand side implies that integration was performed over a four-dimensional domain of size $\bar{\rho}$ with a nearly constant function J, where the dependence on the arguments is indicated explicitly (the absolute value of the integral is immaterial). On the other hand, the explicit form of the instanton in a singular gauge,

$$A^a_\mu(x,z) = -\frac{\bar{\eta}_{a\mu\nu}}{g}\frac{\partial}{\partial x_\nu}\ln\left(1+\frac{\rho^2}{y^2}\right), \quad y = x-z,$$

makes it possible to find straightforwardly that the correction to instanton potential is given by

$$a^a_\mu(x,z) = H^a_{\mu\nu}(x,z)\frac{\partial\rho}{\partial x_\nu}, \quad (9)$$

where $H^a_{\mu\nu}(x,z) = -\dfrac{\bar{\eta}_{a\mu\nu}}{g}\dfrac{2\rho}{y^2+\rho^2}$; to the precision adopted here, it is legitimate to set $\rho(x,z) \simeq \bar{\rho}$—that is, $H^a_{\mu\nu}(x,z) \simeq H^a_{\mu\nu}(x-z)$. Comparing Eqs. (8) and (9), we deduce that the deformation field $\rho_\nu = \partial\rho/\partial x_\nu$ satisfies the equation

$$H^a_{\mu\nu}(x-z)\frac{\partial\rho(x,z)}{\partial x_\nu} = \bar{D}^{ab}_{\mu\nu}(x-z)\bar{J}^b_\nu(z-z_\psi).$$

Since the current $\bar{J}$ can be taken to be constant in the long-wave approximation (that is, its gradients are negligible), we immediately obtain the estimate $|\partial\rho(x,z)/\partial x| \simeq |\partial\rho(z)/\partial z|$ for the rate of deformation. This result seems quite natural, because, in the adiabatic approximation, there are no other fields in the problem. With allowance for the correction from the pseudoparticle-deformation fields, the contribution of deformed (anti)instantons to the path integral can then be estimated as [7]

$$\langle S\rangle \simeq \int dz \int d\rho n(\rho)\left\{\frac{\kappa}{2}\left(\frac{\partial\rho}{\partial z}\right)^2 + s(\rho)\right\}, \quad (10)$$

where κ is a kinetic coefficient calculated semiclassically. To the precision adopted in the present study, the kinetic coefficient must be fixed at some characteristic scale—for example, as $\kappa \sim \kappa(\bar{\rho})$. For this coefficient, the estimations that we performed yield $\kappa \sim c\beta$ (a value on the order of the instanton action functional), with the coefficient c whose specific value ranging between about 1.5 and 6 depends on the ansatz adopted for the saturating configuration. Although the kinetic term could in principle be introduced on a phenomenological basis as well, we note, going somewhat ahead, that there is no significant dependence on κ in the problem being considered. As a result, the action functional per instanton is supplemented solely with a small contribution that is caused by a scalar deformation field and which is of the kinetic-energy type. Its effect on the preexponential factors can be disregarded

because of their logarithmic smallness. The inverse effect is negligibly small as well. It is worth noting here that the deformation fields associated with the shear mode and with rotation in isotopic space lead, respectively, to a trivial and to a singular kinetic coefficient [7]. In order to establish the mass scale corresponding to these modes, it is therefore necessary to invoke additional considerations that are likely to be beyond the theory of instanton liquid and the standard theory of chiral-symmetry breaking.

Within the approximation employed here, we further retain only the second-order terms of smallness in the deviation from the point $ds(\rho)/d\rho|_{\rho_c} = 0$, where the action functional attains a minimum, making use of the approximate expression

$$s(\rho) \simeq s(\bar{\rho}) + \frac{s^{(2)}(\bar{\rho})}{2}\varphi^2, \qquad (11)$$

where $s^{(2)}(\bar{\rho}) \simeq d^2s(\rho)/d^2\rho\big|_{\rho_c} = 4\nu/\overline{\rho^2}$ and where the scalar field $\varphi = \delta\rho = \rho - \rho_c \simeq \rho - \bar{\rho}$ is the field of deviations from the equilibrium value $\rho_c = \bar{\rho}\left(1 - \left(\frac{1}{2\nu}\right)\right)^{1/2} \simeq \bar{\rho}$. Comparing expressions (10) and (11), one can easily see that the deformation field is described in terms of the Lagrangian density

$$\mathcal{L} = \frac{n\kappa}{2}\left\{\left(\frac{\partial\varphi}{\partial z}\right)^2 + M^2\varphi^2\right\},$$

where $M^2 = s^{(2)}(\bar{\rho})/\kappa = 4\nu/(\kappa\overline{\rho^2})$ is the mass gap in the spectrum of phonon-like excitations; $M \approx 1.21\Lambda$ for an instanton liquid in the "quenched" approximation with parameters $N_c = 3$, $c = 4$, $\bar{\rho}\Lambda \approx 0.37$, $\beta \approx 17.5$, and $n\Lambda^{-4} \approx 0.44$ (more detailed data are quoted in the tables given in the Appendix) [7].

Upon a change of variables, the gluon component of the generating functional takes the form

$$\mathcal{Z}'_g \sim \int D\varphi \left|\frac{\delta A}{\delta\varphi\cdots}\right| \times \exp\left[-\frac{n\kappa}{2}\int dz\left\{\left(\frac{\partial\varphi}{\partial z}\right)^2 + M^2\varphi^2\right\}\right],$$

where $\left|\frac{\delta A}{\delta\varphi\cdots}\right|$ is the Jacobian for the transition to new variables that describe the deformation fields. We would like to qualify, from the outset, the above notation as that which is not fully specified, since we do not present the complete set of variables of the transformation in question. As was indicated above, however, the preexponential factor is a c number in the adiabatic approximation, so that its contribution can be disregarded.[5)]

Let us now analyze modifications arising in the quark determinant $\mathcal{Z}_\psi$ (6). For this, we take into account a variation of fermion zero modes that are associated with perturbations of the instanton size, $\Phi_\pm(x-z,\rho) \simeq \Phi_\pm(x-z,\rho_c) + \Phi^{(1)}_\pm(x-z,\rho_c)\delta\rho(x,z)$, where $\Phi^{(1)}_\pm(u,\rho_c) = \partial\Phi_\pm(u,\rho)/\partial\rho|_{\rho=\rho_c}$; in accordance with the adiabaticity condition, we set here $\delta\rho(x,z) \simeq \delta\rho(z,z) = \varphi(z)$. Additional contributions from scalar fields generate corrections in the kernels of the factors $Y^\pm$; we will consider these corrections in the linear approximation in φ, setting everywhere $\rho_c \simeq \bar{\rho}$; that is

$$i\hat{\partial}_x\Phi_\pm(x-z,\rho)\Phi^\dagger_\pm(y-z,\rho)(-i\hat{\partial}_y) \qquad (12)$$
$$\simeq \Gamma_\pm(x,y,z,\bar{\rho}) + \Gamma^{(1)}_\pm(x,y,z,\bar{\rho})\varphi(z),$$

where

$$\Gamma_\pm(x,y,z,\bar{\rho}) = i\hat{\partial}_x \times \Phi_\pm(x-z,\bar{\rho})\Phi^\dagger_\pm(y-z,\bar{\rho})(-i\hat{\partial}_y),$$

$$\Gamma^{(1)}_\pm(x,y,z,\bar{\rho}) = i\hat{\partial}_x \times \Phi^{(1)}_\pm(x-z,\bar{\rho})\Phi^\dagger_\pm(y-z,\bar{\rho})(-i\hat{\partial}_y) + i\hat{\partial}_x\Phi_\pm(x-z,\bar{\rho})\Phi^{\dagger(1)}_\pm(y-z,\bar{\rho})(-i\hat{\partial}_y).$$

Here, the derivative $(-i\hat{\partial}_y)$ acts from the left, and the gradients of the scalar field φ can be disregarded in the adiabatic approximation. It can easily be shown that, in the momentum representation, the result obtained by integrating the expression on the right-hand side of (12) with respect to z and U generates, in formula (6), the kernel

$$\frac{1}{N_c}\left[(2\pi)^4\delta(k-l)\gamma_0(k,k) + \gamma_1(k,l)\varphi(k-l)\right], \qquad (13)$$

where k and l are the relevant momenta. At a fixed value of the parameter $\rho = \bar{\rho}$ (which is henceforth omitted in order to avoid encumbering the presentation), the functions γ_0 and γ_1 are expressed in terms of

[5)] In general, the relationship between the deformation field ρ_ν and the variable a^a_μ of integration in the path integral involves the color-rotation matrix: $\tilde{a}^a_\mu = \Omega_{ab}H^b_{\mu\nu}(x-z)\rho_\nu$. In the long-wave approximation, the function H can be treated as a constant equal to $H^b_{\mu\nu}(0)$ ($x \sim z$). Choosing further the rotation matrix Ω^{-1} in such a way that the color field $a_\mu = \Omega^{-1}\tilde{a}_\mu$ would be associated with some specific direction in isotopic space, one can see that, apart from loop corrections, which can be disregarded, and this insignificant rotation in isotopic space, the gluon-field vector a^z_μ and the deformation-field vector ρ_ν appear to be in one-to-one correspondence and the Jacobian of the transformation reduces basically to an insignificant constant.

the functions $G(k,\rho) = 2\pi\rho F(k\rho/2)$ and $G'(k,\rho) = dG(k,\rho)/d\rho$ as

$$\gamma_0(k,k) = G^2(k),$$
$$\gamma_1(k,l) = G(k)G'(l) + G'(k)G(l);$$
$$F(x) = 2x[I_0(x)K_1(x) - I_1(x)K_0(x)] - 2I_1(x)K_1(x),$$

where I_i and $K_i (i = 0, 1)$ are modified Bessel functions.

Further, we perform auxiliary integration with respect to the parameter λ (see, for example, [2]), whereupon the exponentiated path integral in (6) taken with allowance for the phonon-like component assumes the following form in the momentum representation:[6)]

$$\mathcal{Z}_\psi \simeq \int \frac{d\lambda}{2\pi} \exp\left\{N \ln\left(\frac{N}{i\lambda VR}\right) - N\right\}$$
$$\times \int D\psi^\dagger D\psi \exp\left\{\int \frac{dkdl}{(2\pi)^8}\psi^\dagger(k)\left[(2\pi)^4\delta(k-l)\right.\right.$$
$$\left.\left.\times\left[-\hat{k} + \frac{i\lambda}{N_c}\gamma_0(k,k)\right] + \frac{i\lambda}{N_c}\gamma_1(k,l)\varphi(k-l)\right]\psi(l)\right\}.$$

We everywhere omit normalization factors that are associated with the free Lagrangian and which are irrelevant to our purposes. It can be seen that, as soon as the scalar field is switched off, we arrive at the result obtained by Diakonov and Petrov in [2]. In order to avoid the emergence of a great many redundant coefficients, we simplify the presentation by going over to the dimensionless variables

$$\frac{k\bar{\rho}}{2} \to k, \quad \frac{M\bar{\rho}}{2} \to M, \quad \gamma_0 \to \bar{\rho}^2\gamma_0, \qquad (14)$$
$$\frac{1}{(n\bar{\rho}^4\kappa)^{1/2}}\gamma_1 \to \bar{\rho}\gamma_1$$

for the momenta, masses, and vertices and the dimensionless variables

$$\varphi(k) \to (n\kappa)^{-1/2}\bar{\rho}^3\varphi(k), \quad \psi(k) \to \bar{\rho}^{5/2}\psi(k), \quad (15)$$

for the fields and by using the parameter $\mu = \lambda\bar{\rho}^3/(2N_c)$ instead of λ. In terms of these variables, the generating functional can be written as

$$\mathcal{Z} \simeq \int d\mu \mathcal{Z}_g'' \int D\psi^\dagger D\psi D\varphi \qquad (16)$$
$$\times \exp\left\{-N\ln\mu - \int \frac{dk}{\pi^4}\frac{1}{2}\varphi(-k)4[k^2+M^2]\varphi(k)\right\}$$
$$\times \exp\left\{\int \frac{dkdl}{\pi^8}\psi^\dagger(k)2\left[\pi^4\delta(k-l)\right.\right.$$
$$\left.\left.\times[-\hat{k} + i\mu\gamma_0(k,k)] + i\mu\gamma_1(k,l)\varphi(k-l)\right]\psi(l)\right\},$$

where $\mathcal{Z}_g''$ is that part of the gluon component of the generating functional which survives upon the expansion of the action functional per instanton [see Eq. (11)] in terms of a small deviation from its equilibrium size. Now that indefinite forms have disappeared, the resulting functional, together with all contributions involving the scalar field, provides a closed description of an instanton liquid with allowance for the effect of quarks on it (see also the Appendix). As was indicated above, it is not expected that either this effect or the inverse effect of phonon-like deformations on the quark determinant would strongly change the parameters of the instanton-liquid model or the parameters of chiral-symmetry breaking. The free part of the Lagrangian associated with phonon-like excitations characterizes the reaction of the instanton liquid to an external long-wave perturbation and is likely to be its general property, which is independent of the character of fields that generate this perturbation. The presence of a quark condensate suggests a natural scheme for approximately calculating the generating functional; namely,

$$\psi^\dagger\psi\varphi = \langle\psi^\dagger\psi\rangle\varphi + \{\psi^\dagger\psi - \langle\psi^\dagger\psi\rangle\}\varphi. \qquad (17)$$

3. TADPOLE APPROXIMATION

A formal integration with respect to the scalar field leads to a four-fermion interaction, for which it is impossible to calculate the path integral explicitly. On the basis of the theory of chiral-symmetry breaking and under the assumption that the corrections from the scalar field are small, it is possible, however, to find an approximate form of the effective Lagrangian by replacing one of the quark-field pairs by its condensate value (see Fig. 1*a*): $\psi^\dagger(k)\psi(l) \to \langle\psi^\dagger(k)\psi(l)\rangle = -\pi^4\delta(k-l)\,\mathrm{tr}S(k)$, where $S(k)$ is the Green's function for quarks. In the lowest order of perturbation theory in μ, the diagram with four external fermion legs reduces to a two-fermion diagram of the tadpole type (because of two possible types of quark-field pairing, there are two such contributions). Specifically, we have

$$2(i\mu)^2 \int \frac{dkdldk'dl'}{\pi^{16}}\gamma_1(k,l)\gamma_1(k',l')$$
$$\times \psi^\dagger(k)\psi(l)\psi^\dagger(k')\psi(l')\underline{\varphi(k-l)\varphi(k'-l')}$$

[6)] In coordinate space, we have the nonlocal Lagrangian $\mathcal{L} = \int dx\psi^\dagger(x)i\hat{\partial}_x\psi(x) - \int dz(n\kappa/2)\times\left\{(\partial\varphi/\partial z)^2 + M^2\varphi^2(z)\right\} + (i\lambda_\pm/N_c)\int dxdydzdU\psi^\dagger(x)\times\{\Gamma_\pm(x,y,z,\bar{\rho}) + \Gamma_\pm^{(1)}(x,y,z,\bar{\rho})\varphi(z)\}\psi(y)$, which represents the interaction of the scalar field of phonon-like deformations with quarks and which describes the physically transparent phenomenon consisting in that the propagation of quark fields through an instanton medium is accompanied by its small deformation.

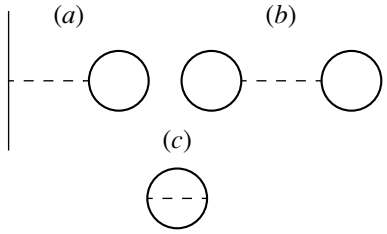

Fig. 1. Diagrams of the tadpole approximation that are taken into account in deriving the equation of the saddle-point method. The solid and the dashed lines represent, respectively, the fermion and the phonon-like fields.

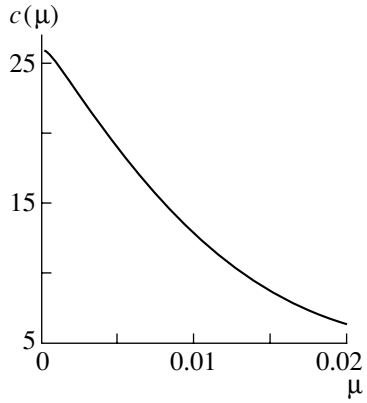

Fig. 2. Function $c(\mu)$ at $N_f = 1$.

$$\simeq 4\mu^2 \int \frac{dk}{\pi^4}\gamma_1(k,k)\psi^\dagger(k)\psi(k) \times \int \frac{dl}{\pi^4}\gamma_1(l,l)\mathrm{tr}S(l)D(0),$$

where we have introduced a natural definition for the convolution of the scalar fields—namely, $\overline{\varphi(k)\varphi(l)} = \pi^4\delta(k+l)D(k)$, with $D(k) = 1/[4(k^2+M^2)]$. The expression in front of the combination $\psi^\dagger(k)\psi(k)$ can be treated as an additional contribution to the dynamical mass

$$m(k) = \mu\gamma_1(k,k)(-2i\mu) \times \int \frac{dl}{\pi^4}\gamma_1(l,l)\mathrm{tr}S(l)D(0). \quad (18)$$

We recall that, in the Lagrangian expressed in terms of the dimensionless variables, the mass term involves an additional factor of 2.

In deriving the equation of the saddle-point method in the same order of perturbation theory, it is necessary to take additionally into account the contribution of the diagrams where all quark fields are paired (see Fig. 1*b*),

$$-2\mu^2\left[\int \frac{dk}{\pi^4}\gamma_1(k,k)\,\mathrm{tr}S(k)\right]^2 \pi^4\delta(0)D(0) = -\frac{\mu^2}{2}\frac{\kappa}{\nu}\frac{V}{\bar\rho^4}\left[\int \frac{dk}{\pi^4}\gamma_1(k,k)\mathrm{tr}S(k)\right]^2,$$

and the contribution of the diagram in Fig. 1*c*,

$$2\mu^2\int \frac{dkdl}{\pi^8}\,\mathrm{tr}\gamma_1(k,l)\gamma_1(l,k)S(k)S(l)D(k-l),$$

where use has been made of a natural regularization of the delta function in terms of the dimensionless variables: $\delta(0) = \frac{1}{\pi^4}\frac{V}{\bar\rho^4}$, since $\delta\left(\frac{k\rho}{2}\right) = \frac{\delta_1(k)}{\rho/2}\cdots\frac{\delta_4(k)}{\rho/2}$, while $\delta_1(0)\cdots\delta_4(0) = \frac{V}{(2\pi)^4}$.

As a result, we reduce the generating functional to the form

$$\mathcal{Z} \sim \int d\mu \int D\psi^\dagger D\psi \exp\left\{ -N\ln\mu + \frac{2N_c^2}{n\bar\rho^4\nu}\frac{V}{\bar\rho^4}\mu^4c^2(\mu) - 2N_c\mu^2\frac{V}{\bar\rho^4}\int\frac{dkdl}{\pi^8} \times \gamma_1^2(k,l)\frac{(kl)-\Gamma(k)\Gamma(l)}{(k^2+\Gamma^2(k))(l^2+\Gamma^2(l))}D(k-l) + \int\frac{dk}{\pi^4}\psi^\dagger(k)2[-\hat k + i\Gamma(k)]\psi(k)\right\} \quad (19)$$

$$= \int d\mu \exp\left\{-N\ln\mu + \frac{2N_c^2}{n\bar\rho^4\nu}\frac{V}{\bar\rho^4}\mu^4c^2(\mu) - 2N_c\mu^2\frac{V}{\bar\rho^4} \times \int\frac{dkdl}{\pi^8}\gamma_1^2(k,l)\frac{(kl)-\Gamma(k)\Gamma(l)}{(k^2+\Gamma^2(k))(l^2+\Gamma^2(l))}D(k-l) + \frac{V}{\bar\rho^4}\int\frac{dk}{\pi^4}\mathrm{tr}\ln[-\hat k + i\Gamma(k)]\right\},$$

where we have defined the vertex

$$\Gamma(k) = \mu\gamma_0(k,k) + m(k)$$

and have introduced the function

$$c(\mu) = -\frac{i(n\bar\rho^4\kappa)^{1/2}}{2\mu N_c}\int\frac{dk}{\pi^4}\gamma_1(k,k)\,\mathrm{tr}S(k),$$

which is convenient for the ensuing calculations. As can be seen from (19), the Green's function for the quark fields is determined self-consistently from the equation

$$2[-\hat k + i\Gamma(k)]S(k) = -1.$$

Seeking its solution in the form $S(k) = A(k)\hat k + iB(k)$, we can easily obtain

$$A(k) = \frac{1}{2}\frac{1}{k^2+\Gamma^2(k)}, \quad B(k) = \frac{1}{2}\frac{\Gamma(k)}{k^2+\Gamma^2(k)}.$$

Using Eq. (18) and substituting the function $B(k)$ into the definition of $\Gamma(k)$, we arrive at the closed integral equation

$$\Gamma(k) = \mu\gamma_0(k,k) + N_c\frac{\kappa}{\nu}\mu^2\gamma_1(k,k)$$

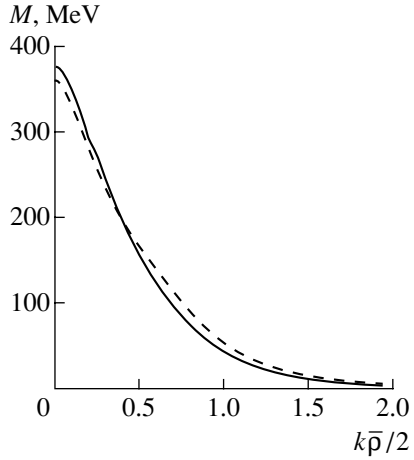

Fig. 3. Dynamical mass M at $\Lambda = 280$ MeV as a function of $k\bar{\rho}/2$ (the dashed curve represents the result obtained by Diakonov and Petrov [2]).

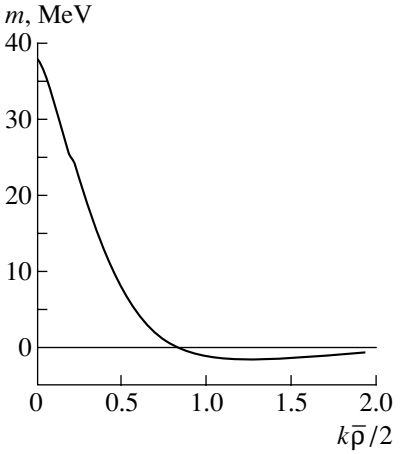

Fig. 4. Correction m to the dynamical mass as a function $k\bar{\rho}/2$.

$$\times \int \frac{dl}{\pi^4}\gamma_1(l,l)\frac{\Gamma(l)}{l^2+\Gamma^2(l)},$$

whence we obtain a solution in the convenient form

$$\Gamma(k) = \mu\gamma_0(k,k) + \frac{N_c}{(n\bar{\rho}^4\kappa)^{1/2}}\frac{\kappa}{\nu}\mu^3 c(\mu)\gamma_1(k,k).$$

For the function $c(\mu)$ in turn, we can easily obtain

$$c(\mu) = \frac{(n\bar{\rho}^4\kappa)^{1/2}}{\mu}\int \frac{dk}{\pi^4}\gamma_1(k,k)\frac{\Gamma(k)}{k^2+\Gamma^2(k)}.$$

Substituting $\Gamma(k)$ into this expression, we can find a closed integral equation for the function $c(\mu)$,[7)] which is displayed in Fig. 2 at $N_f = 1$. We note that the N_f dependence of the function $c(\mu)$ within the range of significant values of μ, this dependence being specified by the position of the saddle point for the functional given by (19), can be disregarded to the precision adopted in the present study. For the additional contribution to the dynamical mass, one can easily obtain

$$m(k) = \frac{N_c}{(n\bar{\rho}^4\kappa)^{1/2}}\frac{\kappa}{\nu}\mu^3 c(\mu)\gamma_1(k,k). \qquad (20)$$

It is interesting to note that, in the tadpole approximation, the dependence on the kinetic coefficient κ is canceled in $m(k)$, so that the exact value of this coefficient is immaterial.

The saddle point of the functional specified by Eq. (19) satisfies the equation

$$\int \frac{dk}{\pi^4}\frac{[\Gamma^2(k)]'_\mu}{k^2+\Gamma^2(k)} \qquad (21)$$
$$-\int \frac{dkdl}{\pi^8}\left\{\frac{\mu^2\gamma_1^2(k,l)[(kl)-\Gamma(k)\Gamma(l)]}{(k^2+\Gamma^2(k))(l^2+\Gamma^2(l))}\right\}'_\mu$$
$$\times D(k-l) + \frac{N_c}{n\bar{\rho}^4\nu}[\mu^4 c^2(\mu)]'_\mu = \frac{n\bar{\rho}^4}{2N_c\mu},$$

where a prime denotes differentiation with respect to μ.

The equation for the saddle point is written under the assumption that the parameters of the instanton liquid do not change; however, this is not quite correct, because it is necessary to take into account effects caused by the quark-condensate-induced change in the equilibrium instanton size. In the perturbation-theory scheme specified by Eq. (17), the first term, which is linear in the scalar field, causes a small shift of the equilibrium instanton size ($\rho_c \sim \bar{\rho}$). In the leading approximation, this shift, which is represented by a simple diagram of the tadpole type, is given by

$$2i\mu\int \frac{dkdl}{\pi^8}\gamma_1(k,l)(-\pi^4)\delta(k-l) \qquad (22)$$
$$\times \mathrm{tr}S(k)\varphi(k-l) = \Delta\cdot\varphi(0),$$
$$\Delta = -2i\mu\int \frac{dk}{\pi^4}\gamma_1(k,k)\mathrm{tr}S(k) = \frac{4N_c}{(n\bar{\rho}^4\kappa)^{1/2}}\mu^2 c(\mu).$$

It should be recalled that $\varphi = \rho - \rho_c$ and that $\varphi(0) = \int dz\varphi(z)$ denotes the scalar field in the momentum representation.

[7)] In the range of μ values that is of prime interest to us, this equation has a unique solution, but it should be noted that, for μ greater than $\mu_c \sim 4\times10^{-2}$, the number of branches of $c(\mu)$ becomes greater. In principle, it would be of interest to find out whether the equation of the saddle-point method holds for these branches, but it is clear a priori that these particles will be heavier than the mass scale of a few hundred MeV, which follows from chiral-symmetry breaking. It is conceivable, however, that, if such solutions exist, they can be associated with some heavy particles.

Table 1. Basic parameters of the theory of chiral-symmetry breaking

N_f	DP			MSZ		
	μ	$M(0)$, MeV	$-i\langle\psi^\dagger\psi\rangle$, MeV^3	μ	$M(0)$, MeV	$-i\langle\psi^\dagger\psi\rangle$, MeV^3
0	5.68×10^{-3}	341	$-(301)^3$	5.68×10^{-3}	341	$-(337)^3$
1	5.24×10^{-3}	361	$-(337)^3$	4.98×10^{-3}	377	$-(326)^3$

This contribution can be taken into account by supplementing the variational procedure for determining the saddle point of the functional in (19) with the variation of the parameters of the instanton liquid as functions of μ [in the case being considered, it is the instanton-liquid density $n(\mu)$ that changes]. In practice, it is quite acceptable to use a simple iterative procedure where the first step consists in determining the saddle point $\mu(\bar\rho)$ without taking these changes into account. The following steps involve determining the new parameters of the instanton liquid (see Appendix) and solving anew the equation for the saddle point, whereupon the procedure is repeated. It turns out that, to the precision adopted in our calculations, the results converge after five to six iterations. The results of our numerical calculations (MSZ) at $N_f = 0, 1$ are quoted in Table 1, along with the results obtained by Diakonov and Petrov in [2], who disregarded the deformation of instantons. In the first row of this table, we present the results for the case of $N_f \to 0$, which formally corresponds to the "quenched" approximation for the parameters of the instanton liquid. Specifically, the table gives the calculated values of the dynamical quark mass

$$M(0) = 2\Gamma(0)\left(\frac{1}{\bar\rho}\right)\ [\text{MeV}]$$

and of the quark condensate

$$-i\langle\psi^\dagger\psi\rangle = i\,\mathrm{tr}S(x)|_{x=0} = -2N_c\int\frac{dk}{\pi^4}$$
$$\times\frac{\Gamma(k)}{k^2+\Gamma^2(k)}\left(\frac{1}{\bar\rho}\right)^3\ [\text{MeV}^3].$$

In the present study, the renormalization constant Λ_{QCD} is everywhere fixed at the scale of $\Lambda = 280$ MeV. The parameters of the instanton liquid differ somewhat from the commonly accepted phenomenological values of $\bar\rho \sim (600\ \text{MeV})^{-1}$ and $\bar R \sim (200\ \text{MeV})^{-1}$ (see the relevant tables in the Appendix). For the constant Λ, it is possible, however, to choose a more appropriate value at which the instanton-liquid parameters found by means of our procedure would be close to the aforementioned phenomenological values. As might have been expected, the changes in the parameters of the quark condensate are insignificant, about a few MeV, which makes it possible to introduce a new soft energy scale caused by effects of quark propagation through an instanton medium. For the sake of comparison, we display, in Fig. 3, the function $M_{\text{DP}}(k\bar\rho/2)$ (dashed curve) and the function $M_{\text{MZS}}(k\bar\rho/2)$ (solid curve) and, in Fig. 4, the function $m(k\bar\rho/2)$ at $N_f = 1$. As might have been expected, the presence of an effective attractive interaction, which appears in the system owing to the scalar field, leads to an increase in the dynamical quark mass. As to the inclusion of the quark effect on the instanton liquid, it reduces to an increase in its density (see Table 1A in the Appendix). This also corresponds to an effective attraction that arises in the system of pseudoparticles; in turn, the attraction in question may obviously serve as a source of inhomogeneity in the ensemble of instantons, leading to the formation of pseudoparticle clusters.

4. GENERALIZATION TO THE CASE OF MANY FLAVORS

Let us now proceed to consider the case of $N_f > 1$, which is more important for phenomenological applications. The quark determinant then has the form [2, 10]

$$\mathcal{Z}_\psi \simeq \int D\psi^\dagger D\psi\exp\left\{\int dx\sum_{f=1}^{N_f}\psi_f^\dagger(x)i\hat\partial\psi_f(x)\right\}$$
$$\times\left(\frac{Y^+}{VR^{N_f}}\right)^{N_+}\left(\frac{Y^-}{VR^{N_f}}\right)^{N_-},$$

$$Y^\pm = i^{N_f}\int dzdUd\rho n(\rho)/n$$
$$\times\prod_{f=1}^{N_f}\int dx_f dy_f\psi_f^\dagger(x_f)i\hat\partial_{x_f}\Phi_\pm(x_f-z)$$
$$\times\Phi_\pm^\dagger(y_f-z)i\hat\partial_{y_f}\psi_f(y_f).$$

The inclusion of the phonon-like component modifies the kernels of the factors $Y^\pm$ similarly to (13).

Therefore, the well-known transformation that is applied to fermion fields and which reduces the factors $Y^{\pm}$ to a determinant form remains in force in our case as well. Integration performed everywhere with respect to z [in the adiabatic approximation, we have $\varphi(x,z) \to \varphi(z)$] leads to correct diagrams conserving the momenta of interacting particles. As a result, we find, in the leading order in N_c, that

$$Y^{\pm} = \left(\frac{1}{N_c}\right)^{N_f} \int dz \det\left(iJ^{\pm}(z)\right),$$

$$J^{\pm}_{fg}(z) = \int \frac{dkdl}{(2\pi)^8}\left[e^{i(k-l)z}\gamma_0(k,l) + \int \frac{dp}{(2\pi)^4} e^{i(k-l+p)z}\gamma_1(k,l)\varphi(p)\right]\psi^{\dagger}_f(k)\frac{1\pm\gamma_5}{2}\psi_g(l).$$

In order to reduce the functional considered here to a Gaussian form, it is necessary to perform, in addition to integration with respect to the auxiliary parameter λ, the bosonization transformation accompanied by integration with respect to the auxiliary $N_f \times N_f$ matrix meson fields $\mathcal{M}$ [10]; that is,

$$\exp\left[\lambda \det\left(\frac{iJ}{N_c}\right)\right] \simeq \int d\mathcal{M} \times \exp\left\{i\mathrm{tr}[\mathcal{M}J] - (N_f-1)\left(\frac{\det[\mathcal{M}N_c]}{\lambda}\right)^{\frac{1}{N_f-1}}\right\}.$$

As a result, the generating functional can be recast into the form

$$\mathcal{Z} \simeq \int \frac{d\lambda}{2\pi}\mathcal{Z}''_g \exp(-N\ln\lambda) \times \int D\varphi \exp\left\{-\int \frac{dk}{(2\pi)^4}\frac{n\kappa}{2}\varphi(-k)[k^2+M^2]\varphi(k)\right\} \times \int D\mathcal{M}_{L,R} \exp\left\{\int dz\left\{-(N_f-1)\right.\right. \times \left[\left(\frac{\det[\mathcal{M}_L N_c]}{\lambda}\right)^{1/(N_f-1)} + \left(\frac{\det[\mathcal{M}_R N_c]}{\lambda}\right)^{1/(N_f-1)}\right]\left.\right\}\left.\right\} \int D\psi^{\dagger}D\psi \times \exp\left\{\int \frac{dk}{(2\pi)^4}\sum_f \psi^{\dagger}_f(k)(-\hat{k})\psi_f(k) + i\int dz\left(\mathrm{tr}[\mathcal{M}_L J^{+}] + \mathrm{tr}[\mathcal{M}_R J^{-}]\right)\right\}, \quad (23)$$

where $\mathcal{M}_L$ and $\mathcal{M}_R$ are meson fields interacting with quark fields of specific helicity. Now, the scalar field interacts with quarks of various flavors, but the main contribution comes, as might have been expected on the basis of the above consideration of the $N_f = 1$ case, from diagrams of the tadpole type, with some pairs of the quark fields involved being considered in the condensate approximation, where $\psi^{\dagger}_f(k)\psi_g(l) \to \langle\psi^{\dagger}_f(k)\psi_g(l)\rangle = -\pi^4\delta_{fg}\delta(k-l)\mathrm{tr}S(k)$. The condensate is obtained as a nontrivial solution to the saddle-point equation for meson fields of the diagonal form $(\mathcal{M}_{L,R})_{fg} = \mathcal{M}\delta_{fg}$. In addition to the transformations specified by Eqs. (14) and (15), it is convenient to introduce dimensionless variables as $(\mathcal{M}/2)\bar{\rho}^3 \to \mu$ and $\left(\lambda\bar{\rho}^4/(2N_c\bar{\rho})^{N_f}\right)^{1/(N_f-1)} \to g$. In terms of this notation, the effective action ($\mathcal{Z} \simeq \int dgd\mu \exp\{-V_{\mathrm{eff}}\}$) has the form

$$V_{\mathrm{eff}} = N(N_f-1)\ln g - \frac{V}{\bar{\rho}^4}(N_f-1)\frac{2\mu^{N_f/(N_f-1)}}{g} - \frac{V}{\bar{\rho}^4}\frac{2N_f^2N_c^2}{n\bar{\rho}^4\nu}\mu^4c^2(\mu) + 2N_cN_f\mu^2\frac{V}{\bar{\rho}^4}\int\frac{dkdl}{\pi^8}\gamma_1^2(k,l) \times \frac{(kl)-\Gamma(k)\Gamma(l)}{(k^2+\Gamma^2(k))(l^2+\Gamma^2(l))}D(k-l) - 2N_fN_c\frac{V}{\bar{\rho}^4}\int\frac{dk}{\pi^4}\ln\{k^2+\Gamma^2(k)\}. \quad (24)$$

The saddle-point equation can be represented as

$$\int\frac{dk}{\pi^4}\frac{[\Gamma^2(k)]'_{\mu}}{k^2+\Gamma^2(k)} + \frac{N_fN_c}{n\bar{\rho}^4\nu}[\mu^4c^2(\mu)]'_{\mu} - \int\frac{dkdl}{\pi^8}\left\{\frac{\mu^2\gamma_1^2(k,l)[(kl)-\Gamma(k)\Gamma(l)]}{(k^2+\Gamma^2(k))(l^2+\Gamma^2(l))}\right\}'_{\mu} \times D(k-l) = \frac{n\bar{\rho}^4}{2N_c\mu}, \quad (25)$$

and formula (20) for the additional contribution to the mass acquires the factor N_f since, in view of the scalar nature of the phonon-like field, a tadpole involving the condensate of quark fields of all N_f possible flavors can be connected to each vertex:

$$m(k) = \frac{N_fN_c}{(n\bar{\rho}^4\kappa)^{1/2}}\frac{\kappa}{\nu}\mu^3c(\mu)\gamma_1(k,k).$$

As a supplement to Table 1, Table 2 illustrates the results of our numerical calculations at $N_f = 2$, displaying, among other things, data for the pion decay constant F_{π} [MeV] given by

$$F_{\pi}^2 = \frac{N_cN_f}{2}\int\frac{dk}{\pi^4} \times \frac{\Gamma^2(k) - (k/2)\Gamma'(k)\Gamma(k) + (k^2/4)(\Gamma'(k))^2}{(k^2+\Gamma^2(k))^2}\left(\frac{1}{\bar{\rho}}\right)^2,$$

Table 2. Basic parameters of the theory of chiral-symmetry breaking at $N_f = 2$

DP					MSZ				
μ	$M(0)$, MeV	$-i\langle\psi^\dagger\psi\rangle$, MeV^3	F_π, MeV	F'_π, MeV	μ	$M(0)$, MeV	$-i\langle\psi^\dagger\psi\rangle$, MeV^3	F_π, MeV	F'_π, MeV
4.81×10^{-3}	388	$-(384)^3$	122	100	4.36×10^{-3}	425	$-(366)^3$	114	94

where $\Gamma'(k) = d\Gamma(k)/dk$, and for its approximate expression F'_π[MeV],

$$F'^2_\pi = \frac{N_c N_f}{2}\int\frac{dk}{\pi^4}\frac{\Gamma^2(k)}{(k^2+\Gamma^2(k))^2}\left(\frac{1}{\bar\rho}\right)^2;$$

the condensate $-i\langle\psi^\dagger\psi\rangle$ is presented there for quarks of one of the flavors.

Expression (23), which was obtained in the present study for the generating functional, makes it possible to describe meson excitations of the quark condensate by using the approach developed previously in [2] and by taking into account the effect of the phonon-like field within perturbation theory. An analysis along these lines has revealed that the parameters of the mesons do not change sizably—in particular, the pion decay constant undergoes virtually no changes.

5. CONCLUSION

A simple scheme has been proposed for describing quark interaction with an instanton liquid. This scheme is based on a special choice of configurations saturating the path integral that have the form of deformable (easily crumpled) (anti)instantons whose parameters $\gamma(x)$ can be varied. In the present study, we have varied the pseudoparticle size $\rho(x,z)$. This choice was motivated by the form of the quark determinant, which, in the theory of chiral-symmetry breaking, depends substantially only on the mean instanton size. In the long-wave approximation, the variational problem of optimally choosing deviation fields reduces to constructing the effective Lagrangian that involves a scalar phonon-like field coupled to quarks by a Yukawa interaction. As might have been expected, the effect of quarks on the parameters of the instanton liquid is insignificant. The parameters of the theory of chiral-symmetry breaking also change insignificantly—in particular, the scale of corrections to the quark condensate is about a few MeV. Within the pattern developed in this study, the propagation of quark-condensate perturbations through an instanton liquid resembles the situation in the polaron problem, where it is necessary to take into account the reaction of the medium in describing elementary excitations.

In the course of solving the problem, we have been getting an ever clearer idea of the problem of describing the penetration of gluon fields into a vacuum (their propagation over a vacuum). The situation here is somewhat paradoxical. In the theory of an instanton liquid, the constant β is determined self-consistently. Its value is large ($\beta \sim 15$–20) and, in general, corresponds to the deconfining region—that is, to the region where gluons are commonly thought to be mediators of interaction. In the presence of a gluon condensate, which is a vacuum proper in the theory, this naive picture seems, however, unrealistic in the region of soft momenta. Indeed, we have to consider, each time, the gluon fields $g_{\mu\nu}$ against the background of the instanton field $G_{\mu\nu}$—say, for the sake of simplicity, in the form of the simple superposition $G'_{\mu\nu} = G_{\mu\nu} + g_{\mu\nu}$. The path integral admits a straightforward calculation, which can be referred to, by convention, as an exact calculation, in two limiting cases. The first is that where $G_{\mu\nu} \gg g_{\mu\nu}$ and where the gluon field $g_{\mu\nu}$ describes quantum corrections to the instanton field, which are eventually reduced to loop contributions, only the vacuum condensate saturated by instantons appearing here as an observable. The other limiting case is that of very strong gluon fields, $g_{\mu\nu} \gg G_{\mu\nu}$. In this case, which corresponds to the region of hard momenta, we merely have free gluon fields, with instanton fields being immaterial. Figuratively, the gluon field is as if lost, in the first case, against the background of the instanton field because of averaging over the pseudoparticle position. Within the scheme developed here for approximately calculating the path integral, perturbations of the quark condensate, pions being the lightest of these, appear to be the source of long-wave phonon-like excitations of the gluon condensate. Closely inspecting the result obtained for the generating functional within the approximation of chiral-symmetry breaking, where the inverse effect of quarks on pseudoparticles is disregarded, one can see that, in the nonperturbative region of soft momenta, the variable mean pseudoparticle size $\bar\rho \to \bar\rho + \delta\rho$, which is the only parameter involved in $\mathcal{Z}_\psi$ and which encodes the state of the instanton liquid, is a convenient variable that makes it possible to take this effect into account. As a result, it turns out that a light particle

possessing the properties of a scalar glueball is a natural candidate for a mediator of the interaction. Therefore, a color-singlet object is likely to be the observable mediator of the interaction even in the deconfining region (large β). The existence of such a color-singet object can then be associated with the unusual properties of the sigma meson [$f_0(400-1200$ MeV)], which is observed experimentally as a broad resonance of width about 600–1000 MeV and which is unsatisfactorily described in terms of a quark–antiquark bound state.[8)]

Thus, it is urgently needed to investigate the Green's function for the mediator of the interaction over the entire range of momenta. Its role is played by a phonon-like excitation of the gluon condensate in the region of soft momenta and by a gluon in the region of hard momenta (at a scale smaller than the mean instanton size). The same circumstance dictates the rescaling of loop corrections in the theory. In a sense, the use of a free gluon propagator is not quite legitimate. The formulas must be corrected in the region of soft momenta, but the large value of β in the theory of an instanton liquid guarantees the smallness of the relevant corrections.

Our calculations cannot be considered as absolutely rigorous because, in a full theory, it is necessary to take into account changes in the instanton profile [11], to describe more realistically the interaction of pseudoparticles (which is likely to be overestimated), to go beyond the long-wave approximation (for example, by taking into account the contribution of the instanton Jacobian $|\delta A/\delta\varphi|$), etc.

ACKNOWLEDGMENTS

We are grateful to N.O. Agasian, M. Musakhanov, Yu.A. Simonov, and J. Ellis for discussions on this study.

This work was supported by the Russian Foundation for Basic Research (project no. 97-02-17491) and INTAS (grant nos. 93-0283 and 96-0678). S.V. Molodtsov and A.M. Snigirev are indebted to Prof. M. Namiki and the HUUJUKAI Fund for a financial support. G.M. Zinovjev and S.V. Molodtsov thank the Fabergé Foundation for providing excellent conditions for work.

[8)] For example, a Yukawa-type effective interaction Lagrangian found in the present article makes it possible to assess the presence of a bound state in the quark–antiquark system within the naive relativistic approximation. The inequality $\frac{\mu\gamma_0(0)}{4\pi M}\frac{\mu^2\gamma_1^2(0)}{n\bar\rho^4\kappa} \geq 2$ serves as a criterion for the emergence of a level. Our estimations yield an $O(1)$ value for the expression on the left-hand side of it.

APPENDIX

The contribution of the quark determinant to the action functional for an instanton liquid is represented by the tadpole diagram [see Eq. (22)]. Upon going over to the dimensionless variables specified by Eq. (15), it assumes the form

$$\Delta\varphi \to \Delta\frac{(n\kappa)^{1/2}}{\bar\rho^3}\varphi(0) = \Delta(n\bar\rho^4\kappa)^{1/2} \times \int d\rho\frac{n(\rho)}{n}\int\frac{dz}{\bar\rho^4}\frac{\rho(z)-\rho_c}{\bar\rho}.$$

The instanton-liquid action functional in Eq. (3) then acquires an additional term, becoming

$$\langle S\rangle = \int dzn\left\{\langle s\rangle - \left\langle\Delta'\frac{\rho-\rho_c}{\bar\rho}\right\rangle\right\},$$

where $\Delta' = \dfrac{4N_cN_f}{n\bar\rho^4}\mu^2c(\mu)$. The mean action functional per instanton is then given by

$$\langle s_1\rangle = \int d\rho s_1(\rho)n(\rho)/n,$$

where $s_1(\rho) = \beta(\rho) + 5\ln(\Lambda\rho) - \ln\widetilde\beta^{2N_c} + \beta\xi^2\rho^2n\overline{\rho^2} - \Delta'(\rho-\rho_c)/\bar\rho$. In order to find the equilibrium parameters of the instanton liquid, we apply the maximum principle

$$\langle e^{-S}\rangle \geq \langle e^{-S_0}\rangle e^{-\langle S-S_0\rangle},$$

employing its simplest version, where the approximating functional is trivial: $S_0 = 0$.[9)] In the equilibrium state, the size distribution of instantons, $n(\rho)$, must depend only on the instanton-liquid action functional; that is, $n(\rho) = Ce^{-s(\rho)}$, where C is a constant.[10)] Further, it is necessary to find the maximum of the mean action functional per instanton with respect to variations of the parameters of the instanton liquid (for example, the mean instanton size $\bar\rho$). We assume that the corrections introduced by the

[9)] In principle, this choice of the approximating functional is expected to be somewhat poorer than the estimate of Diakonov and Petrov [2]. Its advantage is that, in this case, one can obtain explicit expressions for the parameters of the instanton liquid instead of solving a complicated transcendental equation.

[10)] This argument corresponds to the maximum principle [2]. In order to demonstrate this, we note that, if the action functional in (3) is approximated by the local expression $\langle s_1\rangle = \int d\rho s_1(\rho)n(\rho)/n$, where $s_1(\rho) = \beta(\rho) + 5\ln(\Lambda\rho) - \ln\widetilde\beta^{2N_c} + \beta\xi^2\rho^2n\overline{\rho^2}$, this choice of the distribution function $n(\rho)$ makes the problem self-consistent. Varying the difference $\langle s\rangle - \langle s_1\rangle = \int d\rho\{s(\rho) - s_1(\rho)\}e^{-s(\rho)}/n$ of the functionals being considered with respect to $s(\rho)$ and taking into account arbitrariness in the choice of normalization, we obtain $s(\rho) = s_1(\rho) + \text{const}$.

shear term are small and consider them in only in the linear approximation in the deviation Δ, employing the expansion

$$\langle s_1\rangle = \frac{\langle (s+\delta)e^{-s-\delta}\rangle}{\langle e^{-s-\delta}\rangle} \simeq \frac{\langle se^{-s}\rangle + \langle \delta e^{-s}\rangle}{\langle e^{-s}\rangle} + \frac{\langle se^{-s}\rangle\langle \delta e^{-s}\rangle - \langle s\delta e^{-s}\rangle\langle e^{-s}\rangle}{\langle e^{-s}\rangle^2}, \quad (A.1)$$

where δ is a small shear contribution and s is the action functional generated only by the gluon component. The last term is much smaller than the first one and will therefore be disregarded. From relation (A.1), one can see that, in assessing the mean action functional per instanton, it is legitimate to retain, in the exponential, only the gluon-component contribution s (the shear term δ can be disregarded). As a result, we arrive at $\langle s_1\rangle = \int d\rho s_1(\rho) n_0(\rho)/n_0$, where $n_0(\rho)$ is the distribution function n without the inclusion of the shear term.[11] For the mean square of the instanton size and for the instanton-liquid density, we can obtain[12]

$$r^2\overline{\rho^2} = \nu\left\{1 + \frac{\Delta'}{r\bar\rho}\frac{\Gamma(\nu+1/2)}{2\nu\Gamma(\nu)}\right\} \simeq \nu\left\{1 + \Delta'\frac{\Gamma(\nu+1/2)}{2\nu^{3/2}\Gamma(\nu)}\right\}, \quad (A.2)$$

$$n = CC_{N_c}\widetilde\beta^{2N_c}\frac{\Gamma(\nu)}{2r^{2\nu}}, \quad (A.3)$$

where the parameter r^2 is given by

$$r^2 = \beta\xi^2 n\overline{\rho^2}. \quad (A.4)$$

By using the expansion $\ln\rho = \ln\bar\rho + \frac{\rho-\bar\rho}{\bar\rho} + \frac{1}{2}\frac{(\rho-\bar\rho)^2}{\bar\rho^2} + \ldots$ and relation (A.2), it can be shown that

$$\frac{\int d\rho n_0(\rho)\ln\rho}{\int d\rho n_0(\rho)} = \ln\bar\rho + \Phi_1(\nu),$$
$$\frac{\int d\rho n_0(\rho)\rho}{\int d\rho n_0(\rho)} = \bar\rho + \Phi_2(\nu),$$

where Φ_1 and Φ_2 are some functions of ν that are independent of $\bar\rho$. In addition, we note that, to the precision adopted here, the mean square of the instanton size satisfies the equality $r^2\overline{\rho^2} = \Phi(\nu)$, with $\Phi(\nu)$ being a function of only ν. For the mean action functional per instanton, we then have

$$\langle s_1\rangle = -2N_c\ln\widetilde\beta + (2\nu-1)\ln\bar\rho + F(\nu),$$

where $F(\nu)$ is again a function of only ν, its explicit form being irrelevant here. Determining the maximum of the mean action functional per instanton with respect to $\bar\rho$, we obtain

$$\bar\rho = \exp\left\{-\frac{2N_c}{2\nu-1}\right\}, \quad \beta = \frac{2bN_c}{2\nu-1} - \ln C_{N_c}.$$

From relations (A.2) and (A.4), we find that the instanton-liquid density is given by

$$n = \nu\frac{\exp\left(\dfrac{8N_c}{2\nu-1}\right)}{\beta\xi^2}\left\{1 + \Delta'\frac{\Gamma(\nu+1/2)}{2\nu^{3/2}\Gamma(\nu)}\right\}.$$

Further, we determine the constant C using relation (A.3). The parameters of the instanton liquid—they are compiled in Table 1A for $N_f = 0, 1, 2$ and $N_c = 3$ (the instanton-liquid density for $\Delta \neq 0$ at the end of the iteration process is given parenthetically)—prove to be very close to the parameters of the Diakonov–Petrov model [2]. It is interesting to note that, upon taking into account the effect of quarks on the equilibrium state of the instanton liquid, its density becomes higher.

Table 2A displays the calculated values of the mass gap M and of the wavelength in the "time" direction $\lambda_4 = M^{-1}$. Also given there for the sake of comparison is the mean distance between pseudoparticles, which gives sufficient grounds to believe that the adiabatic approximation ($\lambda \geq L \sim \bar R > \bar\rho$ with $\bar R =$

Table 1A. Instanton-liquid parameters

N_f	DP			MSZ		
	$\bar\rho\Lambda$	n/Λ^4	β	$\bar\rho\Lambda$	n/Λ^4	β
0	0.37	0.44	17.48	0.37	0.44	17.48
1	0.32	0.66	18.23	0.33	0.63 (0.71)	18.11
2	0.27	1.06	19	0.28	1.03 (1.37)	18.91

[11] The shear term changes insignificantly the mass of the phonon-like excitation. The equilibrium instanton size determined from the condition $ds(\rho)/d\rho|_{\rho=\rho_c} = 0$ is then given by $\rho_c = (\alpha + \Delta'\beta)\bar\rho$, where $\alpha = \left(1 - \frac{1}{2\nu}\right)^{1/2}$ and $\beta = \frac{1}{4\nu}\left\{1 - \alpha\frac{\Gamma(\nu+1/2)}{\nu^{1/2}\Gamma(\nu)}\right\}$, the second derivative of the action functional being $s''(\rho_c) = \frac{4\nu}{\bar\rho^2}\left\{1 + \frac{\Delta'}{\alpha}(1-2\beta)\right\} \sim M^{-2}$. The inclusion of a variation of the instanton profile in the deformation mode $A \to A + a$, which can be introduced within the superposition ansatz (1) with a subsequent change in the quark zero mode $[D(A+a)\psi = 0]$, where the correction field is $a \sim \partial\rho(x,z)/\partial x|_{x=z}$, is yet another source of corrections to the kinetic coefficient. Numerically, both corrections to the kinetic term are small.

[12] In order to avoid encumbering the displayed equations with factors that reduce then to dimensionless forms and which are proportional to powers of Λ, we omit them in the hope that this will not lead to confusion.

Table 2A. Features of phonon-like excitations

N_f	$M\Lambda^{-1}$	$\lambda_4\Lambda$	$M'\Lambda^{-1}$	$\lambda_4'\Lambda$	$\bar{R}\Lambda$
0	1.21	0.83	0.99	1.01	1.23
1	1.34	0.75	1.09	0.92	1.12 (1.09)
2	1.45	0.69	1.18	0.85	0.99 (0.94)

$n^{-1/4}$) is valid for long-wave perturbations of the pion type. Unprimed (primed) parameters correspond to the kinetic term $\kappa = 4\beta$ ($\kappa = 6\beta$). The values in parentheses are the distances between pseudoparticles at the end of the iteration process.

REFERENCES

1. C. G. Callan, R. Dashen, and D. J. Gross, Phys. Rev. D **17**, 2717 (1978); C. G. Callan, R. Dashen, and D. J. Gross, Phys. Lett. B **66B**, 375 (1977); E.-M. Ilgenfritz and M. Müller-Preussker, Nucl. Phys. B **184**, 443 (1981); E. V. Shuryak, Nucl. Phys. B **203**, 93 (1982); **203**, 116 (1982); **203**, 140 (1982); **328**, 85 (1989); **328**, 102 (1989); T. Schäfer and E. V. Shuryak, Rev. Mod. Phys. **70**, 323 (1998).
2. D. I. Diakonov and V. Yu. Petrov, Nucl. Phys. B **245**, 259 (1984); in *Hadronic Matter under Extreme Conditions,* Ed. by V. Shelest and G. Zinovjev (Naukova Dumka, Kiev, 1986), p. 192; D. I. Diakonov, V. Yu. Petrov, and P. V. Pobylitsa, Phys. Lett. B **226**, 471 (1989).
3. G. 't Hooft, Phys. Rev. D **14**, 3432 (1976).
4. L. S. Brown, R. D. Carlitz, D. B. Creamer, and C. Lee, Phys. Rev. D **17**, 1583 (1978).
5. C. Lee and W. A. Bardeen, Nucl. Phys. B **153**, 210 (1979).
6. M. Musakhanov, Eur. Phys. J. C **9**, 235 (1999); V. F. Tokarev, Teor. Mat. Fiz. **73**, 223 (1987).
7. S. V. Molodtsov, A. M. Snigirev, and G. M. Zinovjev, Phys. Rev. D **60**, 056006 (1999); in *Lattice Fermions and Structure of the Vacuum,* Ed. by V. Mitrjushkin and G. Schierholz (Kluwer, Dordrecht, 2000), p. 307; G. M. Zinov'ev, S. V. Molodtsov, and A. M. Snigirev, Yad. Fiz. **63**, 975 (2000) [Phys. At. Nucl. **63**, 903 (2000)].
8. N. S. Manton, Phys. Lett. B **110B**, 54 (1982); **154**, 397 (1985); G. W. Gibbons and N. S. Manton, Nucl. Phys. B **274**, 183 (1986).
9. A. G. Sergeev and S. V. Chechin, Teor. Mat. Fiz. **85**, 397 (1990).
10. D. I. Diakonov, M. V. Polyakov, and C. Weiss, Nucl. Phys. B **461**, 539 (1996); D. I. Diakonov, hep-ph/9802298.
11. A. B. Migdal, N. O. Agasyan, and S. B. Khokhlachev, Pis'ma Zh. Éksp. Teor. Fiz. **41**, 405 (1985) [JETP Lett. **41**, 497 (1985)]; N. O. Agasyan and S. B. Khokhlachev, Yad. Fiz. **55**, 1116 (1992) [Sov. J. Nucl. Phys. **55**, 628 (1992)]; N. O. Agasian and Yu. A. Simonov, Mod. Phys. Lett. A **10**, 1755 (1995); N. O. Agasyan, hep-ph/9904227; Yad. Fiz. **59**, 317 (1996) [Phys. At. Nucl. **59**, 297 (1996)].

Translated by A. Isaakyan

Physics of Atomic Nuclei, Vol. 65, No. 5, 2002, pp. 943–952. Translated from Yadernaya Fizika, Vol. 65, No. 5, 2002, pp. 974–983.

ELEMENTARY PARTICLES AND FIELDS
Theory

Azimuthal Asymmetry of Jet Production as a Signal of Parton Energy Losses in Semicentral Heavy-Ion Collisions

I. P. Lokhtin, S. V. Petrushanko, L. I. Sarycheva, and A. M. Snigirev

Institute of Nuclear Physics, Moscow State University, Vorob'evy gory, Moscow, 119899 Russia

Received February 14, 2001; in final form, October 11, 2001

Abstract—The question is investigated of whether an azimuthal asymmetry in the hadron-jet spectra can arise because of rescattering and energy losses of partons produced via hard processes in a dense quark–gluon matter formed in the region of the initial nuclear overlap in collisions characterized by a nonzero value of the impact parameter. Methods are discussed for determining the reaction-plane angle in ultrarelativistic heavy-ion collisions with the aid of the flux of semihard particles. © *2002 MAIK "Nauka/Interperiodica".*

1. INTRODUCTION

Considerable advances recently made in a lattice simulation of QCD systems with allowance for, in particular, dynamical quarks have given sufficient grounds to state that the deconfinement of hadronic matter and the restoration of chiral symmetry must occur at high temperatures of $T_c \sim 200$ MeV [1]. An experimental investigation of the properties of quark–gluon plasma formed in ultrarelativistic nucleus–nucleus collisions is one of the main objectives of present-day high-energy physics (for an overview, see, for example, [2–6]).

In recent years, much attention has been given to investigating the potential of hard tests of quark–gluon plasma, such as heavy quarkonia, hard hadrons, jets, and dimuons of high invariant mass. Since hard QCD scattering processes occur at the earliest stage of a nucleus–nucleus collision, particles and parton jets produced in such processes do not belong to a thermalized system, so that they can carry information about initial stages of its evolution. In particular, the suppression of the yield of massive vector mesons J/ψ and ψ' because of the screening of a $c\bar{c}$ bound state (color dipole) in a plasma [7] or because of dynamical dissociation on semihard deconfined gluons [8] was proposed as one of the main signals from the formation of quark–gluon plasma. The observation of such an anomalous suppression of ψ resonances in the most central PbPb collisions at the Super Proton Synchrotron (SPS, CERN) [9] does not comply with models of absorption in cold nuclear matter and a hadronic gas and can be interpreted as an effect due to the formation of quark–gluon plasma [10]. For heavier $b\bar{b}$ systems (Υ resonances), a similar effect of suppression in quark–gluon plasma is possible at temperatures that are higher than those for $c\bar{c}$ and which are expected to be achieved in heavy-ion collisions at RHIC and especially at LHC.

Apart from the suppression of heavy quarkonia, the propagation of hard jets of color-charged partons through quark–gluon plasma, which are produced in pairs at the earliest stage of the collision process ($\tau_{\rm form} \sim 1/p_T \lesssim 0.01$ fm/c) in individual hard nucleon–nucleon (parton–parton) scattering events, may be yet another hard test of plasma formation. Such jets propagate through dense quark–gluon matter formed by a set of minijets over a large time scale ($\gtrsim 0.1$ fm/c) and interact with matter constituents, with the result that their original properties are modified upon additional rescatterings. The inclusive cross section for the production of hard hadron jets [$Q^2 \gg 1$ (GeV/c)^2] is still too small for such events to be analyzed at SPS energies, but it grows fast with increasing energy of colliding nuclei. Hard and semihard processes of parton–parton scattering will play an important role at LHC energies, $\sqrt{s} = 5.5$ TeV per nucleon pair for PbPb collisions. Here, changes in the behavior of a color charge (jet parton) in dense QCD matter [11] that are associated with medium-induced coherent gluon bremsstrahlung [12–17] and with collision energy losses due to elastic rescattering on medium constituents [18–20] present a problem of paramount importance. Since the intensity of rescattering grows sharply with increasing temperature, the formation of a hot quark–gluon plasma with an initial temperature of $T_0 \sim 1$ GeV at LHC [21] is expected to be accompanied by hard-jet energy losses that are much greater than those in the case of cold nuclear matter or a hadronic gas [14, 15].

In order to implement experimental searches for energy losses of hard quarks and gluons in dense QCD matter and to perform a relevant analysis of the

1063-7788/02/6505-0943$22.00

properties of the medium formed in ultrarelativistic nucleus–nucleus collisions, it was proposed to use the suppression of the yield of hard dijets [20, 22], the enhancement of the yield of single jets [23, 24] produced in primary processes of hard parton–parton scattering, and the disbalance of the transverse momentum in the production of a parton jet and a particle that does not undergo strong interaction (such as a Z boson [25] or a high-energy photon [26]). The above features can be investigated in heavy-ion collisions [27] by using the compact-muon-solenoid (CMS) detector, which is being constructed at LHC and which can be optimized for precisely measuring the characteristics of high-energy muons, photons, electrons and hadron jets [28]. The distribution of hard jets with respect to the impact parameter of a nucleus–nucleus collision was considered in [29]. This distribution carries information about the dependence of the parton energy losses on the distance that partons travel in a dense medium (a coherent pattern of medium-induced gluon bremsstrahlung can lead to a nontrivial character of this dependence [14–16]). Among other things, it was shown in [29] that parton rescattering in a medium can modify the impact-parameter distribution of jets, shifting its mean and maximum values.

In the present study, we consider another aspect of the problem of jet suppression in noncentral heavy-ion collisions, that which is associated with the azimuthal asymmetry arising in the jet yield from semicentral nucleus–nucleus collisions because of rescattering and energy losses that partons from hard processes suffer in the asymmetric dense-medium volume produced in the region of the initial overlap of colliding nuclei. Investigation of the azimuthal-angle distribution of jets seems promising from the experimental point of view, since it does not require a precise measurement of the initial jet energy (this would present a rather difficult problem depending on the algorithm for seeking jets and on the angle of a jet cone [27])—it is only necessary to measure the jet angle with respect to the reaction plane. It should be emphasized that, while, in experiments that are being currently performed, the reaction-plane azimuthal angle, which is formed by the directions of the beam axis and the impact-parameter vector, is measured primarily on the basis of the flux of soft ($p_T \leq 2$ GeV/c) particles [30–32], at LHC energies, it would become possible, in all probability, to determine this angle by using the flux of semihard ($p_T \gtrsim 2$ GeV/c) particles originating for the most part from the fragmentation of gluons emitted in the asymmetric volume [33, 34].

The ensuing exposition is organized as follows. In Section 2, we give a brief account of the geometric model for the production and propagation of hard partons through dense matter formed in ultrarelativistic nucleus–nucleus collisions. In Section 3, we present the results obtained by calculating the azimuthal-angle distributions of hard jets with allowance for collision and radiative parton energy losses estimated for PbPb collisions at the LHC energy. In Section 4, we discuss the applicability of known methods for determining the reaction-plane angle in heavy-ion collisions at LHC on the basis of the flux of semihard particles. In the Conclusion, we list the main results of our study.

2. HARD-PARTON ENERGY LOSSES IN AN ASYMMETRIC VOLUME OF A DENSE MEDIUM

A simple geometric model describing the production of hard partons in ultrarelativistic nucleus–nucleus collisions and the propagation of these partons through the dense medium formed was comprehensively investigated in [29]. Here, we briefly dwell upon the basic points directly concerning the calculation of the azimuthal asymmetry of jets. The initial distribution of the jet-production vertex in the nuclear-overlap region is azimuthally isotropic and has the form

$$P_{AA}(\mathbf{r}, b) = \frac{T_A(r_1)T_A(r_2)}{T_{AA}(b)}, \qquad (1)$$

where b is the impact parameter, $\mathbf{r} = r\cos\psi \cdot \mathbf{e}_x + r\sin\psi \cdot \mathbf{e}_y$ is the vector drawn from the jet-production vertex to the beam axis (z axis),

$$r_{1,2} = \sqrt{r^2 + \frac{b^2}{4} \pm rb\cos\psi} \qquad (2)$$

is the distance from the center of each nucleus to the jet-production vertex,

$$T_{AA}(b) = \int_0^{2\pi} d\psi \int_0^{r_{\max}} r dr T_A(r_1)T_A(r_2) \qquad (3)$$

is the nuclear-overlap function, and $T_A(\mathbf{r}) = A\int_{-\infty}^{+\infty}\rho_A(\mathbf{r}, z)dz$ is the nuclear-thickness function for the intranuclear-nucleon density $\rho_A(\mathbf{r}, z)$. The quantity $r_{\max}$ is found by equating the greater value of $r_1(r)$ and $r_2(r)$ to the nuclear radius R_A; that is,

$$r_{\max} = \min\left\{\sqrt{R_A^2 - \frac{b^2}{4}\sin^2\psi} + \frac{b}{2}\cos\psi, \right. \qquad (4)$$
$$\left. \sqrt{R_A^2 - \frac{b^2}{4}\sin^2\psi} - \frac{b}{2}\cos\psi\right\}.$$

By way of example, we indicate that, for the uniform distribution of intranuclear nucleons, $\rho_A^{\mathrm{un}}(\mathbf{R}) =$

$\rho_0\Theta(R_A - |\mathbf{R}|)$, which is used below for numerical estimates, the nuclear-overlap function has the form $T_A^{\rm un}(r) = 3A\sqrt{R_A^2 - r^2}/(2\pi R_A^3)$. The distribution $P_{AA}^{\rm un}(\mathbf{r}, b)$ is then given by

$$P_{AA}^{\rm un}(\mathbf{r}, b) \propto \sqrt{R_A^2 - r_1^2(r,\psi,b)}\sqrt{R_A^2 - r_2^2(r,\psi,b)}. \quad (5)$$

Traveling in a dense medium formed in the initial nuclear-overlap region, hard-jet partons undergo rescattering and lose energy. In general, the energy loss ΔE as a function of the initial energy E and the distance L traveled in the medium can be described in terms of the kinetic equation

$$\Delta E(L, E) = \int_0^L dx \exp\left(-x/\lambda(x)\right) \frac{dE}{dx}(x, E), \quad (6)$$

where dE/dx is the energy losses per unit length, $\lambda = 1/(\sigma\rho)$ is the hard-parton range in the medium, $\rho \propto T^3$ is the medium density at temperature T, and σ is the cross section for parton interaction in the medium. From geometric considerations, it is straightforward to estimate the proper time $\tau_L = L$ ($\hbar = c = 1$) over which the jet resides within the dense region. [1)] The result is [29]

$$\tau_L = \min\left\{\sqrt{R_A^2 - r_1^2\sin^2\phi} - r_1\cos\phi, \quad (7)\right.$$
$$\left.\sqrt{R_A^2 - r_2^2\sin^2(\phi - \varphi_0)} - r_2\cos(\phi - \varphi_0)\right\},$$

where $\phi = \varphi \mp \arccos\{(r\cos\psi + b/2)/r_1\}$ is the azimuthal angle that is distributed isotropically and which specifies the direction of jet motion with respect to the vector $\mathbf{r}_1$, φ is the azimuthal angle between the direction of jet motion and the impact-parameter vector, and

$$\varphi_0 = \pm\arccos\frac{r^2 - b^2/4}{r_1 r_2} \quad (8)$$

is the angle between the vectors $\mathbf{r}_1$ and $\mathbf{r}_2$. The plus (minus) sign in (8) is taken for $\psi > 0$ ($\psi < 0$). From (7), one can see that, in the case of a noncentral collision ($b \neq 0$), the mean value of τ_L depends on φ: it has a maximum value at $\varphi = \pm\pi/2$ and a minimum value at $\varphi = 0$ (see Fig. 1 for PbPb collisions at the impact-parameter values of $b = 0$, 6, and 10 fm). Therefore, the jet energy loss, which is an increasing function of τ_L [29], also depends on the jet azimuthal angle with respect to the reaction plane.

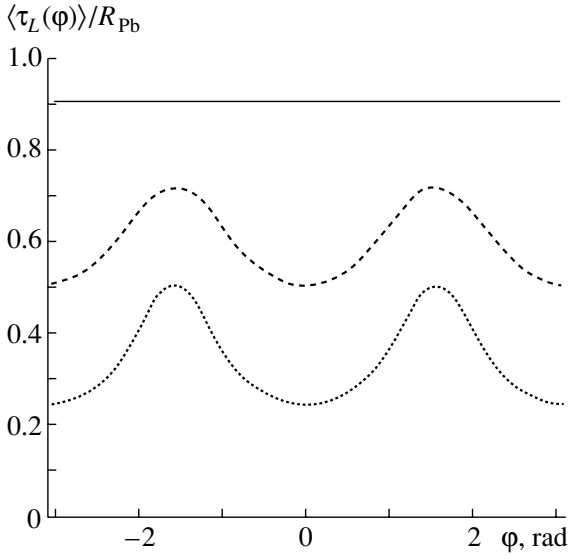

Fig. 1. Mean proper time $\langle\tau_L\rangle/R_A$ of the escape of a hard parton from dense matter as a function of the parton azimuthal angle with respect to the reaction plane for PbPb collisions at the impact-parameter values of $b =$ (solid curve) 0, (dashed curve) 6, and (dotted curve) 10 fm.

In order to illustrate the azimuthal asymmetry of the parton energy loss, we consider the model presented in [29], where the evolution of quark–gluon plasma formed at the initial stage of the reaction at the instant τ_0 in the nuclear-overlap region is considered within one-dimensional Lorentz-invariant hydrodynamics for the case where particles are produced at the hypersurface of the constant proper time $\tau = \sqrt{t^2 - z^2}$ [35]. In this model, collision and radiative energy losses are associated with each scattering event in an expanding medium; interference effects in gluon bremsstrahlung are taken into account by modifying the radiation spectrum as a function of decreasing temperature [$dE/dx(T)$]. In the limiting case of $\Delta E \ll E$, the total hard-parton energy loss in the transverse (with respect to the nuclear-collision axis) direction—it depends on the azimuthal angle φ—can be obtained on the basis of Eq. (6) as the result of averaging over the production vertex $P_{AA}(\mathbf{r}, b)$ (1), over the square t of the momentum transfer in a scattering event, and over spacetime evolution. Specifically, we have

$$\langle\Delta E_T(b,\varphi)\rangle = \int_0^{2\pi} d\psi \int_0^{r_{\max}} r dr \frac{T_A(r_1)T_A(r_2)}{T_{AA}(b)} \quad (9)$$

[1)] In determining τ_L, we assume that a jet moves along a straight line in the azimuthal direction; in fact, the initial azimuthal direction of the jet differs, because of rescatterings, from its final direction by $\Delta\varphi^2 \sim (\mu_{\rm D}^2/E^2)(L/\lambda)$ (here, $\mu_{\rm D}$ is the Debye screening mass, which specifies a typical momentum transfer in a scattering event), but this quantity is negligible for the parameter values used here.

$$\times \int_{\tau_0}^{\tau_L(\varphi)} d\tau \left(\frac{dE^{\rm rad}}{dx}(\tau) + \sigma(\tau)\rho(\tau)\nu(\tau) \right),$$

where τ_0 is the proper time of medium formation.

At temperature T, the thermally averaged energy loss ν of a hard parton of energy (effective mass) $m_0 \sim 3T \ll E$ per event of elastic scattering on a medium constituent can be estimated as

$$\nu = \left\langle \frac{t}{2m_0} \right\rangle = \frac{1}{2} \left\langle \frac{1}{m_0} \right\rangle \langle t \rangle \simeq \frac{1}{4T\sigma} \int_{\mu_{\rm D}^2}^{3TE/2} dt \frac{d\sigma}{dt} t. \quad (10)$$

The energy spectrum of medium-induced coherent gluon bremsstrahlung and the corresponding dominant part of the radiative energy loss, $dE^{\rm rad}/dx$, were determined in [14, 15] for a massless quark from an equation of the Schrödinger type with a potential that is expressed in terms of the cross section for single hard-parton scattering in a medium. Specifically, we have

$$\frac{dE^{\rm rad}}{dx} = \frac{2\alpha_s C_R}{\pi \tau_L} \int_{\omega_{\min}}^{E} d\omega \times \left[1 - y + \frac{y^2}{2} \right] \ln |\cos(\omega_1 \tau_1)|, \quad (11)$$

$$\omega_1 = \sqrt{ i \left(1 - y + \frac{C_R}{3} y^2 \right) \bar{\kappa} \ln \frac{16}{\bar{\kappa}} }, \quad \bar{\kappa} = \frac{\mu_{\rm D}^2 \lambda_g}{\omega(1-y)}, \quad (12)$$

where $\tau_1 = \tau_L/(2\lambda_g)$, α_s is the QCD coupling constant, $y = \omega/E$ is the hard-parton energy fraction carried away by the gluon, and $C_R = 4/3$ is the quark color factor. By making the substitution $C_R = 3$ and by replacing the bracketed expression in Eq. (11) by the result obtained in [14] for gluons, a similar expression can be obtained for the gluon jet. Integration in (11) is performed with respect to the energy from the minimal gluon energy in the coherent Landau–Pomeranchuk–Migdal mode (QCD analog of the Landau–Pomeranchuk–Migdal effect in QED), $\omega_{\min} = E_{\rm LPM} = \mu_{\rm D}^2 \lambda_g$ (λ_g is the gluon range), to the maximum possible energy value, which is equal to the initial hard-parton energy E. We note that coherent Landau–Pomeranchuk–Migdal radiation causes a strong dependence of the jet energy on the angular dimension of the jet cone; at the same time, the jet energy loss by collisions is virtually independent of the angular dimension of the jet cone, since thermal particles that elastically interacted with a hard parton fly at rather large angles with respect to the jet-axis direction [36].

In a superdense system ($\rho^{1/3} \gg \Lambda_{\rm QCD}$), where color interaction is screened because of collective effects, partons are asymptotically free. This makes it possible to determine, on the basis of perturbative QCD, the dominant contribution to the differential cross section $d\sigma/dt$ for hard-parton scattering. The result is [13, 37]

$$\frac{d\sigma_{ab}}{dt} \cong C_{ab} \frac{2\pi \alpha_s^2(t)}{t^2}, \quad (13)$$

where $C_{ab} = 9/4, 1$, and $4/9$ for gg, gq, and qq scatterings, respectively;

$$\alpha_s = \frac{12\pi}{(33 - 2N_f) \ln(t/\Lambda_{\rm QCD}^2)} \quad (14)$$

is the running QCD coupling constant for N_f active quark flavors; and $\Lambda_{\rm QCD}$ is the QCD scale factor, which is on the order of the critical temperature T_c. The integrated cross section

$$\sigma_{ab} = \int_{\mu_{\rm D}^2(\tau)}^{m_0(\tau)E/2} dt \frac{d\sigma_{ab}}{dt} \quad (15)$$

is regularized at the lower limit by the square of the Debye screening mass, $\mu_{\rm D}^2 \cong 4\pi\alpha_s T^2(1 + N_f/6)$, in the high-temperature limit of perturbation theory [38].

In our calculations, we used the Bjorken scaling solution [35] for the energy density, the temperature, and the density of quark–gluon plasma for $T > T_c = 200$ MeV,

$$\varepsilon(\tau)\tau^{4/3} = \varepsilon_0 \tau_0^{4/3}, \quad (16)$$

$$T(\tau)\tau^{1/3} = T_0 \tau_0^{1/3}, \quad (17)$$

$$\rho(\tau)\tau = \rho_0 \tau_0, \quad (18)$$

and disregarded the possible insignificant contribution to the energy losses from the rescattering of hard partons in cold nuclear matter having a much lower density. For the sake of definiteness, we took the initial conditions for the formation of gluon-rich plasma that are expected for central PbPb collisions at LHC [21]: $\tau_0 \approx 0.1$ fm/c, $T_0 \approx 1$ GeV, $N_f \approx 0$, and $\rho_g \approx 1.95 T^3$. The impact-parameter (b) dependence of the initial energy density ε_0 in the nuclear-overlap region has the form [29]

$$\varepsilon_0(b) \propto T_{AA}(b)/S_{AA}(b), \quad (19)$$

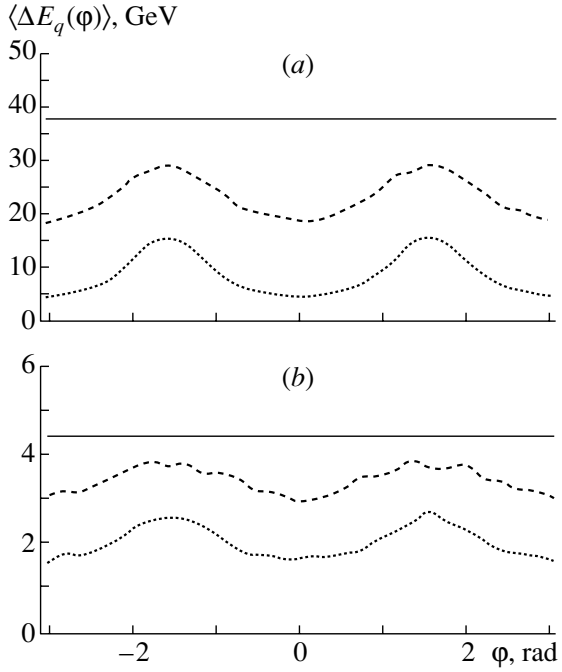

Fig. 2. Mean (a) radiative and (b) collision energy losses of a hard quark with the initial energy of $E_T^q = 100$ GeV versus the quark azimuthal angle for the impact-parameter values of $b =$ (solid curves) 0, (dashed curves) 6, and (dotted curves) 10 fm .

$$\varepsilon_0(b) = \varepsilon_0(b=0)\frac{T_{AA}(b)}{T_{AA}(b=0)}\frac{S_{AA}(b=0)}{S_{AA}(b)},$$

where the effective transverse area of the nuclear-overlap region is

$$S_{AA}(b) = \int_0^{2\pi} d\psi \int_0^{r_{\max}} r dr \qquad (20)$$

$$= \left(\pi - 2\arcsin\frac{b}{2R_A}\right)R_A^2 - b\sqrt{R_A^2 - \frac{b^2}{4}}.$$

That, in the nuclear-overlap region, the initial energy density ε_0 (19) depends only slightly on the impact parameter b ($\delta\varepsilon_0/\varepsilon_0 \lesssim 10\%$) up to $b \sim R_A$ and decreases fast for $b \gtrsim R_A$ is an interesting result obtained in [29]. At the same time, the quantity $\langle\tau_L\rangle$ deduced by averaging, over all production vertices, the time (7) of hard-parton escape from the dense region decreases nearly in inverse proportion to increasing b. This means that, for impact-parameter values in the region $b < R_A$—approximately 60% of dijets are produced in events characterized by such impact parameters—the difference in the intensity of rescattering and in the corresponding energy loss is determined almost completely by the different values of the distance traveled in the dense medium, but not by different values of ε_0.

Figure 2 shows the mean medium-induced (a) radiative and (b) collision energy losses of a hard quark of initial energy $E_T^q = 100$ GeV versus the quark azimuthal angle with respect to the reaction plane at the impact-parameter values of $b = 0$, 6, and 10 fm. It should be noted that the initial-quark-energy scale of $E_T^q \sim 100$ GeV corresponds to the threshold above which it becomes possible to single out, in heavy-ion collisions at LHC, hard QCD jets against the background of spurious jets (statistical fluctuations of the transverse-energy flux that are due to a formidable particle multiplicity in an event) with a fairly high reconstruction efficiency [27]. As might have been expected, the azimuthal asymmetry of the energy losses becomes more pronounced with increasing impact parameter b because the volume becomes more asymmetric, although the mean value of the losses decreases since the mean distance that the jet travels in the medium becomes smaller (for $b \gtrsim R_A$, the initial energy density of the medium begins to decrease significantly). A nonuniform azimuthal-angle dependence of the jet energy losses in semicentral heavy-ion collisions must lead to an azimuthal asymmetry of the spectrum of such jets.

3. AZIMUTHAL ASYMMETRY OF THE JET SPECTRUM IN NONCENTRAL NUCLEUS–NUCLEUS COLLISIONS

The azimuthal-angle distribution of the number of ij dijets having transverse momenta p_{T1} and p_{T2} and originating from initial hard-scattering processes in AA interactions at an impact parameter b can be represented in the form

$$\frac{dN_{ij}}{dp_{T1}dp_{T2}d\varphi_1 d\varphi_2}(b) = \frac{1}{(2\pi)^2}\int_0^{2\pi} d\psi \qquad (21)$$

$$\times \int_0^{r_{\max}} r dr T_A(r_1)T_A(r_2)\int dp_T^2 \frac{d\sigma_{ij}}{dp_T^2}$$

$$\times \delta(p_{T1} - p_T + \Delta E_T^i(r,\psi,\varphi_1,b))$$

$$\times \delta(p_{T2} - p_T + \Delta E_T^j(r,\psi,\varphi_2,b)),$$

where the cross section $d\sigma_{ij}/dp_T^2$ for hard parton–parton scattering in the c.m. frame was calculated on the basis of the PYTHIA model [39] with the structure function taken in the form of the STEQ2L parametrization

$$\frac{d\sigma_{ij}}{dp_T^2} = K\int dx_1 \int dx_2 \int d\hat{t} f_i(x_1, p_T^2) \qquad (22)$$

$$\times f_j(x_2, p_T^2)\frac{d\hat{\sigma}_{ij}}{d\hat{t}}\delta(p_T^2 - \frac{\hat{t}\hat{u}}{\hat{s}}).$$

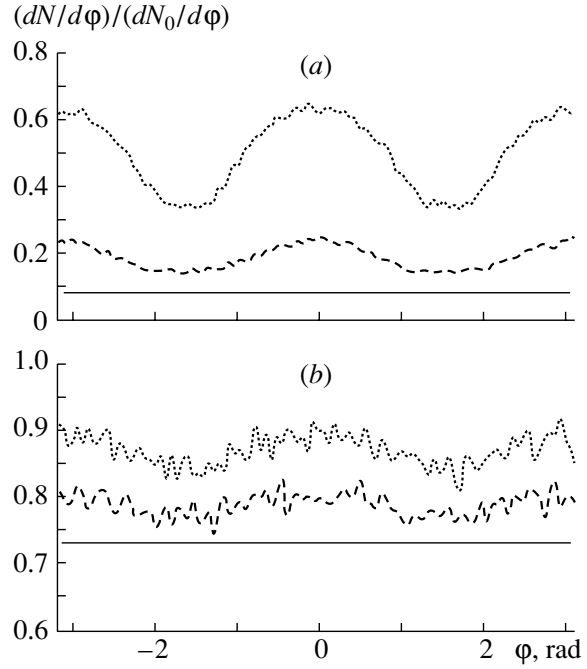

Fig. 3. Azimuthal-angle distribution of $E_T^{\rm jet} > 100$ GeV jets in the rapidity region $|y^{\rm jet}| < 2.5$ (a) with allowance for collision and radiative energy losses and (b) with allowance for only collision energy losses at $b =$ (solid lines) 0, (dashed-line histograms) 6, and (dotted-line histograms) 10 fm.

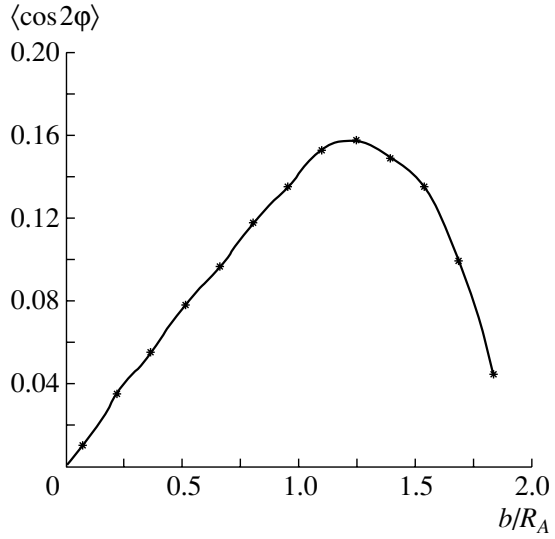

Fig. 4. Jet elliptic-anisotropy coefficient $\langle\cos 2\varphi\rangle$ with allowance for collision and radiative energy losses as a function of the impact parameter.

Here, $d\hat{\sigma}_{ij}/d\hat{t}$ is the differential parton–parton cross section as a function of the kinematical Mandelstam variables $\hat{s}$, $\hat{t}$, and $\hat{u}$; $f_{i,j}$ are the structure functions for the i and j partons; x is the total-nucleon-momentum fraction carried away by a given parton; and the coefficient K takes into account higher order corrections in α_s ($K \sim 1$ for $p_T \geq 50$ GeV/c jets whose typical angular cone dimension is 0.3–0.5 [29]). We note that the inclusion of the initial bremsstrahlung from a hard parton within PYTHIA results in that the jet azimuthal angles no longer satisfy the simple relation $\varphi_1 + \varphi_2 = \pi$.

For the impact-parameter values of $b = 0$, 6, and 10 fm, Fig. 3 shows the azimuthal-angle ($\varphi = \varphi_{1,2}$) distribution of jets (a) for the case where both collision and radiative energy losses are taken into account and (b) for the case where only collision energy losses are taken into account. Only dijets for which the transverse energy of each jet was greater than 100 GeV and the rapidity lay in the region $|y^{\rm jet}| < 2.5$ were selected. The distributions were normalized to the initial azimuthal-angle distributions of jets (without energy losses) in PbPb collisions. We note that, in the kinematical range being considered, approximately 60, 30, and 10% of jets are produced in hard gluon–gluon scattering ($gg \to gg$), quark–gluon scattering ($qg \to qg$), and quark–quark scattering and gluon–gluon annihilation into two quarks ($qq, gg \to qq$), respectively. We can see that the azimuthal asymmetry (the jet yield is maximal at $\varphi = 0$ and is minimal at $\varphi = \pm\pi/2$) is enhanced upon going over from central to semicentral collisions because the volume becomes more asymmetric, although the absolute value of the suppression of the jet yield decreases with increasing b. For jets of finite angular dimension, it is natural to expect that the result would be intermediate between that in case (a) and that in case (b) because, as was mentioned in the preceding section, the radiative loss is dominant at small angular dimensions of the jet cone, $\theta_0(\to 0)$, while the relative contribution of the collision loss grows with increasing θ_0 [36].

In noncentral collisions, the φ distribution of jets is well approximated by the dependence

$$\frac{dN}{d\varphi} = A(1 + B\cos 2\varphi), \qquad (23)$$

where $A = 0.5(N_{\max} + N_{\min})$ and $B = (N_{\max} - N_{\min})(N_{\max} + N_{\min})^{-1} = 2\langle\cos 2\varphi\rangle$. The mean value of the cosine of 2φ for the particle flux is often referred to as the elliptic-anisotropy coefficient v_2 [30–34, 40]. Figure 4 displays the impact-parameter dependence of the jet elliptic-anisotropy coefficient $\langle\cos 2\varphi\rangle$ for the case where both collision and radiative energy losses are taken into account. Within the model used, the azimuthal-asymmetry effect increases with b almost linearly, reaching a maximum value at $b \sim 1.2R_A = 8.2$ fm, whereupon the jet elliptic-anisotropy coefficient decreases in the region of b values where the

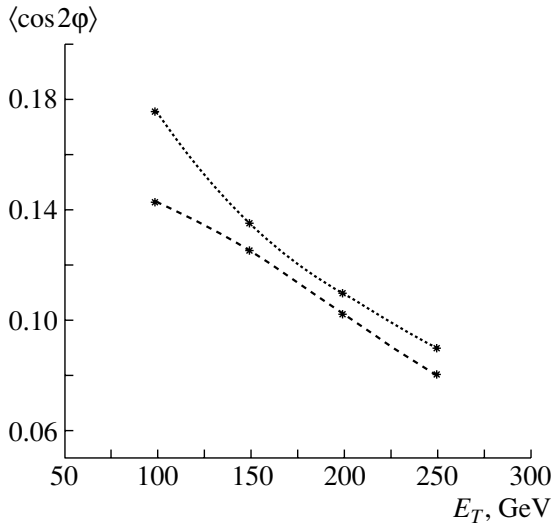

Fig. 5. Jet elliptic-anisotropy coefficient $\langle \cos 2\varphi \rangle$ with allowance for both collision and radiative energy losses as a function of the initial transverse energy E_T of a jet at the impact-parameter values of $b =$ (dashed curve) 6 and (dotted curve) 10 fm.

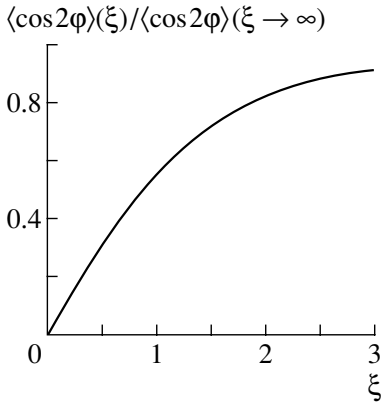

Fig. 6. Ratio of the jet elliptic-anisotropy coefficient $\langle \cos 2\varphi \rangle$ as a function of the parameter ξ that characterizes the accuracy in determining the azimuthal angle of the reaction plane to the value of $\langle \cos 2\varphi \rangle$ for $\xi \to \infty$.

effect of the reduction of the jet energy loss due to a decrease in the effective dimension of the dense region and in the initial energy density of the medium becomes crucial and is not compensated by the increase in the degree of asymmetry of the volume.

The transverse-momentum (p_T) dependence of the elliptic-anisotropy coefficient is yet another interesting characteristic of the azimuthal asymmetry; its behavior for the flux of particles within hydrodynamic models [40] (linear or quadratic growth of v_2 with p_T) differs qualitatively from that within the models where the elliptic flux stems from the fragmentation of minijets losing energy in the asymmetric volume [34] (reduction of v_2 with increasing p_T). For the impact-parameter values of $b = 6$ and 10 fm, the elliptic-anisotropy coefficient $\langle \cos 2\varphi \rangle$ as a function of the initial transverse energy E_T of a jet is shown in Fig. 5 for the cases where collision and radiative energy losses are taken into account. It can be seen that, with increasing E_T, the azimuthal asymmetry of jets decreases (for collisions characterized by a higher degree of centrality, this decrease is more gently sloping). This can be explained by the fact that the energy losses, which are weakly dependent on E_T, have a less pronounced effect on the yield of jets with high values of the initial energy.

To conclude this section, we note that the impact parameter can be determined experimentally by measuring the transverse-energy flux with the aid of the calorimetric system of the facility used—for example, to within 1 to 2 fm in PbPb collisions at LHC [27, 41]. Thus, the observation of the azimuthal asymmetry of jets in various intervals of the detected transverse energy can carry information about the intensity of parton rescattering in a medium and can serve as a signal of the quark and gluon energy losses in an asymmetric volume of quark–gluon plasma.

4. DETERMINATION OF THE REACTION-PLANE ANGLE FOR A NUCLEUS–NUCLEUS COLLISION FROM THE FLUX OF SEMIHARD PARTICLES

In order to perform an inclusive analysis of jet production versus the azimuthal angle, it is necessary to determine the reaction-plane angle in each event. So far, the existing methods for determining the reaction-plane angle, which were summarized in [30], have been applied to heavy-ion collisions in order to investigate the elliptic flux of soft particles ($p_T \leq 2$ GeV/c) in experiments at SPS [31] and RHIC [32]. The resulting pattern of the elliptic flux of soft particles proved to be in qualitative agreement with the predictions of hydrodynamic models [40].

It was shown in [30] that, if there are no correlations between particles, the distribution in the reaction-plane angle Ψ_n measured on the basis of the nth harmonic of the particle flux (see below) with respect to the true angle Ψ^0 is independent of Ψ^0 and has the form

$$\frac{dN}{d(n\Psi_n)} = \frac{1}{2\pi}\left\{ e^{-\xi^2/2} + \xi\sqrt{\frac{\pi}{2}}\cos(n\Psi_n) \right. \quad (24)$$

$$\left. \times \left[e^{-\xi^2 \sin^2 (n\Psi_n)/2} \left(1 + \mathrm{erf}\left(\frac{\xi \cos (n\Psi_n)}{\sqrt{2}} \right) \right) \right] \right\},$$

where the dimensionless parameter ξ depending on the multiplicity of particles and on the degree of their anisotropy characterizes the precision in determining the azimuthal reaction-plane angle: $\Psi_n \to 0$ for $\xi \to \infty$. Figure 6 shows the ratio of the "observed" jet elliptic-anisotropy coefficient $\langle \cos 2\varphi \rangle$ as a function of the parameter ξ for $n = 2$ to the idealized value of $\langle \cos 2\varphi \rangle$ for $\xi \to \infty$. We note that this dependence has a universal character for different absolute values of the jet elliptic-anisotropy coefficient $\langle \cos 2\varphi \rangle$; this can be demonstrated analytically, provided that the approximation (23) of the azimuthal-angle distribution of jets is valid (see also [30]). By way of example, we indicate that the value of $\xi = 2.5$ leads to a decrease in the observed effect of jet azimuthal asymmetry by 10% and that the value of $\xi = 0.8$ corresponds to a 50% reduction of the effect (see Fig. 6).

As was noted in the Introduction, jet production in heavy-ion collisions can be analyzed in an experiment with the CMS detector, which will be installed at the LHC collider under construction at CERN and which can be optimized, in particular, for precisely measuring the properties of hard-hadron jets [27, 28]. The special features of CMS make it possible to measure, to a fairly high precision, the momenta of charged particles from heavy-ion collisions with the aid of a tracking system only from relatively high values of p_T. Nevertheless, the reaction-plane angle can be determined, in principle, on the basis of the flux of such semihard particles (which do not belong to hard dijets) owing to the following two factors: a rather high multiplicity of these particles at the LHC energy (it is commensurate with the multiplicity of soft particles at the SPS energy) and the sensitivity of semihard particles, which originate predominantly from the fragmentation of gluons emitted in the asymmetric volume, to the azimuthal asymmetry of noncentral nucleus–nucleus interactions [33, 34].

For the nth harmonic, the azimuthal reaction-plane angle Ψ_n can be derived from the equation [30]

$$\tan n\Psi_n = \frac{\sum_i \omega_i \sin n\varphi_i}{\sum_i \omega_i \cos n\varphi_i}, \qquad (25)$$

where φ_i is the azimuthal angle of the ith particle and ω_i is its weight, the sum being taken over all particles that are used to determine the reaction plane. It should be noted that the weights are optimized in order to achieve the highest precision in determining the reaction-plane angle. Sometimes, this can be done by choosing particles of a specific type or by using the transverse momenta of particles as weights (see [42] for details). We also note that the reaction-plane angle Ψ_n determined by using the nth harmonic falls within the range $-\pi/n \le \Psi_n \le \pi/n$.

In order to illustrate the applicability of the methods for determining the reaction-plane angle, we employed the HIJING Monte Carlo model [43] for nucleus–nucleus interactions, which is based on combining the multiparticle production of minijets within perturbative QCD with the scheme of soft string interactions and hadronization of the Lund type. The interaction of partons in dense matter is simulated as constant energy losses per unit length ($dE/dx = 1$ GeV/fm for a quark and twice that value for a gluon), which are accompanied by a collinear splitting of the emitted gluon from the primary parton.

Since the distribution of semihard particles in the HIJING model used here is elliptically anisotropic, we determined the reaction-plane angle on the basis of the second harmonic—$n = 2$ in Eq. (25). An equivalent method for determining the reaction-plane angle consists in using the maximum principle for the quantity

$$\sum_i \frac{p_{xi}^2 - p_{yi}^2}{p_{xi}^2 + p_{yi}^2} = \sum_i \cos 2(\varphi_i - \Psi_2) \qquad (26)$$

with respect to the angle Ψ_2. For weights, we used $\omega_i = 1$, $\omega_i = p_{ti}$, and $\omega_i = p_{ti}^2$.

For the mean multiplicity of $p_T > 2$ GeV/c, $|\eta| < 2.4$ charged particles (for the sake of definiteness, use is made here of the estimate of the CMS acceptance), the HIJING model predicts the value of $\langle n^{\pm} \rangle \approx 160$ for semicentral PbPb collisions ($b = 6$ fm) at $\sqrt{s} = 5.5$ TeV per nucleon. The best precision in determining the reaction-plane angle in semicentral collisions was achieved at the weights chosen to be $\omega_i = p_{Ti}$; albeit not high, $\xi \sim 0.5$, it is quite acceptable (see Fig. 6). It can be hoped that this precision can be improved by further optimizing the weights ω_i. Moreover, the result that we obtained for ξ is nothing but a lower bound, since the current version of HIJING gives no way to increase the quark energy losses above $dE/dx = 1$ GeV/fm. At the same time, much higher values of the energy losses are expected at the LHC energy (see, for example, [14, 16, 17, 24] and Fig. 2 in the present study), and this would result in the enhancement of the azimuthal anisotropy of semihard particles and, hence, in the improvement of the accuracy in determining the reaction-plane angle.

5. CONCLUSION

We have considered the emergence of the azimuthal asymmetry of the hadron-jet spectrum as a possible signal of the rescattering and energy losses of jet partons in an asymmetric volume of dense quark–gluon matter formed in the region of the initial nuclear overlap in collisions with a nonzero impact parameter.

In order to investigate the azimuthal-angle distribution of jets, it is sufficient to know the jet azimuthal angle with respect to the reaction-plane angle—a precise measurement of the primary jet energy is not required. The elliptic-anisotropy coefficient $\langle \cos 2\varphi \rangle$ for $E_T \geq 100$ GeV jets that was estimated in the present article for semicentral PbPb collisions at the LHC energy ranges between 0.01 and 0.16, depending on the mechanism of the energy losses and on the angular dimension of the jet cone and becoming somewhat less with increasing jet energy.

In order to perform the inclusive analysis of jet production versus the azimuthal angle, it is necessary to determine the reaction-plane angle in each event. The existing methods that make it possible to do this are based on the analysis of the elliptic flux of soft particles ($p_T \leq 2$ GeV/c). We have shown that the reaction-plane angle in semicentral PbPb collisions at the LHC energy can in principle be determined by using the flux of semihard particles ($p_T \gtrsim 2$ GeV/c). This possibility is due to the sensitivity of semihard particles, which are predominantly produced in the fragmentation of gluons emitted in an asymmetric volume, both to the azimuthal asymmetry of noncentral nucleus–nucleus interactions and to a fairly high multiplicity of these particles in an event.

ACKNOWLEDGMENTS

We are grateful to V.V. Uzhinskii for numerous discussions and for placing the modified version of the HIJING model at our disposal. Thanks are also due to P. Filip, U. Wiedemann, and O.L. Kodolova for enlightening discussions.

REFERENCES

1. J. Engels *et al.*, Phys. Lett. B **396**, 210 (1997); E. Laermann, Fiz. Élem. Chastits At. Yadra **30**, 720 (1999) [Phys. Part. Nucl. **30**, 304 (1999)].
2. H. Satz, Phys. Rep. **88**, 349 (1982).
3. I. L. Rozental' and Yu. A. Tarasov, Usp. Fiz. Nauk **163** (7), 29 (1993) [Phys. Usp. **36**, 572 (1993)].
4. J. W. Harris and B. Müller, Annu. Rev. Nucl. Part. Sci. **46**, 71 (1996).
5. I. P. Lokhtin, L. I. Sarycheva, and A. M. Snigirev, Fiz. Élem. Chastits At. Yadra **30**, 660 (1999) [Phys. Part. Nucl. **30**, 279 (1999)].
6. S. A. Bass, M. Gyulassy, H. Stöcker, and W. Greiner, J. Phys. G **25**, R1 (1999).
7. T. Matsui and H. Satz, Phys. Lett. B **178**, 416 (1986).
8. D. Kharzeev and H. Satz, Phys. Lett. B **334**, 155 (1994).
9. NA 50 Collab. (M. C. Abreu *et al.*), Phys. Lett. B **410**, 337 (1997); **450**, 456 (1999).
10. R. Vogt, Phys. Rep. **310**, 197 (1999).
11. R. Baier, D. Schiff, and B. G. Zakharov, Annu. Rev. Nucl. Part. Sci. **50**, 37 (2000).
12. M. G. Ryskin, Yad. Fiz. **52**, 219 (1990) [Sov. J. Nucl. Phys. **52**, 139 (1990)].
13. M. Gyulassy and X.-N. Wang, Nucl. Phys. B **420**, 583 (1994); X.-N. Wang, M. Gyulassy, and M. Plümer, Phys. Rev. D **51**, 3436 (1995).
14. R. Baier *et al.*, Phys. Lett. B **345**, 277 (1995); Nucl. Phys. B **483**, 291 (1997); **531**, 403 (1998); Phys. Rev. C **58**, 1706 (1998).
15. B. G. Zakharov, Pis'ma Zh. Éksp. Teor. Fiz. **64**, 737 (1996) [JETP Lett. **64**, 781 (1996)]; **65**, 585 (1997) [**65**, 615 (1997)]; **70**, 181 (1999) [**70**, 176 (1999)]; Yad. Fiz. **61**, 924 (1998) [Phys. At. Nucl. **61**, 838 (1998)].
16. U. Wiedemann and M. Gyulassy, Nucl. Phys. B **560**, 345 (1999); U. Wiedemann, Nucl. Phys. B **588**, 303 (2000); hep-ph/0008241.
17. M. Gyulassy, P. Levai, and I. Vitev, Nucl. Phys. B **594**, 371 (2001).
18. J. D. Bjorken, Fermilab Preprint 82/29-THY (1982).
19. S. Mrówczyński, Phys. Lett. B **269**, 383 (1991); M. H. Thoma, Phys. Lett. B **273**, 128 (1991).
20. I. P. Lokhtin and A. M. Snigirev, Yad. Fiz. **60**, 360 (1997) [Phys. At. Nucl. **60**, 295 (1997)]; Z. Phys. C **73**, 315 (1997).
21. K. J. Eskola, K. Kajantie, and P. V. Ruuskanen, Phys. Lett. B **332**, 191 (1994); Eur. Phys. J. C **1**, 627 (1998); K. J. Eskola, Prog. Theor. Phys. Suppl. **129**, 1 (1997); Comments Nucl. Part. Phys. **22**, 185 (1998); K. J. Eskola and K. Tuominen, Phys. Lett. B **489**, 329 (2000); K. J. Eskola, K. Kajantie, P. V. Ruuskanen, and K. Tuominen, Nucl. Phys. B **570**, 379 (2000).
22. M. Gyulassy and M. Plümer, Phys. Lett. B **243**, 432 (1990).
23. M. Gyulassy, M. Plümer, and X.-N. Wang, Nucl. Phys. A **590**, 511 (1995).
24. I. P. Lokhtin, L. I. Sarycheva, and A. M. Snigirev, Yad. Fiz. **62**, 1333 (1999) [Phys. At. Nucl. **62**, 1258 (1999)].
25. V. Kartvelishvili, R. Kvatadze, and R. Shanidze, Phys. Lett. B **356**, 589 (1995).
26. X.-N. Wang, Z. Huang, and I. Sarcevic, Phys. Rev. Lett. **77**, 231 (1996).
27. M. Bedjidian *et al.*, CERN CMS Note 2000/060 (2000).
28. CMS Collab., Technical Proposal, CERN/LHCC 94-38.
29. I. P. Lokhtin and A. M. Snigirev, Yad. Fiz. **64**, 1563 (2001) [Phys. At. Nucl. **64**, 1487 (2001)].
30. S. Voloshin and Y. Zhang, Z. Phys. C **70**, 665 (1996); A. M. Poskanzer and S. A. Voloshin, Phys. Rev. C **58**, 1671 (1998).
31. NA49 Collab. (H. Appelshäuser *et al.*), Phys. Rev. Lett. **80**, 4136 (1998).
32. STAR Collab. (K. H. Ackermann *et al.*), Phys. Rev. Lett. **86**, 402 (2001).
33. A. S. Galoyan and V. V. Uzhinskii, hep-ph/0007122.
34. X.-N. Wang, nucl-th/0009019; M. Gyulassy, I. Vitev, and X.-N. Wang, nucl-th/0012092.
35. J. D. Bjorken, Phys. Rev. D **27**, 140 (1983).
36. I. P. Lokhtin and A. M. Snigirev, Phys. Lett. B **440**, 163 (1998).

37. M. G. Mustafa, D. Pal, D. K. Srivastava, and M. Thoma, Phys. Lett. B **428**, 234 (1998).
38. S. Nadkarni, Phys. Rev. D **33**, 3738 (1986).
39. T. Sjostrand, Comput. Phys. Commun. **82**, 74 (1994).
40. P. F. Kolb, J. Solfrank, and U. Heinz, Phys. Rev. C **62**, 054909 (2000); P. F. Kolb, P. Huovinen, U. Heinz, and H. Heiselberg, hep-ph/0012137.
41. M. V. Savina, S. V. Shmatov, N. V. Slavin, and P. I. Zarubin, Yad. Fiz. **62**, 2263 (1999) [Phys. At. Nucl. **62**, 2084 (1999)].
42. P. Danielewicz, Phys. Rev. C **51**, 716 (1995).
43. M. Gyulassy and X.-N. Wang, Comput. Phys. Commun. **83**, 307 (1994).

Translated by A. Isaakyan

Physics of Atomic Nuclei, Vol. 65, No. 5, 2002, pp. 953–958. Translated from Yadernaya Fizika, Vol. 65, No. 5, 2002, pp. 984–989.

ELEMENTARY PARTICLES AND FIELDS
Theory

On Coefficients of the Brody–Moshinsky Type

K. J. Yankauskas*

Klaipeda University, 5805 Klaipeda, Lithuania

Received November 1, 2000; in final form, April 24, 2001

Abstract—Brody–Moshinsky coefficients of the axial type are introduced. It is shown that Brody–Moshinsky coefficients represent a particular case of Petrauskas coefficients. Analytic expressions for some sums of Petrauskas coefficients are obtained, and the examples of their application to calculating matrix elements are given. A number of analytic expressions for axial Petrauskas coefficients are presented in the Appendix. © *2002 MAIK "Nauka/Interperiodica".*

1. INTRODUCTION

Calculations dealing with the spectroscopy of nuclei widely employ not only Brody–Moshinsky coefficients [1] in translation-invariant bases of the $U(3(A-1))$ scheme [2, 3] (A is the number of nucleons in a nucleus) and in allied models (the K-harmonic method [4, 5], the method of generalized hyperspherical harmonics [6], and so on) but also their modifications and generalizations. In this article, we give a review of all these coefficients. More specifically, we present expressions for them, study relationships between coefficients of different types, find some of their sums, discuss the problem of phase matching, and propose a terminology for coefficients of various types.

This article is organized as follows. In Section 2, we introduce Brody–Moshinsky coefficients of the axial type and derive some expressions for them. In Section 3, we present expressions for two types of Petrauskas coefficients and show their relationship with the corresponding Brody–Moshinsky coefficients. Using the bases of the $U(3(A-1))$ scheme, we calculate radial integrals for harmonic-oscillator functions in the $3(A-1)$-dimensional system of spherical coordinates {in the bases adapted to describing deformed nuclear states [3, 5] in $(A-1)$-dimensional subspaces associated with the coordinates x, y, and z}. Expansion of the above integrals in terms of Talmi integrals (or Talmi-type ones) is performed by using coefficients that were considered for the first time by A.K. Petrauskas and his collaborators (it is natural to call them Petrauskas coefficients). In Section 4, we obtain a number of analytic expressions for Petrauskas coefficients and for some sums of these coefficients and present a few examples of their application (in particular, such sums are employed in calculating matrix elements). In the Appendix, analytic expressions for axial Petrauskas coefficients are given for a number of cases frequently occurring in spectroscopic calculations.

2. TYPES OF BRODY–MOSHINSKY COEFFICIENTS

In representing radial integrals $I_{\epsilon l\epsilon' l'}$ that are calculated for states of a three-dimensional harmonic oscillator in terms of Talmi integrals,

$$I_{\epsilon l\epsilon' l'} = \sum_p \langle \epsilon l \epsilon' l' | p \rangle I_p, \tag{1}$$

we employ the well-known Brody–Moshinsky coefficients [1]

$$\langle \epsilon l \epsilon' l' | p \rangle = \Gamma(p+3/2) \times \sum_{m,m'}^{N,N'} \frac{(-1)^{p-(l+l')2}[N!N'!\Gamma(N+l+3/2)\Gamma(N'+l'+3/2)]^{1/2}}{(N-m)!(N'-m')!m!m'!|\Gamma(l+m+3/2)\Gamma(l'+m'+3/2)}. \tag{2}$$

Here, $N=(\epsilon-l)/2$, $N'=(\epsilon'-l')/2$, and the condition

$$m+m' = p-(l+l')/2 \tag{3}$$

must be satisfied, which implies that summation is actually performed over only one index. In (1), p takes the following values: $p=(l+l')/2, (l+l')/2+1, \ldots, (\epsilon+\epsilon')/2$.

*e-mail: fizkat@jtf.ku.lt

1063-7788/02/6505-0953$22.00

In bases that are adapted to describing deformed nuclear states [3], we calculate integrals involving functions of three one-dimensional (in subspaces associated with the axes x, y, and z) harmonic oscillators,

$$I_{\boldsymbol{\epsilon}\boldsymbol{\epsilon}'} = \int_{-\infty}^{\infty}\int\prod_i d\rho_i H_{\epsilon_i}(\rho_i)O(c\rho)\prod_i H_{\epsilon'_i}(\rho_i) \quad (4)$$
$$(i = x, y, z).$$

Hereafter, vectors stand for triples of numbers—that is, $\epsilon = (\epsilon_x\epsilon_y\epsilon_z)$; $H_{\epsilon_i}(\rho_i)$ are Hermite polynomials; the numbers ϵ_x, ϵ_y, and ϵ_z specify the distribution of the oscillator quanta ϵ ($\epsilon = \epsilon_x + \epsilon_y + \epsilon_z$) among the axes x, y, and z and characterize the separated-quasiparticle functions depending on the Jacobi coordinates ρ_i ($\rho^2 = \rho_x^2 + \rho_y^2 + \rho_z^2$); $O(c\rho)$ is an arbitrary translation-invariant one- or two-particle operator {$c = -[(A-1)/A]$ or $c = 2^{1/2}$ for one- or two-particle operators, respectively}. In the expansion

$$I_{\boldsymbol{\epsilon}\boldsymbol{\epsilon}'} = \sum_{\mathbf{P}}\langle\boldsymbol{\epsilon}\boldsymbol{\epsilon}'|\mathbf{p}\rangle I_{\mathbf{p}} \quad (5)$$

of the integrals in (4) in Talmi-type integrals

$$I_{\mathbf{p}} = \prod_{i'}\frac{2}{\Gamma(p_{i'}+1/2)a^{2p_{i'}+1}} \quad (6)$$
$$\times\int_0^{\infty}\int\prod_i d\rho_i\rho_i^{2p_i}e^{-\rho_i^2/a^2}O(c\rho)$$

(here, a is a scale parameter), there appear the coefficients $\langle\boldsymbol{\epsilon}\boldsymbol{\epsilon}'|\mathbf{p}\rangle$ of the Brody–Moshinsky type [7], which are given by

$$\langle\boldsymbol{\epsilon}\boldsymbol{\epsilon}'|\mathbf{p}\rangle = \prod_{i=x,y,z}\langle\epsilon_i\epsilon'_i|p_i\rangle = \prod_i\frac{2^{2p_i-\epsilon_i-k_i}}{\pi^{1/2}}\Gamma(p_i+1/2)[\epsilon_i!(\epsilon_i+2k_i)!]^{1/2}(-1)^{\epsilon_i-p_i} \quad (7)$$
$$\times\sum_{s_i=\max(0,\epsilon_i-[\epsilon_i/2]-p_i)}^{\min([\epsilon_i/2],\epsilon_i+k_i-p_i)}\frac{1}{s-i!(\epsilon_i+k_i-s_i-p_i)!(\epsilon_i-2s_i)!(2p_i+2s_i-\epsilon_i)!},$$

where $\epsilon'_i = \epsilon_i + 2k_i$ and the parameter p_i can take the values of $p_i = (\epsilon_i+\epsilon'_i)/2, \ldots, 1$, or 0 (the symbol $[\epsilon_i/2]$ stands for the integral part of $\epsilon_i/2$). The coefficients given by (7) will be referred to as axial Brody–Moshinsky coefficients. It is worth noting that the phase of the coefficients (7) is matched with that of the axial Petrauskas coefficients $D^{\mathbf{N}l\mathbf{N}'l'}_{\mathbf{p},\boldsymbol{\alpha}}$ (see Section 3 below) and differs from the phase in (2.8) from [7] by the factor $(-1)^{k_i}$. A set of analytic expressions for the coefficients $\langle\epsilon l\epsilon' l'|p\rangle$ and $\langle\boldsymbol{\epsilon}\boldsymbol{\epsilon}'|\mathbf{p}\rangle$ can be obtained by means of a direct summation in (2) and (7) and can be found in [3], along with tables of their numerical values.

It can be shown that the axial Brody–Moshinsky coefficients $\langle\epsilon_i\epsilon'_i|p_i\rangle$ satisfy another formula, that which is obtained from (2) upon replacing 3/2 by 1/2 in the arguments of Γ functions and making the substitution $l = l' = l_{\min}$ ($l_{\min} = 0$ or 1 for even or odd ϵ_i, respectively).

3. RELATIONSHIP BETWEEN PETRAUSKAS AND BRODY–MOSHINSKY COEFFICIENTS

Petrauskas coefficients appear in the expansion of radial integrals [calculated for the oscillator functions depending on $3(A-1)$-dimensional distance ρ] in terms of Talmi integrals and have the form [8]

$$D_{p,\alpha}^{Nl_KN'l'_K} = \frac{[\Gamma(N+l_K+3/2)\Gamma(N'+l'_K+3/2)N!N'!]^{1/2}}{\alpha!} \quad (8)$$
$$\times\frac{\Gamma((l_K+l'_K)/2+3/2)\cdot\Gamma(p+\alpha+3/2)}{\Gamma((l_K+l'_K)/2-p)\Gamma(p+3/2)}\sum_{m.m',s}^{N,N',m+m'}(-1)^{m+m'}$$
$$\times\frac{(m+m')!\Gamma((l_K+l'_K)/2-p+s)}{s!m!m'!(N-m)!(N'-m')!\Gamma(l_K+m+3/2)\Gamma(l'_K+m'+3/2)},$$

where $N = (E-K)/2$, $N' = (E'-K')/2$, $l_K = K + 3(A-2)/2$, $l'_K = K' + 3(A-2)/2$, and $K' = K + 2n$ ($n = 0, 1, \ldots$). Here, E and K are the number of oscillator quanta and the multidimensional

angular momentum, respectively. These numbers also label irreducible representations of the $U(3(A-1))$ and $O(3(A-1))$ groups, respectively. The Petrauskas coefficients depend on two variables, p and α. The integer-valued variables p and α can take the following values: $p = 0, 1, 2, \ldots, (l_K + l'_K)/2$ and $\alpha = 0, 1, \ldots, N + N'$. The constraint

$$m + m' - s = \alpha \tag{9}$$

is imposed on summation in (8), so that it is actually performed over two indices. The coefficients in (8) obviously satisfy the symmetry relation

$$D_{p,\alpha}^{Nl_KN'l'_K} = D_{p,\alpha}^{N'l'_KNl_K}. \tag{10}$$

In spectroscopic calculations employing bases that are adapted to describing deformed nuclear states [such as the generalized orthogonal scheme or the $SU(3)$ canonical basis of the unitary scheme]—in particular, in equations for the $SU(3)$-irreducible density matrix for excited $U(3(A-1))$ states [3]—use is made of the axial Petrauskas coefficients [3, 7]

$$D_{\mathbf{p},\boldsymbol{\alpha}}^{\mathbf{Nl\,N'l'}} = \prod_{i=x,y,z} D_{p_i,\alpha_i}^{N_il_{K_i}N'_il'_{K_i}}. \tag{11}$$

The coefficients in (11) appear in the expansions of the integrals in (5) [calculated with radial harmonic-oscillator functions depending on multidimensional distances ρ_x, ρ_y, and ρ_z in $(A-1)$-dimensional subspaces associated with the Jacobi coordinates X, Y, and Z] in terms of Talmi-type integrals. A formula for the factors $D^{N_il_{K_i}N'_il'_{K_i}}$ can be obtained from (8) upon replacing 3/2 by 1/2 in the arguments of the Γ functions involved and setting $l_{K_i} = K_i + (A-2)/2$.

In spectroscopic calculations [for example, in calculating the $SU(3)$-irreducible density matrix for excited $U(3(A-1))$ states], it is often more convenient to use the coefficients $\tilde{D}_{p_i,\alpha_i} = N_{K_iK'_i}D_{p_i,\alpha_i}$, which differ from D_{p_i,α_i} by the factor

$$N_{K_iK'_i} = \frac{[\Gamma(l_{K_i} + 1/2)\Gamma(l'_{K_i} + 1/2)]^{1/2}}{\Gamma((l_{K_i} + l'_{K_i})/2 + 1/2)}. \tag{12}$$

In the Appendix, analytic expressions for the coefficients $\tilde{D}^{N_il_{K_i}N'_il'_{K_i}}$ are given at $l'_i = l_{K_i}$, $l_{K_i} + 2$, $l_{K_i} + 4$, and $l_{K_i} + 6$ for $N_i + N'_i \leq 3$. More complete tables can be found in [3].

The coefficients $D_{p,\alpha}$ and $D_{\mathbf{p},\boldsymbol{\alpha}}$ represent a generalization of the Brody–Moshinsky coefficients given by (2) and (7). We will now show that expression (2) for the Brody–Moshinsky coefficients is a particular case of expression (8). For this, we consider that the Petrauskas coefficients for $p = p_{\max} = (l_K + l'_K)/2$ use $p_{\max} + \alpha$ instead of α; upon introducing the notation p for $p_{\max} + \alpha$ and considering that, in the 3-dimension case, $K = l$ and $K' = l'$, we then indeed obtain expression (2) from (8). Summation over s is removed since, in the case of $p = p_{\max} + \alpha$, the constraint in (3) for the coefficients in (2) leads to $m + m' = \alpha$ and $s = 0$.

Similarly, it can easily be shown that the axial Brody–Moshinsky coefficients (7) represent a particular case of the coefficients in (11).

4. SOME SUMS OF PETRAUSKAS COEFFICIENTS

In calculating matrix elements with allowance for excited $U(3(A-1))$ states, it is necessary to know the sums

$$\sum_\alpha D_{p,\alpha}^{Nl_KN'l'_K} = S(Nl_KN'l'_K), \tag{13}$$

$$\sum_\alpha \alpha D_{p,\alpha}^{Nl_KN'l'_K} = S_1(pNl_KN'l'_K). \tag{14}$$

The general form of the functions S and S_1 is not known. In contrast to the sum in (14), that in (13) is independent of the parameter p. At $l_K = l'_K$, the following equality (normalization condition) holds:

$$S(Nl_KN'l_K) = \delta(N, N'). \tag{15}$$

In the cases of $l'_K = l_K$, $l_K + 2$ and $N' = N$, $N \pm 1$, which are of importance for spectroscopic calculations, explicit expressions for the sums S and S_1 can be obtained by using the results presented in [3] (see the table, where the subscript K on l_K is suppressed for the sake of simplicity).

Upon making the substitutions $p \to p_i - 1$, $l \to l_{K_i} - 1$, $N \to N_i$, $l' \to l'_{K_i} - 1$, and $N \to N'_i$, it turns out that the formulas presented in the table are valid for the sums $\sum_{\alpha_i} D_{p_i,\alpha_i}$ and $\sum_{\alpha_i} \alpha_i D_{p_i,\alpha_i}$ of the coefficients $D_{p_i,\alpha_i}^{N_il_{K_i}N'_il'_{K_i}}$ as well.

To exemplify the application of the formulas given in the table, we consider the orthogonal scheme described in [2]. For $E > K$ excited $U(3(A-1))$ states, the matrix elements of operators O involving r^2 (mean-square radii, monopole and electric quadrupole moments, transition probabilities, etc.) can be directly expressed, within this scheme, in terms of the matrix elements for $E = K$:

$$\langle EK\Gamma_0|O|E'K'\Gamma'_0\rangle = A(Nl_K, N'l'_K)\langle KK\Gamma_0|O|K'K'\Gamma'_0\rangle. \tag{16}$$

Here, Γ_0 stands for the set of the remaining quantum numbers that label the function of the orthogonal scheme. The matrix elements in (16) are nonzero only

Table

$Nl\,N'l'$	$S(Nl\,N'l')$	$S_1(p\,Nl\,N'l')$
$Nl\,N-1\,l$	0	$-\dfrac{(2p+3)\sqrt{2N(2l+2N+1)}}{2(2l+3)}$
$Nl\,Nl$	1	$\dfrac{2(2p+3)N}{2l+3}$
$Nl\,N+1\,l$	0	$-\dfrac{(2p+3)\sqrt{2(N+1)(2l+2N+3)}}{2(2l+3)}$
$Nl\,N-2\,l+2$	0	$\dfrac{(2p+3)\sqrt{N(N-1)}}{2l+5}$
$Nl\,N-1\,l+2$	$-\sqrt{\dfrac{2N}{2l+2N+3}}$	$-\dfrac{(2p+3)(2l+4N+1)}{2(2l+5)}\sqrt{\dfrac{2N}{2l+2N+3}}$
$Nl\,N\,l+2$	$\dfrac{2l+3}{\sqrt{(2l+2N+3)(2l+2N+5)}}$	$\dfrac{2(2p+3)N(2l+N+4)}{(2l+5)\sqrt{(2l+2N+3)(2l+2N+5)}}$
$Nl\,N+1\,l+2$	$\dfrac{(2l+3)\sqrt{2(N+1)}}{\sqrt{(2l+2N+3)(2l+2N+5)(2l+2N+7)}}$	$-\dfrac{(2p+3)(2l+3)\sqrt{2(N+1)}}{2\sqrt{(2l+2N+3)(2l+2N+5)(2l+2N+7)}}$

for $E'=E,\ E\pm 2$, in which case the factors A are given by (see the Appendix)

$$A(Nl_K,N-1l_K)=-\frac{\sqrt{N(l_K+N+1/2)}}{l_K+3/2};\quad(17)$$

$$A(Nl_K,N+1l_K+2)=0;$$

$$A(Nl_K,Nl_K)=\frac{l_K+2N+3/2}{l_K+3/2};$$

$$A(Nl_K,Nl_K+2)$$

$$=\sqrt{\frac{(l_K+N+5/2)(l_K+N+3/2)}{(l_K+5/2)(l_K+3/2)}};$$

$$A(Nl_K,N+1l_K)=-\frac{\sqrt{(N+1)(l_K+N+3/2)}}{l_K+3/2};$$

$$A(Nl_K,N-1l_K+2)$$

$$=-\sqrt{\frac{4N(l_K+N+3/2)}{(l_K+5/2)(l_K+3/2)}};$$

$$A(Nl_K,N'l'_K)=0,\quad |N-N'|>1;$$

$$A(Nl_K,N-2l_K+2)=\frac{\sqrt{N(N-1)}}{l_K+5/2};$$

$$A(Nl_K,N'l_K+2)=0,\quad N-N'>2.$$

REFERENCES

1. M. Moshinsky, *The Harmonic Oscillator in Modern Physics: from Atoms to Quarks* (Gordon and Breach, New York, 1969; Mir, Moscow, 1972).
2. V. V. Vanagas, *Algebraic Methods in the Theory of the Nucleus* (Mintis, Vilnius, 1971).
3. K. J. Jankauskas and A. K. Petrauskas, *Density Matrix for Excited $U(3(n-1))$ States of Nuclei and Its Application* (Klaipeda Univ., Klaipeda, 1997).
4. E. D. Surkov, Yad. Fiz. **5**, 908 (1967) [Sov. J. Nucl. Phys. **5**, 644 (1967)].
5. Yu. T. Grin', Yad. Fiz. **12**, 927 (1970) [Sov. J. Nucl. Phys. **12**, 506 (1970)].
6. G. F. Filippov, B. I. Ovcharenko, and Yu. F. Smirnov, *Microscopic Theory of Collective Excitations of Nuclei* (Naukova Dumka, Kiev, 1981).
7. A. K. Petrauskas, K. J. Jankauskas, and V. M. Bondarenko, Yad. Fiz. **55**, 3082 (1992) [Sov. J. Nucl. Phys. **55**, 1723 (1992)].
8. A. K. Petrauskas, K. J. Jankauskas, and G. P. Kamuntavicius, Litov. Fiz. Sb. **12**, 229 (1972).

APPENDIX

Coefficients $\tilde{D}^{N_i l_K N'_i l'_{K_i}}$ at $l'_{K_i} = l_{K_i}, l_{K_i}+2, l_{K_i}+4, l_{K_i}+6$ and $N_i + N'_i \le 3$ (to simplify the presentation, the indices i and K_i are suppressed; S is the sum of the relevant coefficients over α)

α	$\tilde{D}^{1l\ 0l}_{p,\alpha}$	α	$\tilde{D}^{1l\ 0l+2}_{p,\alpha}$	α	$\tilde{D}^{1l\ 0l+4}_{p,\alpha}$
0	$\dfrac{2p+1}{\sqrt{2(2l+1)}}$	0	$\dfrac{2p-1}{\sqrt{2(2l+1)}}$	0	$\dfrac{2p-3}{\sqrt{2(2l+1)}}$
1	$-\dfrac{2p+1}{\sqrt{2(2l+1)}}$	1	$-\dfrac{2p+1}{\sqrt{2(2l+1)}}$	1	$-\dfrac{2p+1}{\sqrt{2(2l+1)}}$
S	0	S	$-\dfrac{\sqrt{2}}{\sqrt{(2l+1)}}$	S	$-\dfrac{2\sqrt{2}}{\sqrt{(2l+1)}}$
α	$\tilde{D}^{1l\ 0l+6}_{p,\alpha}$	α	$\tilde{D}^{0l\ 1l+2}_{p,\alpha}$	α	$\tilde{D}^{0l\ 1l+4}_{p,\alpha}$
0	$\dfrac{2p-5}{\sqrt{2(2l+1)}}$	0	$\dfrac{2p+3}{\sqrt{2(2l+5)}}$	0	$\dfrac{2p+5}{2\sqrt{2(2l+9)}}$
1	$-\dfrac{2p+1}{\sqrt{2(2l+1)}}$	1	$-\dfrac{2p+1}{\sqrt{2(2l+5)}}$	1	$-\dfrac{2p+1}{2\sqrt{2(2l+9)}}$
S	$-\dfrac{3\sqrt{2}}{\sqrt{(2l+1)}}$	S	$\dfrac{\sqrt{2}}{\sqrt{(2l+5)}}$	S	$\dfrac{2\sqrt{2}}{\sqrt{(2l+9)}}$
α	$\tilde{D}^{2l\ 0l}_{p,\alpha}$	α	$\tilde{D}^{2l\ 0l+2}_{p,\alpha}$	α	$\tilde{D}^{2l\ 0l+4}_{p,\alpha}$
0	$\dfrac{(2p+1)(2p+3)}{2\sqrt{2(2l+1)(2l+3)}}$	0	$\dfrac{(2p+1)(2p-1)}{2\sqrt{2(2l+3)(2l+1)}}$	0	$\dfrac{(2p-1)(2p-3)}{2\sqrt{2(2l+1)(2l+3)}}$
1	$-\dfrac{(2p+1)(2p+3)}{\sqrt{2(2l+1)(2l+3)}}$	1	$-\dfrac{(2p+1)^2}{\sqrt{2(2l+3)(2l+1)}}$	1	$-\dfrac{(2p-1)(2p+1)}{\sqrt{2(2l+1)(2l+3)}}$
2	$\dfrac{(2p+1)(2p+3)}{2\sqrt{2(2l+1)(2l+3)}}$	2	$\dfrac{(2p+1)(2p+3)}{2\sqrt{2(2l+3)(2l+1)}}$	2	$\dfrac{(2p+1)(2p+3)}{2\sqrt{2(2l+1)(2l+3)}}$
S	0	S	0	S	$\dfrac{2\sqrt{2}}{\sqrt{(2l+1)(2l+3)}}$
α	$\tilde{D}^{1l\ 1l}_{p,\alpha}$	α	$\tilde{D}^{1l\ 1l+2}_{p,\alpha}$	α	$\tilde{D}^{1l\ 1l+4}_{p,\alpha}$
0	$\dfrac{4l+4p^2+1}{2(2l+1)}$	0	$\dfrac{4l+4p^2+1}{2\sqrt{(2l+5)(2l+1)}}$	0	$\dfrac{4l+4p^2-7}{2\sqrt{(2l+1)(2l+9)}}$
1	$-\dfrac{(2p+1)^2}{(2l+1)}$	1	$-\dfrac{(2p+1)^2}{\sqrt{(2l+5)(2l+1)}}$	1	$-\dfrac{(2p+1)^2}{\sqrt{(2l+1)(2l+9)}}$
2	$\dfrac{(2p+3)(2p+1)}{2(2l+1)}$	2	$\dfrac{(2p+1)(2p+3)}{2\sqrt{(2l+5)(2l+1)}}$	2	$\dfrac{(2p+1)(2p+3)}{2\sqrt{(2l+1)(2l+9)}}$
S	1	S	$\dfrac{2l+1}{\sqrt{(2l+5)(2l+1)}}$	S	$\dfrac{2l-3}{\sqrt{(2l+1)(2l+9)}}$

APPENDIX (Contd.)

α	$\tilde{D}^{2l\ 0l+6}_{p,\alpha}$	α	$\tilde{D}^{0l\ 2l+2}_{p,\alpha}$	α	$\tilde{D}^{0l\ 2l+4}_{p,\alpha}$
0	$\frac{(2p-3)(2p-5)}{2\sqrt{2(2l+1)(2l+3)}}$	0	$\frac{(2p+3)(2p+5)}{2\sqrt{2(2l+5)(2l+7)}}$	0	$\frac{(2p+5)(2p+7)}{2\sqrt{2(2l+9)(2l+11)}}$
1	$-\frac{(2p+1)(2p-3)}{\sqrt{2(2l+1)(2l+3)}}$	1	$-\frac{(2p+1)(2p+5)}{\sqrt{2(2l+5)(2l+7)}}$	1	$-\frac{(2p+1)(2p+7)}{\sqrt{2(2l+9)(2l+11)}}$
2	$\frac{(2p+1)(2p+3)}{2\sqrt{2(2l+1)(2l+3)}}$	2	$\frac{(2p+1)(2p+3)}{2\sqrt{2(2l+5)(2l+7)}}$	2	$\frac{(2p+1)(2p+3)}{2\sqrt{2(2l+9)(2l+11)}}$
S	$-\frac{6\sqrt{2}}{\sqrt{(2l+1)(2l+3)}}$	S	$\frac{2\sqrt{2}}{\sqrt{(2l+5)(2l+7)}}$	S	$\frac{6\sqrt{2}}{\sqrt{(2l+9)(2l+11)}}$

α	$\tilde{D}^{0l\ 1l+6}_{p,\alpha}$	α	$\tilde{D}^{1l\ 1l+6}_{p,\alpha}$	α	$\tilde{D}^{0l\ 2l+6}_{p,\alpha}$
0	$\frac{2p+7}{\sqrt{2(2l+13)}}$	0	$\frac{4l+4p^2-23}{2\sqrt{(2l+1)(2l+13)}}$	0	$\frac{(2p+7)(2p+9)}{2\sqrt{2(2l+13)(2l+15)}}$
1	$-\frac{2p+1}{\sqrt{2(2l+13)}}$	1	$-\frac{(2p+1)^2}{\sqrt{(2l+1)(2l+13)}}$	1	$-\frac{(2p+1)(2p+9)}{2\sqrt{2(2l+13)(2l+15)}}$
–	–	2	$\frac{(2p+1)(2p+3)}{2\sqrt{(2l+1)(2l+13)}}$	2	$\frac{(2p+1)(2p+3)}{2\sqrt{2(2l+13)(2l+15)}}$
S	$\frac{3\sqrt{2}}{\sqrt{(2l+13)}}$	S	$\frac{2l-11}{\sqrt{(2l+1)(2l+13)}}$	S	$\frac{12\sqrt{2}}{\sqrt{(2l+13)(2l+15)}}$

α	$\tilde{D}^{2l\ 1l+2}_{p,\alpha}$	α	$\tilde{D}^{3l\ 0l+6}_{p,\alpha}$
0	$\frac{(2p-1)(4p^2+8l+11)}{4\sqrt{(2l+5)(2l+3)(2l+1)}}$	0	$\frac{(2p-5)(2p-3)(2p-1)}{4\sqrt{3(2l+1)(2l+3)(2l+5)}}$
1	$-\frac{(2p+1)(12p^2+8p+8l+13)}{4\sqrt{(2l+5)(2l+3)(2l+1)}}$	1	$-\frac{3(2p-3)(2p-1)(2p+1)}{4\sqrt{3(2l+1)(2l+3)(2l+5)}}$
2	$\frac{(2p+3)(2p+1)(6p+5)}{4\sqrt{(2l+5)(2l+3)(2l+1)}}$	2	$\frac{3(2p-1)(2p+1)(2p+3)}{4\sqrt{3(2l+1)(2l+3)(2l+5)}}$
3	$-\frac{(2p+5)(2p+3)(2p+1)}{4\sqrt{(2l+5)(2l+3)(2l+1)}}$	3	$-\frac{(2p+1)(2p+3)(2p+5)}{4\sqrt{3(2l+1)(2l+3)(2l+5)}}$
S	$-\frac{2(2l+3)}{\sqrt{(2l+1)(2l+3)(2l+5)}}$	S	$-\frac{4\sqrt{3}}{\sqrt{(2l+1)(2l+3)(2l+5)}}$

Physics of Atomic Nuclei, Vol. 65, No. 5, 2002, pp. 959–961. Translated from Yadernaya Fizika, Vol. 65, No. 5, 2002, pp. 990–992.

LETTERS TO THE EDITOR

Comparative Analysis of Channels Involving the Formation of Three α Particles and ^{12}C Nuclei in ^{16}Op Collisions at 3.25 GeV/c per Nucleon

M. A. Belov[1], K. G. Gulamov[2], V. V. Lugovoi[2], S. L. Lutpullaev[2], V. D. Lipin[2], K. Olimov[2], Kh. K. Olimov[2], A. A. Yuldashev[2], and B. S. Yuldashev[1]

Received January 19, 2001

It is well known that light nuclei whose mass numbers A (≤ 20) are integral multiples of 4 have an α-cluster structure and that many of their properties are adequately described by models that take this fact into account [1]. By studying the fragmentation of relativistic oxygen nuclei interacting with protons [2–7], our group revealed some features of this phenomenon. In particular, it was shown that, among multiply charged fragments, doubly charged ones, which contain more than 80% ^{4}He nuclei (α particles), have the highest emission probability [3]. The breakup of relativistic oxygen nuclei into multiply charged fragments whose total charge is equal to the charge of the primary nucleus [5] is realized only through the even-charge topologies of (224), (2222), and (26), where the numbers in parentheses are the charges of nuclear fragments. At the same time, the (44), (35), and (233) channels were not observed experimentally [if the two colliding nuclei are those of ^{8}Be, their decay leads to the (2222) final state—the combination of ^{9}Be and ^{7}Be was not found], which may be due to a higher threshold energy required for their realization.

The above experimental results show that the structure of the primary nucleus manifests itself significantly in peripheral collisions. In view of this, we performed a comparative analysis of the properties of the reactions

$$^{16}\mathrm{O} + p \to 3\alpha + X, \quad (1)$$

$$^{16}\mathrm{O} + p \to {}^{12}\mathrm{C} + X, \quad (2)$$

where X is an arbitrary singly charged fragment (p_f, d, t) or a doubly charged fragment of mass number $A \leq 3$ (^{3}He); in addition, there can appear charged pions and a recoil proton (p_r) if such a proton was not involved in the charge-exchange process resulting in the formation of a neutron and a π^+ meson.

The experimental data are compared with the predictions of the cascade–fragmentation–evaporation model (CFEM) [8]. The CFEM employs the intranuclear-cascade model [9, 10] combined with a modification of the Fermi statistical model of multiparticle production [11]. Within this model, the fragmenting nucleus is assumed to consist of a perfect Fermi gas. Once the intranuclear cascade has passed, a statistically equilibrium state is established, in which the probability of each channel is proportional to the relevant phase space. In the case of the light nucleus ^{16}O, Fermi breakup (that is, the explosive disintegration of nuclei) is considered as a dominant mechanism of fragment formation in the model.

The experimental data that we consider here were obtained from stereoscopic photographs of the 1-m hydrogen bubble chamber installed at the Laboratory of High Energies at the Joint Institute of Nuclear

Table 1. Mean multiplicities of charged secondaries and fragments in reactions (1) and (2)

Particle type	Mean multiplicity	
	$^{16}\mathrm{O} + p \to 3\alpha + X$	$^{16}\mathrm{O} + p \to {}^{12}\mathrm{C} + X$
π^-	0.28 ± 0.03	0.31 ± 0.03
π^+	0.55 ± 0.04	0.50 ± 0.04
p_r	0.55 ± 0.03	0.57 ± 0.03
p_f	1.41 ± 0.06	1.46 ± 0.06
d	0.23 ± 0.02	0.23 ± 0.02
t	0.04 ± 0.01	0.05 ± 0.01
^{3}He	0.03 ± 0.01	0.03 ± 0.01

[1]Institute of Nuclear Physics, Uzbek Academy of Sciences, pos. Ulughbek, Tashkent, 702132 Republic of Uzbekistan.
[2]Institute for Physics and Technology, Fizika–Solntse Research and Production Association, Uzbek Academy of Sciences, ul. Timiryazeva 26, Tashkent, 700084 Republic of Uzbekistan.

1063-7788/02/6505-0959$22.00

Table 2. Mean values of the total and transverse momenta (GeV/c) of charged secondaries and fragments in reactions (1) and (2)

Particle type	$^{16}\mathrm{O} + p \to 3\alpha + X$		$^{16}\mathrm{O} + p \to {}^{12}\mathrm{C} + X$	
	$\langle P \rangle$	$\langle P_\perp \rangle$	$\langle P \rangle$	$\langle P_\perp \rangle$
π^-	0.41 ± 0.03	0.19 ± 0.01	0.39 ± 0.03	0.21 ± 0.01
π^+	0.46 ± 0.02	0.24 ± 0.01	0.48 ± 0.02	0.23 ± 0.01
p_r	2.34 ± 0.05	0.39 ± 0.02	2.28 ± 0.05	0.39 ± 0.02
p_f	0.32 ± 0.01	0.24 ± 0.01	0.32 ± 0.01	0.25 ± 0.01
d	0.34 ± 0.02	0.26 ± 0.02	0.32 ± 0.02	0.25 ± 0.02

Research (JINR, Dubna) [12] and irradiated at the JINR synchrophasotron by ^{16}O nuclei accelerated to a momentum of 3.25 GeV/c per nucleon and are based on an analysis of 11 098 measured $^{16}O p$ events. It should be noted that the experimental conditions made it possible to detect all charged secondaries, to identify unambiguously their charges, to measure the momenta of fragments to a high precision, and to determine their masses.

The fragments were separated in mass according to the measured momenta and charges. We considered fragments whose tracks were longer than 35 cm, which was necessary for more reliably separating them in mass and for analyzing their kinematical features. For reactions (1) and (2), there remained, respectively, 399 and 405 events satisfying these conditions and selection criteria for charged secondaries and fragments [3, 4]. Taking into account the loss of events in the interaction of α particles and ^{12}C over the length of $L = 35$ cm in the sensitive volume of the chamber, we finally find that the cross sections for these reactions have the close value of $\sigma_{\mathrm{in}}(3\alpha) = 25.7 \pm 1.5$ mb and $\sigma_{\mathrm{in}}(^{12}\mathrm{C}) = 22.8 \pm 1.4$ mb. The corresponding CFEM values are $\sigma_{\mathrm{in}}(3\alpha) = 6.2 \pm 0.3$ mb and $\sigma_{\mathrm{in}}(^{12}\mathrm{C}) = 11.5 \pm 0.4$ mb, which differ from each other nearly by a factor of 2 and which differ significantly from their experimental counterparts. In all probability, this discrepancy between the model results and the experimental data is due to the disregard of the α-cluster structure of the primary nucleus ^{16}O in the CFEM.

The threshold energies for reactions (1) and (2) differ by 7.3 MeV, the species of X particles and their kinematical features being identical. This energy is insufficient for the breakup of a residual nucleus of mass number $A_f = 12$ to occur through channels other than that of reaction (1), which also includes the cascade decay of excited nuclear states: $^{12}\mathrm{C}^* \to {}^{8}\mathrm{Be}^* + \alpha$, $^{8}\mathrm{Be}^* \to 2\alpha$. In view of this, many features of reactions (1) and (2) are likely to be identical. Indeed, the data in Table 1 demonstrate that the experimental mean multiplicities of charged secondaries and fragments from the two reactions agree within the statistical errors. As to the results of the CFEM calculation [8], the features of all particles and fragments, with the exception of π^+ mesons, are different in the different reactions and deviate from the experimental data.

The mean total ($\langle P \rangle$) and transverse ($\langle P_\perp \rangle$) momenta of charged secondaries and fragments formed in reactions (1) and (2) are displayed in Table 2. The mean momenta of secondary particles and fragments are given in the rest frame of the oxygen nucleus. It can be seen that the mean momentum characteristics of secondary particles and fragments in the two reactions agree within the statistical errors. In the CFEM [8], the momentum characteristics of secondary particles and fragments (except for those of deuterons) are very close to their experimental values.

The agreement between the above experimental features of reactions (1) and (2) suggests that these processes proceed under close physical conditions, the α-cluster structure of the ^{16}O nucleus playing a significant role here. All this indicates that the α-cluster structure of light nuclei must be taken into account in constructing a realistic model of their fragmentation at high energies.

REFERENCES

1. B. R. Fulton, in *Proceedings of the Conference Requiem for an Accelerator, Oxford, 1993,* p. 83.
2. A. S. Botvina, W. Wislicki, Sh. Gaitinov, *et al.*, Z. Phys. A **345**, 413 (1993).
3. V. V. Glagolev, K. G. Gulamov, M. Yu. Kratenko, *et al.*, Pis'ma Zh. Éksp. Teor. Fiz. **58**, 497 (1993) [JETP Lett. **58**, 497 (1993)]; **59**, 316 (1994) [**59**, 336 (1994)].
4. V. V. Glagolev, K. G. Gulamov, M. Yu. Kratenko, *et al.*, Yad. Fiz. **58**, 2005 (1995) [Phys. At. Nucl. **58**, 1896 (1995)].

5. K. N. Abdullaeva, M. Azimova, K. G. Gulamov, *et al.*, Dokl. Akad. Nauk Resp. Uzb. **5**, 21 (1996).
6. V. V. Glagolev, K. G. Gulamov, V. D. Lipin, *et al.*, Yad. Fiz. **61**, 2132 (1998) [Phys. At. Nucl. **61**, 2021 (1998)].
7. V. V. Glagolev, K. G. Gulamov, V. D. Lipin, *et al.*, Yad. Fiz. **62**, 1472 (1999) [Phys. At. Nucl. **62**, 1388 (1999)].
8. A. S. Botvina, A. S. Iljinov, and I. N. Mishustin, Nucl. Phys. A **507**, 649 (1990); Preprint No. 626, OIYaI (Joint Inst. for Nuclear Research, Dubna, 1989).
9. V. S. Barashenkov and V. D. Toneev, *Interactions of High-Energy Particles and Nuclei with Nuclei* (Atomizdat, Moscow, 1972), p. 648.
10. V. S. Barashenkov, A. S. Il'inov, N. M. Sobolevskiĭ, *et al.*, Usp. Fiz. Nauk **109**, 91 (1973) [Sov. Phys. Usp. **16**, 31 (1973)].
11. E. Fermi, Prog. Theor. Phys. **5**, 570 (1950).
12. A. V. Belonogov, A. A. Belushkina, *et al.*, Nucl. Instrum. Methods **20**, 114 (1963).

Translated by V. Bukhanov